# Honda R&D

# Technical Review



April 2004



## Comment on the Cover

When I was in elementary school, I used to enthusiastically root for the F1 racing machines that had the Honda mark on them. I recall feeling oddly proud that a vehicle with the same logo as the car we had at home was so active on the world stage.
A decade or more later, the same Honda is challenging an entirely new world as its airplane flies the skies. As I see this happening, I have that same proud feeling that I did as a child.
In drawing this cover, I wanted to cherish that long-ago pride that the Honda jet brought back to me, as well as the feelings like it in the future.



Asakahigashi
R&D Center
Masato Fujiwara

# Development of New Intelligent Tourer 2004 Model INSPIRE

Shigehiro YASUKI* Yasuaki ASAKI* Hiroshi TASHIRO*
Hideki MATSUOKA* Taku KONO**

## ABSTRACT

The new model, INSPIRE was developed based on the concept of a “New Intelligent Tourer.” The aim was to produce a new luxury sedan offering users a high degree of satisfaction through the achievement of superior luxury sedan performance while maximizing the advances and sportiness for which Honda is known.

The vehicle’s refined design gives it a tremendous sense of presence, individuality and quality, and a superbly quiet ride. Numerous new technologies are employed to fully realize the “New Intelligent Tourer” development concept.

The following give the INSPIRE a level of advancement and sportiness that is Honda-unique: (1) a balance between incredible driving performance and high fuel economy offered by the V6 3.0L i-VTEC variable cylinder system engine; (2) a body and suspension designed for a superbly comfortable ride belying the power of the vehicle; and (3) the employment of HiDS to offer stress-free high-speed cruising and an advanced safety support system that includes collision mitigation braking (a world first) and E-pretensioners.

The new luxury sedan is aptly named “INSPIRE,” offering as it does a level of driving appeal that competitors’ vehicles cannot match.

## 1. Introduction

Since the first-generation INSPIRE went on the market in 1989, it was well received as a Honda specialty - the four-door model. The vehicle evolved through similarly well-received second- and third-generation models. However, in recent years the market for sedans in Japan shrank and the severe decline in sales of high-class small sedans like the INSPIRE continues.

In the development of the fourth-generation INSPIRE, the target was to achieve the level of advancement and sportiness worthy of the Honda name, with the sense of quality offered by a luxury four-door sedan. These goals were to be realized in a user-centered package. Target users covered a broad range: intellectually curious individuals from ages 30 to 60 who retain a feeling of being “young at heart.” The concept for this vehicle is established based on repeated group interviews and dealer surveys primarily focused on exactly what type of sedan the target users desire.

* Tochigi R&D Center
** Wako R&D Center

## 2. Concept and Development Targets

Characteristics of the ways in which target users employ their vehicles were clarified through numerous user surveys. It was discovered that they frequently covered medium to long distances on the highways not only in their daily lives but also in their business activities. Knowing this enabled the fixing of a concept for the new INSPIRE that offers an overwhelming appeal to consumers - the "New Intelligent Tourer," which employs the most advanced technology and which displays performance at the top of its class in city driving and ahead of its class on the highway.

The following three targets were set to realize the design concept:

(1) Achievement of top-class basic performance
- Design offering a sense of presence and classiness
- Clean, precise lines for a high-quality feeling
- Top-class smoothness of ride and quietness for a high-class sedan
- Highest standard of collision safety performance in its class

(2) Achievement of a level of advancement worthy of the Honda name

The target for the engine was a fuel economy of 11.6 km/l, equivalent to that of a 2.5L direct-injection engine, and the achieving of a Japanese three-star Ultra-Low Emission Vehicle certification, to comply with "Green Tax" regulations. A cylinder on demand system would be employed to achieve this. An additional target was the achievement of NV performance equivalent to that displayed by a standard V6 vehicle, through the use of active NV control technology.

To help provide safe and comfortable cruising, a collision mitigation system (CMS) and E-pretensioners were developed and employed. These are part of an advanced safety support system to help prevent or reduce the effects of rear-end collisions.

(3) The target for engine power was set at 250 ps to achieve the sportiness worthy of a Honda vehicle.

High standards, beyond those normally associated with a high-class sedan, were set to achieve a smoothness of ride belying the power of the vehicle and a stability of steering and high-speed performance.

## 3. Design

### 3.1. Package

The Accord model marketed in North America was used as the base vehicle in designing the packaging of the new INSPIRE. 3D moving outlines of test subjects entering and exiting the vehicle were analyzed. This resulted in a number of changes (including increases to the angle of the front pillar and the size of the rear door opening around the rear pillar) to give the vehicle a greater feeling of spaciousness and to increase the ease with which users can get in and out. The rear window has been pulled towards the back and the roof lengthened to style a long, spacious cabin. This also is a benefit because it reduces the amount of direct sunlight shining on passengers in the rear seat. By not merely changing the dimensions but also increasing the quality of the cabin space in this way, the designers succeeded in creating a welcoming space that is both classier and easier to use, and that is compatible with a dynamic and powerful exterior design.

### 3.2. Styling

The exterior design of the new INSPIRE is also based on the North American Accord, and centered around a "Classy and Aggressive" design concept (Figs. 1 and 2). The front of the vehicle, with an advanced milli wave radar unit built in, sweeps back from the Honda logo to the hood, emphasizing the sense of V6 power. From the side the spacious long cabin and sporty high deck styling are visible. At the rear, crystalline high-mounted lights and integrated dual exhaust finishers contribute to the aerodynamics of the vehicle, and are suggestive of speed with style. Every part of the vehicle brings classiness and aggressiveness together in a superb balance. As a result, the vehicle not only possesses the sense of quality and refinement expected of a sedan in its class, but its individual styling gives it a presence that makes it stand out among other sedans.




Fig. 1 Exterior styling image



Fig. 2 Exterior styling

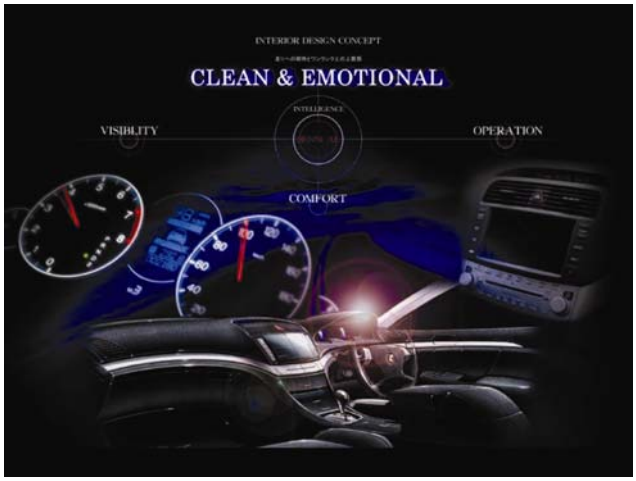



Fig. 3 Interior image

To design the interior of the new INSPIRE, the interior design of the US Accord was revamped based on a concept of "Clean and Emotional" styling (Fig. 3). The instrument panel and the door linings form a smooth curve in a wrap-around interior accented with metal ornamentation. This gives the sense of being surrounded by personal space and the luxury distinctive to sedans. The features designed to give the cabin as a whole a clean and emotional atmosphere include the minimization of the lines of the door linings, and the use of luminous meters and blue illumination.

## 4. Engine

### 4.1. Engine Development Goals

The concept for the power plant of the new INSPIRE is the achieving of a level of fuel economy and environmental performance that is beyond the vehicle's class. To achieve this, the engine employed in the US Accord was used as a base. A cylinder on demand system (cylinder stop mechanism)[(1)] was added, and the following basic performance targets, difficult to achieve in a direct-injection engine, were established:

(1) Equivalent fuel economy performance to competitors' direct-injection engines (2000 regulation values +10%)
(2) Low emissions (Achievement of ULEV certification)
(3) Top-class running performance




Fig. 4 View of V6 i-VTEC Engine

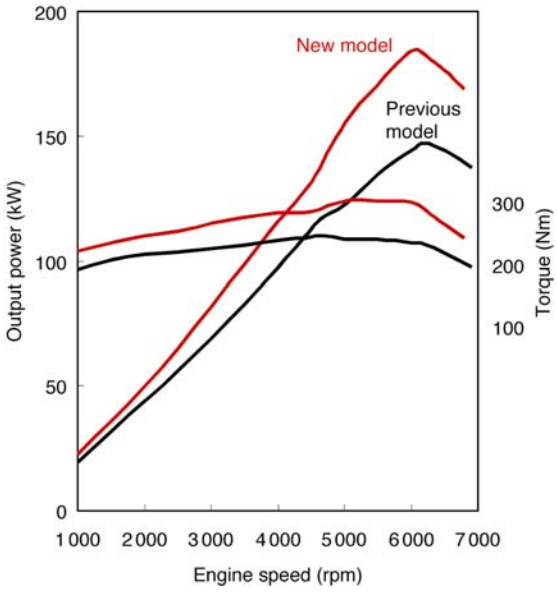



Fig. 5 Output performance

Table 1 Main engine specifications

| | Previous model | New model |
|---|---|---|
| Engine type | 60°V-6 SOHC VTEC | 60°V-6 SOHC I-VTEC |
| Displacement | 2495cc | 2997cc |
| Compression ratio | 10.5 | 10.5 |
| Fuel | Premium | Regular |
| Max.power (kw/rpm) | 147/6200 | 184/6000 |
| Max.torque (N·m/rpm) | 240/5000 | 296/5000 |
| Transmission | 5AT | 5AT |
| Fuel economy (10-15 Mode) | 10.2 | 11.6 |
| Emissions level | J-LEV ★★ | J-ULEV ★★★ |

### 4.2. Overview of Engine and Main Specifications

Figure 4 shows a view of the V6 i-VTEC engine employed in the new INSPIRE. Figure 5 shows the power characteristic of the engine, and Table 1 provides the main specifications.

In this engine, excellent dynamic performance has been balanced with fuel economy through the employment of a mechanism to stop the operation of the intake or exhaust valves of one bank (rear bank) of three cylinders as required. This enables the actual volume of exhaust to be varied.

### 4.3. Increasing Fuel Economy

In attempting to increase fuel economy, individual targets as shown in Fig. 6, were set for the contributions to be realized by engine, AT and body technologies. As a result, while the displacement of the engine has been increased to 3.0L, it displays a 14% improvement in fuel economy over the 2.5L engine employed in the previous INSPIRE 25V model, recording a fuel consumption of 11.6 km/l in Japanese 10-15 mode. The fuel economy of the improved engine equals that of a 2.5L direct-injection engine.

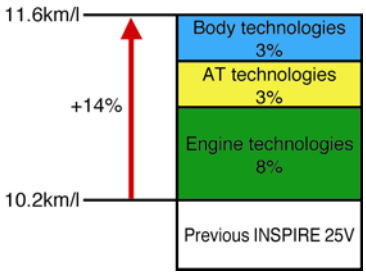



Fig. 6 Ratio of contribution to improvement of 10-15 mode fuel economy

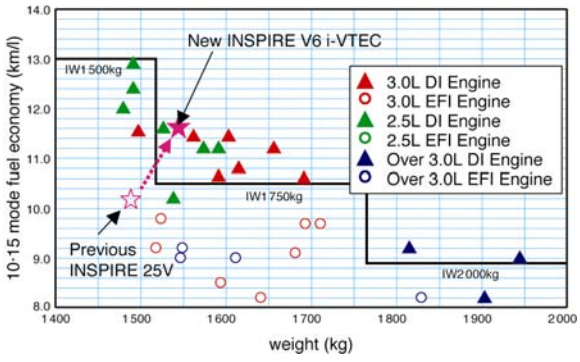



Fig. 7 10-15 mode fuel economy

### 4.4. Environmental Performance

Figure 8 shows a diagram of the system employed to reduce emissions in the new engine. The system enables independent reduction of exhaust gases in both banks of the V6 i-VTEC engine.

The employment of highly-accurate A/F ratio control in combination with the emission control system has enabled the achievement of a high level of environmental performance in the engine. As Fig. 9 shows, the system has recorded a low fuel consumption figure of 11.6 km/l in Japanese 10-15 mode. It complies with the Japanese three-star Ultra-Low Emissions standards. And, it has emissions figures that are only 25% of those stipulated in 2005 domestic standards, giving it a Japanese four-star rating.

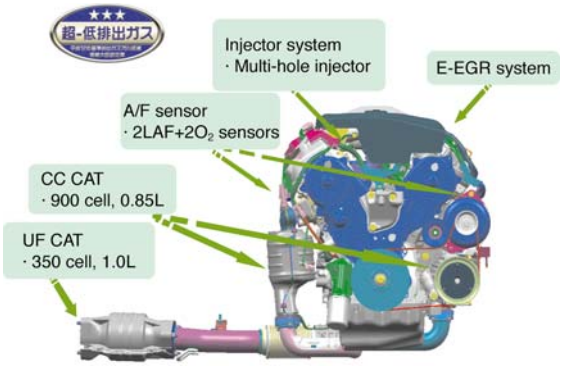



Fig. 8 Emission control system

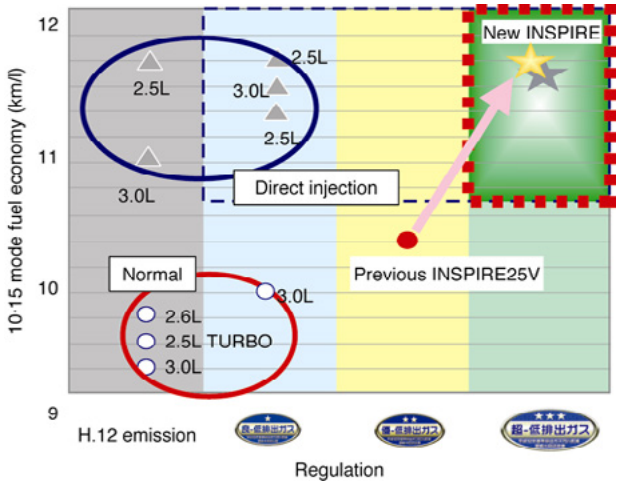



Fig. 9 Achievement of clean emissions and compliance with 2010 fuel economy standards

## 5. Transmission

To further increase the fuel economy of the variable cylinder engine, cooperative control with a cylinder stop mechanism has been employed in the AT. At the same time, a long torsion damper has been used in the lockup clutch to increase commercial appeal through improving NV performance during three-cylinder operation (Fig. 10).

As Fig. 11 shows, the damping (with a one-dimensional spring with a low spring constant up to the maximum torque produced during three-cylinder operation) has enabled fluctuations in the rotation of the main shaft to be maintained at the same level as the level occurring during six-cylinder operation. This is equivalent to a reduction of 5 dB in drive system vibration and 3 dB throughout the cabin.

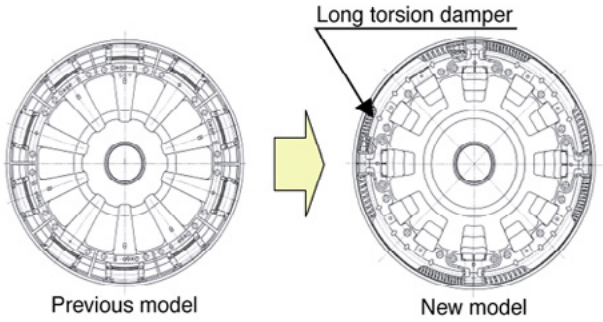



Fig. 10 Optimization of torsion damper characteristic for lock-up clutch

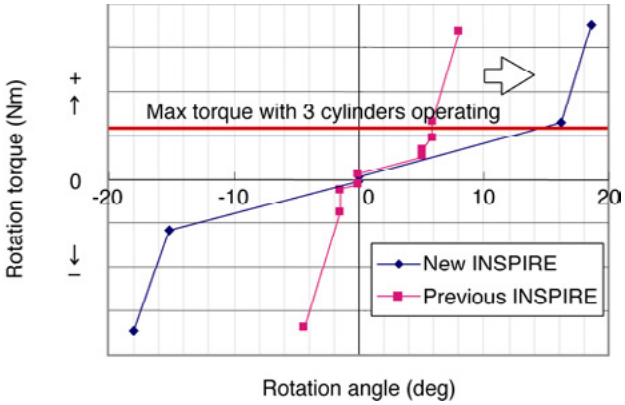



Fig. 11 Damper characteristics

## 6. Noise and Vibration

A cylinder on demand system has been employed in the engine of the new INSPIRE to achieve a balance between running performance and fuel economy. Because the number of cylinders in which combustion is occurring is reduced when one bank of cylinders is stopped, the frequency of vibration is reduced and the combustion pressure in each active cylinder increases. This significantly increases the amplitude of vibrations, the level of intake and exhaust noise, and torque fluctuations. This leads to a serious concern that NV performance and, hence, market appeal would decline. Two new technologies have been employed to prevent this: Active control engine mount (ACM) technology[2] and active noise control technology (ANC)[3]. Conventionally, these are both high-cost systems. However, costs were reduced in the case of the new INSPIRE through the development of a new control logic and by employing existing vehicle systems, enabling both technologies to be offered as standard features. Once again the US Accord was used as the base vehicle in design relating to NV performance. By using additional soundproofing materials and by changing the materials employed, road noise performance is improved in line with the expectations consumers have of a domestic high-class sedan.

### 6.1. Active Control Engine Mount Technology

ACMs have been employed to counter the increased engine vibrations generated when one bank of cylinders is

stopped (Fig. 12). Two ACMs are used, at the front and the rear of the engine. The ACM ECU is located in the cabin, and is connected to the engine ECU.

This system uses the crank pulse signal (an existing engine control signal) to detect variations in crank rotation produced by combustion. The system employs the cylinder pulse as a standard for phase in the application of control. This enables the system to estimate the size and phase of engine vibrations, and to use those estimates in driving the excitation plate located in the hydraulic mount section of the ACM by means of an actuator. This control system eliminates the need for extraneous equipment such as special load sensors - enabling significant cost reductions in comparison to conventional systems employed by competitors. The actuator was specially designed for use in this system. It is a linear solenoid-type that generates a low level of heat. In terms of packaging, the positioning of an air release diaphragm in the top section improves heat resistance, and a reduction in total height ensures commonality with standard mounts. The use of this system reduces the transmission of engine vibrations with one bank of cylinders stopped by approximately 10 dB, making it possible to significantly reduce booming noise and body vibrations.

### 6.2. Active Noise Control Technology

Figure 13 shows the configuration of the ANC system. The control unit for this system is located on the top of the audio unit, and features a built-in microphone for compensation in the front seats. The microphone for compensation in the rear seats is located in the center of the rear tray. Adaptive feedforward control is applied to minimize the square of the noise signals from the two microphones. A filtered-reference SAN algorithm was developed for the system to enable low-priced microchips to be used in place of high-priced DSP. This results in a significant reduction in the amount of calculation required. The existing audio system is used for output. Integration of the output of sound to cancel noise and the normal audio functions has made high performance compatible with low cost. The system reduces booming noises in the front and rear seats originating in the exhaust and drive systems by approximately 10 dB and, in combination with the ACM, it enables the achievement of a level of NV performance that makes cylinder stop undetectable.




Fig. 12 Cutaway view of ACM

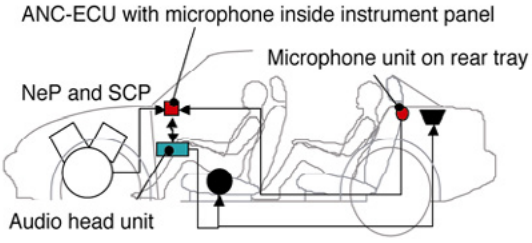



Fig. 13 On-board system configuration of ANC

### 6.3. Improvement of Road Noise Performance

Taking the high-rigidity body framework and the suspension system used in the US Accord as a base, additional soundproofing materials are employed, and the quality of the materials themselves are improved. Specifically, soundproofing materials are newly applied to the middle floor, felt materials are replaced by Thinsulate™, and the density of the backing of the carpeting on the floor is increased, resulting in the achievement of top-class road noise performance for a high-class small sedan (Fig. 14).

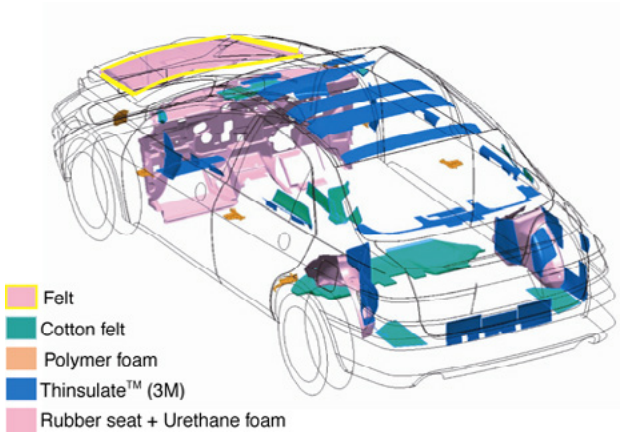



Fig. 14 Placement of soundproofing/sound absorbing materials

## 7. Chassis

The target in the design of the chassis is the achievement of excellent running performance, with the emphasis on superb handling and stability (especially during high-speed driving) and to offer the comfortable ride expected of a high-class sedan. The world's first collision mitigation system (CMS)[4] is employed in the vehicle as an original Honda pre-crash safety technology.

### 7.1. Suspension

The well-received US Accord was once again taken as a base, and the double wishbone suspension employed in the vehicle is further advanced and matured to continue to help enable both steering stability and ride comfort (Table 2).

The front suspension in the US Accord employs an A-type lower arm and a high-capacity compliance bush, with optimized geometry and mounting points. In the new INSPIRE, the settings of the springs and damper mounts are

Table 2 Suspension dimensions

| | | New INSPIRE | US Accord |
|---|---|---|---|
| Front | Spring | 5.5 | 5.6 |
| | Stabilizer | $\phi$ 25.4 × 4.5t | $\phi$ 25.4 × 4.5t |
| | Damper Mt. | 77.5kgf/mm | 100kgf/mm |
| Rear | Spring | 2.9 | 3.1 |
| | Stabilizer | $\phi$ 15 | $\phi$ 13 |
| | Damper Mt. | 100kgf/mm | 100kgf/mm |

altered to increase the comfort of the ride. Optimizing the balance between front and rear, and increasing the rigidity of the body and dampers ensure steering stability.

A five-link double wishbone system with optimized geometry and a higher-capacity and optimized bush was employed in the US Accord to increase stability and smoothness of ride. This system is used as the base for the rear suspension of the new INSPIRE. In addition to softening the springs and dampers to provide a smoother ride, the diameter of the stabilizer and the rigidity of the body is increased to ensure an even higher level of stability (Fig. 15).

205/60R16 size tires are employed in the new INSPIRE. To balance a smooth, comfortable ride with a powerful grip, the height and the hardness of the bead filler sections are adjusted.

The innovations described above result in a drive feel that is not merely softer but also possesses excellent convergence and a level of steering stability offering users a relaxed driving experience.

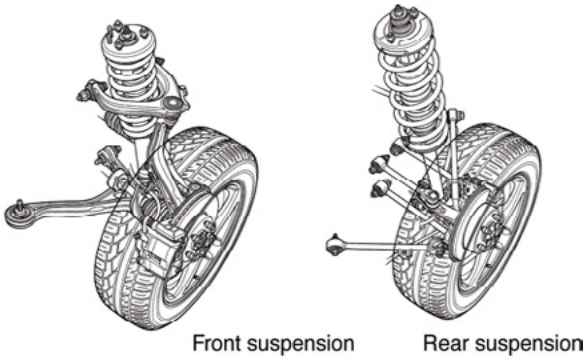



Fig. 15 View of suspension

## 7.2. Steering

Electronic power steering (EPS) is employed in the new INSPIRE to contribute to the achieving of excellent low-speed handling and high-speed stability and superb fuel economy, in addition to the enabling of HiDS[5] to be used in the vehicle.

The increase in the power of the motor to match the V6 engine, the reduced inertial mass and increased rigidity of the mounts results a stable and precise steering characteristic. Tuning with particular attention to the region around the center offers both a smooth steer feeling and superb responsiveness (Fig. 16).

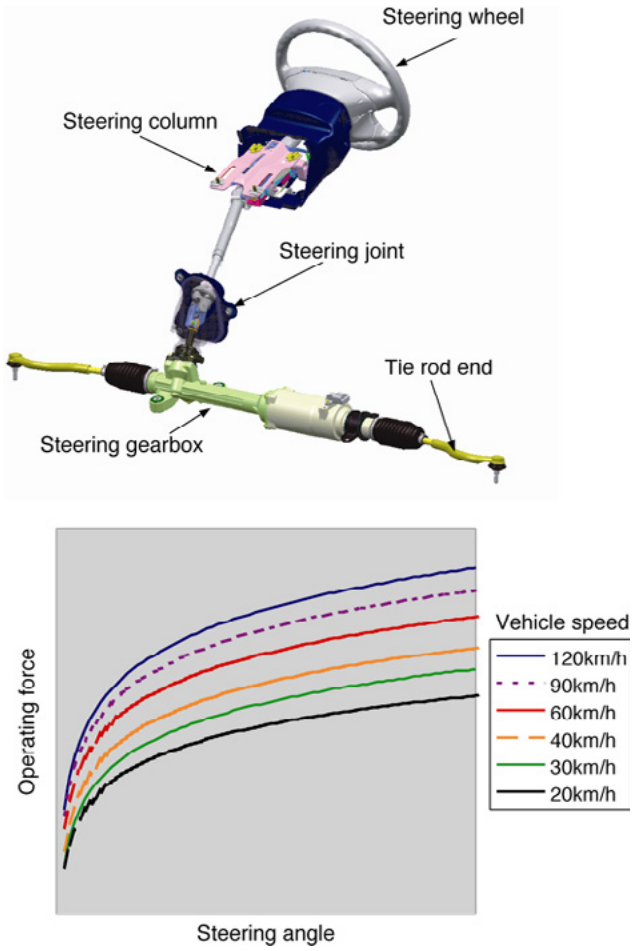



Fig. 16 View of steering system

## 7.3. Brake

Fuel consumption performance is further improved by reducing the drag resistance of the brakes to reduce rolling resistance. At the same time, the following are improvements to the calipers for both enhanced brake performance and feeling:

(1) Altering the shape of grooves in the piston seals ensures clearance between the disc and the pad.
(2) The shape of the retainer is altered to reduce the sliding load on the pad.

These changes reduce drag resistance by 75%, contributing to improved fuel economy (Fig. 17).

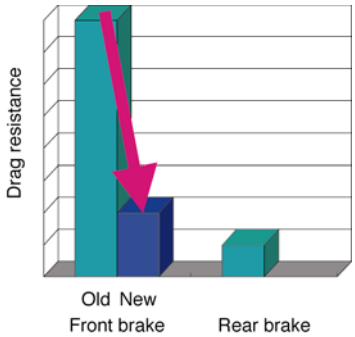



Fig. 17 Brake drag resistance

### 7.4. Improvement of Aerodynamics

Reducing aerodynamic resistance is generally effective in improving actual fuel economy at high speeds. Reducing aerodynamic resistance becomes even more effective when the range of three-cylinder operation is increased in the cylinder on-demand system. The following elements are established as contributing to a reduction of aerodynamic resistance on the basis of digital wind tunnel simulations and wind tunnel tests:

(1) 3D round cabin (Fig. 18)
(2) Flush surfaces
(3) Aerodynamic under floor styling (Fig. 19)
(4) Aerodynamic high-mounted stop lights integrated with the trunk
(5) Aerodynamic door mirrors

These improvements allow the achievement of a coefficient of drag of 0.29. Increasing the range of three-cylinder operation also contributes to improved fuel economy.

## 8. Body

"Body with Confidence" – a body providing tremendous confidence and peace of mind – is the concept employed in developing a body befitting the expectations for a high-class sedan.

### 8.1. Body Rigidity

Dynamic rigidity was a particular focus in the development of the new INSPIRE - to achieve superior stability in all driving conditions, from city driving to high-speed driving. As a result of the improvements based on structural analysis and driving tests, the body displays both high dynamic rigidity and considerably improved static rigidity, increasing the vehicle's competitiveness in the market.

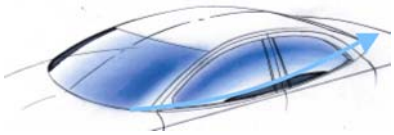


Fig. 18 3D round cabin

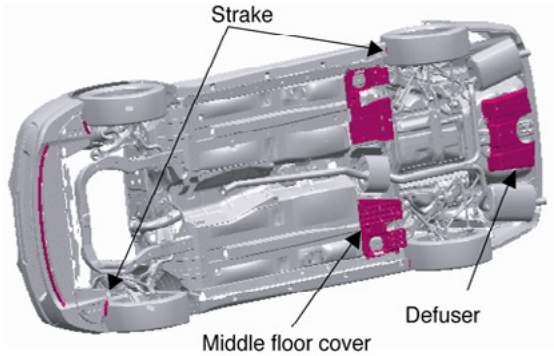



Fig. 19 Aerodynamic under floor styling

The right-left mode of front active rigidity is enhanced to improve responsiveness and to enable direct and supple cornering. A continuous closed cross-sectional structure is adopted in the front bulkhead. This highly efficient continuous structure enables control of displacement at the very front of the vehicle. In addition, the up-down mode of rear dynamic rigidity is enhanced to achieve stability and a level of comfort belying the power of the vehicle. A large stiffener is employed in the center of the rear pillar, and reinforcement is applied from the roof to the rear panel. The front of the vehicle is strongly reinforced as a collision safety measure. To ensure that the rear of the vehicle does not seem weak in comparison, major connecting sections are effectively reinforced to achieve an excellent balance of rigidity from front to rear (Fig. 20).

### 8.2. Collision Performance

The new INSPIRE is the first Honda vehicle to receive the highest rating (six stars for both seats) in the JNCAP collision safety performance evaluation. To achieve a six-star rating, it is necessary for a vehicle to receive high points in a 64 km/h offset collision, a 55 km/h flat barrier collision, and a 55 km/h side collision. This achievement is made possible in the new INSPIRE by reducing deformation of the body through side frame bending mode control, steering column stroke load control and under floor reinforcement. In addition, high-tensional materials have been used at many points in the body framework. Lightweight but strong, these materials improve both front and side collision performance. 48% of the framework consists of high-tensional materials, of which approximately 2/5 is the even more highly effective 590 MPa-grade (Fig. 21).

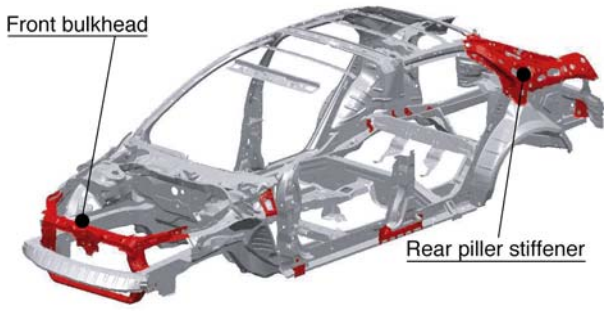



Fig. 20 Body construction

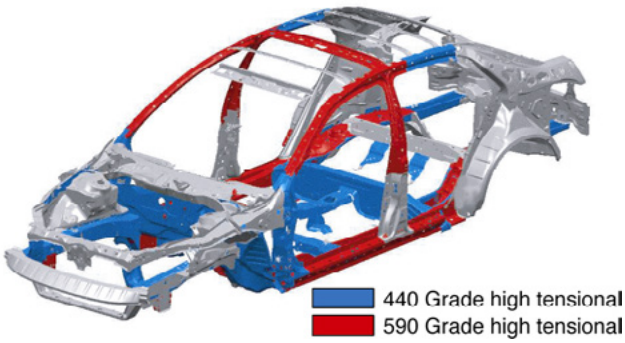



Fig. 21 High tensional strength

## 9. Interior

The interior design of the new INSPIRE is based on the concept of “Smart, Emotional, Clean.” The driver interface is improved, and is centered on a center module, while the instrument panel and the door trim achieve a wrap-around effect with a high-quality and “emotional” styling. The high-class impression generated by the vehicle is further enhanced by features such as seats having an all-new framework designed to reduce fatigue on long drives and electrically operated rear sunshades.

E-pretensioners have been employed in the seatbelt system of the new INSPIRE as yet another Honda pre-crash safety technology.

To reduce the environmental impact associated with the soft pads on the surfaces of the instrument panel and the door trims, the standard PVC skin has been changed to a spray urethane skin (Fig. 22). With PVC coatings, a slush is conventionally produced by heating and liquefying powdered PVC in a metal mold, after which rapid chilling forms a skin. In the spray method used for the new INSPIRE, in contrast, liquid urethane is sprayed onto a metal mold and the skin is formed by means of a chemical reaction. This enables the mold to be maintained at a fixed temperature, reducing the amount of energy expended in the production process.

The freedom of form offered by the spray method has been exploited to form a high-quality exterior surface. The design carefully eliminates breaks or joins between different components. To achieve this, the skin of the meter visor, the inside door handles, etc. are formed in one piece. The opening on the lid of the front passenger seat airbag is produced by a laser from the rear surface of the instrument panel, making the cut in the lid invisible. This laser operation is optimized based on a variety of conditions for airbag operation to help ensure the same high reliability in the new lid as is displayed by conventional lids.

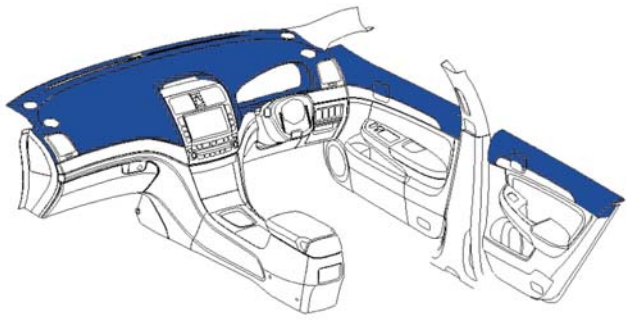


Fig. 22 Area of spray urethane application

## 10. Electrical Equipment

To realize the “Cruising Smart” concept established for the electrical equipment employed in the new INSPIRE, development proceeded with the following targets:

(1) Reduced driving burden in highway cruising;
(2) Making equipment designed for user comfort smarter.

Line beam headlights with a new reflector structure are employed to reduce the burden of night time driving. HiDS is employed to reduce driver load during highway driving and this further increases the safety of the vehicle in combination with the CMS and E-pretensioner pre-crash safety technologies. Cylinder stop cooperative control has been added to cruise control, to improve fuel economy when cruising and to increase commercial appeal. On the instrument panel, a center module brings together displays and controls for vehicle operation. The large, luminescent displays make it easy for the driver to read a variety of information on vehicle status.

### 10.1. Line Beam Headlights

Low beam line beam headlights featuring reflectors are used in the new INSPIRE. The reflectors are capable of directing light in the upper part of the beam, which is normally ineffective for illumination, in a tight forward beam. This increases luminous flux intensity by approximately 50% and extends the beam cast by the lights for long distances without diminution of the range illuminated, including the area directly in front of the vehicle. As a result, visibility during night driving is increased helping to reduce the burden on the driver (Figs. 23 and 24).

### 10.2. HiDS Coordinated with CMS

To bolster the CMS, a high-resolution milliwave radar unit is installed to conduct mechanical scans and increase the ability of the system to detect targets (vehicles in front) (Fig. 25).

A deceleration control logic employing a VSA hydraulic unit was developed to establish a balance between the sudden responses of the automatic brake system and the deceleration feeling produced by the IHCC headway control - making a system designed for user safety and comfort even smarter.



Fig. 23 Line beam

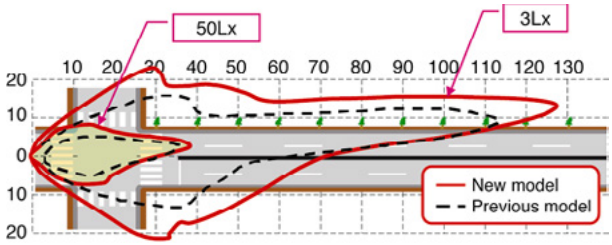



Fig. 24 Area of line beam illumination

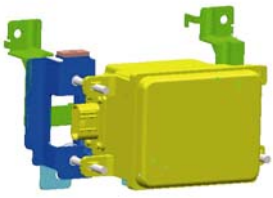


Fig. 25 Milli wave radar

### 10.3. Cruise Control – Cylinder Stop Cooperative Control

By limiting the changes in the degree of opening of the throttle when the vehicle is in cruise control mode to the extent that changes in vehicle speed are not apparent to vehicle users, the frequency of three-cylinder operation can be increased. This results in a roughly 3% improvement in fuel economy relative to fuel economy prior to the introduction of cooperative control.

### 10.4. Meters

Large, easy to read, luminescent meters are employed in the new INSPIRE (Fig. 26). A liquid crystal multi-information panel is located within the meter display, centralizing information on the vehicle and on running status. This makes accurate information easily available to the driver. Increasing visibility of the HiDS and CMS systems status, information on fuel consumption, and warning messages, raises the commercial appeal of the vehicle. Fig. 27 shows an example of the meter displays.




Fig. 26 Meter panel display




Fig. 27 Multi-information display

## 11. Conclusion

Numerous new devices and technologies are employed in the new INSPIRE. However, no matter how superb the technology developed, ultimately it must be functional for users, rather than simply drawing attention to its existence. Development of the technologies employed in the new vehicle was predicated on the fundamental concept that technologies should have the maximum possible effect, and that they should also offer their benefits effortlessly and without nuisance to users. Many new technologies employed in the new INSPIRE are merged and sublimated into the overall vehicle – the “New Intelligent Tourer.” As a result, the vehicle is the very embodiment of a high-class sedan with a new level of appeal not matched by competitors. As such, it is truly capable of “inspiring” its users.

This development reached fruition with the generous assistance of many individuals, both on the Honda team and from other companies. The authors wish to take this opportunity to offer their sincere thanks to all who assisted in the project.

## References

(1) Noguchi, K., et al.: Development of V6 i-VTEC Engine with Variable Cylinder Management, Honda R&D Technical Review, Vol. 16, No. 1, p. 85-92

(2) Matsuoka, H., et al.: Development of Active Control Engine Mount, Honda R&D Technical Review, Vol. 15, No. 2, p. 209-214

(3) Inoue, T., et al.: Development of Active Noise Control System for Engine Booming Noise, Honda R&D Technical Review, Vol. 15, No. 2, p. 201-208

(4) Kodaka, K., Otaba, M., Urai, Y., Koike, H.: Rear-end Collision Velocity Reduction System, SAE paper 2003-01-0503

(5) Ishida, S., Tanaka, J., Kondo, S. Shingyoji, M.: Development of a Driver Assistance System, SAE Paper 2003-01-0279

■ Authors ■


Shigehiro YASUKI


Yasuaki ASAKI


Hiroshi TASHIRO


Hideki MATSUOKA


Taku KONO

# Development of New Model LIFE Incorporating Concept of “Technology with Heart”

Norio IGARASHI* Takuya AOKI* Yoshiharu UCHIDA*
Takahiro SUGAWARA* Katsumi KANASUGI* Tomoyuki UEMURA*

## ABSTRACT

The new model Honda LIFE was developed based on the concept of “Technology with Heart.” The aim was to achieve high performance levels in the areas of safety, design, packaging, utility and driving. The engine, transmission and platform are entirely redesigned, making the vehicle more compact, with a resulting 95 mm increase in effective cabin area and increased collision safety performance. The vehicle has a high fuel economy of 19.8 km/L in Japanese 10-15 mode, and is certified as an Ultra Low Emission Vehicle (ULEV). The superior aerodynamic characteristics of the vehicle’s exterior provide a high level of driving stability and NV performance. With its front-to-rear walk-through seating arrangement, a multi-information display and a variety of other distinctive features, the new LIFE is a next-generation small car offering a high degree of utility and driving pleasure.

## 1. Introduction

Honda’s mini-compact car history commenced in 1966 with the N360. This was the very beginning of automobile manufacture at Honda, and the philosophy developed centered on safety as the most important consideration. In addition, the company wanted the vehicle to provide a comfortable space for users despite its size, and for it to be fun for anyone to drive. This human-centered approach has been passed down as an unbroken tradition at Honda, and is still very much alive in the company’s current automotive manufacturing operations. 20th century technology enriched our lives, but tended to stress efficiency above all else. The development team behind the new LIFE felt that 21st century technology should be kinder to humans, more in tune with their senses, something that provides everyone using it with a feeling of comfort. In developing the vehicle, the team wanted to ensure the excellent economy, environmental performance and the other benefits that mini-compact cars have traditionally been known for. But, the team also wanted to make the vehicle more pleasurable to use, a mini-compact that users would drive with pride and abundant feelings of warmth. The exterior of the new LIFE developed on this basis is shown in Fig. 1.




Fig. 1 Exterior view of LIFE

* Tochigi R&D Center

## 2. Concept and Development Goals

The development concept for the new LIFE is "Technology with Heart." This means not merely attempting to achieve physical efficiency to increase the number of functions or the level of performance, but rather to apply technologies on the basis of empathetic thinking, seeking to help users gain a sense of genuine satisfaction. The team believed that applying this perspective to the development process would enable them to produce a small car suited to the future - one that would emotionally effect users, to afford a sense of intimacy and which would be loved by all users.

The following themes and objectives were put in place to do this:

(1) Safety: Safety technologies which are effective in vehicle-to-vehicle collisions, to enable users to feel the vehicle is designed with safety in mind.
(2) Design: A design that expresses the functionality of the vehicle with beauty, to generate excitement and have an emotional resonance
(3) Packaging: Packaging which is efficient, but also user-friendly
(4) Utility: Utility designed from the user's perspective and focusing on even the smallest details
(5) Driving: Design of a new power train to provide a level of driving performance combining environmental friendliness with driving pleasure

## 3. Package Layout

### 3.1. Long Room Package

A long room package was selected for the new LIFE to provide the "total comfort cabin," one that not only enables users to feel the sense of comfort and well-being associated with a more spacious cabin, but one that is also beautiful to the eye, easy to use, and easier to drive. The total height of this long room package is reduced to help driving stability, and this also reduces aerodynamic resistance, thereby contributing to increased fuel economy. Working within the standard dimensions for a mini-compact car, the space required for mechanical devices is reduced to increase space available to users. A variety of measures, including the use of a newly developed 60 mm shorter engine, enable the total engine room to be shortened by 95 mm. In this way, distance from the accelerator pedal to the tailgate lining increases 95 mm relative to the previous model. Shortening the nose of the vehicle enables the luggage compartment to be lengthened by 15 mm. Use of a newly developed rear suspension system enables a low floor to be employed in the luggage compartment (525 mm above the ground), increasing storage capacity to a volume of 200 L (VDA system).

### 3.2. Driving Position

To provide a driving position that is comfortable for users of various physiques even if driving for extended periods, we raised the steering shaft angle and positioned the shaft higher to increase the amount of space around the driver's knees. The upper part of the steering wheel was also brought closer to the driver, to offer both excellent operability and sufficient upper body room. In addition, the accelerator pedal was brought closer to the floor, to help reduce the burden on the driver's ankle. To allow easy driver ingress and egress and to help with visibility, the hip point was set 580 mm above the ground. The front edge of the side belt line descends smoothly. A seat height adjuster enables the seat to be raised or lowered 30 mm, which allows drivers to set their eye point to match their height. Triangular windows are used to help reduce the blind spot caused by the front pillar, providing excellent visibility in all directions, front and rear, left and right, and diagonally.

## 4. Engine

### 4.1. Engine Development Goals

The following are the four development targets established for the new engine to produce a compact vehicle that consumes little energy and is kinder to people and the environment:

(1) Improved environmental performance (Increased fuel efficiency and compliance with ultra-low emissions standards)
(2) Significantly improved torque in the practical use range
(3) Reduced weight and compact size
(4) Reduced noise and vibration

### 4.2. Engine Overview and Specifications

#### 4.2.1. Overview

Engines of mini-compact cars are frequently subject to high loads in actual use. The new engine is therefore designed with the following characteristics:

(1) Reduced friction at high engine speeds by means of short stroke
(2) Increased valve diameter and reduced pumping loss by employing a big bore
(3) High compression ratio achieved by use of two valves and two spark plugs

Table 1 shows the main engine specifications, and Fig. 2 shows an external view of the engine. The use of a bore/stroke ratio of 0.78 and a low piston speed (average = 12.4 m/sec at engine speeds generating the highest power) reduces friction at high speeds, while the employment of two large-diameter valves controls increases in pumping loss. The compression ratio is set at 11.2 in the NA model, the highest level for a regular gasoline engine.

Table 1 Engine specifications

| Engine | NA model | Turbo model |
|---|---|---|
| Cylinder configuration | In-line 3-cylinder | In-line 3-cylinder |
| Bore × stroke (mm) | 71 × 55.4 | 71 × 55.4 |
| Displacement ($cm^3$) | 658 | 658 |
| Compression ratio | 11.2 | 8.5 |
| Valve train | SOHC 2valves | SOHC 2valves |
| Number of valves | 2 per cylinder | 2 per cylinder |
| Valve diam. (mm) Inlet | 35 | 35 |
| Valve diam. (mm) Exhaust | 30 | 30 |
| Fuel supply system | Programmed fuel injection | Programmed fuel injection |
| Ignition system | Dual point sequential ignition | Dual point sequential ignition |
| Max. power (kW/rpm) | 38/6 700 | 47/6 700 |
| Max. torque (N·m/rpm) | 61/3 800 | 93/3 800 |

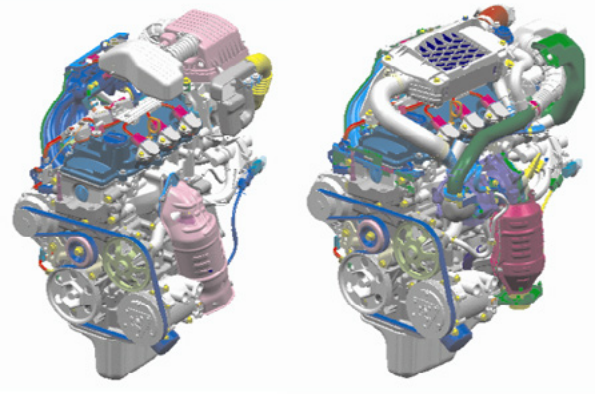



Fig. 2 Engine models

#### 4.2.2. Reducing weight and increasing compactness

The angle of mounting of the engine is changed from a forward inclination of 60 deg in the previous model to 5 deg in the new LIFE; together with direct mounting of the auxiliary equipment on the cylinder block and the direct mounting of a catalyzer (NA model) or a turbocharger (turbo model) underneath the cylinder head which is integrated with the exhaust manifold. These changes reduce engine room by 95 mm relative to the previous model, increasing the compactness of the vehicle. Optimization of the crankshaft, the shape of the area around the cylinder block and the overall layout, together with the employment of a resin intake manifold, cylinder head cover, oil strainer and oil level gauge, enable the mass of the engine to be reduced by 9%.

### 4.3. Engine Performance

#### 4.3.1. Fuel economy

The stoichiometric air-fuel ratio employed in the new engine has reduced BSFC by 7%. In addition to using a short stroke to reduce friction at high engine speeds, a variety of other friction reduction methods are employed in the new engine. The diameters of the roller follower and the crank journals have been reduced in size and OW-20 low-viscosity engine oil is employed. A variety of features found in the Civic Hybrid are also used – plateau honing, an offset cylinder structure, an ion plated piston ring, burring of the main metal and conrod metal, and molybdenum disulfide shot peening of the piston skirts.

#### 4.3.2. Power

Figure 3 shows engine performance curves. The maximum torque of the new engine is identical to that of the previous model, but it displays an average increase in torque of 7% up to 4 000 rpm. Both engines have the same practical power characteristic, producing maximum power at the low engine speed of 500 rpm. The superior knocking performance of the engine has been exploited to enable turbocharging from a lower speed in the turbo engine, ensuring smooth acceleration performance.

#### 4.3.3. Emission reduction technology

The main emission reduction technologies employed in the new engine are discussed below. The turbo model is the first turbocharged engine to achieve compliance with ultra-low emissions standards.

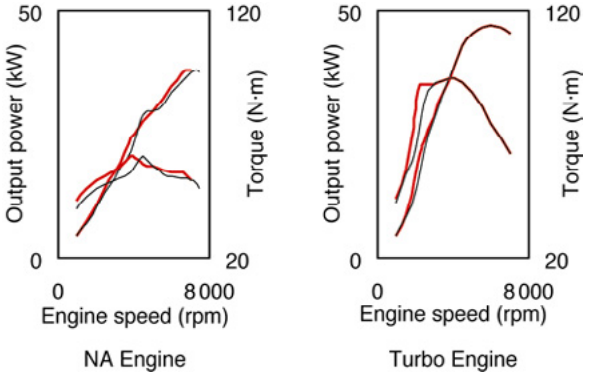



Fig. 3 Engine performance

(1) Highly accurate air-fuel ratio control
- The positioning of an A/F sensor in front of the catalyzer and an $O_2$ sensor downstream from the catalyzer enables highly accurate air-fuel ratio control.
- The positioning of a multi-hole fuel injector in the cylinder head port reduces the delay in providing fuel.

(2) Rapid heating of catalyzer
- Integration of the cylinder head with the exhaust manifold
- Positioning of the catalyzer directly underneath the engine
- Direct mounting of the turbocharger on the cylinder head (turbo model)

(3) Application of stoichiometric air-fuel ratio control directly after cold start is enabled by stabilization of combustion

(4) Control of delay angle at large ignition timing for early activation of catalyst

#### 4.3.4. Technologies to improve engine NV performance

A lower block structure is employed in the cylinder block to increase quietness and to reduce the amount of noise and

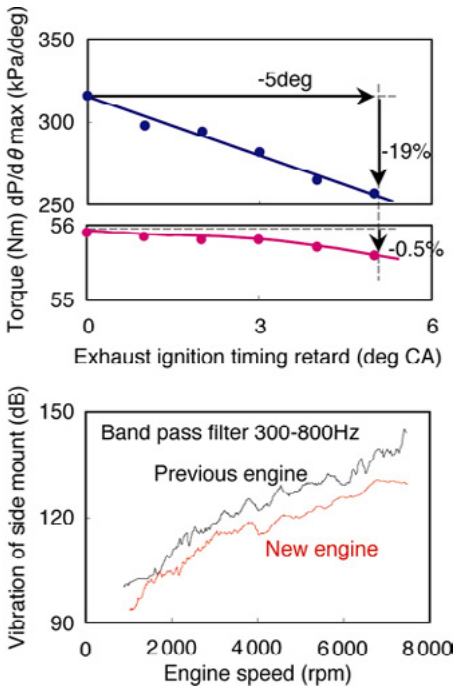



Fig. 4 Vibration level of new engine

vibration produced by rapid combustion. Each journal is integrated with the outer wall of the lower block, and its curvature and the placement of ribs are optimized, resulting in a 38% increase in the rigidity of the journals. In addition, the structure employed eliminates the need for reinforcement to ensure coupling rigidity between the engine and the transmission. The use of a short stroke enables the overlap in the diameters of the crankshaft journals and pins to be increased, ensuring a highly rigid structure effective for reducing knocking noise. Vibration is suppressed by the use of a full balance weight. Phased ignition control between the two spark plugs effectively reduces crank knocking noise. The use of a 5 deg delay angle when sparking on the exhaust side reduces (dP/dθ) max by 19% and externally transmitted engine noise by 17% relative to simultaneous sparking, while maintaining engine torque at virtually the same level. The increased rigidity of the engine framework and the phased ignition control discussed above reduce mid-frequency vibrations at the engine mounts by 5-10 dB as shown in Fig. 4.

## 5. Transmission

To enable the development concept established for the new LIFE to be realized, the transmission had to be made compact, contribute to improved fuel economy, and to offer a commercial appeal beyond the vehicle's class. While the previous model employed a hydraulically controlled 3-speed AT, the new LIFE employs a newly developed electronically controlled 4-speed AT provided with a lockup mechanism.

### 5.1. Compact Structure

To help achieve a reasonably safe level of collision safety performance while increasing cabin space, a parallel three-shaft layout has been adopted for the new 4AT, shown in cross-section in Fig. 5. The third gears and the idle gears are common, reducing the total and longitudinal length of the transmission.

In order to avoid any increase in length despite the addition of a lockup clutch, a new highly efficient torque converter has been developed, which maintains the same high torque ratio as a conventional 3AT but has a flow channel flatness ratio (torus cross-section) of 81%. As a result, despite using a 4AT with a lockup clutch, the total length of the unit is 13 mm shorter than the previous 3AT. The vehicle is also made more compact in the longitudinal direction thanks to a layout in which the differential shaft is located towards the bottom of the engine, as shown in Fig. 6.

### 5.2. Technologies for Improved Fuel Economy

Because the absolute value of engine torque is low in mini-compact cars, the ratio of friction loss, a cause of poor fuel economy, increases. Reducing friction loss was therefore a major focus in developing the new 4AT. A low drag torque-type clutch pack is used at all stages in the clutch to reduce drag torque. The shape of the grooves in the friction materials of the friction plate was studied, and redeveloped to enable lubricating oil to flow away more easily. Various measures, including the optimizing of lubrication specifications, are adopted to reduce oil pump driving loss and agitation resistance in the differential. As a result, while the shift

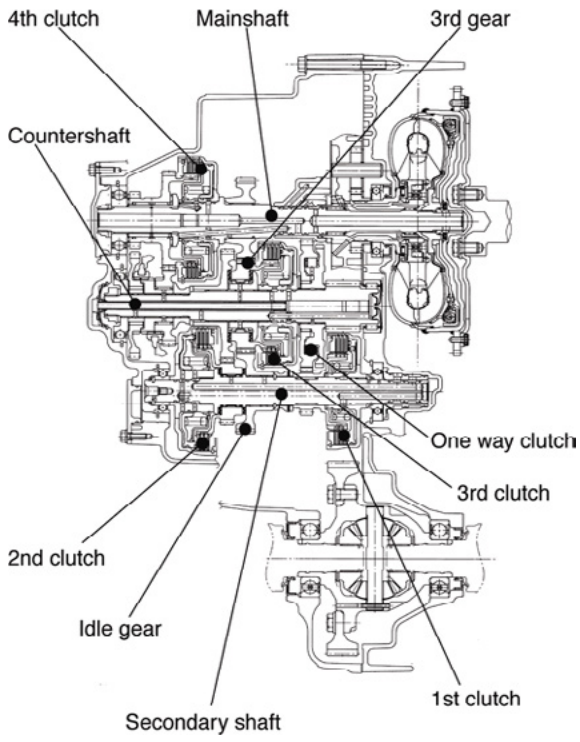



Fig. 5 Cross-section view of new 4AT

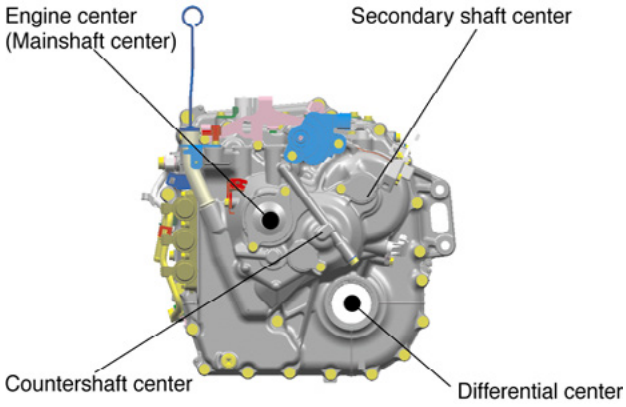



Fig. 6 Side view of new 4AT

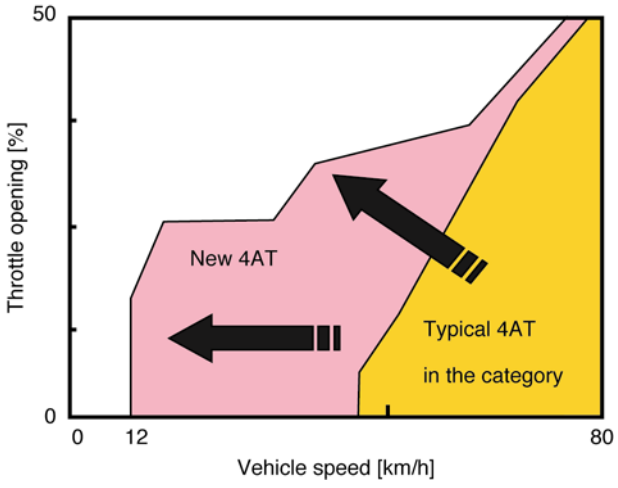



Fig. 7 Comparison of lock-up control area

stages are increased, the new 4AT has the same level of friction as the previous 3AT. A lock-up clutch is employed to both increase fuel economy and ensure drivability. The use of the Active Lock-up II system, which is provided with a lock-up clutch and which uses a linear solenoid for control in all vehicle variations, enables lock-up from 2nd to 4th gears, including shift transitions. In this system, the lockup clutch uses a long torsion damper to attenuate variations in torque from the engine. A linear solenoid provides highly accurate oil pressure control, enabling more precise feedback control in the transient area. As Fig. 7 shows, these measures enable lockup from 12 km/h in 2nd gear, significantly expanding the lockup range when the vehicle is cruising and accelerating.

### 5.3. Commercial Appeal Beyond the Vehicle’s Class

#### 5.3.1. Shift

Direct control of clutch pressure by means of a linear solenoid that uses a control logic normally employed in high-class vehicles is used in the new LIFE to achieve a smooth and highly responsive shift feeling. The structure of the clutch enables centrifugal hydraulic cancellation from 2nd to 4th gears, improving the accuracy of clutch hydraulic control and realizing a smooth shift feeling with excellent stability of quality.

#### 5.3.2. Climbing and descending slopes

To respond to the load generated by climbing or descending a slope, PROSMATEC (PROgressive Shift schedule MAnagement TEChnology) is used in all variations to enable optimal selection of the shift stage from 2nd to 4th gears. This eliminates unnecessary shifting when climbing or descending and enables optimal control of the engine brake when descending, thereby increasing drivability.

#### 5.3.3. NV performance

The idle gears are positioned in the center of the shafts, controlling the effect of the misalignment of meshing generated by changes in input load. Together with new settings for the mesh ratio of the gears, this contributes to the quietness of the vehicle.

## 6. Suspension

In addition to focusing on excellent city driving performance as an aspect of the basic performance of the vehicle, the development team became convinced (by repeated driving tests in Europe, where the driving environment is tougher than Japan’s) that ready high-speed driving performance also is important. The following performance improvements were therefore required:

(1) Stable high-speed running and solid steering close to neutral
(2) Linear and confident responsiveness up to high speeds
(3) Suspension with a great deal of give to absorb the tossing of the vehicle when driving on roads with large undulations and a matching body, to ensure a flat, smooth ride in which passengers are not shaken around excessively and do not experience high Gs
(4) Smooth response to steering input and reliable transmission of road surface information to the driver when the steering wheel is turned

To help ensure rigidity and precision in the mounts of the front suspension, a Macpherson strut provided with a high-rigidity L-shaped lower arm connected to the subframe is adopted. A compact new H-beam is redesigned for the 2WD rear suspension. There are no variations in the scuff. The difference between left and right in the jack up position is reduced to zero. The wheel base is increased by 60 mm, but an increased tire angle ensures that the turning radius of the vehicle is unchanged from the previous model, at 4.5 m (Fig. 8). The EPS system is redesigned to achieve a more natural steer feel, and employs a CPU with approximately three times the power of the previous model to provide more subtle assist settings (Fig. 9).

### 6.1. Brakes

The pedal ratio and the brake master power characteristic are optimized to help produce a stable brake feeling and to provide a solid pedal feel and a brake response in line with the amount of pressure put on the pedal. A wheel geometry is employed whereby, when braking during a turn, the front TOE points outside the turn for both the inner and outer wheels. This helps prevent the vehicle from being oversteered in a turn, and helps allow the vehicle to stop stably. Brake assist enables a higher braking force to be generated. To help prevent the tires from locking and to assist the stability and maneuverability of the vehicle, electronic brake-force distribution (EBD) is employed in the ABS throughout the vehicle, enabling optimal distribution of braking force between the front and rear wheels and enabling the vehicle to make maximum use of braking force. The use of ABS throughout reduces unpleasant braking noise and

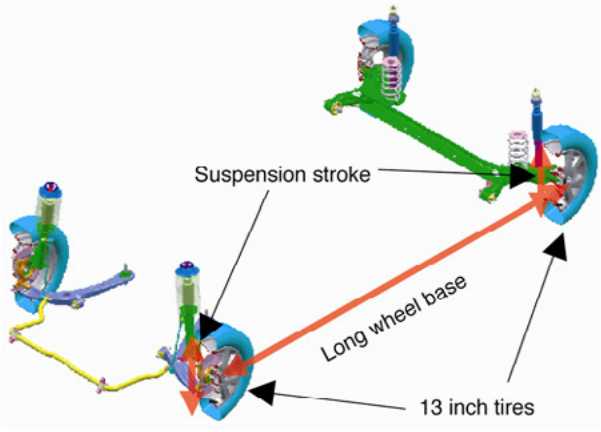



Fig. 8 New suspension system

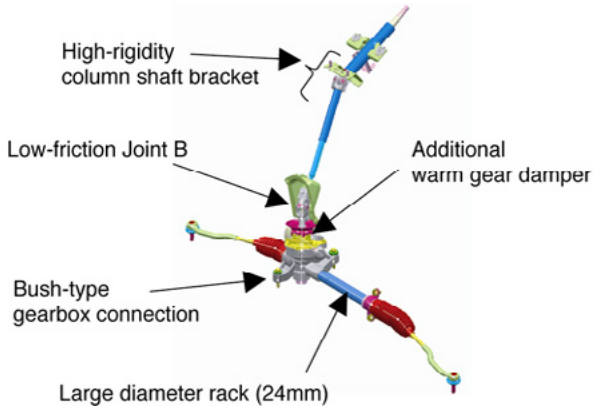



Fig. 9 New EPS system

vibration to the maximum extent, so the vehicle is more comfortable for users even in situations in which the brakes are applied frequently. To allow a front-rear and side walk-through layout, the parking brake has been changed from the former hand brake to a foot-operated type. The height and position of the pedal have been optimized, and the required force and stroke are set to allow comfortable operation by female users. The amount of sound generated by operation and release of the ratchet has also been reduced.

## 7. Body/Fittings/Electrical System

### 7.1. Body Framework

To enable a long frame package to be employed and to provide excellent stability, fuel economy and running performance, the vehicle was redesigned from the platform. As Fig. 10 shows, higher strength 780/980 MPa grade high tensile strength steel has been employed in the new vehicle. Including the 440/590 MPa grade materials that were carried over from the former model, the ratio of high tensile strength steel is 32% of the mass of the body-in-white, and 71% if looking only at framework components. Appropriate use of high tensile strength steel and soft steel with consideration of the purpose of the relevant part has helped in achieving a high level of collision safety performance while reducing the weight of the vehicle.

### 7.2. Body Rigidity

A bulkhead has been added to the tailgate opening and stiffeners have been used in the suspension system mounts in order to achieve excellent steering stability and NVH performance. In terms of static rigidity, this has resulted in improvements of 55% in bending rigidity and 16% in twisting rigidity against the previous model. From the perspective of dynamic rigidity, a significant improvement of 11 Hz has been achieved in both front goose-necking and rear twisting.

### 7.3. Door

To allow for a variety of conditions of use, the degree of opening of both the front and rear doors is increased, and they can lock in three separate positions. Because the rear door is often used to stow large parcels or bags in the vehicle, the angle of opening is increased to 79°. The multi-angle door handles are not only a design accent, but ensure that the handles function at the various angles they can be gripped from, increasing ease of use. A new door lock is employed to reduce the sound when the door is closed, resulting in a high-class, refined sound with reduced high-frequency components.

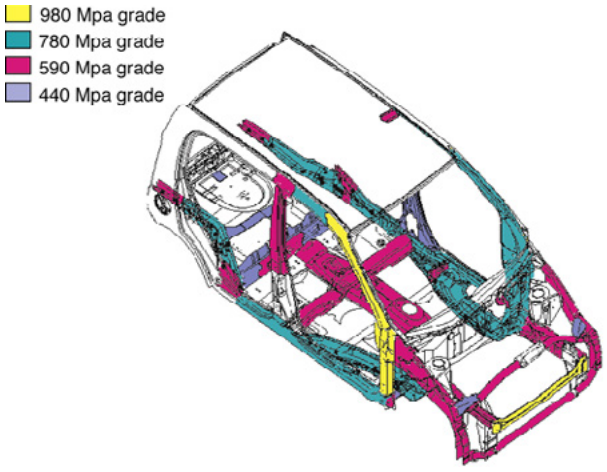



Fig. 10 Area of application of high tensile strength steel

### 7.4. Collision Safety Performance

Compatibility improvement technology[1], developed as a result of research on car-to-car crashes[2], is employed in the body framework of the new LIFE (Fig. 11). A pretensioner is also used for both the lap belt and the shoulder belt at the driver's seat. This helps assist the vehicle in achieving the established collision safety performance target in a 50% offset collision with a vehicle of up to two tons when both vehicles are traveling at 50 km/h. The vehicle also performs well in a frontal full-wrap collision at 55 km/h and a frontal offset collision at 64 km/h. Together with measures helping the vehicle perform well in a side collision of 55 km/h and a rear collision of 50 km/h, this enables the vehicle to achieve a level of collision safety performance at the top of the mini-compact class. The body, incorporating these compatibility measures, is able to disperse impact and help absorb the

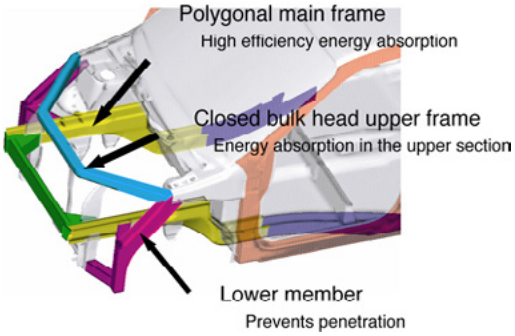



Fig. 11 Layout of new body structure

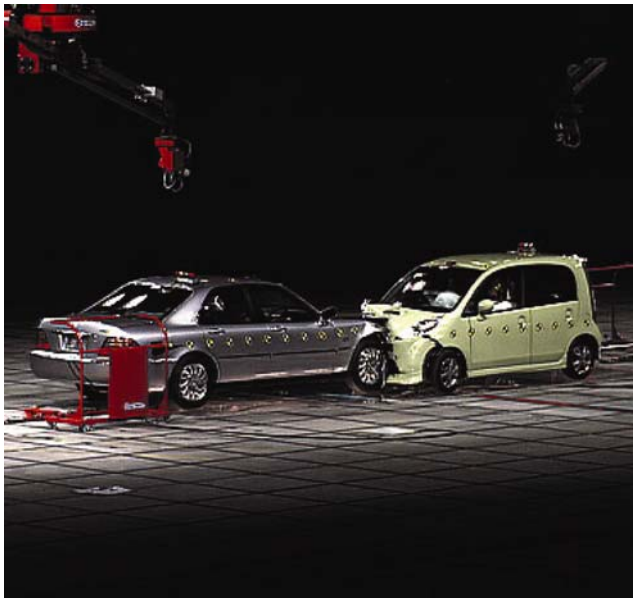


Fig. 12 Car-to-car crash test

energy of a collision. Not only is damage to the vehicle itself reduced, but also the effect of the collision on the other vehicle is reduced. Inside the cabin, head protecting interiors in the side of the roof and the pillars help reduce potential injuries to passengers. Pedestrians have also been considered, as the body includes features to help reduce injuries to pedestrians in the event of a collision. The front of the body has a structure enabling it to soften in a collision, to help reduce the degree of injury to a pedestrian’s head and legs. Figure 12 shows a car-to-car crash test.

## 7.5. Improved Noise and Vibration Performance

Making the cabin quiet during driving was an indispensable element in realizing the development concept, which stressed achieving a level of comfort that exceeds expectations for a mini-compact vehicle. Noise and vibration were reduced at the source with the newly designed engine and transmission discussed above. Simultaneous with the additional car-to-car collision measures, the body features gains from the commercial appeal of improved noise and vibration performance. The change to an H-beam in the rear suspension reduces the road noise caused by vibration permeating from the suspension. The use of a new platform specifically designed for a mini-compact vehicle enables the achievement of a level of noise and vibration in which there is a balance between input and response, improving quietness to the level normally associated with the small car class.

An inertial main axis mount system, which provides support at three points, is positioned to wrap around the center of gravity of the power plant. This increases the support rigidity of the engine as compared with the previous model (despite the smaller engine room) and reduces the vibration. Hydraulic envelope mounts are used for the side engine mounts. Side and transmission mount brackets are constructed of high-rigidity aluminum materials to increase passenger comfort, reduce the transmission of vibration to the body, and lower weight. Increased rigidity in the subframe and the body, including the power plant and underbody mounts, significantly reduces input from the body (Fig. 13). A lightweight but highly effective asphalt vibration damping material is used for soundproofing on the surface of the floor panel. The material has the added benefit of reducing the weight by 40%. Optimum deployment and placement of vibration damping, soundproofing and sound absorbing materials, including the use of a high-performance urethane sound-proofing material in the dashboard, and a sound absorbent roof lining, increases cabin quietness in the high-frequency range. (Fig .14)

## 7.6. Fittings

### 7.6.1. Interior

Color coordination of the interior fittings is employed to make the cabin bright, unique, and to display a high quality. A two-tone effect is achieved by coordinating the color of the coating on the instrument panel and the skin on the doors with the bright beige used on the seats. Metallic accents are used on the operating equipment, producing a bright but high-quality impression. The employment of plastic of a single color and finish without surface treatment for all the interior fittings further increases the sense of quality. The plastic materials and skins are redesigned to achieve a high-quality gloss. In addition, a texturing surface treatment for the metal surfaces and a new maintenance method are developed.

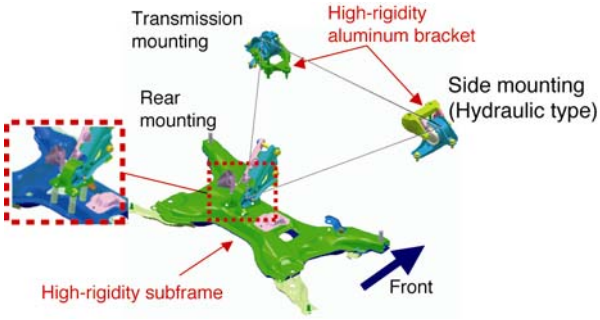



Fig. 13 Engine mounting system

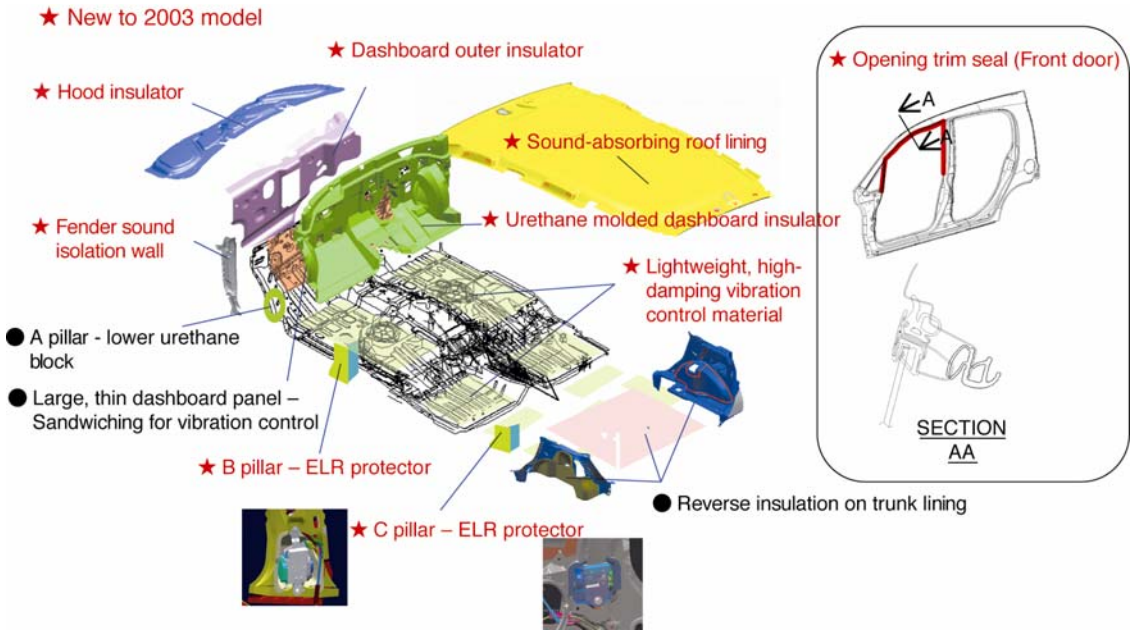



Fig. 14 Packaging employs high-efficiency soundproofing (Sound- and vibration-absorbing)

### 7.6.2. Instrument panel/Passenger seat airbag

Join lines and seams between the components on the instrument panel are eliminated and the components are arranged in a stepped layout both to produce quality and to increase ease of use. The lid of the passenger seat front airbag is integrated with the panel, and the opening is formed from behind with a laser to make it invisible and seamless. This has also contributed to the production of a well-constructed instrument panel with an integrated color scheme and finish. A large tray is used to increase ease of use. There is a divider between the upper box and the inside of the tray, and sufficient storage space is ensured for items like ticket holders, etc.

### 7.6.3. Seats

The seats are redesigned to make them more user-friendly - both relaxing and enveloping and to help provide safety for the occupant. The size of the seats is increased over the previous model, and the urethane along with the other materials used in the skin are improved to produce a soft and comfortable surface capable of distributing pressure while also maintaining a firm grip on the occupant. Convenience is further increased by using tip-up and long slide seat adjustment mechanisms in the F-grade passenger seats to enable side and front-rear walkthrough accessibility (Fig. 15).

### 7.7. Air-conditioner

The target for the air-conditioner was to achieve improved performance while reducing operating noise and energy consumption, and to produce extremely easy-to-use controls on the instrument panel. The performance of the unit itself remains equivalent to the previous model, but resistance to the air flow is dramatically reduced, resulting in a 10% decrease in operating noise and a 10% increase in the volume of air. To reduce energy consumption, the compressor is redesigned; a resulting 20% increase in cycle efficiency contributed to improved fuel economy. The panel, designed for ease of use, features three continuous dials for normal operation, making it possible to make fine adjustments – four stages are available for FAN SW, for example. Full auto air-conditioning is available as an option, and features a large dial for adjusting temperature and a large liquid crystal display to make it even easier to use.

### 7.8. Multi-information Display

Because it is important to help reduce anxiety in driving situations, a new multi-information display is being provided in the new LIFE. The display features a full-dot liquid crystal screen and offers the freedom to choose display content in order to be able to offer drivers more vehicle data (Fig. 16).

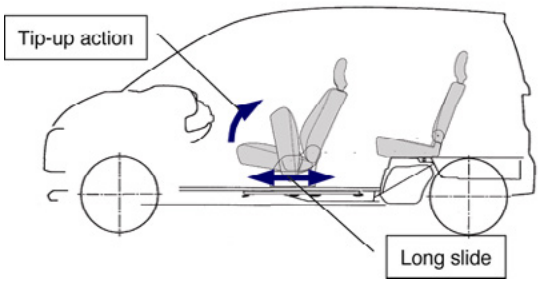



Fig. 15 Seat mechanism for walk-through

The vehicle employs newly developed engine and transmission ECUs, EPS ECU, integrated units, etc. The port output and analog output of each unit was developed from the outset by considering the provision of data to the meter displays. Figure 17 shows examples of displays available on the meters.

(1) Standard screen

During normal driving, the driver can easily select between three screens with the push of a button: one shows an odometer, a trip meter and outside air temperature, another moment-by-moment fuel consumption and average fuel consumption, and the third a tachometer. To help achieve a higher level of safety performance, the fuel meter is accessible from any of the screens. On the fuel consumption

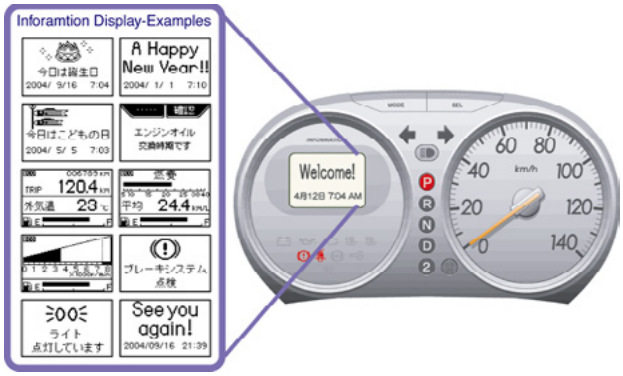



Fig. 16 Information display in instrument panel

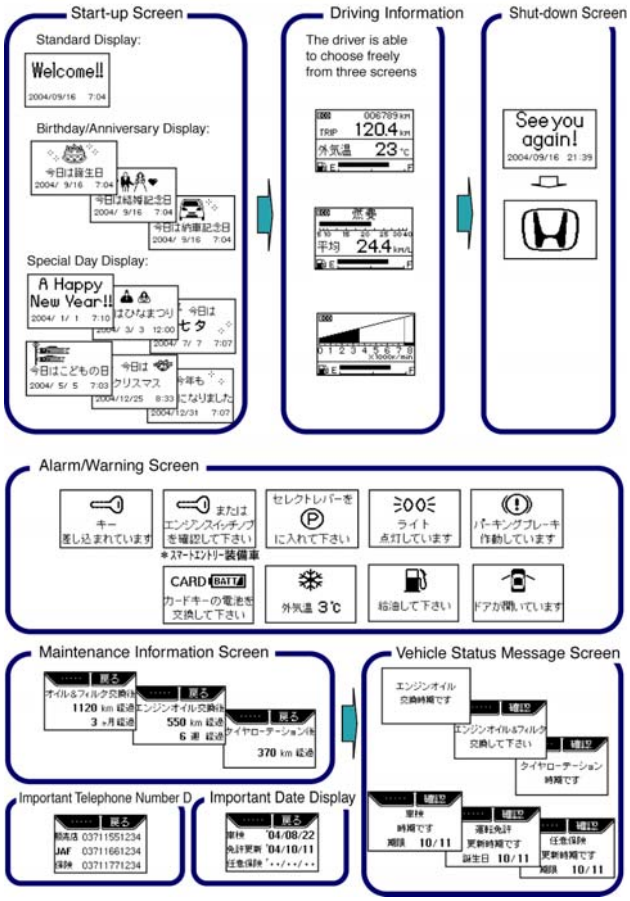



Fig. 17 Functional display

screen, a display of moment-by-moment fuel consumption makes it easier for the driver to be aware of changes in fuel consumption under different driving conditions. This information is displayed as a bar graph to make it easier to read while driving.

Average fuel consumption is numerically displayed, and, to increase convenience, the display is linked to the trip meter, enabling the driver to easily understand the correlation between the displayed average fuel consumption and the fuel consumption, which can be determined by dividing the distance traveled by the amount of fuel consumed before the tank is filled again. Outside air temperature is directly linked to driving conditions, as for example in situations in which ice forms on road surfaces during winter. An external air temperature sensor has therefore been employed (in models with manual air-conditioning), and a picture of a snowflake and a warning appears on the display when the temperature drops below 3 °C.

(2) Warning screens (Linked to sounding of an alarm)

If certain conditions occur during vehicle operation, an alarm sounds, and in five seconds the display changes from the standard screen to a warning screen. These screens show the driver the location of the condition in easy-to-understand pictures and text (Fig. 17). Driving with a door not properly closed or with a seat belt unbuckled will also cause warning screens to be displayed.

Because the parking brake is operated by foot, it is harder for the driver to see whether it is on or not. If the vehicle commences motion with the parking brake on, an alarm will sound and a warning screen will be displayed when the speed goes above 7 km/h. In addition, if the key has been removed and the lights are left on, an alarm will sound and the standard screens will be displayed despite the fact that ignition is off.

(3) Maintenance information

A screen informing the driver of the need for maintenance is displayed as the vehicle approaches the time for its periodic oil changes or tire rotations, enabling the driver to use the vehicle over the long-term with confidence. The requirement for an oil change is estimated from the elapsed time and number of kilometers driven, while the need for tire rotation is calculated from the distance traveled. A screen is also available which shows the number of days and the distance traveled since the last maintenance, enabling the user to check it as required.

(4) User data/Vehicle-related data

Another screen enables the user to easily input information such as the telephone numbers of the dealer, JAF (equivalent to AAA in the United States) and his or her insurance company, enabling the user to access it as needed. The user can also input dates like his or her birthday, his or her driver’s license renewal date, and vehicle inspection validity periods. An information screen will be displayed on or shortly prior to each date.

### 7.9. Honda Smart Card Key System

To increase convenience for users, the new LIFE features key-free operation. Doors can be locked and unlocked and the vehicle started with a thin card key. The card key also has an immobilizer function to prevent car theft. When the user with a card key approaches the car (around 80 cm), the doors unlock and the vehicle can be started by simply turning the key knob if the card is in the vehicle. The doors will lock automatically when the user gets out of the vehicle, closes the door and walks away. All the doors and the tailgate can detect the presence of the card key, a feature added to increase convenience for users who might be carrying parcels or small children. A new communications system is developed to enable operation in the detection areas with fewer antennas than used in standard card key systems. Antennas are positioned in four places (left and right door mirrors and inside left and right RR bumpers) to increase the detection area and reduce power consumption. Inside the vehicle, two antennas are located in the front and rear, and these will enable ignition if the card key is on any seat. This is convenient for users who may have their card key inside a bag, a briefcase, or a purse that they have placed on the passenger seat or the rear seat.

## 8. Environmental Performance

### 8.1. Elimination of PVC from Interior Components

Polyvinyl chloride (PVC) is said to be difficult to recycle. Designers of the new LIFE have succeeded in eliminating its use from the main interior components (Fig. 18).

(1) Thermoplastic olefin (TPO) is employed in the sun visor, run channel and weather strip. The shift knob is thermoplastic urethane (TPU), the seat coverings are fabric, and felt is used as the insulator under the floor carpet. Urethane rather than olefin is employed in the shift knob because of its excellent wear resistance, a particular requirement of materials used in the knob.

### 8.2. PVC in Exterior Components

New materials have been used in all the moldings (door, window and roof) and the quarter seals in order to eliminate PVC (Fig. 19). The moldings and seals are prone to damage, and the form of TPO used is selected from a variety of others for its toughness, on the basis of a cost-benefit analysis. To increase toughness even further, a multi-layered structure is employed, in which other materials are bonded to the TPO during the extrusion process.

### 8.3. Reduction in the Use of Lead

The amount of lead employed in the vehicle is reduced dramatically, to one-tenth the level stipulated by 1996 regulations, and the vehicle meets, in advance, the target as stipulated by the 2006 regulations of Japan Automobile Manufacturers Association, Inc. (JAMA) guidance. This is possible due to the development of substitutes for balance weight and the previously-employed paints, which contained a high quantity of lead.

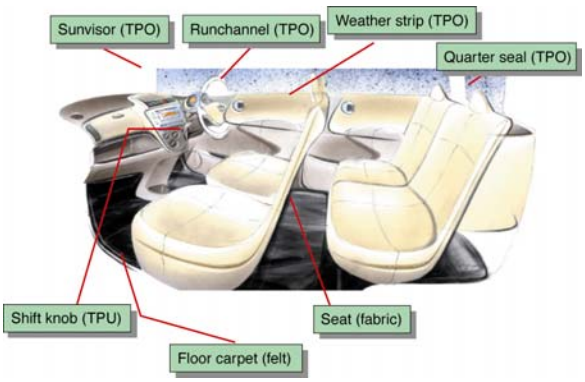



Fig. 18 Interior non-PVC parts

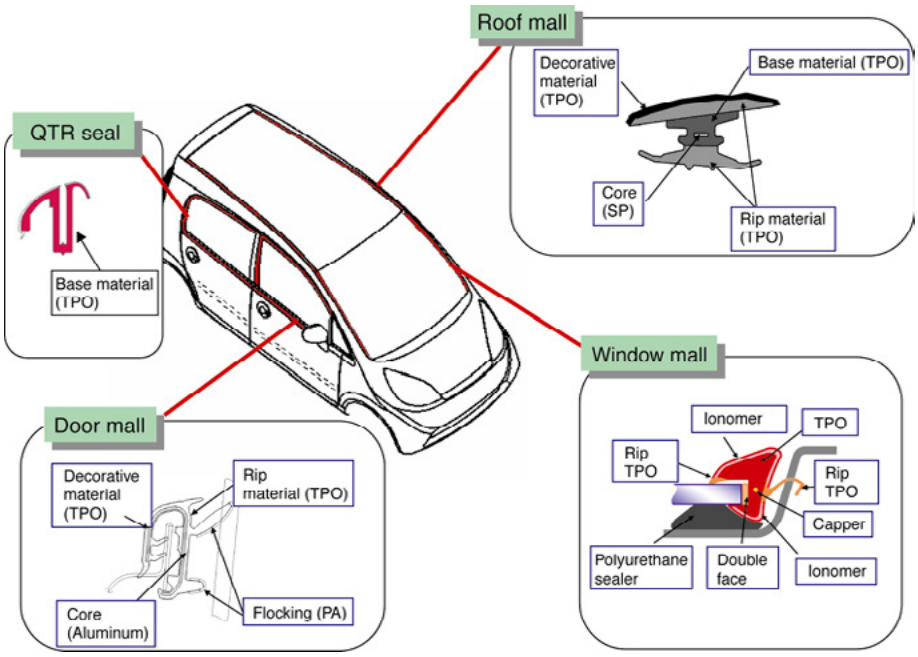



Fig. 19 Exterior non-PVC parts

## 9. Conclusion

The development of the new LIFE is based on the concept of "Technology with Heart." Precisely because mini-compact cars are often used every day, the developers strived not only for superb performance in basic areas such as collision safety, running, turning and stopping, they also sought to fill the vehicle at every point with "Technology with Heart," to provide a driving experience that is comfortable, enjoyable and tension-free. The development team is proud of its success with the new LIFE mini-compact vehicle.

## References

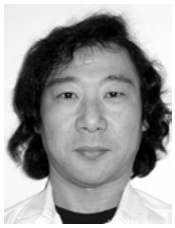
(1) Takizawa, S., Sugimoto, T., Suzuki, H.: A STUDY OF COMPATIBILITY TEST PROCEDURE IN FRONTAL IMPACT, Proceeding 18th International Technical Conference on the Enhanced safety of vehicles Paper Number 437 (2003)

(2) Saito, M., Gomi, T., Taguchi, Y., Yoshimoto, T., Sugimoto, T.: INNOVATIVE BODY STRUCTURE FOR THE SELF-PROTECTION OF A SMALL CAR IN A FRONTAL VEHICLE-TO-VEHICLE CRASH, Proceeding 18th International Technical Conference on the Enhanced safety of vehicles Paper Number 239 (2003)

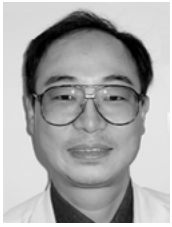
■ Authors ■

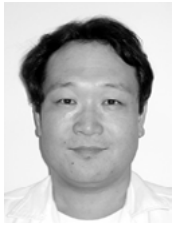

Norio IGARASHI


Takuya AOKI


Yoshiharu UCHIDA


Takahiro SUGAWARA


Katsumi KANASUGI


Tomoyuki UEMURA

# Prototype Motorcycle for Lower Limb Physically Disabled “Super EARA”

Kunihiko HASHIMOTO* Yutaka MURATA* Yukiya UEDA*
Takashi KUDO* Kousuke TSUNASHIMA* Kyo TAKAHASHI*

## ABSTRACT

A prototype motorcycle called the “Super EARA” has been developed that wheelchair users can get on and off, drive and stop by themselves. The functions that the motorcycle should be equipped with were considered in development. The functions are starting, driving and stopping without the using of lower limbs. A vehicle height adjustment system for getting on and off, and an outrigger and a gas pressure type emergency stand to help prevent stack are also equipped. Operation of the newly designed equipment was confirmed by actual driving tests at the Suzuka and Motegi circuits.

## 1. Introduction

A contest for one’s own dreams was started in the year 2000 at the Asaka R&D Center in order to spark the imagination of the employees. This contest is held by the in-house personnel development committee to promote imaginative ideas. The ideas chosen would be developed into a project and their realization would be pursued by the company. This is also a method for passing on a part of Honda’s culture “pursue development of all types.” The dream of “2-wheeled vehicle touring for people in wheelchairs” was chosen in the 2001 dream contest and the development of the “Super EARA” began.

In order to realize this dream, Honda Sun Co., Ltd. employees who require the use of a wheelchair (who had ridden a motorcycle prior to becoming physically disabled) were consulted. Their desire was to be able to ride a motorcycle that is as close as possible to those ridden by physically unimpaired people. They had a deep desire to control the motorcycle themselves without assistance. In order to respect these desires, the development needed to produce a system that has the handling sense of a motorcycle and that looks like a motorcycle. Therefore, the special wheel designs and gyro based self-supported traveling device considered during preliminary investigation were abandoned. Instead, the characteristics focused on were its handling, handling sense and external view.

* Asaka R&D Center

## 2. Development Details of the Super EARA

Figure 1 shows an external view of the Super EARA and its main specifications are given in Table 1.



Fig. 1 Super EARA

Table 1 Specifications

| Items | | Specification | |
|---|---|---|---|
| Overall length | (m) | 2.265 | |
| Overall width | (m) | 0.880 | |
| Overall height | (m) | 1.080 | |
| Groud clearance | (m) | Upper | 0.120 |
| | | Lower | 0.075 |
| Seat height | (m) | 0.630 | |
| Vehicle mass | (kg) | 220 | |
| Engine type | | Liquid-cooled V-type two-cylinder | |
| Displacement | ($cm^3$) | 249 | |
| Fuel tank capacity | (l) | 7.0 | |
| Starting system | | Electric starter | |
| Clutch type | | Wet-type multiple disk clutch, coil spring | |
| Transmission type | | Motor-driven shifting, constant-mesh | |
| Caster angle | (degree) | 31.5 | |
| Trail | (mm) | 130 | |

## 2.1. Development Concept

The development of the Super EARA had the goals of allowing a person who cannot use his lower limbs to get on and off, run, and stop the motorcycle and to provide them the characteristic feeling of riding a motorcycle. It also has the goal of giving riders the enjoyment of being able to ride their motorcycle at their own will and pleasure. The targeted audience for the development was people who required the use of a wheelchair because they could not use their lower limbs, yet had previous experience riding a motorcycle. The following conditions were also placed on the development:

(1) Ability to move to and from a wheelchair to the motorcycle without assistance.
(2) Ability to start, control, and stop without requiring any use of the legs.
(3) Ability to store a wheelchair on the motorcycle without assistance from others.

## 2.2. Investigation of the Completed Vehicle Image

Three image sketch ideas were developed to embody the above stated conditions.

Figure 2 shows a rear entry American type. It has equipment that allows the rider to move alongside the rail on top of the rear fender while still in a specialized wheelchair and then to move to the motorcycle seat. Getting off the motorcycle is done using these steps in reverse. The exclusive wheelchair is equipped with small wheels and moves by electric drive. Figure 3 shows an idea that is primarily the same as the one shown in Fig. 2; it is just a design that allows the rider to better become one with the motorcycle. Figure 4 shows a swing type tricycle that allows the rider to bank the entire bike besides the rear two wheels when running, giving a feeling of riding on a motorcycle. This has a swing mechanism below the springs and allows for use of a large displacement engine. The construction is a step through type with a flat floor for the feet making it easy to get on and off. This is an advantage of this type of motorcycle.

The above images and ideas were discussed with people who use wheelchairs. This brought up the fact that they needed to be able to use their regular wheelchairs, not a special wheelchair discussed in Fig. 2 and 3. It was also found that they do not like large-scale devices. Concerning Fig. 4, it was found that though it has the appearance of a motorcycle, the fact that it has 3 wheels lead to the opinion that it would not sufficiently satisfy their dream of riding a motorcycle.

Next, American Scooters, Super Sports, and Touring motorcycles were brought to Honda Sun Co., Ltd. to provide people with disabled lower limbs the opportunity to feel how it felt to sit on a motorcycle. Of course, they did not actually drive any, but instead they just sat on the motorcycle. The severity of those with lower limb disability varied; one person who had a spinal injury did not have any feeling below a few centimeters under his armpits and had very few abdominal muscles as well. Generally, motorcycles require control by a rider's lumbar region. Determining the ability of a person with handicapped legs for maintaining balance of his body and the bike, as well as controlling the motorcycle during banking with just arm strength was something that we were concerned with and needed to be addressed carefully.

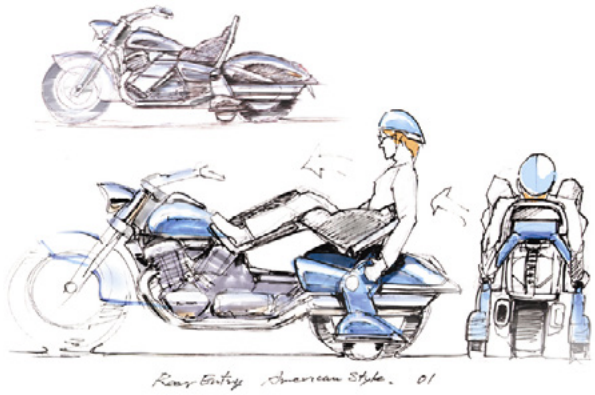


Fig. 2 Rear entry American type

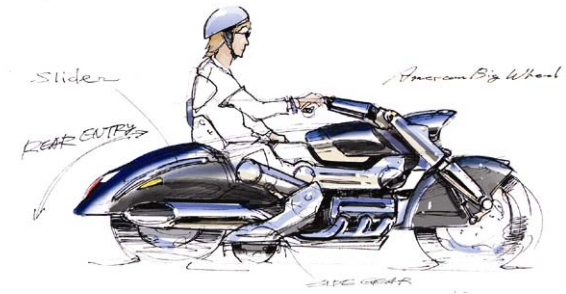


Fig. 3 New American type

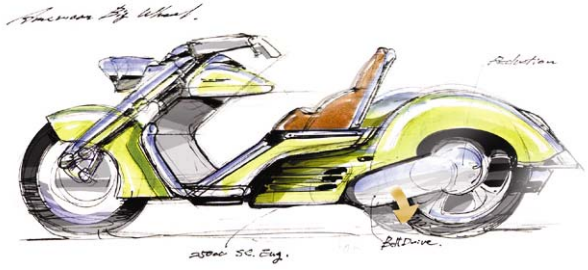


Fig. 4 Swing-type tricycle

### 2.3. Issue Discovery using Precedential Experimental Vehicle

A precedential experimental vehicle was prepared so that a person who uses a wheelchair could (according to our hypothesis) control it in a limited manner. This was used to discover and confirm issues. The base motorcycle chosen was the Honda Magna 250 as it has a low seat and the following changes were made:

(1) The rear suspension was fully bottomed out.
(2) A fixed type outrigger where the width and height could be adjusted was added to keep the motorcycle upright and set at a slight distance above the ground so that the motorcycle could be driven at a low speed.
(3) The motorcycle was changed so that the lever on the right handle controlled both the front and rear brakes (the rear brakes were converted to disk brakes).
(4) A high back rest that came to the subscapular, side supports for the lower back and a special soft seat were added.

At Honda Sun Co., Ltd. two experienced riders were asked to try and ride this precedential experimental vehicle. One of the persons asked to perform this test drive did not have any feeling in his body lower than a few centimeters below his armpits; therefore the backrest was strengthened near the shoulder blade so that he could sense the movements of the motorcycle there. The outrigger was set just above the ground on the right and left side to hold the motorcycle in an upright position. The motorcycle was also set so that it could be driven at low speeds (it was set so that it could not come out of low gear). We supported the motorcycle on both sides to keep it straight when taking off. However, after just a few meters, the motorcycle leaned to one side when the outrigger came into contact with the ground, and it stopped. The second person to test the motorcycle was a person that had raced motorcycles previously. He was successful at balancing the motorcycle and riding it on his first try.

### 2.4. Concept Definition

Through this type of investigation, the type of motorcycle that needed to be realized became more apparent. The type of motorcycle that will fulfill the dream of people who require a wheelchair is simply not a specialized vehicle that is operated by electricity or has a unique appearance. It is important that mechanisms used for support be kept to a minimum, allowing the rider to enjoy controlling the motorcycle on his/her own. And, while being a motorcycle built for people who require a wheel chair, it should have an appealing look to all who behold it. In order to realize the dream of being able to use the motorcycle for touring, it is necessary that the rider be able to completely get on and off, and handle it by himself/herself.

### 2.5. Choice of Engine

In order to preserve the feeling of riding a motorcycle (such as turning while banking) and for the enjoyment of acceleration as well as deceleration, a sufficiently large engine displacement is needed. It was considered that a 250 cc level of power was desirable to meet these needs. The following were also considered in this choice.

In order to preserve the ability of the rider to get on and off the motorcycle, it is important to make the area where the gasoline tank is normally situated on a regular motorcycle as low as possible, making it easy to ride. Therefore the VT250 engine, which has intake valves in front and is short was chosen for the application (as use of a commercial engine was a primary condition). Using a V-style 2 cylinder engine also proved effective in reducing the overall width and weight of the motorcycle.

### 2.6. Discovery of Technical Issues

In order for a rider without the use of his lower limb to drive the motorcycle by himself/herself, the following additional functions were required:

(1) In order to be able to move from the wheelchair to the motorcycle without assistance, the motorcycle needs to stand up on its own while the rider is getting on and off, when first starting to move, and while stopped.
(2) Equipment needs to be added so that the hands can perform all of the functions performed by the feet.
(3) After riding, the vehicle needs to support the rider from the forward and reverse directions.
(4) Structural elements that are in the way of the rider getting on and off the motorcycle need to be removed to the extent possible.
(5) A wheelchair provides the same function as a physically unimpaired person’s legs. Therefore, the wheelchair and wheelchair cushion need to be able to be loaded on the motorcycle.

The original layout is shown in Fig. 5 while the illustration of the final specification is shown in Fig. 6.

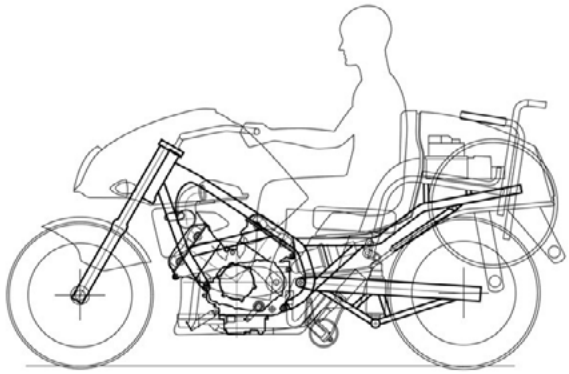


Fig. 5 Layout of Super EARA



Fig. 6 Illustration of Super EARA

## 3. Technologies Implemented on the Super EARA

### 3.1. Vehicle Self-supported System

In order for a rider with physically disabled lower limbs to ride a motorcycle, it is necessary that the motorcycle stand up with stability when the rider is getting on and off and while it is stopped. For example, a retractable outrigger has been considered as a mechanism to support the vehicle when stopping. However, in order for the outrigger to provide sufficient stability the outrigger needs to have sufficient span when lowered and significant strength. It was therefore believed that it would become fairly big and heavy. On the other hand, in order to preserve the image of the motorcycle and maneuverability, the outrigger needs to be stowed quickly and be as compact as feasible when traveling. To resolve these conflicting issues, a self-supported system developed by Honda with the combination of a mechanism for lowering the height of the motorcycle and a compact outrigger is used for when the Super EARA is stopped. In order to ensure operation and preserve safety, ideas for various mechanisms were generated. The details of these are described below.

#### 3.1.1. Vehicle height adjustment mechanism

In order to make it easier for the rider to get on and off when it is stopped, a height adjustment mechanism was attached to the motorcycle's rear wheel suspension. The motorcycle's height adjustment mechanism is shown in Fig. 7. When a switch on the right handle is lowered, two actuators begin to operate and through a link turn the upper suspension pivot lowering the motorcycle height by about 50 mm. When the same switch is raised the opposite actions occur and the motorcycle height is returned to the correct height for traveling.

#### 3.1.2. Outrigger

The outrigger that is placed low on the motorcycle is operated with the same mechanism as the motorcycle height adjustment. When the switch on the right handle is lowered, the outrigger is lowered through a link and opens a distance of roughly 25 mm between the wheel and the road surface. When the switch is raised, the opposite action occurs and it is retracted inside a cover that is behind the footrest to the side of the swing arm. The outrigger is shown in Fig. 8.

When the rider gets onto the motorcycle, it is parked slightly inclined to either the right or the left. The rider places his hand on the end of the handle bars when getting on the motorcycle. When starting, the motorcycle makes contact with the ground at three points. The rider engages the clutch, begins to travel at his discretion, providing 2-wheel driving, then retracts the outrigger. For the outrigger, there are two possibilities for operation, automatic (speed response type) and manual. At the current time, the best speed for starting to retract the outrigger depends on the conditions. As it was not necessary to satisfactorily provide control in all conditions at this stage of the development of this technology, this prototype used manual control.



Fig. 7 Vehicle height adjusting system



Fig. 8 Outrigger

### 3.2. Actuator Control System

The new electrical equipment on the Super EARA are the actuator control unit, outrigger monitor display, and each of the actuators. The actuators are the height adjustment, outrigger drive, and shift pedal operation and each of them are controlled with the actuator control unit. A block diagram of the electrical structure is shown in Fig. 9.

The control unit is mounted in the motorcycles rear seat cowl. The actuators are driven with 24 V electricity.

### 3.3. Visual Monitor for Outrigger Motion

The visual monitor is shown in Fig. 10. When the motorcycle comes to a stop it is essential that the outrigger be lowered, otherwise, the motorcycle will fall over. Therefore, an indicator showing the outrigger’s position was installed; however, it did not completely reconcile the fears of the rider. In order to resolve this issue, a camera with the ability to capture both the right and left side was mounted at the pivot point of the outrigger and a monitor that continually displays the condition of the outrigger was mounted on top of the tank shelter. When the outrigger is down the wheel is shown in the middle of the monitor allowing for better visibility and abating an element of the rider’s anxiety.

### 3.4. Gas Pressure Emergency Stand

The gas pressure emergency stand is shown in Figs. 11 and 12. The gas pressure emergency stand was developed for dealing with the situation where both the non-operation of the outrigger and stalling of the engine occur simultaneously. In order to make the system as compact as possible, an inflatable mat was used for the system. When it deploys, it is required to hold up the weight of both the motorcycle and the rider, therefore it requires considerable strength. To meet these requirements and to increase the capability to withstand pressure, polyester textile base, which is durable and does not stretch, was used for the mat. In addition, polyester thread and circumferential nylon belts were added to give it more rigidity. It operates instantly through the simple pulling of a rope with the right hand causing a hole to be opened in the system gas cylinder. Through optimizing the hole size, the air tube and flow resistance in the joints, the speed of the emergency stand expansion is sufficient. The mats are mounted under the footrests on the right and left sides (10 liters in total), can be inflated to 100 kPa, and through coming in contact with the ground help prevent the motorcycle from falling over.

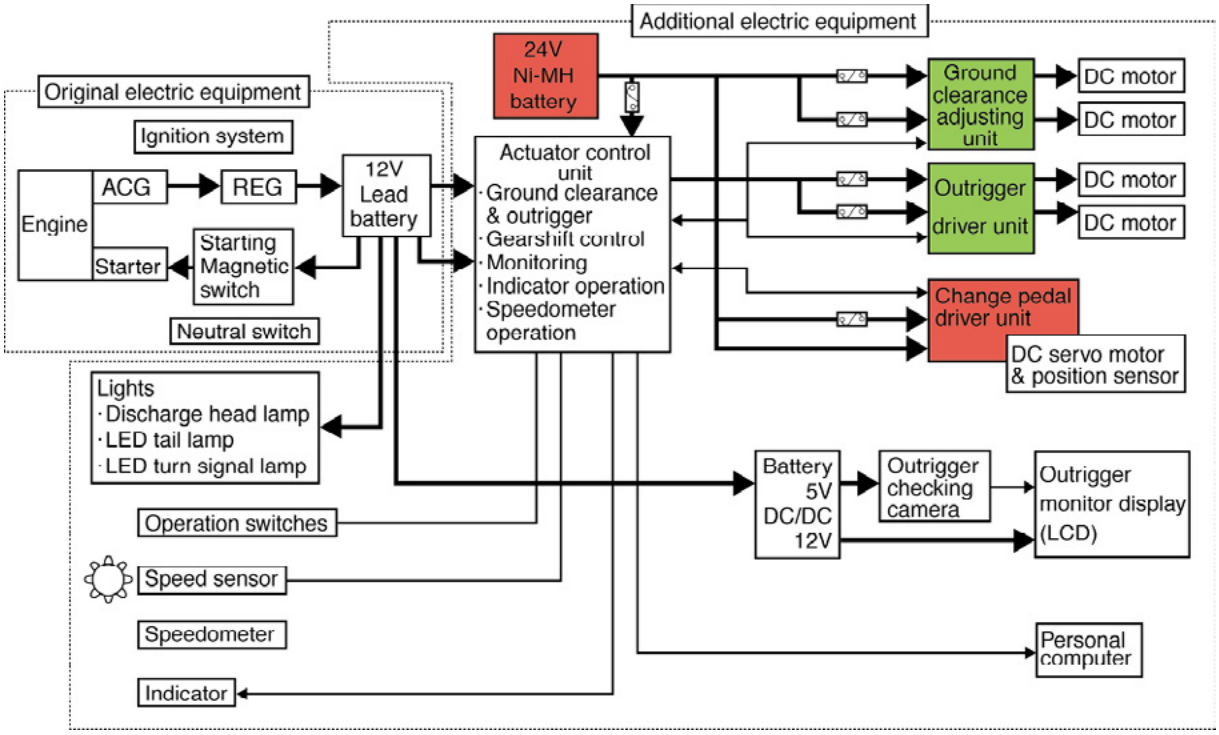



Fig. 9 Illustration of electric circuit



Fig. 10 Monitor of outrigger position

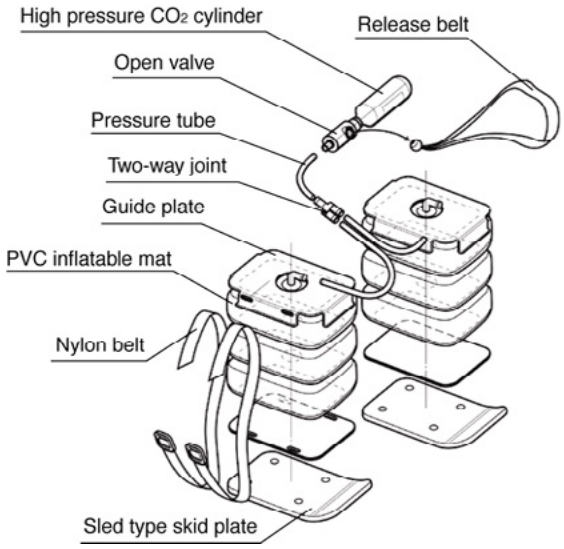



Fig. 11 Structure of gas pressure type emergency stand

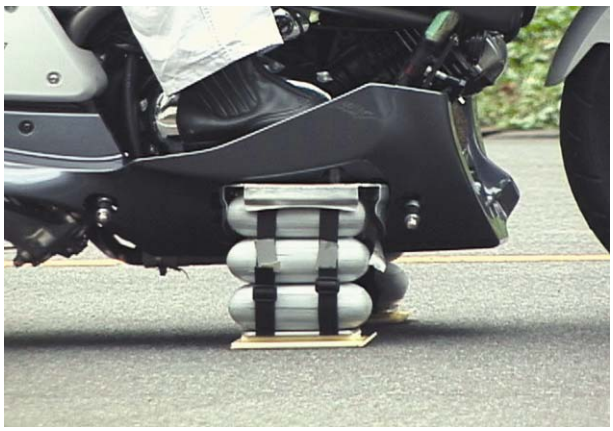


Fig. 12 Side view of gas pressure type emergency stand

### 3.5. Manual Control Gear Shift Mechanism

The manual control gear shift mechanism is shown in Fig. 13. When the paddle switch on the left handle is lowered, an actuator with a 24 V power supply is activated and through a link the shift spindle is rotated. This causes a gearshift into low gear or down one gear, depending on the original gear (if this paddle switch is pushed up, the opposite of what has been describe occurs and causes a gearshift up one gear). If the button on top of the handlebars is pressed while in low gear, the motorcycle shifts into neutral. The clutch lever is the same one that is used on the base motorcycle, the Magna 250.

In order to help reduce rider errors to the extent possible, the operating systems for the brake (front and rear combined) were placed by the right hand, and for shifting (electric shift) a button was placed by the left hand.




Fig. 13 Manual control gearshift system

### 3.6. Moveable Tank Shelter that also Serves as Support when Getting On and Off

The moveable tank shelter is shown in Figs. 14 and 15. When getting on and off the motorcycle from a wheelchair, a large fuel tank in a high position becomes an obstacle. Therefore, the fuel tank was installed to the bottom of a shelter, providing a “tank shelter”. When getting on and off, it is possible to lift up the entire tank shelter. When the tank

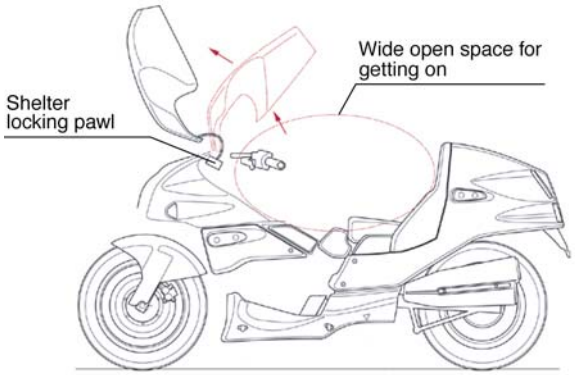



Fig. 14 Layout of movable shelter

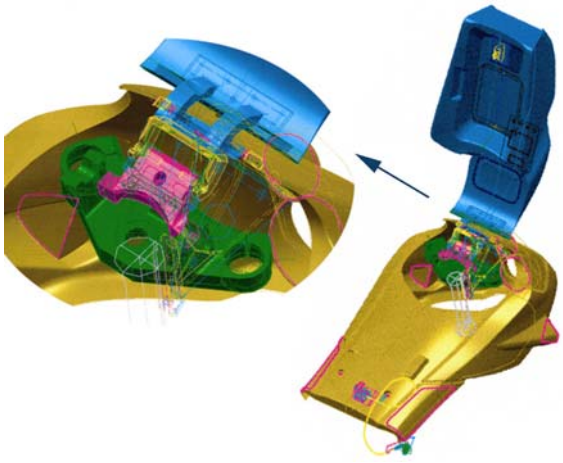


Fig. 15 3D drawing of movable shelter

shelter is raised, the projection of the hinge fits into the handle bars making it so they can not move. As a result, a large open space is generated in front of the seat allowing the rider to easily lift and move his legs and straddle the seat. Also, as the rider moves from the wheelchair to the motorcycle, the fixed handlebars can be used for support. When the fuel tank shelter is then lowered it helps prevent the rider from moving forward or backward on the seat providing a more stable seat position. Also, the step board and the half step on the left side, as well as the form of the specially shaped seat help provide handling support and aid in getting on and off.

### 3.7. Loading Device of Wheelchair

The equipment used to load the wheelchair is shown in Fig. 16. To the rider, the wheelchair provides the same functions as legs to a person who is not disabled, and is something that can not be parted with in order to move freely. Therefore the wheelchair needs to be with the rider at all times, making the ability to carry the wheelchair an obvious requirement and the rider needs to be able to easily and quickly load and unload the wheelchair. The following instructions show how this is done:

(1) After getting on the motorcycle, the rider folds up the wheelchair. Next he/she pulls the wheelchair in until the inside wheel comes into contact with guide rail ‘A’ by his/her right hand.
(2) Using the rotation of the wheelchair’s inside wheel, the rider uses his right hand to lift the wheelchair onto guide rail ‘A’.
(3) When the wheelchair is lifted it comes into contact with guide rail ‘B’ where its leaning is corrected and rolls up onto guide rail ‘C’. The upper surface of guide rail ‘C’ is smooth and the wheelchair slides to the rear of the motorcycle under its own weight and is locked into place due to contact with the end plate.

The process of loading the wheelchair can be performed in a matter of seconds.

## 4. Running Test

The running tests were performed at the Suzuka and Motegi circuits where the maximum speed reached was 130 km/h.

It was possible for a person without the use of his legs, whom requires the use of a wheelchair, to get on and off and to control this motorcycle by him/herself without assistance. The goal of having the feel of a motorcycle and allowing its riders to fully enjoy controlling it without assistance was considered fulfilled.

Figure 17 shows the driving condition of the test and Fig. 18 shows a standstill condition.



Fig. 17 Running view of Super EARA



Fig. 18 Stopping view of Super EARA

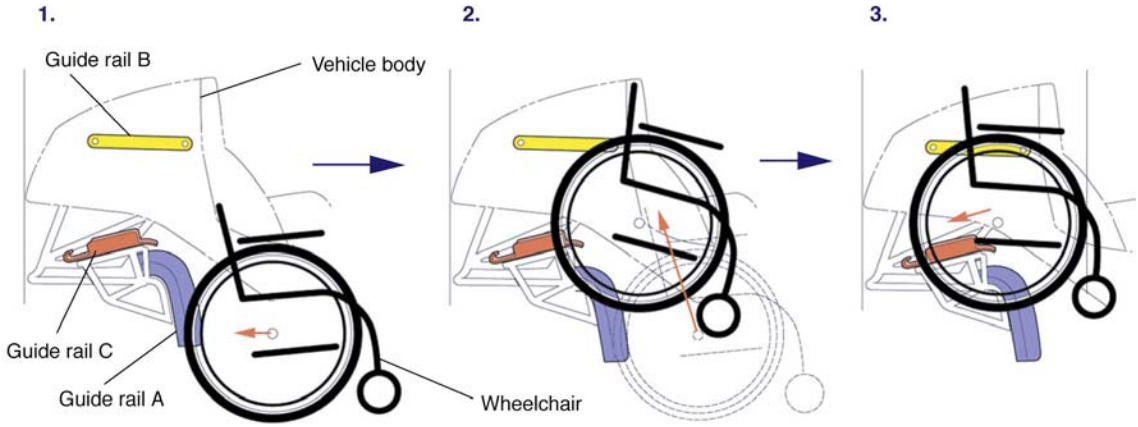



Fig. 16 Wheelchair carrying equipment

It was also possible to test the motorcycles ability for self-support, though on a limited course; however, the expected operation of the system was confirmed. As the riders gained experience they became better at retracting and lowering the outrigger when starting and coming to a stop. They also became faster at adjusting the height of the motorcycle and became very good at driving it smoothly. They were also able to easily use the visual monitor to confirm operation of the outrigger.

## 5. Conclusion

The technology achieved at this time is such that it can only be used for driving on a circuit track or other limited courses. The motorcycle was demonstrated at some major events such as Moto-GP (Suzuka, Motegi) and the Suzuka eight-hours endurance race. This provided a good opportunity to display the technology and numerous motorcycle fans as well as people who live with wheelchairs have given their warm approval.

## 6. Afterword

It is possible for disabled persons to drive a car on public roads. In the future we hope that through the development of this technology that this will also be realized for motorcycles.

■ Authors ■


Kunihiko HASHIMOTO


Yutaka MURATA


Yukiya UEDA


Takashi KUDO


Kousuke TSUNASHIMA


Kyo TAKAHASHI

# Development of High-power, High Fuel Economy BF150 Outboard Motor

Makoto YONEZAWA* Yoshiyuki MATSUDA* Hiroki TAWA*
Sadafumi SHIDARA* Keiichiro BUNGO* Yukio SUZUKI*

## ABSTRACT

Honda has developed a 4-stroke (4st) 110 kW (150 hp) engine for the highly popular 150 hp class of the outboard engine market. A variety of technologies have been employed to increase power and reduce weight to produce a 4st engine in a horsepower class normally associated with 2-stroke (2st) engines and equal the performance of competitors' 2st engines.

To increase the power of the engine, automotive engine technologies including DOHC-VTEC were employed, together with a dual control cooling system (unique to outboard motors) and a variable intake port system utilizing butterfly valves. Improved performance was achieved through the application of weight saving technologies including a resin engine undercover manufactured using a new production process and a new oil case structure and the employment of a gear case that lowers the gear ratio to cope with the demands of the large propeller.

Increased fuel efficiency was achieved through the employment of lean-burn using linear air/fuel ratio (LAF) sensor control in a world first for an outboard motor.

As a result of the technologies outlined above, a 15% increase in specific power (kW/L) was achieved in the new outboard versus previous Honda models. The motor satisfies the emission requirements stipulated in the 2008 CARB regulations while increasing fuel efficiency by 20% versus the previous model in the same output range, and offers an excellent balance between running performance and fuel economy. In actual offshore use, the top speed and acceleration of the new outboard match those of competitors' 2st engines.

## 1. Introduction

Large-class outboard motors (74 kW [100 hp] and over) account for approximately 22% of all outboard motors in use around the world (FY2000; Honda research), and the total number is approximately 144 000 units.

Honda first marketed a model in this class in 1998, with the BF130/115[(1)]. The company continued its production of engines in the class with the BF225/200[(2)] in 2001, and the BF175, a detuned BF200, in 2002.

Sales of engines in this class are increasing with the general expansion of the total market for outboard motors. Against this background, the market demand for engines in the output class between 110 kW and 147 kW

* Asakahigashi R&D Center

(150 hp-200 hp) has increased rapidly as a result of their excellent fuel economy and ease of use and increased environmental consciousness among users. However, at present, outboards fitted with 2-stroke direct-injection engines (2st DI) have the strongest commercial appeal from the perspective of fuel economy, and make up close to half the market share in the class. For Honda to really compete in this class it was essential not only to produce an outboard that bettered the economy and environmental performance of other motors on the market, but to employ technologies giving the motor a market-leading fuel economy and a low weight and level of power output equal to competitors' 2st outboards while maintaining the high reliability of a normal 4st outboard.

## 2. Development Goals

The target in the development process was the achievement of a superb balance between running performance and fuel economy. Specifically, this meant the achievement of the top level of specific power (kW/L) for a 4st outboard motor, and the top level of fuel economy for any outboard motor.

The achievement of these targets would involve employing;

- DOHC-VTEC
- A resin variable intake manifold
- A dual controlled cooling system (A first for an outboard motor) to increase engine power.

The improvement of running performance would involve;

- Reduction of the weight of the outboard (Target: lower weight than the BF130)
- Employment of a gear case designed for use with a large propeller.

Fuel economy was improved through the achievement of;

- Lean-burn employing an LAF sensor control (a first for an outboard motor).

In addition, the new outboard was provided with the various alert control mechanisms employed in the flagship of the Honda outboard range, the BF225, and the use of stainless steel in the bracket system components was increased, as part of efforts to enhance the commercial appeal of the motor through the achievement of class-topping reliability and thorough consideration of ease of operation and maintenance.

As indicated above, the BF150 was developed to be the top of its class in running performance, fuel economy, reliability, and handling, in fact in every aspect of outboard performance.

The external design of the new outboard is based on the integrated lines of the Wing Form which was extremely well received in the market when employed in the BF225, and the motor strongly reflects the high level of advancement of Honda outboards. Figure 1 shows an external view of the BF150.

## 3. Main Specifications and Overview

The main specifications of the BF150 are shown in Table 1.

The engine shares the main drive components, including the crankshaft and connecting rods, with the 2.4L in-line 4-cylinder engine employed in the 2003 US Accord. A 4-valve DOHC system, which features a 3-rocker arm VTEC mechanism on the intake side only, was employed for the valve system. To modify the engine for use in an outboard motor and enable it to be positioned vertically, the lubrication and cooling systems utilized in the automotive engine were extensively redesigned, based on knowledge obtained from the development of the BF130. The BF150 employs the automotive cylinder head used in the BF225, meaning that no special facilities are required for the production of a cylinder head exclusively designed for this outboard, thereby lowering production costs. The dimensions of the engine cover were established on the basis of considerations of interchangability of installation with competitors' 2st motors. The total width was set to enable the pitch with two motors mounted to be compatible with that of already available 26-inch (660 mm) models.

To enable the outboard to be used on high-speed boats, the transom height was reduced by 29 mm against the BF130, and the water screen was positioned lower, ensuring that the motor is able to take in a sufficient amount of cooling water even when trimming up and planing.

Ease of handling was a serious consideration in the design of the new outboard, therefore the BF150 was fitted with a small engine cover, a rear grommet was provided to enable minor adjustments and the maintenance points were concentrated on the starboard side, enabling ease of maintenance. A polypropylene injection-molded undercover was employed to reduce the weight of the motor. A new structure was used in the undercover, designed to ensure rigidity and enable the number of components to be reduced. The number of link components in the shift mechanism was reduced against the previous model, improving the shift feel.




Fig. 1 External view of BF150

Table 1 BF150 L-type Specifications

| | |
|---|---|
| Overall length (mm) | 845 |
| Overall width (mm) | 580 |
| Overall height (mm) | 1 665 |
| Transom height (mm) | 508 |
| Dry weight (kg) | 217 |
| Engine type | 4stroke<br>L-type 4 cylinder |
| Displacement ($cm^3$) | 2 354 |
| Bore (mm) × stroke (mm) | 87 × 99 |
| Compression ratio | 9.6 : 1 |
| Valve train | DOHC-VTEC 16 valves |
| Number of valves | 4/cylinder |
| Maximum power (kW/rpm) | 110 / 5 500<br>(150 PS / 5 500 rpm) |
| Maximum torque (N·m) | 202 |
| Recommended engine rpm range | 5 000 - 6 000 |
| Fuel supply system | Programmed Fuel Injection |
| Ignition system | Programmed Ignition (with Plug Hole Coil) |
| Charge output (A) | 40 |
| Cooling system | Water cooling (with 2 thermostats) |
| Exhaust system | Through propeller hub |

The LAF sensor employed to achieve lean-burn is based on the model utilized in automotive applications, but was altered to enable it to be fitted directly to the exhaust manifold and to increase its toughness with regard to water immersion from the exhaust pipe. The newly developed ECU employs the various alert mechanisms utilized in the BF225, and is based on an automotive program, but utilizes special settings for an outboard motor.

## 4. Component Technologies

### 4.1. Technologies Employed to Increase Engine Power

#### 4.1.1. Dual controlled cooling system

The BF150, in a first for an outboard motor engine, was provided with independent cooling systems for the head and the block, increasing both the knock limit and the power output of the motor.

In a normal engine, the cylinder head and cylinder block water jackets are connected by the gasket face, and one thermostat is employed to control water temperature.

However, when an outboard employing this conventional system directly takes in sea water, etc., for cooling, excessive cooling on the cylinder block side may cause oil dilution. Therefore, it is not practical to lower the set water temperature in the control system below a fixed point. This prevents more effective cooling being provided to the cylinder head side, which represents an obstacle to increasing power.

In the BF150, therefore, the head gasket was used to completely separate the cooling water routes for the cylinder head and the cylinder block, making them entirely independent. Two thermostats are used to provide separate water temperature control for each route. This means it was possible to make the control temperature for the thermostat on the cylinder head side (50 °C) lower than the control temperature on the block side (60 °C), leading to an increase of approximately 8° in the knock limit and approximately 2.5% in engine power.

In addition, the exhaust manifold and oil gallery are cooled by cooling water routes which are divided from the cylinder head and block routes. Figure 2 shows a diagram of the cooling water routes in the BF150.

#### 4.1.2. Resin variable intake manifold

To balance high torque at low and medium engine speeds with high power at high engine speeds while at the same time as reducing weight and increasing corrosion resistance, an all-resin variable intake manifold was employed in the BF150.

The variable intake port system in the BF150 employs butterfly valves to vary the length of the intake pipe in two stages. The effect of this system is multiplied through its employment in combination with VTEC, enabling the outboard to display both flat torque from low to high engine speeds and high power. Figure 3 shows an outline of the variable intake port system, and Fig. 4 shows a graph of the power curve of the BF150.

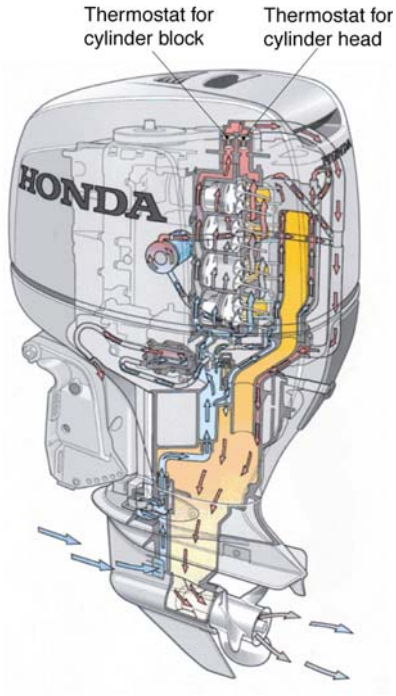



Fig. 2 Dual control cooling system

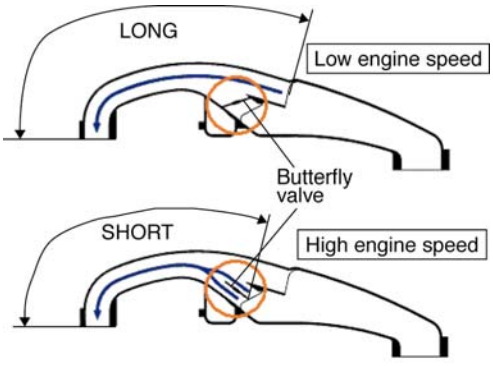



Fig. 3 Variable air intake port system

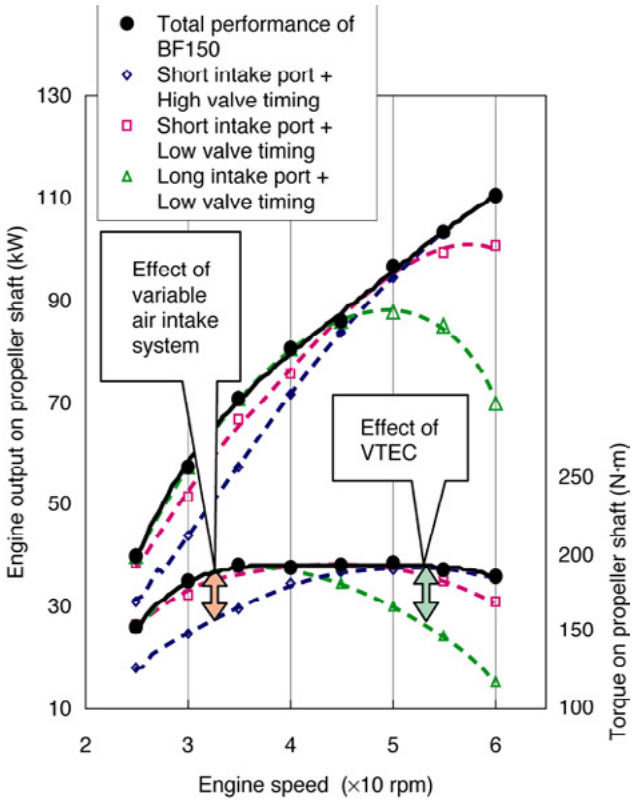



Fig. 4 Power curve of BF150

The number of component parts was reduced by integrating the vacuum tank used to operate the valves, the diaphragm body and the check valves with the main body. In combination with the use of resin materials, this reduced the weight and increased corrosion resistance. The butterfly valves that enable switching between intake lengths were also made of all-resin, with resin materials employed in the main body and the bearings. This reduced the weight by 2.7 kg against the aluminum die cast model. Figure 5 shows a cutaway view of the variable intake system.

The technologies described above were employed to increase the power of the motor, and enabled specific power (kW/L) to be increased by 15% against the BF130, and gave the motor the highest specific power of any 4st outboard. Figure 6 shows a graph comparing the specific power of the BF150 with other models.

## 4.2. Technologies Employed to Improve Running Performance

### 4.2.1. Weight reduction technologies

To reduce weight, in addition to the resin variable intake manifold, a lightweight resin engine undercover manufactured using a new production process was employed, and the oil case was integrated with the upper section of the extension case.

(1) Lightweight resin engine undercover (manufactured using new production process)

When a resin engine undercover is employed in a conventional outboard, metal components are used to reinforce the interior to prevent deformation of the cover when the motor is being carried horizontally. In the BF150, a blow-molded internal frame is welded to the interior of an injection-molded external cover in order to lower weight and reduce the number of components in the support structure. The employment of this structure reduced the weight by 1 kg. Figure 7 shows the structure of the engine undercover.

(2) Oil case structure

In conventional oil case structures, the oil pan is covered by the extension case with the exhaust pipe mount on it and cooling water flows inside the case in the form of a shower to reduce transmitted noise from the exhaust. In an effort to achieve significant weight reductions in the BF150, the oil pan and exhaust pipe were integrated, and the oil case was integrated with the upper section of the extension case. The exhaust pipe is positioned in the approximate center of the oil case. In addition to ensuring that the exhaust outlet is located at a sufficient distance from the external cover, this structure

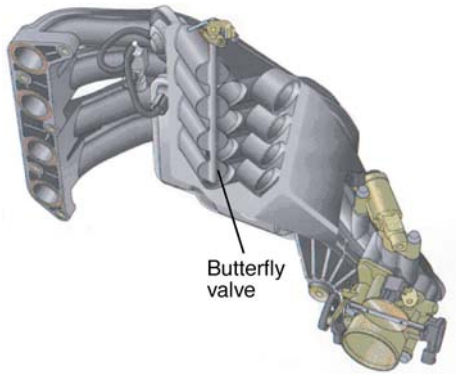



Fig. 5 Cutaway view of intake manifold

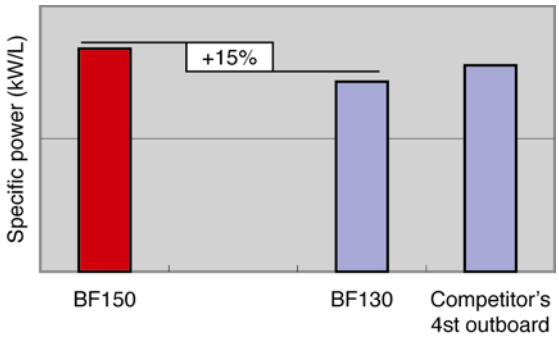



Fig. 6 Comparison of specific power

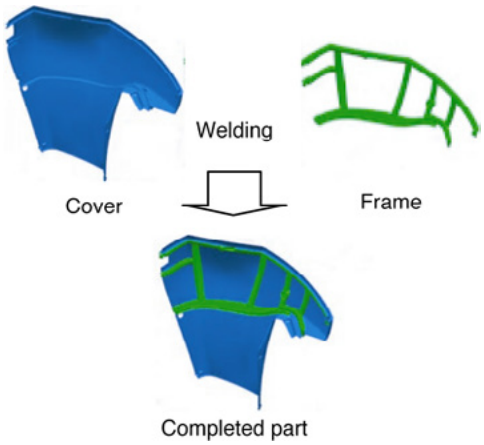



Fig. 7 New product engine undercover

divides the interior of the oil case by means of the oil pan, minimizing the resonating internal surface area and suppressing transmitted noise from the exhaust. The new structure also reduced the weight by 2 kg. Figure 8 shows a cutaway view of the oil case structure.

### 4.2.2 Redesign of the drive system

The gear case of the new outboard was redesigned to enable weight to be reduced in spite of the increased diameter of the housing required for the large diameter propeller, formerly used in the BF225.

To match the gears with the large diameter propeller, the gear ratio was lowered, and the gears were increased in diameter in accordance with the increased diameter of the housing, thereby increasing durability. As a result, the BF150 equaled the top speed and acceleration time over 200 m from a standstill of a competitor's 2st DI outboard in the same class.

Figures 9 and 10 show comparisons of the top speed and acceleration time of the BF150 with a competitor's 2st DI respectively.

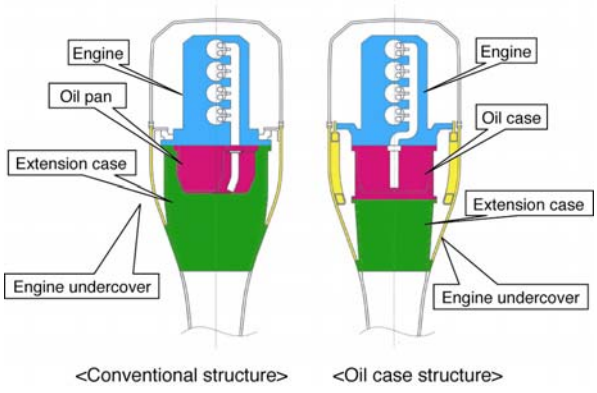



Fig. 8 Cutaway view of oil case

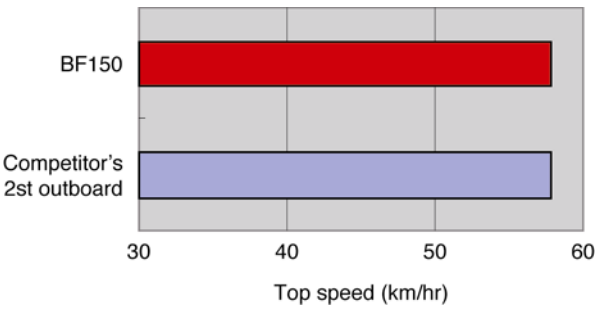



Fig. 9 Top speed

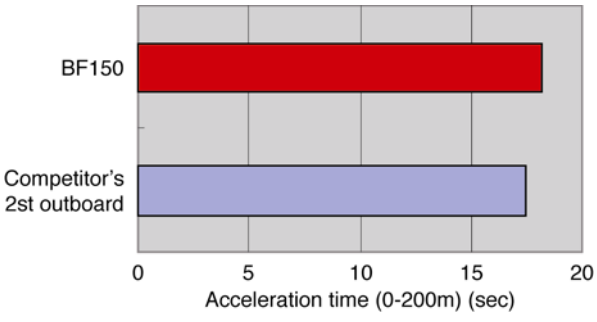



Fig. 10 Acceleration performance

## 4.3. Technologies Employed to Increase Fuel Economy

### 4.3.1. Achievement of high fuel economy with lean-burn

PGM-FI is used in the intake and fuel systems of the BF150 to enable the motor to both meet a variety of international exhaust emissions regulations and significantly exceed the fuel economy performance of competitors' outboard motors. In addition, lean-burn control using LAF sensors was utilized for the first time in an outboard motor. As a result, the fuel consumption of the BF150 in emission measurement mode is 20% lower than the Honda BF130 and 15% lower than a competitor's 2st DI outboard with the same power rating. A comparison of fuel consumption is shown in Fig. 11.

For users to clearly recognize how good the fuel economy of an outboard motor is, it is essential for the motor to display excellent fuel economy at cruising speeds, which are used most frequently. The BF150 employs lean-burn up to an engine speed of 4 700 rpm, enabling users to be aware of its excellent fuel economy when used with any watercraft.

The air-fuel ratio for lean-burn was set at A/F = 18 to achieve a balance between fuel economy and drivability. To control sudden increases in power output when the motor goes from a lean to a rich ratio, the BF150 was provided with a throttle cam with a nonlinear opening characteristic ensuring excellent output control.

Figure 12 shows the effect of lean-burn in reducing fuel consumption in use on a standard boat, and Fig. 13 shows the lean-burn area. The throttle body is shown in Fig. 14.

The BF150 cleared the final year (2008) values for the CARB marine emissions regulations, and achieved an ULTRA-LOW emissions rating. The motor also passed in advance the emissions regulations that go into effect in the EU in 2006. Figures 15 and 16 show the emissions levels achieved by the BF150.

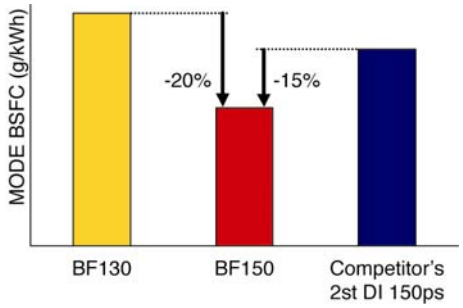



Fig. 11 BSFC in emission measurement mode

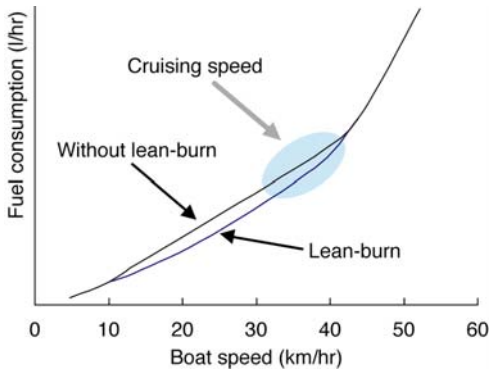



Fig. 12 Effect of lean-burn

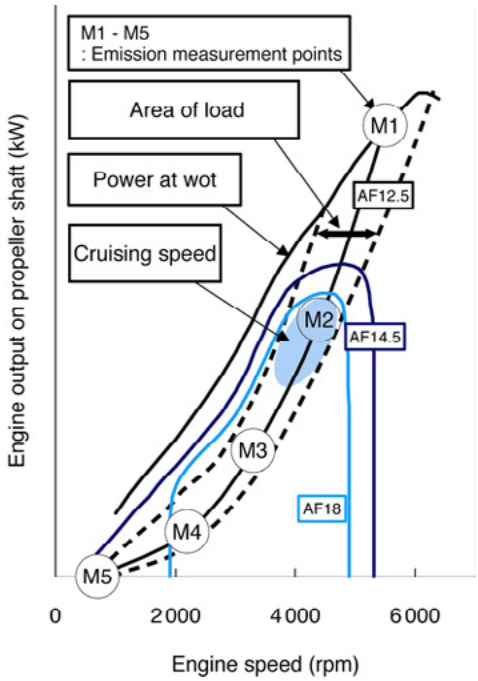



Fig. 13 BF150 lean-burn area

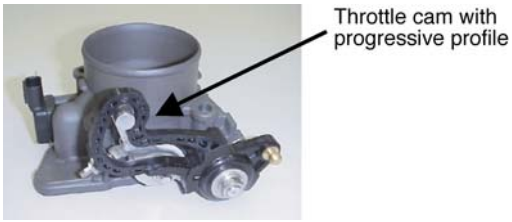



Fig. 14 Throttle body

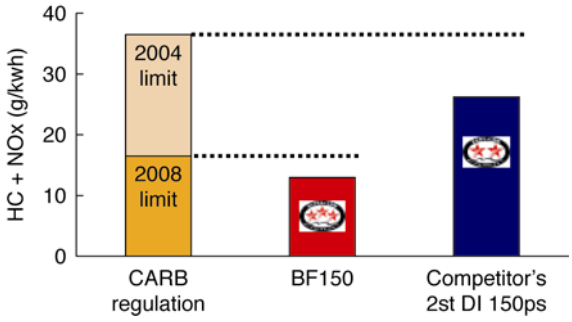



Fig. 15 Level of exhaust emissions (CARB)

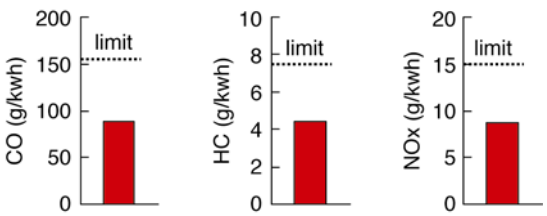



Fig. 16 Level of exhaust emissions (EC)

### 4.3.2. Adapting LAF sensor to outboard use

The LAF sensor employed in the BF150 was based on the model used in automotive applications, but was altered to fit the special conditions of use in an outboard. Specifically, it was modified to enable direct mounting on the exhaust manifold and to increase its resistance to taking in water from the exhaust pipe.

The vibration experienced by the LAF sensor when mounted directly on the exhaust manifold differs from the vibration experienced in an automotive application, and its internal structure was therefore modified.

Because the exhaust channel is in direct contact with sea water, the positioning of the LAF sensor on the exhaust outlet side meant that the unit would sometimes take in sea water. To minimize the amount of water coming into contact with the sensor elements, the sensor was therefore positioned against the upper edge of the exhaust manifold, corresponding to the topmost section of the exhaust channel flow path, and the shape of the sensor protector was redesigned.

## 4.4. Other Element Technologies Employed to Increase Commercial Appeal

### 4.4.1. Chain system for marine use

The BF150 is the first Honda outboard motor to employ a chain to drive the camshaft and balancer shaft.

The design of the system was based on the layout of an automotive engine, and aimed both to reduce the total height of the motor when mounted and to make the system maintenance-free through the use of an autotensioner.

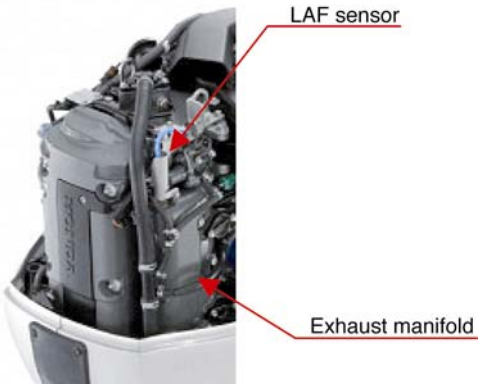



Fig. 17 LAF sensor layout

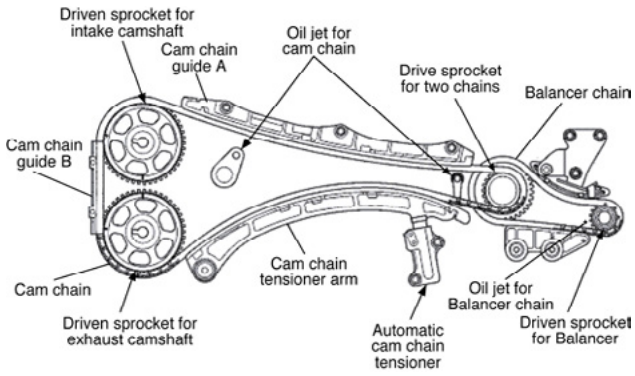



Fig. 18 Camshaft and balancer driving system

The system in the BF150 employs the same components as the automotive system, but the method of lubrication was changed for application in an outboard motor.

In the BF150, the crankshaft is perpendicular and the flywheel is positioned on the underside of the engine. The chain was therefore positioned in the topmost section of the engine. For this reason, if a standard automotive system was employed, in which the oil used to lubricate the cylinder head was then used to lubricate the chain, very little oil would be available to lubricate the chain.

To solve this situation, in addition to employing three new oil jets to provide lubricating oil, the shape of the area around the sprocket was redesigned to hold oil, and oil is directly provided to the chain. This ensures that a sufficient amount of oil is provided to lubricate the chain, helping prevent it from stretching and enabling the achievement of an equally high level of durability and reliability to that of the system employed in automotive engines. Figure 18 shows a diagram of the chain system.

### 4.4.2. Improvement of shift feel

The reduction of the number of links in the shift mechanism against the conventional structure reduced mechanical loss in the connecting sections and increased transmission efficiency, reducing the shift load and improving the smoothness of the shift feel. Figure 19 shows a diagram of the shift mechanism, and Fig. 20 shows a comparison of transmission efficiency under an operating load.

### 4.4.3. Improvement of ease of maintenance

The following structural modifications were made to increase ease of maintenance:

1) The oil level gauge, oil cap, oil filter and the oil drain and check bolts for the gear case were all positioned on the starboard side to offer ease of access.

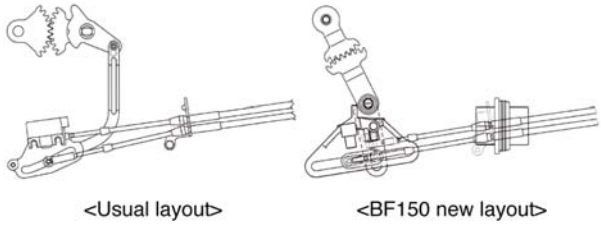



Fig. 19 Comparison of shift change system

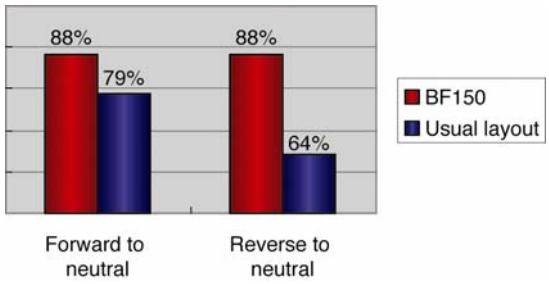



Fig. 20 Power efficiency of newly designed shift change system

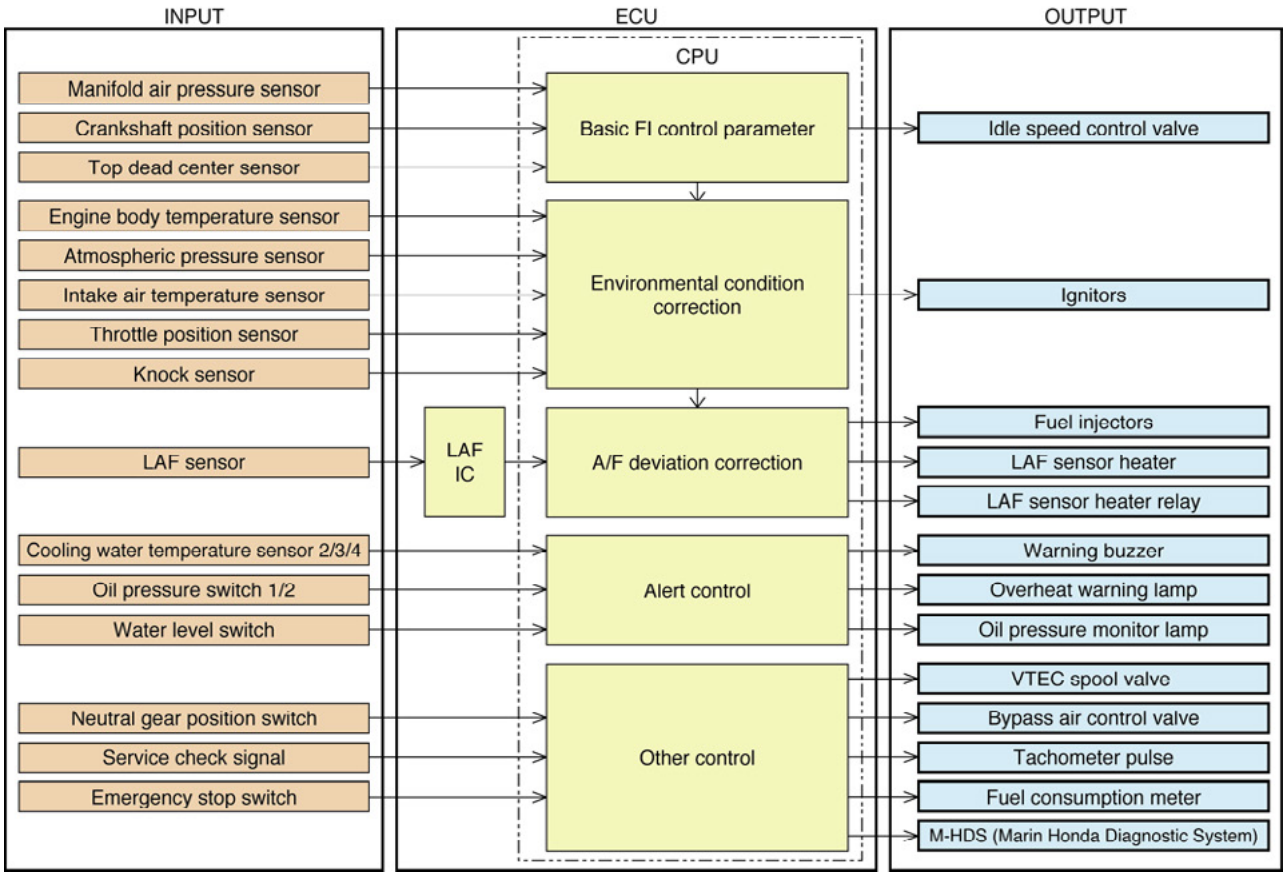



Fig.21 BF150 engine control system

2) The drain plug cover was placed in the engine undercover, which can be removed and replaced in one step, and can also be used to hold the drain oil.
3) The undercover grommet was placed in the rear of the engine cover so that it would be possible to inspect and clean the spark plug of the No. 4 cylinder without removing the engine undercover.
4) A two-part engine undercover was employed to increase ease of disassembly and reassembly.

#### 4.4.4. Engine control system

##### (1) Overall system outline

The engine control system is based on an automotive system, but employs an LAF sensor to enable lean-burn for improvement of fuel economy and an alert system specifically designed for the usage of outboard motors, which has been used since the BF130 model. The utility of the system was increased through the use of digital meters and diagnostic mechanisms. Figure 21 shows a diagram of the control system.

##### (2) Alert and control systems

The following alert and control systems were employed to ensure that the BF150 has an equivalent level of reliability to the flagship model, the BF225.

1) Overheat alert

The cooling system of an outboard motor directly takes sea water, etc., into the engine. Matter floating on the surface of the water may therefore block the water inlets or the cooling routes, causing cooling performance to fluctuate. The cooling system of the BF150 employs a new structure, and overheat detection sensors were positioned at the cylinder head, the cylinder block and the exhaust manifold to accurately detect blockages in any of the cooling routes. This system helps ensure that an overheating alert is given if the temperature at any of these detection points increases over a predetermined level for each point. When overheating is detected, the algorithm cuts the fuel supply, stops the spark plug firing, and progressively reduces engine speed. If this does not correct the overheating, the system finally shuts down the engine. During this period, a buzzer and a warning light indicate the situation to the user.

2) Other alert systems

To help prevent oil pressure from becoming low when the user forgets to adequately fill the oil, the BF150 is provided with high and low oil pressure switches, as employed in the BF225/200. The system monitors oil pressure, and sounds an alert if the oil pressure is too low for a particular engine speed. Buzzers and warning lights also indicate malfunctions in the alternator as well as if there is water pooled in fuel tank, so as to help keep it from infiltrating into the fuel lines.

##### (3) Backlash detection and control system

Because an outboard motor has no brakes, there are times when the shift lever is suddenly changed from forward to reverse to avoid danger when the engine is running at high speed. When this happens, the momentum of the boat causes backlash in the engine through the propeller. The control system in the BF150 monitors changes in the angular velocity of the crankshaft and can detect the transition to backlash the instant it occurs, ensuring that the engine can be brought to a smooth stop without the adverse affects of backlash.

#### 4.4.5. Utility

##### (1) Digital meters

There has recently been a high level of demand for digital meters to be offered as options on outboard motors, in order to provide the user with a higher quantity of more accurate information and make that information easier to read. The BF150 is the first Honda outboard to employ digital meters. In addition to displays showing craft speed and engine speed, the motor has a fuel consumption display which accurately calculates the amount of fuel injected from the time required for injection. The digital meter is shown in Fig. 22.

##### (2) Diagnostic mechanism

As an aid to service and maintenance, as on Honda's other outboards, if a sensor failure or other malfunction is detected, buzzers and warning lights indicate the malfunction and the number of times the warning light flashes indicates where the malfunction is occurring. In addition, the system remembers the status of the control systems in the engine when the malfunction occurred, and the Marine Honda Diagnostic System (M-HDS) can be used to read it from the diagnostic communications port, enabling the malfunction to be easily located. The M-HDS is shown in Fig. 23.

## 5. Conclusion

The application of the component technologies described in Section 4 has resulted in the following improvements to the BF150 against the BF130:

(1) Specific power (kW/L): 15% increase (Top level for a 4st outboard motor)
(2) Mode fuel consumption: 20% decrease (Top level for an outboard motor; 15% decrease against competitor's 2st DI)
(3) Total weight: 5 kg decrease (15% decrease in power-weight ratio)
(4) In terms of running performance (in an offshore boat), the BF150 has an identical top speed and acceleration over 200 m as a 2st DI motor.




Fig. 22 Digital meter with fuel consumption gauge




Fig. 23 M-HDS

## 6. Afterword

The BF150 is a model that will play an extremely important role in establishing Honda's large class outboard motor lineup in the market, looking towards the expansion of the company's OEM business.

The adaptation and employment of existing automotive technologies and structures and the active development and application of new mechanisms and structures unique to outboard motors has given the new model a level of appeal not possessed by other outboards on the market, making it a highly commercially viable product.

The experience of creating the BF150 was an extremely valuable one for the design team. The new motor is an embodiment of their persistence in staying true to "Challenging Spirit," the mainstay of Honda's product development efforts, their active pursuit of their goals from the stage of proposal of product targets and the consistency of their methods of achieving those targets from the initial stages of design.

This development received generous assistance from numerous individuals from Honda and other companies, including staff members of a number of manufacturing centers. In particular, it was of tremendous help to receive direct advice concerning the adaptation of the automotive engine to an outboard motor application from the team which developed the engine[3]. The authors wish to take this opportunity to once again offer their sincere thanks to everyone who assisted in this project.

## References

(1) Tsunoda, M., Shidara, S., Shimazaki, W., Rinzaki, S.: Development of Large-sized 4 Stroke Outboard Motor "BF115/130", HONDA R&D Technical Review, Vol. 11, No. 1, p. 15-22 (1999)

(2) Tsunoda, M., Furuya, K., Ohsumi, M., Shidara, S., Yonezawa, M., Kimata, R.: Development of Honda Flagship Outboard Motor "BF225/200", Honda R&D Technical Review, Vol. 14, No. 1, p. 11-20 (2002)

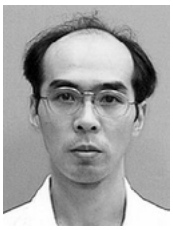
(3) Niizato, T., Hayashi, A.: Development of New 2.0L Lean-burn Engine, HONDA R&D Technical Review, Vol. 12, No. 2, p. 45-54 (2000)

■ Authors ■


Makoto YONEZAWA


Yoshiyuki MATSUDA


Hiroki TAWA


Sadafumi SHIDARA


Keiichiro BUNGO


Yukio SUZUKI

# Development of High-performance and Low-emission Direct Injection Gasoline Engine

Yutaka KOHDA* Tomoji SUGANAMI*
Hiroyuki KOBAYASHI* Ken OGAWA*

## ABSTRACT

Honda has developed the first-ever 2.0L i-VTEC I direct injection gasoline engine employing a center injection system in which a high-pressure fuel injector is located in the center of the combustion chamber. This engine significantly improved fuel economy and emissions performance. Optimization of in-chamber fuel flow through a redesign of piston shape, the spray characteristics of the high-pressure fuel injector, and the application of VTEC has enabled the achievement of stable combustion of a stratified ultra-lean air-fuel mixture. Due to the VTEC mechanism and the continuous variation of the camshaft phase enabled by VTC, the engine has achieved top-class power for a high fuel economy engine. The new engine is fitted in the 2004 Stream that, in combination with the CVT employed in the vehicle, has enabled the Stream to achieve a low fuel consumption figure of 15.0 km/l in Japanese 10 - 15 mode. A large amount of EGR and a high-performance lean NOx catalyst to reduce emissions has further enabled the Stream to become the first vehicle with an engine employing ultra-lean stratified charge combustion to achieve an emissions level of only 25% of the level stipulated by the Japanese 2000 emissions regulations and obtain Ultra Low Emission Vehicle (ULEV) certification.

## 1. Introduction

The automotive industry has progressed with the development of power plants with a focus on the achievement of high fuel economy and low emissions. This focus has been in response to increasing concern towards the global environment. In particular, a variety of direct in-cylinder fuel injection gasoline engines have been developed, given the efficacy of direct injection in increasing the fuel efficiency of spark ignition internal combustion engines[1), 2)]. Honda has also responded to the challenge by putting its next-generation power plant, the i-series[3), 4)], into production. In a further development, the 2.0L i-VTEC lean-burn engine developed for the 2000 model Stream[3)] has been used as a base in the development of the world's first 2.0L i-VTEC I direct injection gasoline engine. An original concept of center direct injection was employed in the new engine to enable the achievement of ultra-lean stratified charge combustion in order to improve fuel economy and reduce emissions. This paper discusses the technologies employed to achieve ultra-lean combustion in the 2.0L i-VTEC I direct injection engine, which was previously considered a challenging issue in a direct injection gasoline engine.

## 2. Development Goals

The development concept for the new model Stream, in which this engine is installed, was to achieve a balance between superior environmental performance and sportiness.

* Tochigi R&D Center

A CVT is employed to take the significant gains in fuel efficiency achieved through the use of a direct injection engine to an even higher level. The increased power of the direct injection engine and the optimization of the ratio through the use of CVT would enable the achievement of both excellent dynamic performance and a high level of environmental performance. The specific targets of the development were as follows:

(1) High fuel economy (10 - 15 mode: 15.0 km/l)
(2) Low emissions (Ultra low emissions level – Reduction of emissions level by 75% against values stipulated by 2000 regulations)
(3) High power for sporty performance

## 3. Overview of Engine / Specifications

Figure 1 shows an external view of the engine, and Table 1 shows a comparison of the specifications of the newly developed K20B engine and the previous K20A engine. The effectiveness of direct in-cylinder fuel injection in increasing intake air charging efficiency and suppressing knocking is well known[5, 6]. The most distinctive feature of the new engine is the employment of a center injection system, which makes use of these characteristics of direct injection to achieve ultra-lean stratified charge combustion. This application results in significant improvements in fuel economy, emission performance, and increased power. Figure 2 (a) shows the positioning of the high-pressure fuel injector in the center of the combustion chamber, and Fig. 2 (b) shows the positioning of the spark plug between the exhaust valves. To reduce the space required for this configuration, the diameters of the inlet and exhaust valves have been reduced by 1 and 2 mm respectively compared to the previous model. Optimization of the valve lift profile and the shape of the inlet and exhaust ports has ensured that intake and exhaust efficiency is equivalent or superior to that demonstrated by the previous model, despite the reduction in the diameter of the valves.

In the valve system, VTEC and cam shaft phase continuation variable timing control (VTC) have been employed to balance ultra-lean stratified charge combustion with high power. The higher compression ratio and redesigned intake and exhaust layout of the K20B give it increased torque in the medium- to high-speed range compared to the previous K20A engine. This results in improved fuel economy and running performance. Figure 3 shows the power characteristic of both engines with the throttle fully open.




Fig. 1 K20B direct injection gasoline engine

Table 1 Engine specifications

| Engine Code | | K20B | K20A |
|---|---|---|---|
| Cylinder configuration | | In-line 4-cylinder | In-line 4-cylinder |
| Bore × stroke (mm) | | 86 × 86 | 86 × 86 |
| Displacement ($cm^3$) | | 1998 | 1998 |
| Compression ratio | | 10:1 | 9.8:1 |
| Valve train | | DOHC VTEC | DOHC VTEC |
| Number of valves | | 4 per cylinder | 4 per cylinder |
| Valve diameter (mm) | In. | 34 | 35 |
| | Ex. | 28 | 30 |
| Fuel supply system | | Programmed fuel injection | Programmed fuel injection |
| Fuel injection pressure (MPa) | | 8 - 10.5 | 0.34 |
| Ignition system | | Programmed ignition | Programmed ignition |
| Max.power (kW/rpm) | | 115 / 6300 | 113 / 6500 |
| Max.torque (N·m/rpm) | | 188 / 4600 | 186 / 4000 |

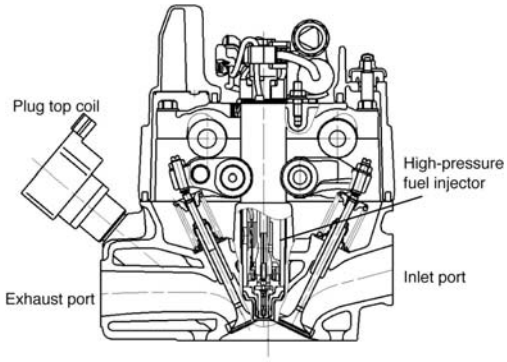



Fig. 2 (a) Section view of cylinder head

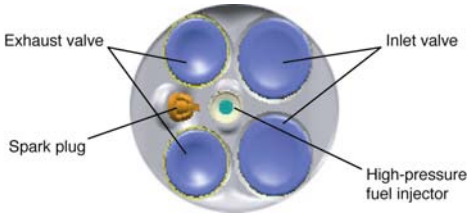



Fig. 2 (b) Configuration of cylinder head

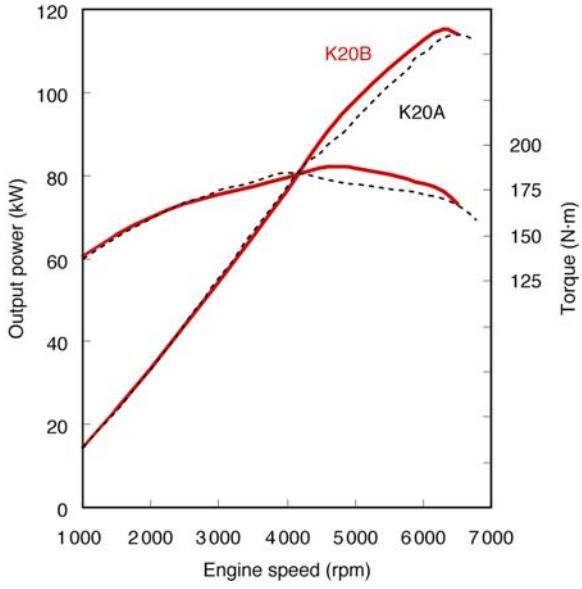



Fig. 3 Engine performance

Figure 4 shows the high-pressure fuel injector and the high-pressure fuel pump that utilizes a single plunger driven by the exhaust cam. Figure 5 shows the spray characteristics of the high-pressure fuel injector. The fuel pressure is controlled within a high range between 8 and 10.5 MPa depending on driving conditions. The pressurized fuel is converted to atomized droplets by the swirl guide channel in the injector before being injected into the cylinder. Atomization brings the diameter of the droplets in the spray to less than SMD12 $\mu$m. The spray characteristic is set for high penetration at an oblique angle to increase the ability to maintain the air-fuel mixture.

## 4. Combustion Concept

The achievement of ultra-lean stratified charge combustion requires the formation and maintenance of a combustible air-fuel mixture and rapid combustion after sparking. The least amount of in-cylinder intake air flow is desirable to form and maintain the air-fuel mixture. On the other hand, it is desirable for in-cylinder flow and turbulence to be stronger to achieve rapid combustion of the air-fuel mixture after sparking in order to increase thermal efficiency. The concept proposed to balance these antagonistic demands was to form and maintain the air-fuel mixture by spray flow using a high-penetration fuel injector positioned in the center of the cylinder and a cavity piston, and to employ the swirl produced by the closure of one valve by the VTEC mechanism to achieve rapid combustion (Fig. 6).

When high power is demanded from the engine, the VTEC mechanism switches to operation of both inlet valves to increase volumetric efficiency, fuel is supplied into the intake stroke, and combustion becomes homogeneous at a stoichiometric air-fuel ratio. This configuration gives the engine high power and high responsiveness. Given that no fuel adheres to the wall of the cylinder in the combustion chamber in this system, it reduces the level of unburned HC compared to the former side injection system. Figure 7 shows the range of each combustion mode in the K20B engine. The figure demonstrates the high degree of freedom of fuel injection timing and the broad stratified charge combustion range achieved by this system.

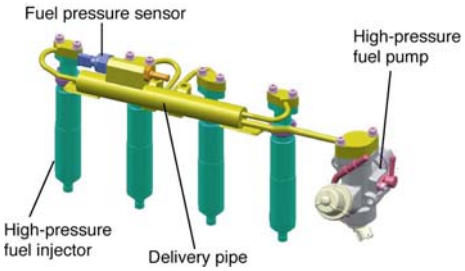



Fig. 4 High pressure fuel system

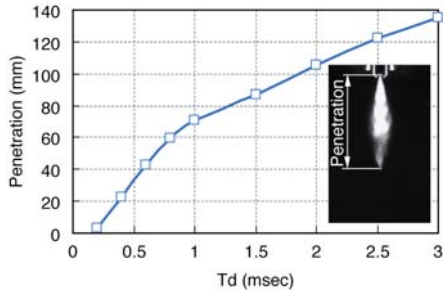



Fig. 5 High-pressure injector spray characteristics

### 4.1. Shape of Piston Cavity

Figures 8 (a) and 8 (b) show external views of the piston. The cavity piston is positioned so that the bottom of the cavity has a slope angle to the spark plug, and the cavity is deeper on the spark plug side. The deepest part of the cavity is deflected towards the upstream side of the swirl. This enables the swirl of air-fuel mixture to be formed in the cavity by the high-speed spray from the injector, maintained,

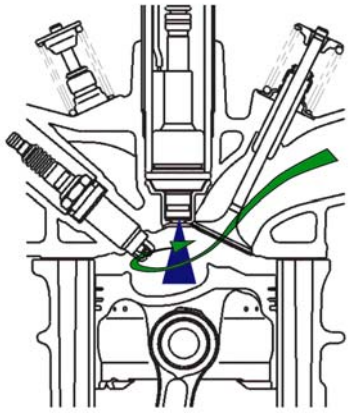


Fig. 6 Combustion chamber configuration

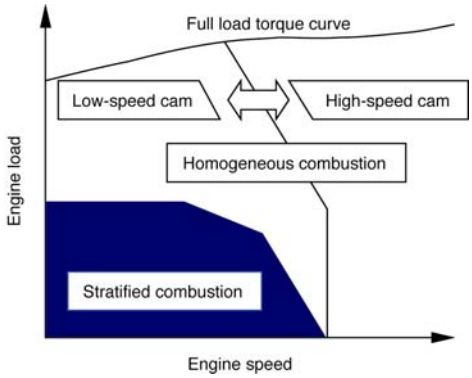



Fig. 7 Map of combustion mode

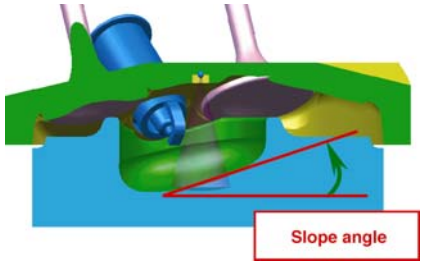



Fig. 8 (a) Section view of piston

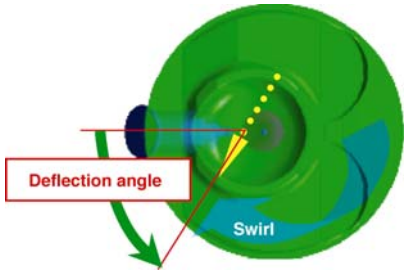



Fig. 8 (b) Top view of piston

and carried by the swirl flow to the spark plug. The volume of the cavity and the angles of slope and deflection were optimized by actual engine tests, visualization of air-fuel mixture in the combustion chamber, and simulations of air-fuel mixture distribution.

### 4.1.1. Establishing cavity specifications

Figure 9 shows the indicated specific fuel consumption (ISFC) characteristic with changes in the cavity volume ratio (ratio of cavity volume to total combustion chamber volume) during stratified combustion. As the cavity volume decreases, ISFC at low loads improves and stratification increases. But, at high loads, the air-fuel mixture in the cavity tends to become over-rich, with a negative effect on ISFC. A cavity volume ratio of 26% was established for the new engine to produce an optimum balance of stratified charge combustion across all engine loads.

The influence of the slope angle of the bottom of the cavity on ISFC is shown in Fig. 10, and the influence of the deflection angle in Fig. 11.

When the slope angle of the bottom of the cavity is low, the air-fuel mixture is not strongly directed to the spark plug. This has a negative effect on ISFC at low loads when the amount of fuel injected is low. The optimum value for the deflection angle of the cavity varies with the strength of the swirl in the cylinder. An angle of slope of 15° and an angle of deflection of 45° were established for the K20B.

### 4.1.2. Distribution of air-fuel mixture

Figure 12 shows the simulation results of the distribution of the air-fuel mixture and air motion during stratified charge combustion. The spray injected into the cylinder during the compression stroke follows the slope of the bottom of the cavity and is guided to the deepest part of the cavity, which deviates towards the upstream of the swirl. The high spray penetration achieved by high-pressure injection creates vertical vortexes from the walls towards the center of the cylinder. These vertical vortexes prevent the dispersion of the air-fuel mixture and increases maintainability, forming a compact agglomeration of the mixture.

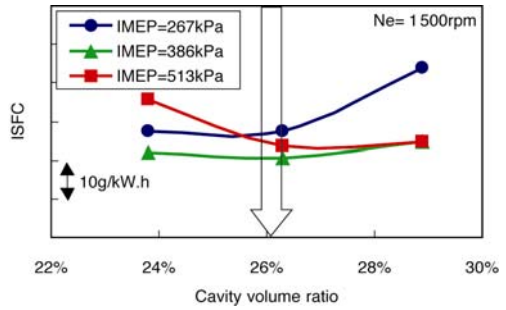



Fig. 9 Influence of cavity volume ratio on ISFC

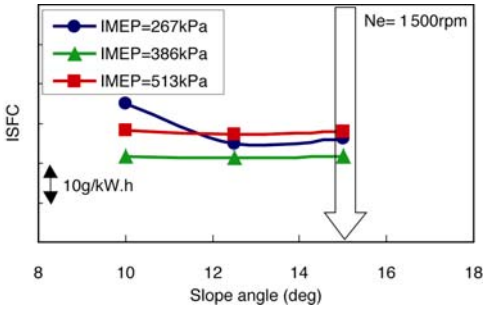



Fig. 10 Influence of slope angle on ISFC

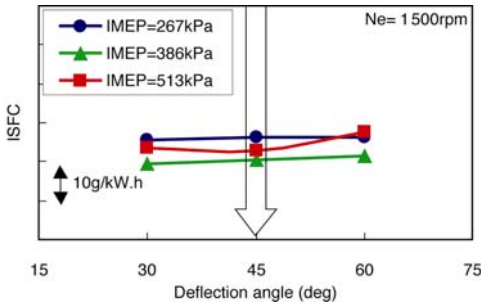



Fig. 11 Influence of deflection angle on ISFC

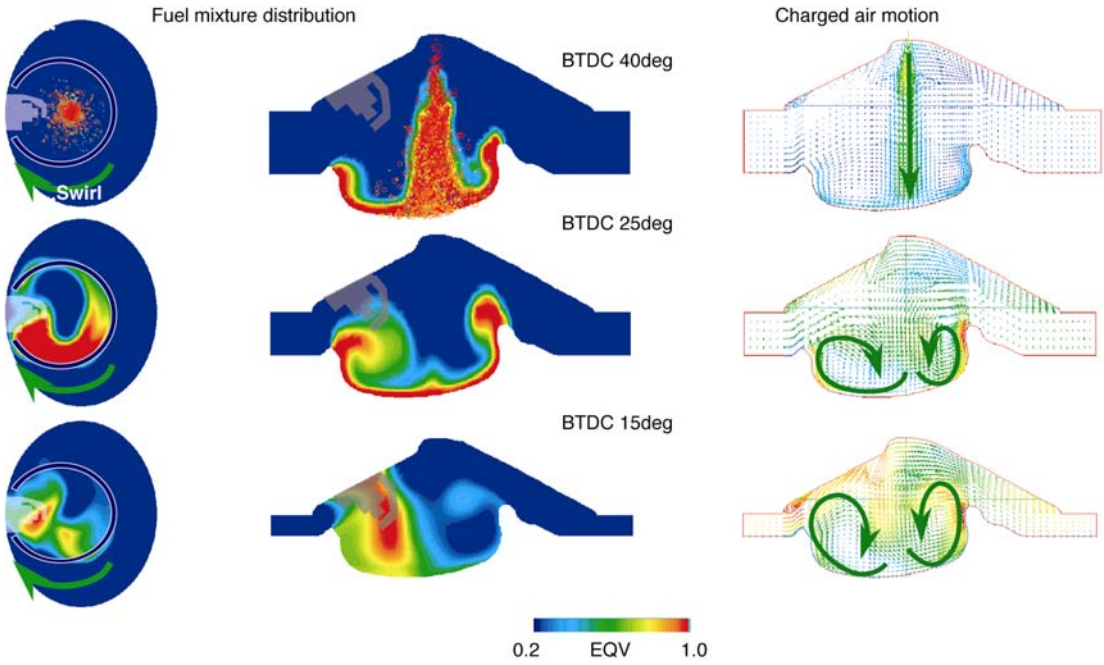



Fig. 12 Simulation of fuel mixing process and air motion in stratified charge combustion

After colliding with the piston cavity, the gasified air-fuel mixture is carried in the direction of the spark plug by the in-cylinder swirl. A stable, combustible mixture is therefore present around the spark plug at the spark timing of BTDC 15°, ensuring stable combustion in the ultra-lean stratified charge combustion range.

## 4.2. Combustion Characteristics

Figure 13 shows data from analyses of ISFC, HC and NOx emissions and in-cylinder pressure against injection timing with the engine in DISC mode at 1 500 rpm.

The employment of a piston cavity shape ensuring high maintainability of the mixture and the use of center injection have enabled the achievement of stable combustion at a broad range of injection timings, from BTDC 20° to 50°. The optimum injection timing for this load in terms of fuel consumption, emissions and combustion stability is BTDC 40°. If injection timing is advanced to BTDC 60°, the mixture disperses, stratification is reduced, and combustion fluctuates. By contrast, if injection timing is retarded to around BTDC 20°, fuel efficiency is reduced. The increased HC emissions at this injection timing indicate that this is caused by an increase in the amount of afterburn, lengthening the time required for combustion and thus increasing ISFC. There are therefore injection timings at which ISFC in the DISC area reaches its lowest level. Injection timings in the K20B have been optimized to enable the achievement of an excellent balance between ISFC and emissions levels at different engine speeds and loads.

Figure 14 shows data for brake specific fuel consumption (BSFC), NOx emissions, air-fuel ratio and in-cylinder pressure against EGR rate with ultra-lean stratified charge combustion at an engine speed of 1 500 rpm. Combustion is stable even at an EGR rate of 40%, at which BSFC is at its lowest level. In addition, mass EGR has reduced feed NOx by approximately 80%.

Figure 15 shows the results of analyses of in-cylinder pressures for DISC and stoichiometric combustion at Ne = 1 500 rpm and BMEP = 118 kPa. The stratification of the air-fuel mixture in the piston cavity during DISC reduces sparking delay compared to the homogeneous combustion occurring at stoichiometric air-fuel ratios. In addition, combustion is initiated more quickly after sparking, resulting in rapid combustion. This rapid combustion has been enabled by the employment of an atomized high-penetration spray and a piston cavity which maximizes maintainability to form the air-fuel mixture and the generation of an in-cylinder swirl flow.

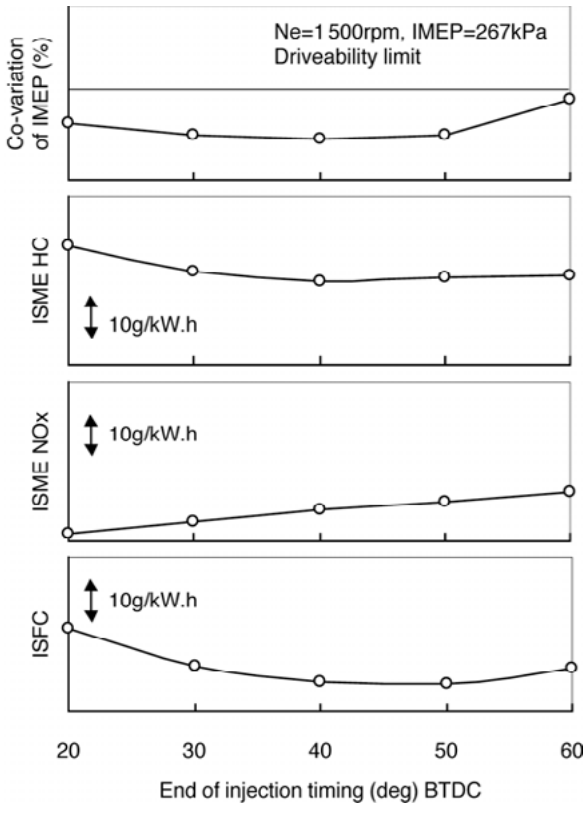



Fig. 13 Influence of injection timing on combustion characteristics

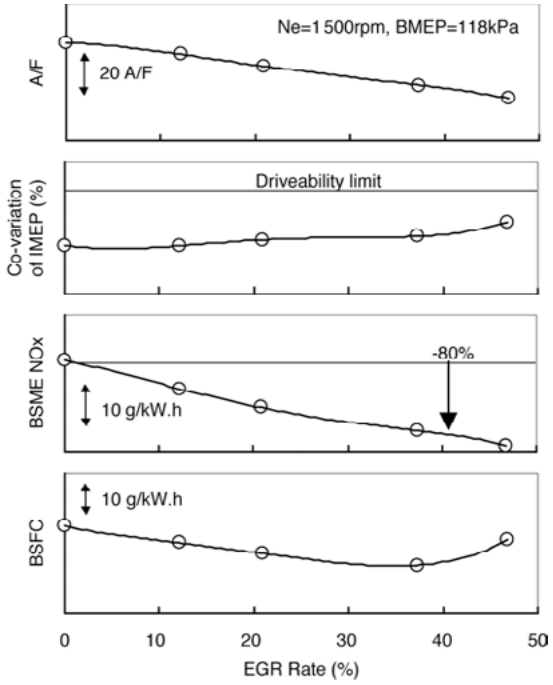



Fig. 14 BSFC, NOx combustion characteristics

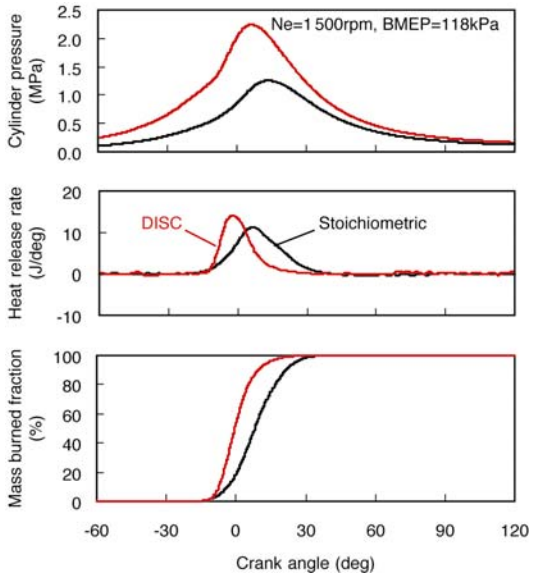



Fig. 15 Comparison of combustion characteristics

## 5. Engine Unit Fuel Efficiency and Vehicle Fuel Efficiency

### 5.1. Engine Unit Fuel Efficiency

Figure 16 shows the relationship between total engine displacement and BSFC. The reduction of heat loss and pumping loss and the increase in specific heat ratio achieved through ultra-lean stratified charge combustion in the direct injection engine has reduced BSFC by 20% against a conventional stoichiometric air-fuel ratio combustion engine.

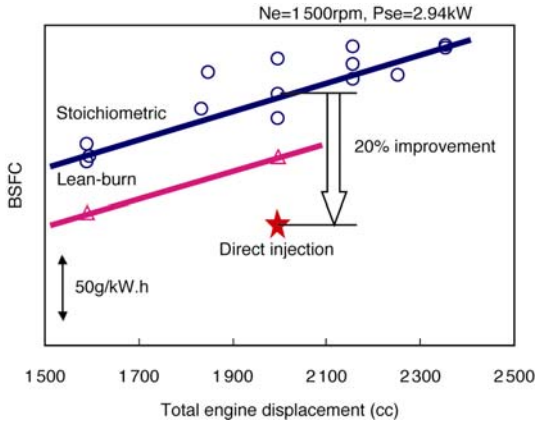



Fig. 16 Improvement of BSFC

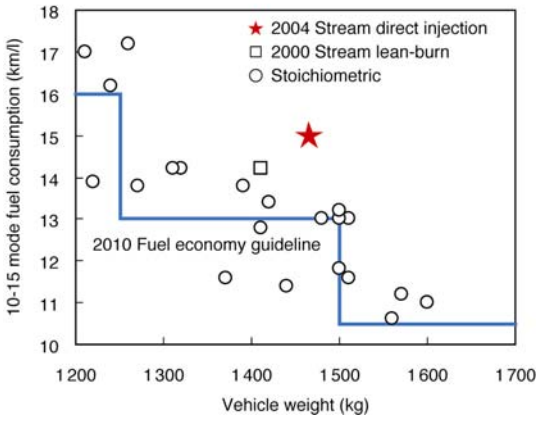



Fig. 17 Relationship between vehicle weight and 10 - 15 mode fuel economy in production gasoline vehicles

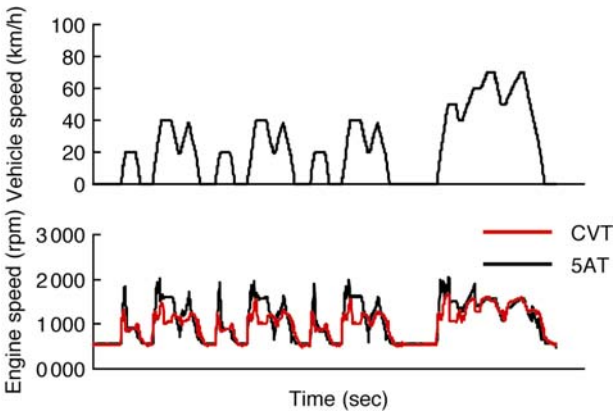



Fig. 18 Comparison of 10 - 15 mode engine speed between CVT and 5AT

### 5.2. Vehicle Fuel Efficiency

Figure 17 shows the relationship between vehicle weight and fuel consumption in Japanese 10 - 15 mode. Figure 18 compares engine speed in 10 - 15 mode in vehicles fitted with a CVT and a 5AT. Cooperative control of the engine and CVT is set to hold the engine operating range at low speeds, and therefore the engine operate at low BSFC. In 10 - 15 mode, the vehicle fitted with a CVT is able to cruise and accelerate at lower engine speeds than the vehicle fitted with a 5AT.

The improved fuel economy achieved through ultra-lean stratified charge combustion and the application of cooperative control with the CVT has enabled the reduction of fuel consumption. The resulting fuel economy in the 10 - 15 mode has been reduced by approximately 15% compared to the vehicle with a stoichiometric engine, achieving a low fuel consumption of 15.0 km/l. This is excellent fuel consumption performance, well below the standards established in the 2010 fuel consumption regulations.

## 6. Emissions Control Technology

Stratified charge combustion had never previously been employed in a direct injection engine. The emissions control system for the new engine was developed with the target of reducing emissions in a direct injection engine by 75% against the values stipulated in 2000 regulations, which meets the J-ULEV. Development proceeded with a major focus on reducing feed gases in the lean area and increasing the NOx purification rate.

### 6.1. Exhaust System

The exhaust system of the new engine is shown in Fig. 19. A 4-1 system with a rear exhaust was adopted to balance high power and purification performance. The catalyst and sensor configuration was selected to enable purification during a cold start at a stoichiometric air-fuel

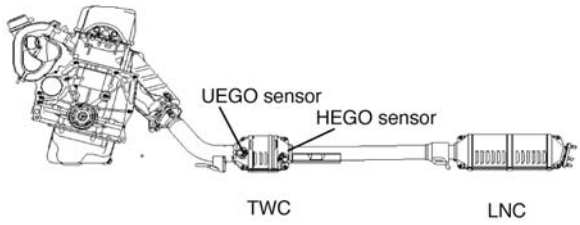



Fig. 19 Configuration of exhaust system

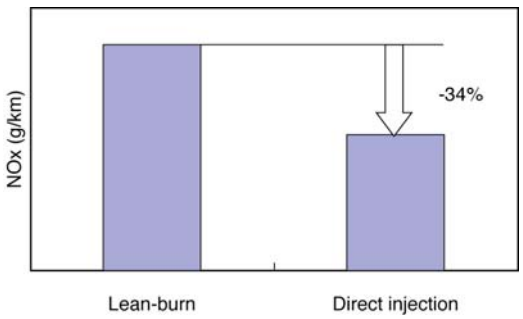



Fig. 20 Comparison of feed NOx emission in 10 - 15 mode between lean-burn engine and direct injection engine

ratio and HC purification during lean operation. A universal exhaust gas oxygen (UEGO) sensor was positioned upstream of the three-way catalyst (TWC), and a heated exhaust gas oxygen (HEGO) sensor was positioned downstream, to ensure high-accuracy control of air-fuel ratio. In addition, a NOx adsorption reduction-type TWC was positioned under the floor to enable NOx purification when the engine operates in the lean area.

### 6.2. Achieved Emissions Values

Figure 20 shows a comparison of the feed NOx level in the lean area in conventional lean-burn combustion and ultra-lean stratified charge combustion. The possibility of employing mass EGR during ultra-lean stratified charge combustion in the new engine has resulted in a 34% reduction in feed gases in the 10 - 15 mode.

Figure 21 shows the purification characteristics of the lean NOx catalyst by differences in concentration of NOx in exhaust gas. The lower the concentration of NOx in the feed gases, the higher the purification rate of the lean NOx catalyst. The mass EGR achieved with ultra-lean stratified charge combustion in the direct injection engine has enabled a reduction in the concentration of NOx. Also, improvements to the lean NOx catalyst have enabled it to control NOx to a lower volume than the lean NOx catalyst employed in the 2000 model lean-burn engine (Table 2).

Control for switching from ultra-lean stratified charge combustion to stoichiometric combustion has been optimized. This enables the vehicle to achieve both a high fuel economy of 15.0 km/l in Japanese 10 - 15 mode and to reduce emissions by 75% against the values stipulated in 2000 regulations, leading to the vehicle receiving ULEV Certification.

## 7. Conclusion

The i-VTEC I direct injection gasoline engine has the following technological characteristics:

(1) Ultra-lean stratified charge combustion has been achieved by the employment of a center injection system, an original cavity piston, and the formation of the air-fuel mixture using the in-cylinder swirl produced by VTEC.

(2) The vehicle has a top-class fuel economy of 15.0 km/l in 10 - 15 mode.

(3) The employment of a stratified charge combustion control system using mass EGR and a high-performance lean NOx catalyst in an engine that switches from stratified to homogeneous combustion has enabled the reduction of emissions by 75% against 2000 regulation values, which lead to ULEV certification.

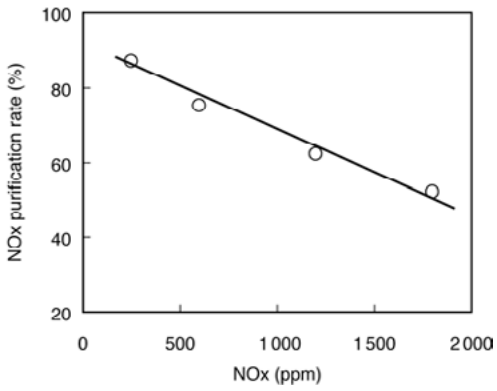



Fig. 21 NOx purification characteristics

Table 2 Catalytic converter specifications

| | 2004 Model direct injection | 2000 Model lean-burn |
|---|---|---|
| TWC | 1.0L 600cell | 0.7L 400cell |
| LNC | 1.4L 400cell Improved | 2.4L 400cell Adsorption type |

## References

(1) Ashizawa, T., Saitoh, K., Tamura, Y., Sakai, T.: Development of a New In-line 4-cylinder Direct-Injection Gasoline Engine, JSAE Annual Congress Proceedings, No. 71-98, JSAE9838237

(2) Norota, K., Harada, J., Abe, S., Yoshioka, Y., Aoyama, K.: Development of a New L-4 Direct Injection SI Gasoline Engine, JSAE Annual Congress Proceedings, No. 78-00, JSAE20005525

(3) Niizato, T., Hayashi, A.: Development of New 2.0L Lean-burn Engine, HONDA R&D Technical Review, Vol. 12 No. 2, p. 45-54 (2000)

(4) Nakayama, Y., Suzuki, M., Iwata, Y., Yamano, J.: Development of a 1.3L 2PLUG Engine for the 2002 year Model Fit, Honda R&D Technical Review, Vol. 13, No. 2, p. 43-52 (2001)

(5) Kuma, T., Iwamoto, Y., Iida, K., Murakami, M., Akishino, K., Ando, H.: Combustion Control Technologies for Direct Injection SI Engine, SAE Paper 960600

(6) Okamoto, K., Ichikawa, T., Saitoh, K., Oyama, K., Hiraya, K., Urushihara, T.: Study on Relationship between Octane number and anti-knock performance in Direct Injection Spark Ignition Gasoline Engine, SAE Annual Congress Proceedings, No. 73-02, JSAE20025175

■ Authors ■



Yutaka KOHDA



Tomoji SUGANAMI



Hiroyuki KOBAYASHI



Ken OGAWA

# Development of High-pressure Fuel System for Direct Injection Gasoline Engine

Hiroyuki GOTO* Kenji HIROSE* Masayoshi SAITOH*
Seiji MATSUMOTO* Satoshi IITAKA* Kazuhiro TAKASHIBA*

## ABSTRACT

A center injection system in which a high-pressure fuel injector is located in the center of the combustion chamber is employed in a newly developed direct injection gasoline engine. The high-pressure fuel injector is highly responsive, with a minimum injection timing of 0.7 msec, and injects an ultra-atomized spray with an average droplet diameter of less than 12 $\mu$m. To ensure durability and reliability in this original center injection system, the high-pressure fuel injector mounting employs a layout in which arm holders secure the unit. The design of the high-pressure fuel supply lines is optimized using simulations. In addition, high reliability is achieved by the reduction of stress and the adoption of a structure to dampen fuel pulsation. A simple plunger and spill solenoid system is employed in the high-pressure fuel pump enabling the reduction of the required driving force, the reduction of the component size, and the achievement of high-accuracy fuel pressure control.

## 1. Introduction

In response to the increasing demand for fuel economy in recent years, Honda developed a 2.0L direct injection gasoline engine. Mass production direct injection gasoline engines to date have most often been side injection systems with the injectors located on the side of the engine's combustion chamber.

This new engine gives the maximum in fuel economy improvements with ultra lean stratified charge combustion available in a direct injection gasoline engine, and at the same time adopts a center injection system to achieve excellent emission and power performance. As a result, best-in-class fuel economy is achieved by combining a highly accurate fuel injection control system and a high-performance lean NOx catalyst. At the same time, the engine meets the strictest Japanese emissions standards.

This paper reports on the newly developed high-pressure fuel system and components for the center injector, direct injection engine.

## 2. System Outline

Figure 1 shows the fuel supply system adopted in the newly developed direct injection gasoline engine. The fuel is sent from the fuel tank by a low-pressure fuel pump at a pressure of 343 kPa. This is the same pressure as the port injection fuel supply system. The pressure of the fuel is raised by a high-pressure pump located on the engine, and the fuel is supplied to the high-pressure fuel injectors (referred to as injectors hereafter) through a delivery pipe. The fuel pressure is controlled so that it is normally 10 MPa, 8 MPa when idling, and 10.5 MPa at full load. The major features of

* Tochigi R&D Center

the high-pressure fuel system for direct injection gasoline engines are as follows:

(1) Adoption of highly responsive, ultra-atomization spray injectors that meet the requirements of a center injection system.
(2) Adoption of mountings that secure the injectors using arm holders, giving both combustion gas seal reliability and injector durability and reliability.
(3) Adoption of a fuel pulsation damper delivery pipe having a large capacity chamber and fuel feed pipe orifice structure; as well as a high-pressure fuel relief return system in case of an abnormal fuel pressure rise.
(4) Adoption of a high-pressure fuel pump that uses a simple plunger and spill solenoid control system, providing a compact system and a cam drive requiring low drive force.

Details of each of these features are given below.

## 3. High-pressure Fuel Injector

### 3.1. Injector Structure

The injector structure is shown in Fig. 2. The basic structure follows that of an electromagnetic solenoid system injector used in port fuel injection gasoline engines. The features of an injector for direct injection gasoline engines are as follows:

(1) Adoption of a high efficiency magnetic circuit that satisfies the requirements for high responsiveness and a wide range of flow characteristics.
(2) Adoption of an inner collar that reduces the diameter of the fuel passage, thereby reducing pulsation occurring inside the injector.
(3) Adoption of a swirl chip that creates an ultra atomized, narrow angle, high-penetration spray.
(4) An outer case at the end of the injector is provided that forms a combustion gas sealing gasket surface between the engine head and the injector.
(5) A seal ring is provided, which uses poly tetra fluoro ethylene resin (referred to as PTFE resin hereafter) to make a combustion gas seal between the outer case and the valve seat.
(6) The elimination of a direct connector and using of a harness drawing structure that seals the wire connection part.

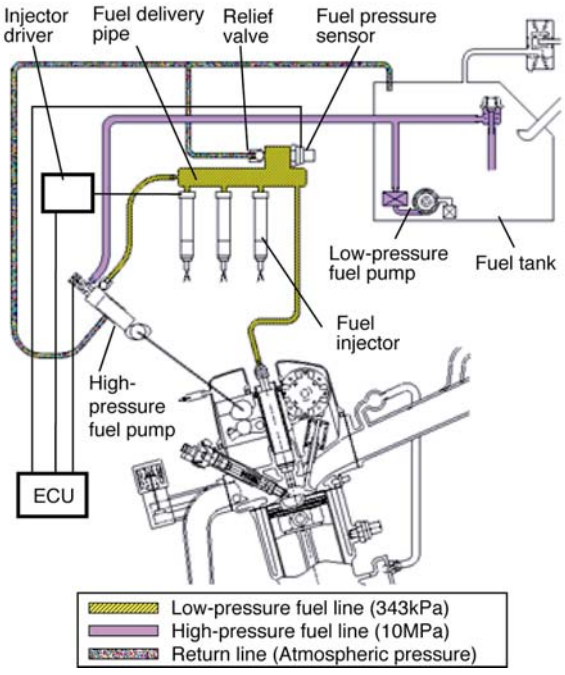



Fig. 1 High pressure fuel supply system

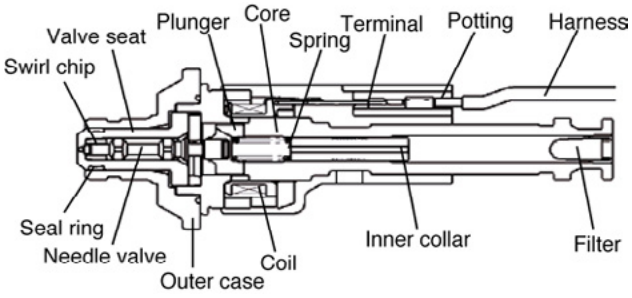



Fig. 2 Cutaway view of high-pressure fuel injector

### 3.2. Highly Responsive with a Wide Range

In the ultra lean stratified charge combustion range of the injector for direct injection gasoline engines, it is necessary to discharge the fuel in a short period towards the rising piston cavity to form a stratified charge fuel mixture. In the fully loaded driving range, it is necessary to complete injection in the period from intake process through compression process. Therefore, high responsiveness and large flow characteristics are required.

In order to satisfy these requirements and maintain linear flow characteristics from the idling range to fully loaded driving range, the injector is designed with a high-efficiency magnetic circuit, providing the highest magnetic flux density in the aspiration gap section between plunger and core, without losses in the magnetic circuit. The design work was carried out with a magnetic simulation, as shown in Fig. 3. In addition, to reduce closed valve dispersion due to needle

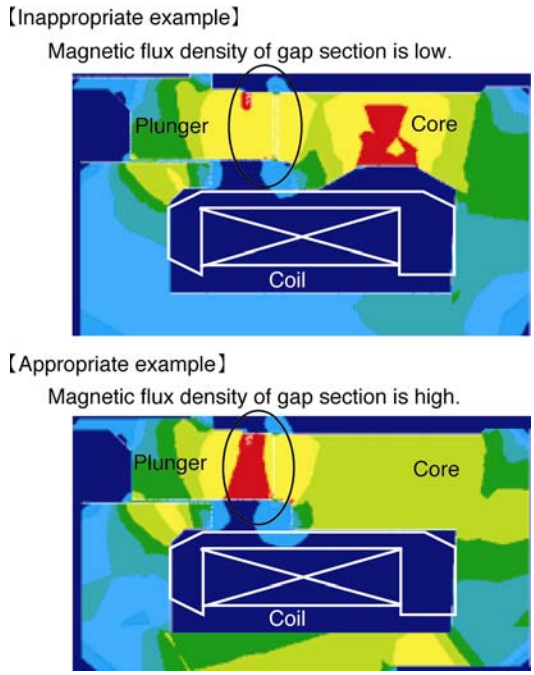



Fig. 3 Results of magnetism simulation

valve bouncing, the inner collar's fuel passage diameter was made smaller (diameter ϕ1 mm), and fuel pulsation occurring within the injector was damped, working toward stabilized flow in the low-pressure injection range.

The drive driver uses a 150 V voltage converter, and employs a drive current wave peak hold type driver, as shown in Fig. 4, thereby raising responsiveness. As shown in Fig. 5, peak current value is set at the point where open valve responsiveness is at its best and current value is at its lowest.

As shown in Fig. 6, these improvements result in highly responsive and wide range flow characteristics. Linearity is maintained to the shortest injection time of 0.7 msec, and at the same time, an injection flow rate at least twice that of a port injection injector is obtained.

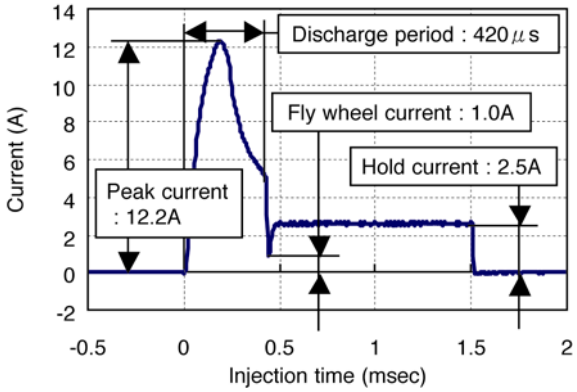



Fig. 4 Injector current wave

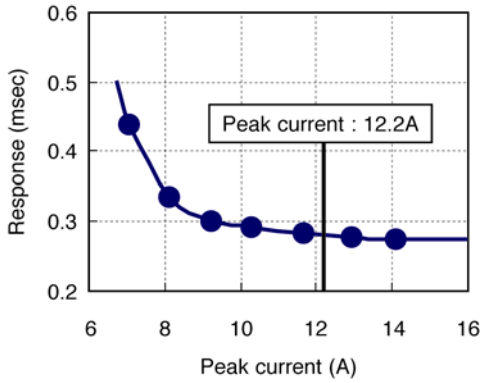



Fig. 5 Needle valve response and peak current

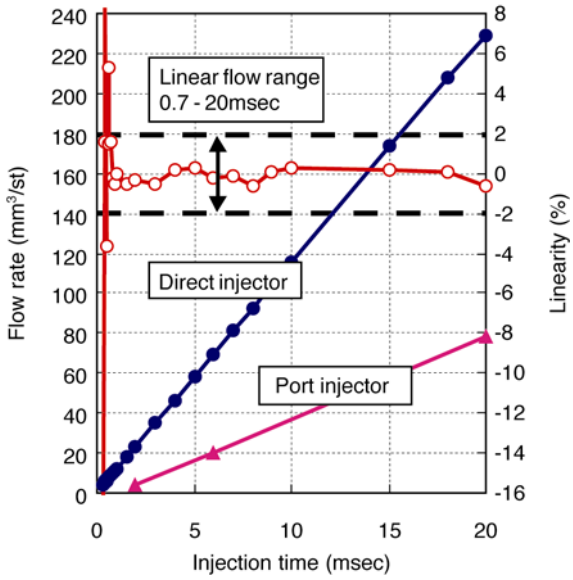



Fig. 6 Injector flow rate

## 3.3. Spray Characteristics

With direct injection gasoline engines, the injectors inject fuel directly into the combustion chamber and the air-fuel mixture burns. This requires the injectors to have ultra atomized spray. In addition, in order to create the stratified charge fuel mixture according to the independent center injection combustion concept, as shown in Fig. 7, the injector must have a spray with a tight spray angle of 25 deg., and have a high spray penetration. Figure 8 shows the spray angle when the injector is spraying its full amount. Figure 9 shows the spray penetration at a fixed time after the injector has completed injection.

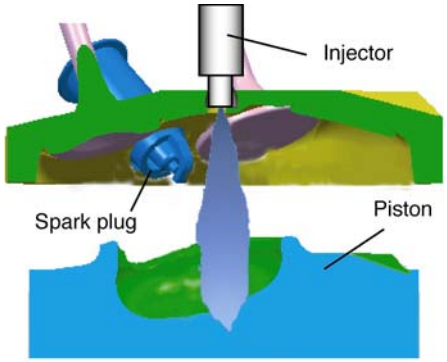



Fig. 7 Concept of combustion in direct injection gasoline engine

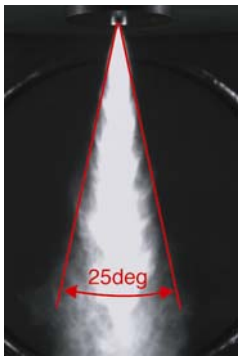



Fig. 8 Spray angle of newly developed injector

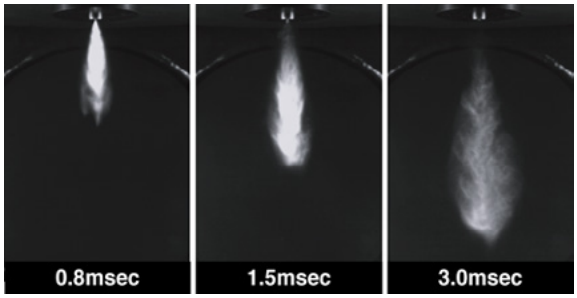



Fig. 9 Spray penetration of newly developed injector

In order to obtain ultra-atomization spray, a normal fuel pressure of 10 MPa was adopted, making it possible to create droplets having Sauter's Mean Diameter (referred to as SMD hereafter) of 12 μm or less, as shown in Fig. 10. It is known that the higher the fuel pressure is, the smaller the particle diameter becomes (ultra atomization)[(1)], and as shown in Fig. 11, this injector is designed so that particle diameter is at its best at 10 MPa.

In spray creation, by optimizing the proportion of straight flow and swirl flow using the swirl chip flutes positioned at the very end of the passage within the injector, as shown in Fig. 12, it is possible to obtain a superior balance between spray angle, spray penetration, and particle diameter.

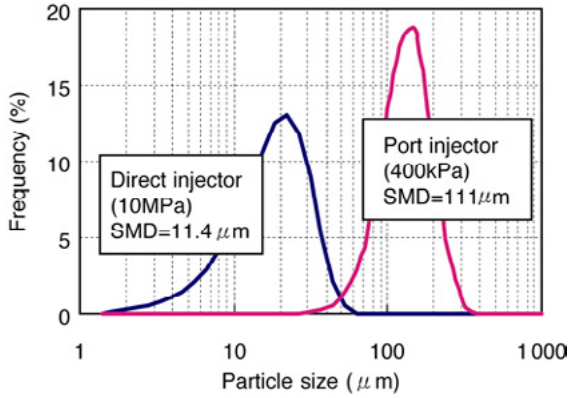



Fig. 10 Comparison of SMD between conventional port injector and high-pressure direct injector

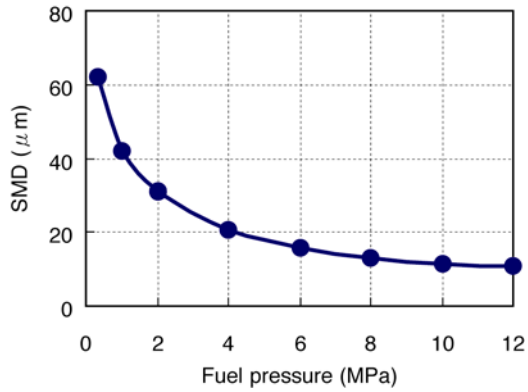



Fig. 11 Relationship of SMD and fuel pressure

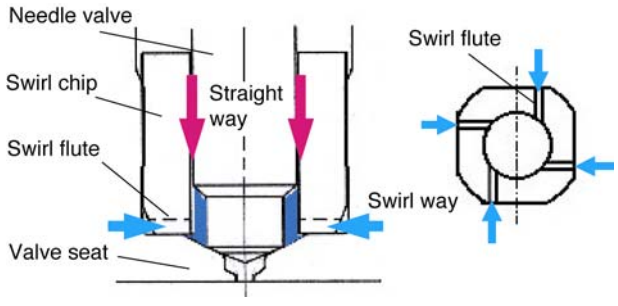



Fig. 12 Configuration of injector swirl guide

## 3.4. Center Injector Mounting Structure

In order to establish the independent center injection layout, it is necessary to resolve the following issues:

(1) Combustion gas seal that is highly reliable.

(2) Lowering of injector valve seat temperature as a countermeasure to deposits clogging the injector nozzle.

In order to achieve these, an arm holder structure is adopted, as shown in Fig. 13. This structure can often be seen as a mount for fuel injection nozzles used on diesel engines, and is adopted for this direct injection gasoline engine as well.

A metal gasket is adopted for the combustion gas seal around the outside of the injector, as shown in Fig. 14, and by setting the injector seat on the cylinder head side, a gasket seal surface is formed. On the injector tip gasket on the combustion chamber side, a gasket without a rubber coating is established as a firewall, and the valve seat tip temperature is lowered. A gasket with rubber coating is used at the upper levels of the injector, creating a complete seal structure. In order to seal these gaskets, a holder is placed around the outside of the injector, and an outer case at the end of the injector. Then, axial force is applied through the medium of an arm from the top of the cylinder head.

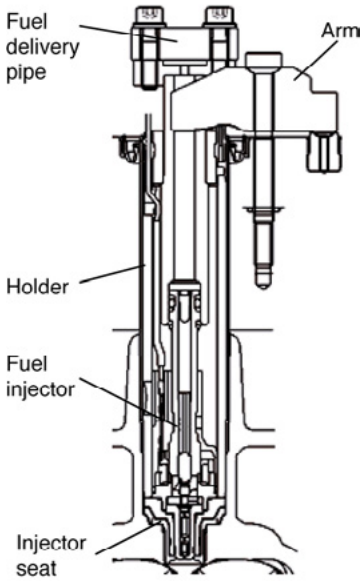



Fig. 13 Installation of injector

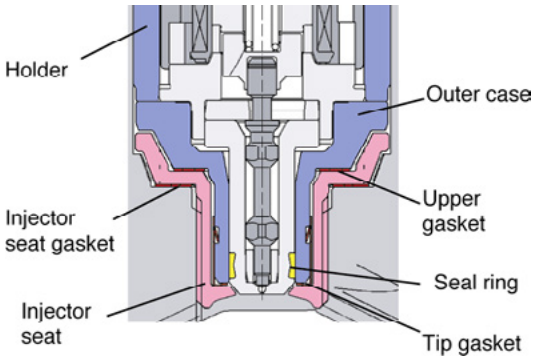



Fig. 14 Cutaway view of seal mechanism

In addition, a PTFE resin seal ring is used between the outer case and the valve seat to help prevent valve seat temperature rise due to combustion gas penetration. The PTFE resin in this seal ring behaves such that at low temperatures the volume reduces and there is a drop in seal performance. However, as shown in Fig. 15, by setting the volume of the seal ring at a charging rate of 100% or more of the volume of the seal groove in the valve seat, it is possible to have a combustion gas seal in an extremely low temperature environment.

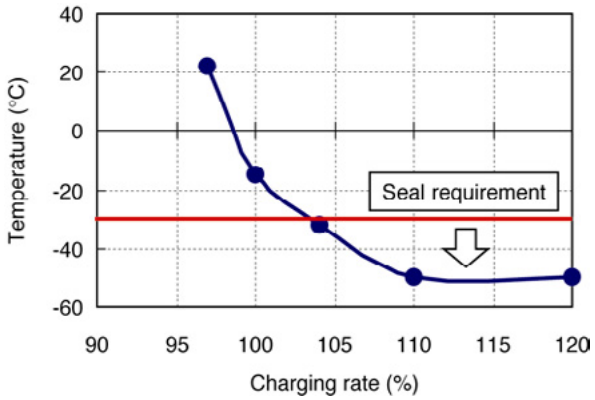



Fig. 15 Low temperature seal ability of seal ring

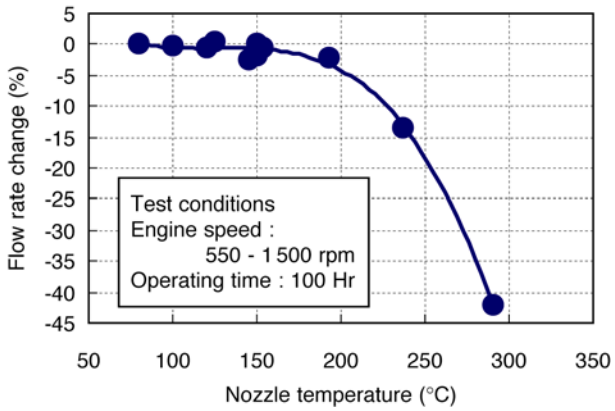



Fig. 16 Influence of nozzle temperature on flow rate

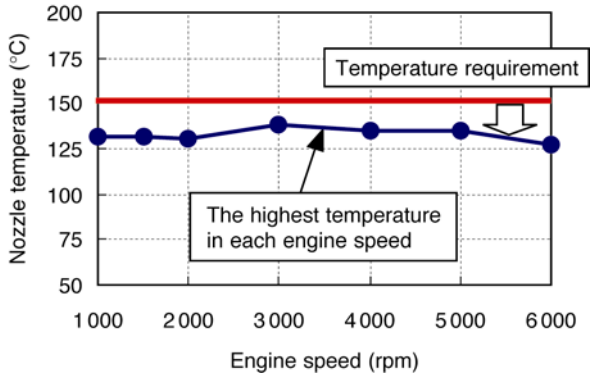



Fig. 17 Relationship of nozzle temperature and engine speed

It is known that if the valve seat temperature of injectors for direct injection engines exceeds 160 °C, there is a tendency for an increase in flow deterioration due to adhesion of deposits in the nozzle[(2), (3)].The test results for the new engine are shown in Fig. 16. By using the aforementioned combustion gas seal structure, the injector valve seat temperature, as shown in Fig. 17, remains below the development target of 150 °C at all engine speeds, preventing any reduction in injector flow after actual vehicle endurance driving.

In addition, by giving the injector end a shape that follows that of the combustion chamber, creating a structure whereby the combustion gas flow continually interferes with the nozzle, any accumulation of deposits on the injector edge is prevented.

## 4. High-pressure Fuel Supply Line

### 4.1. Fuel Delivery Pipe Reliability

The high-pressure fuel supply line structure, centered on the fuel delivery pipe, is shown in Fig. 18. For the fuel delivery pipe material, stainless steel for its corrosion resistance and superior resistance to stress caused by engine vibration. The feed pipe, which connects the high-pressure pump to the chamber, and the chamber to the injector, is designed using simulations. As shown in Fig. 19, simulations are made of static stress, considering location dispersion of fastening flange on the delivery pipe side and mounting flange on the mating side, and of dynamic stress considering engine vibration. It is confirmed there are no points of stress concentration. As a result, it is possible to create a reliable high-pressure fuel supply system, ensure reliability through simulation design, and confirm reliability through vehicle durability tests.

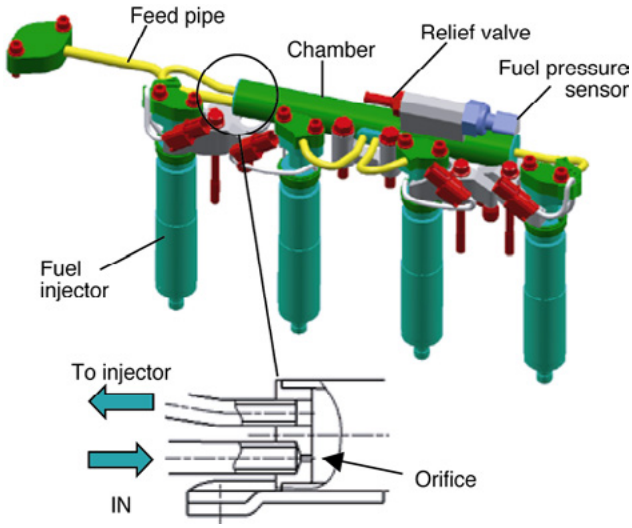



Fig. 18 Fuel delivery pipe

### 4.2. High-pressure Fuel Pulsation Countermeasures

The delivery pipe chamber has a capacity of approximately 80 $cm^3$, with damping of pulsation occurring due to the high-pressure fuel pump discharge or injector operation working towards pressure stabilization. In the feed pipe that connects the high-pressure fuel pump and the chamber, an orifice is made at the chamber inlet. This orifice has the effect of damping resonance in the feed pipe that occurs due to high-pressure fuel pump discharge pulsation. This raises the durability and reliability of the O-ring seals in the fuel pipes. Figure 20 compares high-pressure fuel pump discharge pulsation waveforms with and without the orifice. It is clear that there is a dramatic reduction in pulsation due to the orifice.

### 4.3. High-pressure Fuel Relief System

Figure 21 shows the high-pressure fuel relief system. The pressure relief valve has a simple structure – a ball valve is seated in the valve seat with a spring. The relief valve's valve opening pressure is set at 12 MPa, for pressure relief in case of an abnormal fuel pressure rise. The structure is such that fuel discharged from the relief valve is released into the fuel tank through a return pipe placed under the floor of the vehicle. The fuel delivery pipe relief valve discharges into the high-pressure fuel pump return line inside the engine bay.

## 5. High-pressure Fuel Pressure Control System

Figure 22 shows the high-pressure fuel pump structure. The exhaust camshaft is extended to have a double peak cam on it for the pump drive. The cam let the single plunger piston rise and fall, taking in and discharging fuel. As for fuel metering, the intake check valve opening and closing timing is controlled using a spill solenoid. Any excess fuel is emitted on the low-pressure fuel line side, with the required fuel discharged on the high-pressure line side. By using this spill solenoid fuel metering method, it is possible to drive the pump with the minimum required amount of work, and at the same time the unit can be very compact.

A large capacity pulsation damper is placed at the fuel inlet of this high-pressure fuel pump, absorbing pulsation that occurs when the excess fuel is emitted, raising the durability and reliability of the low-pressure fuel line.

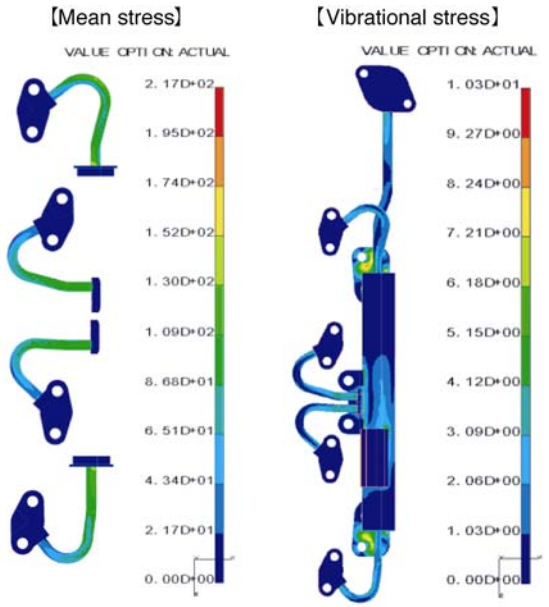



Fig. 19 Simulation results for mean stress and vibrational stress

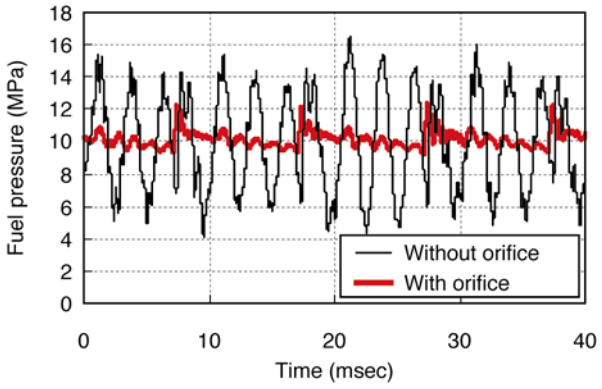



Fig. 20 Pulsation of high-pressure fuel pump

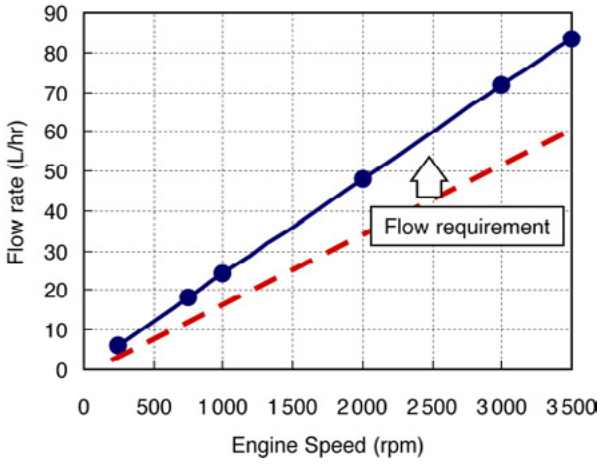



Fig. 21 High-pressure fuel relief system

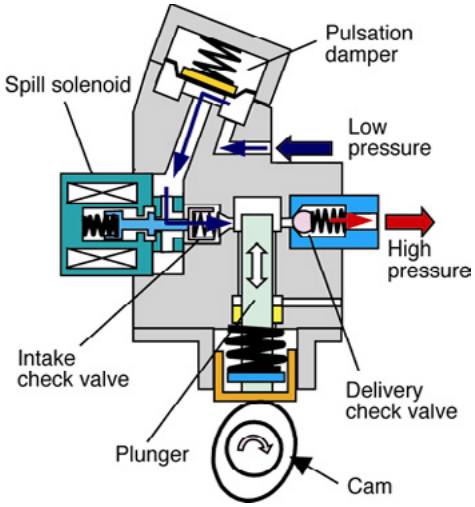



Fig. 22 Cutaway view of high-pressure fuel pump

The flow characteristics of the high-pressure fuel pump are shown in Fig. 23. It is clear that in comparison with the flow required when the vehicle is fully loaded, it is possible to obtain flow beyond the required amount.

The fuel pressure control method is shown in Fig. 24. As for the amount of discharge from the high-pressure fuel pump, the basic control variable is determined by the spill solenoid operation map, which is obtained according to the engine speed and injector discharge amount. Furthermore, by implementing feedback control that corrects the deviation between the pressure measured by a fuel pressure sensor placed in the fuel delivery pipe and the target fuel pressure using PID control, it is possible to control pressure at the target fuel pressure value. Adopting this fuel pressure control method enables highly accurate fuel pressure control.

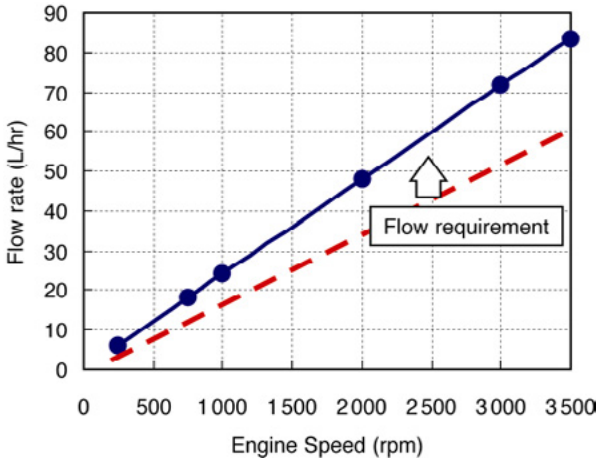



Fig. 23 Flow rate of high-pressure fuel pump

## 6. Conclusion

The following results are achieved in the development of a high-pressure fuel supply system for direct injection gasoline engines:

(1) It is possible to obtain, with this high-pressure injector, linear flow characteristics from no load idling through fully loaded driving, through a high-efficiency magnetic circuit design, a smaller inner collar diameter, and a specially designed driver. In addition, by optimizing high fuel pressure and swirl guide settings, it is possible to obtain spray characteristics including particle diameter, spray angle and spray penetration, that match the center injection combustion concept.

(2) By adopting an arm holder structure as the center injection system's injector mounting structure, combustion gas seal performance and injector tip temperature targets are met, making it possible to ensure durability and reliability.

(3) Using various stress simulations for the feed pipe, and by placing a large capacity chamber and an orifice in the fuel feed pipe, it was possible to create a very reliable high-pressure fuel supply. In addition, providing a relief return system helps provide additional safety in the event of an abnormal fuel pressure rise.

(4) By adopting a simple, cam driven plunger and spill solenoid control system, a compact and low drive force high-pressure fuel pump was achieved. The high-pressure fuel pressure control system enables highly accurate control by carrying out feedback control using a fuel pressure sensor, in addition to a basic control variable using a map.

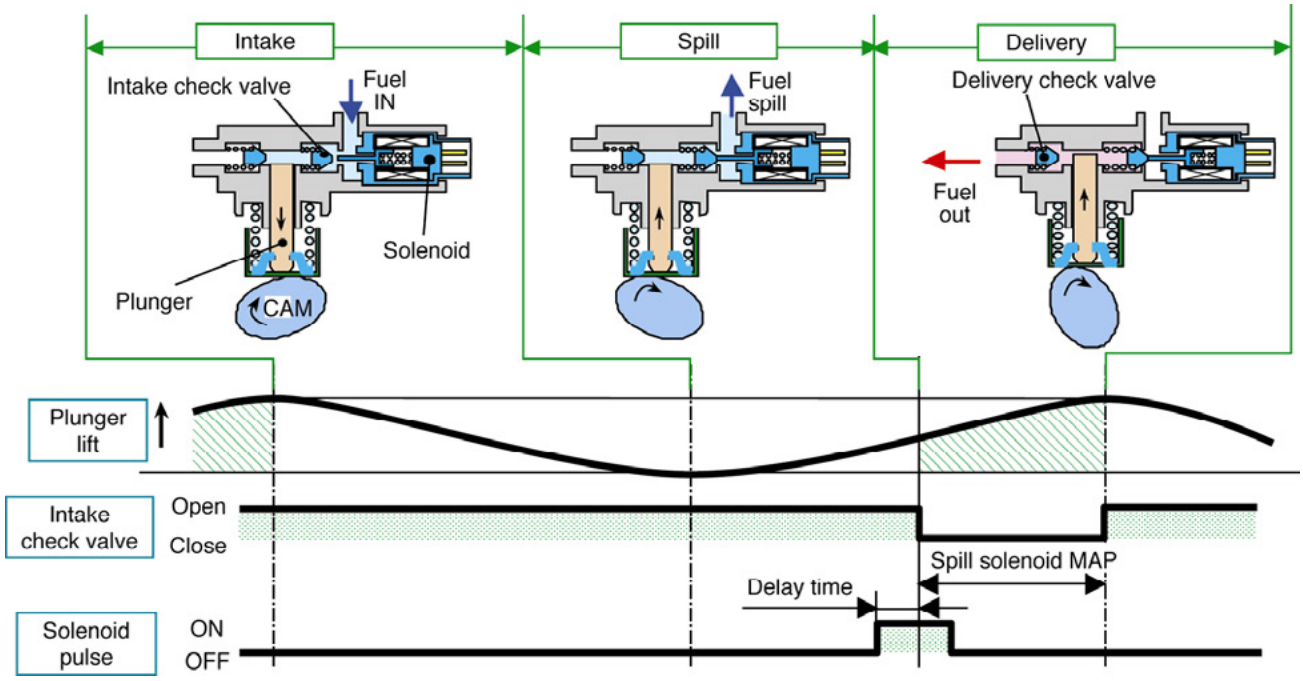



Fig. 24 Diagram of spill solenoid control

## Acknowledgments

Finally, the authors would like to express their deep and sincere gratitude to those at Keihin Corporation, Sanoh Industrial Co. Ltd., and Hitachi, Ltd. who generously cooperated in this development project.

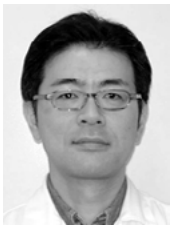
## References

(1) Matsushita, S., Nakanishi, K., Gohno, T., Sawada, D.: Mixture Formation Process and Combustion Process of Direct Injection S. I. Engine, JSAE Annual Congress Proceedings, No. 965 p. 102 (1996)

(2) Kinoshita, M., Saito, A., Matsushita, S., Shibata, H., Niwa, Y.: Study of Nozzle Deposit Formation Mechanism for Direct Injection Gasoline Engines, JSAE Annual Congress Proceedings, No. 976 p. 23-24 (1997)

(3) Ashida, T.: Effects of Fuel on Deposits in Gasoline Engines, JSAE Annual Congress Proceedings, No. 08-00, p. 25-26 (2000)

## ■ Authors ■

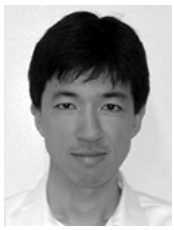

Hiroyuki GOTO


Kenji HIROSE


Masayoshi SAITOH


Seiji MATSUMOTO


Satoshi IITAKA


Kazuhiro TAKASHIBA

# Development of Electronically Controlled Hydraulic Steering Damper for Motorcycles

Takeshi WAKABAYASHI* Kiyotaka SAKAI*
Shinichi YAMADA* Takehiko NANRI*

## ABSTRACT

The world's first electronically controlled hydraulic steering damper for motorcycles, HESD (Honda Electronic Steering Damper), has been developed. The HESD gives optimum damping characteristics during running. Handling characteristics and the "Kickback" phenomenon were analyzed using a motorcycle with and without a steering damper. The steering damper with optimum damping characteristics according to the speed and acceleration of the vehicle reduced the "Kickback" phenomenon. An electronically controlled linear solenoid is applied to alter flow resistance of the damper. The HESD reduced kickbacks while maintaining sporty handling at low speed running.

## 1. Introduction

Kickback is a vibration phenomenon (vehicle behavior) arising in motorcycles running at high speed. Kickback is a sharp change in the steering angle which occurs as the vehicle passes over bumpy road surfaces. This can lead to rider discomfort and fatigue.

Typical measures employed to reduce kickback include setting adjustments to the tires, suspension characteristics and vehicle alignment. However, another device for reducing kickback is a steering damper. A steering damper adds a damping torque to the steering axis and suppresses any sudden movement to the handlebar. Hydraulic types have been the main types of damper control used to date. The issue with steering dampers is that when the damping torque required to reduce kickback is applied it can affect the handling when the vehicle is running at low speed. Consequentially, such steering dampers have only been applied to racing motorcycles and some commercial motorcycles.

An analysis of the handling characteristics and kickback phenomenon was conducted and the damping characteristic requirements for these were observed. This paper describes the development of a new technology with the application of an electronically controlled rotary steering damper that applies variable damping characteristic. This new technology successfully reduces kickback phenomenon without deterioration of the light handling when the vehicle runs at low speed.




Fig. 1 Appearance of the HESD

Figure 1 shows the newly developed Honda Electronic Steering Damper (HESD) system and Fig. 2 shows the 2004 CBR1000RR model with the new steering damper system.

* Asaka R&D Center




Fig. 2 Appearance of the CBR1000RR

## 2. Development Goals

In order to apply the system to mass-production motorcycles, development goals were set up as follows.

(1) To reduce the magnitude of kickback without deterioration of light handling when running at low speed.
(2) Design the system to be light and compact.

## 3. Kickback Phenomenon

The Japanese Automobile Standard Organization, JASO, has defined kickback as the sudden change in the steering angle of a motorcycle caused when passing over bumpy road surfaces[(1)]. Kickback can affect handling and stability.

Figure 3 shows a graph of the steering angle and front suspension behavior when the kickback phenomenon occurs. When a front wheel of the motorcycle passes over a bumpy road surface, a load is exerted to the vehicle's forward direction. If the direction of the front wheel and direction of the force to that wheel are not the same, a torque is exerted on the steering axis according to the steering angle, the bump height on the road surface, and the contact load to the front wheel. As the steering system turns, the rider's steady state steer force and tire's self aligning torque cause the steering direction to shift back to the direction prior to the load impact. When the torque is excessive, however, the steering is forced in the opposite direction. This repetition increases the steering amplitude. The operational frequency of the steering angle is 5-10 Hz and is believed to be determined by such factors as vehicle weight and alignment. The operational frequency of the front suspension when kickback occurs is approximately twice that of the steering angle.

The load exerted to the motorcycle's forward direction, which is input to the steering system, increases along with greater road surface irregularities and higher running speeds. This consequentially leads to greater kickback occurrence. Even as the direct contact load to the front wheel decreases, for example, as the speed is accelerated, the steering angle increases in reaction to the exerted load and also greater kickback occurs. The excessive kickback transmits greater force on the rider's arms such that the rider can have discomfort and fatigue.

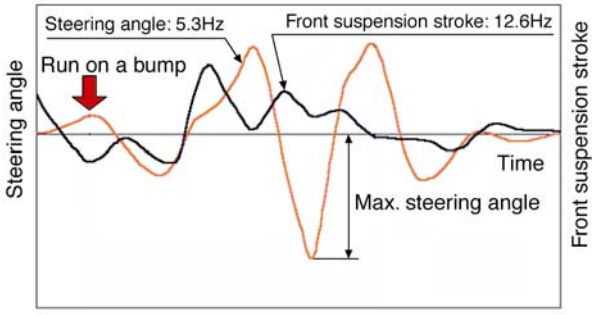



Fig. 3 Explanation for "Kickback" phenomenon

## 4. Evaluation Method of Running Test

A large super sport motorcycle was used in all running tests of this research. Table 1 shows the major specifications of the test motorcycle. The following test method was used to evaluate light handling (steering effort) and kickback.

### 4.1. Evaluation of Steering Effort at Low Speed

As shown in Fig. 4, the test motorcycle goes into the test course with straight running at a constant speed of 30 km/h. From point "A", the motorcycle changes lanes to the right or left by two meters and then reverts to its straight running. The steering torque fluctuation in this lane change test mode at the change in steering angle was defined as "low speed steering torque fluctuation" and was evaluated. See Fig. 5. The test rider also rated the steering effort according to the sensory test. Figure 6 shows the rating scale of the test

Table 1 Major specifications

| Item | | Specifications |
|---|---|---|
| Engine type | | Liquid cooled 4-stroke DOHC 4-cylinder |
| Engine displacement | ($cm^3$) | 998 |
| Transmission | | 6 speed constant mesh |
| Vehicle dimension | (mm) | 2 025 × 720 × 1 120 |
| Wheel base | (mm) | 1 410 |
| Vehicle mass | (kg) | 179 |
| Tire size | Front | 120/70-17 |
| | Rear | 190/50-17 |
| Suspension | Front | Telescopic |
| | Rear | Swing arm |

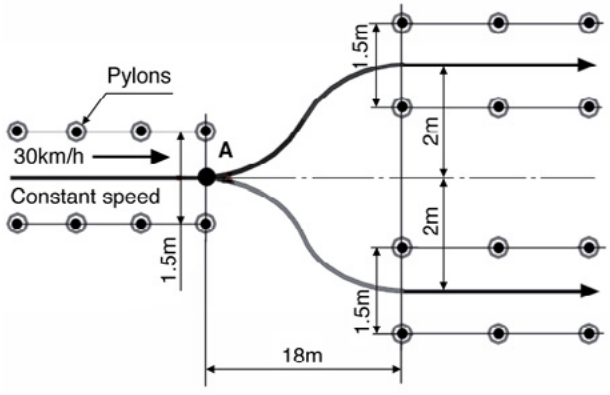



Fig. 4 Test condition of lane change at low speed

rider's sensory evaluation. The above-mentioned test method has been defined as the "low speed lane change test."

### 4.2. Evaluation Method of Kickback

As shown in Fig. 7, the motorcycle enters the test course with straight running at a constant speed of 120 km/h using sixth gear. From point "A," the motorcycle enters a bumpy road surface at full throttle condition. The greatest steering angle that occurs in the test was defined as the "maximum kickback steering angle," and then evaluated as shown in Fig. 3. The test rider also conducts sensory evaluation. The same criteria for evaluating the ride sensation used in the low-speed lane change test as shown in Fig. 6 are also used in this test. This test has been defined as the "kickback test." The demanding conditions were used in the testing to generate the kickback phenomenon.

## 5. Target Damping Characteristics

A running test was conducted to determine the target damping characteristics. Tests were conducted by using a steering damper with manual control damping characteristic.

### 5.1. Target Minimum Damping Characteristics

Light handling can be achieved by decreasing the damping torque generated by a steering damper. The low speed lane change test was repeated while gradually increasing the damping torque of the steering damper. The sensory evaluation was also conducted. If the increase in steering torque fluctuation at low speed is less than 10%, it was confirmed that there was no change in the rider's evaluation of steering effort as shown in Fig. 8. As shown in Fig. 9, this test verified that the fluctuation in steering torque at low speed increased proportionally for damping torque applied in almost maximum steering angular velocity. From the results of these analyses, the target value for the steering torque fluctuation at low speed was determined within 10% of the test motorcycle without steering damper system. It was also verified that the damping characteristics to achieve the target is characteristic of line 1 shown in Fig. 10. This was defined as the target minimum damping characteristic.

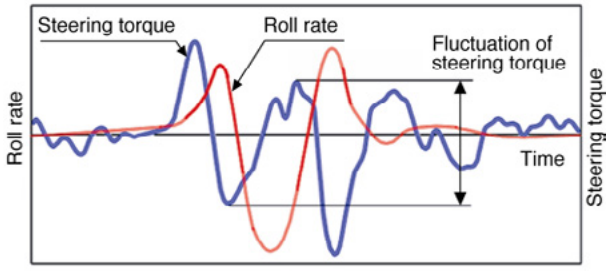



Fig. 5 Definition of steering torque fluctuation at low speed

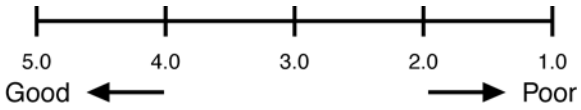



Fig. 6 Rating scale

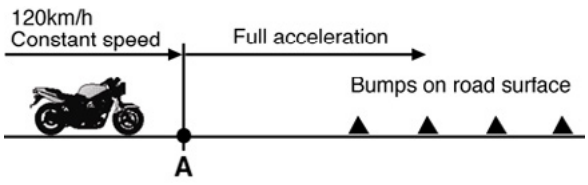



Fig. 7 Condition of Kickback test

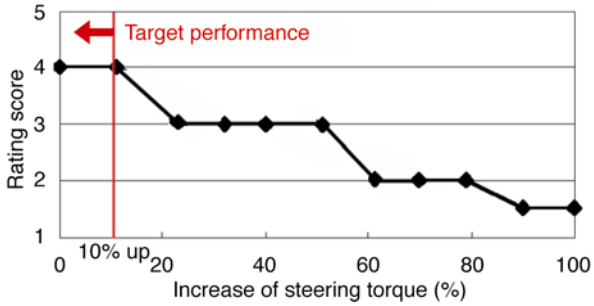



Fig. 8 Rating of handling heaviness

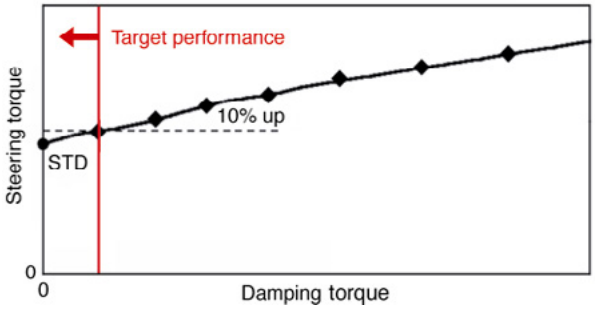



Fig. 9 Relationship between steering torque and damping torque

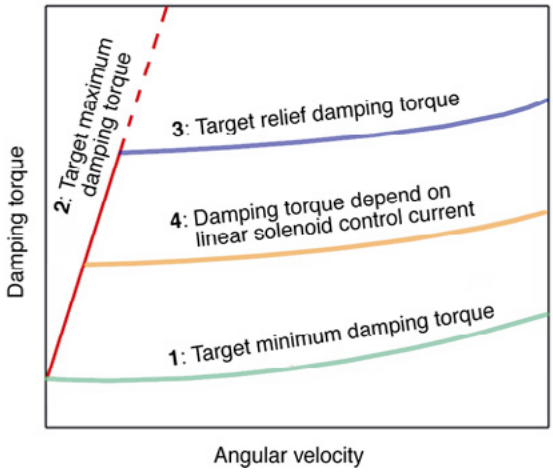



Fig. 10 Target characteristics on relationship between damping torque and angular velocity

### 5.2. Target Maximum Damping Characteristics

A steering damper that can exert a large damping torque will help reduce the level of kickback. The kickback test was repeated while gradually increasing the damping torque on the steering damper. Test rider evaluation of the kickback feeling showed a 4-point rating increase when the maximum kickback steering angle was reduced by 75% or more compared to without a steering damper. This reduction of 75% was set as the target value. Figure 11 shows the target performance. It was also confirmed that the maximum kickback steering angle tended to converge as the damping torque increases as shown in Fig. 12.

It was also found that exerting a larger damping torque at lesser steering angles and steering angular velocity is effective for reducing the kickback.

However, test results also showed that applying an excessive damping torque at low steering angular velocity affects the straight line running stability. When a motorcycle leans to the right or left, the front wheel turns to that leaning direction to maintain stability. Turning of the front wheel is delayed when the damping torque is greatly increased.

The maximum damping torque characteristic without affecting the straight running stability was obtained from the above-mentioned test results. Line 2 shown in Fig. 10 was determined as the target maximum damping characteristic.

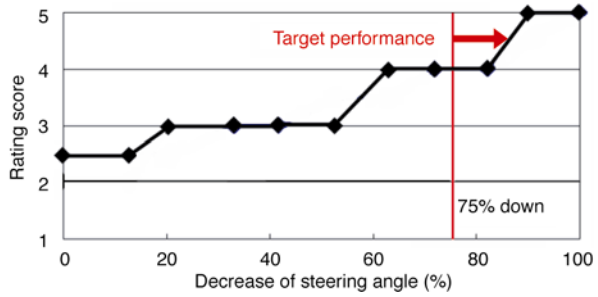



Fig. 11 Rating of kickback performance

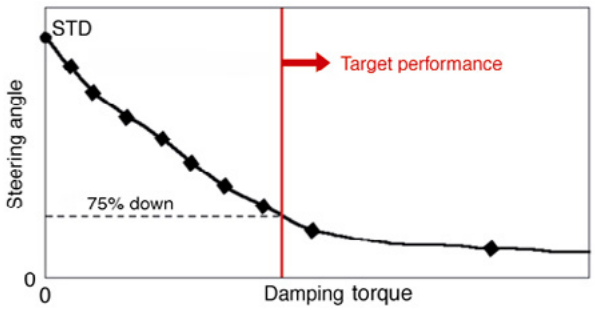



Fig. 12 Relationship between steering angle at kickback test and damping torque

### 5.3. Relief Valve System

In the targeted maximum damping torque characteristic described in the section 5.2., damping torque is raised in conjunction with increasing steering angular velocity and the higher strength is required for the damper body because the damper pressure is greatly increased. As a result, the body becomes large and heavy. If a suitable damping torque can be applied in low steering angular velocity, the kickback can be sufficiently reduced by a minimal damping torque. By fitting an adjustable relief valve, increasing damping torque was controlled by releasing more than certain specific pressure.

The working pressure characteristics of relief valve satisfying the target of kickback reduction were obtained from the test results. The characteristics are represented in line 3 shown in Fig. 10 and it was defined as the target relief valve characteristics. The optimum damper body size and specifications were determined by applying these characteristics.

## 6. Damping Characteristic Control with Vehicle Speed and Acceleration

### 6.1. Requirements of Controlling Mechanism

From the above-mentioned test results, it was found that the damping characteristic of the steering damper needs to change according to the required performance. Some steering dampers currently available on the market have an adjustable damping characteristic with manual operation. The newly developed system is fitted with an automatic controlling device that electronically controls the damping characteristic to generate the optimum damping characteristics according to running conditions.

### 6.2. Control Parameters

The conventional steering damper creates a substantial heaviness of steering effort during low speed operation. As the operation speed decreases, the rider controls the motorcycle largely by adjusting the steering angle. This increases the steering angular velocity as shown in Fig. 13. The kickback occurs more readily when running at high speed where the steering system receives larger impact loads, when accelerating where the contact load of the front tire decreases.

Speed and acceleration have been applied to the controlling parameter for the damping characteristics. The conditions for controlling are as follows:

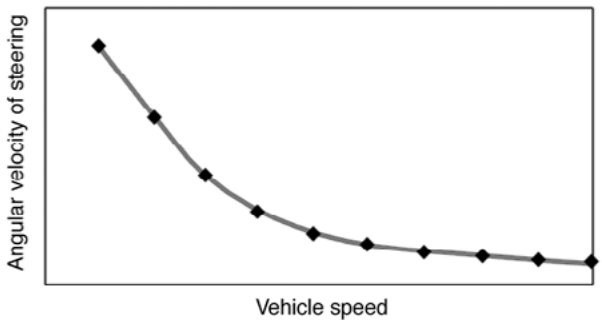



Fig. 13 Characteristics of angular velocity of steering

- Damping torque is reduced to enable light handling when running at low speed.
- Damping torque is increased to reduce kickback when running at high speeds and accelerating.

## 7. System and Control

### 7.1. Damper System

There are generally three types of steering damping systems; friction type dampers, hydraulic type dampers and electromagnetic type dampers. Table 2 shows the characteristics for each damper system and the verified results on each type. As a result, the hydraulic system was selected for this development. Hydraulic type dampers provide a damping mechanism with fluid resistance of the hydraulic oil and can generate a damping torque according to the actuation speed of the dampers.

Hydraulic steering dampers are classified into a linear actuation type and a rotary actuation type. The rotary type adopted in this development has the following advantages:

- There is no reciprocating part between the hydraulic oil chamber and the outside, so little oil is consumed by raking out.
- Steering axis and damper rotational axis are set on the same axis to provide a working damping angle in proportion to the steering angle.

### 7.2. System and Damper Configuration

Figure 14 shows the system configuration of the newly developed HESD. The ECU of the controller segment determines the control current value for the linear solenoid housed in the damper based on information from a vehicle speed sensor. The linear solenoid is attached to the main valve and adjusts the pushing force according to the control current value calculated by the ECU. The reason for using a linear solenoid is to achieve an actuation response at sudden acceleration and deceleration, and a linear change in damping characteristics according to the change in current value.

Figure 15 shows the internal structure of the HESD. The damper body consists of an oil chamber divided into right and left by the vane and oil lines for controls. The hydraulic oil fills the oil chamber. The damper body is fixed on the motorcycle body frame. The vane is located in the oil chamber and is connected to the steering system via a link. Both the steering system and vane share the same rotational axis and rotate on a 1:1 ratio. When the vane rotates, the hydraulic oil begins to flow between the right and left oil

Table 2 Investigation of types

| Types / Items | **Friction Type** Use of mechanical friction | **Hydraulic Type** Use of fluid resistance | **Electromagnetic Type** Use of magnets and coils |
|---|---|---|---|
| Damping characteristics | Unsuitable | Suitable | Suitable |
| Generated damping force | Small | Large | Medium |
| Controllability | Low | Medium | High |
| Size | Small | Small | Large |
| Cost | Low | Medium | High |

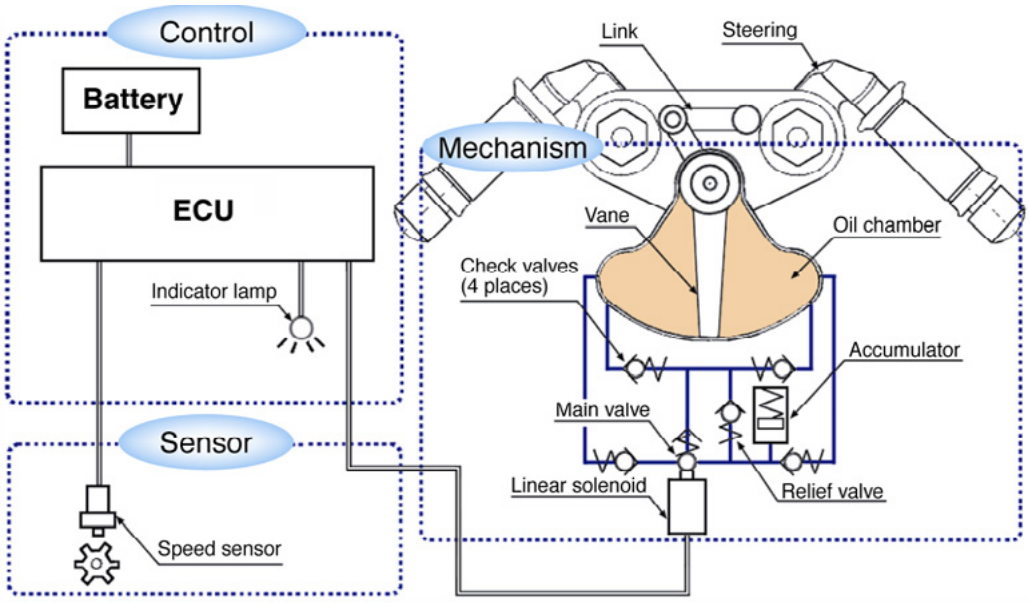



Fig. 14 System diagram of the HESD

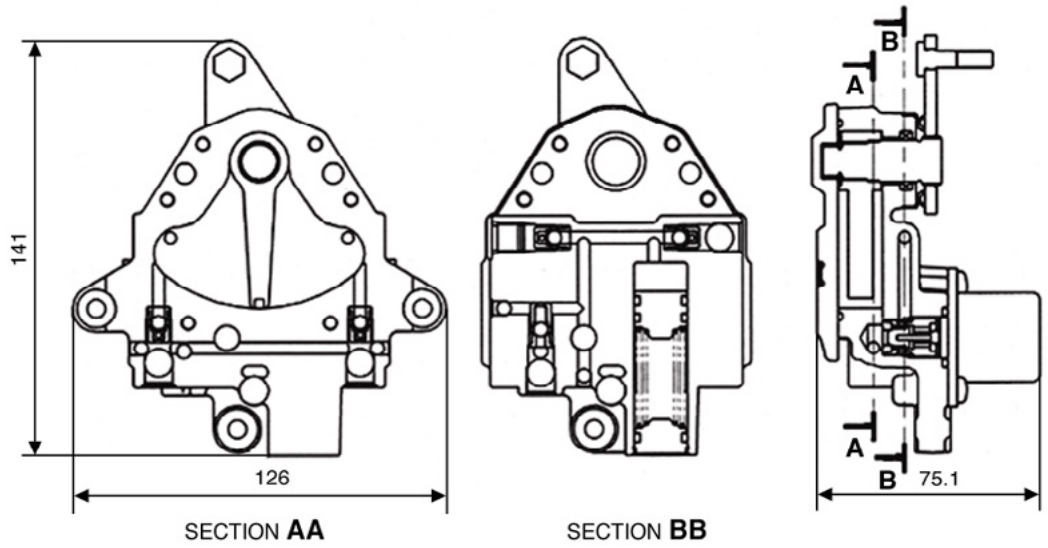



Fig. 15 Inner structure of the HESD

chambers. At the same time, the fluid resistance and the friction inside of the damper is transmitted to the steering system as a damping torque around the common rotational axis. The controlling oil lines were designed as three-dimensional piping with excellent space efficiency to achieve a light weight and compactness. The main valve, check valves, a relief valve and an accumulator are placed in the controlling oil lines. The functions of each component are described below.

The main valve regulates the magnitude of fluid resistance according to the valve opening conditions. The check valves ensure a one-way flow of the hydraulic oil to the main valve. The relief valve is located in the oil line parallel to the main valve and limits the maximum generating damping torque. The accumulator serves to stabilize the damper inner pressure though the volume of the hydraulic oil changes according to the operational temperature.

### 7.3. Control of Damping Characteristics

The fluid resistance varies according to the angular velocity of the vane and the opening area of the main valve. The opening area of the main valve is set according to the balance between the pushing force by the linear solenoid and the return force of the pressure adjusted by the main valve.

#### 7.3.1. Damping characteristics under de-energized

The damping characteristic of line 1 shown in Fig.10 was realized by a fully opened main valve actuating the spring in the main valve under de-energized. The fluid resistance of the hydraulic oil is generated mostly in the main valve and increases according to the steering angular velocity.

#### 7.3.2. Damping characteristics under energized

At low steering angular velocity, the pressure generated from the pushing force initiated by the linear solenoid is larger than a return force by the generated pressure, which allows the main valve to stay closed. When the main valve is closed, the hydraulic oil does not flow into the control oil line, but flows into the gap between the oil chamber and vane. The target maximum damping torque of line 2 shown in Fig. 10 was achieved. As the steering angular velocity increases and the return force due to the pressure exceeds the pushing force of the linear solenoid, the main valve opens. Damping characteristics change from line 2 to line 4 based upon the control current value as shown in Fig. 10.

### 7.4. Electronic Control

An electronic control system has been adopted to achieve excellent damper control functionality with high accuracy and high actuation response. The ECU calculates vehicle speed and acceleration by using signals of vehicle speed and determines the control current value for the linear solenoid by a three-dimensional map. As the control current value increases, the damping characteristics change continuously from line 1 to line 3, as shown in Fig. 10. Figure 16 shows the control map. The control current of the linear solenoid is dropped at low speeds and increases according to an increase in the vehicle speed. When the vehicle accelerates, the control current value increases according to the acceleration. During deceleration, the control current value is set equal to that of the constant speed.

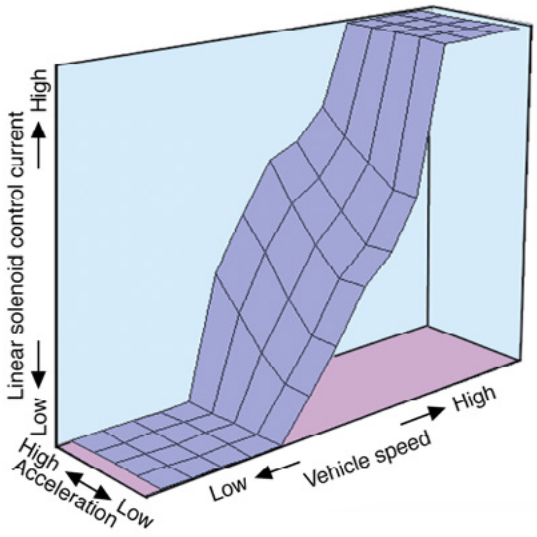



Fig. 16 Control mapping

## 8. Results of Effect Verification

The following test was conducted with an HESD fitted vehicle to verify the efficiency of the system configuration and specifications described herein. A vehicle without a steering damper and a vehicle with a conventional steering damper were used in the comparative testing. Two types of conventional steering dampers with the target specification of this development were used. One has the characteristic of fluctuation in the low speed steering torque increased by approximately 10% (conventional specification 1). The other has the maximum kickback steering angle reduced by approximately 75% (conventional specification 2).

### 8.1. Low Speed Lane Change Test

This test verified whether the HESD made steering heavy when running at low speeds. Figure 17 shows the distribution of steering torque fluctuation during the low speed lane change test. The horizontal axis shows the maximum steering velocity. The average values for ten evaluations of each specification are shown with the horizontal line. Fluctuation in steering torque at low speed was increased by 8%, when comparing between the vehicles with the HESD and without a steering damper. This is a favorable result even in comparison with the conventional damper specification 1 configured with the target value. On the other hand, that was increased by 52% on the vehicle with conventional damper specification 2. Table 3 shows the sensory evaluation results. The vehicle fitted with the HESD was rated with the same score as the vehicle without a damper. It was further verified the HESD vehicle was ratable as the same level as that without a steering damper.

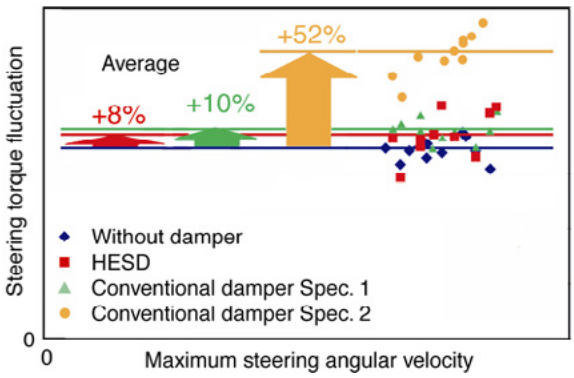



Fig. 17 Low speed lane change test results

Table 3 Steering heaviness evaluation result

| | Rider A | Rider B | Rider C |
|---|---|---|---|
| Without damper | 4.0 | 4.0 | 4.0 |
| HESD | 4.0 | 4.0 | 4.0 |
| Conventional damper Spec. 1 | 4.0 | 4.0 | 4.0 |
| Conventional damper Spec. 2 | 3.0 | 2.0 | 3.0 |

### 8.2. Kickback Test

Figure 18 shows the time-series change for the steering angle of tested vehicles as they passed over the tested road surfaces. The HESD has reduced the maximum steering angle by approximately 85%. This was a better result than that achieved by the target conventional damper specification 2. In contrast, conventional damper specification 1 achieved only a 19% reduction in steering angle. Table 4 shows the sensory evaluation results of kickback characteristic. The vehicle with the HESD received high ratings compared with that for the vehicle without a damper.

These test results have demonstrated that the HESD has suitable damping characteristics for riding conditions. Those provide light handling when running at low speeds while reducing kickback occurrences when running at high speeds, which is not possible on vehicles with conventional steering dampers.

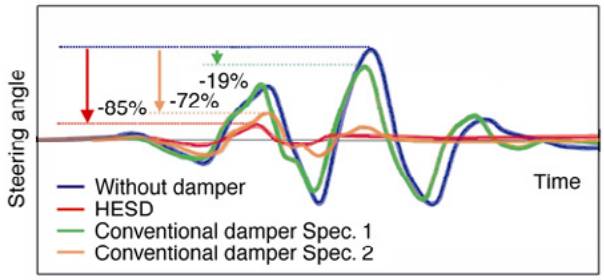



Fig. 18 Kickback test results

Table 4 Kickback performance evaluation result

| | Rider A | Rider B | Rider C |
|---|---|---|---|
| Without damper | 3.0 | 2.5 | 2.5 |
| HESD | 5.0 | 4.0 | 4.0 |
| Conventional damper Spec. 1 | 3.0 | 2.5 | 3.0 |
| Conventional damper Spec. 2 | 4.0 | 4.0 | 4.0 |

## 9. Conclusion

(1) Handling characteristics and kickback phenomenon characteristics were analyzed. Optimal steering damping characteristics for speed and acceleration were found.
(2) An electronically controlled linear solenoid was used to alter the internal damper fluid resistance. This reduced kickback occurrences while maintaining light handling at low speed running.
(3) Maximum damping characteristics and oil line layout were optimized. A lightweight and compact electronically controlled steering damper for motorcycles was achieved.

## References

(1) Society of Automotive Engineers of Japan, Inc.: JASO T803-96, Glossary of terms relating to motorcycle and moped stability and controllability, p. 22 (1996)

■ Authors ■


Takeshi WAKABAYASHI


Kiyotaka SAKAI


Shinichi YAMADA


Takehiko NANRI

# Development of Electronic Control System for Small Hybrid Snow Thrower

Tsutomu WAKITANI* Yoshihiko YAMAGISHI*
Toshiaki KAWAKAMI* Tsutomu MIZOROKE*

## ABSTRACT

An electronic control system has been developed for a small snow thrower for general home use. The new system provides stable propulsion and smooth turning. Development focused on the major requirements of stable operational behavior in changing conditions and responsiveness to operator input. The new system has eliminated the need for variations in speed control, and even more complicated turning maneuvers can be conducted more easily. Both high torque and high speed are required from the drive motor, which employs a 12 V battery power supply. A brushless DC motor was utilized and flux-weakening control was adopted to enable these requirements to be balanced. The new control system achieves good performance, and the integration of components has resulted in a 10% reduction in the size of components compared to the current hybrid snow thrower.

## 1. Introduction

With the recent technology trend of hybrid systems, Honda has introduced a parallel hybrid system for the Integrated Motor Assist (IMA) system[(1)]. Automobiles released for sale on the market have already adopted this hybrid system. The hybrid system has also been adopted by working tools such as the medium-sized snow thrower, which has been available on the market since 2000[(2)].

Incorporation of the hybrid system to snow throwers has made the machines easier to control by reducing the operation load. These advantages are now being sought in small-size snow throwers.

Among the characteristics associated with snow throwers configured with a hybrid system are: adoption of a series hybrid system that uses an engine for the snow clearing work and power generation and uses DC motors for axle driving only; use of drive motors powered by a lead acid battery for automobiles; use of minimal sensor data to allow for a simple and inexpensive system construction; driving with a continuous high load torque at low speed ranges; stable performance over changing load conditions including a variety of surface conditions; driving speed control in response to the work load; independent control of left and right mounted motors to achieve smooth turning maneuverability; and synchronized control of forward propulsion.

This paper introduces the control methods and the various device technologies used in the development of the small-size hybrid snow thrower.

* Asakahigashi R&D Center

## 2. Development Goals

The goals set for this development were to further enhance the electrical control system of the current medium-size hybrid snow thrower by incorporating an even simpler operator interface in addition to achieving a level of stabilized performance response. Also, higher motor drive efficiency, overall system compactness, and lower costs were targeted in the development of the small-size hybrid snow thrower.

Figure 1 shows an electrical system concept.

### 2.1. Applications for Small Type Hybrid Snow Thrower

Conventional small type snow throwers configured with typical engine formats are approximately 60% in both weight and size compared with similarly configured medium-size snow throwers. While the small-size snow thrower is comparatively easier for an operator to maneuver, it exhibits considerable variation in behavior as conditional disturbances arise according to the work conditions. More specifically, the operator needs to exert frequent path correction movement to maintain forward propulsion and turning stability regardless of whether the machine is traveling or being engaged in work activity.

This development has quantitatively eliminated such factors and targeted good performance responsiveness and stable maneuverability.

### 2.2. Ease of Operation

Hybrid snow throwers configured with steering systems control turning operations (during decelerated speeds) with left and right mounted drive motors by assigning the target speed to each drive motor independently. On medium-size snow throwers, the target speed is derived from an analog signal initiated by the speed lever as shown in Fig. 2.

While the operator is able to arbitrarily control the turning speed according to the degree of control exerted on the speed lever, stable turning motion is dependent on the operator.

The need for controlling speed deceleration with a speed lever has been eliminated in the new system as shown in Fig. 3. To achieve ease of operation, On/Off push switches have been adopted to automatically control acceleration and deceleration according to the targeted turning requirement.

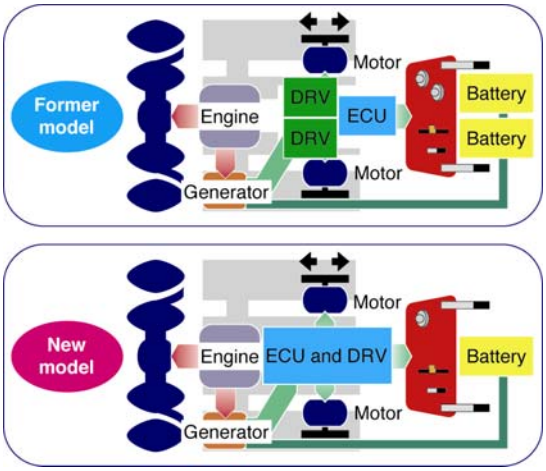



Fig. 1 Electrical system concept for hybrid snow thrower

### 2.3. Motor Drive

The existing medium-size hybrid snow thrower is configured with 24 V motor driven power sources to provide the required running torque during work conditions and satisfy the adopted brush motor characteristics. The system's power source is also 24 V. This configuration therefore necessitates the adoption of two 12 V batteries. However, one battery is preferable when considering a design of a small-size snow thrower. Achieving a 12 V DC power source system would enable the installation of the battery to the limited space of a small-size snow thrower. Also, general in-vehicle electrical devices could be used in the configuration, which would contribute to the overall cost reduction.

However, adopting the 12 V motor drive has created a challenge in achieving the required motor speed and torque. A snow thrower requires gearless speed change capability from a stationary position to the highest running speed to accommodate work requirements at low and medium speed ranges as well as movement at higher speed ranges. A motor shaft speed of 2 500 rpm is required for the gear ratio demand to provide the necessary torque during work operations.

To address this challenge, a brushless motor as shown in Fig. 4 was utilized to achieve high efficiency and variable speed control at the lower 12 V-voltage level. This has achieved a highly efficient drive system with a broad speed range.

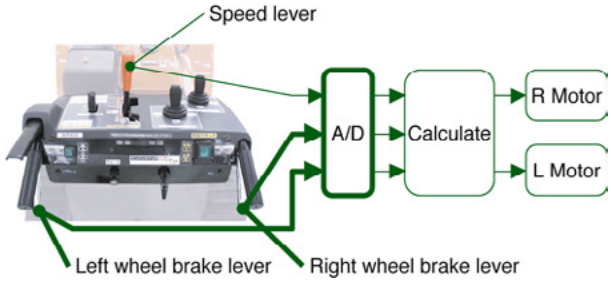



Fig. 2 Control panel of former model

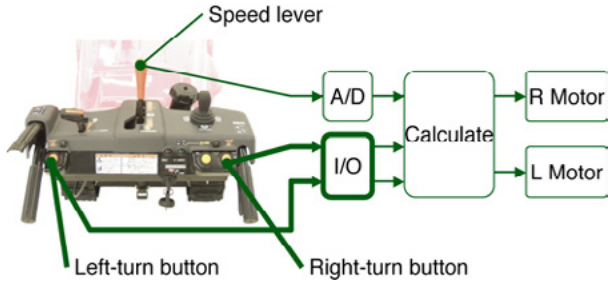



Fig. 3 Control panel for new model

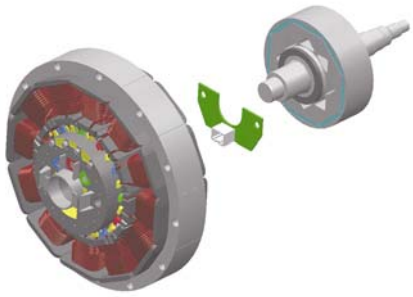


Fig. 4 Brushless DC motor

### 2.4. Compact Configuration

Multiple controlling devices including man-machine interface components, system controls, relays for initiating driving of devices, and motor driving devices were required to achieve a hybrid system configured with independent left and right mounted motor drives. A 10% reduction in size compared with the previous configuration was targeted through the integration of these devices. The integration of the devices has eliminated electrical connection between the devices, increased wire harness reliability, and reduced overall system cost.

## 3. System Controls

In integrating the multiple devices, the Electronic Control Unit (ECU) and motor driver (hereafter referred to as DRV) used in the medium-size hybrid snow thrower have been configured to control the main functions as follows:

- ECU – total system control and interface
- DRV – motor drive with load control

Microcomputer chips (hereafter referred to as CPU) are used selectively to regulate processing as follows:

- One high-performance CPU for integrated data processing
- Multiple common CPUs for individual processing

Applying the latter CPU configuration to the system formulates a master-slave method of control. The signal interface between CPUs is mainly digital by means of the bus connectivity but analog interfaces are also employed. This configuration reduces the number of debugging checks by allowing distribution of CPU processing and also maintains system integrity when CPU inconsistencies occur. Figure 5 shows a block diagram of the electronic control unit.

### 3.1. Automatic Turning Control

To achieve ease of operation, automatic deceleration and acceleration in a smooth response without any unusual feeling of movement is required when the operator uses the push switches to initiate a turning operation. While the motor drive is operating, the snow thrower must evaluate the various possible drive conditions such as whether it is driving on a paved surface, moving over snow (especially when a crawler drive is employed the influence to the running movement is significant because of the large surface contact) or conducting snow-cleaning work. Such variable factors were set as parameters, and the targeted speeds, *SPm* and *SPm'* were obtained from model Eqs. (1) and (2). These represent the target speed for the left and right driving shaft respectively and are calculated in the master CPU.

The targeted forward speed is determined according to the target speed data of forward *ACC* input by the speed adjustment lever. The same target speed value is indicated to the two slave CPUs to perform the forward running motion.

The turning instruction command is entered with the R or L mounted push switches. This initiates a request for the target speed data of deceleration *SPm* and the target speed data of counter side deceleration *SPm'* and then executes automatic deceleration in a timed series control.

$$SPm = (a1 \times DECm \times ACC) - (a2 \times DECm' \times ACC) \quad (1)$$

$$SPm' = a1 \times DECm' \times ACC \quad (2)$$

*SPm* : target speed data for deceleration
*SPm'* : target speed data for counter side deceleration
*ACC* : target speed data of forward
*DECm* : speed reduction for deceleration (parameter)
*DECm'* : speed reduction for counter side deceleration (parameter)
*a1* : rate of deceleration contribution 1 (parameter)
*a2* : rate of deceleration contribution 2 (parameter)

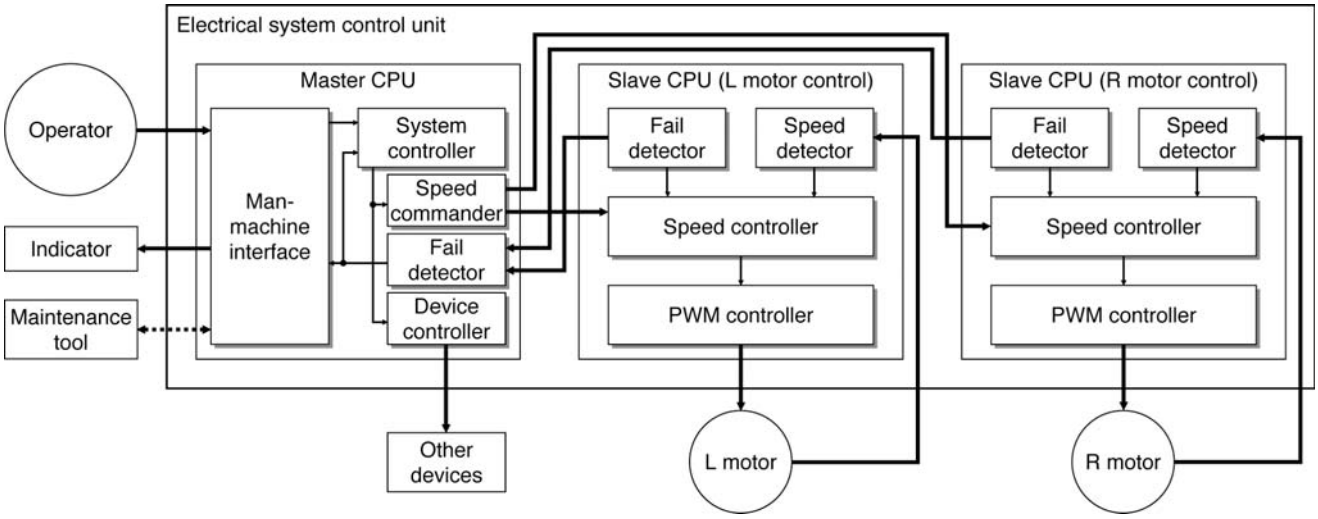



Fig. 5 System block diagram

Using *DECm*, the time series control and the rate of deceleration required for the automatic deceleration pattern after the push switch is activated are determined. The running speed when the push switch is activated and running load influence the location of the vehicle's center of gravity and produces a difference in running behavior and deceleration. In determining the deceleration pattern, these parameters are optimized through actual vehicle tests so that there would be no unusual feeling in behavior to the operator under each condition. Figure 6 shows a graph of the *DECm* MAP data.

*a1* and *a2* are independent parameters for the snow thrower's left and right mounted motor drive system. Turning of the snow thrower is carried out by slowing down the speed of the wheels on one side. Reducing the speed slightly on the counter deceleration side as well as on the deceleration side yields a smooth turning feel. The Map data is derived in the same way as that for *DECm*.

The *ACC* input on the actual snow thrower is operated by the acceleration lever positioned on a straight line. The total operation range comprises of the speed range of the forward motion, the stop position (neutral position) and the reverse motion. This data is converted into analog signal and inputted into the model equation. However, the mounting tolerance of the analog potentiometer and other factors create reading variation on individual units. In order to retain reliable operation of this system in respect to such variable factors, the *ACC* calculation has also been set to a model pattern where the initial operation is to compensate for such deviations.

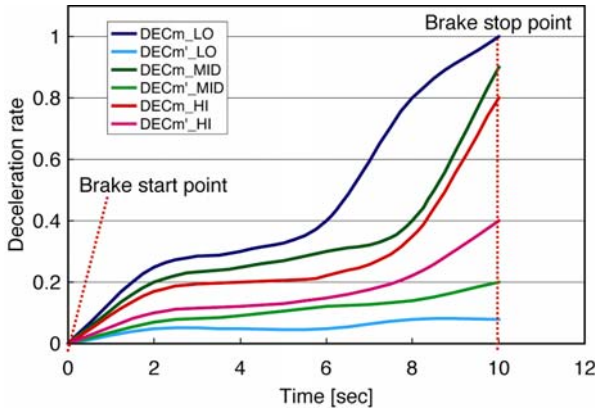



Fig. 6 DECm MAP data

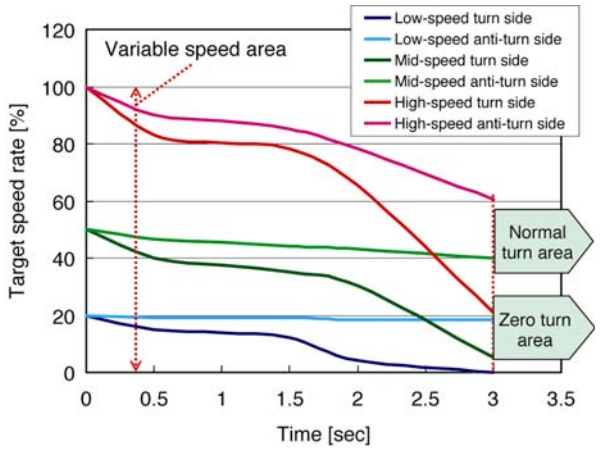



Fig. 7 Brake timing chart

Figure 7 shows a deceleration curve obtained from Eqs. (1) and (2) when each of the parameters is fixed. This yields a correlative output according to each of the running conditions.

These results are illustrated in the automatic turn control image as shown in Fig. 8.

### 3.2. Motor Drive Control

The maximum torque for the driving motor required by the small-size snow thrower is 4.5 Nm; the maximum motor speed is 2 500 rpm. Figure 9 shows the relationship between the motor speed and motor torque required for the driving motor. Control must be implemented to quickly reach the target speed calculated by the master CPU without any noticeable disruption of movement, ensuring a desired level of operational ease. Also, a stable speed control is required while the system is conducting snow-clearing work at low speeds under a 12 V power source.

In resolving these issues the following controls have been implemented to satisfy configuration demands of the small-size snow thrower:

- Motor speed control
- Switching of high-side with low-side
- Phase change by force
- Cancellation of zero start synchro control

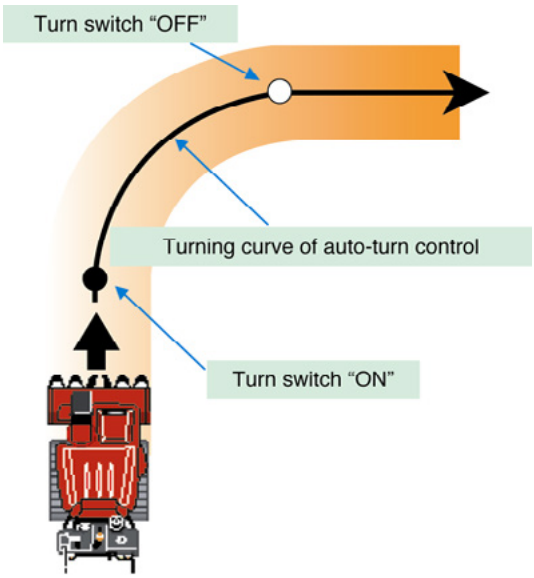



Fig. 8 Turning curve line of auto-turn control

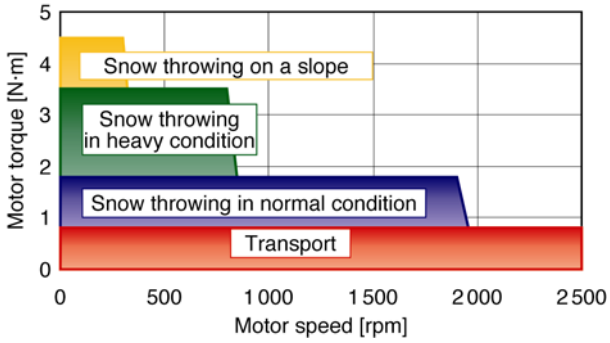



Fig. 9 T-N curve of brushless DC motor

### 3.2.1. Motor speed control

As mentioned earlier, this system comprises three CPUs. The calculation for target speeds that regulate the vehicle speed in response to the operator's control input is conducted by the master CPU, which determines the *SPm* and *SPm'* parameters for the R and L motors. The two slave CPUs for controlling the left and right mounted motors provide speed feedback in accordance with the values calculated by the master CPU and provide follow-up control to changes of the vehicle's speed due to the surface conditions and workload. Each slave CPU executes control regulation independently without any interference to one another. This configuration is able to assign the highest priority response to change the vehicle speed. Additionally, the resulting imbalance in the right and left motor speeds has been addressed by assigning synchro control to the master CPU that responds after receiving motor speed data in real time from each slave CPU.

The slave CPUs carry out feedback control with the PI method control function and use the feed forward control for the targeted speed to achieve quick responsiveness and prevent speed overshooting in response to variations in vehicle speed and target speed. Figure 10 shows a slave CPU control block diagram. Figure 11 shows target speeds and Map data for feed forward control speeds.

The integral coefficient for feedback control as shown in Fig. 12 provides Map data for deceleration and acceleration values and provides a stabilized response across the range of speeds.

### 3.2.2. Switching of high-side with low-side

To provide the necessary running torque for driving the vehicle powered with a 12 V source, an increase in current is required. With switching elements (hereafter referred to as FET), a larger capacity configuration is preferred in order to accommodate occurrences of heat generation by switching loss and withstand current. However, a larger capacity FET would be physically larger and more costly. This development has enabled the adoption of a small capacity FET by implementing a motor drive with an improved switching efficiency rate that has reduced the level of heat loss and provides a reliable safeguard.

The motor drive is configured with a bridge circuit three-phase motor on the high side and low side. The motor drive controls equalization of FET loss balance. The issue of heat generation in real mode operation has been solved as shown in Fig. 13 where the difference in temperature on the high side and low side does not exceed Δt=20.

### 3.2.3. Phase change by force

The maximum torque required while the unit is running or when conducting work operation is 4.5 Nm. However, if the crawler becomes locked while the machine is running, there are situations when the lock cannot be released even when maximum torque is reached. In such situations, the system will conduct a series of protection processes when either the master CPU detects the locked condition or a slave CPU detects an over voltage reading. However, there is a need for the working unit to run continuously even though the crawler remains in the locked position. When an over voltage is detected in the conventional machine, more power is required for retry action. This is not possible however in a 12 V system. Furthermore, the crawler locked condition causes continuous electrical input to the same single phase and carries a large flow of current flow. This eventually leads to over voltage output. Therefore, the method is employed in which a phase change control is forcibly exerted to cause the lock to be released and send electricity to a new phase. Figure 14 shows the torque level during a crawler lock condition.

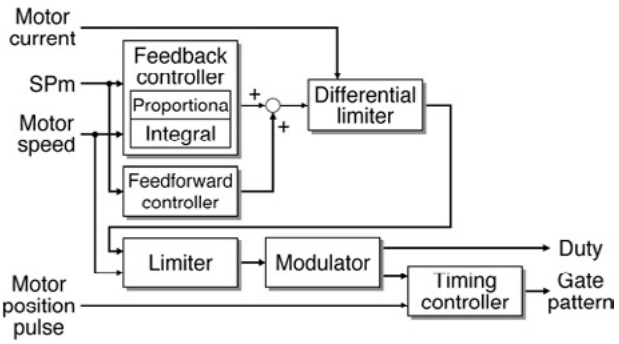



Fig. 10 DRV control block diagram

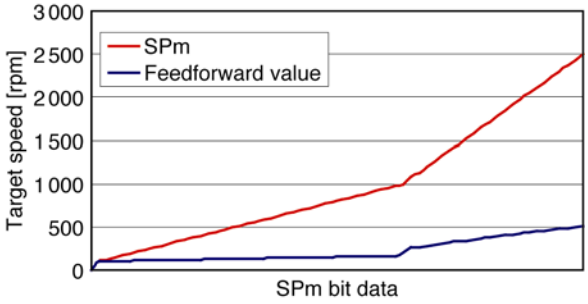



Fig. 11 Feedforward value

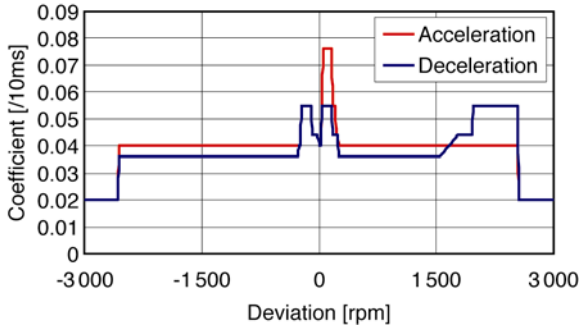



Fig. 12 Integral coefficient MAP

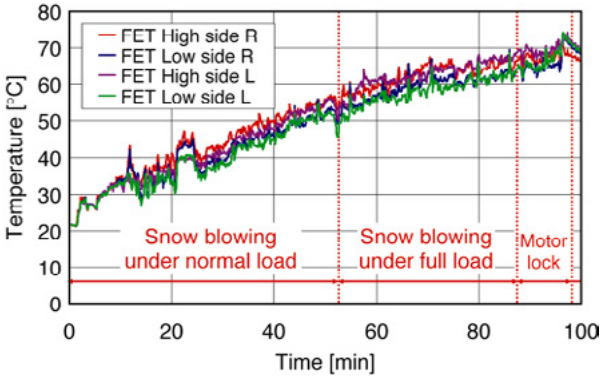



Fig. 13 Result of measurements temperature of drive FET

### 3.2.4. Cancellation of zero start synchro control

With the implementation of the 12 V DC power source, there are cases where the motors are powered with an impressed voltage level of 3 V when running at low speeds. When the applied voltage for the target speed is so low, the start response of the forward propulsion synchro control, which reliably compensates for the speed difference in the independent left and right mounted motors, deteriorates.

It was discovered that not synchronizing the left and right motors at the drive startup provides a better initial response. Consequentially, it was decided to cancel the synchro control of the left and right motors until a speed was reached wherein the machine's forward propulsion motion was not adversely affected. This process was removed immediately after an initial speed was reached. Testing of whether this had any negative influence on the synchro control while the machine was running has shown that this is not a concern. The process has been applied only from the initial zero speed up until the machine begins to move. Normal processing has otherwise been applied at deceleration of forward speeds and when the unit is being turned.

The results gathered from this section have been effectively applied to the working machine where the drive is running at high resistance with crawler work activity.

## 4. Hardware Configuration

The previous section dealt with the counter measures applied to the system software. This section will discuss hardware related issues and countermeasures.

Over voltage resulting from the application of regenerative braking current is characteristic of hardware configured around a 12 V DC power source. This development has successfully determined the circuitry voltage specification from the peak voltage levels applied to the controller and driver components respectively. Protection of over voltage level occurrences has also ensured voltage reliability. Figure 15 shows the circuit board for the ECU/DRV unit.

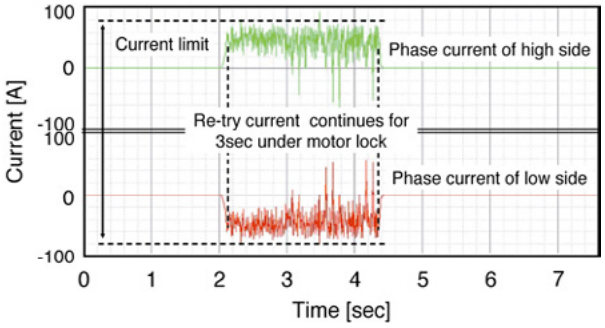



Fig. 14 Results of lock current measurements

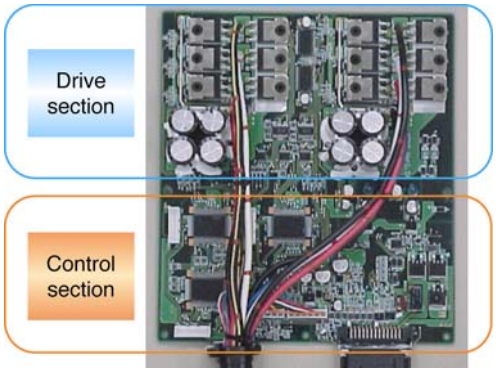



Fig. 15 Circuit board of ECU/DRV unit

### 4.1. Integrated Circuit Board

The large scale integration layout has been applied on a print circuit board consisting of four glass epoxy layers. The pattern line of power ground (hereafter referred to as GND) was taken into consideration in the board design to prevent any negative influence on the controller when conducting large current flow switching at the motor drive. Each GND was adapted to a common configuration to minimize the pattern surface area. The CPU GND however was configured separately and the GND location is set close to the connector pattern in conjunction with the common condenser with surge-suppression elements. This has also succeeded in maintaining GND noise integrity.

### 4.2. Control Power Source Configuration

The device is integrated in a single unit construction wherein multiple power sources are configured on the same circuit board. The following power source configurations have been integrated to achieve a small power source construction:

- Shared motor drive power and DRV control power sources
- Independent system control power source

After establishing the startup time difference for each power source regulator, the hardware was configured so that the master CPU would start before the slave CPUs when the power is initiated.

### 4.3. Input/Output Line

As shown in Fig. 16, the signal and device power interface lines have been designed as a direct coupler on the circuit board. This has eliminated the need for a wire harness in the unit, improving reliability and reducing cost. The battery power source input line and motor drive output power line have been connected to the circuit board via a direct cable. This has eliminated the need for a circuit board pattern for power lines to carry large current flow. Improving the efficiency of the circuit board layout pattern and minimizing the overall line length have reduced the overall circuit board surface area and 10% reduction in the volume compared with the previous device configuration was achieved.

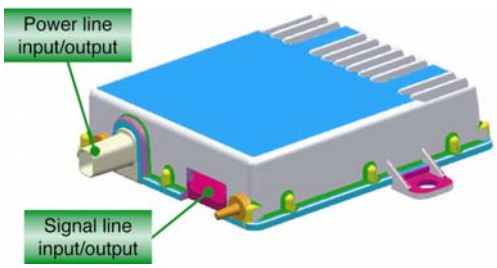



Fig. 16 Overview of ECU/DRV unit

Table 1 Major specification of hybrid snow thrower

| Items | Former hybrid model | New hybrid model |
|---|---|---|
| Type | Medium | Small |
| L × W × H [mm] | 1 650 × 920 × 1 340 | 1 500 × 725 × 1 155 |
| Outfitted weight [kg] | 265 | 163 |
| Snow-clearing width [mm] | 920 | 710 |
| Snow-clearing height [mm] | 580 | 510 |
| Maximum snow-clearing volume [ton/h] | 80 | 60 |
| Drive system | Dual drive for DC motor | Dual drive for brushless DC motor |
| Speed control | Pulse Width Modulation (PWM) control with unipolar drive | Pulse Width Modulation (PWM) control with bipolar drive |
| Motor reduction gear ratio | 61 : 1 | 36.4 : 1 |
| Maximum speed [m/sec]<br>Maximum motor speed [rpm] | 0.78<br>3 000 | 0.8<br>2 500 |
| Maximum motor output [N·m] | 4.5 | 4.5 |
| Turning | Manual operation with analog switches | Automatic control with digital switches |
| Power source | 12V battery ×2 | 12V battery |
| Control device | Electronic Control Unit (ECU)<br>Motor Driver (DRV) ×2 | Unified controller |

## 5. Unit Test Results

Figure 17 shows an overview of the hybrid small-size snow thrower used in the evaluation testing of the running speed response from the time the machine is started through its maximum running speed and for the evaluation of user feeling while the machine is in work mode. Table 1 lists the major specifications of the small-size hybrid snow thrower. The successful developments carried out for the hybrid small snow thrower have enabled the introduction of a new snow thrower model that offers significant enhancements over previous models including the adoption of an electronic control system and the improvement of snow-cleaning efficiency by 30% over conventional mechanical small-size snow thrower. Furthermore, the full cover construction has reduced the machine's working noise level and overall mechanical vibration. The results of the actual working test conducted on this small-size hybrid snow thrower clearly demonstrate a level of performance that satisfies the running requirements for small-size snow thrower units.

### 5.1. Snow Thrower Running Speed Response

Influences to the motor speed control for driving the snow thrower unit include: 1) changes initiated by the operator to speed operation, 2) surface changes ranging from tiled surfaces having a low friction coefficient (μ) to a partially melted snow surface having a high μ value, 3) changes in snow removal performance according to the work load. Figure 18 shows the time variables associated with the motor speed response in relation to the motor's actual speed and the internal variable *SPm* (the target speed calculated by the master CPU). The graph shows the response characteristics of the actual motor speed against the optimal target speed *SPm* under different load conditions when the speed control by an operator ranges from the initial low speed to the maximum speed.

Even with the previously described changes, the unit was able to achieve a linear response to deliver a highly satisfactory level of operational ease.




Fig. 17 Overview of hybrid small snow thrower

### 5.2. Performance Behavior of the 12 V DC Power Source Configuration

The following results were observed in the actual unit test conducted on the 12 V DC power source configuration where voltage drops during high load runs and changes in drive speed caused by fluctuating primary voltage due to varying work loads were measured:

- Lowest voltage level when voltage dropped during performance run 11.4 V
- Deviation in rated speed for varying voltage levels ± 6%

These results indicate that the voltage level did not exert any influence to the system controls or responsiveness and also shows that the performance levels were well within the permissible rated speed range.

### 5.3. Stability During Turning Operation

Maintaining stability when performing turning operations is essential particularly when exposed to a range of variables during snow-cleaning work. Figure 19 shows an analysis of the yaw rate. These results confirm that a stable yaw rate was achieved during turning operation without creating any noticeable disruption of movement to provide an overall favorable level of responsiveness.

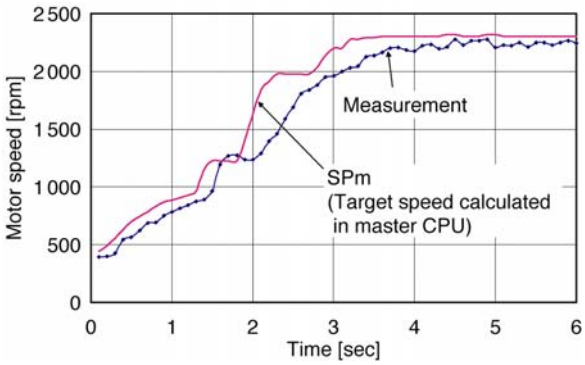



Fig. 18 Response time graph for different load characteristics

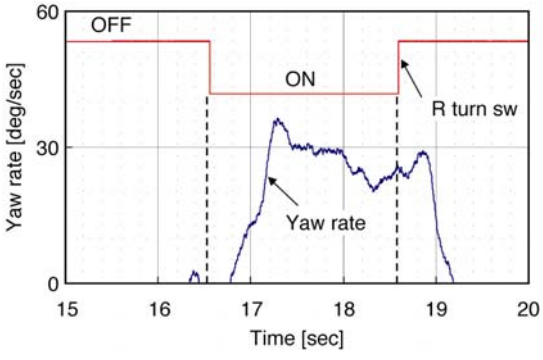



Fig. 19 Response time graph of vector curve

## 6. Conclusion

The development of an electronic control system for a small-size hybrid snow thrower has yielded the following:

(1) Automatic turning control that provides stable turning performance with automatic speed deceleration and acceleration, which is operated by an easy to use push switch.

(2) Motor speed control provides stable control even with variable factors including load condition and fluctuation of voltage. Additionally, switching control of high-side with low-side, phase change by force and cancellation of zero start synchro control have achieved the necessary running torque and speed with a 12 V drive power source, enabling complete system configuration under the 12 V DC power source.

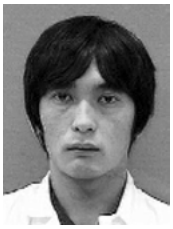
(3) Integrated circuit board and miniaturized control power source configuration; direct coupler configuration for input/output lines and shared cable connectivity on the circuit board - have reduced the volume of the control unit by 10% compared with the control device employed in the medium-sized hybrid snow thrower.

## References

(1) Matsuki, M., Wakashiro, T., Kamiyama, T., Sato, T., Kaku, T., Kanda, M.: Development of a New Power Train for the Civic Hybrid, Honda R&D Technical Review, Vol. 14, No. 1, p. 39-48 (2002)

(2) Hanafusa, J., Wakitani, T., Yamamoto, T., Inui, T.: Development of Hybrid HS1390i Snow Thrower, Honda R&D Technical Review, Vol. 14, No. 1, p. 31-38 (2002)

■ Authors ■


Tsutomu WAKITANI


Yoshihiko YAMAGISHI


Toshiaki KAWAKAMI


Tsutomu MIZOROKE

# Establishment of Rapid Manufacturing System for Dies to Produce Hydraulic Valve Body Prototype

Hiromi SHIMADA* Yoichiro ISHIHAMA* Yoshihisa HAYAKAWA*
Shigemi KAWATA* Takanao UCHIDA*

## ABSTRACT

The use of different casting methods causes differences in the detailed shapes of mass-production and prototype models of the hydraulic valve bodies which make up the hydraulic circuits employed for shift control in automatic transmissions. These differences make it necessary to reset the shift control specifications in mass-production models after their initial setting in the prototypes. This issue could be resolved by replacing the sand molds currently used to cast prototypes with the dies used in mass production, but the length of time required to produce prototypes with the dies renders this method impractical. Therefore, new production techniques were proposed and the production workflow was studied in order to reduce the period required to produce dies. As a result, prototype hydraulic valve bodies can now be produced using dies in a shorter period than previously required when using sand molds.

## 1. Introduction

The hydraulic control units of automatic transmissions are used to perform smooth, shock-free shift control. The hydraulic control specifications are set using hydraulic circuits that are formed by hydraulic valve bodies which are aluminum diecast (hereafter, “diecast”) parts. Differences occur in the detailed shapes of mass-production and prototype models of hydraulic valve bodies such as the draft angles and corner roundness of the bottom of the hydraulic circuit as shown in Fig. 1. As automatic transmission control has become more precise in recent years, these differences in the detailed shapes can affect the hydraulic characteristics. This made it necessary to reset the hydraulic control specifications in mass-production models after their initial setting in the prototypes.

These differences in the detailed shapes of mass-production and prototype models of hydraulic valve bodies are caused by the use of different casting methods for mass-production and prototype models. Figure 2 shows the manufacturing processes for mass-production and prototype models. The product designer creates the detailed 3D model shown in Fig. 2 by reflecting the parting lines, draft angles, fillet roundness and other specification requests from the manufacturing side to the model using 3D CAD. This detailed 3D model is used in the same manner for both mass-

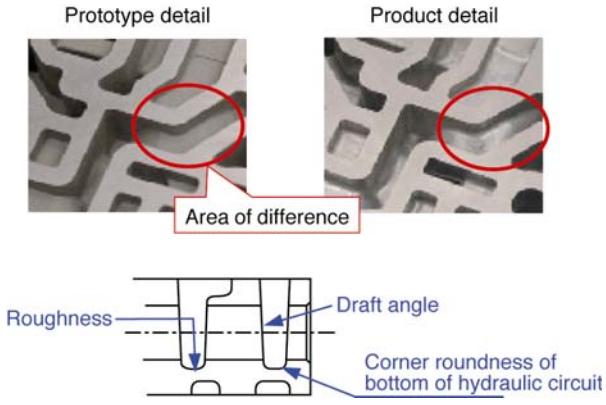



Fig. 1 Comparison of detail shape in prototype, and product

* Tochigi R&D Center

production and prototype models. In the mass-production model manufacturing process, the detailed 3D model is used for the CAM model, and the die is carved by a CNC machine and used for diecasting. The detailed 3D model is also used for the CAM model in the prototype model manufacturing process, but in this case a wood mold is carved by a CNC machine, and this wood mold is then used to make a sand mold for diecasting. In the prototype model manufacturing process, the sand mold is made manually, and it is in this process that differences occur in the detailed shapes of mass-production and prototype models due to the following factors:

(1) Wood mold matching defects due to sand entering between the layers of the slice type wood mold. (Fig. 2)
(2) Slice type wood mold wear.
(3) Misalignment when joining the sand molds for the hydraulic circuit shape portions to the main sand mold.
(4) Misalignment when matching the upper and lower sand molds.
(5) Sand mold tip deformation.

These factors were investigated to propose a countermeasure to make the detailed shapes for prototypes the same as those for mass-production models, but variance in manual work could not be eliminated, so no solution was reached.

Therefore, in order to make the detailed shapes of hydraulic valve body prototypes the same as mass-production models, it was necessary to manufacture prototype models using dies.

## 2. Goals of Constructing a Rapid Manufacturing System

Normally, a diecast die is manufactured specially for each part type. This is the same when manufacturing prototypes using dies, so the lead time is doubled when compared to manufacturing prototypes using conventional sand molds as shown in Fig. 3. The die manufacturing period in this case accounted for 3/4 of the total manufacturing period from when the Product Design Division issued the detailed 3D model drawings until completion of the prototype as shown in Fig. 4. Furthermore, the manufacturing process for the main die required the most time within the die manufacturing period, and accounted for half of the total manufacturing period.

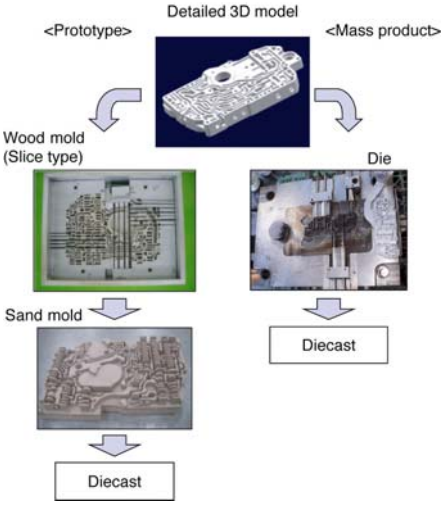



Fig. 2 Manufacturing process

The diecast manufacturing specifications are determined by performing a number of casting tries (Fig. 4) to eliminate casting defects such as casting cavities (Fig. 5), cold shut and surface folding. The various casting try processes are described below.

(1) Die casting: The die is placed in a diecast machine at the diecast factory, the liquid metal controls such as the liquid metal speed during diecasting are set, and diecasting is performed.
(2) Machine work: The diecast materials are machined at the machine work factory, and the worked surfaces are inspected for casting defects.
(3) Casting plan modification: When casting defects are found, the casting plan, which consists of gates, runners, backups, air vents and other die shapes such as shown in Fig. 11, is reviewed and modified at the die factory to improve the liquid metal flow.

A single casting try consists of all three processes (1), (2) and (3) above. In addition, these processes are each performed at a separate factory, and shifting between processes requires time to transport the die and the casting try

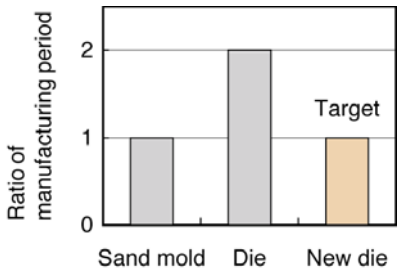



Fig. 3 Comparison of manufacturing periods

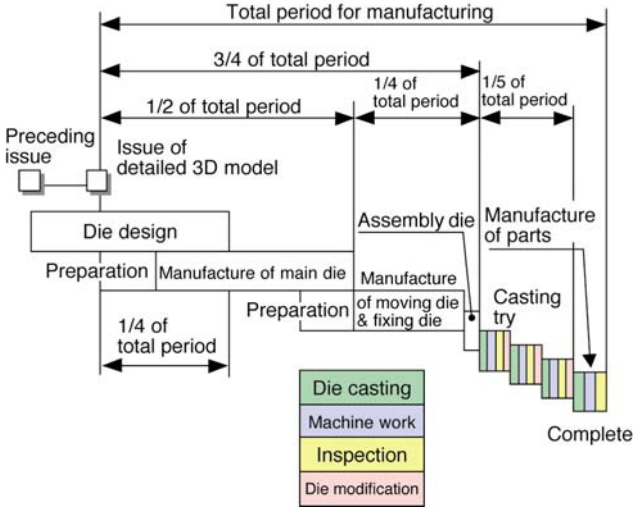



Fig. 4 Workflow of manufacture by die

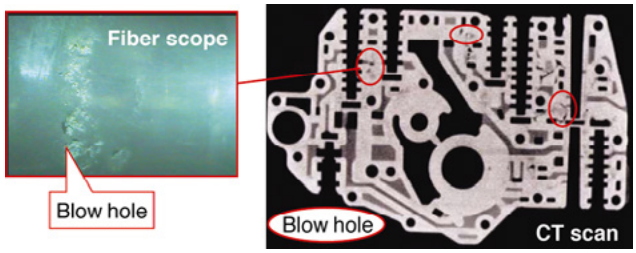



Fig. 5 Casting cavity

product to each factory. Normally around three casting tries are required to eliminate the casting defects. For these reasons, the casting try period accounted for approximately 1/5 of the total manufacturing period. (Fig. 4)

Die design starts when the preceding drawings are received from the Product Design Division. After that, the official detailed 3D model drawings are received and the details are designed. For this reason, the die design process in Fig. 4 was included in the manufacturing period, and accounted for 1/4 of the total manufacturing period.

Therefore, the following issues were raised as measures for shortening the manufacturing period using dies to the same as the manufacturing period using sand molds.

(1) Shortening the die manufacturing period
(2) Reducing the number of casting tries
(3) Advancing the die design timing

## 3. Construction of a Rapid Manufacturing System

### 3.1. Shortening the Die Manufacturing Period

#### 3.1.1. Characteristics of the hydraulic valve body die shape

The characteristics of the hydraulic valve body shape are as follows.

(1) Hydraulic circuits are present on the front and reverse surfaces. (Fig. 6)
(2) Holes for inserting hydraulic valves are present on the right and left sides. (Fig. 6)
(3) An exclusive shape is used for each type of automatic transmission, but all shapes resemble each other.

In order to support these hydraulic valve body shape characteristics, the die structure consists of a moving die and a fixing die that assemble the die of the product shape to the main die, and slide pins located on the left and right sides of the moving die as shown in Fig. 7. Here as well, all die shapes resemble each other. Therefore, a study was made as to whether this similarity in die shape characteristics could be used to create standard main die and slide base units.

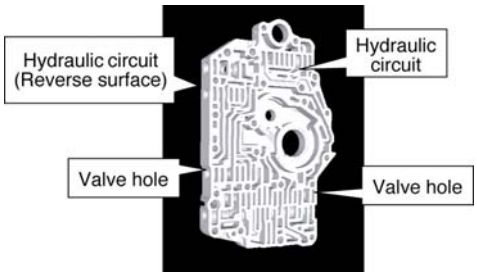



Fig. 6 Shape of hydraulic value body

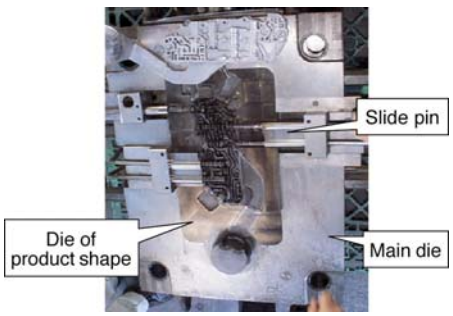



Fig. 7 Moving die

#### 3.1.2. Creating standard main die units

Creating a standard main die unit entails standardizing the dimensions of the moving die and fixing die portions that assemble the die of the product shape to the main die, and the width dimensions of the moving die portion that assembles the slide base as shown in Fig. 8. In order to investigate this standardization, a survey was made of all Honda hydraulic valve body types to obtain the maximum projected area of the hydraulic valve body outline and the maximum installation width dimension of the hydraulic valve holes. These results were then used to study the creation of a standard main die unit that supports the maximum projected area of the hydraulic valve body. However, the following issues were found for the hydraulic valve body with the minimum projected area.

(1) The wasted material area for the product shape die (Fig. 8) increased, resulting in excess material costs.
(2) Larger diecast machines than the necessary size were required, resulting in excess facility costs.
(3) The area of the product shape (Fig. 8) that contacts the liquid metal decreases relative to the size of the die, making it difficult for the die to reach the set temperature during the diecast process, which can easily lead to surface folding and other casting defects.

In order to resolve these issues, the standard dimensions of the product shape die were divided into two sets of dimensions for hydraulic valve bodies with large and small projected areas, and two types (large size and small size) of standard main die units were set. In addition, the slide base width dimension was set at the maximum installation width dimension of the hydraulic valve holes to support small-size and large-size main dies.

#### 3.1.3. Creating standard slide base units

Two types of standard slide base unit were also set to support the slide base width dimensions of the standard main die units. In addition to the horizontal direction, an inclined valve hole insertion direction is also present as shown in Fig. 8. For this reason an adapter was set between the slide base and the slide pin.

#### 3.1.4. Exclusive die parts

When manufacturing a hydraulic valve body prototype die using standard main die and slide base units, it is necessary to newly manufacture or perform additional machine work only for the following die parts which are exclusive to each hydraulic valve body type.

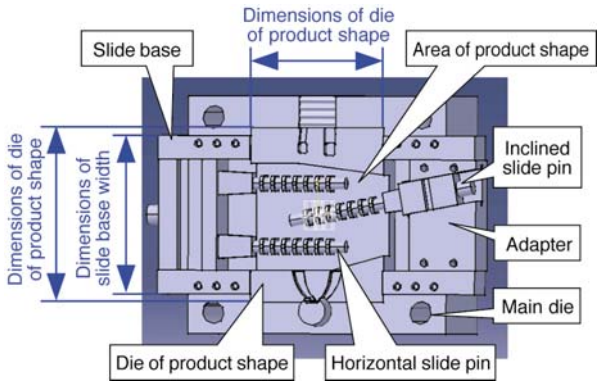



Fig. 8 Standard main die unit

(1) Newly manufacture the product shape die (Fig. 9)
(2) Newly manufacture the slide pins (Fig. 8)
(3) Perform additional work as necessary for the cooling hose holes in the back block (Fig. 9)
(4) Newly manufacture an adapter as necessary (Fig. 8)

Creating standard main die and slide base units and reducing the number of exclusive die parts reduced the die manufacturing period to 1/3 the previously required period. As a result, the total manufacturing period was halved. Fig. 10 shows an example of a hydraulic valve body prototype die manufactured using standard main die and slide base units.

## 3.2. Reducing the Number of Casting Tries

### 3.2.1. Hydraulic valve hole casting cavities

The greatest issue in terms of hydraulic valve body casting defects is that of casting cavities occurring on the inner surface of the machine-worked holes where the hydraulic valves are inserted (Fig. 5). The cause of these casting cavities is that these parts are located at deep positions from the outside of the die, so cooling is slow during the diecast process. In addition, these parts are the hydraulic valve sliding surfaces, so the quality standards for casting cavities are quite strict. Therefore, methods for improving the cooling performance and reducing the machine work allowance around the valve holes were investigated to resolve the above issue and reduce the number of casting tries.

### 3.2.2. Reducing the number of casting tries to one time

The following methods were investigated to reduce the number of casting tries.

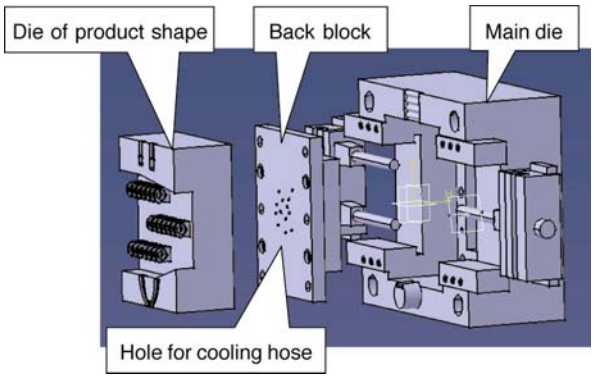



Fig. 9 Configuration of main die unit

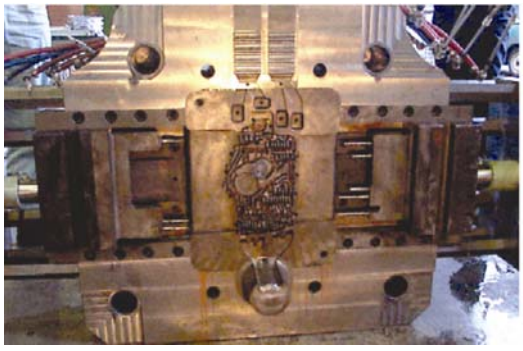


Fig. 10 New prototype die produced by standard main die unit

(1) Application of specifications that prevent casting defects to dies Casting plans with proven results in mass-production and prototype dies were used, and the following new specifications were applied to new prototype dies in order to prevent casting defects and especially hydraulic valve hole casting cavities from occurring during the casting tries.

a. Improvement of cooling performance around the valve holes Cooling in the slide pins, line cooling and spot cooling were added as shown in Fig. 11.

b. Reduction of the machine work allowance The depth from the casting surface at which casting cavities occurred was analyzed, and the results showed a correlation between casting cavity occurrence and depth, with fewer casting cavities forming near the cooling surface. Reducing the slide pin draft angle to the low angle at which raw cast can be removed from a die was also studied as shown in Fig. 12. This reduced the machine work allowance.

These measures made it difficult for casting cavities to occur on the machine-worked surfaces of the valve holes during the casting tries.

(2) Integration of casting try processes to the diecast factory Applying specifications that prevent casting defects to dies eliminated the need for major modifications to the casting plan that were formerly performed at the die factory. This made it possible to integrate the following processes that were formerly performed at the machine work and die factories to the diecast factory. (Fig. 13)

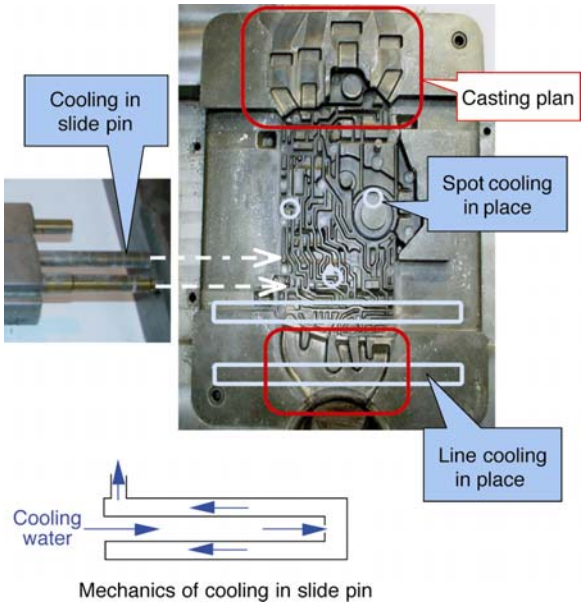



Fig. 11 Improvement of cooling capability of die

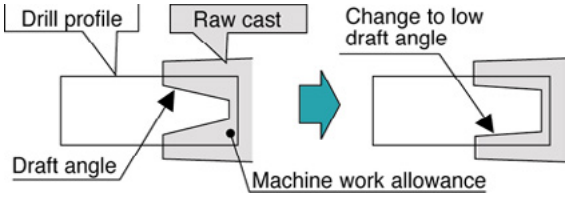



Fig. 12 Low draft angle slide pin

(a) Machine work for valve hole and other inspections
(b) Casting defect inspections of the valve holes and other machine-worked surfaces
(c) Modification work of the casting plan

This eliminated the need to transport dies and casting try products between factories when shifting processes.

By applying specifications that prevent casting defects to dies and integrating the casting try processes to the diecast factory, the number of casting tries could be reduced from three times to just one time. This in turn reduced 1/8 of the total manufacturing period.

## 3.3. Advancing the Die Design Timing

### 3.3.1. Utilization of product shape layout drawings

Advancing the die design start timing in the workflow shown in Fig. 4 was investigated. Die design performed in the initial stages consists of investigating the die concept and designing the material procurement and other preparation processes shown in Fig. 4. These processes are preparation for manufacturing the moving die, fixing die, slide pins and other parts (manufacture of the moving die and fixing die in Fig. 4). In order to start these die design processes, product shape layout drawings that show the hydraulic valve body profile, the number of valves and the valve positions are required. Therefore, the new workflow shown in Fig. 14 added a process for sending the layout drawings from the Product Design Division to the Die Design Division before the preceding drawings.

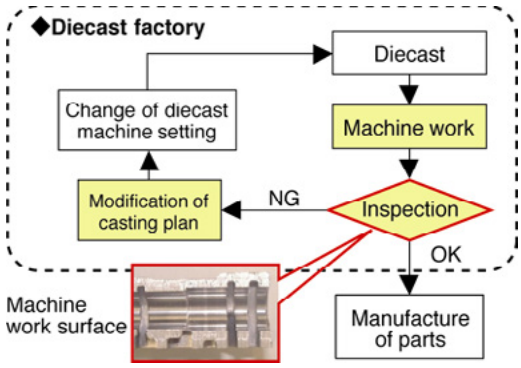



Fig. 13 Flow of casting try for one time

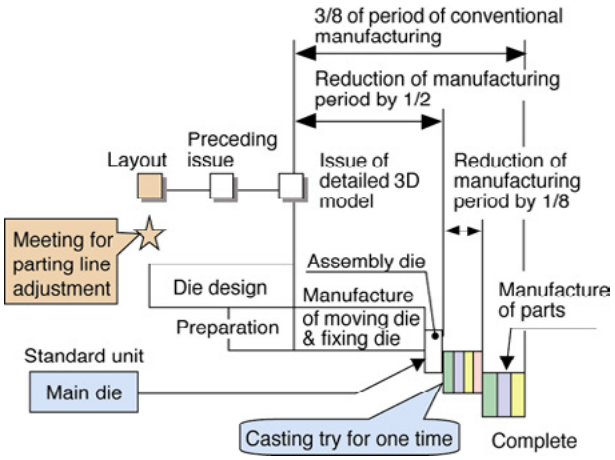



Fig. 14 Workflow of manufacture by new die

### 3.3.2. Setting meetings for parting line adjustment

In order to make the detailed die design, the parting lines must first be set. Therefore, the new workflow shown in Fig. 14 set a meeting to coordinate between the product designers and the die designers at the same time as the layout drawings are sent from the Product Design Division to the Die Design Division. In addition, the mass-production die designers also attend this meeting to ensure that the parting lines are the same in the mass-production and prototype dies.

As a result of these changes, the die design process was moved before the manufacturing process as shown in Fig. 14. This eliminated the need to consider the die design period as part of the manufacturing period.

# 4. Effects of the Rapid Manufacturing System

## 4.1. Shortening the Manufacturing Period

By shortening the die manufacturing period and reducing the die design period, the prototype manufacturing period using dies was shortened to half the previously required manufacturing period as shown in Fig. 14. In addition, reducing the number of casting tries further shortened the manufacturing period by 1/8, which resulted in a manufacturing period only 3/8 as long as the conventional prototype manufacturing period using dies as shown in Fig. 15. This period is also just 3/4 the conventional prototype manufacturing period using sand molds.

## 4.2. Equalizing the Detailed Shapes of Mass-production and Prototype Models

The detailed shapes such as the hydraulic circuit draft angle, hydraulic circuit bottom corner roundness, and surface roughness that differed between mass-production and prototype models of hydraulic valve bodies were normalized by manufacturing the prototype models using dies. In addition, having prototype and mass-production die designers coordinate the parting lines also equalized the detailed shapes of mass-production and prototype models.

# 5. Conclusion

The following techniques were established and the workflow was reviewed in order to manufacture prototype models of hydraulic valve bodies using dies.

(1) Creation of standard main die and slide base units
(2) Reducing the number of casting tries to a single time
(3) Advancing the die design timing

These improvements have resulted in the creation of a system that can manufacture prototype models of hydraulic

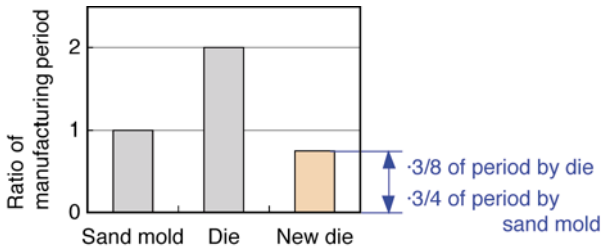



Fig. 15 Period required for manufacture by new die

valve bodies using dies in 3/4 the manufacturing period using conventional sand molds. In addition, the prototype models of hydraulic valve bodies have the same detailed shapes as mass-production models, which helps to increase the specification setting accuracy for hydraulic control in the development of automatic transmissions.

The manufacturing system presented in this report is a comprehensive technology consisting of 3D design technology capable of accurately expressing product shapes, high-speed die manufacturing technology, technology for preventing casting defects in diecast products, and workflow design technology. Construction of this type of technology is still limited to injection molding fields such as diecast and plastics. However, it is thought that comprehensive technology combining 3D design technology and manufacturing technology will also be established in other manufacturing fields such as machine working, and that this will foster workflow innovation that will spread throughout the manufacturing industry in the future.

## Acknowledgements

The authors wish to express their deepest gratitude to related parties those at Matsuoka Die and Mould Manufacturing Co., Ltd. for their cooperation in establishing technology for manufacturing dies and for resolving casting defects in a short period.

## References

(1) Uchida, T., Nagai, S., Koyama, S.: Practical Examples and Future Directions for CAE-Based Development for Automobile Transmission by Designers, Honda R&D Technical Review, Vol. 15, No. 1, p. 109-114 (2003)

(2) Shimada, H., Ishihama, Y., Kubota, N., Uchida, T.: Establishment of Design Method for Transmission by 3D Media, Honda R&D Technical Review, Vol. 14, No. 2, p. 107-114 (2002)

(3) Uchida, T., Nagai, S.: Practical Examples of Virtual Development for Automotive Transmission, JIDOSYA-GIJUTSU, Vol. 56, No. 6, p. 71-76 (2002)

■ Authors ■



Hiromi SHIMADA



Yoichiro ISHIHAMA



Yoshihisa HAYAKAWA



Shigemi KAWATA



Takanao UCHIDA

# Development of Modeling System for Data Proto Model

Hiroshi UEDA* Masaaki NAKAZATO* Akio KAGAYA*
Tadashi NAKAMURA* Teppei MORO* Hideyuki TANAKA*

## ABSTRACT

Honda's Data Proto Model (DPM) is a digitally-modeled prototype vehicle generated through the formulation of three-dimensional data for a complete vehicle and the input of the collected data into a computer. This paper discusses the development of two three-dimensional modeling systems for the vehicle body, which forms part of the DPM. One of these systems makes use of global time differences to enable modeling before the issue of design drawings, making an image of the latest body constantly available to designers. The other is a modeling system based on the BOM (Bill of material) established after the issue of design drawings. These systems enable other designers and members of the manufacturing division to refer on a daily basis to the latest form of the body. The DPM also enables constant review of specifications in the initial stages of design. A system was developed to facilitate DPM verification meetings; these bring together specialists to run checks on interference between components, review the design layout, etc., using DPM. As a result, any designer is able to use DPM for verification of the appropriateness of design, and the system is now in use in Honda's design departments.

## 1. Introduction

Among product developments in the global manufacturing industry, especially in the aeronautical and automotive industries, new product developments began through input of three dimensional data of all parts of a product in the computer from the early nineties, to perform product verification in the engineering design process, manufacturing process and testing process. (Fig. 1)[(1) – (11)]

Boeing was the first to input the three-dimensional data of all the parts of the product into the computer and use the data for development. Data of approximately 250 000 parts of the full-size models were converted to digital data in the development of the B777. Boeing called this Digital Pre-Assembly (DPA). DPA was used to start the simulation of assembly before the issue of design drawings. Even though the system development cost 500 billion yen, it has reaped huge benefits in terms of (1) reduction in development costs, (2) improvement in initial quality, (3) reduction in development time, and (4) increase in customer satisfaction[(1), (2)].

In 1995, for the first time in the field of vehicle development, Chrysler Corporation input the three-dimensional data of a complete car in the computer for the development of LH car. This was called Digital Model Assembly (DMA), and it marked the start of the assembly simulation of vehicles[(4)]. In recent years, some automotive companies that can develop vehicles without the physical prototype have also emerged[(10), (11)].

Honda started development of automobiles using DPM

* Tochigi R&D Center

from August 1996, but Honda had concerns regarding DPM. Sometimes, the input of three-dimensional data of all bodies could not be completed; therefore, a complete DPM could not be obtained. Moreover, the demands from all design departments, other than the body department, to create the body surface at the day-to-day design layout stage was high. On the other hand, improved CAD modeling was demanded for the CAD vendors[12), (13)], but no CAD package with innovative surface modeling techniques appeared in the market.

These concerns were resolved by developing a modeling process system before issue of design drawings using time differences between two nations and global networks, and by developing a modeling process system after issue of design drawings. The development of a system for DPM verification also enabled the DPM verification meetings to be held without any concerns.

This document introduces the DPM concept, system development for creating the body surface, and system development for DPM verification.

## 2. DPM Concept

Honda follows the 'Sangen' (the three-gen) concept[(14)]. The concept is to grasp facts and information and to develop products enhancing customer satisfaction by touching the actual object (Gen-butsu) on the actual place (Gen-ba) and by observing the actual fact (Gen-jitsu), at the development site. The Sangen concept is also important in the development of vehicles using the computer. Development equivalent to that of actual vehicles is possible using the computer only if actual data (facts, information) of the vehicles can be simulated[(15)]. That is, actual data exists in the real world in the form of data based on tests and data based on experience. Three-dimensional data and the data of results of computer analysis also exist in the computer simulation world. The developers need to grasp the data of both worlds to develop a product. Therefore Honda has taken "Data" as the first word in the expression "Data Proto Model". (Fig. 2) The prototype based on the data in the computer simulation world was named "Data Proto Model," corresponding to the "Physical

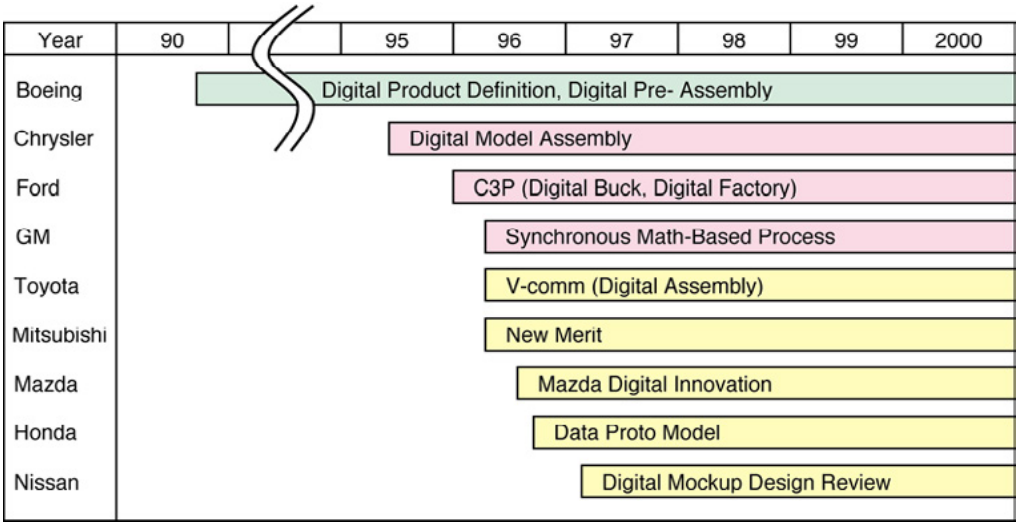



Fig. 1 History of employment of digital modeling in vehicle and airplane development

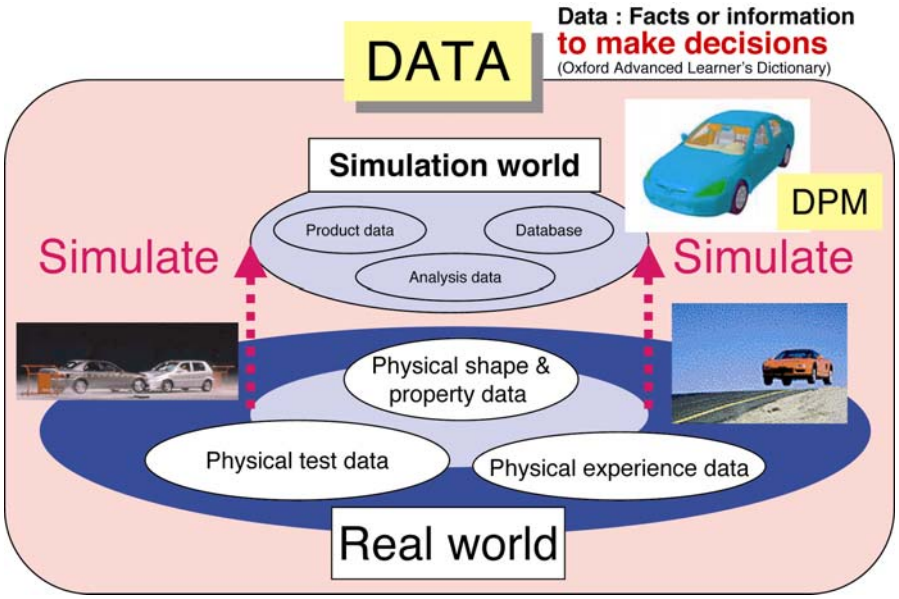



Fig. 2 Image of DPM

Proto Model" for objects. The first vehicle manufactured for tests is called a "Prototype" but it is abbreviated to "Proto" here.

## 3. Creation of Body Surface

Described here are the issues and their solutions when creating the body surface.

### 3.1. Issues Faced by Honda in the Conventional Modeling of Body Surface

The following issues have occurred since 1996 in the development of vehicles using DPM.

(1) As the surface elements are expressed and managed by complex tree structures (Fig. 3) in CAD, the creation and modification of surface data is laborious for the body designers. (Fig. 4)

(2) Wire frames are mainly used in the body design layout; therefore, it takes time for the manufacturing department and design department other than the body design to understand the body form and to make many sections of body form. As a result, demands for creating the day-to-day body surface at the design layout stage increased constantly.

(3) During the initial development stage, sometimes the DPM of the complete body could not be used since the three dimensional form data of the complete body was not available although the three dimensional model of the components such as the engine and chassis were available.

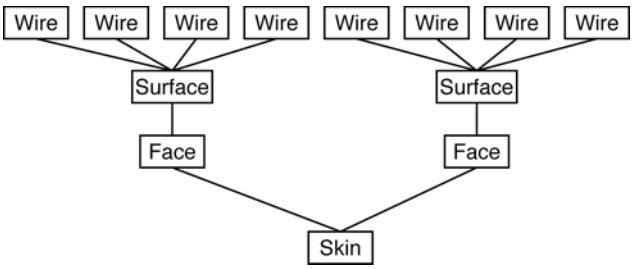



Fig. 3 Structure of elements in CAD

### 3.2. Modeling Using Time Differences Between Two Nations

The authors considered a modeling system using global network to meet the demands for the constant creation of the body surface (Fig. 5). The modeling support system using the global network was being used since 1997, and thus the foundation for continuous modeling using global time differences was already available. Hence the issues related to constantly creating the body surface could be resolved by using the processes mentioned below (Fig. 6).

(1) Preparations at the research center
- Registration of the latest wire frame model by the body designer.
- Data transmission daily by using the global network to the overseas modeling department.

(2) Work in the overseas modeling department
- Laying the surface on the body form by referring to the received wire model.
- Sending the created body surface to the research center at the decided time on the following day.

(3) Open work at the research center
- Registration of the body surface model in the open FILE.
- Referencing and verification by all departments.

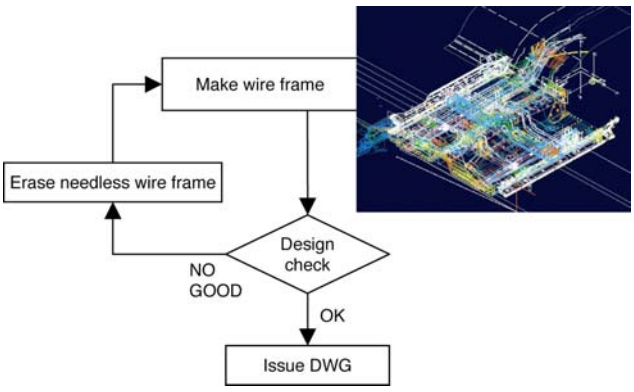
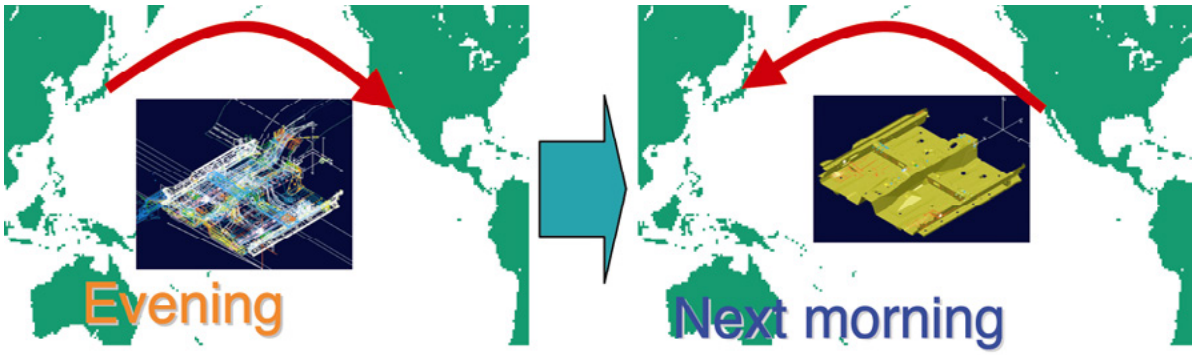



Fig. 4 Former body modeling process




(a) Send wire frame (a) Received skin model

Fig. 5 Modeling of body using time difference

The body surface emerges gradually by repeating these processes.

Since this body surface is conceived and created by persons other than designers, it is set as a tentative surface. It is given a yellow color (signal yellow)and assigned the name Yellow Body (YB) to serve as a warning that it is tentative. Finally, the designers confirm it and determine the body design surface.

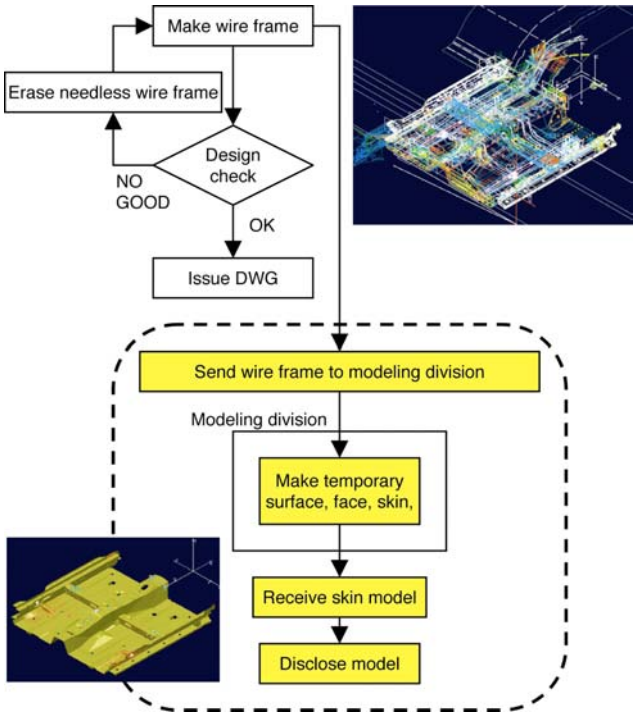



Fig. 6 New modeling of body using time difference

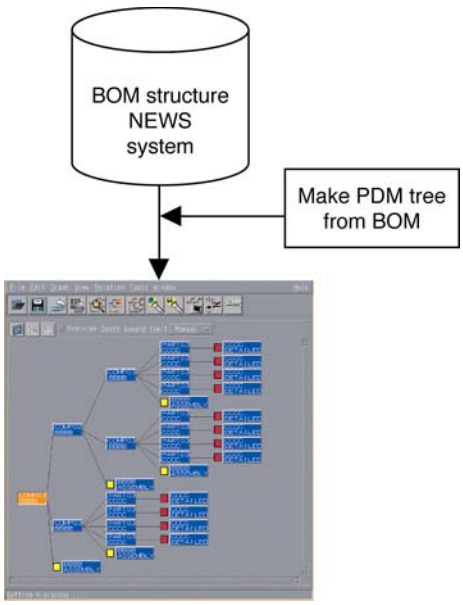



Fig. 7 PDM tree

## 3.3. Modeling After Issue of Design Drawings

The number of wire frame design drawings issued at the initial stage of development is extremely large, and it is necessary to create an efficient body surface after the formal issue of design drawings. The developed system is described below. This body data is used in DPM verification and analysis, where a more detailed check for interference between parts is required.

### 3.3.1. Extracting the body parts tree structure data

To efficiently manage the modeling requests and storage of the body data after the issue of design drawings, a function was developed to remove the parts tree structure (tree structure of parts) from the Bill of Materials (BOM) system (Fig. 7) and register it in the Product Data Management (PDM) of the body data.

The process flow is shown below.

(1) The BOM system outputs the parts tree structure based on information such as a car project name and car variation.
(2) Delete unnecessary parts tree structure (reference drawing, assembly diagram, and specifications, etc.), and use only the parts tree structure of the design drawings required for the body surface.
(3) Register the parts tree structure in PDM.
(4) Automatically link the issued body design drawings to the PDM.

In the data management by body PDM, the relationships between the parts are managed by a car variation information and the date.

This enables a total car variation management, where day-to-day changes can be managed.

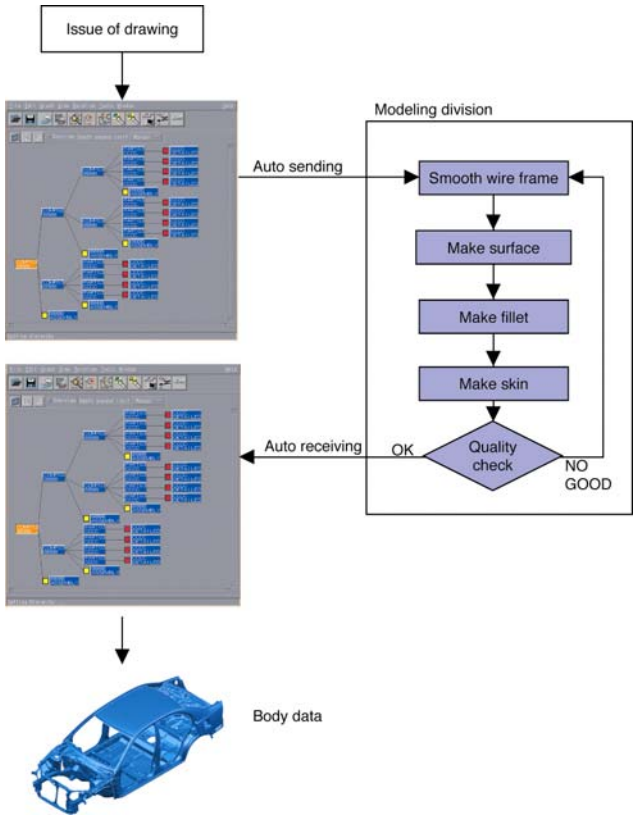



Fig. 8 Body modeling using PDM

### 3.3.2. Body surface modeling flow after formal issue of design drawings

The body surface modeling flow-using PDM is shown below (Fig. 8).

(1) The research center simultaneously sends the parts tree structure and design drawings of the body to the modeling department.
(2) The modeling department creates full data including fillets, and sends that data to the research center.
(3) The research center registers the received full data in the PDM.

STandard for the Exchange of Product model data (STEP) is used for the exchange of parts tree structures of the body. This body data is created according to the formally issued design drawings. It is colored in blue (signal blue) to signify safety and is called Blue Body.

## 4. Development of DPM Verification System

For efficient verification using DPM, a system that can verify DPM was created consisting of a line up ranging from DPM room facility with large screens to notebook type Mobile PC (Fig. 9).

(1) DPM room

DPM rooms were provided enabling a large number of people to perform DPM verification simultaneously. The switching operations are likely to become complicated in a system using multiple screens of the 70 to 110-inch class. Accordingly, the operations were simplified by creating a user-friendly interface that could be understood easily by any designer. The 70-inch class screen system was designed such that it was possible to move the projector and the operations table integrated in the Engineering Work Station (EWS).

(2) Mobile PC

An optimum performance and low cost Mobile PC tool was introduced to view both the physical vehicle and the DPM at the inspection location (next to the actual vehicle) where there is no network.

## 5. DPM Usage Example

The development of this DPM system enabled various types of verifications and applications to be implemented.

Introduced here is one usage example shown by simple illustrations.

- Extract the necessary parts model from DPM and use the parts in the analysis model (Fig. 10)[16]
- Wiring and piping interference check (Fig. 11)
- Body thickness interference check (Fig. 12)
- Engine room regular meeting (Fig. 13)
- Assembly review in the manufacturing division (Fig. 14)
- Application to TV advertisements (Fig. 15)

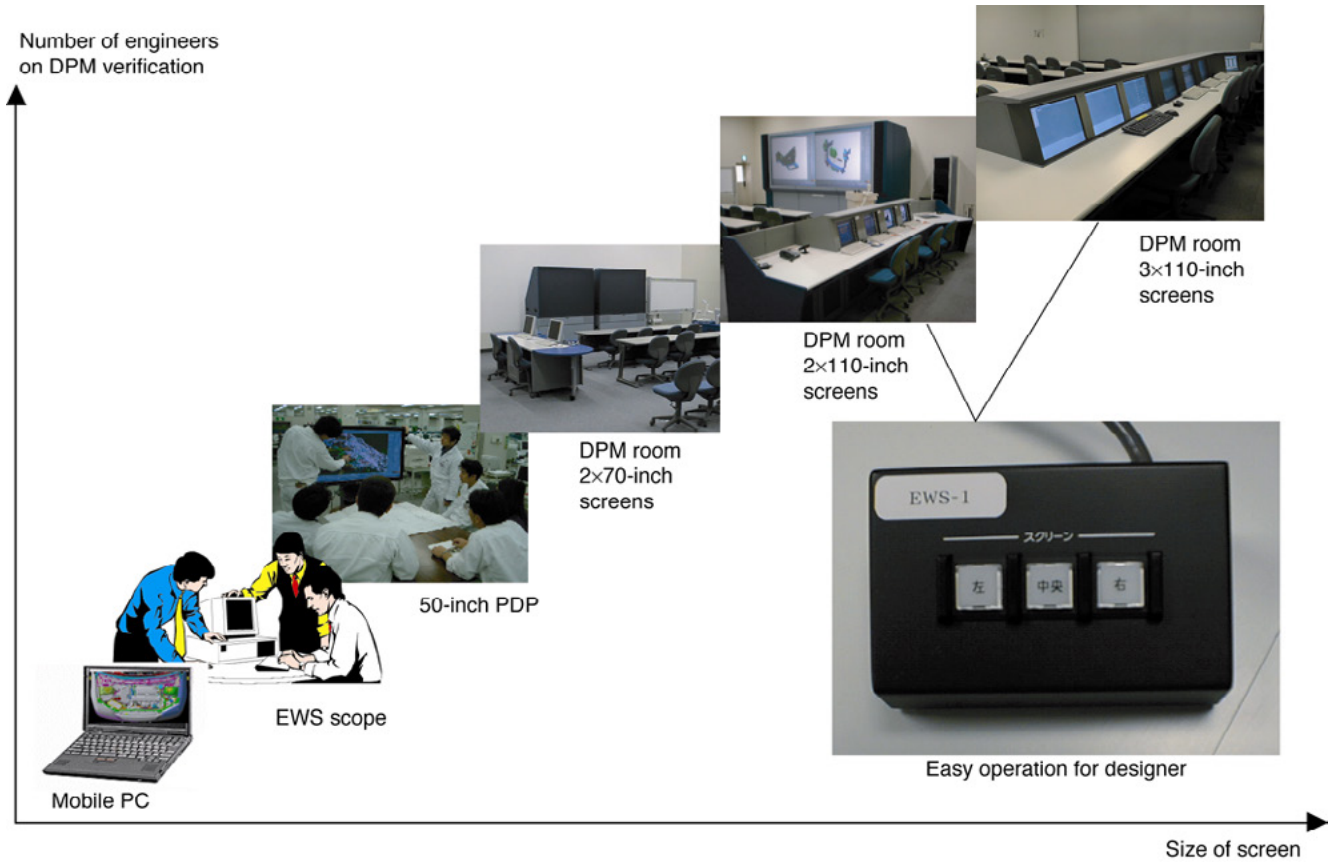



Fig. 9 DPM verification facility

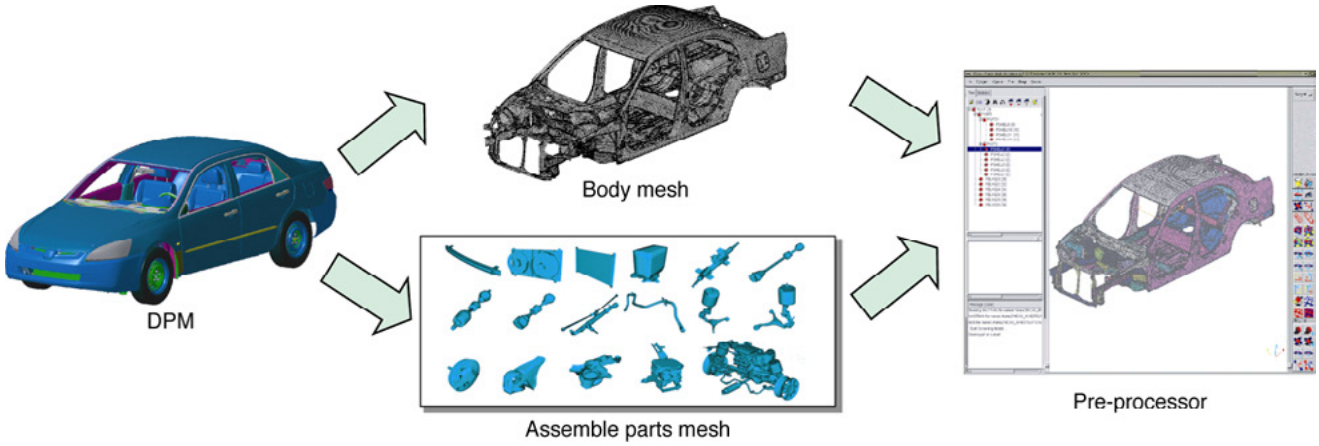



Fig. 10 CAE using DPM

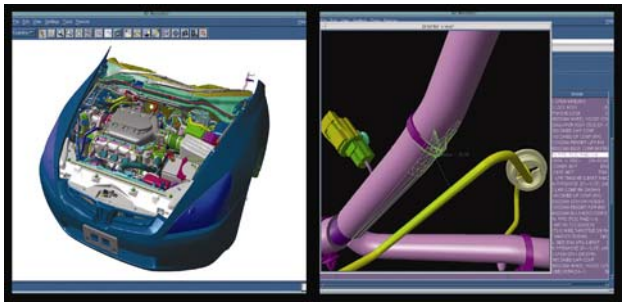


Fig. 11 Verification of wiring using DPM

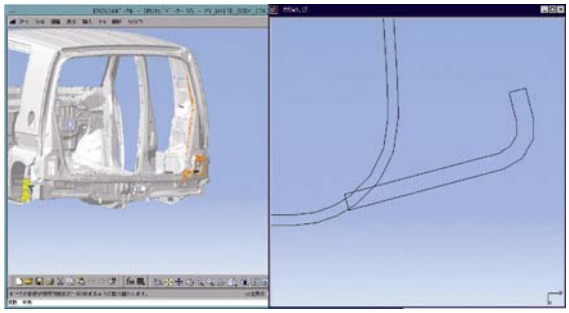


Fig. 12 Thickness interference check using DPM

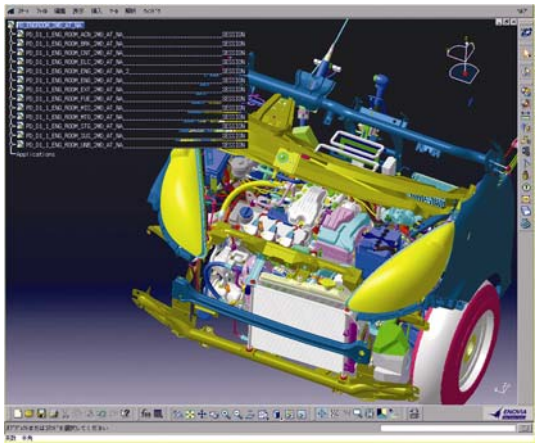


Fig. 13 Engine room layout meeting using DPM

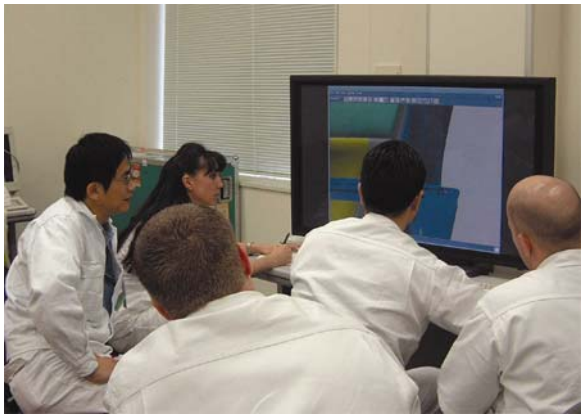


Fig. 14 Manufacturing division staff using DPM




Fig. 15 TV commercial using DPM

## 6. Conclusion

(1) The development of a system for creating a vehicle body surface enabled the following:
- Viewing of the latest body surface on the computer even at the initial design stage.
- The complete DPM.

(2) Development of the DPM equipment systems facilitated DPM verification

As a result, DPM could be used in every area (all design departments, analysis department, manufacturing department, etc.). The aim henceforth is to promote the usage of DPM and other sophisticated technologies so as to conform to various laws and regulations, and to further reduce the weight of vehicles considering the global environment.

## References


(1) Yoshimura, H.: B777 Kaihatsu ni okeru Concurrent Engineering oyobi korewo sasaeru Computer Communication System, Die & Mold Technology, Vol. 11, No. 3-No. 8 (1996) (in Japanese)

(2) Araki, H.: Seihin Kaihatsu Process Henkaku no tameno Kyoucho Sagyou Kankyou ni kansuru Kenkyu, the Doctoral thesis in Tokyo University, p. 96-104 (2001) (in Japanese)

(3) Brooke, C L: Creating the Best CAD/CAM System, Automotive Industries, p. 66-69, December (1996)

(4) Kobe, C.G.: The Paperless Car, Automotive Industries, p. 43, May (1997)

(5) Negishi, T.: Innovative Vehicle Development Process using Digital Engineering, Journal of Society of Automotive Engineering of Japan, Vol. 56, No. 12, p. 43-47 (2002)

(6) Ampo, H.: Toyota Jidoushiya Seisan Gijyutsu Bumon no Digital Assembly Senriyaku, Nikkei Computer Graphics, p. 140-145 (1999) (in Japanese)

(7) Okada, Y.: Presentation of MDI Support System, Journal of Society of Automotive Engineering of Japan, Vol. 56, No. 6, p. 65-69 (2002)

(8) Oki, S.: Computer Application to New Model Car Development, Mitsubishi Motors Technical Review, No. 11, p. 8-15 (1999)

(9) Shimomura, D., Yamamoto, Y., Etou, Y., Kouno, S., Osaka, T., Kurihara, K., Saitou, Y.: Utilizing Three-Dimensional Geometry Data in Vehicle Development, Nissan Technical Review, No. 47, p. 5-9 (2000)

(10) Nakajima, K.: Improvement of the Standard Development and Manufacturing Processes Centering Around 3D-CAD, Nissan Shatai, Text of 12th Design and Manufacturing Solutions Show Seminar, p. 45, July (2003)

(11) Toyota Kanzen Kasou Shisaku wo Honkaku Dounyu he, Nihon Kougyo Shinbun, 2003/10/7 (2003) (in Japanese)

(12) Ueda, H.: User proposals for future CAD, Daratech CAD/CAM/CAE, Product Process Management Strategy Workshops 1999, Chicago, March (1999)

(13) Ueda, H.: CAD in the 21st century?, Daratech CAD/CAM/CAE Product Process Management Strategy Workshops 2000, Boston, March (2000)

(14) Sakazaki, Y.: Honda no Idenshi, Yamato Shuppan, p. 80-81 (2003) (in Japanese)

(15) Ueda, H.: The Concept of making a product and CAD, Daratech CAD/CAM/CAE, PDM Summit 2001, Boston, February (2001)

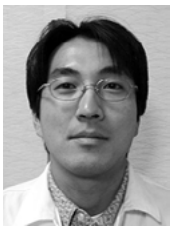
(16) Takada, K., Matsuura, N., Iwamoto, A., Nakano, F.: Development of New Pre-Processor for Car Body Analysis, The Japan Society for Computational Engineering and Science, Proceedings of Computational Engineering Conference, Vol. 7, p. 263-266 (2002)

■ Authors ■


Hiroshi UEDA


Masaaki NAKAZATO


Akio KAGAYA


Tadashi NAKAMURA


Teppei MORO


Hideyuki TANAKA

# Development of V6 i-VTEC Engine with Variable Cylinder Management

Katsumi NOGUCHI* Mikio FUJIWARA* Makoto SEGAWA*
Kazutomo SAWAMURA* Shigeru SUZUKI*

## ABSTRACT

A V6 i-VTEC engine equipped with a variable cylinder system has been developed to achieve high output, high fuel economy and low emissions. The variable cylinder system uses the VTEC mechanism to close the rear bank of three cylinders. To increase the accuracy of switching control, it is essential to increase the responsiveness of switching when oil pressure is low at low engine speeds. High responsiveness has been ensured in this engine by contriving the way of switching synchro pin and spool valves. The increased accuracy of control has enabled valve close timing to be synchronized with the stopping of the fuel supply to the deactivated cylinder bank. As a result, the system is able to switch instantaneously between three- and six-cylinder operation to enable engine output to respond to the different driving conditions with no loss of drivability. The new engine has been employed in the new model INSPIRE. It is a high-power (184 kW [250 ps]) and high-torque (296 Nm [30.2 kgm]) engine, and achieves a fuel consumption of 11.6 km/l in Japanese 10 - 15 mode and meets ultra-low emissions standards while maintaining regular gasoline specifications.

## 1. Introduction

As environmental protection and economical operation are becoming a higher priority, the development of the next generation i-series engine and power train with improved environmental characteristics, fuel economy, and driving performance is being pursued. The new V6 Variable Cylinder Management (VCM) system engine has been developed as the V6 i-VTEC engine by adding VCM system to a Honda VTEC engine.

A V6 engine can be thought of as two 3 cylinder engines put together. When the ECU deems the conditions to be suitable, it instantly stops the movement of the valves of 1 bank 3 cylinders of the V-style engine. The engine then runs on the 3 remaining cylinders only. This defines the VCM System.

When the accelerator is firmly pressed or if conditions are deemed correct, the engine is instantly returned to full 6 cylinder power. Thus the implementation of an engine with the high power of a large displacement engine and the fuel economy and low emissions of a small displacement engine has been successful.

This report discusses the increase in power output, low emissions, and better fuel economy technologies, used in the development of the V6 3.0L i-VTEC VCM engine (Fig. 1), which is being used in the new model INSPIRE.

## 2. Development Goals

The development goals of the new V6 i-VTEC VCM system engine were, as environmental protection and fuel

* Tochigi R&D Center




Fig. 1 View of V6 3.0L i-VTEC engine

economy requirements become more strict, to decide what technologies would be needed for future large displacement superior engines as well as cost reduction, and to pursue technologies that were desired throughout the world. From these goals a superior vehicle engine was developed for the environmentally conscious.

Specific goals are listed below:

(1) Fuel Economy of a typical 2.0L base engine.
(2) Environmental protection; meet Japans ultra low emission standard.
(3) A power output appropriate for a superior V6 class engine.
(4) Power output control at time of switchover through the electronic control of the throttle.

## 3. Engine

### 3.1. Engine Specifications

The main specifications of the J30A V6 3.0L i-VTEC VCM engine that is mounted in the new INSPIRE are shown in Table 1.

### 3.2. Structure of the Variable Cylinder Management System

Figure 2 (a) shows the rear bank 3 cylinder VCM system valve structure and the hydraulic passage while Fig. 2 (b) shows an overall structural view of the system. When in normal driving mode, with the synchro pin in place, the valve lift rocker arm and valve stop rocker arm move back and forth in tandem, as shown in Fig. 3 (a) for operation of the intake and exhaust valves. When the ECU recognizes that the vehicle has entered cruise mode, a synchro-piston is pushed into and stored in the stop rocker arm by hydraulic pressure. As can be seen in Fig. 3 (b) the interlock of the rocker arm is in inactive mode and though the cam continues to operate the valve lift rocker arm, it is just moving. In this condition, the stop rocker arm as well as the intake and exhaust valves cease operation, leading to a sealing in the cylinders and reducing engine pumping losses.

In an existing VTEC engine, hydraulic pressure pushes the synchro-pin, coupling the rocker arms. A spring is then used to return the synchro-pin, separating the rocker arms. In order for the decoupling to occur swiftly and reliably, a spring with a significant amount of reaction force was required. Therefore, in order for the hydraulic pressure to interlock the mechanism, it had to have enough pressure to overcome the spring force.

Table 1 Engine main specifications

| | | |
|---|---|---|
| Cylinder configuration | | 60° V-6<br>Variable Cylinder Management (VCM) |
| Bore × Stroke (mm) | | 86 × 86 |
| Displacement ($cm^3$) | | 2 997 |
| Compression ratio | | 10.5 : 1 |
| Valve train | | SOHC i-VTEC |
| Number of valves | | 4 per cylinder |
| Valve diameter (mm) | Inlet | 35 |
| | Exhaust | 30 |
| Exhaust manifold | | Includes cylinder head |
| Fuel | | Regular |
| Max. power (kW[PS]/rpm) | | 184[250]/6 000 |
| Max. torque (N·m[kgm]/rpm) | | 296[30.2]/5 000 |

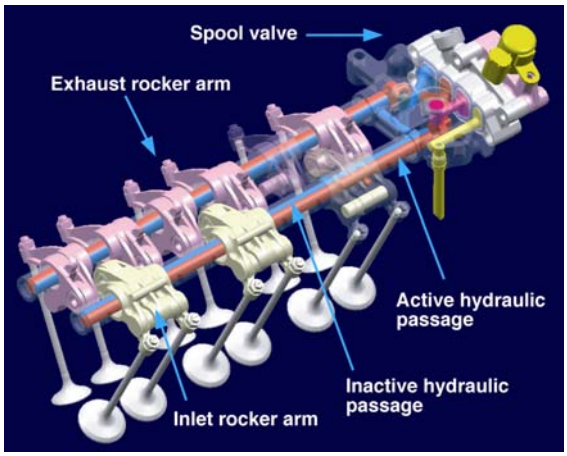



Fig. 2 (a)

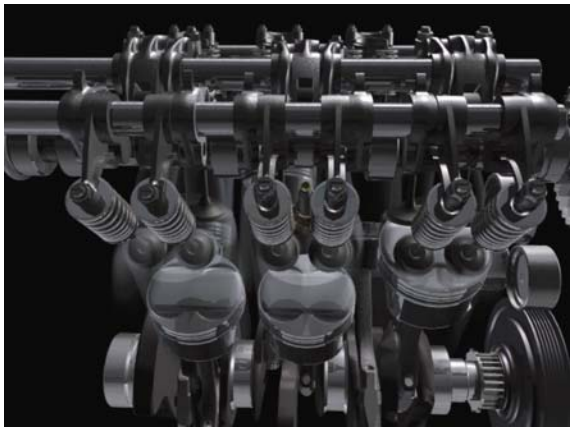


Fig. 2 (b) View of valve train

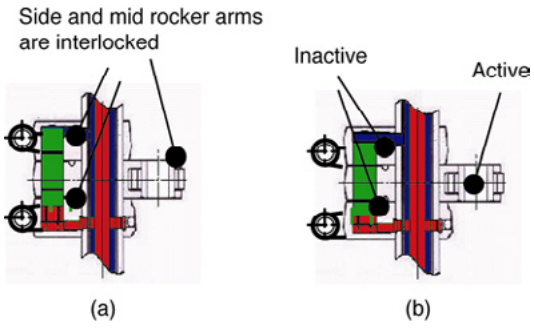



Fig. 3 Valve active and inactive condition

The VCM system is required to have a quick switchover response for valve operation and stop even at low hydraulic pressure generated at low engine speeds. To make the all hydraulic system feasible a new technology 2 way hydraulic circuit[(1)] was developed. This new technology is used for the new VTEC hydraulic switchover system. Figure 4 shows the previous VTEC and new VTEC systems.

As can be seen in Fig. 5, the hydraulic pressure required for switchover in this newly developed VTEC engine is 1/5 the pressure of the previous design. Therefore, a new oil pump or other additional equipment is not necessary and it is possible for the system to switchover at low rpm and low hydraulic pressures such as at idle. This makes it possible for the VCM system to provide maximum fuel economy improvement.

Another important technology for this VCM system is an improvement in switchover responsiveness. The VCM system is required to be able to change from 3 to 6 cylinders and accelerate the instant the driver steps on the accelerator, taking the vehicle out of a cruise condition. In order to ensure this response, a newly developed 3 way solenoid spool valve, as can be seen in Fig. 6, is used. Through the use of this 3 way solenoid valve, the system stop side of the hydraulic circuit is not connected to the drain. Thus it has become possible to quickly move the synchro-piston leading to fast decoupling of the rocker arm. When switching to normal operation mode, the hydraulic oil pressure that had been used for decoupling is lowered by allowing the oil to flow out the drain while instantly raising the coupling pressure. It was possible to improve the switchover response time to 1/3 that of the previous system, as can be seen in Fig. 7.

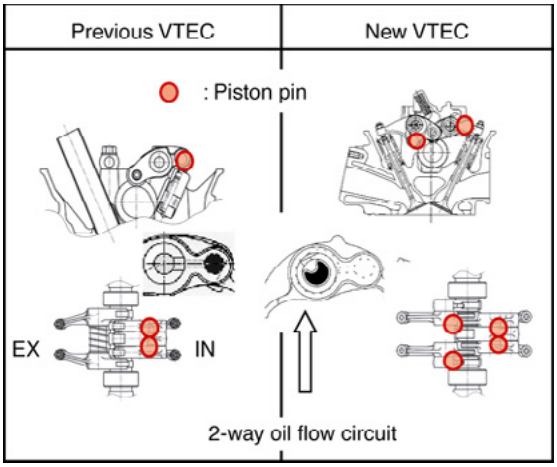



Fig. 4 Previous VTEC and new VTEC

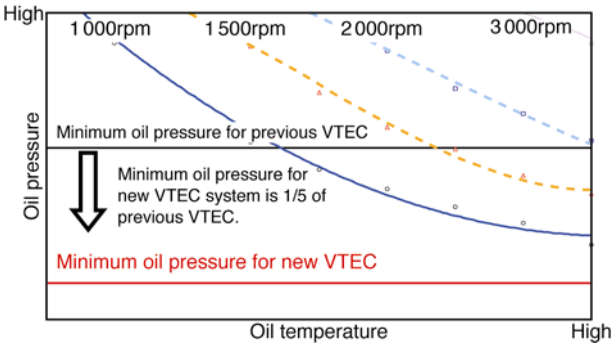



Fig. 5 Minimum oil pressure for VTEC

## 3.3. Variable Cylinder Management System Control and Area of Operation

The VCM system mainly uses the throttle opening information along with vehicle speed, engine speed, and gear location to determine if the vehicle is in either cruise mode or deceleration. The system then turns off the cylinders switching over to 3-cylinder operation, as can be seen in Fig. 8. Also, in order to perform switchover precisely, it also judges whether or not the hydraulic oil temperature and the converter temperature are within an appropriate range.

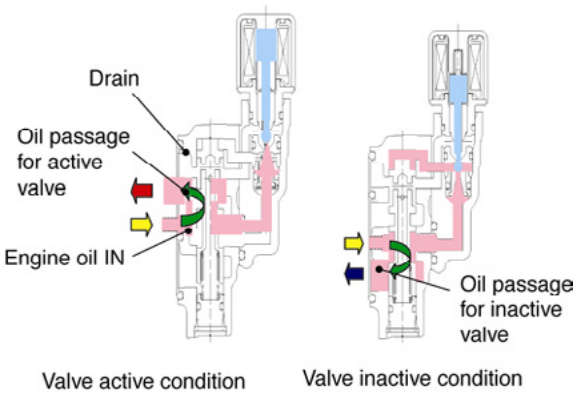



Fig. 6 Spool valve and hydraulic passage

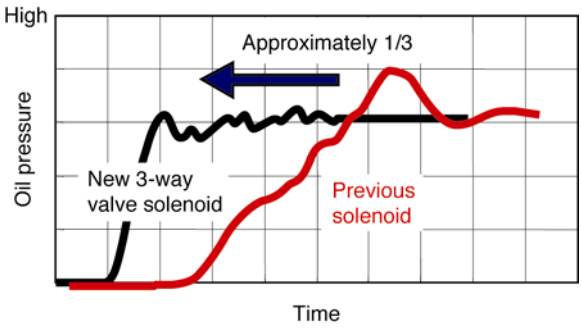



Fig. 7 Spool valve response

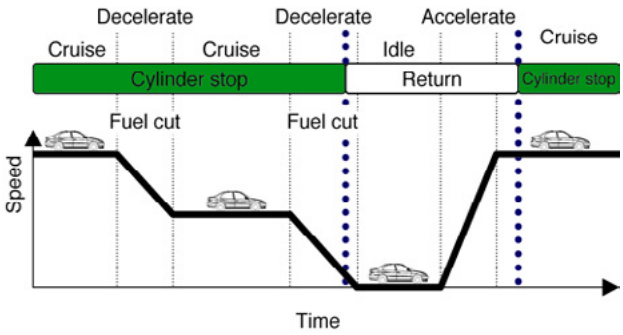



Fig. 8 Operation of cylinder stop system

An actual example is shown in Fig. 9. For instance, in the event the valves incorrectly return to operation before the fuel injection returns to operation, after the pumping cycle in which intake and exhaust valves work without fuel injection, the engine returns to the normal all-cylinder operation. On the other hand, in the event the valves incorrectly return to operation late, the intake valve stays shut while fuel is injected and on the next cycle there will be 2 cycles worth of fuel pulled into the cylinder. These types of incorrect operation cause fluctuations in the air fuel ratio. This results in the torque change shown in Fig. 10 at the time of switchover and causes deterioration in drivability. In order to overcome these types of malfunctions the switchover response accuracy has been improved by adopting this new VTEC engine. It has been possible to develop smooth switchover without any torque changes, through being able to start and turn off fuel simultaneously with that of the operation of the intake and exhaust valves.

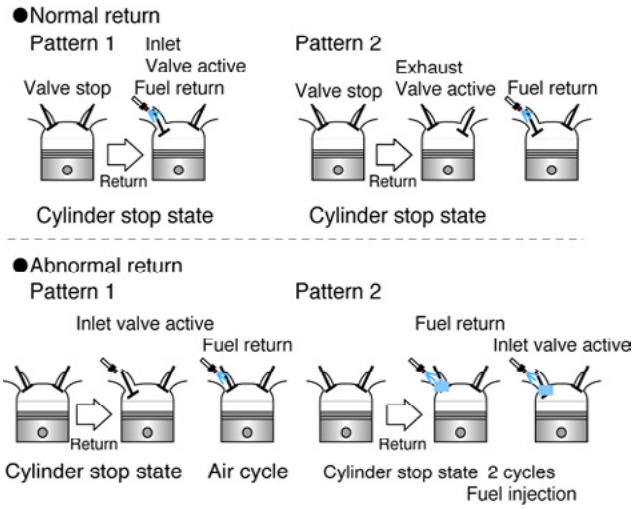



Fig. 9 Pattern at time of fuel return

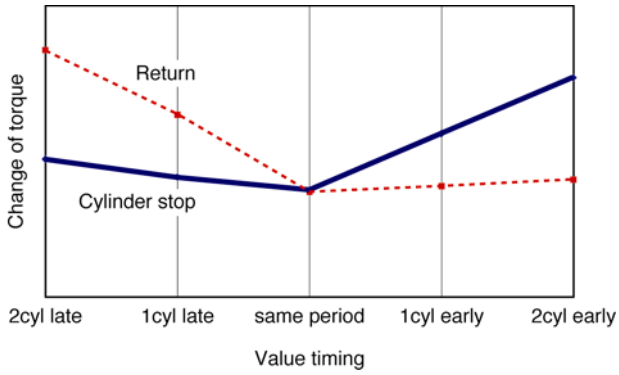



Fig. 10 Effect of change in timing on torque

At the time of VCM switchover, the switchover synchro-piston using hydraulic oil pressure, the spark timing control, the throttle control using electronic throttle control and the AT lock-up control are simultaneously carried out. Through this type of cooperative control, it has been possible to develop a switchover that is smooth and that does not contain any torque changes as can be seen in Fig. 11.

### 3.4. Engine Performance

The output performance characteristics of the J30A V6 3.0L i-VTEC engine are shown in Fig. 12. Even when using regular gasoline, this engines characteristics are: maximum power of 184 kW [250 ps] at 6 000 rpm and maximum torque of 296 Nm [30.2 kgm] at 5 000 rpm, achieving performance at the top of its class.

This power output has become possible through improvement in air intake efficiency through the use of a resonance type manifold with a switchover mechanism, and enlarging the valve diameter. Placing the catalytic converter directly under the cylinder head makes it unnecessary to keep the exhaust hot for the catalytic process. This allows for an exhaust pipe layout that improves exhaust flow efficiency and favors increase in power output.

### 3.5. Fuel Economy

In the V6 VCM system engine, the valves for 1 bank of 3 cylinders, are turned off instantaneously and the engine runs on the 3 remaining cylinders. This reduces the pumping losses of the bank that has been turned off, and engine friction associated with valve drive losses. Further opening of the throttle gives much less pumping losses of the operating bank. Through using a more favorable load area of the engine, the engines thermal efficiency is improved. And the fuel economy is improved by expanding the amount of time for fuel-cut mode.

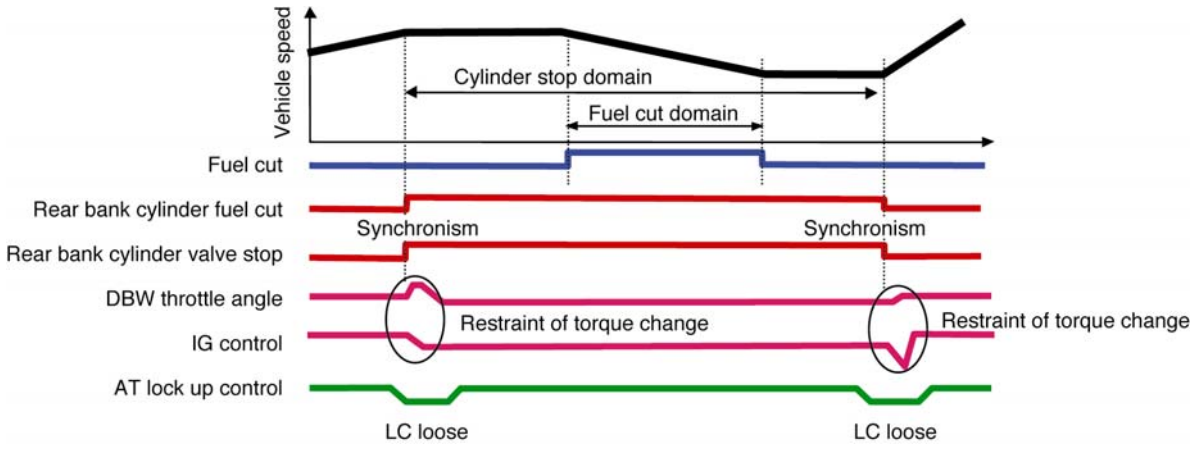



Fig. 11 Pattern of VCM operation

Figure 13 shows the base engines fuel economy improvement rate when it has switched over from 6 cylinders to 3 cylinders. Also, Fig. 14 shows the relationship between BSFC and the engines complete displacement while it is running at an engine speed of 1 500 rpm with a power output of 2.94 kW. The switchover from 6 to 3 cylinders provides the base engine a 30% improvement in fuel economy, and while it is a 3.0L displacement engine, it has achieved the same BSFC as a 1.7L displacement engine.

The new INSPIRE's main technology for fuel economy improvement is the VCM system. Other technologies employed are precise control of the lock-up mechanism of the Automatic Transmission, EPS (Electric Power Steering) and friction reduction. As can be seen in Fig. 15, while this has a displacement of 3.0L, it has a 14% improvement in fuel economy as compared to the previous INSPIRE's 25V 2.5L displacement engine. This new engine achieved an 11.6 km/l fuel economy in Japanese 10 - 15 mode equivalent to that of the 2.5L direct injection engine.

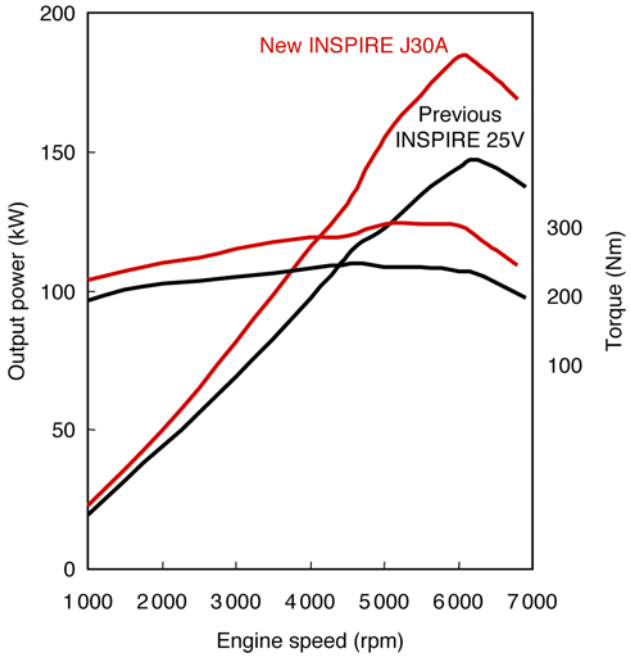



Fig. 12 Output performance

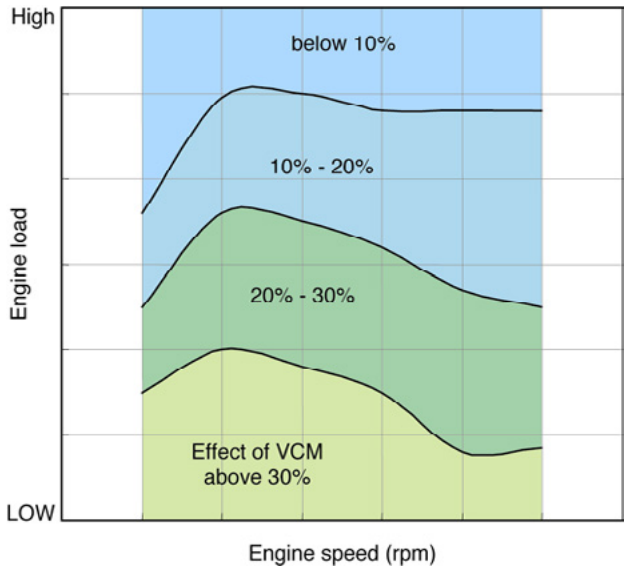



Fig. 13 Effect of VCM on fuel economy

## 3.6. Environmental Performance

As this system does not use lean burn to improve fuel economy, specific equipment such as a NOx adsorption reduction type catalytic converter is not needed. This leads to both a lower cost and a reduction in $CO_2$. It is therefore a system that has realized high performance in both fuel economy and environmental areas.

The diagram of the system used for low emissions in this engine is shown in Fig. 16. There are separate exhaust clean up systems on both banks of this V6 VCM system engine. A high density 900 cell 3-way catalytic converter has been placed just under the cylinder head of each bank, eliminating the exhaust manifold. Through this arrangement, the heat capacity of the system has been reduced and the warm up characteristics in cold area have improved leading to excellent emissions clean up performance. Running the engine on only one bank leads to a temperature difference between the banks. In order to maintain very precise control of the air fuel ratio even in these conditions a LAF (Linear A/F) sensor and $O_2$ sensor have been placed on each of the banks. This gives excellent responsiveness while not being affected by the other bank and is perfect for the air fuel

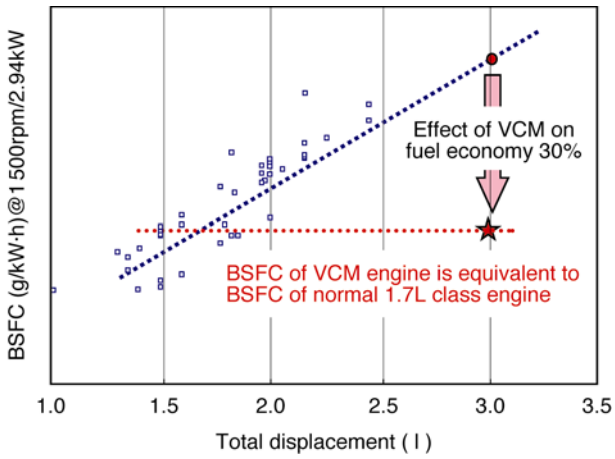



Fig. 14 VCM effect on BSFC

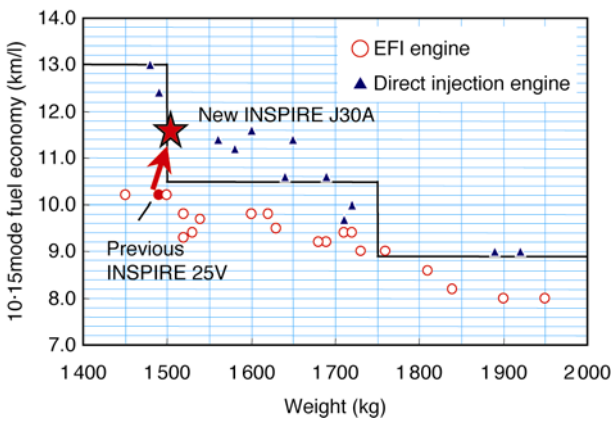



Fig. 15 10 - 15 mode fuel economy

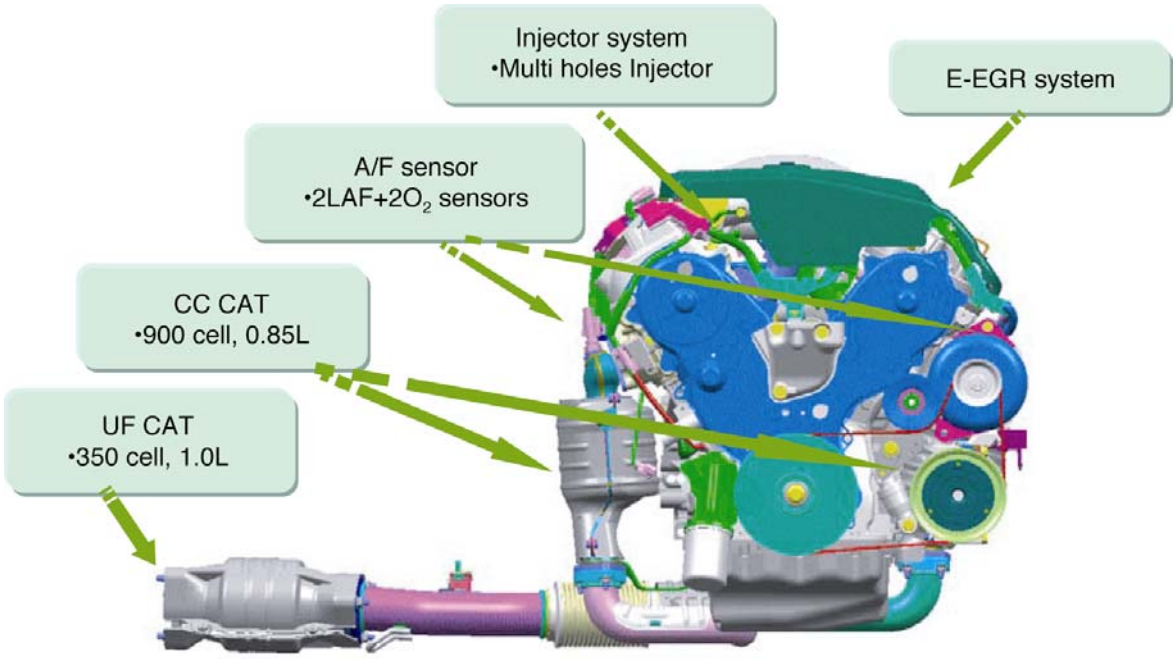



Fig. 16 Engine configuration and control system enable three-stars clean emission rating

control of this V6 VCM system engine. A 350 cell catalytic converter has been placed under the floor, after the $O_2$ sensor, in order to both ensure excellent emission clean up capability. It also reliably cleans the exhaust of the bank that stops because that bank's catalyst is not always warmed up.

In addition to the exhaust gas related technology listed above, a 12 hole injector with improved fuel atomization capability is used. Also, an electric EGR valve with high precision control has been applied. As can be seen in Fig. 17, the engine has a fuel economy of 11.6 km/l in Japanese 10 - 15 mode and meets the ultra low emissions standard, thus it has achieved both a high standard of emissions and of environmental protection.

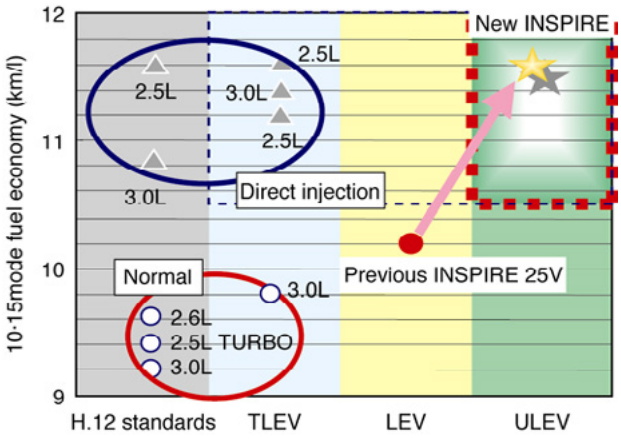



Fig. 17 Achievement of both ULEV emissions rating and conformity with 2010 fuel economy standard

## 4. Comfort

One of the important elements of being able to deliver a comfortable superior vehicle is its NV (Noise and Vibration) performance. The V6 i-VTEC engine has vibration patterns during 3 cylinder operation that do not exist on the previous V6 engine. Trying to find a way of suppressing this vibration became a subject of study. As a countermeasure, a long torsion spring is used on the lock-up damper of the transmission in order to reduce the drive train vibration during 3 cylinder operation. This countermeasure resulted in a 3 dB reduction of the noise level in the front seat and a 5 dB reduction in the vibration level of the drive train. A newly developed ACM (Active Control engine Mount) that predicts engine vibration and actively reduces the vibration is used[(2)]. Also, ANC (Active Noise Control) which reduces cabin noise and does not add very much weight has been adapted[(3)]. Thus both fuel economy and a product appropriate for the superior class have been achieved.

## 5. Conclusion

An engine with the VCM system as a core technology was developed with the reduction of friction and improvement in combustion. This has lead to a system that has high power output, high fuel economy, and high environmental performance. This system was developed in a lower weight and lower cost package. The following results have been obtained through the development of this V6 i-VTEC VCM system engine.

(1) Through development of the new VTEC engine, the hydraulic pressure required for switchover is 1/5 that of the previous system and the response time has been reduced to 1/3 of what the previous system requires. At an engine speed of 1 500 rpm and output power of 2.94 kW, the VCM system provides roughly a 30%

improvement in fuel economy and has the same BSFC as a 1.7L displacement engine though this engines displacement is 3.0L.

(2) This engine has a 14% improvement in fuel economy as compared to the previous INSPIRE's 25V 2.5L engine, achieving 11.6 km/l in Japanese 10 - 15 mode.

(3) Through the use of a LAF sensor and $O_2$ sensor for each bank of the VCM system engine, precise control of the air fuel ratio has been made possible and the above-mentioned fuel economy has been achieved. It also passes the ultra low emissions vehicle standard as certificated by the Ministry of Land, Infrastructure and Transport Government of Japan, meeting standards that have been set for the year 2010. In these ways, the engine meets the needs of the environment.

(4) While achieving the fuel economy and meeting environmental standards described above, the engine has a maximum power of 184 kW [250 ps] at 6 000 rpm and a maximum torque of 296 Nm [30.2 kgm] at 5 000 rpm, while using regular gasoline, achieving a power output at the top of its class.

## References

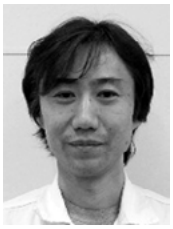
(1) Matsuki M. et al.: Development of a Lean Burn Engine with a Variable Valve Timing Mechanism, SAE Paper 960583

(2) Matsuoka, H., Mikasa, T., Nemoto, H.: Development of Active Control Engine mount, Honda R&D Technical Review, Vol. 15, NO. 2, p. 209-214 (2003)

(3) Inoue, T., Takahashi, A., Minowa, S., Sano, H.: Development of Active Noise Control System for Engine Booming Noise, Honda R&D Technical Review, Vol. 15, No. 2, p. 201-208 (2003)

■ Authors ■


Katsumi NOGUCHI


Mikio FUJIWARA


Makoto SEGAWA


Kazutomo SAWAMURA


Shigeru SUZUKI

# Development of i-DSI 2Plug Engine for 2004 Model Year Honda LIFE

Yusuke WADA* Keiji OHTSU*
Kennosuke NARITA* Toshimitsu SHINOHARA*

## ABSTRACT

A 660 $cm^3$ 3-cylinder engine has been developed for the new model of the Honda Life. The basic structure of the engine has been redesigned to achieve increased environmental performance, increased compactness, a reduced weight, and a higher level of quietness.

The development concept was to produce an engine that excelled under normal driving conditions. To respond to the high frequency of high engine loads and engine speeds in minicars, the i-DSI engine employs a short stroke to reduce friction. The use of i-DSI twin plug ensures rapid combustion, enabling fuel economy and output to be increased through the use of a high compression ratio.

The innovations outlined above have increased torque by 7% under normal driving conditions, and enabled the achievement of a class-topping fuel economy of 19.8 km/L in Japanese 10 - 15 mode. The increased idling fuel economy achieved by improved combustion and reduced emissions, and the reduced noise and vibration make the new engine an extremely high-quality unit.

## 1. Introduction

With the goals of environmental protection and resource conservation, Honda has developed the “i-series” of power trains - lightweight, compact power trains giving lower emissions, enhanced fuel economy, and better drive performance. With the lean-burn i-VTEC used in the Stream, the i-DSI[(1)] providing rapid combustion through dual and sequential ignition used in the Fit, and the i-VTEC cylinder idling system used in the INSPIRE, these new engines were launched into the market providing advanced fuel control.

In the development of this engine, studies were carried out concerning how minicars are used and what would be the best type of engine for them. Development proceeded with the goals of a simple structure and high performance. This paper reports on the engine concept, as well as on the technologies introduced and the performance achieved.

## 2. Development Goals

The 2004 Model Honda Life, for which this new engine was designed, was developed according to the concept “Pride and Dream.” Corresponding to this, studies were made into engine specifications to achieve a small vehicle with low energy consumption that is friendlier towards the environment and mankind. In particular, the following four items were set as environmental performance targets for the small car engine.

(1) Environmental performance; improved fuel economy and conformity to ultra-low emissions standards
(2) Dramatically improved torque in the practical range
(3) A lightweight and compact engine
(4) Reductions in engine vibration and noise

* Tochigi R&D Center

## 3. Overview of the Engine and Specifications

### 3.1. Overview

To study the engine operating range, minicar driving load information was analyzed. Figure 1 shows the results of a comparison of driving frequencies when driving in the Japanese 10 - 15 mode, by engine displacement. For 660 cm$^3$, there is a high usage frequency of relatively high load at high engine speeds.

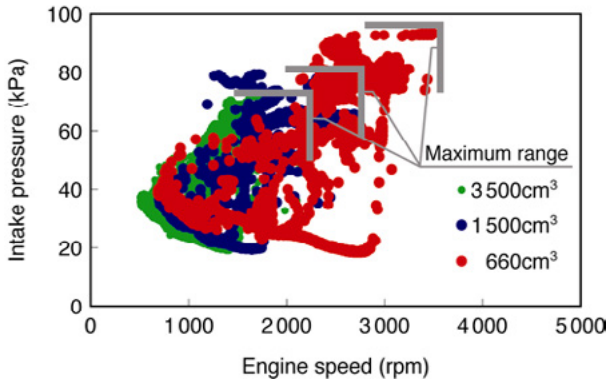



Fig. 1 Comparison of range of operating loads for engines of different displacement in 10 - 15 mode

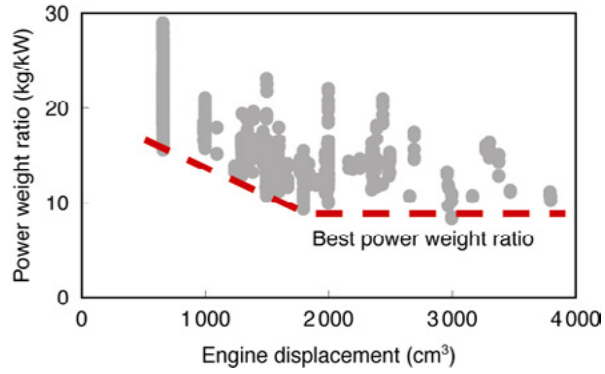



Fig. 2 Best power weight ratio for engines of different displacements

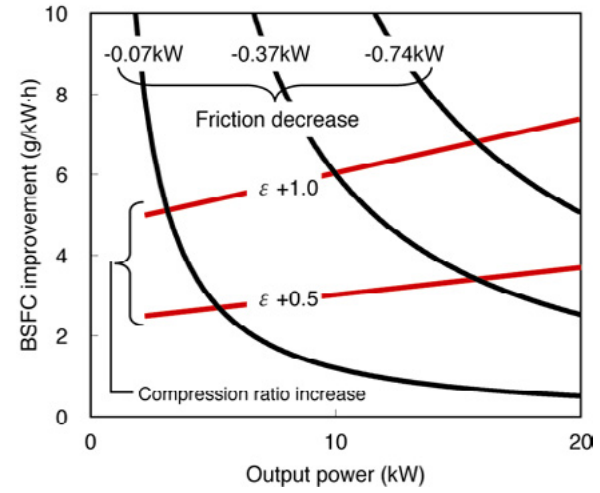



Fig. 3 Improvement of BSFC by friction and compression ratio

Table 1 Engine specifications

| Engine | Developed model | Previous model |
|---|---|---|
| Cylinder configuration | In-line 3-cylinder | In-line 3-cylinder |
| Bore × stroke (mm) | 71 × 55.4 | 66 × 64 |
| Displacement (cm$^3$) | 658 | 656 |
| Compression ratio | 11.2 | 10.5 |
| Valve train | SOHC 2 valves | SOHC 4 valves |
| Number of valves | 2 per cylinder | 4 per cylinder |
| Valve diam. (mm) Inlet<br>Exhaust | 35<br>30 | 24.5<br>21 |
| Fuel supply system | Programmed fuel injection | Programmed fuel injection |
| Ignition system | Dual point sequential ignition | Single point ignition |
| Max. power (kW/rpm) | 38/6 700 | 38/7 200 |
| Max. torque (N·m/rpm) | 61/3 800 | 61/4 500 |

Figure 2 shows the relationship between naturally aspirated engine power to weight ratio and engine displacement. The minimum power to weight ratio for minicars is equivalent to 1.5 times that of a vehicle of 15 kg/kW and 1 800 cm$^3$ or larger. This is the reason for the increase in use frequency of high load, high engine speed in minicar.

Focusing on environmental performance, particularly on the improvement of fuel economy, it is best to have both rapid and stable combustion, regardless of the engine displacement. On the other hand, focusing on minicars, high engine loads are frequently used and therefore the effectiveness of pumping loss reduction methods, such as large volume EGR, is limited. Therefore, the effect of fuel economy improvement methods was checked against desired output.

Figure 3 gives the tests results concerning Brake Specific Fuel Consumption (BSFC) improvements, using a previous 660 cm$^3$ Engine. BSFC improvements through friction reduction are limited when accompanied by an increase in the required output. In contrast, it is clear that using a higher compression ratio to reduce BSFC is an effective method, showing improvements accompanying an increase in required output.

Consequently, it is clear that for minicar engines, the following methods are effective in the significant reduction of high engine speed friction, while avoiding knocking and at the same time setting a high compression ratio.

(1) High engine speed friction reduction, through the use of a short stroke.
(2) Pumping loss reduction by larger valves using a bigger bore.
(3) High compression ratio, through a 2-valve combustion chamber, using 2 plugs for both dual and sequential ignition.

From above, the short stroke frame and i-DSI adoption was determined for the engine basic concept. Table 1 shows the main specifications, and Fig. 4 shows the appearance of the engine.

The features of the engine combustion chamber and the area around it are given in Fig. 5. First, note the big bore, short stroke frame. By applying a bore stroke ratio of 0.78 and a low average piston speed of 12.4 m/sec at the maximum output, friction at high engine speeds was reduced. The adoption of a 2-valve configuration with large diameter

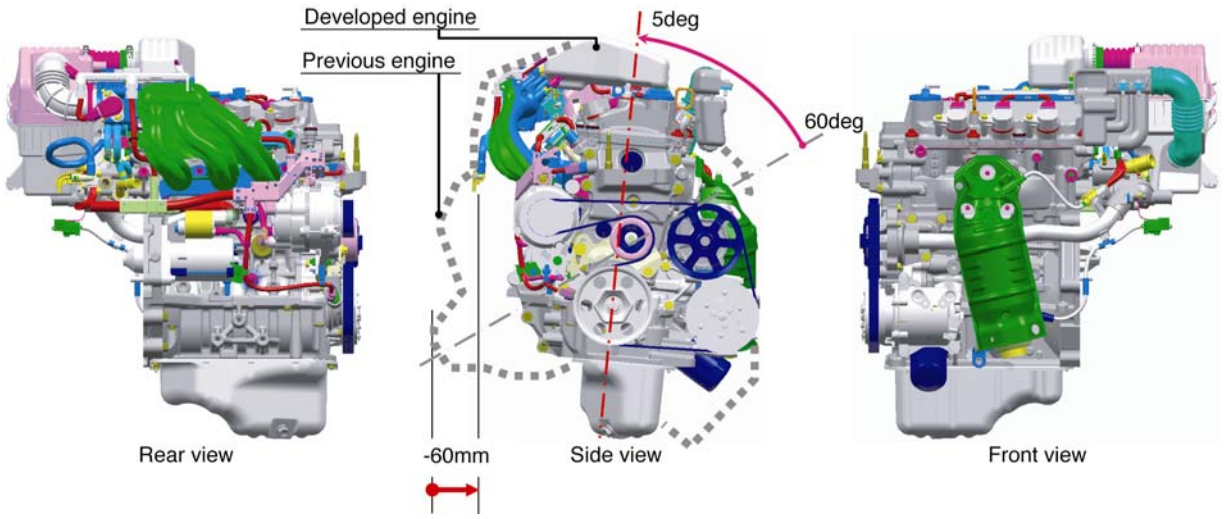



Fig. 4 View of new engine

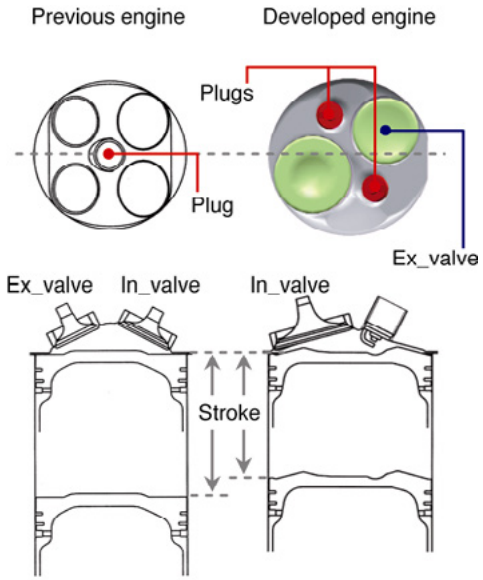



Fig. 5 Comparison of combustion chambers configuration of previous and new engines

valves enabled any increase in pumping losses to be kept to a minimum.

In addition, the i-DSI, already used in the Fit, which has two spark plugs placed diagonally in each cylinder, was adopted for the important purpose of creating a high compression ratio through dual and sequential rapid combustion characteristics.

As a result, the compression ratio was set at a maximum level of 11.2 for the regular gasoline (RON91) specification. In addition, mid to high engine speed torque (which has a high usage frequency) was raised, while keeping the maximum torque and power equivalent to the output of the previous model.

### 3.2. Reduction in Weight and Size

It is very important that minicars are given small engines, in order to maintain a reasonably sized cabin space within the vehicle. Innovations that result in a compact layout include direct attachments of auxiliary equipment to the cylinder block and an exhaust manifold-integrated cylinder head connecting directly with catalytic converter. Changing the engine-fitting angle from a forward 60° tilt to a forward 5° tilt enabled the total fitting length to be shortened by 60 mm.

In addition, placing the concentrated resonator type air cleaner on top of the transmission contributes to making the total power train more compact.

Moreover, by optimizing the shapes and layout of the areas around the crank shaft and cylinder block, and by making the intake manifold, cylinder head cover, oil strainer, and oil level gauge out of plastic, an engine weight reduction of 9% was achieved.

## 4. Achieved Performance

### 4.1. Improved Fuel Economy

Figure 6 shows engine unit fuel consumption and combustion stability under a light load. A 7% reduction of BSFC in stoichiometric air fuel ratio was achieved, and combustion limit air fuel ratio (A/F) was made a leaner 3 A/F. In addition, combustion duration of stoichiometric air fuel ratio was shortened by 13°. This is the effect of rapid combustion. The following are details of the element technologies.

#### 4.1.1. i-DSI application effects

When applying the i-DSI to the short stroke frame, studies were made of fuel consumption effects from the i-DSI cylinder head spec in comparison with the 4-valve cylinder head spec represented in Fig. 5.

The test engine used was a previous engine modified as much as possible to give it a short stroke. Specifically, a bore diameter of 68 mm, stroke of 60.4 mm, compression ratio of 11.5, and valve pinch angle of 30° were set. The inlet and exhaust valves were with diameters of 25 mm and 21 mm for 4-valve spec, and 33 mm and 28 mm for the i-DSI spec.

To evaluate the fuel economy effects accompanying this change, 3 modes were established, including the minicar actual driving range.

(1) Combustion evaluation mode 1 500 rpm, BMEP=358 kPa
(2) Light load mode 2 650 rpm, BMEP=171 kPa
(3) High load mode 4 000 rpm, BMEP=838 kPa

As shown in Fig. 7, the i-DSI spec achieves a 2 - 6% reduction in Indicated Specific Fuel Consumption (ISFC), and a 20 - 50% reduction in HC emissions. These reductions are due to the benefits of increased port flow speed with a single inlet valve, giving a stronger flow within the cylinder, and rapid combustion created by having dual and sequential ignition. The details of this rapid combustion are shown in Fig. 8. In the combustion evaluation mode, it is possible to fully understand rapid combustion, whereby the total combustion period is shortened by 8%, delaying the Minimum Spark Advance for Best Torque (MBT) ignition timing and advancing the maximum cylinder internal pressure generating angle. As a result, fuel economy was improved by raising the average effective pressure through raising the maximum cylinder pressure.

The results of i-DSI rapid combustion benefits are clear. The mass production spec, which aims at a further reduction in friction, has a bore pitch of 80 mm, a cylinder bore diameter of 71 mm which makes the distance between bores 9 mm. The stroke length corresponding to this is 55.4 mm, fulfilling the short stroke specification.

Next, studies were carried out to optimize swirl and tumble ratios through inlet port modifications aiming at improved fuel economy.

(1) a_Port: Tumble port (base spec)
(2) b_Port: Strengthen swirl ratio to 4 times that of a_Port.
(3) c_Port: Further enhance tumble ratio 25%, swirl ratio 12%.

Figure 9 shows the results of a distribution simulation of intake airflow velocities around the inlet valve seat, during

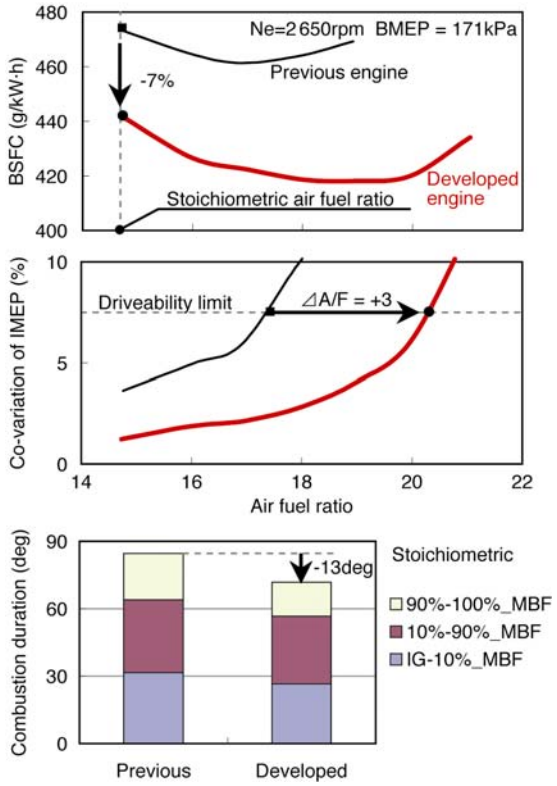



Fig. 6 BSFC and combustion characteristics

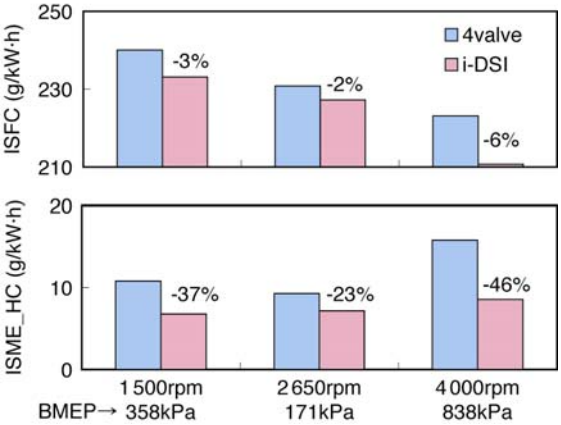



Fig. 7 Effect of i-DSI on ISFC and ISME_HC

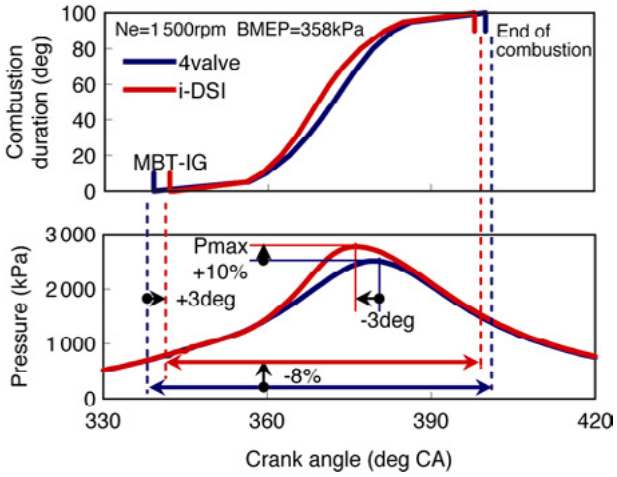



Fig. 8 Effect of i-DSI on combustion characteristics

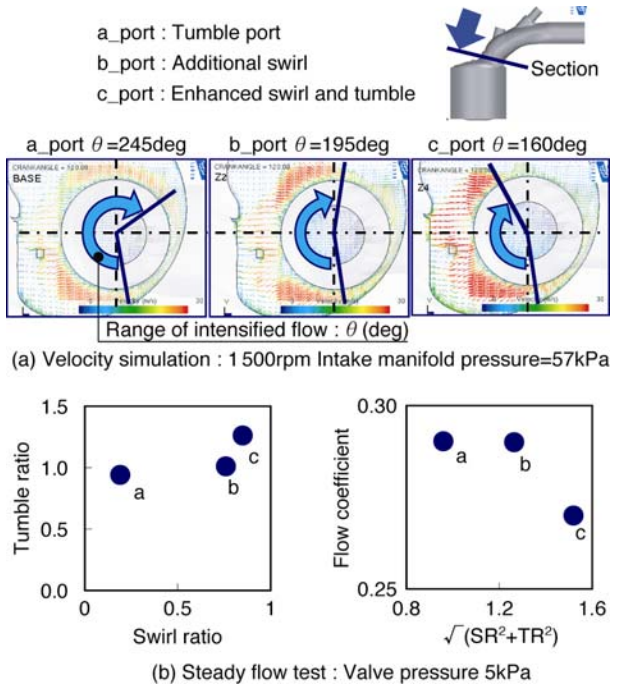



Fig. 9 Inlet port flow characteristics

the intake stroke. It is clear that in the proposed port order of a, b and c, the flow directivity is strengthened. Comparing flow characteristics in terms of average flow coefficient and vortex intensity[2], there was a drop in the average flow coefficient against a relative rise in c_Port vortex intensity, so a drop in output was expected. The vortex intensity used here is defined as composition value $\sqrt{(SR^2+TR^2)}$, with SR the swirl ratio TR the tumble ratio.

Figure 10 shows the result of actual ISFC measurements. The ISFC reduction allocation against a_Port is 0.5% at b_Port and 1.0% at c_Port, so by raising vortex intensity, ISFC was improved. In the end, port specifications showed a 2.5% drop in maximum power output with the c_Port, so the b_Port was selected for mass production.

### 4.1.2. Friction reduction

Aiming for a reduction in friction in the mid and high engine speed range, which sees high use frequency with minicars, a short stroke frame was adopted, and the crank journal diameter was reduced.

It is known that making a short stroke results in a reduction in piston speed, and there is a reduction in oil membrane shear resistance between the piston sliding surface and cylinder sleeve wall surface, and a reduction in pumping loss. In addition by using a short stroke, it is possible to expand the overlap formed by journal diameter and pin diameter, thereby increasing crankshaft rigidity, which is beneficial in terms of crank rattling noise. As a result of studies of friction reduction in the crank journal part, higher crankshaft rigidity, and metal seizure, the diameter of the crank journal was reduced from 40 mm to 38 mm in the new engine.

Other adopted friction reduction techniques included the continued use of the roller follower used on the current model engine, and applying OW-20 low viscosity engine oil. Also contributing to reduced friction is the newly adopted plateau honing used on the Civic Hybrid's engine[3], an offset cylinder structure, ion plated piston ring, main metal and connecting rod metal streaking, and molybdenum disulfide shot peening on the piston skirt[4].

The friction reduction effects are shown in Fig. 11. These results are from a comparison of motoring friction when the throttle is fully open, including pumping losses. Throughout almost all of the engine speed range, there was a reduction in friction of 10% or more. Figure 12 shows the breakdown of friction reductions. Friction at 5 000 rpm showed a 13% reduction in comparison with the previous engine. Of this reduction 55% comes from around the piston, 11% from around the crankshaft, and a 34% from the valve system drive.

### 4.1.3. Idling stability improvements

Idling engine speed reduction is very important in reducing fuel consumption. The idling engine speed with the newly developed engine is 50 rpm less than the previous engine, making it 750 rpm. This is a benefit of the rapid and stable combustion of the i-DSI.

Figure 13 shows the engine speed fluctuation and its frequency for each target idling engine speed. The measurements were taken in a bench test with the engine

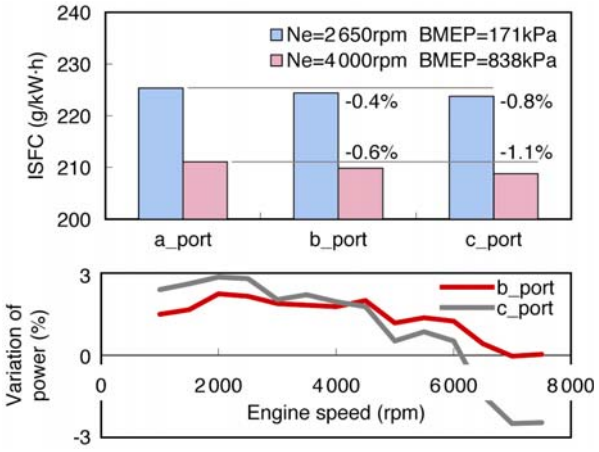



Fig. 10 Comparison of ISFC and power by inlet port

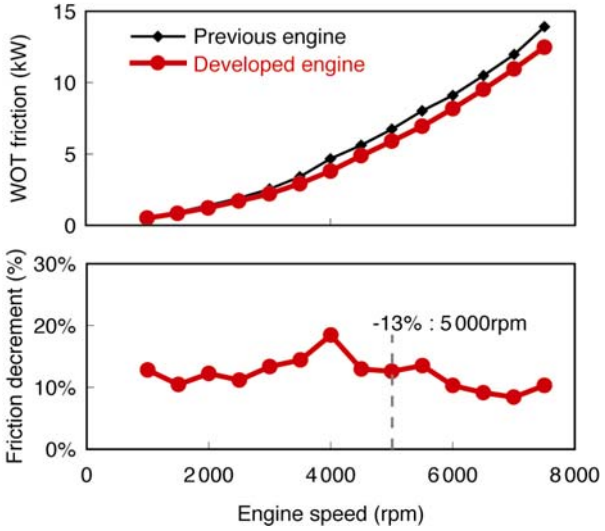



Fig. 11 Decrement of WOT friction

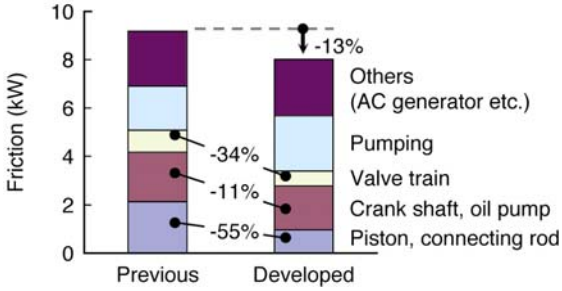



Fig. 12 Comparison of friction distribution

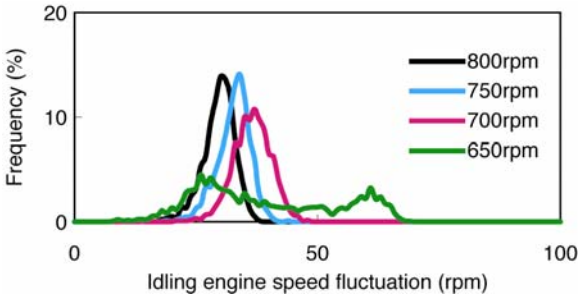



Fig. 13 Stability of idling engine speed

connected to an automatic transmission. The automatic transmission selector was set in the D range, and after fully warming the engine, the air fuel mixture was kept stoichiometric. In this measurement, a tendency was found that engine speed fluctuation range increases by lowering the target idling engine speed. At idling engine speed of 650 rpm, idle stability worsens due to a widening of engine speed fluctuation range and frequency dissipation.

In contrast, Fig. 14 shows the standard deviation of maximum cylinder pressure (Pmax) against target idling engine speed. At 650 rpm, Pmax standard deviation rises, and it enters the unstable combustion range. These results closely follow the tendencies in engine speed frequency characteristics previously noted, and combustion stability greatly affects idling engine speed stability.

The mass production spec sets the engine speed at 750 rpm, including idling controllability during transient periods such as electrical load changes, etc.

### 4.2. Power

Figure 15 shows the engine performance curve. As for power characteristics, resonant engine speed adjustments are carried out using intake system specifications. While the maximum torque value is equivalent to the previous engine, there is an average torque improvement of 7% in the engine speed range up to 4 000 rpm. In addition, the same maximum power value occurs at an engine speed that is 500 rpm lower, giving practical power characteristics.

Furthermore, various types of knocking suppression technologies have also contributed to modifications to the new engine's power characteristics. The application of i-DSI rapid combustion, swirl and tumble ports, and a new coolant path are given as specific examples.

In the same way as with fuel economy improvement, the effect on power of the i-DSI cylinder head spec using short stroke spec modified from the previous engine was confirmed. Figure 16 compares the volumetric efficiency characteristics against engine speed. Thanks to the 2-valve spec, the i-DSI advanced volumetric efficiency in the engine speed range up to roughly 5 000 rpm. Figure 17 shows the MBT torque characteristics at 3 500 rpm, and the set ignition timing. According to this, with i-DSI spec, the high MBT torque occurs with the ignition timing on the delay angle side, and at the same time, because the knocking margin is the same, set torque is raised 3%.

As a result of volumetric efficiency improvements and knocking suppression effects, the power characteristics of i-DSI from low to high engine speed are equal to or better than those of the previous 4-valve engine.

Concerning the coolant path, modifications were made to suppress knocking. Figure 18 shows the changes to the coolant path. Rather than flowing first to the cylinder block as the conventional coolant path would, this system has the recirculated coolant from the radiator flow first to the cylinder head. Thanks to this, recirculated coolant at a comparatively low temperature is provided around the combustion chamber at a high flow speed. This means that

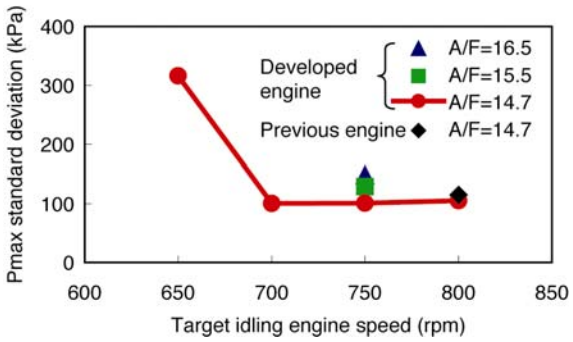



Fig. 14 Stability of idling Pmax

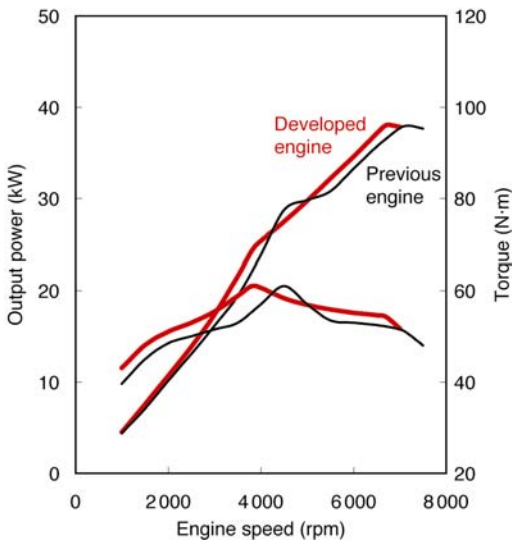



Fig. 15 Engine performance

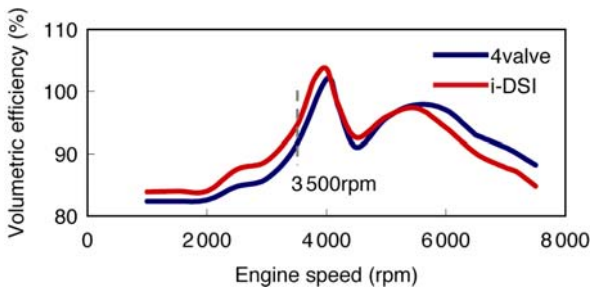



Fig. 16 i-DSI volumetric efficiency

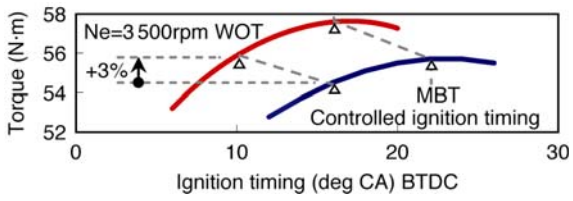



Fig. 17 Effect of i-DSI on torque

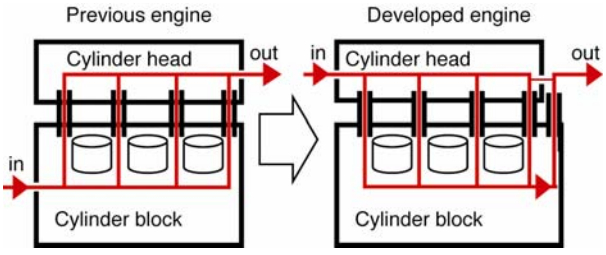



Fig. 18 Comparison of coolant circuit

there is a knocking suppression of 1-2° across the entire engine speed range, despite a higher compression ratio, which contributes to fuel economy and power improvements.

In addition, with the adoption of a cylinder head with integrated exhaust manifold, coolant flow speed distribution in the entire cylinder head water jacket was optimized so that it was possible to maintain sufficient cooling performance even with the heat flux from catalyzer flange to cylinder head. Specifically, through the coolant flow speed simulations in Fig. 19, visualization, and multi-point temperature measurements of actual engine firing, the shape was determined to minimize coolant stagnation and localized temperature rise.

### 4.3. Low Emission Technology

The major technologies for lowering emissions, as applied to the newly developed engine, are outlined in the four items below.

(1) Highly accurate air fuel ratio control
  1-1 Highly accurate air fuel ratio control through the use of an A/F sensor before the catalyzer and an $O_2$ sensor downstream from the catalyzer
  1-2 Reduction in fuel transportation delay by placing multi-hole injectors in the cylinder head ports
(2) A low heat mass structure around the exhaust system
  2-1 Cylinder head with integrated exhaust manifold
  2-2 Catalyzer located immediately under the engine
(3) Stoichiometric air fuel ratio control immediately after cold start, through combustion stabilization
(4) A large ignition timing delay angle control for early activation of the catalyst.

Here the results of application of early catalyst activation technology will be introduced. The goal of this technology is to reduce HC emissions immediately after cold start, as stated in (4) above[(5)].

To have early activation of the catalyst, it is most effective to have an exhaust temperature rise through a large delay angle in ignition timing. However, in applying a large delay angle, it is assumed that stable combustion will be maintained.

Figures 20 and 21 show the results of engine unit tests of combustion stability, using the new engine at low water temperatures. With a water temperature of 35 °C, the ignition timing delay angle and intake air amount was adjusted so that the Brake Mean Effective Pressure (BMEP) is uniform. As a result, even with a delay angle of 25° from MBT ignition timing, the combustion fluctuation rate does not reach 5% and stable combustion is maintained, and an exhaust temperature rise of roughly 200 °C could be reached.

The results of applying this control to actual vehicles are shown below. Figure 22 shows the catalyst temperature and 11 mode HC emissions 54 seconds after engine cold start, against the ignition delay angle amount. In comparison with having no ignition timing delay angle control, even with a maximum 15° delay angle, the HC emissions reduction tendency is maintained. Eventually, the mass production spec

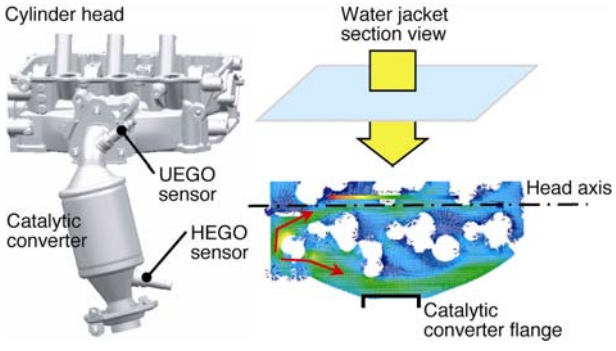



Fig. 19 Result of simulation of coolant flow to siamese exhaust port

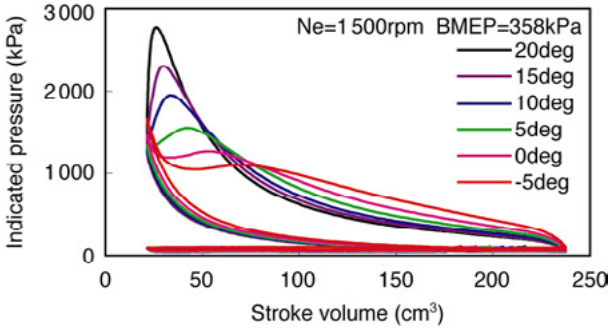



Fig. 20 Relationship between indicated pressure and ignition timing retard at constant BMEP

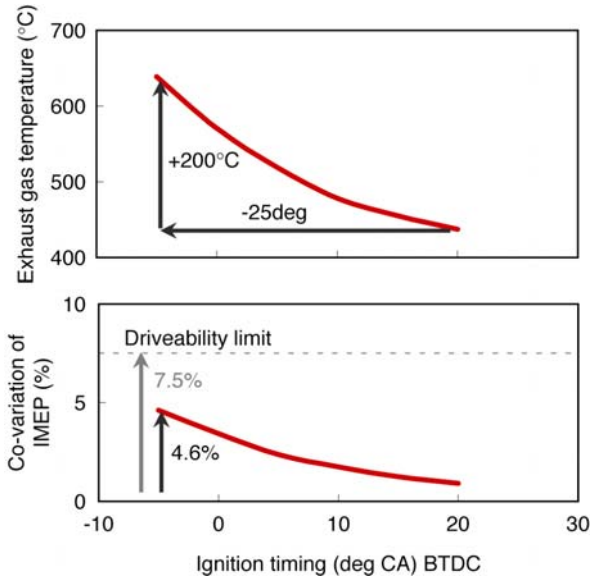



Fig. 21 Influence of ignition timing retard on exhaust temperature and combustion stability

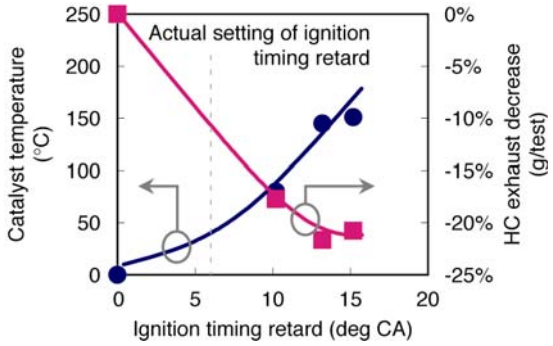



Fig. 22 Catalyst temperature rise and HC decrease

was set with an ignition delay angle of 6°, to balance fuel economy with catalyst early activation. In addition, as shown in Fig. 23, combined with the low heat mass structure around the exhaust system, a 220 °C catalyst temperature rise was achieved, making the system conform to ultra-low emissions standards.

### 4.4. Engine Vibration and Noise Reduction Technologies

Concerning engine vibration and noise, in order to actualize a competitive engine structure for the future, progress was first made in raising rigidity and reducing vibration around the major drive systems. To begin, high crankshaft rigidity was ensured through a short stroke structure, and vibration was suppressed through the use of full balance weights. By adding a twist process to the crankshaft forging and machining, a lighter weight was achieved while still having full balance. In 1-throw rigidity evaluations using computer aided engineering (CAE), crankshaft bend rigidity shows a 26% improvement over the previous model.

On the other hand, the lower block design in the cylinder block structure greatly contributes to engine frame rigidity. In this lower block, each journal is integrated into the lower block's outer wall, and through optimization of the curved surface shape and of the rib locations, the journal's bending stiffness is improved by 38%. In addition, CAE studies made it possible to maintain engine and transmission connection rigidity, without any need for auxiliary parts.

Secondly, there is i-DSI sequential ignition control for engine vibration and noise reduction. Figure 24 shows the simultaneous ignition of two spark plugs in each cylinder at 5 500 rpm WOT, and the (dP/dθ) max reduction effect through the delay angle control on exhaust side only. The mass production spec has, in contrast with simultaneous ignition, a 5° delay angle in the exhaust side ignition timing, thereby (dP/dθ) max is reduced by 19% and engine external noise is reduced by 17%, while the engine torque remains roughly the same.

By applying the above high rigidity engine structure and i-DSI technologies the mid frequency mount point vibrations, shown in Fig. 25, are reduced by 5 - 10 dB.

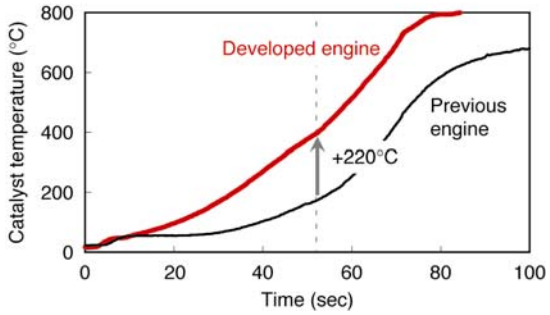



Fig. 23 Effect of siamese exhaust port and ignition timing retard on catalytic converter warm-up characteristics

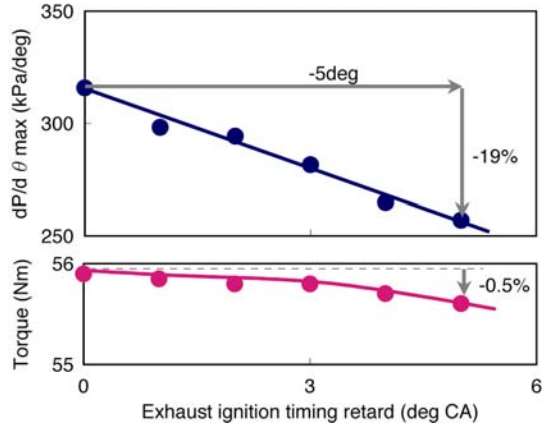



Fig. 24 (dP/dθ) max decrease and torque

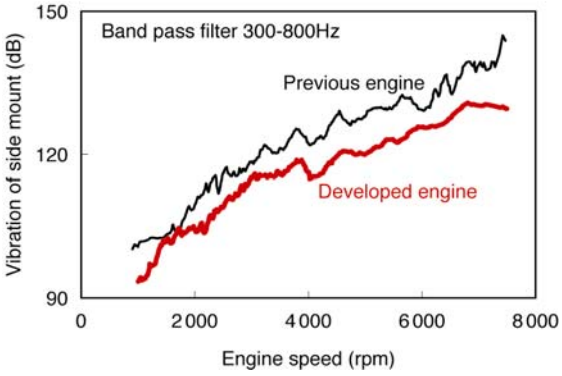



Fig. 25 Effect of i-DSI sequential ignition timing on improvement of engine noise

## 5. Conclusions

In the development of engines for minicars, the knowledge listed below was gained. By applying this knowledge, it was possible to achieve a commercial product that provides best-in-class environmental performance, excellent power, fuel economy and quietness.

(1) Reducing piston speed by applying a shorter stroke enables a 10% reduction in friction. In addition, rapid combustion using dual ignition improves performance against knocking. Combined with a high compression ratio of 11.2, it is possible to improve BSFC by 7%, achieving a 10 - 15 mode fuel consumption of 19.8 km/L.

(2) As for Wide Open Throttle power, in addition to the aforementioned rapid combustion and high compression ratio, volumetric efficiency is improved through a two-valve system, and knocking suppression performance is improved through changes to the coolant paths. These improvements mean that while reducing maximum torque engine speed by 500 rpm, there is a 7% torque improvement.

(3) In terms of environmental performance, improvements include a catalyzer directly beneath the engine, a low heat mass exhaust system, and early catalyst activation through an ignition timing delay angle. Furthermore, the air-fuel ratio was stabilized using a highly accurate air fuel ratio control. These measures have enabled the vehicle to meet the ultra-low emission standards.

(4) Changing the angle at which the engine is fit from 60° to 5° means that the front to rear length is reduced by 60 mm. Making the cylinder head cover and intake system parts out of plastic has reduced the engine's weight by 9%.

(5) Examining noise and vibration performance, action was

taken to create a high-rigidity crankshaft and to increase the connection rigidity with the transmission based on CAE analysis. Moreover, by reducing $(dP/d\theta)$ max through the use of an ignition timing delay angle control the mount vibration could be reduced by 5 - 10 dB.

## References

(1) Nakayama, Y., Suzuki, T., Iwata, Y., Yamano, J.: Development of a 1.3L 2-Plug Engine for the 2002 Model “Fit”, Honda R&D Technical Review, Vol. 13, No. 2, p. 43-52 (2001)

(2) Hayashi, A., Sakurahara, I., Takahashi, T., Endo, T.: Development of 1.8L Lean Burn Engine for the Accord/Torneo, Honda R&D Technical Review, Vol. 10, p. 52 (1998)

(3) Matsuki, M., Wakashiro, T., Kamiyama, T., Sato, T., Kaku, Y., Kanda, M.: Development of a Power Train for Honda’s Hybrid Car, the “Civic Hybrid”, Honda R&D Technical Review, Vol. 14, No. 1, p. 43 (2002)

(4) Ogiwara, H.: Individual Lubricant Application Technologies for Internal Combustion Engine Piston Skirts, and Their Effects, Honda R&D Technical Review, Vol. 14, No. 1, p. 85-92 (2002)

(5) Kitagawa, H., Minobe, T., Okamatsu, K., Yasui, H.: Ultra-Low Emission System for the “Accord SULEV”, Honda R&D Technical Review, Vol. 12, No. 2, p. 37-44 (2000)

■ Authors ■



Yusuke WADA



Keiji OHTSU



Kennosuke NARITA



Toshimitsu SHINOHARA

# Development of New Turbocharged Common Rail Diesel Engine

Tomoya ABE* Kenichi NAGAHIRO* Yoshihito TSUJI*
Kiyoshi TSUKIMURA* Hirokazu OHSAKI* Kazunori OZAWA*

## ABSTRACT

Honda has developed its first 2.2L 4-cylinder diesel engine for the 2004 model Accord being marketed in Europe.

The newly developed engine has a number of distinctive features. The employment of the latest 1 600 bar common rail control system, an EGR cooler and an after-treatment system has enabled the engine to comply with the EURO-IV regulations. The application of a variety of technologies to make the engine both lighter and more compact, including a new casting process for the cylinder block, and the use of advanced combustion and friction reduction technologies have resulted in a balance of power output, fuel efficiency and quietness at the top of this engine class. The employment of these original technologies has fully realized the development concept, which stresses both power and refinement. The new Accord equipped with this newly developed diesel engine has been well received in the European market.

## 1. Introduction

Concern for environmental issues is growing world wide, including in Europe where there is a strong sense of urgency concerning global warming. Europe has been striving to continue to reduce $CO_2$ emissions and has recently developed a large market focused on diesel engines, as they provide high performance. Honda has been engaged in the development of fuel economic and environmental futuristic technologies such as: Compound Vortex Controlled Combustion (CVCC)[1], Variable Timing and Lift Control Technology (VTEC)[2], Compressed Natural Gas Engine (CNG)[3], Electric Vehicle (EV)[4], Hybrid[5] and Fuel Cell vehicles[6]. The most recent development is a Turbocharged Diesel Engine, the Intelligent Common Rail Turbocharged Direct Injection (i-CTDi), which is the first for Honda.

Figure 1 shows an external view of the engine while Table 1 shows its main specifications.



Fig. 1 External view of i-CTDi diesel engine

* Tochigi R&D Center

Table 1 Main specification of i-CTDi diesel engine

| Engine type | DOHC-4VLV |
|---|---|
| Displacement ($cm^3$) | 2204 |
| Bore × Stroke (mm) | 85 × 97.1 |
| Compression ratio | 16.7 |
| Fuel injection system | Common rail |
| Maximum power (kW/rpm) | 103/4000 |
| Maximum torque (Nm/rpm) | 340/2000 |

## 2. Development Concept

The design goals for this project were to develop the diesel engine's strength of good fuel efficiency to the extent possible while holding its weaknesses of noise and vibration to a minimum.

The newest diesel engines are not inferior to gasoline engines on a comparison of power output; in fact there are many cases where diesel engines surpass gasoline engines. This can be considered to be one of the strengths of diesel engines; however, the diesel's very good fuel efficiency, not achievable by current gasoline engines, is considered as its most significant strength.

In comparison with a gasoline engine, a diesel engine loses some appeal due to its vibration and noise. In recent years, along with power output, progress has been made in these areas; however, its unique combustion noise cannot be overlooked. It is expected that an engine that overcomes these demerits, and achieves the same levels of noise and vibration (NV) as a gasoline engine, would be widely accepted.

Another natural basic consideration of an engine development project is the environment. If the engine can be developed to meet EURO-IV emissions regulations, which will be required in 2005, while keeping superior fuel economy and achieving gasoline engine alike NV, the engine is considered well balanced.

An engine with these merits is defined as a "First Class Diesel Engine" in a general term. Once the targets were clarified, the direction of development was easily established. The following three core technologies were pursued to achieve this concept.

(1) Lightweight, highly rigid structure
(2) Highly precise combustion control
(3) Extremely efficient exhaust cleanup system

## 3. Lightweight, Highly Rigid Structure

A lightweight rigid structure is very important for achieving high fuel efficiency and low NV. During the development of the new diesel engine, Honda expanded its strength capability with casting aluminum[(7) - (9)] and developed a closed deck aluminum cylinder block with a high productivity.

One of the most prevalent methods for manufacturing aluminum blocks is the use of high pressure casting. This has a high productivity; however, difficulties arise such that sand cores cannot be used due to the high pressure and gas intrusion leading to heat processing difficulties. On the other hand, the cylinder pressure in a diesel engine is high; therefore a closed deck type is advantageous. Thus, to meet both of these criteria, a manufacturing method injecting semi-solid aluminum into a metal mold at low pressure referred as "Advanced Semi-solid Casting Technology" (ASCT) was developed. This provides both high productivity and a closed deck engine structure. Figure 2 shows an overall diagram of the cylinder block. In addition, an annealing process and thinner walls make it possible to achieve a 30% reduction in weight when compared to cast iron block diesel engines in the same class. This is described in Fig. 3.

The sleeves are made of cast iron using a spin casting process. The thickness other than the outer spines (protrusions used for adherence) was reduced to 3 mm. Also, the thickness of the aluminum between the sleeves is 3 mm, giving a total of 9 mm between cylinders, which is the same as for a gasoline engine.

Another characteristic of the cylinder block is the cylinder offset. The crank center was offset 6.5 mm to the thrust side of the bore center. This has reduced the impact energy of the piston by 30%. Figure 4 shows the simulation results. This has produced both a reduction in NV and an improvement in fuel efficiency.



Fig. 2 Photograph of ASCT aluminum cylinder block

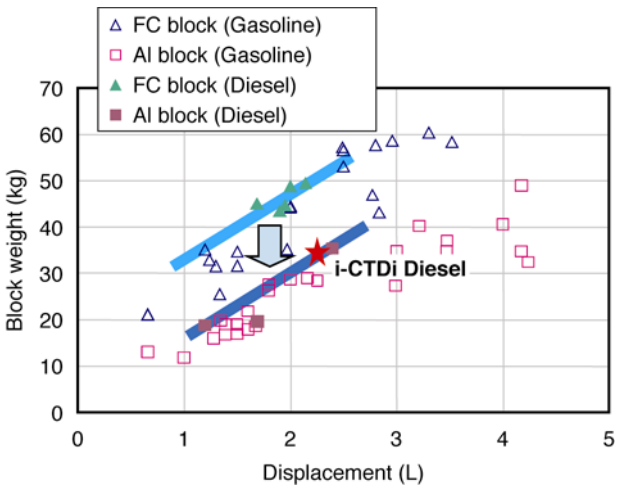



Fig. 3 Effect of ASCT on weight of cylinder block weight

The main bearing is supported by the lower block structure that is made of die cast aluminum, which contributes to the engines high rigidity.

In order to reduce friction at low coolant temperatures, cast iron bearing holders are being cast in a mold. Through this type of construction, as can be seen in Fig. 5, this aluminum block has achieved the same high rigidity as one made of cast iron.

In order to reduce the weight of the crankshaft, a four counterweight type was adopted and the crankshaft was strengthened using high frequency quenching[10]. The diameter of the main/pin journal is 60/50 mm. The bearing includes a recently developed high surface pressure solid lubricant overlay to respond to the low viscosity of the recent engine oil. This improved the boundary lubricant characteristics and made possible the use of low viscosity 0W-20 class engine oil. Furthermore, targeting improvement during the breaking in period, a molybdenum disulfide coating was added to the surface.

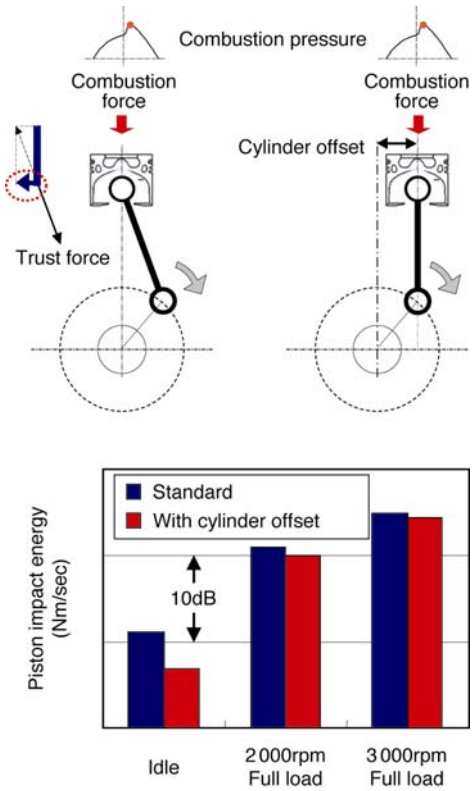



Fig. 4 Effect of offset cylinder on thrust force

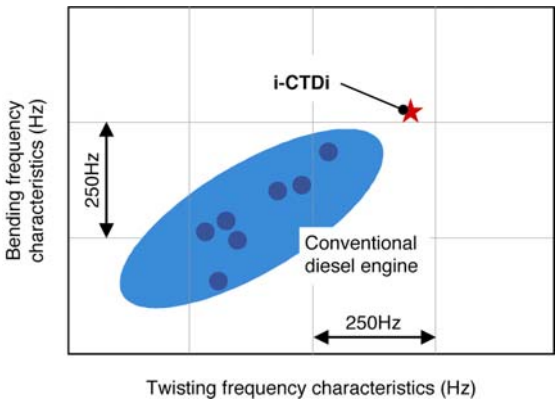



Fig. 5 Dynamic characteristics of cylinder block

The cylinder head contains vertical valves, direct injectors, glow plugs, etc. in a small area leading to a complex structure that has a high thermal load. Therefore, a top-feed cooling method is applied, that is, coolant that has been cooled by the radiator first cools the cylinder head, then the cylinder block and then each of the auxiliary systems. A cylinder head diagram is shown in Fig. 6 while Fig. 7 shows the schematic diagram of the cooling system. Through use of this cooling method, as can be seen in Fig. 8, heat removal of all parts of the head was improved compared to the conventional cooling method, where the cylinder block is cooled first.

In order to use center injection, DOHC 4 valves were used for the valve train. Coupling with the roller rocker arm contributes to the lowering of friction. Also, to help make it maintenance free, hydraulic lash adjusters (HLA) are used.

A single roller chain is used to move the valves. A diesel engine has large fluctuations of engine rotation that place a large load on the drive chain, therefore a silent chain would

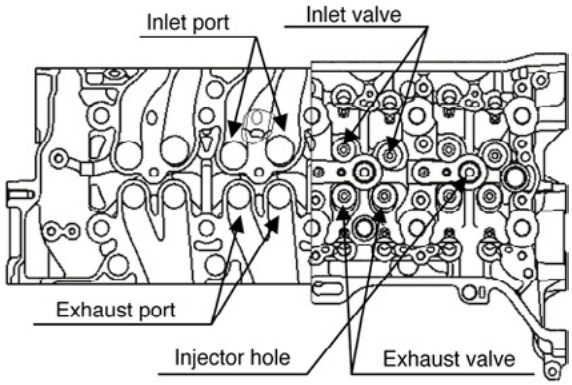



Fig. 6 Detail of cylinder head

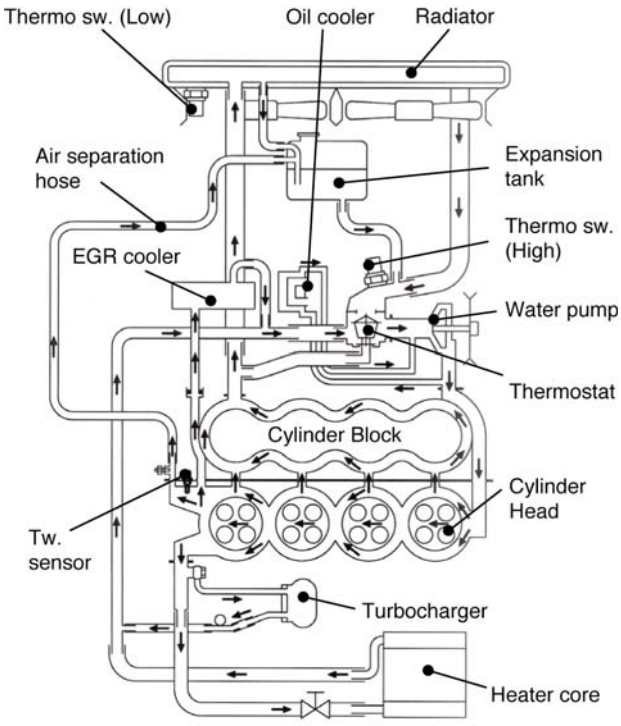



Fig. 7 Schematic diagram of cooling system

be required to be extremely wide. Also, soot in the engine oil causes pitting wear on a bush chain. Therefore, a roller chain that is processed with Vanadium Carbide (VC), which has excellent wear resistance, is used. Drive transfer between the intake and exhaust camshafts is performed by a helical gear with a scissors gear attached. This provides both a reduction in NV and compactness.

In order to reduce NV, a secondary balancing system is used. Targeting the compactness, the balancing unit is driven by a single chain, like the camshaft and is placed in the oil pan. Figure 9 shows an overall diagram of the drive train system. In order to reduce both aeration of the oil and friction, optimization of the balancing unit case structure was performed. Also, the oil pump is driven from the same shaft as the balancer unit providing a synergistic use of components.

The auxiliary systems are grouped at the front of the engine and driven with a serpentine belt. This helps make the system compact. Also, the aluminum housing of the recyclable oil filter is put to further use as an auxiliary bracket providing synergy and making the system more lightweight. The auxiliary systems are shown in Fig. 10.

In order to reduce NV of the i-CTDi a duel mass flywheel is used along with a torque fluctuation absorbing crank pulley used to reduce tension in the auxiliary system belt. However, because the system passes through a resonance area during start up, a pulley with a one-way clutch was applied to the alternator, which has the most inertial mass of the auxiliary systems.

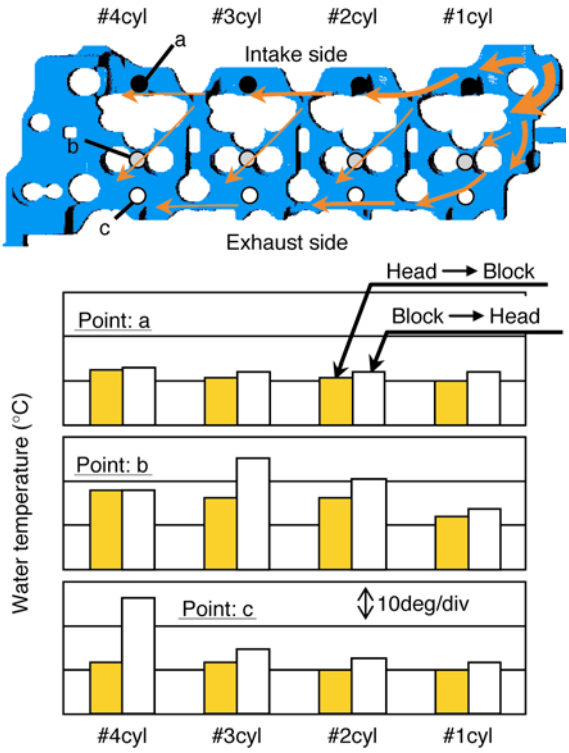



Fig. 8 Effect of top feed cooling system

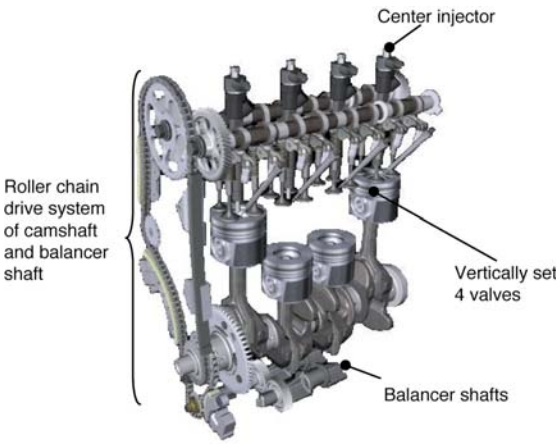



Fig. 9 Schematic diagram of drive train system

## 4. Highly Precise Control of Combustion

The combustion chamber is a re-entrant style 4 valve central injection chamber. To develop a combustion that produces high fuel efficiency, low noise and clean exhaust it needs to be homogeneous and smooth. As shown in Fig. 11, the chamber shape was optimized after reviewing several types of combustion chambers. Also, the compression ratio is set to 16.7, which reduces friction. Afterglow control, energizing the glow plugs after startup, was implemented for combustion improvement at a low coolant temperature and it ensured a stable combustion during this period. Arranging the valves vertically and eliminating the valve pockets in the upper surface of the piston led to a low Surface to Volume (S/V) ratio of 0.643 (1/mm), compatible with the clean concept. Details of the shape of the combustion chamber can be seen in Fig. 12.

To achieve the best possible combustion, having many degrees of freedom of control as well as highly precise control is essential. Several of the devices used on the i-CTDi are changed to electronic control. The control system diagram is shown in Fig. 13.

The fuel injection system used for the engine is the BOSCH common rail system. The high pressure injection pump is driven by a sub-shaft placed at the end of the exhaust camshaft and achieves a maximum pressure of 1 600 bar. To obtain optimal efficiency in the reduction of gear ratio, it is set at a rotational speed of 5/6 of the engine speed. Targeting

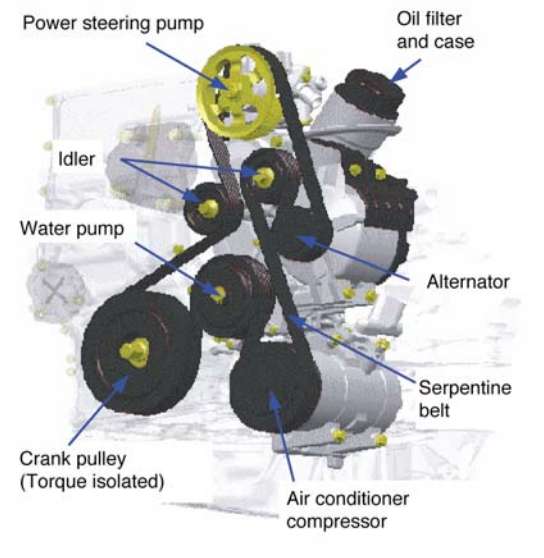
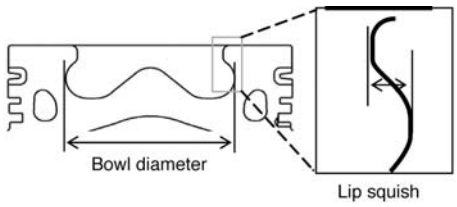



Fig. 10 Schematic diagram of auxiliary device drive system

low NV between the camshaft and sub-shaft a helical gear with a scissors gear attached is used for transfer of power. Also, an Oldham coupling is used to transfer power from the sub-shaft to the high pressure pump. A system overview diagram is shown in Fig. 14. Also, a 6 hole micro-sac spray nozzle that has small spray pattern variability and suppresses Particulate Matter (PM) emissions was adopted.

The i-CTDi is equipped with a variable linear swirl control valve (SCV). This provides optimum and precise swirl control over the entire range of engine speeds leading to optimum combustion. As can be seen in Fig. 15, the SCV valve is placed upstream of the tandem intake manifold, containing two independent ports and chambers, and is situated to avoid direct contact with exhaust gas recirculation (EGR) gases. This has provided a simple yet highly reliable SCV system. The two ports are the primary port, which is a swirl port and the secondary port which is a straight port arranged directly in line with the combustion chamber. As can be seen in Fig. 16, swirl ratios from 1.2 to 4.0 are achieved with low intake resistance. A sensor is used to




| | 1 | 2 | 3 | 4 | 5 | 6 | Best |
|---|---|---|---|---|---|---|---|
| Lip squish | S | M | L | L | L | S | L |
| Bowl diameter | M | M | M | S | M | L | M |

S : Small M : Medium L : Large

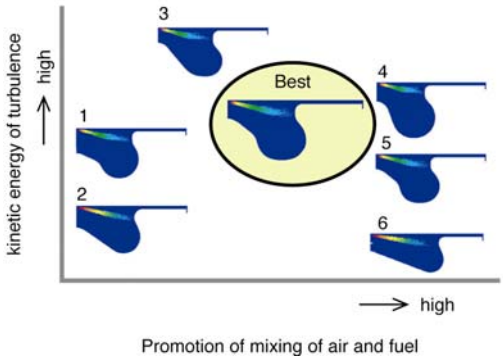



Fig. 11 Test result of various type of combustion chamber

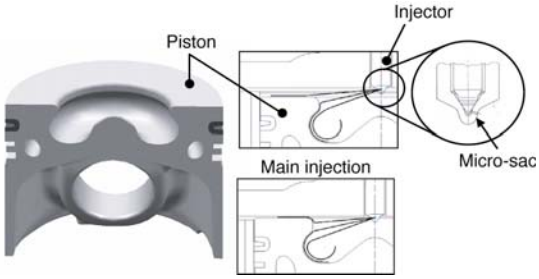



Fig. 12 Detail of the combustion chamber

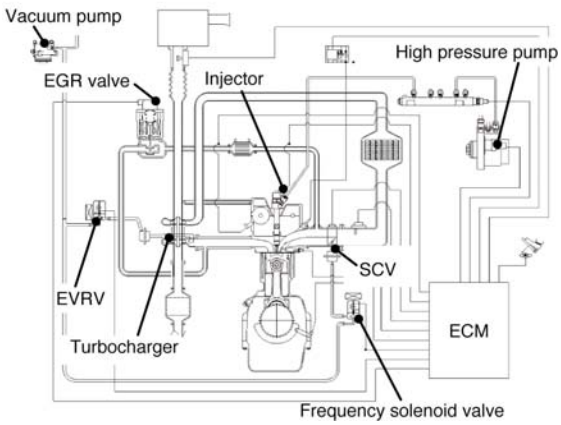



Fig. 13 Schematic diagram of total control system

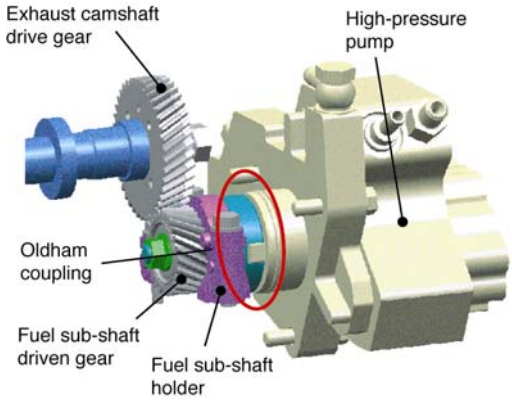



Fig. 14 Schematic diagram of drive system of high-pressure pump

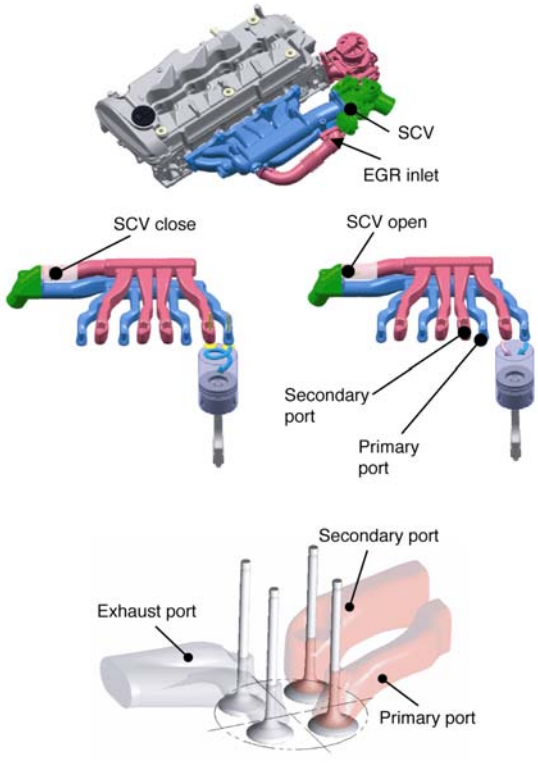



Fig. 15 Schematic diagram of intake system

determine how much the SCV valve is open and a frequency solenoid valve with electronic control is used to operate the valve with vacuum. Figure 17 shows the settings of the SCV valve opening.

EGR, used for NOx reduction has a large effect on combustion quality. Therefore, the EGR valve is controlled with an electronically controlled linear solenoid that provides unparalleled control capability, high precision, and improved response. As the linear solenoid type requires less force to operate compared to the vacuum driven type, the double poppet type is used in a structure that cancels the characteristic exhaust back pressure of a turbocharged engine. This is described in Fig. 18.

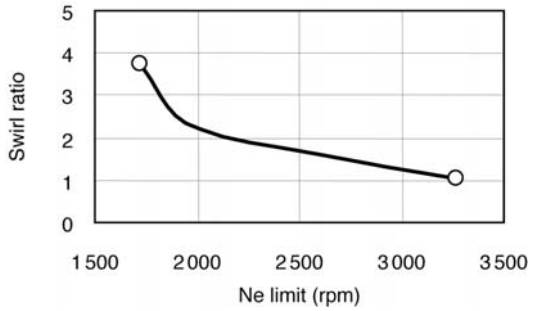



Fig. 16 Relationship between Ne limit and swirl ratio

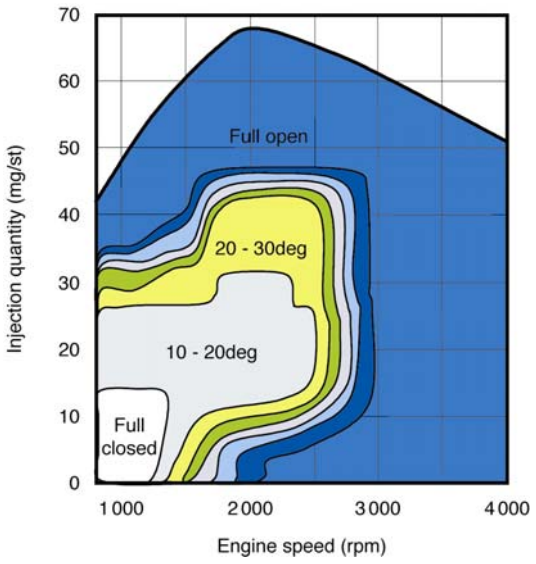



Fig. 17 Control map of SCV

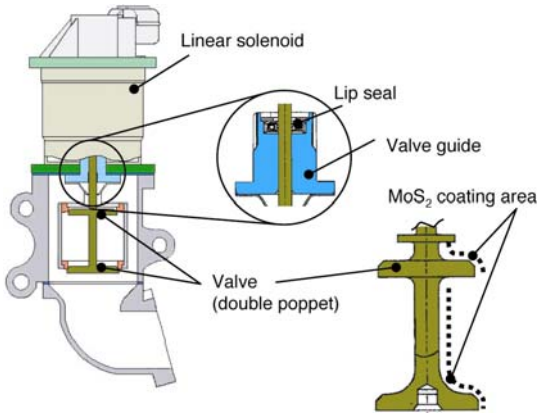



Fig. 18 Cross-section of electrically controlled EGR valve

A shield was placed to suppress exhaust from penetrating the valve guide and a $MoS_2$ coating is used to prevent sticking on the valve seat of residue from unburned fuel. High reliability was achieved. Also, the water cooled EGR cooler is placed downstream from the EGR valve and through increasing the density of the EGR, it improved the efficiency of reducing NOx.

For the turbocharging system a variable geometry turbo charger is employed. Through optimizing the settings of both the compressor and the turbine, optimized turbo charging is available at all speeds. The geometry is controlled with an Electric Vacuum Regulating Valve (EVRV), a vacuum electronic control. The targeted turbo charger pressure is detected inside the intake manifold and the vanes are opened or closed accordingly for geometry control. The center housing is cooled by coolant, protecting the materials that can be damaged by heat such as the engine oil and the bearings. Also, an air to air intercooler is used, concluding with a maximum turbo-charger pressure of 130 kPa being obtained.

## 5. Highly Efficient Exhaust After-treatment System

On top of reducing the amount of engine feed gas, a highly efficient exhaust after-treatment system is essential to achieve EURO-IV exhaust regulations. A new diesel engine exhaust after-treatment system was developed for the i-CTDi engine. Figure 19 shows a system diagram of this exhaust after-treatment system.

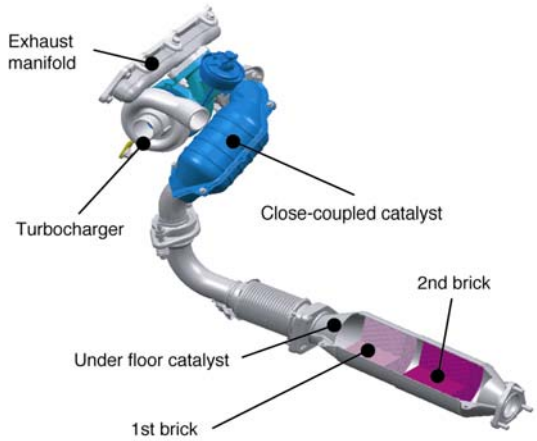



Fig. 19 Schematic diagram of exhaust system

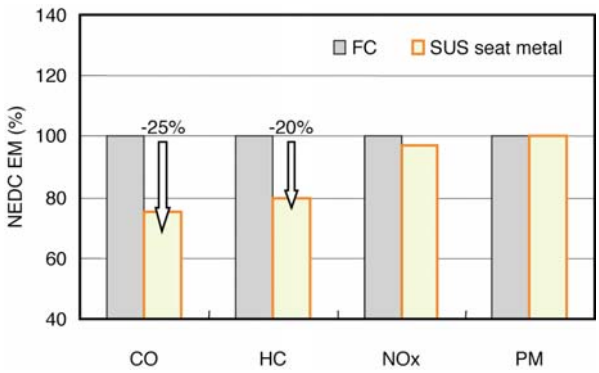



Fig. 20 Effect of seat metal exhaust manifold

Table 2 Main specification of catalyst

| | Close-coupled catalyst | Under floor-catalyst | |
|---|---|---|---|
| | | 1st brick | 2nd brick |
| Type | Oxidation | De-NOx | De-NOx |
| Volume (L) | 0.7 | 1.0 | 1.3 |
| Substrate | Metal foil | Metal foil | Metal foil |
| Foil thickness (mm) | 0.03 | 0.03 | 0.03 |
| Cell density (cpsi) | 400 | 400 | 400 |
| Coating | Pt base | Pt base | Pt base |
| Zeolite | A | A | B |

Through using an extremely compact press type exhaust manifold made of stainless steel, its thermal mass was reduced, therefore the light off characteristics of the catalyst is improved. As can be seen in Fig. 20, compared to a cast iron manifold, CO and HC emissions were reduced 20 to 25 %.

The main specifications for the catalyst are shown in Table 2. The catalysts consist of a close coupled oxidation catalyst and an under floor catalyst with 2 De-NOx reduction catalytic beds with different temperature based selective NOx clean up capabilities, shown in Fig. 21. This expands the temperature window of and optimizes NOx clean up. Also, on a component basis, 0.03 mm thick metal foil has better heat transfer and heat diffusion characteristics than ceramic. Through using metal foil for the catalyst, low temperature oxidation light off performance improved, and oxidization and NOx clean up performance is maintained in a high level balanced design.

## 6. Main Performance Characteristics

Figure 22 shows the power output performance of the i-CTDi engine. The maximum output of the i-CTDi shows a performance at the top of its engine displacement class. The acceleration capability in low to mid speeds is an important output setting. Therefore it is considered that the engine will perform well from city to freeway driving in a wide range of driving conditions.

The European Accord that is equipped with this i-CTDi engine coupled with a 5MT achieved a fuel efficiency of 5.4 L/100 km in the EUDC mode, the top of its class. It also meets the EURO-IV emission requirements.

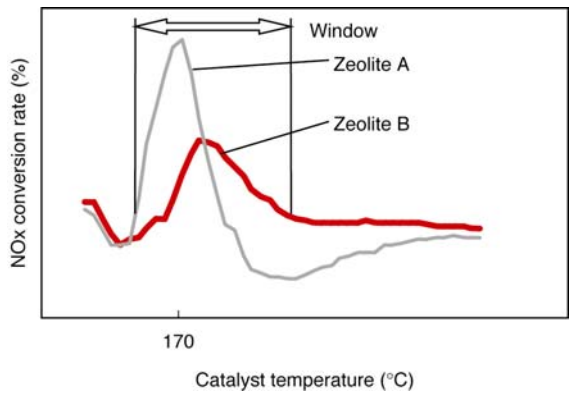



Fig. 21 Thermal characteristics of De-NOx catalyst

This Accord also has the best NV level of all of the diesel engines in the same class as shown in Fig. 23. Therefore, it is considered that the fundamental design concepts were achieved.

## 7. Conclusions

From a fundamental concept of “First Class Diesel Engine”, a turbocharged diesel engine, the i-CTDi, was developed with the goals of achieving high fuel efficiency and low NV.

(1) The combustion is optimized by using a 1 600 bar common rail system. EURO-IV emissions regulations are met early through the combined use of De-NOx catalysts, a water cooled EGR cooler, and a continuously variable swirl control valve.

(2) Through a new manufacturing process, starting with a lightweight aluminum cylinder block and roller chain, engine frame technology has led to a more compact engine with a large reduction in weight.

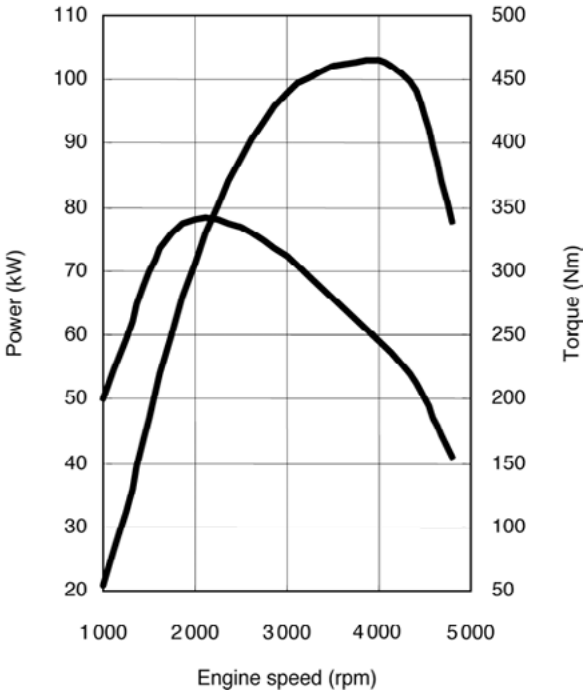



Fig. 22 Power curve of i-CTDi diesel engine

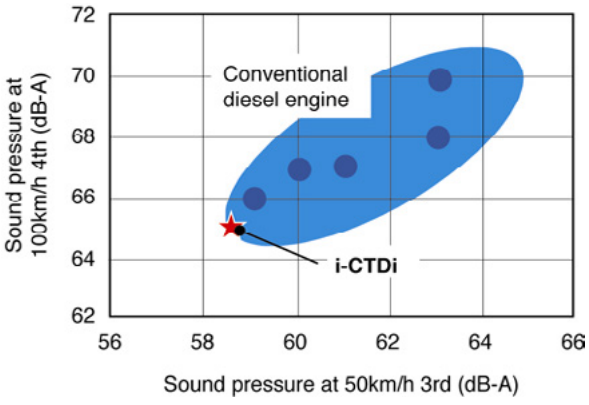



Fig. 23 NV level of i-CTDi diesel engine

(3) Through low friction technologies, including combustion technology, a variable turbo charger, and an offset crankshaft, the engine has simultaneously achieved power output and fuel efficiency at the top of its class.
(4) Through combustion control and increasing the engine frame rigidity, this engine achieved a level of silence similar to that of a gasoline engine.

## References


(1) Yagi, S., Fujii, I., Hatanaka, T.: CVCC Ennjinn no Shotokusei ni Tsuite, JSAE Annual Congress Proceedings, No. 741, p. 285-289 (1974)

(2) Ohura, H., Miura, K.: Development of high-efficiency gasoline engine with variable valve lift and timing system, Journal of Society of Automotive Engineers of Japan, Vol. 45, No. 8, p. 93-98 (1991)

(3) Toda, T., Matsuki, M., Ohmori, T., Yamamoto, H.: Development of a 1.7L CNG Engine for the 2001 CIVIC GX, Honda R&D Technical Review, Vol. 14, No. 1, p. 49-56 (2002)

(4) Ogura, M., Suzuki, S., Matsumoto, K.: Introduction of Electric Vehicle “HONDA EV PLUS”, HONDA R&D Technical Review, Vol. 9, p. 1-10 (1997)

(5) Fukuo, K., Fujimura, A., Saito, M., Tsunoda, K., Takugichi, S.: Development of the Ultra-Low-Fuel-Consumption Hybrid Car-INSIGHT, HONDA R&D Technical Review, Vol. 11, No. 2, p. 1-8 (1999)

(6) Kawasaki, S., Ogura, M., Ono, T., Kami, Y.: Development of the Honda FCX Fuel Cell Vehicle, Honda R&D Technical Review, Vol. 15, No. 1, p. 1-6 (2003)

(7) Mitobe, K., Itakura, K.: New Accord and Vigor, Journal of Society of Automotive Engineers of Japan, Vol. 40, No. 5, p. 611-618 (1986)

(8) Hayashi, T., Ushio, H., Fujisawa, Y., Hata, T., Shibata, K., Ebisawa, M.: The Properties of Hybrid Fiber Reinforced Metal and its Application for Engine Block, HONDA R&D Technical Review, Vol. 1, p. 55-65 (1989)

(9) Shinohara, M., Hata, T., Kato, H.: Development of new type aluminum die-cast cylinder block. Aluminum die-cast cylinder block with cast-iron one piece liner, JSAE Annual Congress Proceedings, No. 954, p. 257-260 (1995)

(10) Onda, H., Asai, T., Fujiki, K., Kudo, H., Murofushi, K.: Development of High-strength Induction Hardened Crankshaft, Honda R&D Technical Review, Vol. 15, No. 2, p. 175-182 (2003)



■ Authors ■


Tomoya ABE


Kenichi NAGAHIRO


Yoshihito TSUJI


Kiyoshi TSUKIMURA


Hirokazu OHSAKI


Kazunori OZAWA

# Development of Aluminum Cylinder Block for Diesel Engine

Masakazu YAMAZAKI* Atsushi TAKAI* Osamu MURAKAMI*
Mitsuhiko KAWABATA* Osami ITO** Koichi KUROKI**

## ABSTRACT

A high-strength aluminum cylinder block manufactured using a new production process, ASCT (Advanced Semisolid Casting Technology) has been adopted for the newly developed 2.2L 4-cylinder i-CTDi (Intelligent Common rail Turbo Diesel Injection) diesel engine fitted in the 2003 Accord marketed in Europe. In the production process, semi-solid aluminum is used during high pressure die-casting. In addition, newly developed pressure-proof sand cores are used to mold the closed deck, and heat treatment is conducted to ensure a high level of material strength.

To respond to the high load on the crankshaft journal, die-cast aluminum lower block and cast iron bearing caps are employed. Adopting the dummy head honing and offset cylinders to reduce bore deformation have enabled the achievement of a lightweight, compact cylinder block configuration matched to the high combustion pressure of the latest diesel engines, while maintaining a high level of quietness.

Thanks to these counter measures, a 30% weight reduction for the new cylinder block has been achieved compared to that of the conventional cast iron diesel engine of the same displacement.

## 1. Introduction

Diesel engine performance has recently increased dramatically with advances in fuel system technologies, in particular the common rail. Increased performance has led to consequent increases in combustion pressure, and greater durability is now required in the structural components of the engines, including cylinder blocks. On the other hand, the achievement of compactness and low weight is also a factor in the over-all reduction of $CO_2$ levels in automobiles, making it extremely important to achieve weight savings in the cylinder block, which represents the heaviest component in the engine[1), 2)]. This has led to the increased use of aluminum alloy cylinder blocks in diesel engines[3)].

Aluminum alloy cylinder blocks are already widely used in gasoline engines, and the majority of these are produced by high-pressure die casting (HPDC) to ensure productivity. Undercut forms cannot be produced using HPDC. When the HPDC method is employed it is necessary to use an open structure in the deck section that forms the mating surface with the cylinder head. It is also difficult to increase the strength of the cylinder block with solution heat treatments because of difficulty in ensuring material quality. However, productivity declines noticeably if low-pressure die-casting

* Tochigi R&D Center
** Honda Engineering Co., Ltd.

(LPDC) is used to enable heat treatments to be applied and allow the formation of a closed deck. In this case, it becomes difficult to mold the thin sections of the block, the dimensions between the cylinder bores increase, and the overall weight of the block increases[4].

The development of an aluminum alloy cylinder block for a high-performance diesel engine without sacrificing performance or productivity necessitated a detailed study of structure and the development of a new production technology. The challenges outlined above were overcome through the employment of semi-solid die casting and the development of pressure-proof sand cores, enabling weight reduction of the cylinder blocks while maintaining good machinability.

## 2. Concept Behind Development of a Cylinder Block for a High-performance Diesel Engine and Performance Requirements

The cylinder block is a key component of the engine, and since the development of the original Civic model, Honda has been producing these components from aluminum to make its engines both lightweight and compact. The cylinder block used in the newly developed i-CTDi diesel engine (Fig. 1) was required to use the same packaging and production equipment as the cylinder block employed in the 2.0 – 2.4L class intelligent variable valve timing and lift electronic control system (i-VTEC) series (K24A) gasoline engines. And, therefore, during its design the K24A cylinder block was employed as a base. The concept behind the development was the production of a high-performance cylinder block that matched the functions and performance of the cast blocks employed in competitors' high-power diesel engines with a minimum increase in weight over the base gasoline engine cylinder block. Table 1 shows a comparison of the basic specifications of the diesel and gasoline engine cylinder blocks, and Fig. 2 shows an exterior view of the diesel cylinder block.

Table 1 Specifications of engines and cylinder blocks

| | i-CTDi Diesel | i-VTEC Petrol |
|---|---|---|
| Total displacement (cc) | 2204 | 2354 |
| Bore (mm) | 85 | 87 |
| Stroke (mm) | 97.1 | 99 |
| Bore pitch (mm) | 94 | 94 |
| Compression ratio | 16.7 | 10.5 |
| Maximum output /engine speed | 103kW (140PS)/ 4000rpm | 147kW (200PS)/ 6800rpm |
| Maximum torque /engine speed | 340Nm/2000rpm | 225Nm/4500rpm |
| Configuration | Closed deck/ Lower block configuration | Open deck/ Lower block configuration |
| Block height (mm) | 247.1 | 231.5 |
| Cylinder offset (mm) | 6.5 | 0 |
| Upper block material | Aluminum alloy | Aluminum alloy |
| Liner material | FC (Centrifugal casting) | FC (Centrifugal casting) |
| Liner thickness (mm) | 3 | 2 |
| Lower block material | Aluminum alloy | Aluminum alloy |
| Lower block height (mm) | 75 | 60 |
| Bearing cap material | FCD450 | FC250 |
| Bearing cap bolt size | M11 × 102 | M11 × 95 |
| Weight (kg) | 34.0 | 28.6 |

### 2.1. Changes, Issues and Solutions in Converting Cylinder Block from Gasoline to Diesel Engine Use

The major points of difference between a diesel engine and a gasoline engine taken into consideration when establishing the specifications of a cylinder block are as follows:

(1) Increased combustion pressure
(2) Increased engine heat at full load
(3) Effect of increased soot concentration in lubricating oil and sulfur content in fuel

The following sections will discuss the issues generated by each of these topics and the counter measures employed as solutions.




Fig. 1 External view of i-CTDi engine



Fig. 2 External view of cylinder block

### 2.1.1. Dealing with increased combustion pressure

It was necessary to consider a figure of 16 MPa, including fluctuations, as the maximum combustion pressure in the i-CTDi engine, when compared to 8 - 10 MPa in a gasoline engine. Figure 3 shows a graph comparing combustion pressure in a gasoline and diesel engine. The counter measures employed to deal with this issue generated by increased combustion pressure are discussed below.

(1) Closed deck design A closed deck configuration was employed in the cylinder block to ensure sufficient rigidity in the cylinder bore section and toughness of the gas seal in the head gasket to resist high combustion pressure. Unit tests to measure stress produced by hydraulic pressurization, and FEM analysis, were carried out to enable optimization of the distribution of thickness in the liner and aluminum, the external shape of the liner, the thickness of the deck and the shape of the water jacket. An example of FEM analysis of the deck and surrounding areas is shown in Fig. 4. Figure 5 shows a comparison of line pressure in the head gasket bead with an open deck and the closed deck employed in the new cylinder block, demonstrating that a greater amount of line pressure is generated against the head bolt axial force in the closed deck configuration.

(2) High-quality aluminum materials and heat treatment To enable the closed deck design to be employed and weight to be lowered, a new production process (Advanced Semi-solid Casting Technology as ASCT), was applied to the upper block. This enabled both the achievement of high quality while maintaining the same material thickness as in HPDC and the application of heat treatments to increase strength. FEM analysis was conducted to optimize thickness and structure in this production process. Figure 6 shows an FEM analysis of the cylinder head when connected and tightened as an example of strength analysis of the cylinder block.

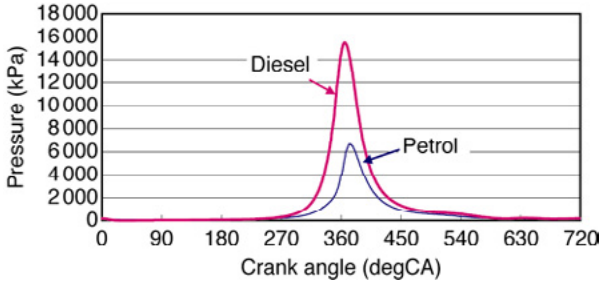



Fig. 3 Comparison of diesel and Petrol engine combustion pressure

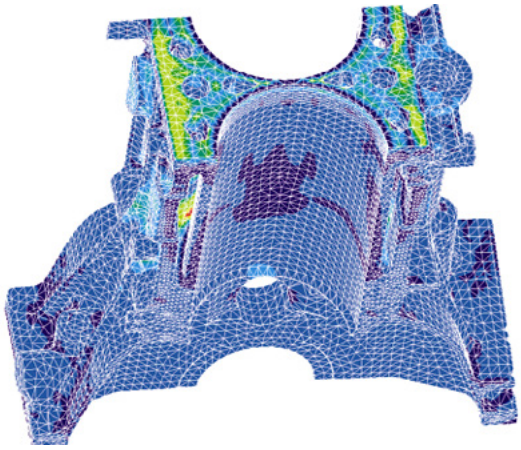


Fig. 4 FEM analysis of deck and surrounding sections

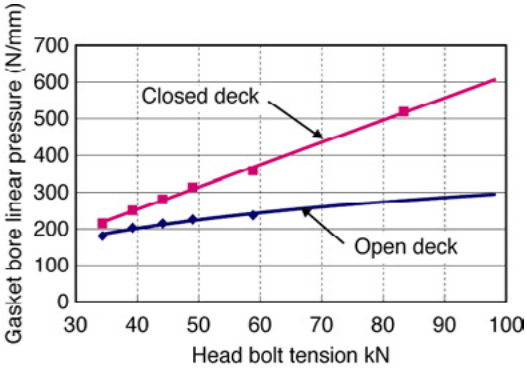



Fig. 5 Comparison of line pressure of head gasket bore

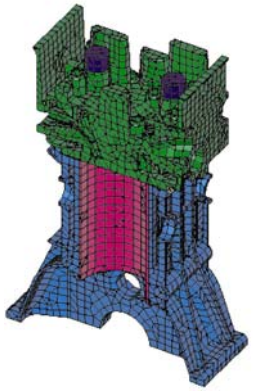


Fig. 6 FEM analysis of tightening cylinder head

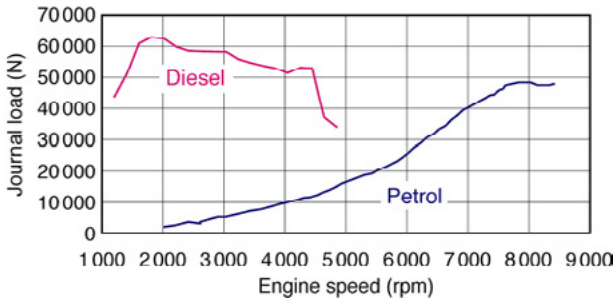



Fig. 7 Comparison of journal load



Fig. 8 Analysis of lower block load

(3) High-rigidity aluminum block In a gasoline engine, the maximum load is produced on the #3 crank journal. This load is produced from the inertial load at high engine speed and the behavior determined by rigidity of the crankshaft and supporting cylinder block rather than combustion pressure. In a diesel engine, by contrast, explosive loads are dominant, and downward loads in journals #2 and #4 will be the maximum loads. Figure 7 shows a comparison of load on the crank journals in a gasoline and diesel engine. As per the example shown in Fig. 8, FEM analysis was employed to design the entire structure of the cylinder block, enabling the optimization of the basic dimensions for the bearing cap, material selection, and the establishment of specifications for the bearing cap bolt and the peripheral structure. FEM analysis was also used to optimize the height of the lower block, the cast form of the bearing cap and the connecting structure with the outer wall in order to increase the bending and torsional rigidity of the entire block.

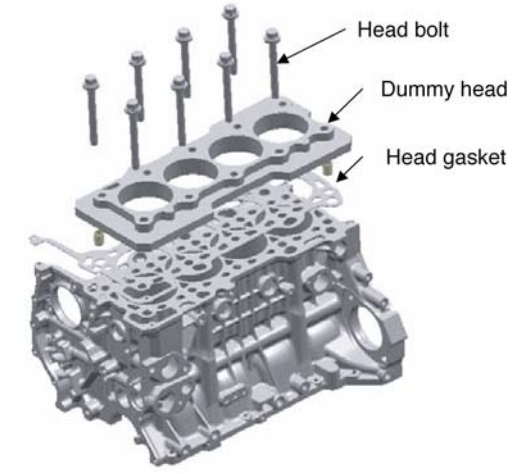



Fig. 9 Dummy head honing method

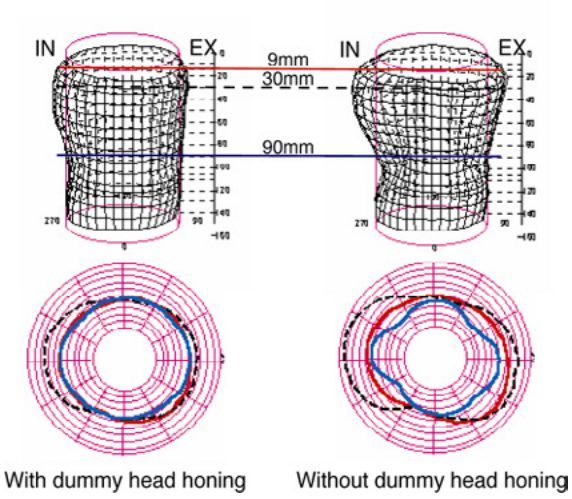



Fig. 10 Effects of dummy head honing

(4) Dummy head honing A large M13 × 1.25 plastic region bolt, of a type not previously employed in a gasoline engine, was utilized for the head bolt in order to produce sufficient head gasket surface pressure. The rigidity of the cylinder head, the positioning of the head bolt, the depth of the female screw section and the peripheral structure were all optimized in the design process. There were concerns over deformation of the cylinder bore caused by the high-axial force head bolt. To ensuring rigidity in the bore and surrounding sections, dummy head honing, which honing is conducted with a dummy head tightened to the cylinder block, was used to minimize bore deformation when assembled. Figures 9 to 11 show the dummy head honing method and the results in reduction of bore deformation. The use of this technique has controlled oil consumption and suppressed piston slap noise, and reduced sliding wear on the pistons by stabilizing piston behavior.

(5) Offset cylinders High combustion pressure and variation in combustion pressure cause an increase in piston slapping sound. An increase in side pressure causes friction to increase. An offset cylinder configuration, in which the cylinders are offset from the crank center in the direction of anti-thrust, was employed to counter the increases in piston slap and friction. The degree of offset was optimized by estimating the piston behavior and the friction caused by side pressure using simulations. Figure 12 shows the reduction in side pressure on the piston achieved by using the offset configuration.

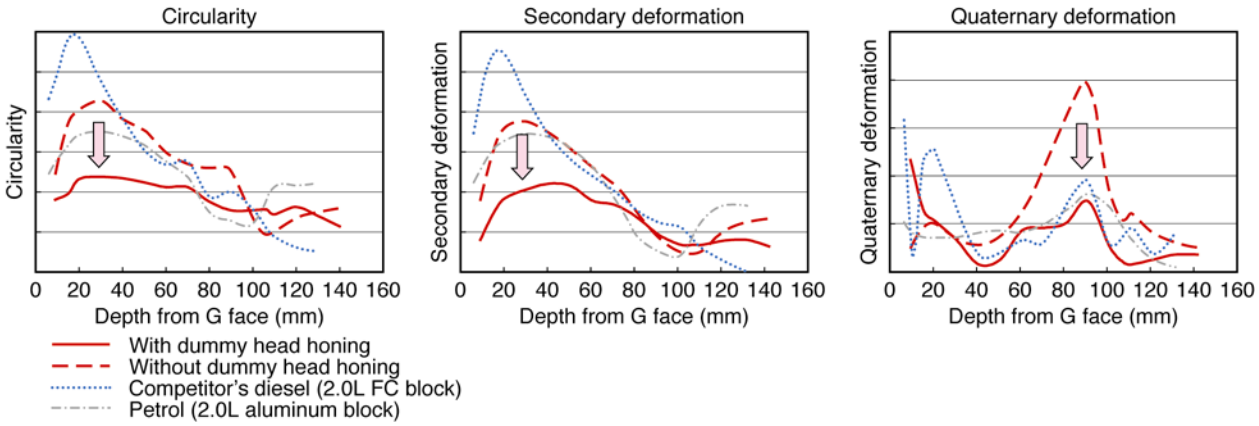



Fig. 11 Effects of dummy head honing

### 2.1.2. Increased engine heat at full load

Diesel engines require a higher degree of cooling at all levels of output than gasoline engines.

Figure 13 shows a comparison of the required cooling performance in gasoline and diesel engines.

There were concerns with cylinder blocks that increased temperature of the aluminum sections between the cylinder bores would reduce strength, causing the seal of the head gasket to deteriorate and the cylinder bore deck section to deform. To prevent this, a simulation of the water flow through the entire water jacket, including the cylinder head, was conducted, and measurements of temperature were taken. The results were utilized to tune the flow to ensure that the cooling water did not back up at any point.

This enabled the temperature to be controlled to under 190 °C, the temperature which aluminum strength begins to drop, without any loss of cooling performance in the cylinder head.

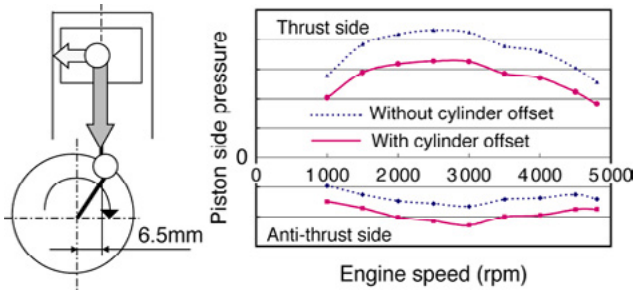



Fig. 12 Reduction of piston impact load due to offset cylinders

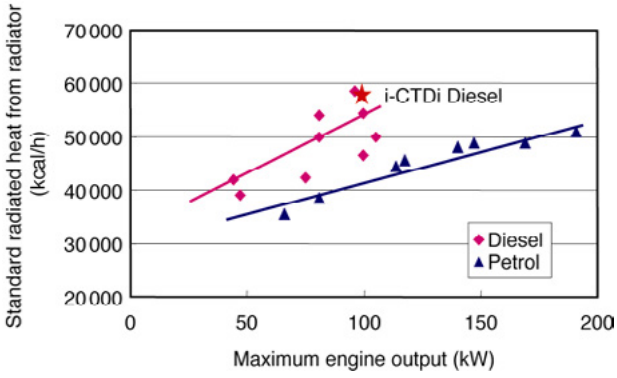



Fig. 13 Comparison of required cooling performance by output

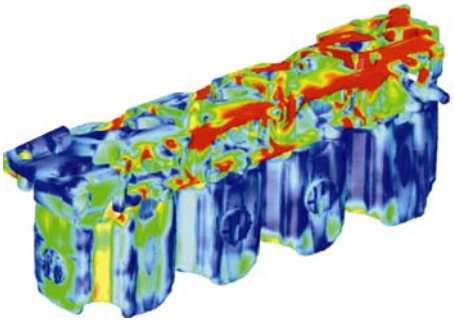


Fig. 14 Example of simulation of flow of water through water jacket

Figure 14 shows the simulation of the water flow through the water jacket, and Fig. 15 shows the temperature characteristics between the deck bores.

### 2.1.3. Effect of increased soot concentration in lubricating oil and sulfur content in fuel

The liner of the new cylinder block is produced by centrifugal casting. The optimal addition of P, Cu and Mo, not used in materials for liners employed in standard gasoline engines, enabled the new cylinder liner to display the same level of workability as the conventional liners, while resisting corrosion caused by the sulfur components in the fuel, and wear caused by high loads and soot in the engine oil. A large liner with a spiny outer (columnar projection) surface and a standard thickness of 3 mm formed by centrifugal casting has been employed. In addition to distributing residual stress in the aluminum section of the outer circumference, mechanical coupling to the circumference provides increased reliability against potential breakdown at the cylinder bore and surrounding sections. Figure 16 shows the spiny appearance of the outer circumference of the liner.

## 3. Overview and Characteristics of New Production Process

### 3.1. Aims of Development of New Production Process

The production process was examined to enable the following four concepts for the upper block to be realized.

(1) Closed deck configuration to provide high rigidity
(2) Thickness of 3 mm between shafts and a standard thickness of 4 mm, to achieve weight savings and compactness
(3) Use of high-quality materials and heat treatment to achieve high strength
(4) Achievement of high level of manufacturability

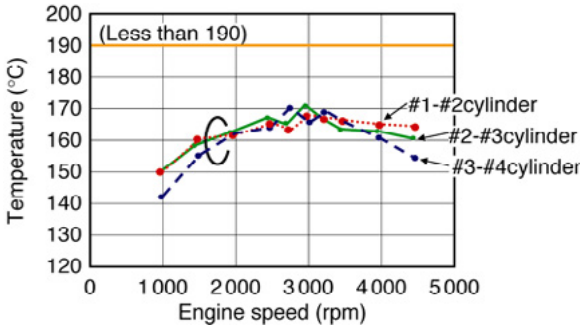



Fig. 15 Aluminum temperature characteristics between deck bores

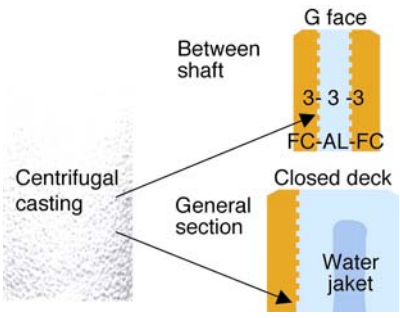



Fig. 16 Spiny exterior of liner

Table 2 Production targets and production methods

| | Flexibility of shape | | | Function | | Cost | |
|---|---|---|---|---|---|---|---|
| | Closed deck | Reduction of thickness | Reduction of machining | Heat treatments T6 and T7 | Strength | Cycle time | Investment |
| LPDC | Good | Poor | No good | Possible | Excellent | No good | Large |
| HPDC | No good | Excellent | Good | Impossible | Poor | Excellent | Small |
| NDC | Good | Good | Good | Poor | Poor | Good | Large |
| ASCT | Good | Good | Good | Possible | Excellent | Good | Small |

As Table 2 indicates, LPDC is a production method well suited to the demands of forming the closed deck structure and the application of heat treatment. However, a new method of production was required which would enable thin materials and a high level of productivity (usually achieved with HPDC) to be balanced.

From the mid-1980s through the 1990s, Honda employed the low-speed, medium-pressure casting (New die cast as NDC) method to produce the closed deck configuration, but this method necessitated higher material quality to cope with heat treatment and the use of different casting equipment to HPDC. For these reasons, the rationalization of production facilities required a new method capable of producing higher quality components and ensuring greater productivity to be found.

## 3.2. Overview and Characteristics of ASCT

In a cylinder block, there are thick sections such as the journals and thin sections such as the cylinder bore and surrounding sections and regular sections. To control internal imperfections such as shrinkage (imperfections caused by solidification and shrinkage), gas inclusions during production process, etc., which are difficult to avoid using the standard casting method, a die cast technique has been employed in which aluminum is injection formed in a semi-solid state, which enables stable and highly efficient production of strong, high-quality components to which heat treatment can be applied. With the semi-solid casting method as a base, Honda has independently developed ASCT as a packaging system which has further evolved and integrated the conventionally employed element technologies, in order to enable the various requirements for the finished cylinder block described previously to be met.

ASCT is made up of the following element technologies:

(1) Casting — Aluminum in a semi-solid state is injected into a metal mold in a laminar flow at low speed and high pressure

(2) Slurry production — Production process for semi-solid slurry using mechanical stirring

(3) Sand cores — Uses pressure-proof cores formed by coating the surfaces of shell cores

## 3.3. Element Technologies

### 3.3.1. Casting

Techniques of injection forming aluminum in a semi-solid state can be classified into thixocast, in which aluminum is used in a semi-molten form, and rheocast, in which aluminum is used in a semi-solid form[5), 6)]. Both these methods use agitation and pulverization to convert the dendrite, which is produced when the normal aluminum alloy is gradually cooled, to granular crystal, and apply shearing force to reduce viscosity and increase the flowability of the metal (thixotropy) (Fig. 17).

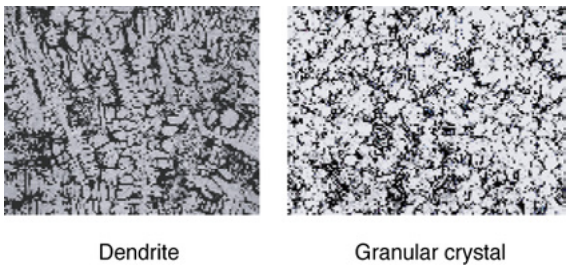



Fig. 17 Comparison of microstructure

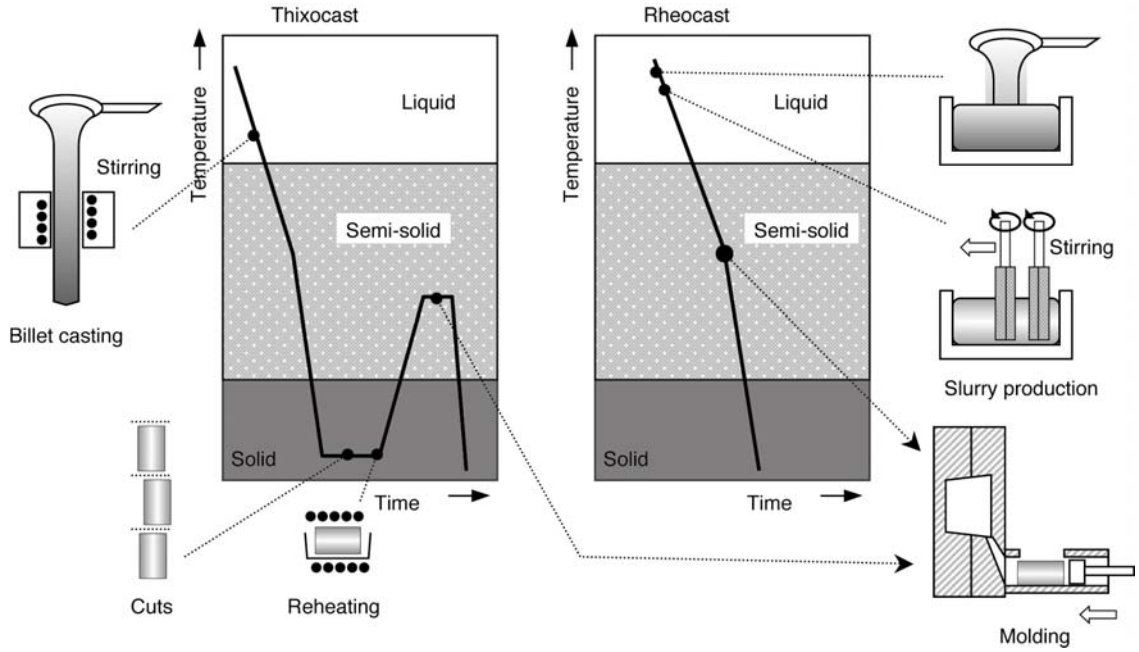



Fig. 18 Production efficiency of thixocast and rheocast methods

Rheocast was utilized in the production of the new cylinder block, to enable the production process to be simplified and increase energy efficiency[7]. Figure 18 shows a comparison of the energy efficiency of thixocast and rheocast.

### 3.3.2. Semi-solid slurry production

The most important element in the rheocast process is the production of the semi-solid aluminum slurry. In this process the molten metal is maintained at a set temperature in a furnace, after which a specified amount is poured into a crucible (an insulated container used to transport the molten metal to the die) preheated using a heater. Chillers and stirrers are then immersed in the molten metal. These rotate while sliding through the metal in a set trajectory, enabling the achievement of uniform semi-solid state. Figure 19 shows an overview of the process.

The issue the project faced here was how to create a semi-solid slurry with a higher degree of applicability to forming. In the conventional production process, it is usual to control the temperature of the molten metal directly before forming, but the presence in the aluminum alloy of alloy ingredients such as Mg, Cu, and Si with different contents means that at the same temperature some components are more solid than others. Figure 20 shows the differences in solidity for different components at the same temperature. The different solidities of these components make it difficult to produce a semi-solid slurry with a stable formability by controlling only the temperature of the molten metal.

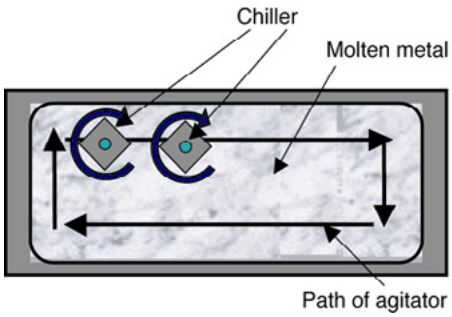



Fig. 19 Diagram of mechanical stirring

To produce a stable semi-solid slurry that was not affected by variations in alloy ingredients, crucible temperature, temperature of the molten metal in the mold, etc., this project focused on controlling the kinetic viscosity of the slurry.

Control of the kinetic viscosity of the slurry is applied during the stirring process in the crucible discussed above, and employs the kinetic viscosity measurement device shown in Fig. 21.

Conducting the kinetic viscosity measurements during the process of stirring and cooling the semi-solid slurry means that the process can be stopped when the slurry reaches the necessary kinetic viscosity, enabling a semi-solid slurry of uniform viscosity to be formed. Compared to the conventionally employed control of temperature, this measurement method enables more accurate control of the consistency of the semi-solid slurry at a predetermined temperature.

The application of these methods produces a stable slurry that has excellent formability, and has enabled significant improvements in the interior and external quality of the molded component.

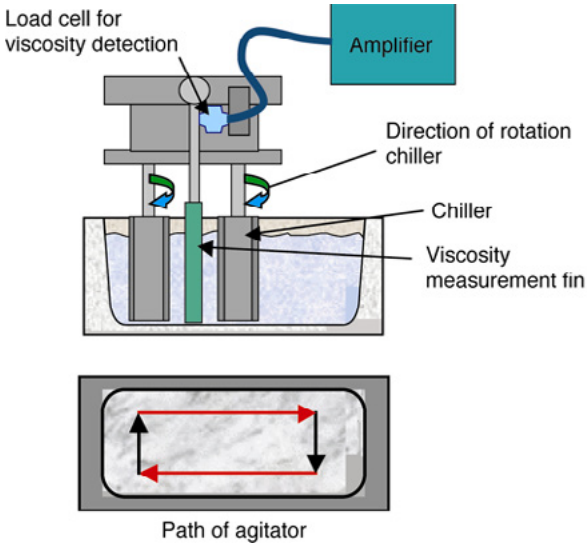



Fig. 21 Diagram of mechanical stirring and viscosity measurement unit

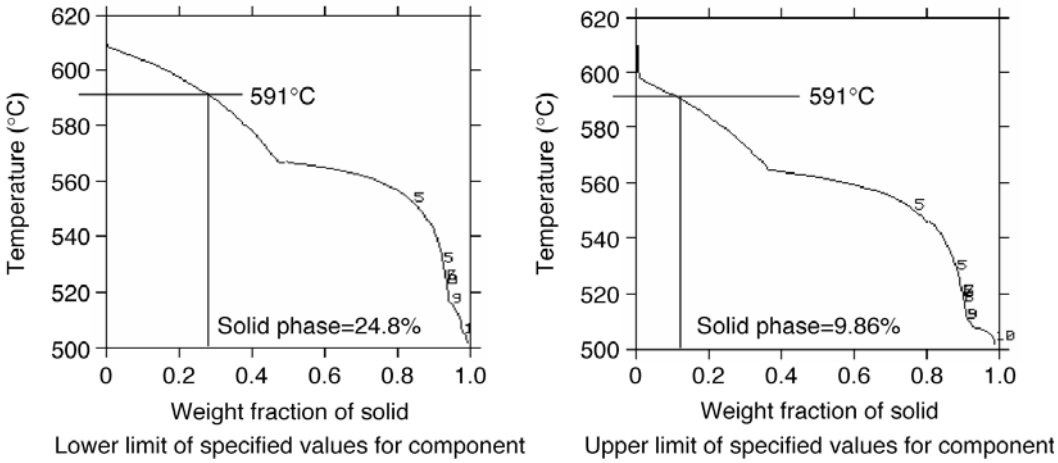



Fig. 20 Thermo calculation graphs: Change in solid phase due to change in components at identical temperature

### 3.3.3. Sand cores

Sand cores are used to mold the water jacket section, which is undercut during forming (Fig. 22). Because these sand cores are used with semi-solid aluminum, large-scale improvements over the sand cores used in conventional molten molding were required, in particular improvements in strength. The requirements for the sand cores employed in ASCT casting are as follows:

(1) Strength to resist molding pressure (≈ 100 MPa).
(2) Sufficient dimensional accuracy to satisfy design values.
(3) Clean removal from mold for post-processing after molding.

To achieve pressure resistance, the filling density of the sand was increased and a coating was applied, enabling the production of sand cores with a deflecting strength of 11 - 12 MPa, resistant to failure or penetration of the molten metal when subjected to high casting pressures. Artificial ceramic casting sand (ceramic beads) was selected as the framework due to the uniform diameter of the grains and the ability of the material to expand at low temperatures. A high-strength resin capable of expanding at low temperatures was employed as the binder. A two-layer coating was employed to balance pressure resistance in the core with separability (sand removability). The first coating functions as an ultra-fine skin, increasing pressure resistance, while the second coating promotes peeling of the aluminum from the mold. This has resulted in the production of a high-strength sand core, with a 15% higher filling density and a 20% higher deflecting strength than a normal silica core. Figure 23 shows a comparison of cross-sections of a conventional core and the newly developed core.

### 3.3.4. Quality

To meet the high performance requirements demanded of the new cylinder block, the block combines thin sections of 3 mm between the cylinder bores, and thick sections of 20 mm in the journals, etc. Preheating of the cylinder liner and the bore pin was employed to ensure the flow of the semi-solid slurry to mold the thin sections. Laminar flow was used to prevent inclusions during filling. The semi-solid slurry was used to reduce the shrinkage in the molding of the thick sections. Together, these methods enable the achievement of a stable quality in the cast block with no imperfections (blowholes, etc.).



Fig. 22 External view of pressure-resistant sand cores

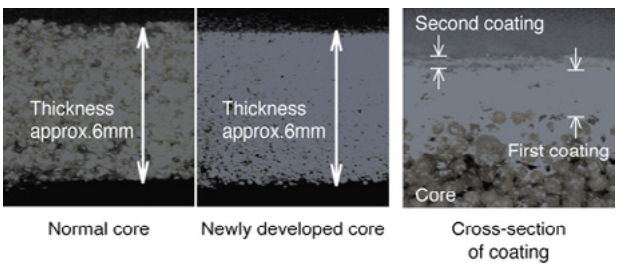



Fig. 23 Comparison of cross-sections of sand cores

### 3.3.5. Heat treatment

To achieve the required strength, T7 heat treat (a treatment applied when the metal is in the molten state to prevent overageing) was chosen for application to the new cylinder block. Balance between strength and dimensional stability was considered. In conventional die casting, inclusions when the mold is being filled trap gas in the component being formed, causing blisters (surface swelling caused by gas) to form when the gas pressure increases with heat. This makes T6 and T7 solution heat treatments impossible. In the new production process, the semi-solid slurry fills the mold in a laminar flow, significantly reducing the amount of gas and enabling heat solution treatments without creating blisters. Figure 24 shows a comparison of proof stress and tensile strength.

### 3.3.6. Productivity

Figure 25 shows a comparison of productivity of various processes, as judged from cycle time. The newly developed ASCT improves cycle time by approximately 20% against NDC, and has an almost equivalent cycle time to HPDC. Productivity with the new process is approximately 4 times that of low-pressure casting, another process which enables sand cores to be used. In addition, because the new process uses a relatively low temperature semi-solid slurry, it reduces heat fatigue in the mold and significantly increases the life of the mold over the HPDC method.

## 4. Results and Performance

The discussion above has provided details of the development of a high-performance diesel engine cylinder block molded from aluminum. The following discussion will focus on the noise reduction and vibration characteristics of the new cylinder block and the weight savings it enabled.

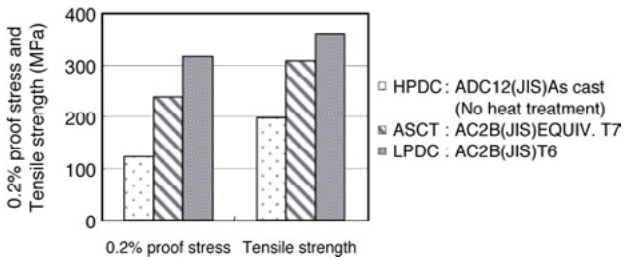



Fig. 24 Comparison of materials strength

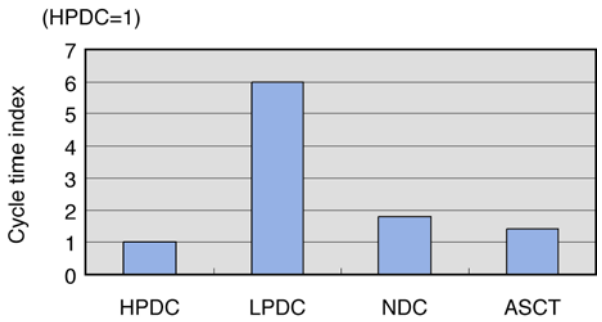



Fig. 25 Cycle time by production process

### 4.1. Noise Reduction and Vibration Characteristics

The use of the closed deck and new lower block structures, in combination with increased rigidity achieved by optimization of overall thickness and rib positioning has resulted in a reduction of engine noise. Figure 26 shows a comparison of structural attenuation using an index expressing the level of noise from the engine.

The aluminum cylinder block equaled the performance of cast cylinder blocks displaying ideal attenuation characteristics produced by competitors for vehicles of the same displacement.

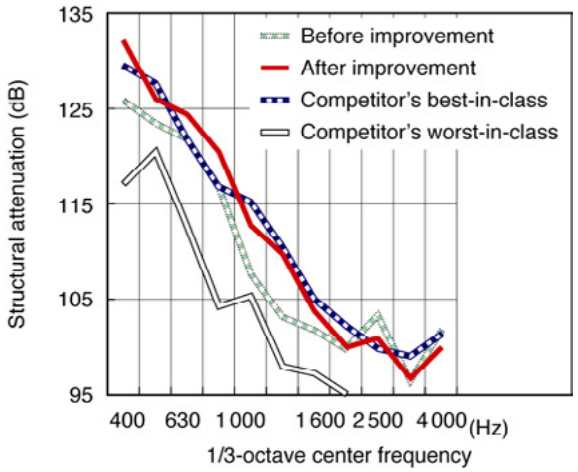



Fig. 26 Structural attenuation

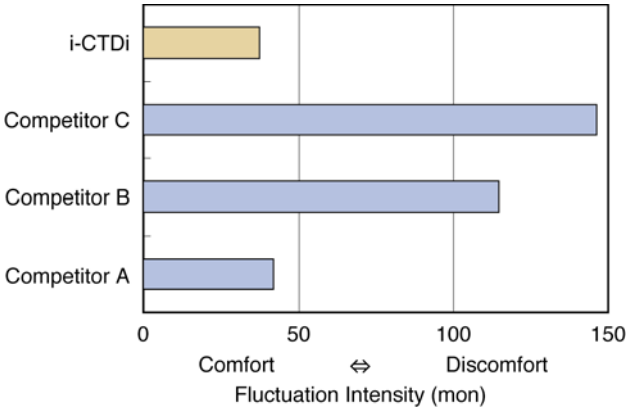



Fig. 27 Quietness at idling (1 m, diagonal and upwards)

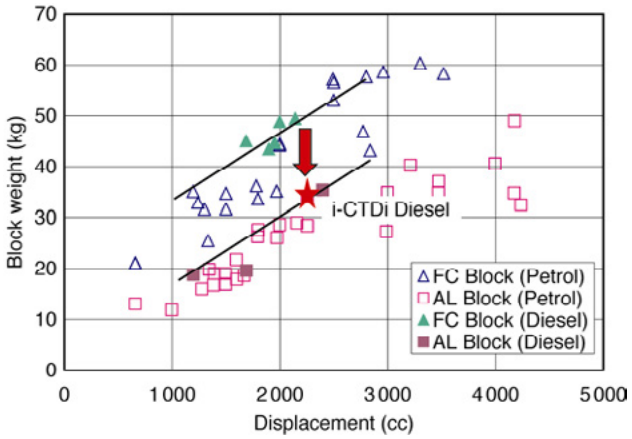



Fig. 28 Comparison of weight of cylinder blocks

In addition, the employment of offset cylinders and dummy head honing has made a significant contribution to reduce piston slapping noise. This, together with the reduction in excitation force due to optimization of combustion, enabled the achievement of class leading engine quietness. Figure 27 shows the extent of change in engine noise using an index representing the level of discomfort caused by slapping noise[8), (9)].

### 4.2. Weight Savings

Figure 28 shows the relationship between displacement and the weight of the cylinder block. As discussed above, the cylinder block employed in the i-CTDi engine possesses a high level of functions and performance for use in a high-performance diesel engine, while being approximately 30% or 15 kg lighter than the cast cylinder blocks used in diesel engines of the same displacement. This is close to 10% of the unit weight of the engine.

If this reduction in cylinder block weight had not been achieved, the necessity for structural reinforcement when it was installed in a vehicle would have resulted in an overall increase in the vehicle weight, which would have led to a decline in vehicle performance, such as running characteristics and fuel consumption. This consideration indicates the significance of this development of a lightweight diesel engine cylinder block from the perspective of the performance of the vehicle as a whole.

## 5. Conclusion

(1) A new production process has been developed which displays equivalent productivity to HPDC and enables the employment of a closed deck configuration and heat treatment through the development of a semi-solid die casting technique and coated pressure-proof shell cores.

(2) The closed deck configuration, a new lower block structure, and high-strength materials were employed to produce a lightweight aluminum cylinder block that can resist the high combustion pressures of the latest diesel engines, and has a low level of structural response, giving it noise reduction and vibration characteristics equivalent to the best of class cast cylinder blocks.

(3) The use of offset cylinders and dummy head honing have reduced piston slapping noise and sliding friction caused by combustion.

(4) The new cylinder block is approximately 30%, or 15 kg, lighter than the cast cylinder blocks used by competitors in vehicles of equivalent displacement.

This paper discussed the element technologies employed in the high-strength aluminum cylinder block used in the i-CTDi, the first diesel engine independently developed by Honda, and the advantages the cylinder block possess. The authors hope that the research described in this paper will contribute to future reductions in the weight of diesel engines, which will in turn contribute to the reduction of $CO_2$ emissions in automobiles.

## References

(1) Miyahara, F., Ohshima, H., Ohtsuka, M.: Development of Cosworth process, Mazda Technical Review, No. 20, p. 97-102 (2002)

(2) Hayashi, T., Ushio, H., Ebisawa, M.: The Properties of

Hybrid Fiber Reinforced Metal and It's Application for Engine Block, SAE-Paper 890557

(3) Hashimoto, H., Kibe, K., Nouno, Y., Sasaki, T.: Development of New 1.4DI Diesel Engine with Aluminum Die-cast Cylinder Block, TOYOTA Technical Review, Vol. 52, No. 1 (2002)

(4) Uebayashi, H., Kadono, H.: Production Engineering for Aluminum Cylinder Block made by High-Pressure Die Casting, JSAE journal, Vol. 57, No. 6 (2003)

(5) Saito, N., Nakamura, T., Ohtani, T., Kuroki, M., Masuda, E., Idegomori, T.: The development of joint parts for automobile body by thixocasting, JSAE20014005 (2000)

(6) Idegomori, T., Hirono, H., Ito, O., Kimijima, S.: Application of SSC method to automobile components, Journal of JSTP, Vol. 41, No. 479, p. 1201-1205 (2000-12)

(7) Adachi, M., Sato, S.: New Rheocasting process without stirring, Journal of JSTP, Vol. 41, No. 479, p. 1191-1197 (2000-12)

(8) Noumura, K., Okada, Y.: Sound Quality Evaluation Technique of Vehicle in Consideration of Auditory Characteristic, HONDA R&D Technical Review, Vol. 9, p. 131-139 (1997)

(9) Noumura, K., Yoshida, J.: Quantification of Luxury and Sporty Car Interior Sounds Perceived by the General Public in Different Markets, Honda R&D Technical Review, Vol. 14, No. 1, p. 237-246 (2002)

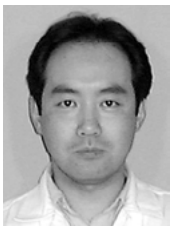
■ Authors ■

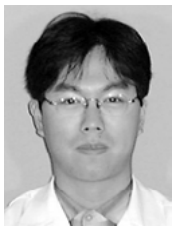

Masakazu YAMAZAKI


Atsushi TAKAI


Osamu MURAKAMI


Mitsuhiko KAWABATA


Osami ITO


Koichi KUROKI

# Increase of Knock Limit in Outboard Motor Through Employment of Dual Control Direct Cooling System

Yoshihiko FUKUDA* Hiroki TAWA* Atsuo MAKISE*


## ABSTRACT

Cooling performance of the outboard engines, which pump ambient water to cool the engine and discharge it, has been improved in a direct-cooled outboard motor without a radiator in order to increase knock limit.

The research project leading to this improvement tested a conventional single control cooling system and a new dual control cooling system in which the cylinder head and cylinder block were made independent and each were provided with a thermostat to enable temperature to be controlled.

Tests were conducted under full engine load. Measurements of the temperature of the cooling water inside the water jacket were taken to evaluate the cooling performance. Knock limit was evaluated through measurements of the combustion chamber pressure using a gasket type combustion pressure sensor positioned at the spark plugs.

These measurements confirmed that the dual control cooling system increased knock limit by 8 deg against the conventional single control cooling system.


## 1. Introduction

With the growing concern for environmental issues in recent years, the transition from the conventional 2-stroke engine to the 4-stroke engine is progressing rapidly in the outboard motor market. On the other hand, compactness and high output equivalent to the 2-stroke engine are demanded in engine size and power, and further improvements are also being demanded in fuel consumption and emissions.

Improving the knock limit is one method to address these issues. If the knock limit is improved, the ignition timing can be set closer to the MBT (Minimum advance for the Best Torque: the ignition timing at which output and fuel consumption rate become optimum), and increased output together with improvement in fuel consumption through high compression can be expected. One method of improving the knock limit is to reduce the temperature of the combustion chamber by enhancing the cooling performance of the cylinder head.

An indirect cooling system is employed in normal water-cooled engines for automobiles, in which the cooling water is circulated in the closed cooling water circuit to cool the engine, and is cooled using heat exchanger including radiator. This cooling water system is mainly a single control cooling system in which the cooling water flows from the water pump to the cylinder block, cylinder head, radiator, and thermostat. Studies have already been conducted on the dual control cooling system in which the temperature of the

* Asakahigashi R&D Center

cylinder head is reduced effectively by controlling the temperature individually using separate routes for the cylinder head and cylinder block systems to improve the knock limit as mentioned above. The effects of this system have already been reported[(1), (2), (3)].

As opposed to automobile engines, existing water-cooled engines for outboard motors employ a direct cooling system. In this system, water from the sea or river in which the boat navigates is sucked in and used for cooling the engine and then discharged. This cooling system is also generally a single control cooling system where the cooling water flows from the water pump to the exhaust manifold, cylinder head, cylinder block, thermostat, and the outlet. If the dual control cooling system mentioned above is employed, the cooling performance of the indirect cooling system can be effectively improved, as the difference in the water temperature in the cooling water intake and the cylinder head temperature is higher than in the indirect cooling system.

This paper describes the characteristics and the effects of improving the knock limit when the dual control cooling system is used in water-cooled engines for outboard motors.

## 2. Issues with the Conventional System and Goals

Preventing overheating of the engine during Wide Open Throttle (hereafter referred to as WOT) operation and inhibiting oil dilution due to excessive cooling during idling operation (hereafter referred to as trolling) should be considered in direct cooling systems to be used in engines for outboard motors. Measures for preventing overheating during WOT operation include setting a low thermostat temperature to reduce the overall temperature. However, the temperature of the cylinder block needs to be high for inhibiting oil dilution during trolling.

If oil dilution occurs, the lubricating ability deteriorates and the engine may seize due to deterioration in the properties of the lubricating oil; therefore, inhibiting oil dilution is a priority. To inhibit oil dilution, the thermostat temperature is set such that the cylinder block temperature is maintained at a high level but outside the range of overheating. The cooling water flows sequentially to the exhaust manifold, the cylinder head, and then to the cylinder block. Means are also provided for raising the cooling water temperature before cooling the cylinder block. On the other hand, reducing the cylinder head temperature is one method for improving the knock resistance. However, the cylinder head temperature is high due to the above-mentioned reasons and this reduces the knock resistance, affects the advance in the ignition timing, and hinders the increase in output.

Accordingly, the dual control cooling system with means for separately controlling the temperature and satisfying cooling performance with conflicting requirements, namely

(1) Maintaining the status of cylinder block temperature and
(2) Reducing the cylinder head temperature. Figure 1 shows the cooling water circuit for the single control cooling system.

## 3. Construction and Characteristics of the Dual Control Cooling System

Two changes were made to the conventional single control cooling system to realize the dual control cooling system.

The first change is to completely isolate the cooling water circuits of the cylinder head and cylinder block using a cylinder head gasket, make them separate and control the water temperature in each circuit using a thermostat. With this change, thermostat-controlled temperature of the cylinder head and cylinder block could be set individually, enabling an optimum controlled temperature to be set for each.

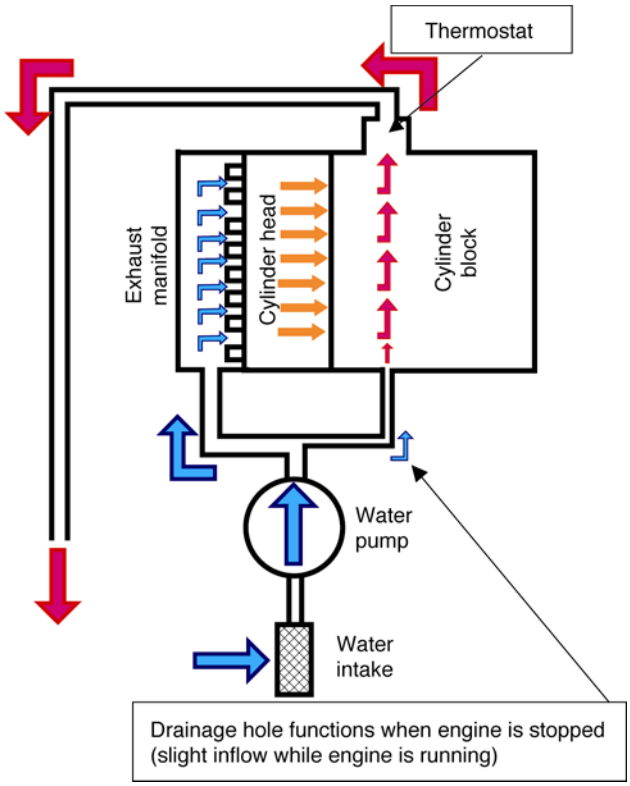



Fig. 1 Cooling water route for single control cooling system

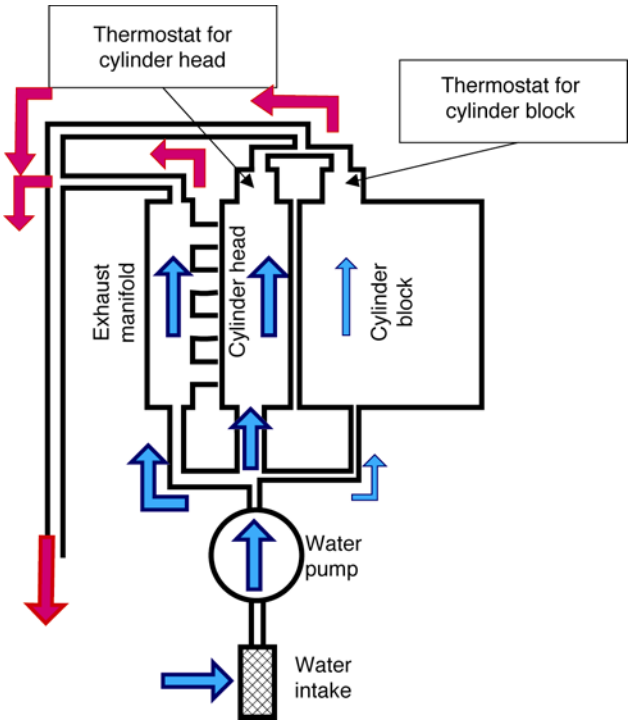



Fig. 2 Cooling water route for dual control cooling system

The second change is that a cooling water circuit was installed for the exhaust manifold completely separate of the cooling circuit for the cylinder head and cylinder block. This circuit introduced cooling water from the lowermost part of the cylinder head and cylinder block.

With this construction,

(1) The cylinder head cooling water is not routed through the exhaust manifold; therefore, the water temperature at the cylinder head intake is reduced.

(2) The cooling water flow is simplified by routing it from bottom to top, thus avoiding stagnation of cooling water.

The temperature of the cooling water in the water jacket of the exhaust manifold is not controlled by the thermostat. Figure 2 shows the circuit diagram of the dual control cooling system.

## 4. Effects of Dual Control Cooling System

### 4.1. Test Conditions

#### 4.1.1. Test engine specifications

Table 1 shows the main specifications of the test engine used in all the tests.

#### 4.1.2. Environmental conditions for tests

Table 2 shows the environmental conditions for the tests.

#### 4.1.3. Temperature measurement points

Figure 3 shows the temperature measurement points on the cylinder head.

### 4.2. Effects of Cooling Performance

In these tests, a 60 °C thermostat was mounted for the test engine with the single control cooling system. For the test engine with the dual control cooling system, 50 °C thermostat and 60 °C thermostat were mounted on the cylinder head and cylinder block, respectively. The water temperature in the water jacket in the cylinder head was measured in order to compare the cooling performance. Figure 4 shows the cooling water temperature in the cylinder head for each cylinder in the single control cooling system when the engine was operated with water temperature of 15 °C, ambient air temperature of 20 °C, and WOT of 6 000 rpm. Figure 5 shows the cooling water temperature in the cylinder head in the dual control cooling system under similar conditions.

Table 3 shows the results of the comparison of Figs. 4 and 5.

As shown in Table 3, the water temperature in the water jacket of the cylinder head could be reduced on average by 23 °C at eight locations by changing over from the single control cooling system to the dual control cooling system.

Figure 6 shows the relationship between the thermostat set temperature and the oil dilution rate.

The relationship between the oil dilution rate due to dilution after 50 hours of trolling and the thermostat set temperature is shown by the blue line for the test engine with the single control cooling system. In the dual control cooling system, the thermostat fixed on the cylinder head side is set at 50 °C and the thermostat fixed on the cylinder block side is set at 60 °C, similar to the single control cooling system. The oil dilution rate after 50 hours of trolling is shown by the star mark.

From these results, it was confirmed that even if the

Table 1 Engine specifications

| | |
|---|---|
| Engine type | 4-stroke vertical L-4 cylinder |
| Displacement ($cm^3$) | 2354 |
| Bore (mm) × stroke (mm) | 87 × 99 |
| Combustion chamber form | Half-globular |
| Compression ratio | 9.6 : 1 |
| Valve train | DOHC VTEC 16 valve |
| Number of valves | 4/cylinder |
| Fuel supply system | Programmed fuel injection |
| Ignition system | Programmed ignition (with Plug hole coil) |

Table 2 Environmental condition for tests

| | WOT running | Trolling running |
|---|---|---|
| Air temperature | 20°C | 10°C |
| Cooling water temp at water intake | 15°C | 5°C |

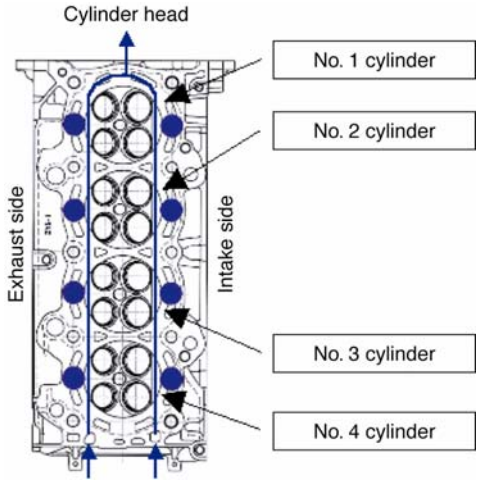



Fig. 3 Temperature measurement points

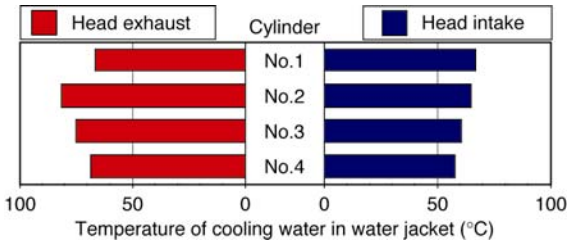



Fig. 4 Single control cooling system

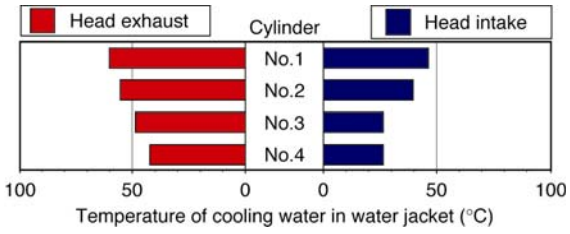



Fig. 5 Dual control cooling system

Table 3 Comparison of temperature in head

| | Single control | Dual control | Mean effect |
|---|---|---|---|
| Intake side (4 points avg) | 63 °C | 37 °C | -26 °C |
| Exhaust side (4 points avg) | 74 °C | 54 °C | -20 °C |
| All 8 points avg | 68 °C | 45 °C | -23 °C |

thermostat set temperature for the cylinder head is lowered by 10 °C from 60 °C to 50 °C, the oil dilution rate is almost unchanged, and this setting does not have a negative effect on dilution.

## 4.3. Effects of Output Performance

### 4.3.1. Improvement in knock limit by using the dual control cooling system

The improvement in knock limit was evaluated by using the dual control cooling system.

Figure 7 shows the comparison of the knock limits up to an engine speed of 4 500 to 6 000 rpm with WOT operation.

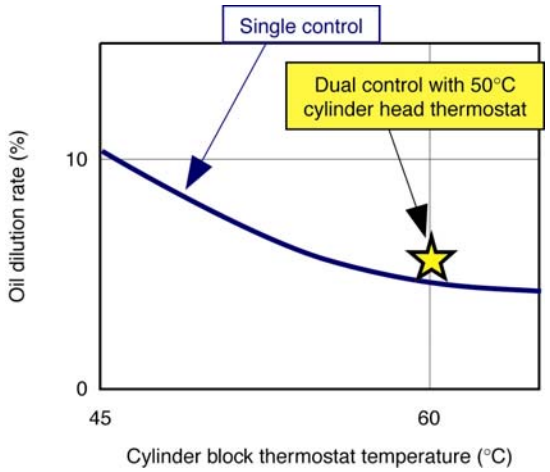



Fig. 6 Thermostat set temperature and oil dilution rate

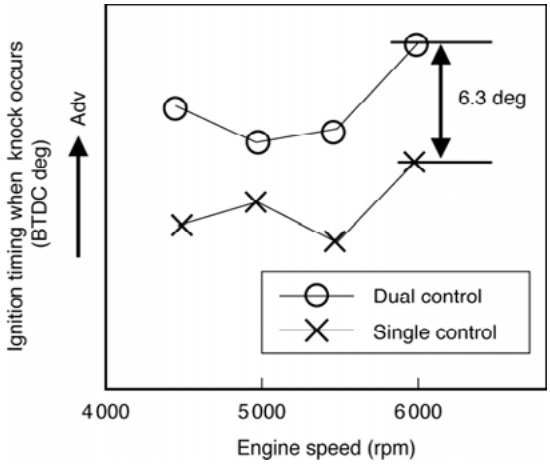



Fig. 7 Comparison of ignition timing when knock occurs single and dual control cooling systems

This test was performed on a completed engine with a gear case assembly. The conditions were identical for important parameters in the knock limit such as the compression ratio, intake air temperature, volumetric efficiency, and air fuel ratio.

The thermostat temperature was set at 60 °C in the single control system test engine. The thermostat temperatures of the cylinder head and cylinder block were also set at 60 °C respectively, in the dual control cooling system test engine.

By changing the single control cooling system to the dual control cooling system, the knock limit is improved by 6.3 deg at an engine speed of 6 000 rpm.

This is the effect of improvement of the cooling performance by changing to the dual control cooling system and eliminating stagnation of cooling water in the cylinder head.

### 4.3.2. Improvement in knock limit due to the low temperature of the head cooling water

Various studies have been conducted on the cylinder head and cylinder block in the dual control cooling system. It is generally known that the knock limit and the volumetric ratio improve due to the low temperature of the cooling water in

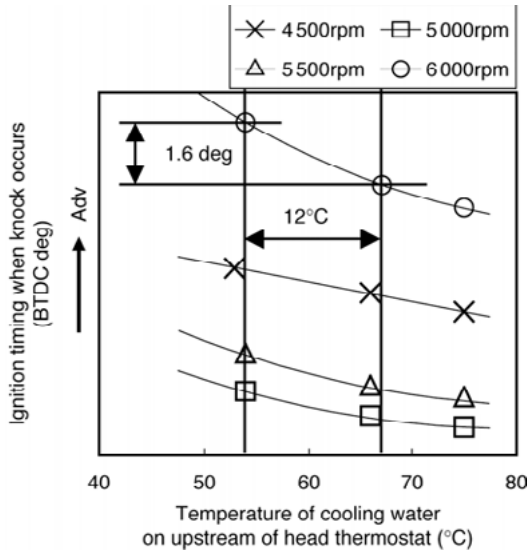



Fig. 8 Effect of cooling water temperature on ignition timing when knock occurs with WOT

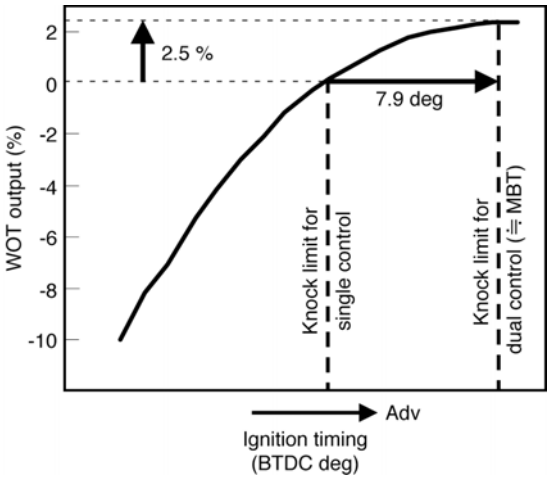



Fig. 9 Correlation between WOT output and ignition timing (6 000rpm)

the cylinder head. Figure 8 shows the temperature of the cooling water upstream of the thermostat on the cylinder head side and the ignition timing when knock occurs. The thermostat on the cylinder block side was set at a constant temperature of 60 °C and only the temperature of the thermostat on the cylinder head side was varied in steps of 10°C from 50 to 70 °C at 4 500 to 6 000 rpm with WOT. As shown in Fig. 8, if the thermostat set temperature is reduced by 10 °C, the temperature cooling water upstream of the thermostat on the cylinder head side is reduced by 12 °C. As a result, the knock limit improves by 1.6 deg during WOT operation at the engine speed of 6 000 rpm.

#### 4.3.3. Increase in maximum output with the improvement in knock limit

As mentioned above, if the 6.3 deg for the improvement in knock limit due to the dual control cooling system is combined with the 1.6 deg for the improvement in knock limit due to the lowering of water temperature by 10 °C, from 60 °C to 50 °C, in the thermostat set temperature on the cylinder head side, the ignition timing could be advanced by a total value of 7.9 deg.

Thus, an increase in output of about 2.5% could be achieved.

Figure 9 shows the correlation between the ignition timing and the output.

## 5. Conclusion

By changing the cooling system from the single control cooling system to the dual control cooling system, the knock limit improved, resulting in an increase in output of about 2.5%.

Further, it was confirmed that the dual control cooling system could be introduced in outboard motors with minor modifications, although the construction may become complex if the system is used for indirect cooling of the engine.

## References

(1) Kobayashi, H., Yoshimura, K., Hirayama, T.: A study on dual circuit cooling for higher compression ratio, IMechE/SAE, International Conference on Fuel Efficient Power Trains and Vehicles London, C427/84, p. 151-158 (1984)

(2) Yamada, T., Furuno, S., Kanda, M., Iwashita, Y., Yokoi, Y., Katagiri, J.: Improvement of Coolant Flow for Reducing Knock, 1990 JSAE Annual Congress Proceedings Fall, 902, Vol. 1, p. 189-192 (1990) (in Japanese)

(3) Ishida, N.: System Sekkei to Engine Seinou, Kouseinou Engine to ha Nanika, Tokyo, Grand Prix, p. 210-216 (1991) (in Japanese)

■ Authors ■


Yoshihiko FUKUDA


Hiroki TAWA


Atsuo MAKISE

# Development of 4WD System for Minivan

Kentaro ARAI* Takaki YAMAOKA*

## ABSTRACT

A torque on demand 4WD system has been developed with a front engine front drive vehicle as a base to balance traction performance and handling characteristics with fuel efficiency in a minivan. The response of torque to front-rear wheel rotation speed difference was studied to ensure traction performance and handling characteristics. The use of an initial torque between the front and rear wheels was considered as a method of improving the response of torque transmitted to the rear wheels when the front wheels slip. Using the Honda dual pump system as a reference, the results of calculations of the required traction force on snow and actual measurement values for tire traction characteristics were employed to find the optimal torque characteristic. As a result, 25% of maximum necessary torque was established as the ideal initial torque. A comparison of the optimal torque characteristic with the torque characteristic of the dual pump system in a simulation of a vehicle starting on snow confirmed the effectiveness of the initial torque. It was possible to achieve the optimal torque characteristic with a simple mechanical structure. A one-way cam and a preset pilot clutch were added to the rear final drive unit of the dual pump system. Good fuel efficiency was ensured through setting an appropriate gear ratio for the rear final drive unit. As a result, the newly developed minivan 4WD system meets vehicle performance requirements while weighing only 54 kg, making it the lightest in its class.

## 1. Introduction

In recent years, through ease of use for both every day and leisure purposes, the minivan, which can hold a lot of people, has become quite popular in Japan. Passenger cars with front engine front drive, with their large interior and comfortable ride, are used primarily as the base structure for minivans. A 4WD system developed for a minivan needs to be lightweight, compact, and not a detriment on fuel efficiency as well as being able to provide traction force according to changes in the number of people riding in the vehicle. This report discusses a minivan 4WD system developed for satisfying these types of needs.

## 2. Development Goals

The number of people in the vehicle changes more significantly for minivans than for passenger cars. The minivan has a higher center of gravity. The change in vertical load on the front wheels, depending on driving conditions, can also be larger[(1)]. Because of this, if the road surface is slippery the front wheels tend to slip, making it more difficult to help ensure traction when starting and handling while turning. In order to help ensure the vehicle's traction force, improving the response of transferring torque to the rear wheels has been considered. An electronically controlled system could provide such response; however, it would require sensors, an ECU, etc., making the system more

* Tochigi R&D Center

complex, which could be a detriment. A full time 4WD system can address this issue, as torque is being transferred to the rear wheels continuously. This type of system requires a central differential and much more durability, as torque is continuously being transferred to both front and rear wheels. This leads to the difficulty of meeting size and weight requirements and improving the vehicle's fuel efficiency. Therefore, the current development has focused on a lightweight, compact, simple 4WD system intended for a minivan. This has been done by developing the idea of a passive torque on demand 4WD system (hereafter, passive 4WD system) that transfers torque to the rear wheels in proportion to the front/rear wheel rotation speed difference. Building on this idea, through simulation, the torque characteristics which best meet the following two requirements have been pursued.

(1) Ability to ensure traction performance and handling characteristics when driving on snow that is the same as an electronically controlled 4WD system.
(2) Maintain the same fuel efficiency as a 4WD system for passenger cars.

## 3. Investigation of the Optimal 4WD Torque Characteristics

The Honda Dual Pump System[2] (DPS) will be explained and will be used for the basis of this passive 4WD system. For a passive 4WD system, a consideration is to have an initial torque defined between the front and rear wheels as a method for improving the response of torque transfer to the rear wheels. In order to determine the preset torque, a 2 400 cc class minivan was used as an example for slope starting on snow. As can be seen in Fig. 1, investigation of the required traction force of the model was performed.

In Fig. 2, the calculation of the required traction force for driving on snow and the measurements of the front tire traction force characteristics are shown, and the area where need of required traction force at the rear wheels can be seen. This is converted to the torque characteristics of the front/rear wheel rotation speed difference in the DPS system (hereafter torque characteristics), and they are both shown together in Fig. 3. It was found that the area in which the DPS torque characteristics was insufficient could be covered by the addition of an initial torque in the amount of 25% of the maximum DPS torque transfer. The initial torque was set such that it does not interfere with the torque limit function[3] set where unneeded torque was cut to lighten the system. It was also set so that it did not interfere with the area where tight corner braking torque is needed. In this way, the optimal torque characteristics were determined.

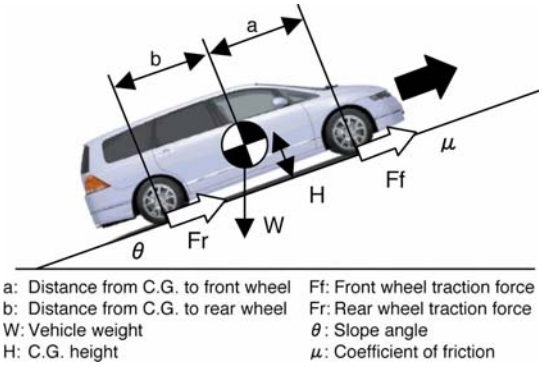



Fig. 1 Study model

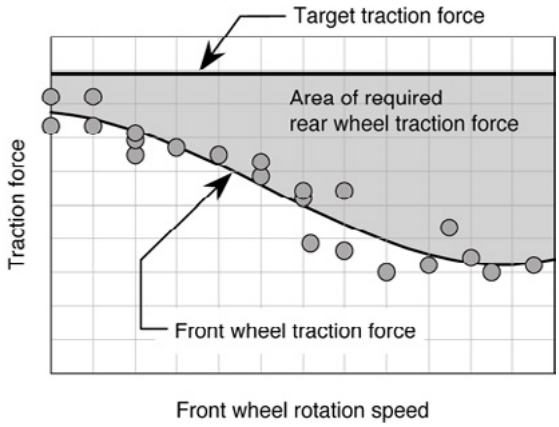



Fig. 2 Tire traction force characteristic on snow

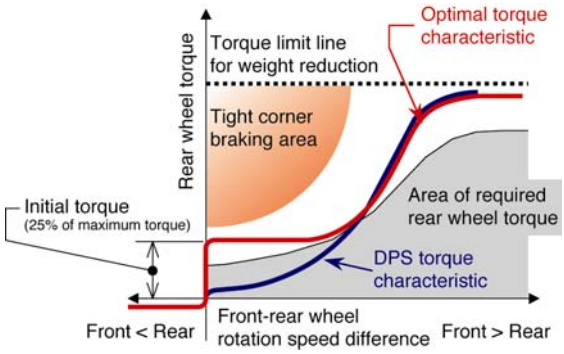



Fig. 3 Torque characteristic

Next, the effect that DPS torque and optimal torque characteristics have on starting performance on snow was confirmed through simulation. This confirmation was performed as defined by the 4WD vehicle model of Fig. 4 showing the coupling between the front and rear wheels and the 4WD system model of Fig. 5 that shows the coupling characteristics used to set the torque characteristics. As a result, through a characteristic of the DPS torque the torque on the rear wheels is delayed and there is a drop in the acceleration of the vehicle, as shown in Fig. 6. Figure 7 shows the characteristics of optimal torque, where the raise in torque is fast, leading to a smooth acceleration when starting.

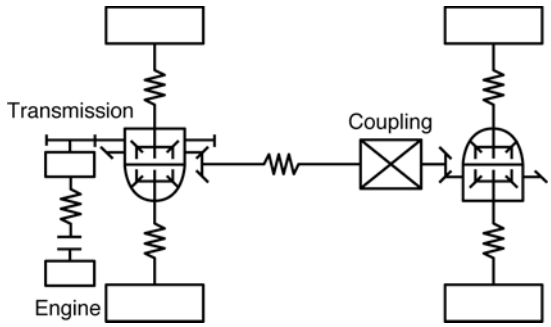



Fig. 4 Vehicle model

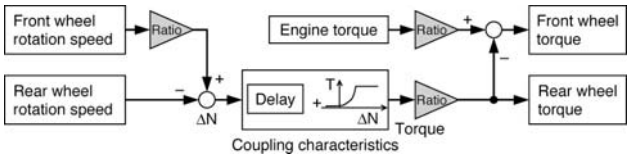



Fig. 5 4WD system model

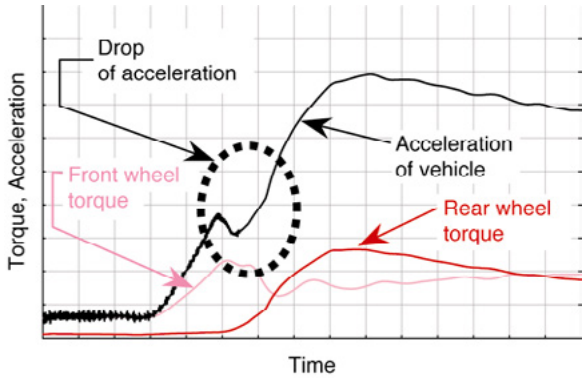



Fig. 6 Simulation data for DPS torque characteristic when starting on snow

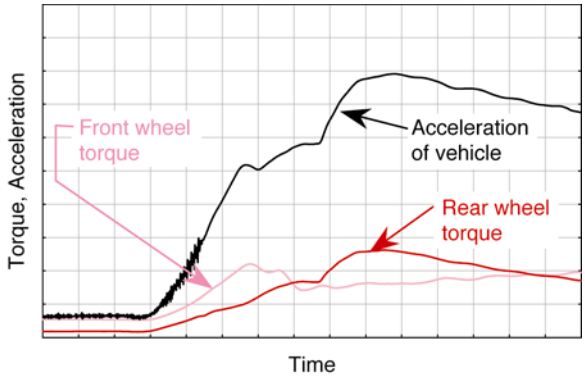



Fig. 7 Simulation data for optimal torque characteristic when starting on snow

## 4. 4WD System

The system structure diagram for this development is shown in Fig. 8.

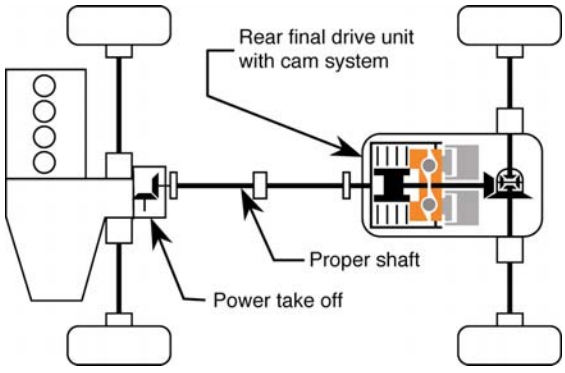



Fig. 8 4WD system

### 4.1. Rear Final Drive Unit

For the rear final drive unit of passive 4WD systems, other than DPS, there are the viscous coupling and the direct hydraulic pressure torque transfer coupling[4]. Both of these systems pose concerns: the viscous coupling system does not provide very much freedom for control, and the hydraulic system requires the system to be quite large in order to provide sufficient torque. In the current development a preset torque was added to a DPS system that uses a multi-plate clutch for transfer of torque. When transferring the torque, the multi-plate clutch is engaged by a hydraulic mechanism that responds to the front/rear wheel rotation speed difference. By using this type of simple mechanical structure, it was possible to achieve optimal torque characteristics. As can be seen in Fig. 9, the mechanism used to add initial torque consists of a pilot clutch that provides a constant torque and a one-way cam structure that engages a clutch only at times of acceleration. As can be seen in Fig. 10, this one-way cam structure responds to slight differences in the angle of the reference cams between the front and rear wheels, at the time of acceleration. The ball rolls against the cam surface, instantly engages the clutch and transfers the preset torque. And during braking, even if there is a difference in the reference cam angle, the ball hits a vertical wall and does not develop any engaging force, maintaining compatibility with the ABS system. The measurements of the torque characteristics of the newly developed rear final drive unit and a DSP system are compared in Fig. 11.

It was possible to make the size of the newly developed rear final drive unit the same as the rear final drive unit of the DPS system by placing the added components effectively, optimizing the BRG size, and reducing the overall length of the pump and hydraulic controls.

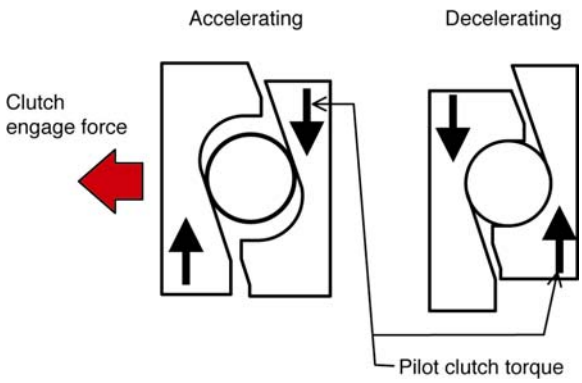



Fig. 9 Working of cam

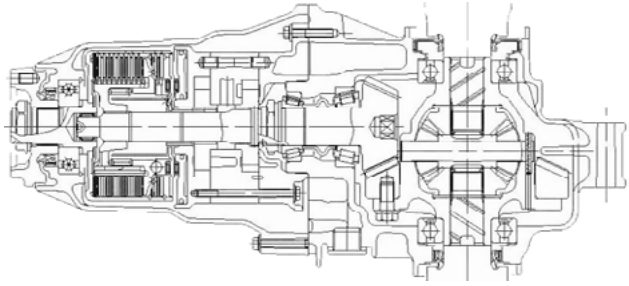


Fig. 10 Sectional view of rear final drive unit

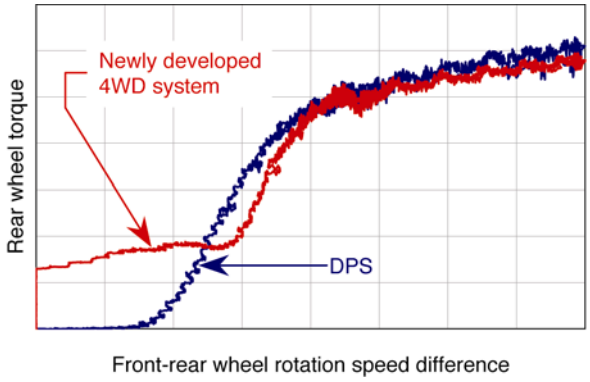



Fig. 11 Torque characteristic

### 4.2. Fuel Efficiency

In the DSP system, torque transmitted to the rear wheels is reduced during normal driving in order to lower fuel efficiency and weight. Therefore, the amount of friction torque is not changed when the ratio in the front/rear wheel rotation speed difference is about 1%. After increasing the response of the torque transferred to the rear wheels, as can be seen in "Modified 1" of Fig. 12, even when there is a small difference in the ratio of the front/rear wheel rotation speed difference, an increase in friction torque delivered to the rear wheels occurs, leading to an increase in friction torque which leads to the issue of a reduction in fuel efficiency. In order to resolve this issue, the ratio between the gear ratio from the front wheels to the propeller shaft and the rear final drive unit gear ratio was reviewed. The gear ratio that generates the front wheels cam structure input rotational speed was set to be roughly 0.5% lower than that of the rear wheels during normal driving. Therefore, the clutch does not cause engaging force, during normal driving, and has the characteristics shown in "Modified 2" of Fig. 12. Through this change, it was possible to reduce the absolute value of the friction torque, for the rear wheels, to that of the DPS system. This gear ratio setting does not have an effect on the systems response as it has been set on the operation side of the cam mechanism when driving in snowy conditions where the slip ratio of the front wheels is such that 4WD is needed.

### 4.3. System Weight

The weights of the 4WD system developed at this time for application to the 2004 model Odyssey is compared to other models in Fig. 13. Preserving a feature of the DPS system this 4WD system weighs only 54 kg, achieving the lightest in its class.

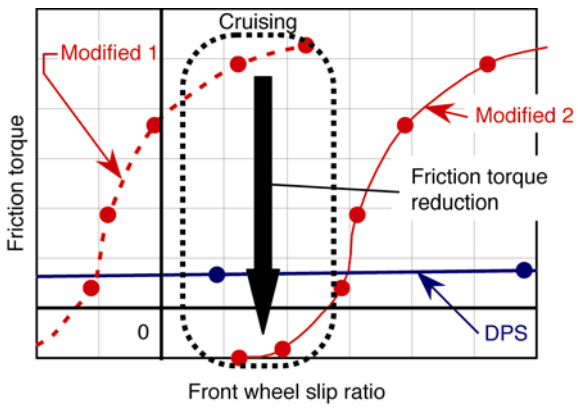



Fig. 12 Friction torque when cruising

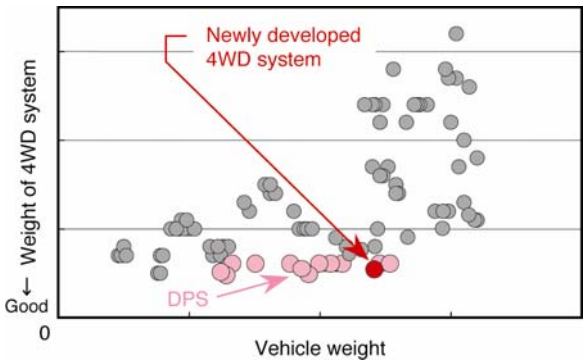



Fig. 13 Weight of 4WD system

## 5. Vehicle Performance

### 5.1. Traction Performance on Snow

As can be seen from the data showing acceleration from a start on snow in Fig. 14 and the data showing climbable grade in Fig. 15, the traction performance of this system is better than that of the DPS system and has achieved the same traction performance as an electronically controlled 4WD system.

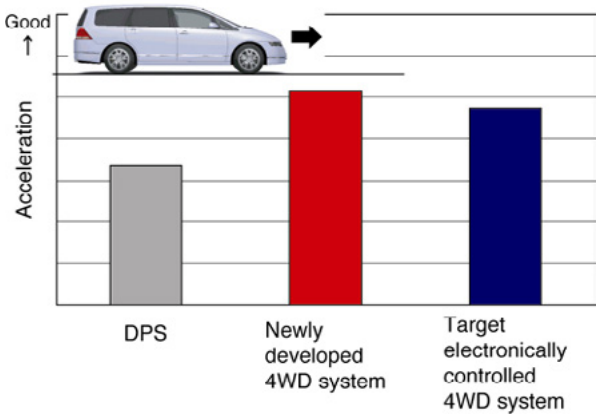



Fig. 14 Starting performance on snow

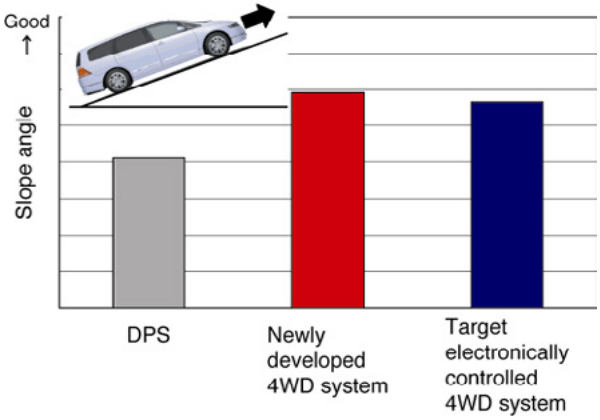



Fig. 15 Slope starting performance on snow

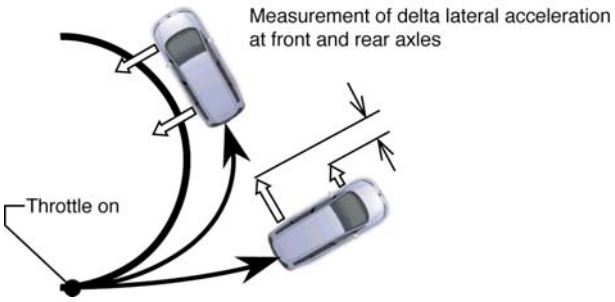



Fig. 16 Cornering test mode

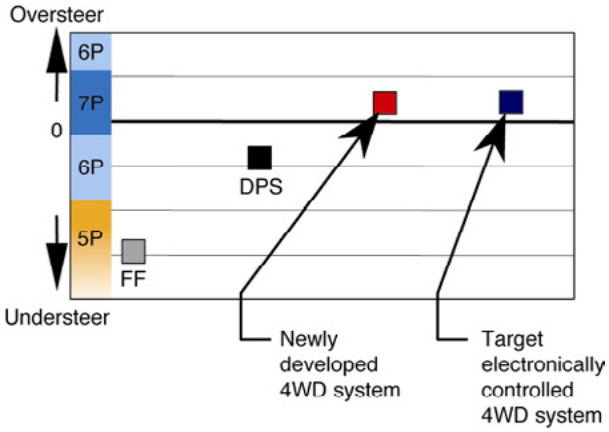



Fig. 17 Cornering performance on snow

### 5.2. Handling in Snow

In the test mode described in Fig. 16, the results of the handling evaluation are, as shown in Fig. 17, that this system has maintained the same handling performance as that of an electronically controlled 4WD system.

### 5.3. Running Resistance

A fuel efficiency parameter that is affected is running resistance while coasting. As described in Fig. 18, the running resistance of this system has been held to the same level as the DPS system.

The reported fuel efficiency in the catalog of this system shows that it has achieved the same fuel efficiency as that of a DPS system and is shown in Fig. 19.

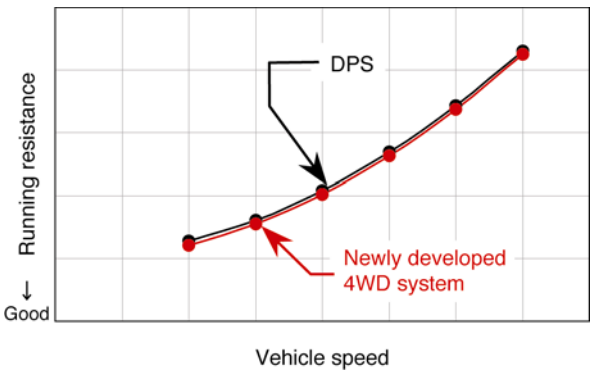



Fig. 18 Running resistance

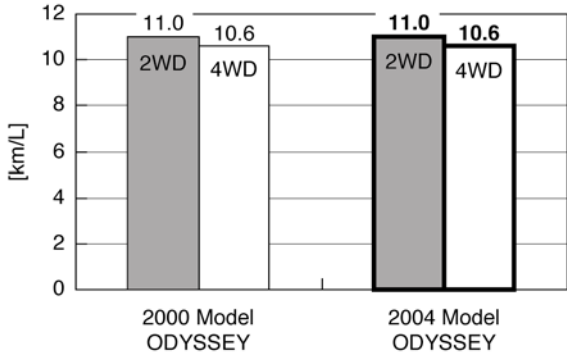



Fig. 19 Fuel efficiency

## 6. Conclusion

A 4WD system developed for a minivan needs to strive to maintain its traction performance and handling characteristics. Focusing on the torque response of a passive 4WD system, while calculating the required traction force on snow and the actual tire traction force, an optimal torque characteristic was sought. The following are the results of this development:

(1) Through combining the characteristics of DPS torque and an initial torque of 25% of the maximum required torque, this system achieved optimal torque characteristics. It was also shown to be effective, through simulation, when the vehicle starts on snow.

(2) In order to show that optimal torque characteristics had been achieved, the system was installed on a minivan where it achieved the same traction performance and handling characteristics on snow as a minivan with an electronically controlled 4WD system installed.

(3) The friction torque during normal driving was developed to be the same as the DPS system, and it has achieved the same level of fuel efficiency as the DPS system.

(4) This system has balanced traction performance and handling characteristics with fuel efficiency while being in a package that weighs 54 kg, the lightest in its class.

This system has been implemented on the 2004 model Odyssey. Honda started to sell this model in Japan in October of 2003 and positive feedback has already been received from customers.

## References

(1) Suzuki, K., et al.: Development of New Electronic Controlled 4WD System for Passenger Cars, 1998 JSAE Annual Congress Proceedings, No. 75-98, p. 1-4 (1998)

(2) Arai, K., et al.: Dual Pump System ni tsuite, Hydraulic and Pneumatics, 401, Vol. 33, No. 7, p. 70-76 (1994) (in Japanese)

(3) Hamada, T., et al.: Weight Savings of 4WD Vehicles by Optimizing Distribution of Torque between Front and Rear Wheels, Transactions of Society of Automotive Engineers of Japan, Vol. 24, No. 4, p. 99-103 (1993)

(4) Matsuno, K., et al.: Present Status and Future Trend of 4WD Technology, Journal of Society of Automotive Engineers of Japan, Vol. 57, No. 1, p. 70-74 (2003)

■ Authors ■


Kentaro ARAI


Takaki YAMAOKA

# Operating Force Simulation for Automatic Transmission Select Lever

Takaki YAMAOKA* Shunichi NOGAMI* Akira KOBAYASHI*


## ABSTRACT

A highly accurate method was developed for simulating the operating force for the select lever of an automobile automatic transmission by considering the internal link mechanism, the contact between parts, the load loss in the wire, and other factors. In order to improve accuracy, an experimental formula was introduced that takes the spring coil angle as a parameter to simulate the hysteresis characteristics of the twisted coil spring that is an essential factor in the mechanism. A method was also created to use mechanical system analysis tools in order to reduce the labor involved in simulation. The use of these means made it possible to simulate the operating force characteristic curve with an accuracy diverging by no more than 5% from measurement values, with half the labor previously required, and with consideration for the main factors influencing the characteristics. As a result, it has become possible to verify issues including excessive operating force and intermediate stopping at the specification study stage.


## 1. Introduction

In recent years, it has become necessary to reduce the operating force for the select lever used to select the position on an automatic transmission of an automobile, in order to improve the product merchantability. At the same time, it is necessary to set the operating force to a somewhat high value in order to prevent intermediate stopping, a phenomenon whereby the select lever stops in an intermediate position outside one of the correct positions such as P, R, N or D. It is also necessary to appropriately set not only the maximum value of the operating force, but also the way in which the operating force rises along with the lever stroke between one position and another, because these factors affect the overall shift feeling.

A very large number of study hours and test man-hours were required for development to ensure that both the merchantability and function of the select lever were satisfactory. For this reason, it was necessary to simulate the operating force of the select lever as a characteristic curve of lever stroke versus force, at an accuracy that enabled the variations in specifications to be judged. However, although there is a reported example of simulation technology related to the operating force of the shift lever for a manual gearbox[(1)], there are no reports related to simulation technology concerning the operating force of the select lever for an automatic transmission, which has an entirely different mechanism.

This paper describes the development of a method to simulate the operating force of the select lever for an automatic transmission.

## 2. Mechanism and Characteristics

### 2.1. Description of Mechanism

Figure 1 shows the position select lever of an automatic transmission. The position selector consists of the select lever on the driver's seat side, a control shaft on the transmission side, and a wire that connects these two parts together. As a result of the lever's operation, the control shaft rotates via the wire. The selection of the hydraulic control system related to each position is made by a manual valve linked to the control shaft. On this control shaft are positioning detents and a

* Tochigi R&D Center

mechanism that locks the driveline when the select lever is in the parking position (hereafter called the “P position”).

Figure 2 shows this mechanical locking device. The parking brake lever, which operates the parking pawl, is pushed against the control shaft by a torsion coil spring. As a result, when the vehicle is parked, the lever can be shifted to the P position regardless of the parking gear phase. Also, if the lever is inadvertently moved to the P position while the vehicle is running, the parking gear will flip out the parking pawl, preventing the driveline from locking.

## 2.2. Operating Force Characteristics of the Select Lever

Figure 3 shows the relationship between the select lever stroke and the operating force, which is the object of the simulation. These force characteristics are determined by the force due to the detent, the mechanical lock mechanism, the force loss due to the wire, the link on the selector lever side, displacement due to looseness and bending of the wire, and the large amount of hysteresis.

Figure 4 shows an explanation of this characteristic curve. During the first half of the lever operation, the operating force is generated in response to the reaction force, and during the latter half a holding force is generated in response to the suction force that prevents the lever from stopping outside the correct position. The directions of these forces reverse when the lever is moved in the opposite operating direction.

The two characteristics between P and R are determined by the operating condition of the mechanical lock mechanism. When the vehicle is parked and the lever is shifted to the P position, the lever will go into either a locked state in which the pawl engages with the parking gear, or an unlocked state in which it is sitting on the gear, depending upon the phase of the parking gear with respect to the parking pawl, as shown in Fig. 5. If the pawl is sitting on the gear, the parking brake lever spring force is added to the operating force. Consequently, the operating force characteristics between P and R differ depending upon whether the pawl is engaged with the gear or is sitting on it.

The main issues during development are the magnitude of the operating force and the existence of suction force which affect the transmission’s merchantability and function. The force near the P position is high due to the mechanical lock mechanism, so the following two items are particularly important. Figure 6 indicates this on the characteristic curves.

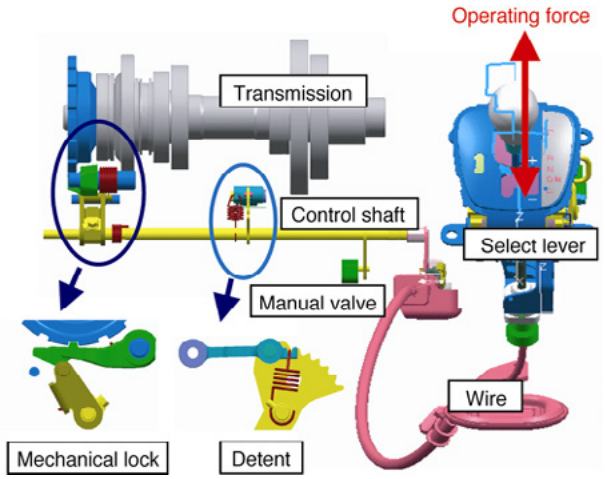



Fig. 1 Position selector

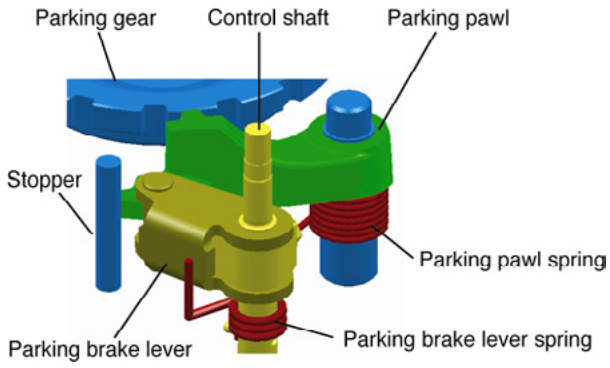



Fig. 2 Components of mechanical locking device

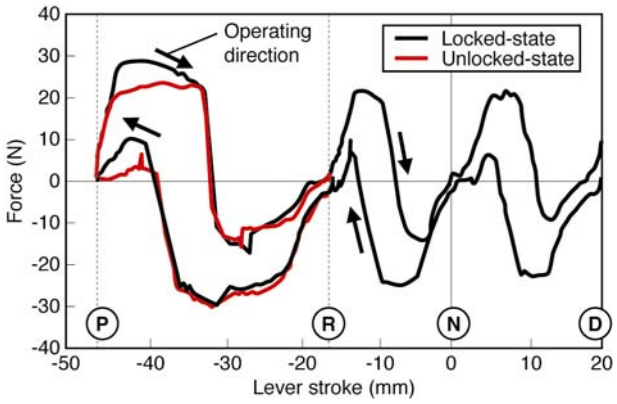



Fig. 3 Operating force characteristic

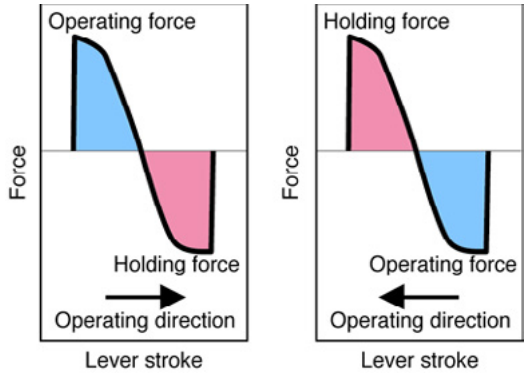



Fig. 4 Explanation of characteristic curve

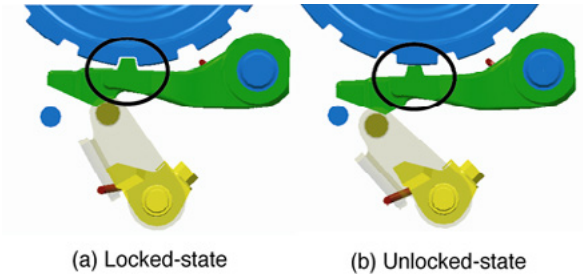



Fig. 5 Position of parking pawl and parking gear

(1) The magnitude of the maximum operating force going from P to R when the pawl is engaged with the gear, from the viewpoint of reduction of the operating force
(2) The existence of a suction force due to shifting of the lever from R to P when the pawl is sitting on the gear, from the viewpoint of preventing intermediate stopping.

Intermediate stopping occurs when the suction force generated at the detent is offset by the force generated by friction and other factors.

If the detent force is reduced in order to reduce the maximum operating force, the suction force will also be reduced, increasing the chances that intermediate stopping will occur. In other words, (1) and (2) are in conflict with each other. In order to both realize a reduction of the maximum operating force and prevent the occurrence of intermediate stopping at the specification study stage, it is necessary to simulate the operating force characteristics.

## 3. Simulation Method

### 3.1. Conventional Simulation Method

The conventional method of simulating the operating force was implemented by checking the joint angle of linkage and the contact angle of the contact part by making a plot for each layout, performing a mathematical calculation of the force transfer efficiency and contact force, and totalizing the calculation results for each element.

However, since there are multiple link mechanisms and force elements, a large number of man-hours are required to perform the simulation. A point calculation was performed at each position and also at several points between P and R. In addition, the simulation accuracy was low, so it was not possible to make a quantitative judgment from the predicted value. Furthermore, the simulation of displacement in the operating direction necessitates simulation of the balance between forces generated at each point in consideration of bending, so it was impossible in practice.

Thus, the issues of simulation accuracy and simulation man-hours were attendant to the conventional method.

### 3.2. Raising the Accuracy and Reducing the Simulation Man-hours

In light of the above, in this development the following methods were used in order to raise the simulation accuracy while reducing the necessary number of man-hours for simulating the operating force characteristics of the lever.

(1) Construction of a method of accurately simulating the component element characteristics in order to raise the simulation accuracy
(2) Simulation of a characteristic curve using a mechanical analysis tool in order to reduce the number of man-hours required.

Details of each of these items are described below.

#### 3.2.1. Raising the accuracy of simulating the hysteresis characteristics

As a result of investigating the component elements that affect the accuracy of the simulation, it was found that there was a large difference in the theoretical force and the actual force generated inside the transmission. Figure 7 shows the operating torque characteristics versus angle of rotation of the control shaft, together with the theoretical values. These characteristics are formed by the force of the detent and the mechanical lock mechanism. The difference between the actual value and the theoretical value is large when the parking pawl is sitting on the parking gear near the P position. Accordingly, attention was paid to the characteristics of the parking brake spring whose characteristics affect only the force characteristics in this vicinity.

As a result of measurement, it was found that the characteristics of the parking brake spring had a large amount of hysteresis. These characteristics are dependent on whether or not the spring turns are touching each other, whether or not the end face of the spring touches the other, and whether or not the spring is tilted. It was found that by using the hysteresis characteristics obtained from measurement in the calculation, the accuracy of the simulated lever force characteristics rose and also the necessary accuracy for quantitatively judging the force was obtained. Accordingly, an attempt was made to predict the hysteresis characteristics.

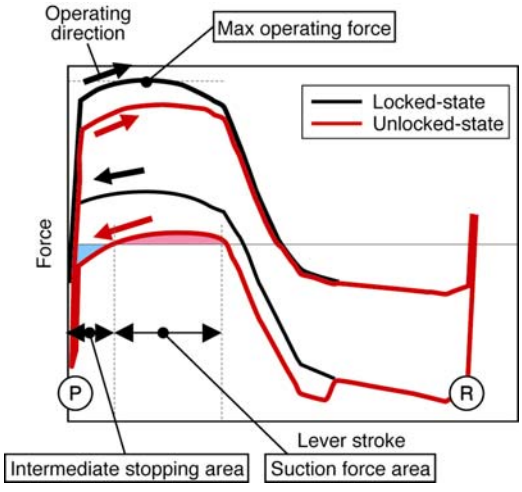



Fig. 6 Max operating force and intermediate stopping

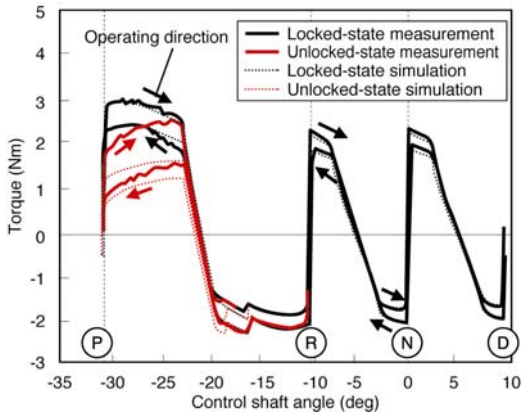



Fig. 7 Operating torque characteristic in transmission

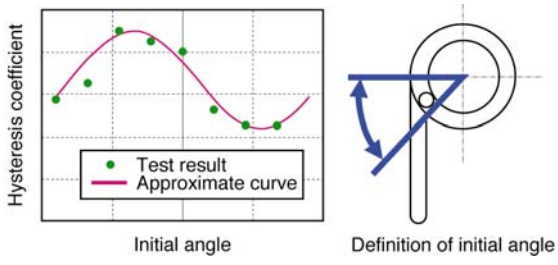



Fig. 8 Result of spring test

In order to investigate the relationship between the hysteresis characteristics and the spring specifications, the state of mutual contact between the turns and the number of turns of the parking brake lever spring were changed, and the characteristics obtained were measured. The hysteresis width is affected by the absolute value of the torque, so the hysteresis width at certain measurement points was divided by the mean value of the torque and arranged as a non-dimensional coefficient. As a result, it was found that there was a constant degree of correlation between this non-dimensional coefficient and the initial phase angle, which is the turn angle between the spring arms shown in Fig. 8. An empirical equation for predicting the hysteresis characteristics was derived using the initial phase angle as a parameter.

In order to verify the appropriateness of this empirical equation, tests were carried out using parking brake lever springs of various specifications. Figure 9 shows an example of a comparison between the measured value of the characteristics, the theoretical value using the conventional calculation formula, and the theoretical value obtained by means of the derived empirical equation. From the above verifications, it was confirmed that the accuracy of simulating the spring hysteresis characteristics rose using the empirical equation.

### 3.2.2. Reduction of simulation man-hours

Figure 10 shows the elements that are taken into account in this simulation. The selection of each element takes into account the effect on the force characteristics.

There were apprehensions that if the number of calculation points were increased in order to take account of these elements and obtain the force characteristics as a characteristics curve, the number of simulation man-hours would increase. For this reason, a simulation was performed by mechanical analysis, using a 3-dimensional CAD layout of the vicinity of the select lever. Previously performed manual calculation was eliminated in order to minimize the increase in man-hours. Also, it was possible to simulate not only the force but also the displacement. A description of a simulation method constructed using a mechanical analysis tool is given below.

(1) Force transfer efficiency The force transfer efficiency changes according to the joint angle of the wire and the position of the link. Previously, the force transfer efficiency for each lever stroke was obtained by plotting a diagram and performing manual calculation. Also, in the case of a link mechanism that had a complicated 3-dimensional layout, there was a risk of an error occurring during the manual calculation process.

In this development, rotational and translational constraint characteristics were made directly from the 3-dimensional layout of the link mechanism, and the force transfer efficiency was automatically calculated.

(2) Contact angle The reaction force to the control shaft changes according to the contact angle between the detent and the detent arm roller, and between the parking pawl and the brake lever roller. Previously, the contact angle of the detent and the parking pawl for each rotational angle of the control shaft was obtained using a calculation formula or by plotting a diagram.

In this development, the contact angle was automatically calculated by means of a constraint definition. The force due to friction of the contact part was also taken into account. However, contact elements should be used in order to define the relationship between the detent and the roller and between the parking pawl and the brake lever in accordance with the actual situation. This requires much calculation time and the analysis becomes unstable. For this reason, it was assumed that for normal operation, the contact between each part was maintained, and point and curve constraint parameters were used on the track of the roller's center.

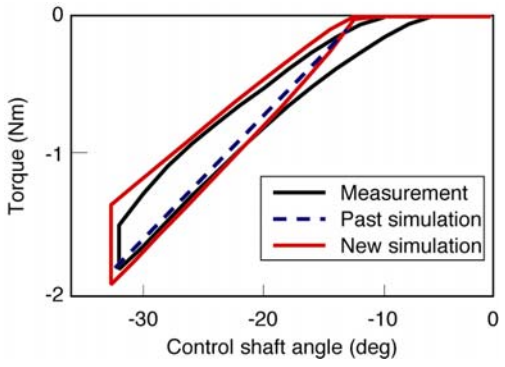



Fig. 9 Parking brake spring characteristic

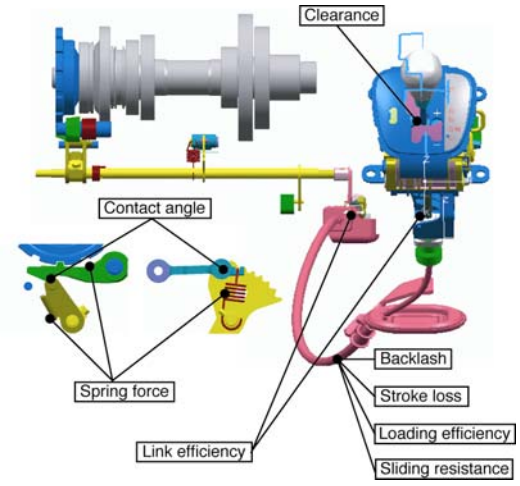



Fig. 10 Factors in select lever operating force

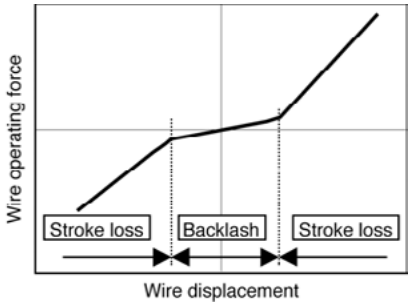



Fig. 11 Non-linear spring for wire displacement

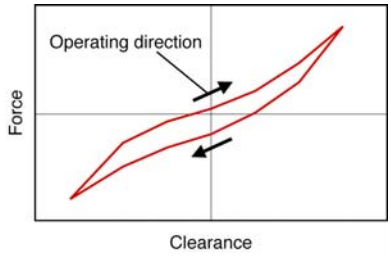



Fig. 12 Non-linear spring for lever stiffness and clearance

(3) Wire characteristics The wire characteristics consist of four elements: force efficiency, sliding resistance which affects force, and backlash and stroke loss which affect displacement. Force efficiency was reproduced by calculating the friction of the rotating shaft for the link on the select lever side in order to generate force loss. The displacement elements of backlash and stroke loss, which could not previously be taken into account, were calculated by dividing the wire into two parts in the model, and connecting the two parts by means of a non-linear spring that exhibited a non-linear displacement to the force shown in Fig. 11.

(4) Select lever characteristics The looseness and stiffness of the select lever affects the displacement. A non-linear spring that had the hysteresis is shown in Fig. 12.

(5) Spring force Load characteristics that vary according to the operating direction were modeled in order to take into account the force of the parking brake lever spring including the hysteresis characteristics obtained in 3.2.1. Also, a non-linear spring that regulated the direction of rotation was modeled in order to reproduce the state in which the parking brake lever is pushed against the control shaft.

(6) Supporting method A method of supporting the creation of a model was constructed in order to permit the designer to readily use this operating force simulation method. Before performing analysis, the designer creates basic constraint parameters in a 3-dimensional CAD layout and a parameter file to which various specifications have been input for the analysis. When the parameter file is executed, the simulation will takes place automatically and the results are output as a graph.

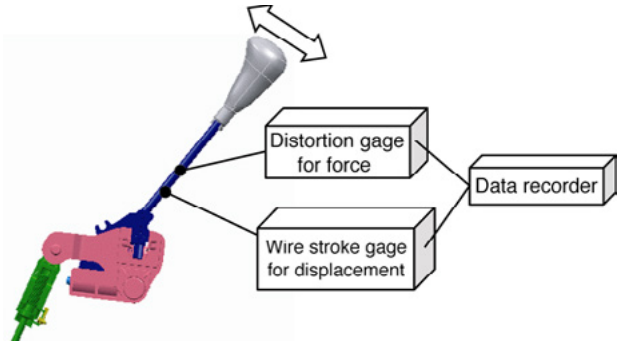



Fig. 13 Operating force test apparatus

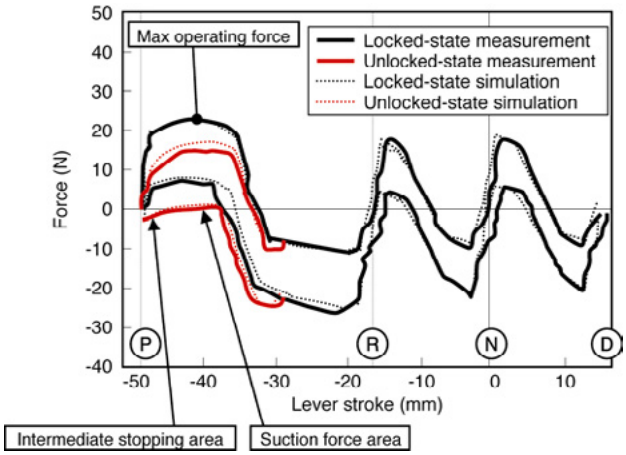



Fig. 14 Comparison of test result and simulation

As a result of performing the above, it became possible to characterize the shift force as a curve, in contrast to the conventional method, which was a method of simulation based on points. Factors that could not previously be taken into account were added. A supporting method was employed, enabling the number of simulation man-hours to be cut in half.

## 4. Verifying the Accuracy of the Simulation

In order to make a detailed comparison of the measured values and the theoretical values over the entire stroke, the select lever operating force and the operating stroke were measured using the distortion gauge and wire stroke gauge shown in Fig. 13. The resulting data was acquired digitally.

Figure 14 shows a comparison of the measured values and the theoretical values obtained using this method. The existence of intermediate stopping when the pawl was sitting on the gear and the maximum operating force when the pawl was engaged with the gear were simulated accurately. Also, the force and displacement were accurately predicted to within ±5% over the entire stroke.

## 5. Conclusion

A method of accurately simulating the operating force characteristics of the shift lever of an automatic transmission to within ±5% was developed. The constructed technology is summarized below.

(1) It was possible to simulate the hysteresis characteristics of the torsion coil spring, which greatly affect the select lever operating force characteristics, by means of an empirical equation.

(2) It was possible to simulate the force characteristic curve while taking into account the main factors that affect the operating force characteristics of the select lever, using one half of the previous number of man-hours.

By adopting this method, it became possible to verify the occurrence of excessive operating load and intermediate stopping at the specification study stage.

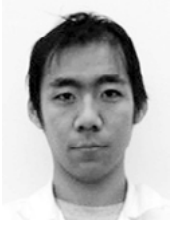
## Reference

(1) Ichikawa, N.: Shift Feeling Evaluation of Farm Tractor by Mechanical Dynamic Analysis, KUBOTA TECHNICAL REPORT, No. 31, p. 87-92 (1996)

■ Authors ■


Takaki YAMAOKA


Shunichi NOGAMI


Akira KOBAYASHI

# Research on Simulation Method for Predicting Rattling Noise in Manual Transmission Drivetrain

Eiji HANAI* Masakazu MITANI* Hiromasa NAKAMURA*

## ABSTRACT

The level of rattling noise in a Manual Transmission (MT) drivetrain system is closely related to the transmission input shaft rotational speed fluctuation. In this research, the loudness of noise, which is proportional to the impact force of the rattling idle gears caused by the rotational speed fluctuation, and the conspicuousness of noise, which is caused by the existence of drivetrain resonance, were clearly identified. Furthermore, a drivetrain simulation method for predicting the rotational speed fluctuation was developed. In this simulation method, a clutch torsional characteristic defined by the dynamic torsion constant and equivalent damping force coefficient is used as the parameter to improve accuracy. Consequently, it is now possible to obtain the optimum specifications of clutch, moment of inertia and torsional rigidity characteristic of the drivetrain to reduce the rattling noise level at an early stage of the development program.

## 1. Introduction

Gear rattling noise in MT vehicles is an important issue that affects the product appeals of comfort and quietness. The source of vibration for this rattling noise is the torque fluctuation caused by engine combustion. This torque fluctuation is inputted into the transmission via the clutch and causes idle gears to impact, producing a rattling noise. In order to reduce the gear rattling noise, it is necessary to suppress the transmission of the torque fluctuation from the engine to the drivetrain. This requires measures to dampen the torsional vibration of the drivetrain in the practical vehicle speed range, and to reduce the rotational speed fluctuation of the transmission input shaft, which causes the rattling noise.

The rotational speed fluctuation of the input shaft is closely related to the torsional characteristics of the clutch[(1), (2)]. Therefore various measures are implemented to reduce this rotational speed fluctuation, such as reducing the torsional stiffness characteristics of the clutch and changing the hysteresis by displacement of the fluctuation angle. However, these measures are limited by the clutch structure, as they require increased spring stress, widening of the operating angle, the addition of a variable hysteresis torque mechanism, etc. Therefore, in order to ensure adequate measures, torsional characteristics of the clutch that can suppress rotational speed fluctuation of the input shaft must be studied and set in the initial design stages. Simulations are conducted to study the rotational speed fluctuation of the input shaft[(3), (4), (5)], but in some cases the results do not match with measured values and the desired effects are not achieved. Therefore, various specifications are currently tested using actual vehicles to determine the specifications.

This paper reports the development of a simulation method that defines and reflects the dynamic torsional characteristics of the clutch in the operating state to accurately predict the rotational speed fluctuation of the input shaft.

## 2. Rattling Phenomenon

The rattling noise of concern becomes noticeable during full-throttle acceleration in high gear and when coasting (natural deceleration) in low gear. Figures 1 (a) and (b) show the actual values for rattling noise measured near the transmission case, engine combustion primary rotational

* Tochigi R&D Center

speed fluctuation, and transmission input shaft rotational speed fluctuation during full-throttle acceleration in 5th gear and when coasting in 3rd gear.

Rattling noise was observed to change in conjunction with the input shaft rotational speed fluctuation. The sum total of the forces during idle gear impact can be considered as an index for the rattling noise loudness, and this is defined as the force of tooth impact $F$ derived from the angular speed fluctuation and moment of inertia of each idle gear as shown in Eq. (1).

$$F = \sum_{i=a}^{b} I_i \frac{d\omega_{Gi}}{dt} = \sum_{i=a}^{b} I_i \frac{d\left(\frac{\Delta N_{IS}}{60} \times 2\pi \times \frac{1}{r_i}\right)}{dt} \quad (1)$$

Here,

$I$ : Moment of inertia of idle gear
$\Delta\omega_G$ : Idle gear rotational speed fluctuation
$\Delta N_{IS}$ : Input shaft rotational speed fluctuation
$r$ : Ratio
$a$ to b : Each idle gear step in the running state

Figure 2 shows the relation between sensory ratings and tooth impact force obtained by Eq. (1) using measured values of the rotational speed fluctuation during resonance of torsional vibration of the drivetrain. This figure shows that the proximate noise level and tooth impact force have a proportional relationship with a high correlation. Conversely, a worsening tendency can be observed for sensory ratings as tooth impact force increases. However, there were a number of cases that received lower ratings even though the tooth impact force was small and the proximate noise level was low.

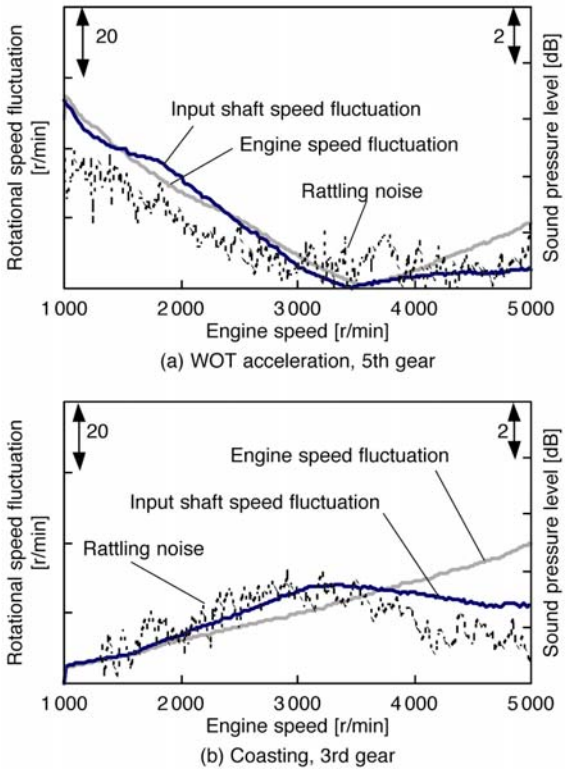



Fig. 1 Rotational speed fluctuation and sound pressure level

Therefore, an index of the rattling noise conspicuousness was defined as the amplification of rotational speed fluctuation, $r_{amp}$, which is the ratio of the input shaft rotational speed fluctuation to the engine rotational speed fluctuation during resonance of torsional vibration of the drivetrain, as shown in Eq. (2).

$$r_{amp} = \Delta N_{IS} / \Delta N_E \quad (2)$$

Here,

$\Delta N_E$ : Engine rotational speed fluctuation

This amplification of rotational speed fluctuation was confirmed to correlate closely with sensory ratings as shown in Fig. 3, with the rating tending to worsen as the rotational speed fluctuation transmission ratio increased. The rating is presumed to worsen because the difference between the rattling noise inside and outside the area of torsional vibration resonance of the drivetrain increases and the rattling noise becomes more conspicuous as the amplification of rotational speed fluctuation increases. Thus, the reason for the poor rating even when the rattling noise is low is thought to be due to the rattling noise conspicuousness.

Based on the above, rattling noise can be rated in terms of loudness, which depends on the absolute value of the sound pressure level, and conspicuousness, which is caused by resonance of torsional vibration of the drivetrain. Furthermore, these characteristics can both be judged by obtaining the input shaft rotational speed fluctuation value.

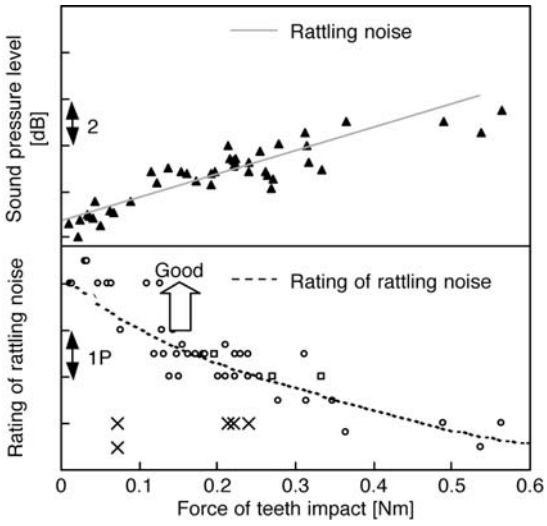



Fig. 2 Relation between rating of rattling noise and force of teeth impact

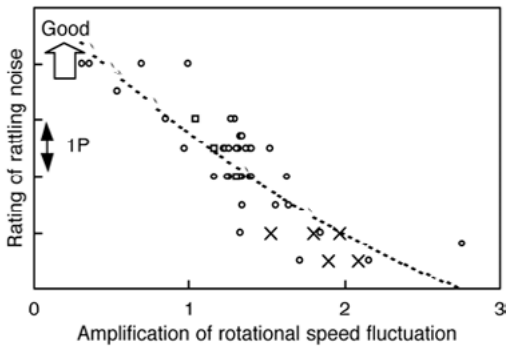


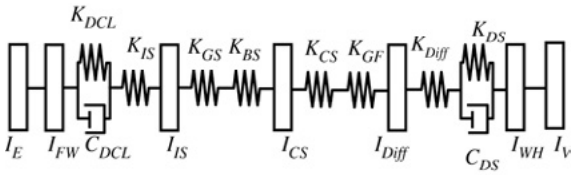

Fig. 3 Relation between rating of rattling noise and amplification of rotational speed fluctuation

## 3. Modeling the Drivetrain Rotation Transmission Mechanism

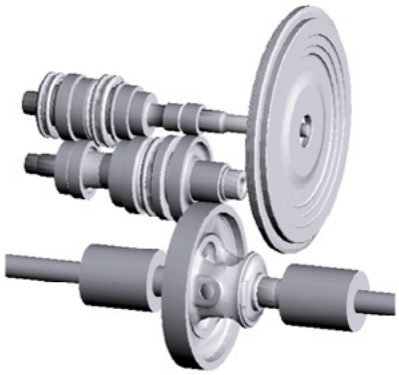
### 3.1. Simulation Model

Figure 4 (a) and (b) shows an outline of the simulation model used to predict transmission input shaft rotational speed fluctuation. The model configuration was set as the range from the crank shaft to the flywheel, clutch, transmission, drive shaft, tire, and body. Equations (3) through (7) show the equations of motion for torsional vibration of the drivetrain used in the simulation model.

Measured values for the input shaft, counter shaft, and differential and calculated values for the drive gear and shaft deflections were used for the torsional stiffness of the transmission.

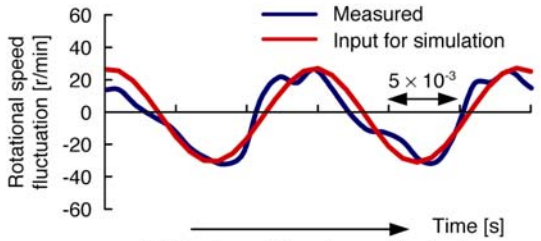



(a) Forced torsional vibration model

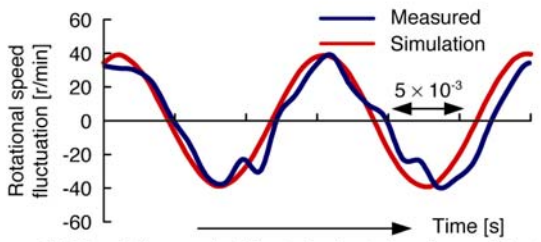


(b) Drivetrain model for simulation

Fig. 4 Simulation model for rotational speed fluctuation




(a) Engine rotational speed fluctuation




(b) Simulation result of input shaft rotational speed fluctuation

Fig. 5 Input wave and simulation result

The measured torsional stiffness and the damping coefficient calculated from experimental equations were used for the drive shaft characteristics.

The torsional characteristics of the clutch reflected the dynamic torsional characteristics in the operating state. These details are described in section 3.2.

The input was a vibration applied in the form of a sine wave that fluctuated at the primary frequency of engine combustion using the measured value of the engine rotational speed fluctuation as the amplitude as shown in Fig. 5 (a). The results reproduced the input shaft rotational speed fluctuation as shown in Fig. 5 (b).

$$I_1\ddot{\theta}_{FW} + C_{DCL}\left(\dot{\theta}_{FW} - \dot{\theta}_{IS}\right) + K_1\left(\theta_{FW} - \theta_{IS}\right) = 0 \quad (3)$$

$$I_2\ddot{\theta}_{IS} + C_{DCL}\left(\dot{\theta}_{IS} - \dot{\theta}_{FW}\right) + K_1\left(\theta_{IS} - \theta_{FW}\right) + K_2\left(\theta_{IS} - \theta_{CS}\right) = 0 \quad (4)$$

$$I_3\ddot{\theta}_{CS} + K_2\left(\theta_{CS} - \theta_{IS}\right) + K_3\left(\theta_{CS} - \theta_{Diff}\right) = 0 \quad (5)$$

$$I_4\ddot{\theta}_{Diff} + K_3\left(\theta_{Diff} - \theta_{CS}\right) + C_{DS}\left(\dot{\theta}_{Diff} - \dot{\theta}_{WH}\right) + K_4\left(\theta_{Diff} - \theta_{WH}\right) = 0 \quad (6)$$

$$I_5\ddot{\theta}_{WH} + K_4\left(\theta_{WH} - \theta_{Diff}\right) + C_{DS}\left(\dot{\theta}_{WH} - \dot{\theta}_{Diff}\right) = 0 \quad (7)$$

$$I_1 = I_E + I_{FW}$$
$$I_2 = I_{IS}$$
$$I_3 = I_{CS}/i^2$$
$$I_4 = I_{Diff}/i^2/i_f^2$$
$$I_5 = \left(I_{WH} + I_V\right)/i^2/i_f^2$$

$$1/K_1 = 1/K_{DCL} + 1/K_{IS}$$
$$1/K_2 = 1/K_{GS} + 1/K_{BS}$$
$$1/K_3 = 1/\left(K_{CS}/i^2\right) + 1/\left(K_{GF}/i^2\right)$$
$$1/K_4 = 1/\left(K_{Diff}/i^2/i_f^2\right) + 1/\left(K_{DS}/i^2/i_f^2\right)$$

Here,

$I_E$ : Moment of inertia of engine
$I_{FW}$ : Moment of inertia of flywheel
$I_{IS}$ : Moment of inertia of input shaft
$I_{CS}$ : Moment of inertia of counter shaft
$I_{Diff}$ : Moment of inertia of differential
$I_{WH}$ : Moment of inertia of wheel and tire
$I_V$ : Moment of inertia of vehicle body equivalent
$K_{DCL}$ : Clutch dynamic stiffness
$K_{IS}$ : Input shaft torsional stiffness
$K_{GS}$ : Gear meshing stiffness
$K_{BS}$ : Shaft deflection stiffness
$K_{CS}$ : Counter shaft torsional stiffness
$K_{GF}$ : Final gear meshing stiffness
$K_{Diff}$ : Differential torsional stiffness
$C_{DCL}$ : Clutch equivalent damping coefficient
$C_{DS}$ : Drive shaft damping coefficient
$I$ : Running gear ratio
$i_f$ : Final gear ratio

### 3.2. Dynamic Torsional Characteristics of the Clutch

The simulation reflected the torsional characteristics of the clutch as the dynamic torsional characteristics in the operating state. Figure 6 shows an example of the dynamic torsional characteristics of the clutch when it is rotating, and the static torsional characteristics when it is not rotating.

The centrifugal force presses the torsion spring toward the outside, which increases the friction force and causes the hysteresis torque of the dynamic torsional characteristics to become larger than the static torsional characteristics. When running, in addition to this increased hysteresis torque, the clutch vibrates with a minute amplitude angle at the engine combustion primary cycle, and can be assumed to operate in a loop form such as shown in Fig. 7.

The clutch stiffness in the running state, the loop shown in Fig. 7, is thought to operate at a higher dynamic stiffness $K_d$ than the static stiffness, and this is defined in Eq. (8). In contrast with the static stiffness, which is a constant value under all conditions, the dynamic stiffness is determined by the hysteresis torque and the fluctuation angle, which change according to the rotational speed and the rotational speed fluctuation, respectively. As a result, the dynamic stiffness changes continuously according to the running state.

Figure 8 shows an example of the dynamic stiffness characteristics calculated by Eq. (8) using the dynamic torsional characteristics of the clutch at each rotational speed.

The damping coefficient produced by the hysteresis torque is defined as the equivalent damping coefficient $C_{eq}$[6] from the area enclosed by the loop shown in Fig. 7, and is calculated as shown in Eq. (9). This equivalent damping coefficient is determined by the hysteresis torque, the fluctuation angle, and the fluctuation frequency caused by engine combustion, so, like the dynamic stiffness, it changes continuously according to the running state.

Figure 9 shows an example of the equivalent damping coefficient characteristics at each rotational speed calculated by Eq. (9), using the dynamic torsional characteristics of the clutch at each rotational speed in the same manner as the dynamic stiffness.

The dynamic stiffness and equivalent damping coefficient characteristics shown in Fig. 8 and Fig. 9 were calculated for each engine rotational speed, rotational speed fluctuation, and operating torque range, and compiled into a simulation database. The simulation continuously varied the characteristics by obtaining the dynamic stiffness and equivalent damping coefficient from this database based on the calculated states and then substituting these values to the clutch characteristics in the simulation model shown in Fig. 4 (a).

$$K_d = \frac{H + K_S \times 2 \times A}{2 \times A} \tag{8}$$

$$C_{eq} = \frac{S}{\pi \times \omega \times A^2} = \frac{H \times 2 \times A}{\pi \times 2\pi f \times A^2} \tag{9}$$

Here,
$K_s$ : Static stiffness
$H$ : Hysteresis torque
$A$ : Crank fluctuation angle
$f$ : Fluctuation frequency
$S$ : Loop area

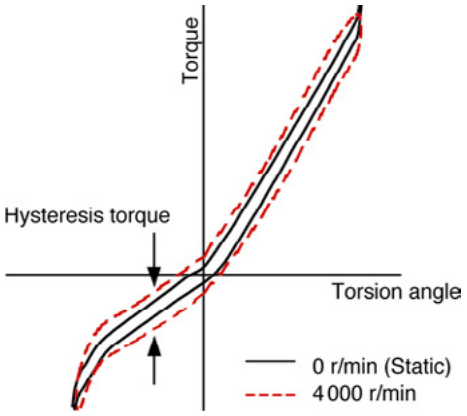



Fig. 6 Rotational characteristics of clutch at 4 000 r/min

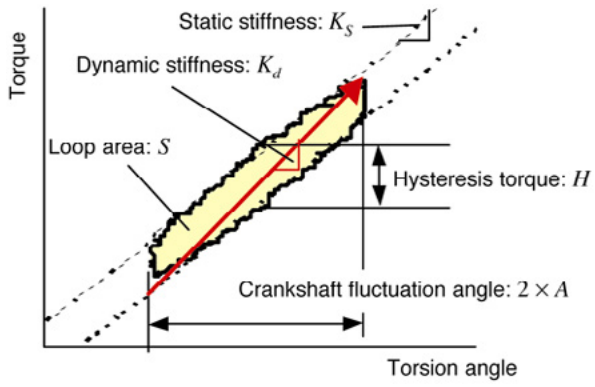



Fig. 7 Dynamic characteristics of clutch

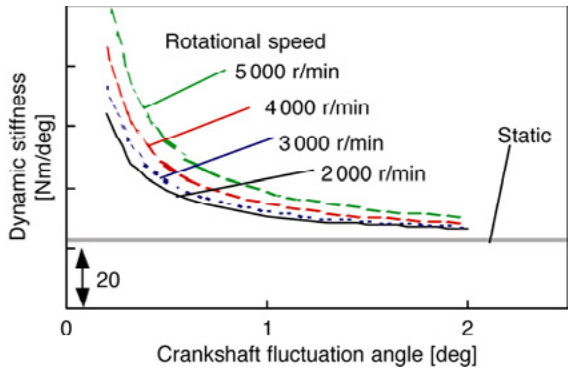



Fig. 8 Calculated results of dynamic stiffness of clutch

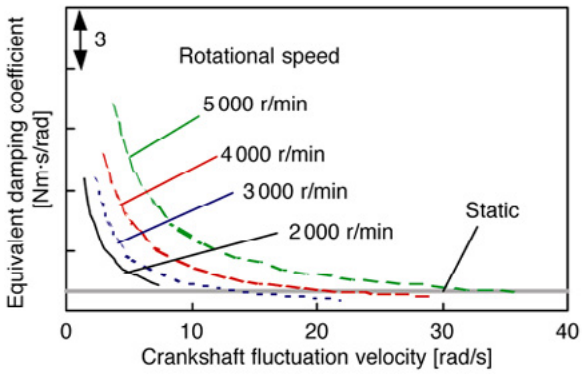



Fig. 9 Calculated results of dynamic damping of clutch

## 4. Analysis Examples

### 4.1. Correlation between Measured Values and Simulation Results

The newly constructed simulation model was applied to a 1.4-liter, 5-speed manual transmission drivetrain, and the results were compared with measured values of the input shaft rotational speed fluctuation.

Figure 10 (a) and (b) shows the simulation results and measured values during full-throttle acceleration in 5th gear and when coasting in 3rd gear.

During full-throttle acceleration in 5th gear, the measured values of the input shaft rotational speed fluctuation increased in amplitude compared to the engine rotational speed fluctuation due to resonance of torsional vibration of the drivetrain at an engine rotational speed of around 2 300 r/min, and the peak value was 40 r/min. The simulation results matched closely with the measured values in terms of the peak value and the engine rotation speed at which that peak occurs due to resonance of torsional vibration of the drivetrain, thus confirming the correlation.

When coasting in 3rd gear, the measured values of the input shaft rotational speed fluctuation increased in amplitude at an engine rotational speed of around 4 000 r/min. In this case as well, the simulation results were to reproduce the same phenomena as the measured values.

These results confirmed that the newly constructed simulation model can accurately reproduce measured phenomena related to input shaft rotational speed fluctuation during both acceleration and deceleration.

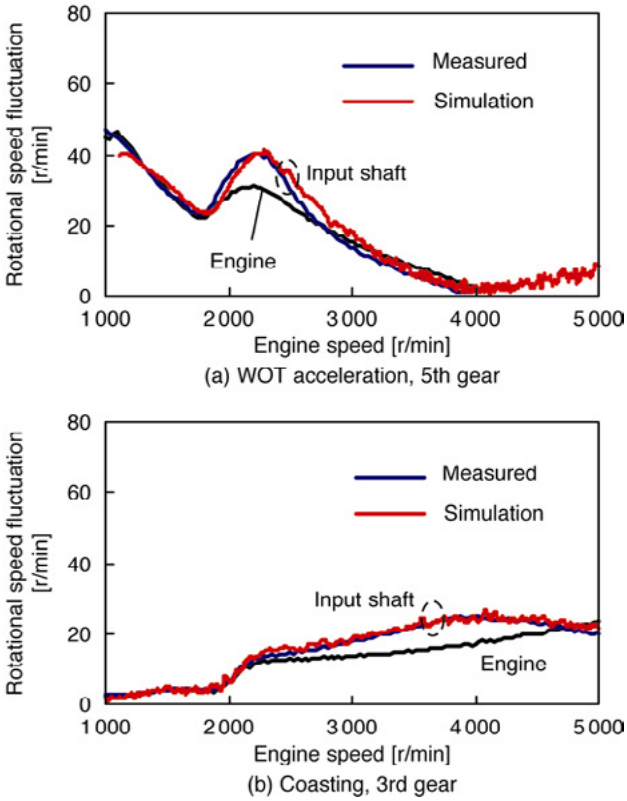



Fig. 10 Comparison of rotational speed fluctuation between measured results and simulation results at 1.4L 5MT

### 4.2. Investigation of Specifications for the Torsional Characteristics of the Clutch

Simulations were conducted to investigate specifications for the torsional characteristics of the clutch during development of a 2.4-liter, 6-speed manual transmission drivetrain. These results were then compared with the results of confirmation testing an actual vehicle.

Figure 11 shows the torsional characteristics during rotation for the two types of clutches investigated. The acceleration side shows the characteristics at 2 000 r/min, and the deceleration side shows the characteristics at 4 000 r/min. On the acceleration side, the same static stiffness characteristics were set for both Type 1 and Type 2, but the hysteresis torque when rotating was set larger for Type 2 than for Type 1. On the deceleration side, the static stiffness was set the same as the acceleration side for Type 1, and half that value for Type 2. In addition, the hysteresis torque when rotating was set smaller for Type 2 than for Type 1.

Figure 12 (a) and (b) shows the simulation results of the input shaft rotational speed fluctuation using the above torsional characteristics of the clutch during full-throttle acceleration in 5th gear and when coasting in 3rd gear.

During full-throttle acceleration in 5th gear, the input shaft rotational speed fluctuation for Type 1 was confirmed to peak due to resonance of torsional vibration of the drivetrain at an engine rotational speed of around 1 850 r/min. The peak value at that time was 55 r/min. Type 2 had reduced rotational speed fluctuation compared to Type 1, and a peak was not observed. For this reason, Type 2 was confirmed to have better characteristics for rattling noise during full-throttle acceleration.

When coasting in 3rd gear, the input shaft rotational speed fluctuation for Type 1 was confirmed to peak due to resonance of torsional vibration of the drivetrain at an engine rotational speed of around 4 000 r/min. The peak value at that time was 40 r/min. Type 2 had reduced rotational speed fluctuation compared to Type 1, and a peak was not observed. For this reason, like full-throttle acceleration in 5th gear, Type 2 was confirmed to have better characteristics for rattling noise during coasting deceleration.

Figure 13 shows the measurement results for input shaft rotational speed fluctuation when these two types of clutches were mounted in an actual vehicle.

The measured values and the simulation results exhibited nearly the same characteristics, and Type 2 was confirmed to achieve the same rotational speed fluctuation and fluctuation reduction effects in an actual vehicle.

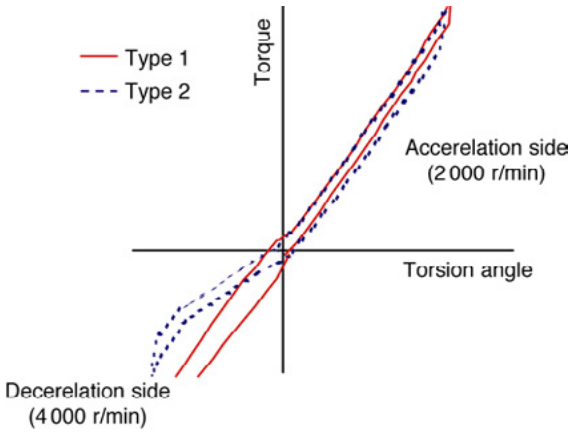



Fig. 11 Rotational speed characteristics of clutch for 2.4L 6MT

Based on these results, the newly constructed simulation model was confirmed to be an effective means for accurately predicting the input shaft rotational speed fluctuation, which is necessary when determining the torsional characteristics of the clutch and the drivetrain specifications.

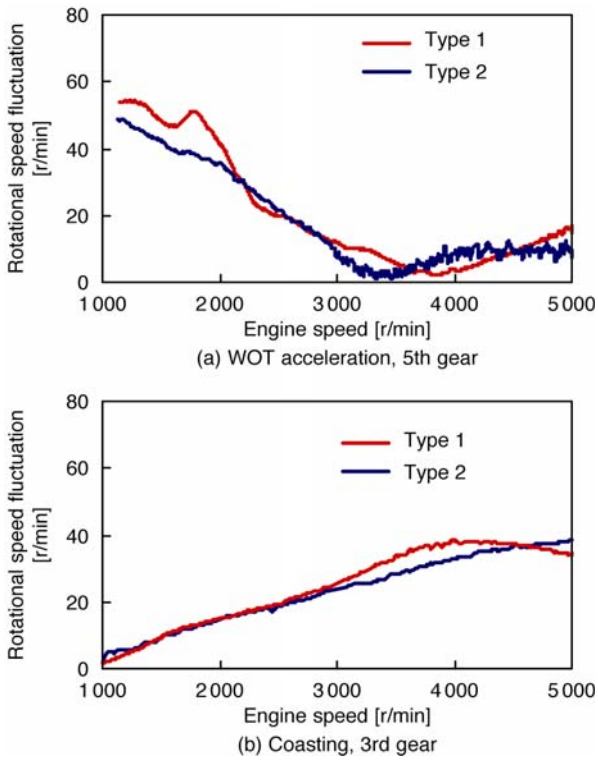



Fig. 12 Simulation results of input shaft rotational speed fluctuation at 2.4L 6MT

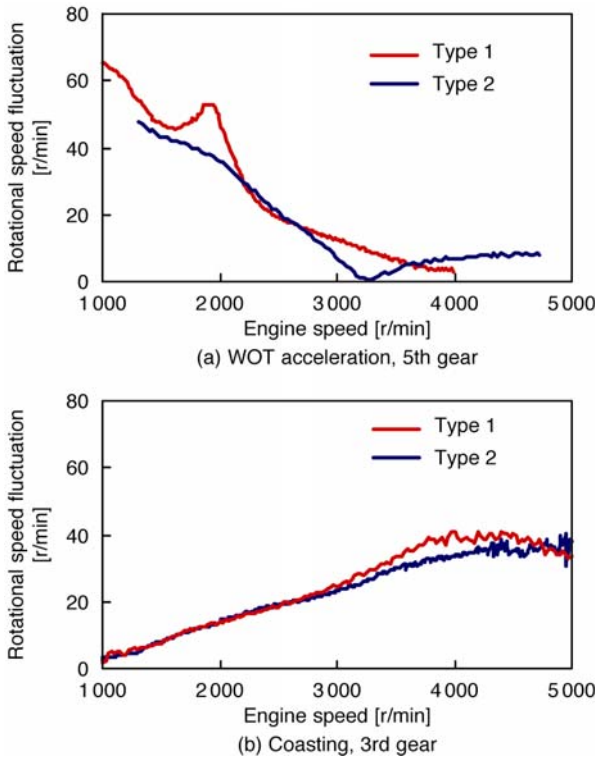



Fig. 13 Measurement results of input shaft rotational speed fluctuation at 2.4L 6MT

## 5. Conclusion

A method for predicting rattling noise in MT vehicles was studied, and the following results were obtained:

(1) Rattling noise can be rated in terms of loudness, which depends on the absolute value of the sound pressure level, and conspicuousness, which is caused by resonance of torsional vibration of the drivetrain. Furthermore, it was shown that both of these characteristics can be judged according to the input shaft rotational speed fluctuation.

(2) The measured values of the input shaft rotational speed fluctuation could be reproduced by defining the dynamic torsional characteristics of the clutch during operation as the dynamic stiffness and the damping coefficient, estimating the characteristics for each engine rotational speed, rotational speed fluctuation, and operating torque range, and then reflecting these values to the simulation model.

(3) Using the newly constructed simulation model made it possible to investigate the optimum specifications for the clutch torsional characteristics and the drivetrain that reduce the input shaft rotational speed fluctuation in each drivetrain.

## References

(1) Mizutani, K., Hata, H.: The Nonlinear Torsional Vibrations of a Shaft System with the Hysteretic and Two-staged Torsional Stiffness, Transactions of The Japan Society of Mechanical Engineers, Vol. B, p. 497-500 (1995)

(2) Doman, Y., Nishikawa, K.: Technique to Solve NV Problems of a Clutch, Journal of Society of Automotive Engineers of Japan, Vol. 54, No. 4, p. 34-40 (2000)

(3) Yahata, S., Kizuka, T., Umemoto, O.: Prediction as to Idling Rattle of Manual Transmission (First Report), Transactions of Society of Automotive Engineers of Japan, Vol. 34, No. 1, p. 96-100 (2003)

(4) Hashimoto, H., Yamada, T., Takatsuki, K., Umezawa, K.: Improvement of Booming Noise Caused by Drive Line Torsional Vibration of a Heavy-duty Truck, Journal of Society of Automotive Engineers of Japan, Vol. 47, No. 6, p. 50-54 (1993)

(5) Sawatsubashi, T., Suzuki, T.: Kudoukei ni Okeru Giya Hauchi no Kaiseki, SUZUKI TECHNICAL REVIEW, Vol. 18, p. 20-25 (1992) (in Japanese)

(6) Tanaka, K., Saegusa, S.: Gensui no Tokusei to Toriatukai, Shindou Model to Simulation, Ouyougijyutu Syuppan, p. 130-142 (1984) (in Japanese)

## ■ Authors ■


Eiji HANAI


Masakazu MITANI


Hiromasa NAKAMURA

# Control Device of Electronically Controlled Fuel Injection System for Small Motorcycle Air-cooled Engine

Kenji TAMAKI* Shiro KOKUBU* Shunji AKAMATSU*


## ABSTRACT

In general, when an on board battery is at low power, the electric power generated from an alternator by a kick-starter operation is consumed by all the electrical loads, including the battery. This causes a voltage drop. To eliminate the power shortage, an installed relay circuit opens all electric loads other than the fuel injection system. This allows the fuel injection system to use all the electric power generated by the kick-starter. An electric power control system was incorporated into the ECU. The control system permits the starting of an engine by using the kick-starter even when the battery is completely discharged. Also, by suitable sensing of the engine oil temperature, the control device permits an efficient compensation of fuel injection quantity and ignition timing even in an air-cooled engine.


## 1. Introduction

Due to increasing global environmental issues in recent years, the emission regulations of small motorcycles have been becoming more stringent than ever in various countries in the world. In Europe, currently the Euro-2 emission control is enforced, and even more stringent, the Euro-3 emission control is due in 2006. In Asia, which is the main market of small motorcycles, China will follow similar to Euro-2 from 2004 and similar to Euro-3 from 2006. In Thailand, the 5th regulations, which are more stringent, will be applied from 2004. The motorcycle exhaust gas emission controls of principal countries or areas are shown in Table 1. Even for small motorcycles, the same level of emission control as for large motorcycles is being required. For emission controls in large motorcycles, the system using fuel

Table 1 Motorcycle emission control in various countries

| Country | Regulations | Period | Exhaust Emission (g/km) | | |
|---|---|---|---|---|---|
| | | | CO | THC | NOx |
| Europe | Euro-2 | 2003 — | 5.5 | 1.2 | 0.30 |
| | Euro-3 | 2006 — | 2.0 | 0.8 | 0.15 |
| China | Current | — 2004 | 13.0 | 3.0 | 0.30 |
| | Future | 2004 — | 5.5 | 1.2 | 0.30 |
| Thailand | 4th level | — 2003 | 4.5 | 3.0 | |
| | 5th level | 2004 — | 3.5 | 2.0 | |
| Japan | Current | — 2006 | 13.0 | 2.0 | 0.30 |
| | Future | 2007 — | 2.0 | 0.5 | 0.15 |

125cm$^3$ - class motorcycles

* Asaka R&D Center

injection (hereinafter referred to as FI) and combining the feedback control incorporating an oxygen sensor and a three-way catalyst is widely applied. Meanwhile in small motorcycles, the system using a carburetor and combining air induction and a catalyst is mainly applied. To make small motorcycles conform to more stringent emission regulations in the future, a fuel supply system that permits more accurate control of the air-fuel ratio is required and for that purpose an FI system is most appropriate at the moment[1]. We therefore researched an electronically controlled FI system that is applicable to small motorcycles using a natural air-cooled four-stroke single cylinder 125 $cm^3$-class engines.

The electric power control at kick-starting of a small motorcycle with an air-cooled engine, the appropriate control of the air-fuel ratio, and their effectiveness are described in this paper.

## 2. Outlines of Test Engine

The air-cooled four-stroke single cylinder 125 $cm^3$-class engine, which is applied to many commuter motorcycles in Southeast Asian countries, is chosen for the test engine. The major specifications are shown in Table 2. The small motorcycle with a test engine mounted is shown in Fig. 1.

## 3. Issues in Application of a Fuel Injection to a Small Motorcycle

Application of an FI system to motorcycles started when component parts for automobile applications were applied to large motorcycles[2]. Therefore, the high cost was an obstacle when considering application to small motorcycles. In recent years, the low-cost FI system, using the modularizing technique with the ECU attached to the throttle body, has been developed and applied to small scooters for export to Europe[3]. There are two major issues mentioned hereafter when applying the above-mentioned system to a small motorcycle using an air-cooled engine.

(1) Simultaneous use of the electric starter and the kick-starter
Usually, when an electric starter is the only starting system for an engine using an FI system, if the battery is completely discharged, not only will the starter motor not work, but also the fuel pump will not function, hence no fuel is supplied and the engine cannot be started. However, in an engine that has a kick-starter and a carburetor, even when the battery is completely discharged, the air-fuel mixture is automatically supplied into the combustion chamber when cranked by the kick-starter. At the same time, AC generator (hereinafter referred to as ACG) starts to supply energy to the ignition system, thus allowing the engine to start. In a small motorcycle, therefore, the engine should be able to start by the kick-starter when the battery is discharged even when an FI system is applied instead of a carburetor.

(2) Choosing a measurement position for engine oil temperature is necessary for system control
Most motorcycles using fuel injection have water-cooled engines, and the fuel injection is controlled based on the water temperature. In natural air-cooled engines, the air temperature after cooling the engine is unstable and difficult to measure. We therefore decided to measure the engine oil temperature. The engine oil for lubrication is distributed to various areas of the engine including the transmission gearbox, and the temperature differs depending on the position. It is therefore necessary to choose an appropriate measurement position for fuel injection control.

Table 2 Major specifications of test engine

| Item | Specifications |
|---|---|
| Engine type | Air cooled 4-stroke single-cylinder |
| Bore × Stroke | 52.4 × 57.9 mm |
| Displacement | 124.8 $cm^3$ |
| Compression ratio | 9.3 |
| Valve train | SOHC 2 valves |
| Valve diameter | IN 24, EX 21 mm |
| Clutch type | Automatic centrifugal |
| Transmission | 4-speed constant mesh |
| Max. output | 6.75 kW/7 500 r/min. |
| Max. torque | 9.74 Nm/5 500 r/min. |



Fig. 1 Overview of small motorcycle with test engine mounted

## 4. Outlines of the Fuel Injection System for Air-cooled Engines

### 4.1. Fuel Injection Control

Figure 2 shows the configuration of the fuel injection quantity control system applied to the test engine. The module unit integrating the throttle body, which controls the intake air volume, and the ECU, which controls the operating conditions of the engine, is incorporated. This module is of the same size as a conventional carburetor for small motorcycles. Figure 3 shows the overview and configuration. Incorporated into the module are the throttle sensor, the intake manifold pressure sensor, and the intake air temperature sensor. The engine oil temperature sensor for control of fuel injection is attached at the oil return passage in the cylinder. The oil temperature sensor sends temperature information to the ECU. The ECU controls the fuel injection quantity, injection timing and ignition timing. For the fuel supply, the power saving fuel pump is installed in the fuel tank, and feeds the pressured fuel to the injector. The fuel pressure is set at 250 kPa. Figure 4 shows the layout of fuel system components.

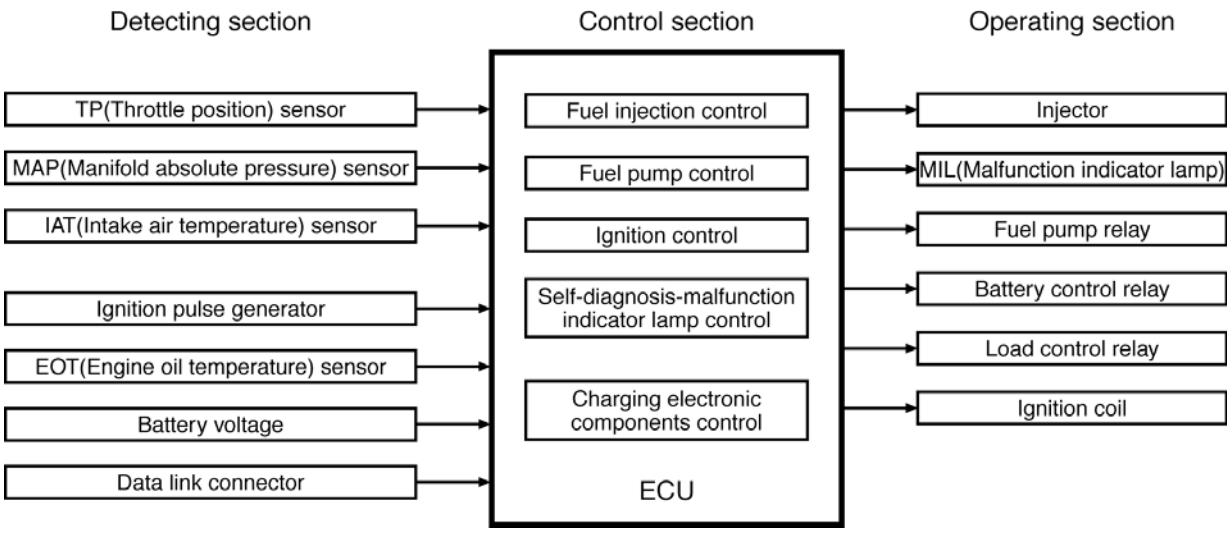



Fig. 2 Configuration diagram of fuel injection volume control system

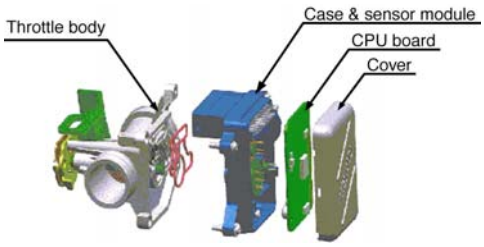



Fig. 3 Overview of module and components

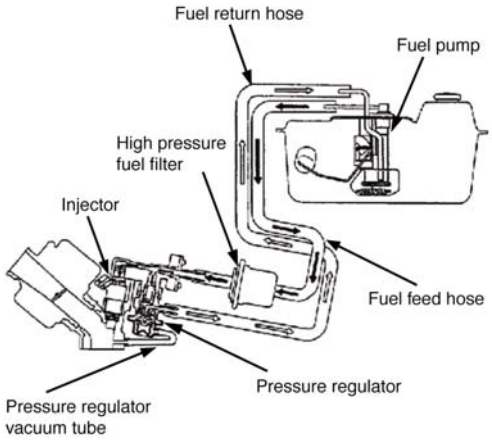



Fig. 4 Layout of fuel supply system

### 4.2. Electric Power Supply Circuit

An ACG is installed for the electric power supply. The power output of the ACG is increased to supply adequate power for the fuel injection system. As shown in Fig. 5, for the electric power supply circuit, a condenser is added in the regulator unit to store energy from the ACG. The relay, (called the battery control relay, load control relay) controlled from the ECU, cuts off the battery and electric loads from the ACG.

## 5. Fuel Injection System

### 5.1. Control of Electric Power Supply on Kick Starting

Usually when starting an engine with an FI system, as well as supplying fuel by operating the ECU, fuel pump and injector with electric power stored in the battery, the electric power is supplied to the ignition coil for sparks. In order to start the engine when the battery is discharged and unable to supply energy to operate the FI system, the electric power generated by the ACG by kick-starting has to be supplied to the ECU, fuel pump, injector and ignition coil. As shown by Fig. 6, however, in the conventional system, the electric power generated by kick-starting is consumed by charging of the battery and other electric loads, causing a voltage drop and not allowing the ECU to function.

To cope with that issue, the ECU in this system starts functioning when the ignition switch is turned on, and detects the battery voltage. The ECU can function when the battery voltage is between six and nine volts, but judges the battery voltage is too low to operate the fuel supply system and the ignition system. The ECU splits the battery and electric loads other than the FI system from the ACG using the relay as shown in Fig. 7. The flowchart of controls is shown in Fig. 8.

When the ECU is activated by the electric power from the ACG, as the battery voltage is less than six volts, just like the above-mentioned conditions, the relay splits the battery and electric loads from the ACG. The voltage lowers and the ECU stops functioning if a large current occurred momentarily in the ignition coil or in the injector of the FI system. The condenser in the regulator stores electric charges to prevent such a voltage drop. Thus the power supply control system mentioned above ensured the starting of the engine by kick-starter, as well as an engine equipped with a carburetor, even when the battery malfunctions, as shown in Fig. 9. After the engine has started or when the battery is in normal condition, the relay is maintained so that power generated by the ACG is supplied to the battery and all electric loads.

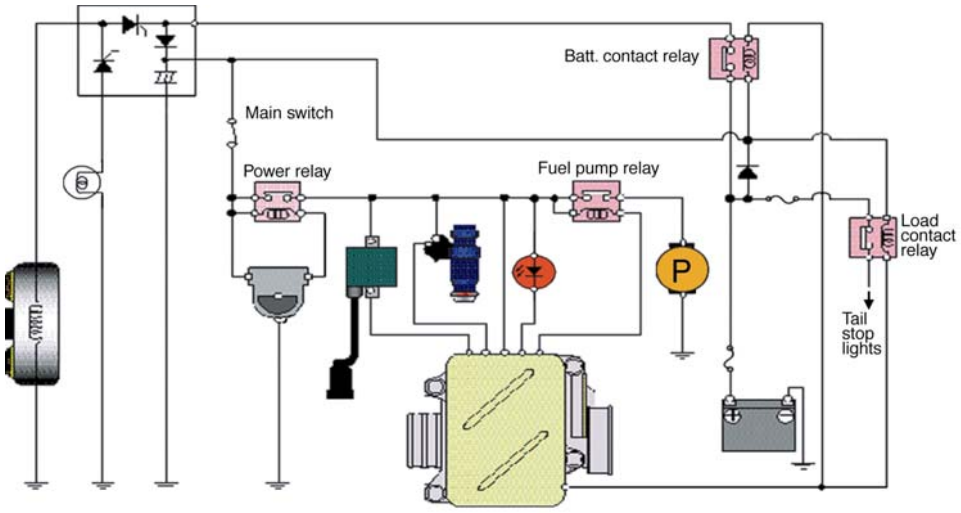



Fig. 5 Power source circuit at normal operation with full charged battery

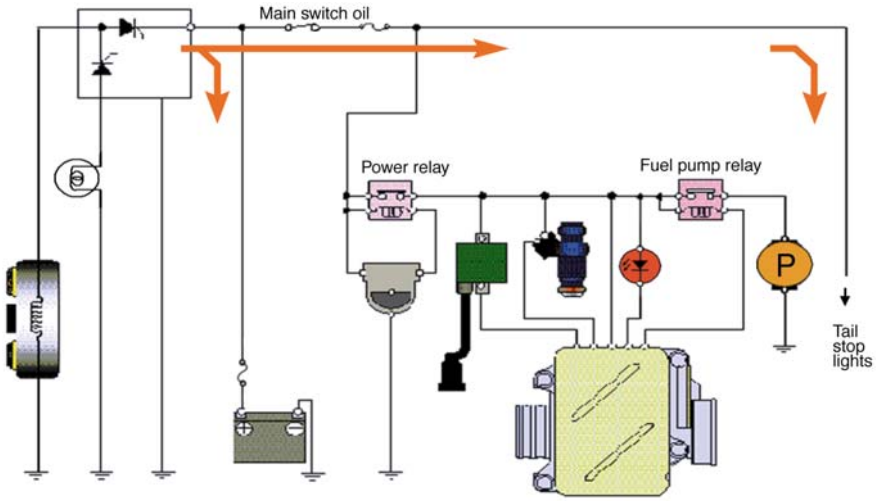



Fig. 6 Usual circuit

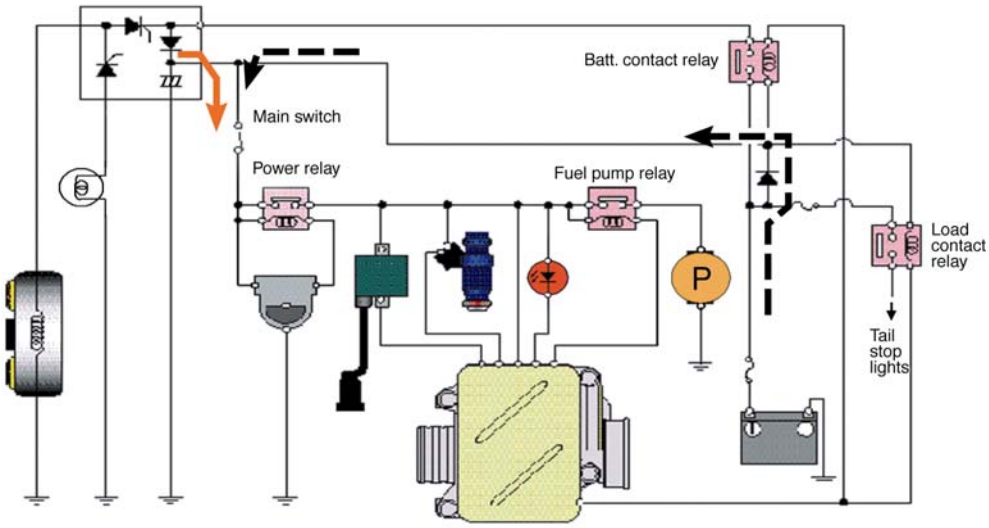



Fig. 7 Cut off of electrical load at kick starting under battery down

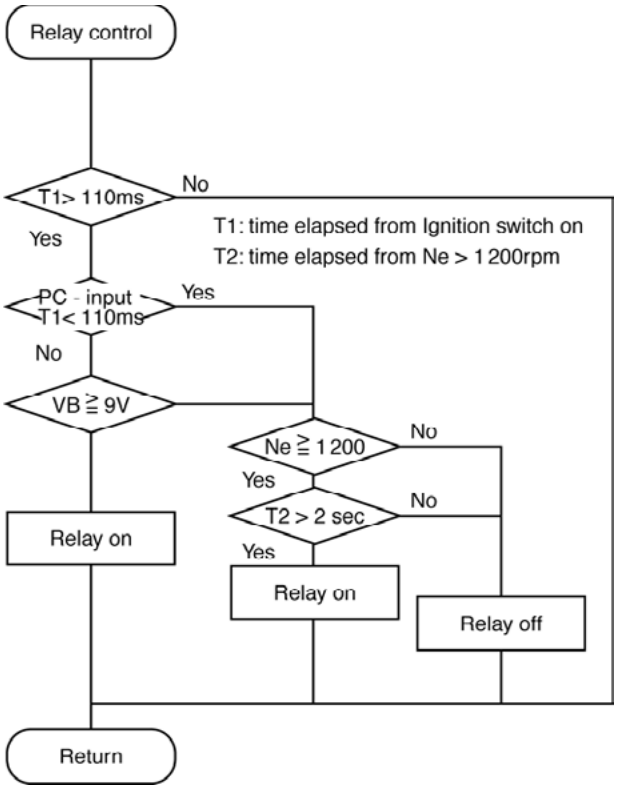



Fig. 8 Flow chart

## 5.2. Fuel Injection Control by Oil Temperature

To allow the ECU to control the air-fuel ratio and the ignition timing appropriately, an output from a sensor is required to understand the engine's warmed-up condition. In case of a liquid-cooled engine, the coolant temperature detected at the exit of the water jacket is used for that purpose. The thermostat regulates the circulating flow rate of the engine coolant to maintain the temperature at the prescribed level. Figure 10 shows an example of such a coolant temperature sensor for a liquid-cooled engine. In case of a natural air-cooled engine, the cooling medium is the air, and it is difficult to measure the air temperature after cooling the engine. Therefore, the engine oil temperature was used to learn the status of the engine warming-up. The engine oil passages of the test engine are shown in Fig. 11. The oil discharged from the oil pump is split between the crankshaft and the cylinder head. The oil supplied to the cylinder head lubricates the camshaft and valves via the cylinder, contacts the cylinder head, then the oil is collected into the passage in the cylinder, and returns to the oil pan. Considering that the oil circulates while absorbing heat from the cylinder and the area close to the combustion chamber, it is said that the engine oil in the air-cooled engine has the same circulation passage as the coolant of a liquid-cooled engine. We therefore consider that the oil temperature in the return passage to the oil pan represents the engine's warmed-up condition, just like the coolant temperature in a liquid-cooled engine. The correlation between the oil temperature and engine's warmed-up condition was confirmed through actual measurements. Figure 12 shows the rise in oil temperature while operating the engine in the exhaust gas emission measurement mode of Thailand.

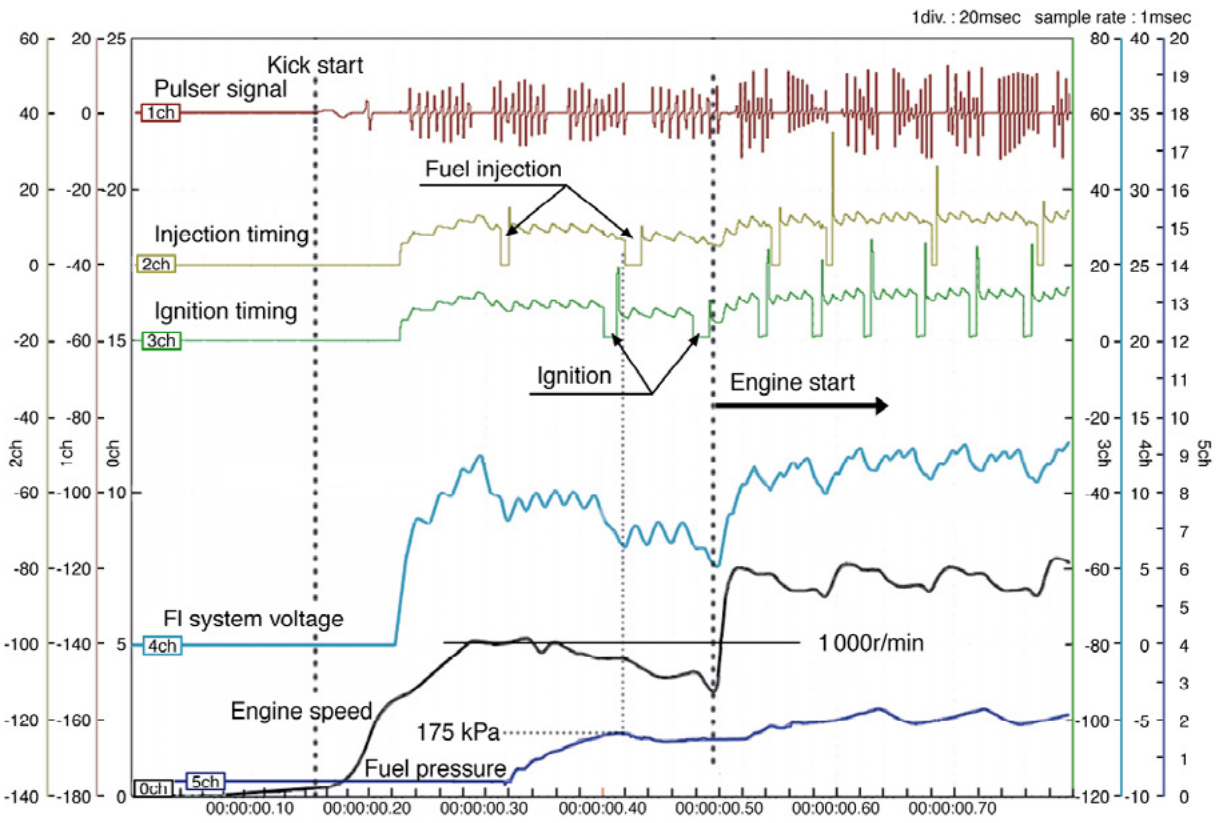



Fig. 9 Measurement data at engine start

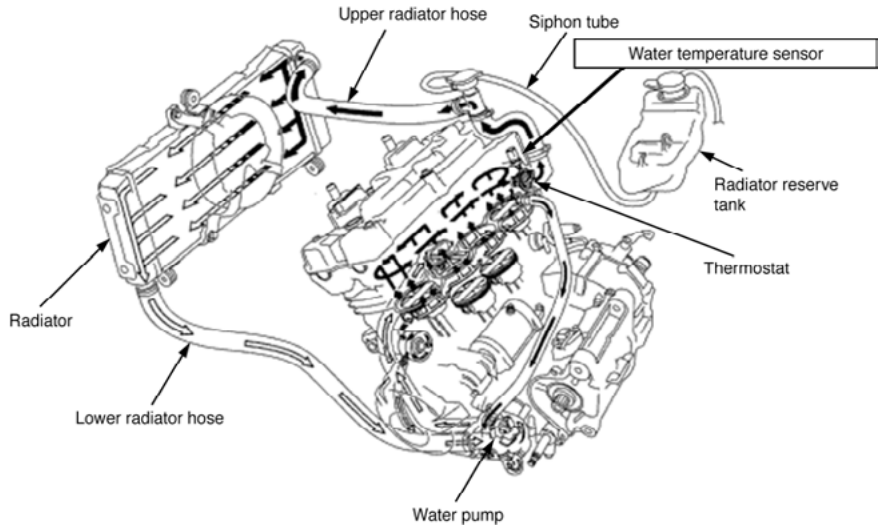



Fig. 10 Water temperature sensor of water cooled engine

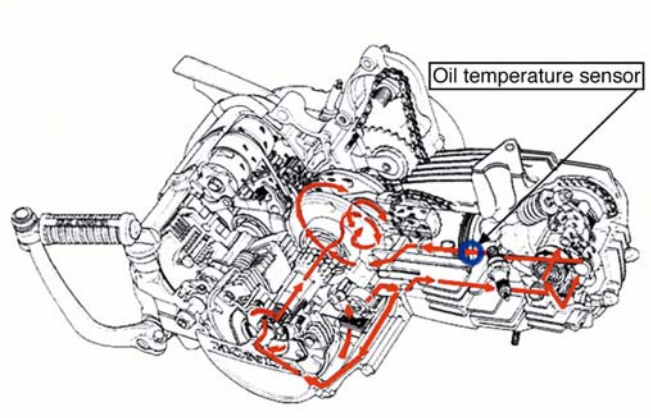



Fig. 11 Layout of oil supply system

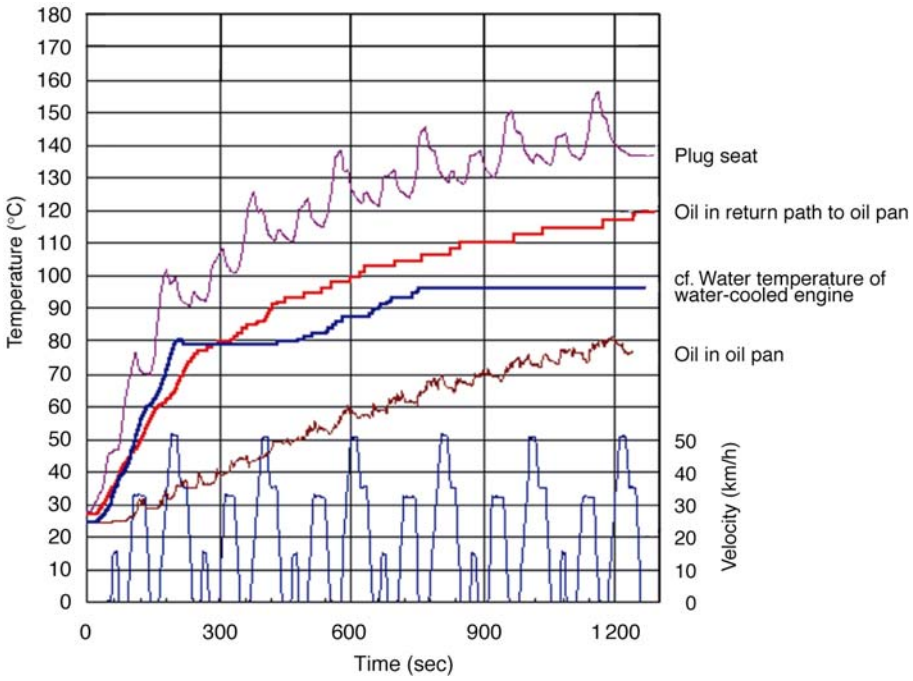



Fig. 12 Rise of temperature in exhaust emission measurement mode of Thailand

In the case of cold starting at an ambient temperature of 25 °C, it takes about 200 seconds to warm up the engine. The oil temperature in the oil pan rises slowly, showing no changes just after starting the engine. The temperature rises approximately 10 °C 200 seconds after starting the engine. Therefore, it is difficult to monitor the engine's warmed-up condition by measuring such small temperature changes. The oil temperature in the oil pan has low correlation with the temperature near the combustion chamber because the engine is fully warmed up 200 seconds after starting. Compared to that, the oil temperature measured at the return passage to the oil pan rises quickly and extensively, by approximately 35 °C, 200 seconds after starting the engine. This results from the oil being directly subjected to high temperatures when passing through the cylinder and cylinder head which creates a high correlation with the temperature near the combustion chamber. Therefore, we have decided to install an oil temperature sensor at the oil return passage in the cylinder, and use the sensor output for the fuel injection control. The output from the engine oil temperature sensor permits control of fuel injection depending on the engine's warmed-up conditions.

### 5.2.1. Actual control by oil temperature

The test engine is mounted behind the front wheel of the test motorcycle with the cylinder head in a flat position. When driving in rain or running through puddles, the water splashed by the front wheel comes directly onto the engine and cools it. The water temperature is close to the ambient air temperature, which is much lower than the engine temperature. As water is much more heat-conductive than air, the temperature of the entire engine lowers considerably. In natural air-cooled engines having no temperature compensation device such as a thermostat in a liquid-cooled engine, even after once warmed up, the engine may be cooled down to the pre-warm up condition in a wet condition. This results in low temperatures around the combustion chamber, and requires compensation of the fuel injection volume. The newly developed control system for fuel injection is very effective under such conditions as mentioned above.

## 6. Effectiveness of Fuel Injection System

By the accurate control of the air-fuel ratio, the exhaust gas emission of the test motorcycle using the FI system has been reduced to such a level that corresponds to 40% of the 4th emission control of Thailand. Figure 13 shows this achievement level. These are results from using only air induction, without using the oxygen concentration feedback control or catalyst. Even when the battery is completely discharged, the engine can be started by the kick-starter. Figure 14 shows the startability of the engine.

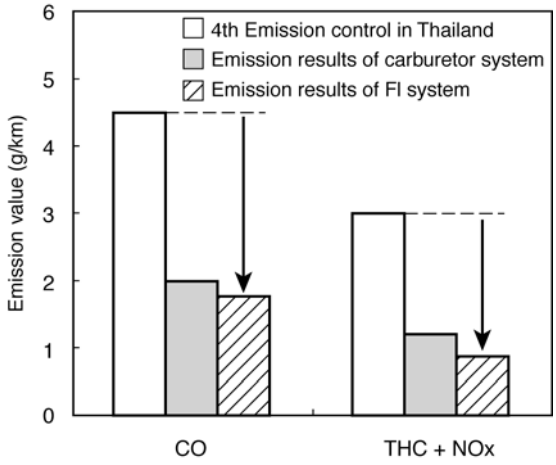



Fig. 13 Results of exhaust gas emission

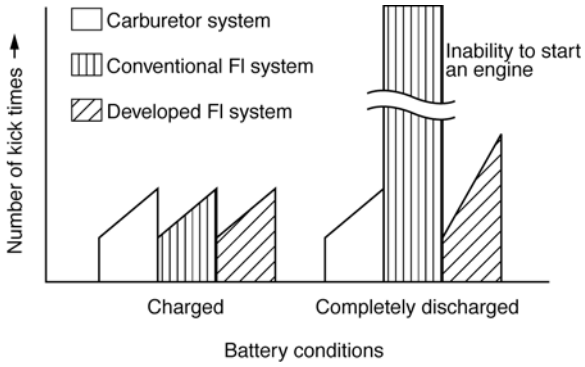



Fig. 14 Startability

## 7. Conclusion

(1) An electronically controlled FI system that permits the starting of the engine by the kick-starter even when the battery is completely discharged has been realized.
(2) By incorporating engine oil temperature detection, the system permits the compensation of fuel injection quantity and ignition timing even in an air-cooled engine.
(3) This electronic control system allows for the application of an FI system to a small, air-cooled engine without the need for major modification to the engine configuration.

This new technology will contribute to the further reduction of exhaust gas emissions for small motorcycles widely used in Asian countries.

## References

(1) Akamatsu, S., et al.: Research for Reducing Exhaust Emission of 4-Stroke Engines for Small Motorcycles Safety Environment Future - International Motorcycle Conference (Organized by Institute for Motorcycle Safety), Munich, Germany (2000)

(2) Abe, M., et al.: Exhaust Emission Reduction for the VFR800FI Safety Environment Future - International Motorcycle Conference (Organized by Institute for Motorcycle Safety), Munich, Germany (1997)

(3) Shimada, N., et al.: Development of an ECU Integrated Throttle Body System Module for Compact Fuel Injection System Used in Small Motorcycles and Scooters, the 12th International Pacific Conference on Automotive Engineering, Bangkok, Thailand (2003)

■ Authors ■



Kenji TAMAKI



Shiro KOKUBU



Shunji AKAMATSU

# Development of PVC-free Mastic Sealer

Takuji ISHIMOTO* Hiroichi KAWASHITA* Kazuyuki OKUI*

## ABSTRACT

A PVC-free mastic sealer has been developed as a recyclable, environmentally friendlier material. Core-shell structure type acrylic resin was selected to replace PVC resin due to its compatibility with the plasticizer in the formulation. The required mechanical properties could not be achieved by simple replacement of the PVC resin with the equivalent amount of acrylic resin. Therefore, we investigated a change in the synthetic rubber component of the sealer to increase strength. As a result, we found that the addition of an SBR rubber with high tearing strength provided the mastic sealer with high strength and high elasticity properties. The fluidity and contamination properties were improved by changing 42% of the calcium carbonate to a surface-treated calcium carbonate and using an inorganic vulcanization catalyst. This provided the PVC-free mastic sealer with the same performance properties as the conventional mastic sealer. Improving the adhesion to aluminum was required due to the increasing application of aluminum for automobile body panels. We focused on the adhesion performance of the sealer by evaluating its absorption of the aluminum stamping oil in the development. Improved adhesion properties to the aluminum was achieved with a solvent that had a low molecular weight of 170. Due to this study, we achieved a PVC-free mastic sealer that is approximately 30% lower in cost than the conventional PVC sealer, which can be used on both aluminum and steel body panels.

## 1. Introduction

With the enactment of the Automobile Recycling Act in Japan, automobile manufacturers are faced with demands to develop technology to reduce the environmental load with automobile designs that use recyclable materials. As a result, it has become necessary to make further efforts for automobile recycling[(1)]. Conventional automobile centers for material recycling consists of breaking down automobiles into components as much as possible and then reusing components or recycling metals, resins and other materials into reusable raw materials[(2)]. Thus far, an effective recycling rate of 85% has been achieved. However, in order to raise the effective recycling to 95% by 2015 as mandated by EU and Japanese regulations, it will be necessary to recycle shredder dust (hereafter “ASR”) into energy by incineration. The main components of ASR include metal, resin, rubber, adhesive, and sealers used in the vehicle. Polyvinyl chloride (hereafter “PVC”) has conventionally been used in the mastic sealer, which is a body sealer. However, when incinerating ASR that contains PVC, a dioxin is produced causing chlorine gas-induced corrosion of the incineration facilities, which is a concern[(3)]. This makes it necessary to reduce the amount of PVC in order to lower the chlorine concentration in the ASR

* Tochigi R&D Center

as much as possible.

Low-strength and high-strength types of mastic sealer are used according to requirements of the outer panel stiffness and deformation of the part. The low-strength type can be substituted with NBR type rubber spot sealer. However, it is necessary to develop a new formulation for the high-strength type.

## 2. Development Goals

Mastic sealer is mainly applied between the skin and the stiffener in the doors, trunk, hood, roof and other parts. This mastic sealer is cured by baking in the paint process. It is applied to prevent interference between the skin and the stiffener to ensure sufficient skin panel stiffness. High-strength type mastic sealer is used when the outer panel stiffness is especially required (Fig. 1). The shear strength of a conventional high-strength mastic sealer is approximately 0.7 to 0.8 MPa. This strength is provided by the PVC component. A key point in developing PVC-free materials was to increase the mastic sealer strength that was set at 0.8 MPa.

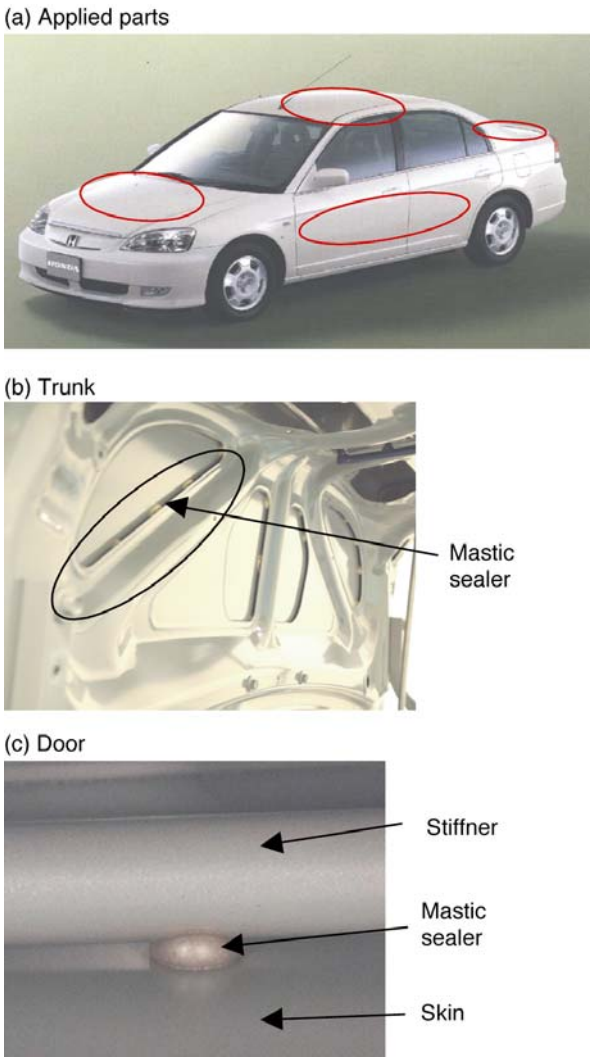



Fig. 1 Examples of application of mastic sealer

Table 1 Main ingredients of mastic sealer

| Main ingredients | Form | Role |
|---|---|---|
| Rubber | SBR/NBR | Elongation; Modulus |
| Vulcanization aid | Organic | Vulcanization for rubber |
| Resin | PVC | Strength |
| Filler | CaCo3 | Workability |
| Plasticizer | DINP | PVC plasticizer; Viscosity adjustment |
| Solvent | High molecular weight | Viscosity adjustment |

In addition, the application of aluminum to the hood and other parts are increasing in order to reduce the vehicle weight. Aluminum has a lower adhesion adaptability, so conventional low-cost mastic sealer for steel sheets cannot be applied. Therefore, the goal for the development of a PVC-free mastic sealer was a low-cost sealer that can be used on both steel and aluminum sheets.

PVC resin is a low cost material that has superior physical properties such as strength and adhesion adaptability. In order to replace PVC resin, components other than the resin were changed in order to maintain these physical properties. The goal was set at maintaining the same performance as the current PVC materials at an equal or lower cost.

The key points when developing a high-strength, high elasticity PVC-free mastic sealer were set as follows:

(1) Technology for maintaining high strength with a PVC-free formulation
(2) Bonding to aluminum sheet
(3) Reducing the cost

## 3. Material Formulation

### 3.1. PVC Replacement and Improvement of Physical Properties

Table 1 shows the main components of the current mastic sealer and the roles of each component.

D-isononylphthalate (hereafter “DINP”) has conventionally been used as the plasticizer in the mastic sealer. DINP is a low cost, general-purpose plasticizer that is a large percentage of the formulation and was used as the plasticizer in this development.

In developing a PVC-free mastic sealer, the formulation was studied as follows in order to satisfy the mastic sealer performance requirements.

#### 3.1.1. Selection of the PVC replacement resin

Acrylic resin was selected to replace the PVC resin material. Acrylic resin has an excellent compatibility with the general-purpose plasticizer DINP, so it is an appropriate replacement resin for PVC resin. The high-strength type mastic sealer has a PVC resin content of approximately 10%, so replacement with the same amount of acrylic resin was attempted. Figure 2 shows the change in the viscosity of a sealer that had the same amount of general-purpose acrylic resin polybutylmethacrylate (hereafter “PBuMA”) as PVC. The viscosity increased after storage (40 °C, 168 hours)

compared to the initial viscosity. The results showed that simply changing to PBuMA causes a decrease in storage stability. Therefore, an acrylic resin formulation with a core-shell structure that uses polymethylmethacrylate (PMMA) that is known to have an excellent stability with DINP as the outer shell in combination with the general-purpose acrylic resin PBuMA as the core was investigated. This formulation achieved the target storage stability as shown in Fig. 2. Based on these results, the decision was made to use acrylic resin with a core-shell structure as the replacement for PVC in the formulation.

Figure 3 shows the shear strength with the equivalent amount of core-shell structure acrylic resin as PVC resin. The results showed that replacement with the same amount of core-shell structure acrylic resin causes the shear strength to drop. Therefore, the decision was made to replace the PVC with the same amount of core-shell structure acrylic resin and to adjust the strength by some other formulation change.

### 3.1.2. Synthetic rubber formulation

An attempt was made to improve the mechanical characteristics with the synthetic rubber. NBR or SBR type synthetic rubber compounds have conventionally been used as the synthetic rubber. NBR has a high polarity, which makes it suitable for use in combination with PVC resin that has a high polarity. However, phase separation occurred and the strength dropped as shown in Fig. 3, when used together with acrylic resin that has a low polarity. Therefore, a SBR type synthetic rubber compound with a low polarity was used. There are different grades of SBR type synthetic rubber compounds each having different mechanical characteristics such as strength and hardness. Therefore, the change in shear strength of the mastic sealer when changing the strength

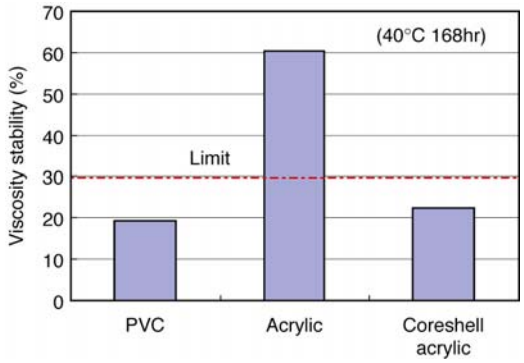



Fig. 2 Influence of different resins on viscosity stability

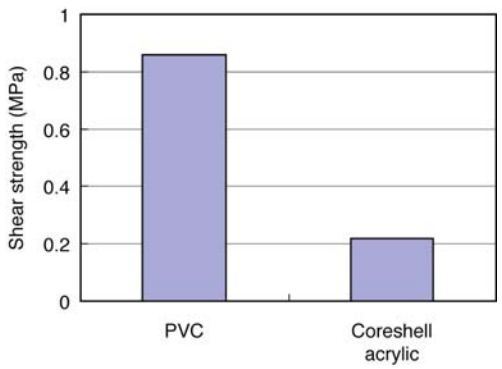



Fig. 3 Influence of different resins on share strength

Table 2 Properties of rubber compound

| Grade (strength) | Low | Middle | High |
|---|---|---|---|
| Tearing strength (kN/m) | 45 | 65 | 75 |
| Hardness (JISA) | 65 | 80 | 90 |

grade of the synthetic rubber compound was investigated. Table 2 shows the tearing strength and hardness of the synthetic rubber compounds used in this study.

Figure 4 shows the relationship of the tearing strength of the synthetic rubber compound versus the shear strength of the mastic sealer containing the synthetic rubber compound.

This figure showed that the tearing strength of the SBR type synthetic rubber compound has a direct relation to the shear strength of the mastic sealer. Therefore, the target shear strength can be obtained by formulating a SBR type synthetic rubber compound with a tearing strength of 75 kN/m or more. In addition, the rubber content can be reduced and with the low cost of SBR type synthetic rubber compounds it provides a cost effective way to improve the shear strength and other mechanical characteristics.

Based on these results, DINP was selected as the plasticizer, acrylic resin with a core-shell structure was selected to replace the PVC resin, and a high-strength type SBR synthetic rubber compound was selected as the rubber component.

### 3.1.3. Pretreatment contamination

In order to obtain high strength by cross-linking the rubber in the curing process, it was necessary to increase the amount of vulcanization catalyst used for SBR type synthetic rubber compounds. However, increasing the vulcanization catalyst amount contaminated the alkali degreasing solution in the pretreatment process.

In the pretreatment process, the mastic sealer is sent through the pretreatment tank before curing, so care must be taken to prevent solution contamination by the extracts from the sealer. Within the pretreatment process, the alkali degreasing solution is particularly susceptible to solution contamination. Yellowing of the solution due to the mastic sealer formulation was a concern. Therefore, an investigation of each component in the formulation was immersed in a

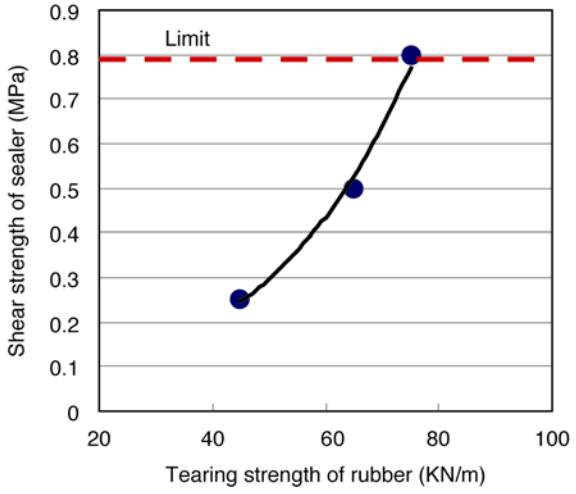



Fig. 4 Relationship of tearing strength of rubber compound and strength of sealer

45 °C degreasing solution for two minutes and the solution was checked for color change. Figure 5 showed the change in color when the vulcanization catalysts were immersed in an alkali degreasing solution and the results when the mastic sealer containing the vulcanization catalyst were immersed in the alkali degreasing solution. The vulcanization catalysts generally used thus far have been organic. The immersion test using only the vulcanization catalyst showed that the organic vulcanization catalyst dissolved and yellowed the alkali degreasing solution. Therefore, the formulation was changed from an organic catalyst that dissolved in the alkali degreasing solution to a chemically stable inorganic vulcanization catalyst.

### 3.1.4. Surface-treated calcium carbonate formulation

Using a high-strength synthetic rubber compound provided sufficient strength even when the synthetic rubber compound content was reduced. However, reducing the rubber compound amount increased the overall liquid component content of the sealer, which was found to increase the fluidity (sagging) when the temperature increased during the curing process. Sagging occurred because the overall liquid component content of the sealer increased, making the sealer more susceptible to drops in viscosity at higher temperatures. Therefore, improvement was attempted by changing the calcium carbonate, which is used in the formulation to adjust the viscosity. Calcium carbonate is included in particle condition as a solid within the mastic sealer paste. The viscosity of the sealer can be increased by the interaction of the liquid components with the solids. It is known that the intermolecular force within the sealer can be raised to further increase the viscosity by altering the surface condition of the calcium carbonate with the particle size and the surface functional group. In this development, the fluidity of the sealer was improved by replacing part of the conventional calcium carbonate with organically surface-treated calcium carbonate in order to increase the intermolecular force with the liquid components that would ultimately increase the viscosity at high temperatures.

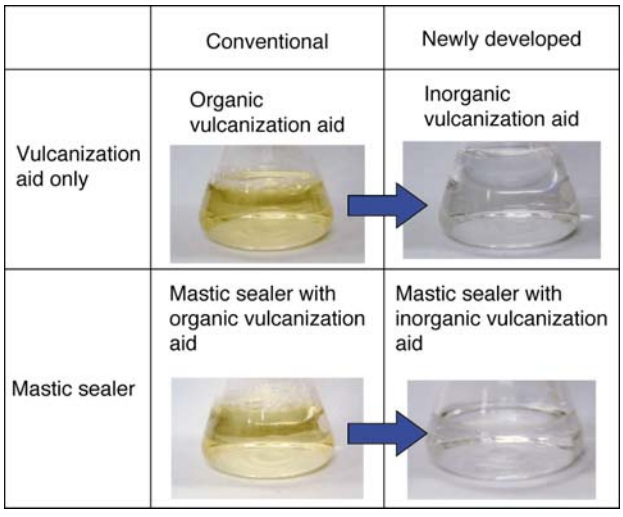



Fig. 5 Pretreatment test

Fluidity was evaluated according to ASTM D2202 and the results are shown in Fig. 6.

When the high-strength synthetic rubber compound was used with conventional non-surface-treated calcium carbonate it resulted in sagging of 8 mm. However, increasing the ratio of surface-treated calcium carbonate to 42% of total calcium carbonate reduced the sagging amount to 0 mm; while still maintaining the same workability as the conventional mastic sealer.

As a result, the decision was made to use a filler formulation fortified with 42% surface-treated calcium carbonate.

### 3.2. Adhesion Performance

Tests were conducted to confirm the adhesion performance to steel sheet with the PVC-free mastic sealer formulation. Figure 7 shows the shear strength test results. The SPCC material and GA material both resulted in cohesive failure, indicating that sufficient adhesion performance was obtained.

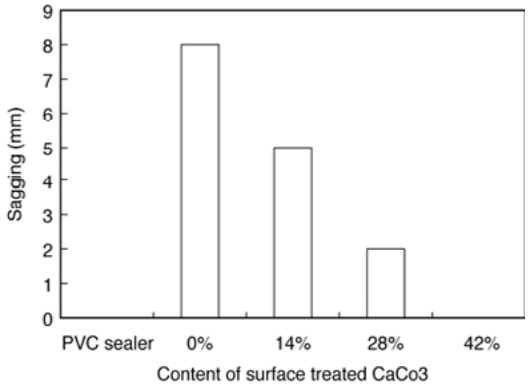



Fig. 6 Influence of surface treatment $CaCO_3$

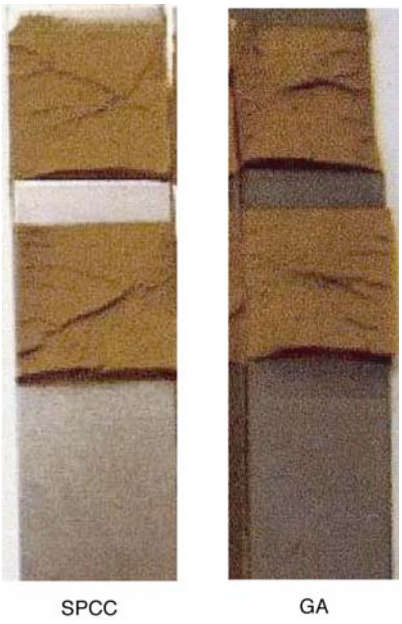
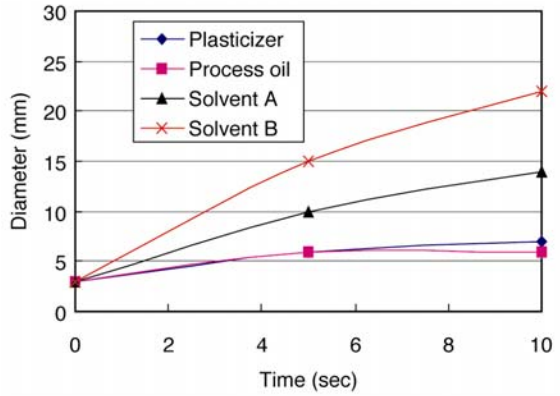



Fig. 7 Shear strength test for steel

## 4. Adhesion to Aluminum

Sealers in the welding process are used on oily surfaces. The conventional mastic sealer was designed to obtain adhesion by absorbing the stamping oil on the steel sheet surface so that the adhesive component inside the sealer contacts the material surface. Different stamping oils are used for aluminum than for steel sheets. The stamping oil for aluminum is not sufficiently absorbed by the mastic sealer developed for steel sheets, so adhesion cannot be obtained. Therefore, the goal of the development of a PVC-free mastic sealer was to improve adhesion by absorbing the aluminum stamping oil. First, improving the wettability between the liquid components of the mastic sealer and the stamping oil was investigated as a means of increasing the amount of stamping oil absorbed by the sealer. Investigation of the wettability of the plasticizer, process oil and solvents are the liquid components conventionally included in the mastic sealer formulation. Measurements were performed by dropping each component onto an aluminum sheet coated with stamping oil and then measuring the increase in the diameter of the drop after 5 seconds and 10 seconds. Figure 8 shows the results.




| | | Plasticizer | Process oil | Solvent | |
|---|---|---|---|---|---|
| | | | | A | B |
| Drop diameter (mm) | 5sec | 6 | 6 | 10 | 15 |
| | 10sec | 7 | 6 | 14 | 22 |
| Molecular weight | | 400 | 500 | 250 | 170 |
| Adhesion to Al | | No good | No good | No good | OK |

Fig. 8 Wettability test




Fig. 9 Shear strength test for Al

The solvents exhibited better wettability than the plasticizers and process oils, which have high molecular weights. The solvent with the lower molecular weight had the best wettability. The results indicated that using a solvent with a lower molecular weight that has a better wettability increases the amount of stamping oil absorbed into the sealer, which can improve the adhesion performance to aluminum. Figure 9 shows the shear strength test results for mastic sealer using a solvent with a molecular weight of 170. Cohesive failure resulted for each type of aluminum material that used a solvent with a higher than 170 molecular weight. Therefore, using a solvent with a molecular weight of 170 ensured sufficient adhesion to aluminum body panels.

Table 3 Ingredients

| | PVC | PVC-free |
|---|---|---|
| Rubber | SBR/NBR | High strength SBR |
| Resin | PVC | Acrylic |
| Filler | CaCo3 | Surfice treatmented CaCo3 |
| Plasticizer | DINP | DINP |
| Vulcanization aid | Organic | Inorganic |
| Solvent | High molecular weight | Low molecular weight |

Table 4 Properties

| | Conventional | Newly developed |
|---|---|---|
| Hardness | 27 | 27 |
| Shear strength (MPa) | 0.69 | 0.8 |
| Elongation (%) | 210 | 160 |
| Density | 1.41 | 1.4 |
| Stability (40°C, 168hr) | ○ | ○ |
| Workability (170°C cure) | ○ | ○ |
| Adhesiveness (Fe) | ○ | ○ |
| Adhesiveness (Al) | × | ○ |

## 5. Formulation Specifications

### 5.1. Formulation Specifications

The following specifications were determined as a result of the above formulation studies. The newly developed formulation achieved a cost reduction of 30% compared to the conventional PVC type mastic sealer.

### 5.2. Physical Property Values

Table 4 shows the various properties of the newly developed sealer. This shows that the newly developed PVC-free mastic sealer has the same performance as the conventional sealer.

## 6. Conclusion

The formulation was adjusted to develop an inexpensive, high-strength PVC free mastic sealer based on acrylic resin. The following results were obtained:

(1) Acrylic resin with a core-shell structure was found to be suitable for developing a high-strength PVC-free mastic sealer.
(2) The sealer strength was improved at a low cost by using a SBR type synthetic rubber compound with a high tearing strength in the formulation.
(3) The vulcanizing catalyst had the greatest effect on contamination of the degreasing solution and was improved by changing from an organic to an inorganic vulcanizing catalyst.
(4) Changing 42% of the calcium carbonate filler to a surface-treated calcium carbonate made it possible to increase the intermolecular force within the system, which improved the fluidity.
(5) Adhesion performance to aluminum sheets were ensured by selecting a solvent with a molecular weight of 170, which has excellent compatibility with the aluminum stamping oil.

This newly developed high-strength PVC-free mastic sealer for both steel and aluminum sheets was first applied to the S2000 released in 2003, making it the first such environmentally friendlier, PVC-free material technology to be applied to the mass production of an automobile.

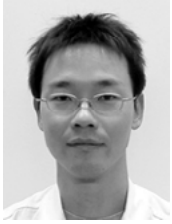
## References

(1) Hosoda, E.: Toward Legislation of Proper Waste Treatment and Recycling of ELV, Waste Management Research, Vol. 12, No. 5, p. 292-302 (2001)

(2) Wada, Y., Miura, H., Nakano, K.: Quantitative Evaluation Method of Recycling and Application to the Automobile Bumper Recycling, Journal of the Japan Society of Waste Management Experts, Vol. 7, No. 2, p. 49-57 (1996)

(3) Ishibashi, N., Okajima, S., Yoshihara, Y., Nishiwaki, K., Hiraoka, M.: De Novo Formation of Polychlorinated Dibenzo-p-Dioxins and Polychlorinated Dibenzofurans during the Gas Cooling Process in a Solid Waste Incinerator, Journal of the Japan Society of Waste Management Experts, Vol. 14, No. 1, p. 17-26 (2003)

■ Authors ■



Takuji ISHIMOTO



Hiroichi KAWASHITA



Kazuyuki OKUI

# Development of Driving Position CAD System Using Digital Human Model

Yasunari KATAGIRI* Kouji MORIYASU* Fuminobu KUROSAWA**
Yoshihiro ABE* Taiichi HASHIMOTO*

## ABSTRACT

The design of automobile packages should generate products that accommodate the diverse body types of vehicle users. The use of digital human model (DHM) technology, which enables designers to more easily reproduce different body types on a computer, has recently become more widespread as a means of enabling this. Honda also employs DHM, but has attempted to produce more customer-oriented designs by analyzing driving position in terms of angles of joints and using the results of these analyses as the basis for evaluation of the operation of the driving position. As a result, the position of the DHM can be evaluated in terms of the angles of the joints, providing the foundation of a system in which the development of a package appropriate for a variety of body types can proceed simultaneously with design.

## 1. Introduction

Advances in body size measurement technology and computer technology have enabled the form and motion of the human body to be more accurately reproduced on a computer. Human factor analysis, which once required test subjects, can now be performed simply, quickly and objectively through simulations employing DHM.

A variety of approaches can be taken when using DHM technology, differing according to the purpose for which the technology is employed.

Experimental approach: The posture and motion of test subjects are measured, and the data obtained are used to construct a database. This approach enables posture and surface morphology to be more accurately reproduced.

Robotics engineering approach: The major methods employed in this approach are inverse kinematics and inverse dynamics. This approach enables dynamic motion to be reproduced on the basis of a limited amount of data.

Biomechanics approach: This approach enables simulation of the internal organs and muscles. The increased accuracy obtained through modeling the internal parts of the body makes this approach the one with the most promise for the future. The research described in this paper focused on posture, and therefore employed a methodology drawn from the experimental approach. A number of software applications have been developed for DHM; this research uses RAMSIS, developed by the German manufacturer Human Solutions, GmbH.

A variety of different studies are required in the actual development process to determine driving position. Of these, examples of the application of RAMSIS have been selected for discussion in this paper. Figure 1 shows an example involving evaluation of the area around the knees and elbows. Here DHM of different body types are employed to

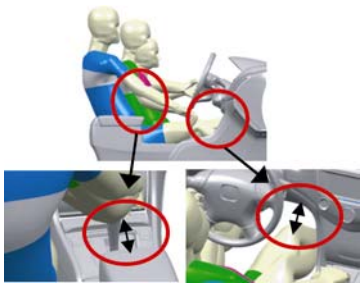


Fig. 1 Driving position evaluation

* Tochigi R&D Center
** Wako R&D Center

measure the clearance between the knees and the lower cover and the elbows and the armrests in order to determine whether there is sufficient clearance to allow comfortable driving operations.

This makes it possible to evaluate whether there is enough clearance to shift gears and operate the pedals; however, it is currently not possible to evaluate ease of operation on the basis of the posture of the RAMSIS DHM. It was therefore necessary to focus on the formulation of indices to enable the quantitative evaluation of posture, and develop a technique employing RAMSIS to enable evaluation based on customer satisfaction.

## 2. Research Goals

The goal of this research was to use the results of analyses of driving postures and joint angles to formulate a quantitative evaluation system employing RAMSIS.

To commence the research, the factors regarding the driving position were abstracted, as shown in Fig. 2. The research focus was restricted to operation, with operation of the steering wheel and pedals becoming the major area of study.

## 3. Test Method

Figure 3 shows an outline of the test method. First, vehicle tests were conducted with test subjects to determine posture and obtain subjective evaluations of the ease of operating the steering wheel and the pedals. Next, the sitting postures of the test subjects in the vehicles were reproduced on a test bench, and the angle of each joint of their bodies was measured using a technique enabling quantification of posture. Finally, indices were formulated by correlating subjective evaluation data with measurements of joint angles.

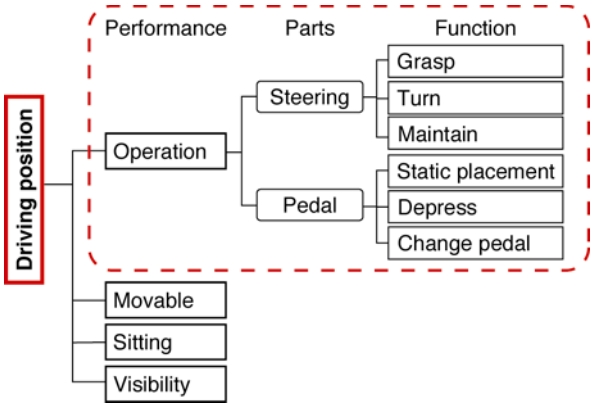



Fig. 2 Factor analysis of driving position

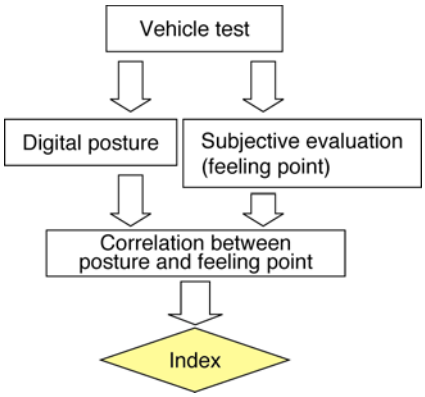



Fig. 3 Test flowchart

Table 1 Definition of 3 style posture

| Posture | Definition |
|---|---|
| Comfort position | Each subject can freely establish driving posture |
| Forward position | Each subject moves to forward position which represents limit for driving |
| Rearward position | Each subject moves to rearward position which represents limit for driving |

Table 2 Subjective evaluation

| Rating | Evaluation |
|---|---|
| 5 | Excellent (Extremely comfortable) |
| 4 | Good |
| 3 | Acceptable |
| 2 | Barely acceptable |
| 1 | Not acceptable |

### 3.1. Vehicle Test Conditions

(1) Test subjects

24 males, mainly in their 30s, ranging from 160 to 190 cm in height

(2) Test vehicle

4-door sedan (AT)

(3) Postures for evaluation

Vehicle tests were conducted using each of three postures shown in Table 1.

(4) Test course

A course in the research facility representing an urban area was selected to enable normal driving postures to be reproduced.

### 3.2. Method of Subjective Evaluation

Subjective evaluation of ease of operation of the steering wheel and pedals in each of the three postures shown in Table 1 was based on the scale shown in Table 2. Test subjects were also interviewed to determine the posture which placed the maximum burden on their bodies during operation of the steering wheel and pedals.

### 3.3. Quantification of Posture

The sitting postures obtained from the driving tests were reproduced using a DP simulator, and the resulting joint angles were measured. Two cameras were employed to record each subject's driving posture from the front and the side, and the posture of each subject was quantified from the image data using specialized software[1]. This data was imported into a CAD program, enabling the dimensions of each body, including joint angles (elbows, knees, ankles), to be measured. Figure 4 shows the flow of the quantification process from a photograph taken from the side.

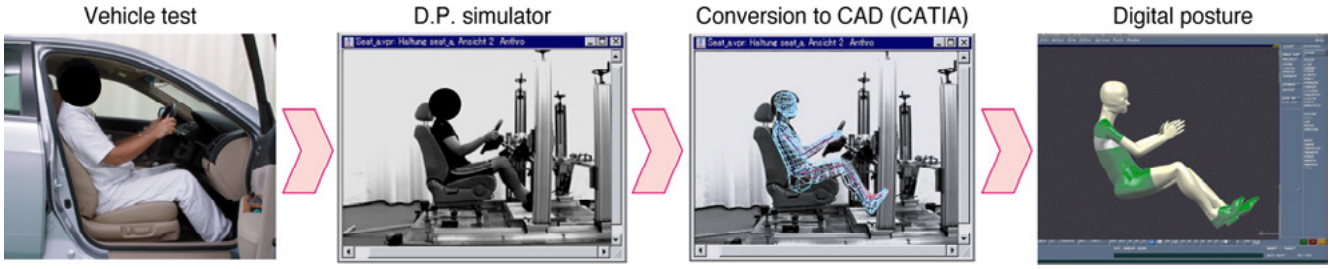



Fig. 4 Flowchart of digital posture simulation

## 4. Determining Areas of Focus

Subjective evaluations of the parts of the body which experienced the maximum burden during vehicle operation were used to abstract the parts of the body with the greatest effect on driving comfort in each of the driving positions employed. The results shown in Figs. 5 and 6 were obtained.

(1) When operating the steering wheel, the angle of the elbows has the greatest effect.
(2) When operating the pedals, the angle of the ankles has the greatest effect.

Analyses were therefore conducted focusing on the elbows and ankles.

## 5. Results of Analyses

The relation between height and elbow angle for each subject in the three driving positions was graphed using a regression line, with the results shown in Fig. 7. The relation between height and elbow angle was shown to be proportional, with the angle decreasing with decreasing subject height. The reason for this is thought to be that shorter test subjects generally possess less muscular strength than taller subjects. It can be predicted that a smaller test subject will slide the seat forward to enable them to exert muscular strength more easily, and this reduces the distance between the steering wheel and their shoulders. As a result, when they grip the steering wheel, the angle of their elbows is therefore smaller than it would be for a taller driver.

The relation between ankle angle and height was graphed in the same way, producing the results shown in Fig. 8. Here, there is a slight inverse relationship between ankle angle and height in the rearward and forward positions, but the relation in the comfort position is basically constant. Ankle angle was therefore judged to be largely unrelated to height, and essentially constant.

This is thought to be because the movements made by the ankle in operating the pedals are small, and produce only a small muscular burden. Because this has no relation to relative muscular strength or weakness, the angle of the ankle

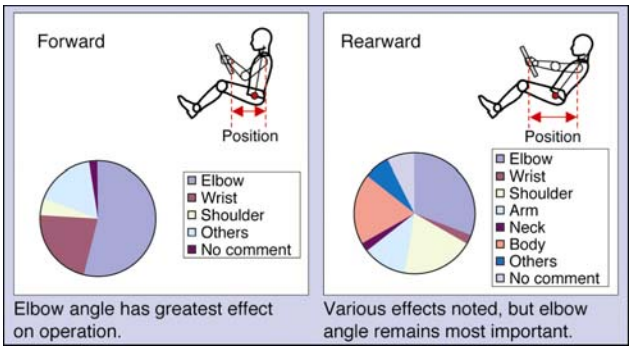



Fig. 5 Steering operation

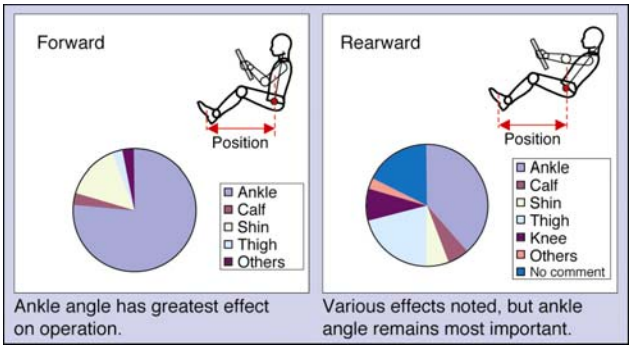



Fig. 6 Accelerator pedal operation

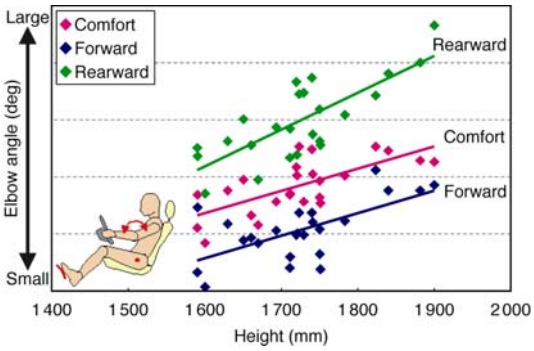



Fig. 7 Relation between elbow angle and height

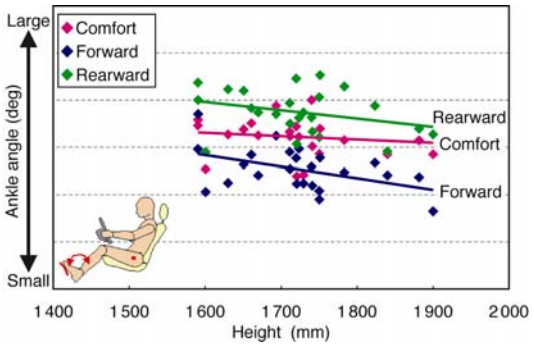



Fig. 8 Relation between right ankle angle and height

at which operation of the pedal is easiest is the same for drivers of different height. It is therefore constant no matter what physical type the driver can be classified as.

At the beginning of the study, it was predicted that subjective evaluations of the ease of operating the steering wheel and the pedals in the forward and rearward postures would cluster around the three-point rating (acceptable) level, but some test subjects recorded two- and one-point ratings (barely/not acceptable). The results from these test subjects were not usable to create indices as the data was originally compiled, and the study therefore continued as described in the next section.

## 6. Establishing Indices

### 6.1. Estimating Joint Angle (Acceptable Point)

Indices enabling evaluation of the ease of operating the steering wheel and the pedals were established on the basis of measurements of joint angles and subjective evaluations of ease of operation. Three-point rating evaluations were considered the acceptable point for indices, and data for test subjects recording one- and two-point evaluations were therefore corrected. A graph of the subjective evaluations of each test subject in each of the three test positions and the angle of their joints in each position was formulated to enable this correction. The subjects' joint angles at the three-point level (acceptable point) for forward and rearward postures were estimated from this graph. Figure 9 shows the method used to estimate the three-point level elbow angle for forward posture for one test subject.

### 6.2. Verification of Appropriateness of Estimated Joint Angle

A test of the appropriateness of the estimates of elbow and ankle angles was conducted with six of the test subjects. The D.P. simulator mentioned above was used to determine the three-point level joint angles for the test subjects, and they were asked to subjectively evaluate the ease of operation of the steering wheel and pedals in that position. Almost all the test subjects evaluated ease of operation at the estimated joint angles at the three-point level.

### 6.3. Indices of Operation

Figures 10 and 11 show, respectively, the indices of operation of the steering wheel and pedals formulated by obtaining joint angles at the three-point level, as described above.

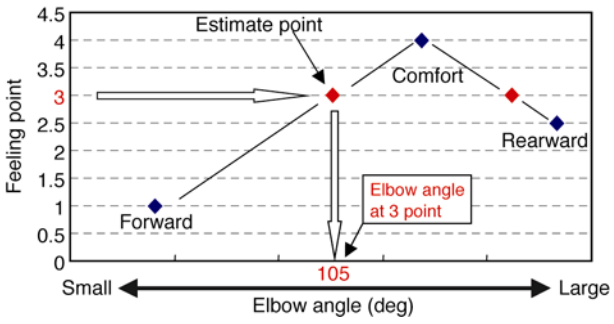



Fig. 9 Relation between elbow angle and feeling point

The following explanation will focus on Fig. 10, the index of steering wheel operation. The straight lines for "rearward" (green) and "forward" (blue) driving positions show three-point subjective evaluations of steering wheel operation for each posture.

The yellow area between these lines represents the recommended area for elbow angles enabling comfortable operation of the steering wheel. The ideal comfort angle is shown by the red line running approximately through the center of the yellow area. Driving posture should be as close as possible to this line. A RAMSIS simulation was conducted using data obtained from two mass-production vehicles, and elbow angles were plotted. The results showed that JM50 percentile and 95 percentile fell within the recommended area. These results are appropriate in consideration of marketplace evaluations.

The indices developed in this study were compared to another set of indices[2] as a reference, and demonstrated the following characteristics:

(1) The restriction of the evaluation zone against the other indices enabled more accurate evaluation of steering wheel operation.

(2) Rigorous and wider range of evaluation was enabled by the fact that the newly developed indices make possible evaluation of comfort for individual body types.

The indices developed in this study can be used in the same way to enable the evaluation of the operation of the pedals.

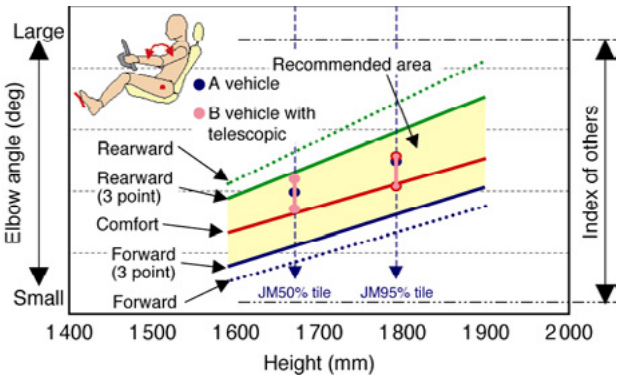



Fig. 10 Index of steering operation

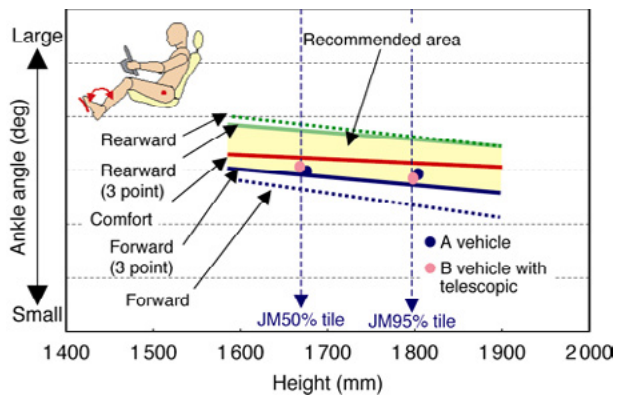



Fig. 11 Index of pedal operation

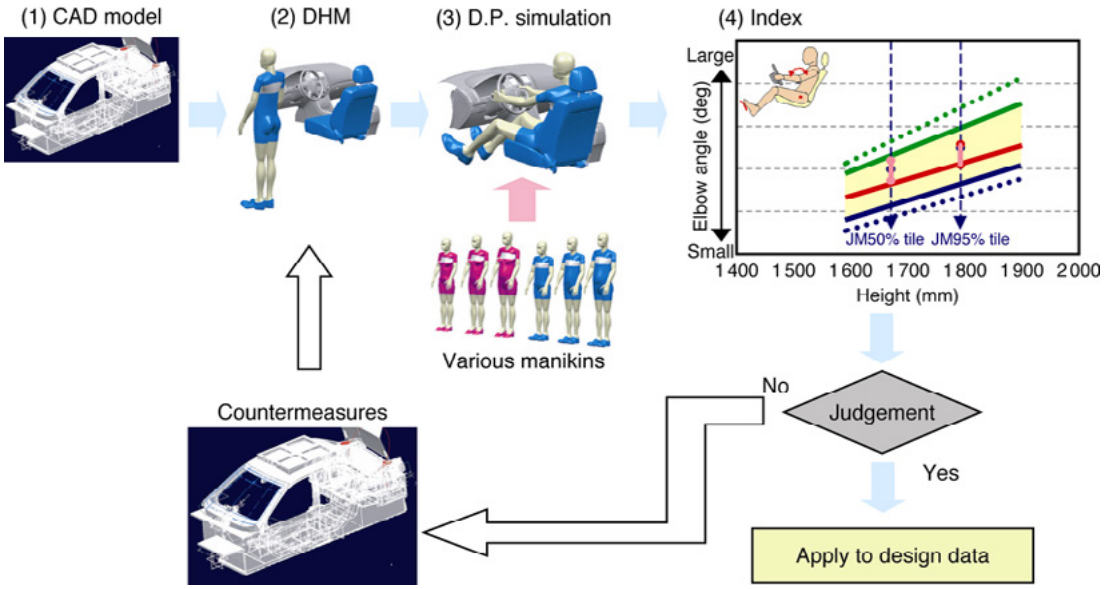



Fig. 12 D.P. evaluation system

## 7. Newly Developed System

Figure 12 shows the newly developed system employing RAMSIS.

(1) The CAD model required for the simulation is formulated.
(2) The parameters (height, seated height, etc.) necessary for selecting a body type from RAMSIS are input.
(3) The RAMSIS model constructed in (2) is seated in the predetermined position.
(4) Posture is evaluated using the newly developed indices.

Following the steps outlined above, the new system enables a human factor analysis to be conducted using CAD.

## 8. Conclusion

The research described in this paper developed indices to act as a foundation in the evaluation of driving position based on customer satisfaction. The newly developed system can be used as part of CAD from the earliest stages of development, enabling human factor analysis to proceed simultaneously with the production of designs.

The indices developed in this study were produced using Japanese males as test subjects. Future research will be required to determine the applicability of these indices to Japanese women and to men and women of different ethnicities.

## References

(1) T. Seitz, H. Bubb: Measuring of Human Anthropometry, Posture and Motion, SAE INTERNATIONAL (1999)

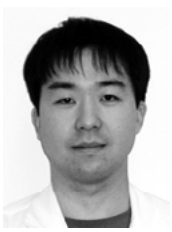
(2) Yanagise, T.: Jidousya no Ningenkogakugijyutu, JSAE, p. 38-41 (1998)

■ Authors ■


Yasunari KATAGIRI


Kouji MORIYASU


Fuminobu KUROSAWA


Yoshihiro ABE


Taiichi HASHIMOTO

# Non-linear, Strain Rate-dependent Behavior of Polymer at Room Temperature: Experimental Findings

Hiroyuki MAE* Kenji TAKADA*
Junichi TAKAHASHI** Toshiharu YAMAMOTO**

## ABSTRACT

Due to the strong non-linearity and the difficulty of obtaining data on the behavior of polymers at high strain rates, most crash simulations use material data based on quasi-static testing.

This study therefore attempted to obtain material data for polymers used in the interior and exterior of automobiles at high strain rates. The material data obtained differs from data obtained through the linear interpolation of stress to model the behavior of polymers at high strain rates. The results of the tests conducted in this project have been compared with results obtained using commercial finite element models.

## 1. Introduction

Recently, crash simulations have been introduced to vehicle body design in automotive development. Crash simulations for steel materials, which are the main materials used in automobiles, currently exhibit high calculation accuracy in axial buckling calculations for structural components, and have reached a level that is sufficient for practical application[(1)]. One factor for this is that the stress-strain behavior of steel materials at high strain rates is accurately obtained[(2)]. On the other hand, in simulations using polymers, the materials exhibit more complex stress-strain behavior, so there have been few research cases[(3)]. In addition, there was also the issue that when attempting to obtain material data at high strain rates, the measurement value fluctuation due to vibration is larger than the stress-strain behavior of the test specimen[(4)].

Therefore, this study constructed a method allowing measurement of stress-strain behavior at high strain rates, which had been difficult for polymers. In addition, findings are also reported regarding the stress-strain behavior of polymers at high strain rates, which is difficult to estimate using conventional extrapolation. Finally, the simulation results of applying the obtained stress-strain behavior to finite element models are presented.

## 2. Mechanical Properties of Polymers

This section describes an overview of the mechanical properties of polymers.

The mechanical properties of polymers include the five items of viscoelasticity, strain rate dependence, hydrostatic pressure dependence, extrusion molding flow direction dependence, and humidity dependence. These properties are known to differ greatly for each polymer type. The main goal of crash calculations is to calculate the high-speed deformation of materials, so the stress-strain behavior of materials during high-speed deformation is an important factor. Therefore, this study focused on the viscoelasticity and strain rate-dependence that are highly dependent on the material deformation rate. Figure 1 shows a typical example of these characteristics.

* Tochigi R&D Center
** Asahi Kasei Corporation

This paper reports on tests conducted to measure the viscoelasticity and strain rate-dependence of polymers in consideration of applying polymers to crash simulations, and presents findings regarding the high-speed deformation of polymers. In addition, a comparison with calculation results using the finite element method is also shown.

## 3. Tensile and Bending Tests

This section describes an overview of the tensile and bending tests performed in this study.

Currently various test apparatuses exist for measuring material properties at high strain rates, and test methods suited to each strain rate range were proposed[5]. According to these methods, the Split-Hopkinson bar method[6] and one bar method[7] are suitable for strain rates from $10^3$ $sec^{-1}$ to $10^5$ $sec^{-1}$, and methods such as the servo-hydraulic systems are suitable for strain rates from $10^0$ $sec^{-1}$ to $10^3$ $sec^{-1}$. In consideration of the effects of different test specimen shapes, this study used a servo-hydraulic system in order to conduct tests using identically shaped test specimens over the widest range possible from the high-speed to low-speed tensile range. These high strain rate test methods consist of accelerating a large mass and impacting it into the piston to start movement of the clamping device before the load is applied to the test specimen. Therefore, the load measurement time becomes shorter at higher strain rates, and the time needed for elastic deformation within the load cell to become uniform is roughly equal. This causes the phenomenon where the elastic wave that reflects multiple times within the load cell becomes noise and has a great effect on the measurement value, and resolving this was an issue for measurement.

Therefore, the high-speed tensile test in this study used a compact and lightweight clamping device and load cell. This increased the natural frequency of the measurement portion to 3.4 times that of the conventional method, and reduced vibration caused by the impact input, making it possible to obtain the measurement value of high-speed tensile test.

### 3.1. Tensile Test Apparatus and Test Method

This study used a Type AG screw-driven system (AGS-1000G: maximum tensile speed 1.7 x $10^{-2}$ m/s) to obtain mechanical characteristics in the static to quasi-static range (strain rate $10^{-4}$ $sec^{-1}$ to $10^{-1}$ $sec^{-1}$), and Type A (EHF-U2H-20L: maximum tensile speed 1.5 x $10^1$ m/s) and Type B (HITS-T10: maximum tensile speed 2.0 x $10^1$ m/s) servo-hydraulic high-speed impact test apparatuses to obtain mechanical characteristics during medium- to high-speed deformation. The Type A and Type B test apparatuses both operate on the same principle. However, the natural frequency of the Type A test apparatus including the load cell is not sufficiently high, so the impact-induced noise was pronounced at a strain rate of $10^2$ $sec^{-1}$, which made it difficult to obtain accurate data. In contrast, the Type B test apparatus differed from the Type A test apparatus in that it used a lightweight and high rigidity load cell. Figure 2 shows the principle of operation for these high-speed impact test apparatus.

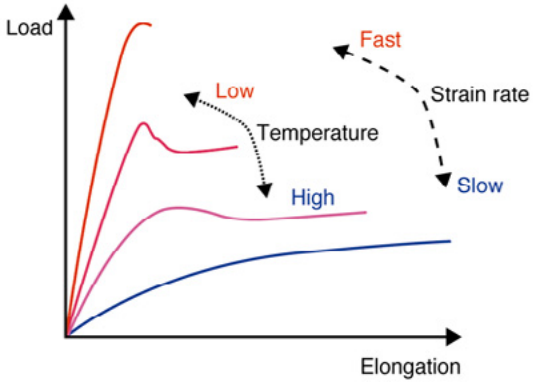



Fig. 1 Dependence of strain rate and temperature in material data

These test apparatuses perform the tensile test after accelerating a hydraulic cylinder to the prescribed speed over the approach (80 mm) of the piston installed on top of the test specimen. This test was used to measure the stress-strain behavior of polymers over the strain rate range from $10^0$ $sec^{-1}$ to $10^2$ $sec^{-1}$. Figure 3 shows a photograph of the high-speed tensile test apparatus.

Note that changes in the cross-section shape of the test specimens were recorded at all times during the tensile test in order to measure changes. This was done using a home video camera (SONY) in the low-speed tensile range, and a high-speed video camera (NAC) capable of recording 20 000 frames/s in the medium to high-speed tensile range.

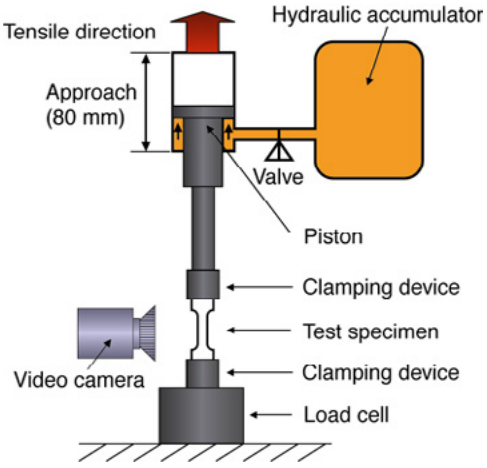



Fig. 2 Schematic illustration of tensile testing apparatus

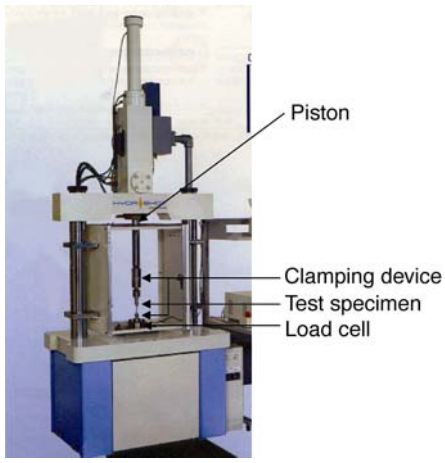



Fig. 3 High-speed tensile testing apparatus

### 3.2. Tensile Test Specimen Materials and Shapes

Three types of test specimen materials were selected for this study from among polymers widely used in the interior and exterior of automobiles. These three types were polypropylene, which is a thermoplastic crystalline material, polycarbonate, which is a thermoplastic amorphous material, and epoxy, which is a thermosetting polymer. These three materials were selected in order to compare and investigate each polymer type.

JISK7113 No. 2 dumbbell shape (parallel portion width 6 mm) test specimens were used from the static tensile to the medium-speed tensile (up to a strain rate of $10^{1}$ $sec^{-1}$) range, and compact test specimens designed exclusively for the test apparatus were used only in the high-speed tensile (strain rate $10^{2}$ $sec^{-1}$) range. Figures 4 and 5 show the respective test specimen shapes.

This test used two types of test specimens with different shapes, so two types of clamping devices were also used. Figure 6 shows a photograph of clamping device A, and Fig. 7 shows a photograph of clamping device B. Clamping device A and B are both made of titanium. Clamping device B has a more compact and lightweight design compared to clamping device A, and while clamping device A has a natural frequency of 5.0 kHz, the natural frequency of clamping device B has been raised to 17 kHz.

### 3.3. Bending Test Apparatus and Test Method

The bending test was performed using the same type of test apparatus as the low-speed tensile test. Figure 8 shows a schematic drawing of the bending test, and Fig. 9 shows a photograph of the bending test apparatus. The distance between the fulcrums is 40 mm, and the test was performed by moving the compression rod at a strain rate from $10^{-4}$ $sec^{-1}$ to $10^{-2}$ $sec^{-1}$. A strain gauge was attached to the reverse side of the contact surface of the compression rod and the test specimen, and a measurement was performed up to the maximum measurable strain of $2.0 \times 10^{-2}$.

### 3.4. Bending Test Specimen Material and Shape

The bending test used only the thermoplastic crystalline material polypropylene, and the test specimen was shaped as a rectangular slab of dimensions 100 x 10 x 3 mm.

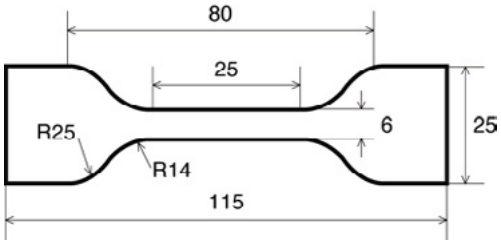



Fig. 4 Schematic illustration of tensile test specimen

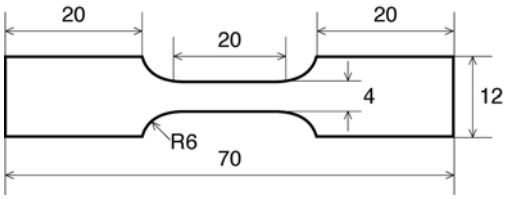



Fig. 5 Schematic illustration of high-speed tensile test specimen



Fig. 6 Clamping device A



Fig. 7 Clamping device B

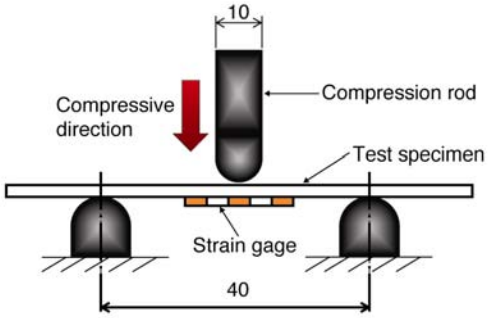



Fig. 8 Schematic illustration of bending test

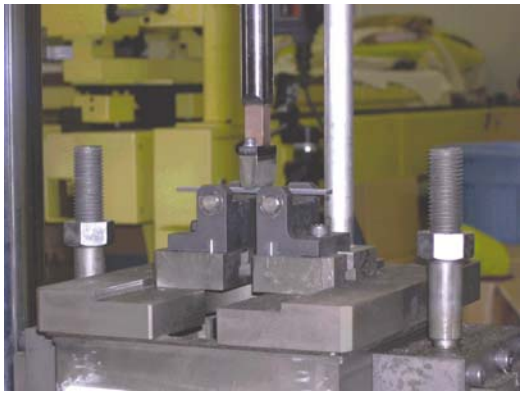


Fig. 9 Bending test apparatus

Table 1 Tensile test conditions

| Crosshead velocity | Strain rate | Testing apparatus |
|---|---|---|
| $8 \times 10^{-6}$ m/s | $10^{-4}$ | Type AG: AGS-1000G JIS2 test specimen |
| $8 \times 10^{-5}$ m/s | $10^{-3}$ | |
| $8 \times 10^{-4}$ m/s | $10^{-2}$ | |
| $8 \times 10^{-3}$ m/s | $10^{-1}$ | |
| $8 \times 10^{-2}$ m/s | $10^{0}$ | Type A: EHF-U2H-20L JIS2 test specimen |
| $8 \times 10^{-1}$ m/s | $10^{1}$ | |
| $4 \times 10^{0}$ m/s | $10^{2}$ | Type B: HITS-T10 Special test specimen |

## 4. Test Results and Findings

Different tensile test apparatus were used for quasi-static, medium and high strain rates, so this section first compares the measurement values for each test apparatus at the same strain rate. Next, the true-stress true-strain curves for each strain rate are shown as the results of the tensile tests using three types of polymers and the bending test using one type of polymer. Finally, calculations using a general finite element method solver are performed for the tensile tests and compared with the tensile test measurement values.

### 4.1. Results due to Differences in Test Apparatuses

These tests used different tensile test apparatuses according to the strain rate as shown in Table 1 for the performance of test apparatus and the elimination of the above-mentioned vibration of the high-speed tensile test.

First, the tensile test was performed at a strain rate of $10^{-1}$ sec$^{-1}$ for polypropylene to verify the difference between the screw-driven system (Type AG) and the high-speed impact test apparatus (Type A). Figure 10 shows the stress-strain curves for these test apparatuses, and the elastic modulus and the stress values were confirmed to match.

Next, the tensile test results for polypropylene at a strain rate of $10^{0}$ sec$^{-1}$ are compared to verify the difference between the two types of high-speed impact test apparatuses (Type A, Type B). These results are shown in Fig. 11, and likewise Fig. 10 the elastic modulus and the stress values were confirmed to match.

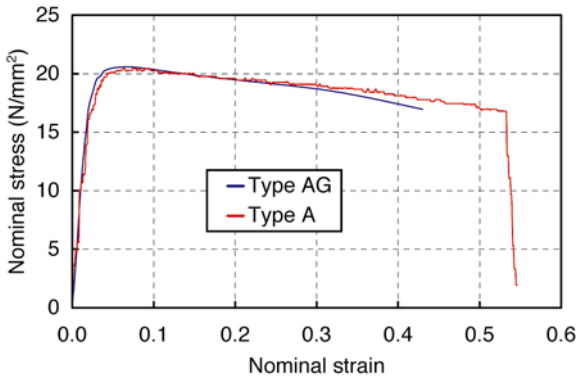



Fig. 10 Stress-strain curves of type AG and A

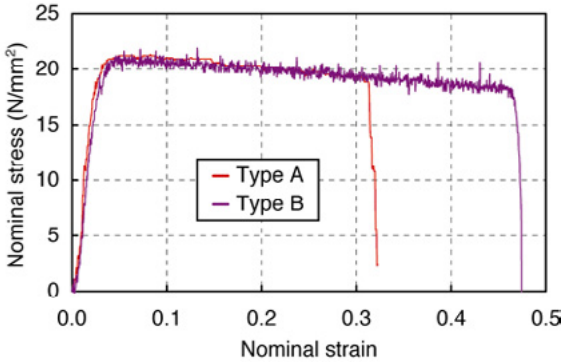



Fig. 11 Stress-strain curves of type A and B

### 4.2. Tensile Test Results

This study obtained tensile test data from the quasi-static to the high-speed ranges using the test apparatuses shown in Table 1 for the three material types of the thermoplastic crystalline polymer polypropylene, the thermoplastic amorphous polymer polycarbonate, and the thermosetting polymer epoxy.

Figure 12 shows the true stress-true strain curves of polypropylene.

As shown in this figure, viscoelastic effects are seen where the elastic modulus increases according to the tensile speed, and the rupture strain also tended to become smaller as the strain rate rose.

Figure 13 shows the difference in the acquired data when using different high-speed test apparatuses for the strain rate $10^{2}$ sec$^{-1}$ data.

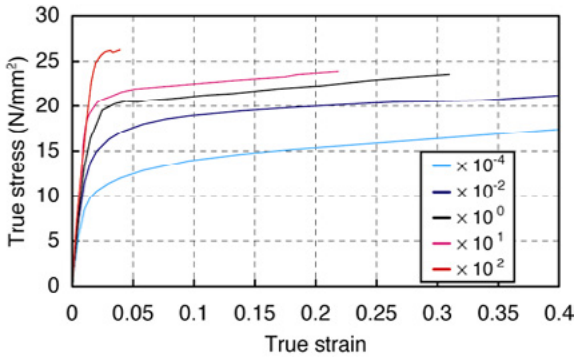



Fig. 12 Stress-strain curves of polypropylene at various strain rates

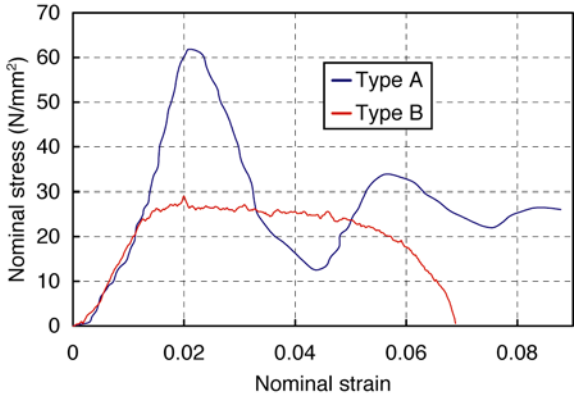



Fig. 13 Stress-strain curves of polypropylene at strain rate 100 sec$^{-1}$

In the data acquired using the high-speed impact test apparatus (Type A), the impact input-induced noise is transmitted through the test specimen as mentioned previously, making it difficult to obtain accurate elastic modulus and stress values. On the other hand, stress-strain curves without impact input-induced noise could be obtained from the data acquired using the high-speed impact test apparatus (Type B).

Next are some observations on the stress values obtained at a strain rate of $10^2$ $sec^{-1}$. Generally there are two methods for handling high-speed deformation such as in crash simulations. The first method interpolates the material properties during high-speed deformation by extrapolation based on the stress-strain curve of the component material obtained in the low-speed to medium speed ranges. The second method uses a strain rate-dependent yielding stress only in the low-speed range, and maintains a constant yielding stress in the medium-speed and high-speed ranges. Comparing the extrapolated values for the high-speed range with the stress increase values obtained in this study show that the stress increase values at strain rates from $10^1$ $sec^{-1}$ to $10^2$ $sec^{-1}$ obtained in this study are much larger than the values calculated based on the stress increase values at strain rates from $10^0$ $sec^{-1}$ to $10^1$ $sec^{-1}$.

The stress values at a strain rate of $10^2$ $sec^{-1}$ is considered based on the relationship between the impact energy absorption of polypropylene and temperature. In terms of the mechanical properties of polymers, the tensile stress-strain curve at high strain rates and the tensile stress-strain curve at low temperatures are known to show the same stress increase tendencies[8]. Figure 14 shows the relationship between the impact energy absorbed by polypropylene and temperature. Here, the impact energy absorption is seen to drop sharply as the temperature decreases[9]. When this impact energy absorption is substituted for the absorbed energy in the tensile stress-strain curve, the sudden decrease in the absorbed energy at a strain rate of $10^2$ $sec^{-1}$ can be assumed to resemble the decrease in energy absorption as the temperature drops. Based on this observation, this study assumed that the above-mentioned rapid change in the absorbed energy exists for polypropylene between the strain rates of $10^1$ $sec^{-1}$ to $10^2$ $sec^{-1}$. However, further investigations are necessary. In addition, tensile tests must be conducted at even more strain rate levels to understand the strain rate boundary values.

Next, Fig. 15 shows the true stress-true strain curves for the thermoplastic amorphous polymer polycarbonate. Likewise for polypropylene, this test data also shows pronounced viscoelasticity and strain rate-dependence. However, polycarbonate differs from polypropylene in that variance was seen in the rupture strain. Figure 16 shows photographs of the entire test specimens following this test, and Figs. 17 and 18 show photographs of craze deformation that occurred on the test specimen surface.

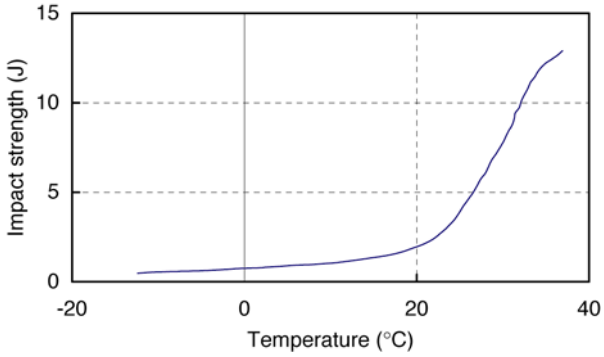



Fig. 14 Temperature dependence at absorption of impact energy in polypropylene

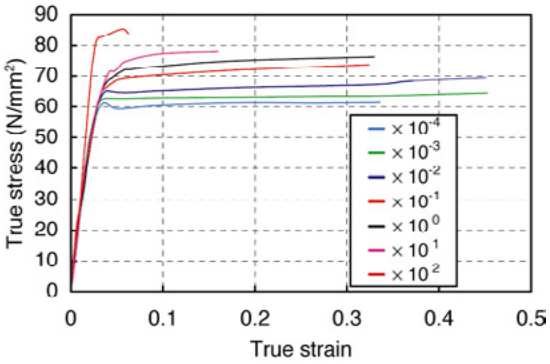



Fig. 15 Stress-strain curves of polycarbonate at various strain rates

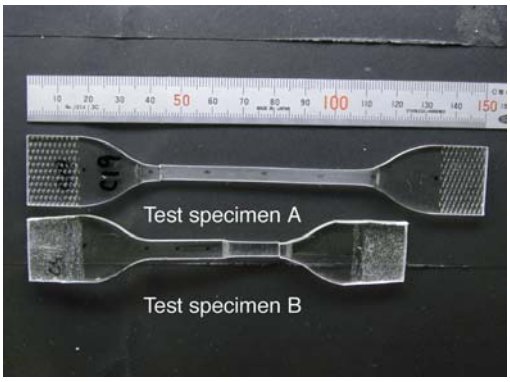



Fig. 16 Photograph of test specimens

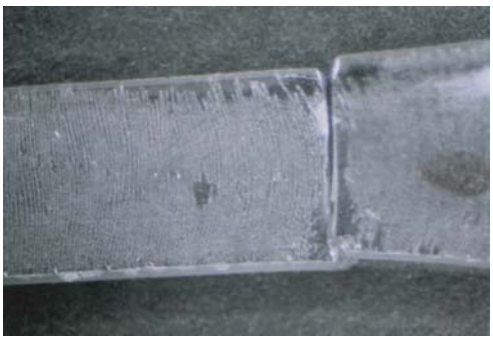


Fig. 17 Magnified photograph of test specimen A

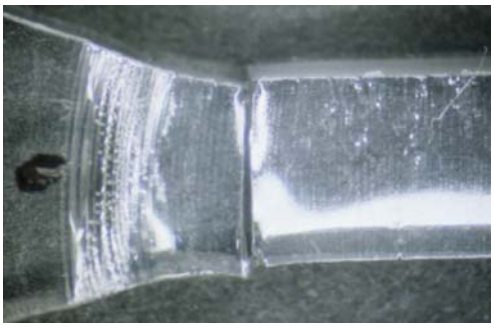


Fig. 18 Magnified photograph of test specimen B

Test specimen A in Fig. 16 is the test piece for a strain rate of $10^{-3}$ $sec^{-1}$, and test specimen B is the test piece for a strain rate of $10^{1}$ $sec^{-1}$. This photograph clearly shows that necking occurred along the entire length of the parallel portion of test specimen A. On the other hand, necking appeared only locally in test specimen B. The necking formation similar to test specimen A was observed at strain rates of $10^{-2}$ $sec^{-1}$ or less, and the necking formation similar to test specimen B was observed at strain rates of $10^{-1}$ $sec^{-1}$ or more.

In addition, craze deformation was observed at a high density on the surface of test specimen A as shown in Fig. 17, but craze deformation occurred only locally on the surface of test specimen B as shown in Fig. 18. Local rupture strain in the necking portions was measured in reference to marks made at 1.0 cm intervals on the surface of each test specimen. The results confirmed that at strain rates of $10^{-1}$ $sec^{-1}$ or more, the rupture strain tended to decrease as the strain rate increased. However, a clear correlation between the local rupture strain and the strain rate was not observed at strain rates of $10^{-2}$ $sec^{-1}$ or less. Based on these observation results, a critical strain rate at which craze occurs at high density is assumed to exist, and it is difficult for a correlation between the strain rate and the rupture strain to appear at strain rates below that level. However, further verification is necessary. In addition, polycarbonate differed from polypropylene in that the rupture strain was smaller in the low strain rate range. This difference in the rupture strain is known to depend largely on whether the material is crystalline or amorphous. For crystalline polymers, the orientation of the polymer chain within the substance faces the loading direction, the rupture strain increases. However, amorphous polymers have a structure with randomly positioned amorphous molecules and do not have a crystal structure, so they are thought to rupture at a smaller strain than for crystalline polymers.

Lastly, Fig. 19 shows the true stress-true strain curves for the thermosetting polymer epoxy. These results show that a strain rate-dependent change in the elastic modulus was observed like for polypropylene and polycarbonate. On the other hand, most rupture occurred within the elastic region.

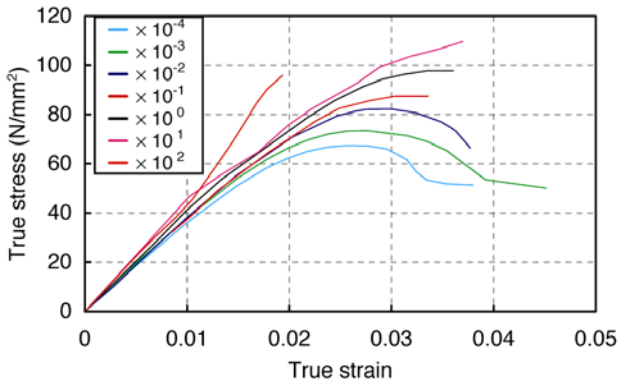



Fig. 19 Stress-strain curves of epoxy at various strain rates

## 4.3. Bending Test Results

In addition to tensile tests, this study also performed bending tests for the thermoplastic polymer polypropylene. The bending test was performed using strain gauges at the strain rates of $10^{-4}$ $sec^{-1}$, $10^{-3}$ $sec^{-1}$ and $10^{-2}$ $sec^{-1}$, and Fig. 20 shows the corresponding bending stress-strain curves. Viscoelastic effects were also observed in the bending test, with the bending elastic modulus increasing together with the strain rate.

## 4.4. Application to Finite Element Models

Verification of the tensile test at a strain rate of $10^{2}$ $sec^{-1}$ for polypropylene was performed by simulation using a general finite element method solver. Calculations were performed for the two conditions of case A, which was based on the stress-strain behavior including the strain rate of $10^{2}$ $sec^{-1}$, and case B, which obtained the stress-strain behavior in the strain rate range in excess of $10^{1}$ $sec^{-1}$ by extrapolation, and these were compared with the maximum load during the tensile test. The maximum load value was 460 (N) for case A and 347 (N) for case B, and the measured value was 445 (N). Figures 21 and 22 show the deformation diagrams of the test specimens for the Von Mises stress distribution at a tensile displacement of 2 mm. Areas with high stress values are indicated by red, and areas with low stress values are indicated by blue.

Figures 21 and 22 clearly show that the case A calculation results have higher stress values than the case B results. This is because in case B, the stress values obtained by linear interpolation from the experimental data at strain rates of $10^{0}$ $sec^{-1}$ and $10^{1}$ $sec^{-1}$ are smaller than the experimental values. These results confirmed that using high strain rate test data enhances simulation reproducibility at high strain rates compared to the extrapolation-based calculation results.

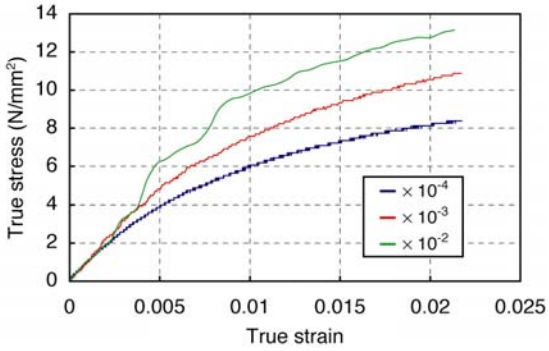



Fig. 20 Stress-strain curves of polypropylene at various strain rates



Fig. 21 Deformation of tensile test piece (Case A)



Fig. 22 Deformation of tensile test piece (Case B)

## 5. Conclusion

Tensile tests and bending tests were performed for polymers used in the interior and exterior of automobiles, and observations were made regarding the non-linear behavior, strain rate-dependence, and rupture behavior of these polymers. In addition, tensile test simulations were performed using a general finite element method solver. In the future, the authors intend to analyze the rupture surface in these polymer tests, and to formulate a new modeling of polymers.

The following conclusions were obtained through this study.

(1) A method was constructed for measuring the high-speed deformation of polymers, which had thus far been difficult to measure.
(2) The stress-strain behavior of polymers at high strain rates, which is difficult to estimate using conventional extrapolation, was understood.
(3) Applying the stress-strain behavior obtained from experiments to finite element models confirmed that simulation reproducibility is enhanced at high strain rates.

## References

(1) Mukai, Y., Watanabe, K.: Estimation Methods and Testing Machines for Evaluation of Impact Deformation Properties in High-strength Steel Sheets, Kobe Steel Engineering Reports, Vol. 52, No. 3, p. 32-34 (2002)

(2) Tanimura, S.: Transaction of the 2nd JSME Materials and Processing Conference, p. 17 (1994)

(3) Fujii, M., et al.: Study of Impact Analysis for Plastic Parts with Rib Structure Part I, JSAE Annual Congress Proceedings (2000)

(4) Keuerleber, M., Eyerer, P.: High-speed tensile testing of polymers -and its application to an instrument panel-, Roell Amsler Symposium (2002)

(5) Mayers, M.: Dynamic Behavior of Materials, John Wiley & Sons Inc. (1994)

(6) Hopkinson, B.: Collected Scientific Papers, Cambridge University Press (1921)

(7) Kawata, K., et al.: Mechanical properties at high rates of strain, Conference series, Institute of physics (1979)

(8) JSTP: Saishin Sosei Kakou Binran, Tokyo, Corona Publishing, p. 278 (1986) (in Japanese)

(9) Miyasaka, K.: Plastic Jiten, Tokyo, Asakura Publishing, p. 356 (1992) (in Japanese)

■ Authors ■



Hiroyuki MAE



Kenji TAKADA



Junichi TAKAHASHI



Toshiharu YAMAMOTO

# Development of Trimmed Body Model for Noise and Vibration

Nobuo AIZAWA* Fumihiko IDE* Yasuhiko KAGIYAMA*

## ABSTRACT

Modeling Technology for a trimmed body that can predict noise and vibration with a short computation time and high accuracy was developed. In order to reduce the total degrees of freedom, parts that exert only a small influence on the acoustic characteristics were simplified from shell elements to concentrated mass models. The acoustic significance of trim parts was determined both experimentally and computationally. Also, Automated Multi-Level Substructuring (AMLS) was applied resulting in a significant reduction in computation time. Finally, the trimmed body prediction results agreed closely with experimental data.

## 1. Introduction

In recent years, improved CAE prediction estimation is being demanded during development in the prediction of noise and vibration in automobiles. Since this requires detailed modeling, the degree of freedom (hereafter referred to as DOFs) of FE models has increased significantly. At the same time, analysis frequency ranges have also expanded leading to an increase in the computation time. The goal of this development is to reduce the computation time while maintaining model accuracy.

Typically, three methods are available for reducing the computation time. The first method is to combine experimental and FE analyses[(1)]. This method makes use of a model with fewer DOFs. In this case, the accuracy of the FE model is supplemented by adjusting stiffness and mass to improve correlation with the experiment. Its application in the development stage is difficult because prototypes typically do not exist. The second method makes use of Component Mode Synthesis (CMS) for converting the FE model to the modal domain by which DOFs not necessary for analysis are eliminated[(2)]. This method requires considerable time since the detailed FE model must be converted to the modal domain. Furthermore, the sub-structuring of the model into modal models requires high-level knowledge and technique. In this research a third method, AMLS was used for reducing the DOFs and the computation time. In addition to using AMLS, many components were reduced to concentrated mass elements if accuracy was not compromised. In this study, the accuracy of AMLS (the newly proposed computation method) was verified and the reduction of computation time was quantified.

## 2. Reducing the Computation Time using AMLS

AMLS is an eigenvalue computation method developed by Bennighof[(3)]. The constrained mode method[(4)], which is

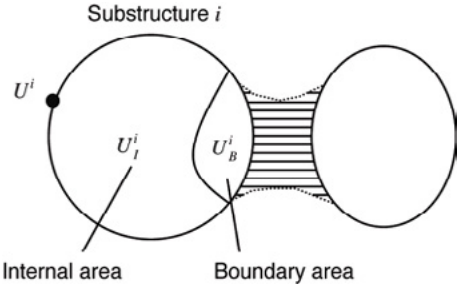



Fig. 1 Definition of substructure

* Tochigi R&D Center

the basis of AMLS, is described here. As shown in Fig. 1, the entire structure is divided into substructures and each substructure is classified into boundary and internal areas. Thus, the displacement $U^i$ of the substructure $i$ is classified into the displacement of the internal area $U_I^i$ , and displacement of the boundary area, $U_B^i$. The displacement of the internal area is expressed as given below, by the displacement of boundary area and modal matrix of the internal area.

$$\{U_I^i\} = [T_B^i]\{U_B^i\} + [\Phi_I^i]\{\xi_I^i\} \quad (1)$$

The first term in Eq. (1) expresses the deformation of the internal area due to displacement of the boundary area, and is a static condensation matrix according to Guyan. The second term expresses the deformation from the mode shape of the internal structure when the boundary area is restrained. It is defined to improve the accuracy of the static condensation in the first term and obtained from Eq. (2).

$$([K_{II}^i] - \omega^2 [M_{II}^i])\{\Phi_I^i\} = 0 \quad (2)$$

The displacement of substructure $i$ can be expressed as below using Eq. (1) and (2).

$$\{U^i\} = \begin{Bmatrix} U_B^i \\ U_I^i \end{Bmatrix} = \begin{bmatrix} I & 0 \\ T_B^i & \Phi_I^i \end{bmatrix} \begin{Bmatrix} U_B^i \\ \xi_I^i \end{Bmatrix} = [A^i] \begin{Bmatrix} U_B^i \\ \xi_I^i \end{Bmatrix} \quad (3)$$

$[A^i]$ represents the conversion matrix by the mode synthesis method. After determining $[A^i]$ from Eq. (3), and pre and post multiplying with the eigenvalue equation of the entire structure, the eigenvalue equation of the entire mode system can be obtained.

$$([\hat{K}] - \omega^2 [\hat{M}]\{\hat{\Phi}\} = 0 \quad (4)$$

Substructure stiffness matrices with several thousand to several tens of thousands of steps are automatically generated by AMLS. As shown in Eq. (2), the substructure matrix is converted to modal DOFs by eigenvalue analysis. As a result, the DOFs of the entire model can be reduced, thereby achieving high-speed computation. Since multiple substructures are used, high-speed processing is also enabled by parallel computation.

Figure 2 shows the flow of computations using AMLS. Special settings are not necessary and the user needs to add only a one-line description to the NASTRAN execution card for running AMLS. Furthermore, since the computed results are output in NASTRAN format, new techniques need not be acquired.

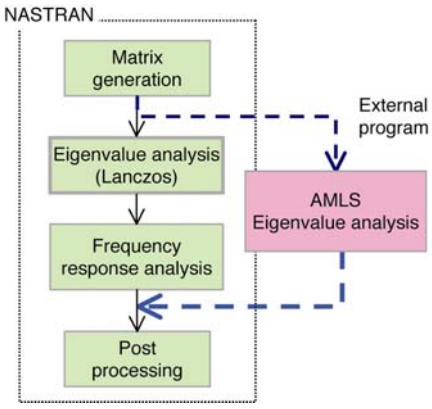



Fig. 2 AMLS process

## 3. Reducing the Degrees of Freedom in the Modeling Method and Maintaining Accuracy

Figure 3 shows the components of the trimmed model and the ratio of DOFs. The DOFs of the model should be reduced to speed up the computation time. On the other hand, if detailed modeling is performed to enhance the accuracy, the DOFs will increase.

If the DOFs are reduced by simplifying the metal structural parts including the Body in White (hereafter referred to as BIW) and door panels, the accuracy of the model cannot be maintained. Therefore, the model should be constructed very accurately according to the drawings. Accordingly, the element size for modeling metallic parts (such as BIW) was approximately 15 mm maximum, where fillets with radius greater than 5 mm were also represented

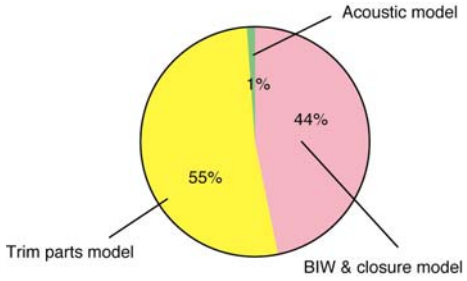



Fig. 3 Degree-of-freedom ratio

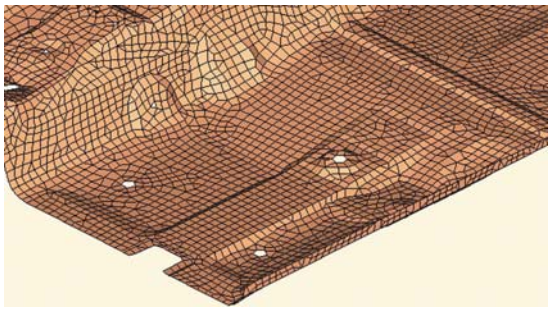


Fig. 4 Floor panel model

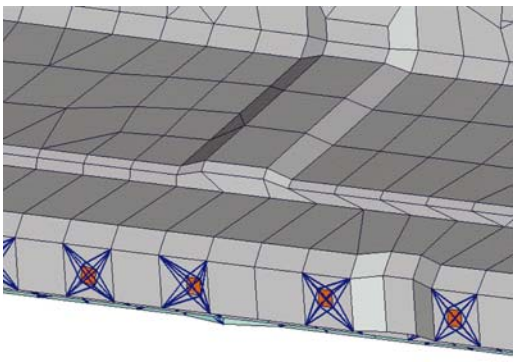


Fig. 5 FE model for Spot welding

(Fig. 4). The diameter of spot welds was also considered important for model accuracy[5]. These were represented using HEXA and RBE3 elements of MSC NASTRAN (Fig. 5).

In considering the number of DOFs needed to model the Acoustic Cavity accurately, it was confirmed that the frequencies and mode shapes of the cavity did not vary appreciably even if the passenger cabin interior surface was reproduced in great detail. Therefore, the element size of the acoustic model was taken to be less than 1/8$^{th}$ of the wavelength of the maximum analysis frequency of interest, thus minimizing the total DOFs for the trimmed body model (Fig. 6).

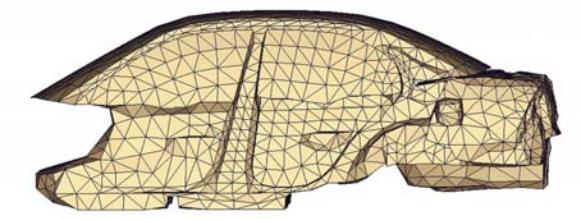


Fig. 6 Acoustic model for cavity




Fig. 7 Excitation points

The effect on model accuracy of reducing each trimmed part from a structural mesh to a concentrated mass was determined. Therefore, where accuracy was not compromised, trim parts were represented as concentrated mass.

### 3.1. Modeling of Trimmed Parts for Reducing the Total Degrees of Freedom

If all the trimmed parts are expressed by concentrated masses, the accuracy deteriorates. If insignificant parts are modeled in detail, the DOFs increase, leading to an increase in the computation time. Therefore, the effect of each trimmed part on the total acoustic response was examined. The trimmed parts were divided into groups that could be modeled by mass only and groups that had to be modeled structurally. The former were replaced by mass models to reduce the DOFs. This procedure is described below.

(1) The trimmed parts were removed individually in an experiment. For parts where the acoustic frequency response function changed, a detailed shell element model seemed to be required, and the remaining parts were modeled using concentrated mass models.

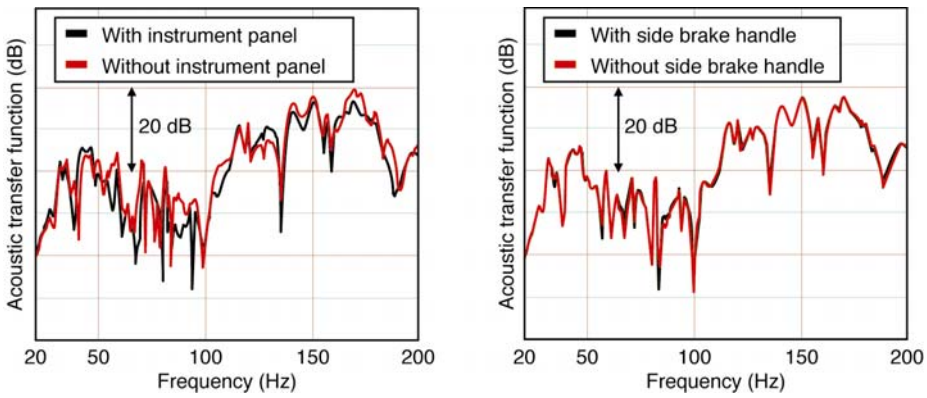



Fig. 8 Influence of trim parts

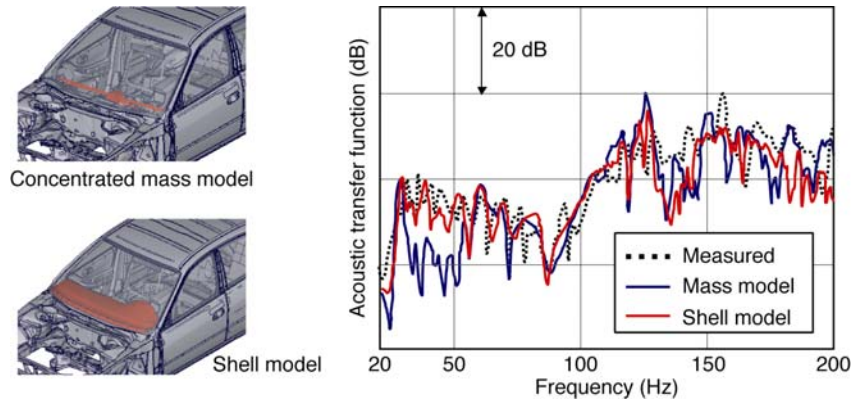



Fig. 9 Influence of instrument panel model

(2) Next, for the sensitive parts in step (1) detailed and concentrated mass FE models were calculated and compared. If the difference in acoustic response was small, a concentrated mass model was used.

### 3.2. Trimmed Part Removal Experiment

The experimental excitation for inducing trimmed part vibration was as follows: forces were input in the vertical direction of the front and rear sub-frames, and in the longitudinal direction of the member front cross. The sound pressure at the front and rear seats and in the trunk was measured (Fig. 7).

All trimmed parts were removed individually, the changes in acoustic response function before and after removal were compared, and priority was determined based on the degree of the changes. Figure 8 shows the frequency response function of the instrument panel with maximum change in acoustic characteristics, and the parking brake with minimum change in acoustic characteristics.

### 3.3. Simplification of Trimmed Parts Model

Trimmed parts judged to have a big influence on the acoustic characteristics in the experiment were modeled in detail using shell elements. Then the shell element model was replaced by a concentrated mass model, and the effects of the simplified model were verified. Figure 9 shows the results for the instrument panel, which had the largest effect on acoustic characteristics. It was confirmed that the correlation with the experiment deteriorated in the range of 30 to 60 Hz when the shell element model was replaced by a concentrated mass model. This indicates that a detailed model is required to ensure accuracy in this frequency band. Next, the replacement of the shell element model of the roof lining by concentrated mass model was studied. Figure 10 shows the results. Since the acoustic characteristics did not exhibit appreciable change, the roof lining was considered to be adequately represented by the concentrated mass model. By similar verification, parts with small effect on the acoustic characteristics were simplified, and the DOFs of the entire trimmed model were reduced by 23%.

### 3.4. Accuracy of Trimmed Body Model

Figure 11 shows the trimmed model consisting of a mix of parts modeled by shell elements and by concentrated mass based on the modeling decision process described earlier. The accuracy of the complete trimmed model was verified by comparing the frequency response function with the experiment. Specifically, the acoustic response due to vertical input on the front sub-frame was calculated. Figure 12 shows the results of the verification. The difference in level between the FE model and experimental values was within ±5 dB up to 200 Hz. It was confirmed that the trimmed model had practical accuracy that could be used during development for the prediction of noise and vibration.

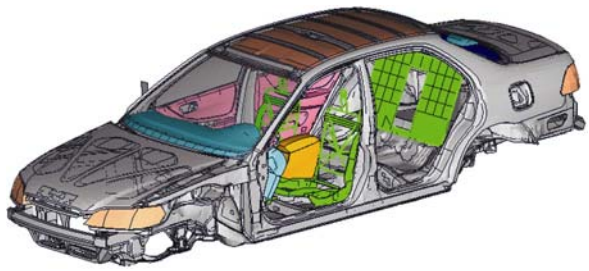


Fig. 11 Trimmed body model

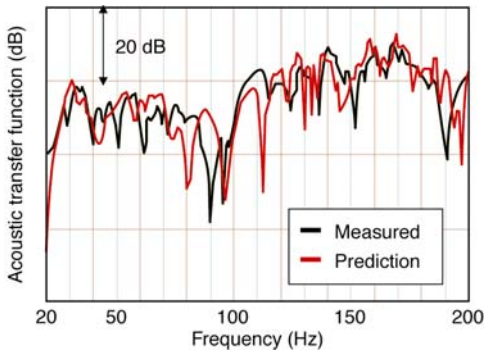
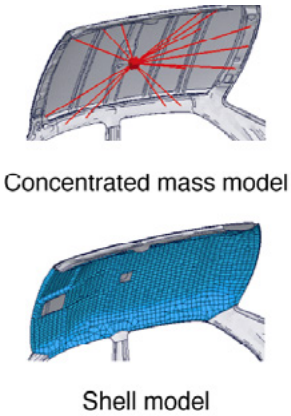



Fig. 12 Verification for trimmed body



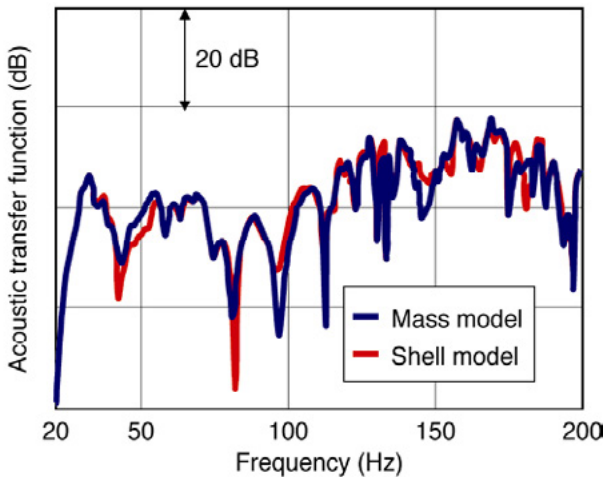




Fig. 10 Influence of roof lining model

## 4. Verification of Computation Speed

Frequency response analysis was carried out up to 300 Hz to verify the computation speed. The computation times were compared for cases where the DOFs of trimmed parts were reduced, were not reduced, and when AMLS was used. Figure 13 shows the computation times. The computation time was shortened by 20% when the DOFs of the trimmed parts were reduced. A further reduction in time of 66% was achieved when AMLS was used. Thus, the effect of reducing the DOFs of the trimmed body and the effect of using AMLS were substantiated.

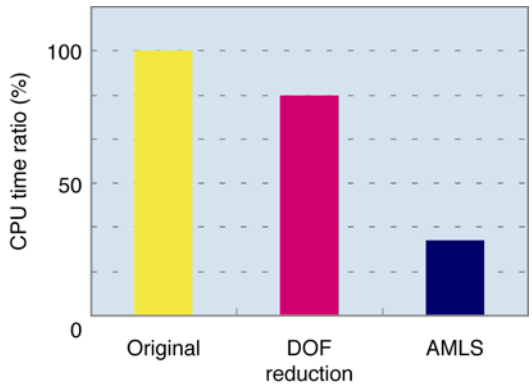



Fig. 13 CPU time ratio

## 5. Conclusion

The results of studies on reducing the DOFs of trimmed parts and computation methods led to the following conclusions:

(1) It was found that treating some of the trimmed parts as concentrated mass elements was an effective and practical method of modeling the trimmed body with high accuracy and reduced computation time.

(2) The effectiveness of this modeling method for reducing the DOFs of trimmed parts and the reduction in computation time of eigenvalue analysis using AMLS were verified.

By application of the modeling technique mentioned above, the development in the prediction of noise and vibration by CAE could be carried out at a higher efficiency especially with regard to accuracy and time.

## References

(1) Kimura, F., Shimizu, H.: Parametric studies on correlation with experiments, Digital Engineering, p. 25, (2002) (in Japanese)

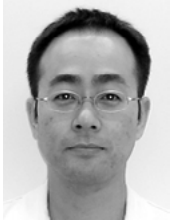
(2) Society of Automotive Engineers: Jidoushagijutu Handobukku Kiso Riron Hen, p. 247 (1991) (in Japanese)

(3) Bennighof, J.K., Kaplan,M.F., Muller,M.B.: Extending the frequency response capabilities of automated multi-level substructuring, SDM Paper AIAA-2000-1574

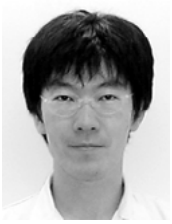
(4) Nagamatsu, A.: Constrained Mode Synthesis, sub-structure synthesis, p. 103-104 (1991) (in Japanese)

(5) Heiserer, D., Sielaff, J., Chargin, M.: High performance, process oriented, weld spot approach, 1st MSC Worldwide Automotive User Conference, (1999)

■ Authors ■


Nobuo AIZAWA


Fumihiko IDE


Yasuhiko KAGIYAMA

# Locating Source of Vehicle Pass-by Noise Using Beamforming Method

Yukihiko HANZAWA* Jun KITAHARA* Shinichi NISHIMURA*

## ABSTRACT

Aiming at reducing vehicle pass-by noise, attention was focused on an analysis method employing high-directivity remote noise source locating technology (beamforming method). The beamforming method is a measurement method that uses a combination of multi-channel sensor technology and signal processing technology. It features the ability to measure the overall noise source in a short time and also the ability to provide a visual indication of the noise source distribution. A study of the shape, arrangement, and other specifications of the beamforming array for analyzing vehicle pass-by noise was carried out. Based on the results, a noise source locating test was performed using both a dummy noise source and an actual vehicle. As a result (1) a noise source locating instrument that had the required locating accuracy and dynamic range was realized, and (2) it was confirmed by using this instrument to analyze vehicle pass-by noise that this method was effective for reducing noise.

## 1. Introduction

Demands for reducing road and traffic noise have increased in recent years around the world. Society is urging for the reduction in the sources of the noise, which is primarily pass-by noise from automobiles. There are several direct sources of pass-by noise: the engine, air intake system, exhaust system, and tires. Many components of these sources are responsible for noise and are widely distributed about the vehicle. There often are contradictions between noise control methods and performance. It is essential to begin efficient reductions of noise in the early stages of development of an automobile. Many analytical methods have been attempted for this purpose.

Some representative methods include contribution analysis by masking[(1)], acoustic intensity[(2)], acoustic holography[(3)], contribution analysis by volume velocity acoustic sources, and the reciprocity principle[(4)]. Since these methods require much time and labor for the testing and analyses, they can often be inadequate methods from the standpoint of the limited time given for current short-term development.

Recently, however, there have been some reports describing the beamforming method, a highly directional technology for noise source location at long distances, which has served the fields of aeronautics[(5)] and the design of high-speed trains[(6), (7)]. This method directly observes a noise source using a combination of multi-channel sensor technology and signal processing technology. It enables quick noise source location in a wide target area in a single measurement, using a 2-dimensional array of microphones.

In this study, a noise source location method using the beamforming method was applied to bench analysis of automobile pass-by noise during acceleration. The microphone array most appropriate for pass-by noise analysis was investigated and noise source location was attempted using the resulting array. Based on these results, noise reduction was conducted and it was confirmed that the newly developed method was effective for noise source location.

* Tochigi R&D Center

## 2. Theory and Characteristics of the Beamforming Method

### 2.1. Theory

Beamforming technology is a method of obtaining highly directional (beam) characteristics from a geometric arrangement of sensors on a 2-dimensional plane (a multi-microphone), using signal processing fitted to the geometric arrangement, to obtain data on the distribution of a source within a group of noise sources. The essentials of this method are described below.

Let us assume that acoustic waves approach from a certain direction and M microphones placed in locations $r_m$ ($m$ = 1, 2, …, $M$) on an XY plane (Fig. 1). It can be assumed that the signals $p_m$ detected by the microphones have certain delay times $\Delta_m$ determined by the direction of approach of the acoustic waves and the position of the microphones. As shown in Fig. 2, by compensating for the delay time of each microphone and summing them, it is possible to highlight the signal coming from a specified direction. "Delay-and-sum beamforming" or just "beamforming" refers to this technique of summation for obtaining highly directional characteristics. The time-base waveform for a specified angle $\kappa$ is given by the following expression:

$$b(\kappa, t) = \sum_{m-1}^{M} p_m(t - \Delta_m(\kappa)) \quad (1)$$

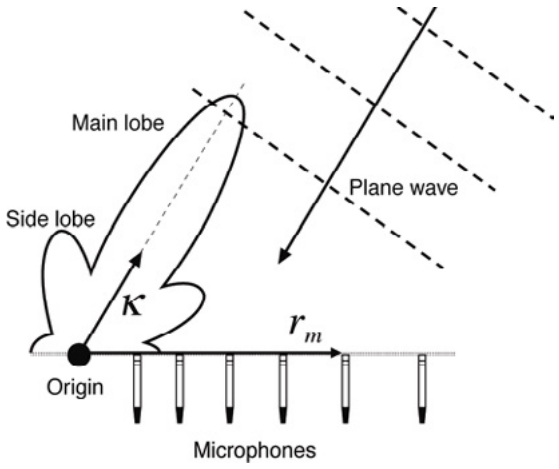



Fig. 1 Beamforming array and directional sensitivity on XY plane

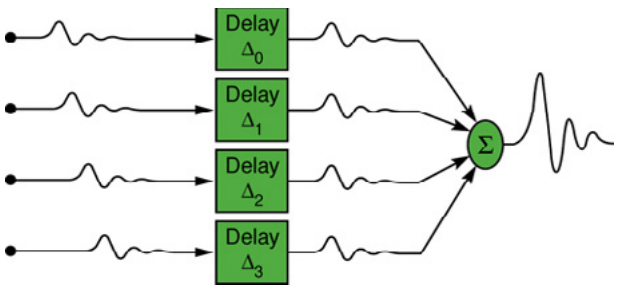



Fig. 2 Principle of beamforming

Since the delay time $\Delta_m$ to be applied to each microphone controls the directionality of that microphone, $\Delta_m$ is determined as a function of the desired direction represented by the unit vector $\kappa$ in that direction. The reason for this is to apply the delays to each of the microphone signals representing the planar wave arriving from direction $\kappa$ coheres the signals before the summing process. The time delay $\Delta_m$ is calculated in the following formula, using the position of each microphone array:

$$\Delta_m = \kappa \cdot r_m / c \quad (2)$$

Here, $c$ is the propagation speed of sound. As shown in Fig. 2, the signals arriving from directions other than the chosen direction are not summed in a coherent way but randomly, so that they cancel each other out. As a result, main directionality for the signals from the chosen direction is obtained and called the "main lobe", while array sensitivity to directionality for the other directions is called the "side lobes".

### 2.2. Characteristics

Beamforming technology allows "one-shot" measurements of distant, large objects, even with arrays of rather small diameters. For example, effective measurement results can even be obtained from objects occupying a solid angle of 30° from the central axis of the array.

Ideally, arrays should have no side lobes. In actual use, arrays show "ghost" indications of noise sources in locations where there are no sources due to the side lobes. Design techniques have been developed which attenuate the maximum side lobe levels (effective dynamic range) in the expected frequency range in order to emphasize the relative difference from the main lobe[8]. These techniques were used in this study.

## 3. Target Setting for Development of Noise Source Location Method

Various methods of analysis of the sources in pass-by noise have been tried, as mentioned above, but many of these require much time and labor for both the tests and the analysis. A beamforming system was constructed as a practical noise source location technology in an attempt to eliminate these issues.

The following targets for our system were set in accordance with the needs of this process of development of an actual automobile:

(1) The accuracy of noise source location shall be within 25 cm at 1 kHz.
(2) In order to accomplish this resolution, it shall be possible to detect two 1 kHz sources at a separation of at least 50 cm.
(3) "One-shot" measurements (a single run per measurement) of the entire vehicle shall be possible.
(4) Results shall be output within 30 minutes of the total processing time.
(5) Effective dynamic range of location results shall be more than 10 dB for the analytical frequency region of 400 Hz – 2.5 kHz.

## 4. Investigation of Microphone Array

Next, an investigation of the following parameters of the microphone array was carried out in preparation for the analysis of noise source location in an entire vehicle: diameter, placement, shapes and number of microphones. The necessary array diameter and placement with respect to the noise source were determined by the desired measurement area and spatial resolution, assuming coverage of an entire vehicle up to 5 m in length and a lower limit of the analytical frequency region of 400 Hz. A semicircular array shape (half-wheel array) was chosen, assuming perfect reflectivity of the floor surface in a measurement environment. This allowed the number of microphones to be cut in half. The number of microphones was set at 42, in consideration of the system structure and the need to obtain adequate spatial position data. The principal specifications of the microphone array are given below and Fig. 3 is a schematic view of the beamforming array.

(1) Array shape and diameter: semicircular (half-wheel type array), 3 m
(2) Number of microphones: 42
(3) Distance between array and noise source: 4 m

## 5. Verifying Characteristics of Half-wheel Array

In order to verify the performance of the microphone array described in the previous chapter, calculations were carried out to find the resolution, the main performance parameter, and the effective dynamic range, which is determined by maximum side lobe characteristics.

### 5.1. Capability to Distinguish Noise Sources

The fundamental characteristics of a half-wheel array are determined by its directionality. Therefore, a simulation was carried out in an effort to predict how well the method would distinguish between two noise sources.

Figure 4 is a contour map showing the results of a calculation carried out for the indicated distribution of noise sources as analyzed by this array resulting from two 1 kHz sources at the desired spacing of 0.5 m. These results show that the observed separation would be slight, but that the array would be able to distinguish two sources.

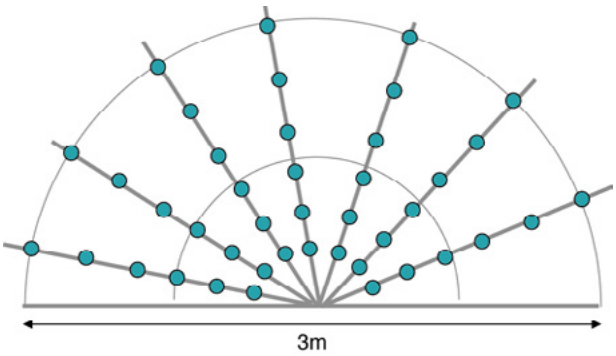



Fig. 3 Typical half-wheel array (42 microphones)

### 5.2. Maximum Side Lobe Characteristics

As described earlier in Section 2, the spatial arrangement of the microphone array determines its directionality. Directionality means a sharp beam shape for the main lobe in the direction of the main axis of the array; it is, therefore, desired that the sensitivity of the side lobes to other directions be kept well below (at least 10 dB below) that of the main lobe. If side lobe sensitivity is insufficiently suppressed, ghost images will appear in the acoustic diagram, making it a challenge to accurately determine the location of the noise source in practical use. Since the location of each microphone in the array is affected by the wavelength, the difference in levels between the sensitivities of the main lobe and the maximum side lobe (the effective dynamic range) can be expressed as a function of frequency. The effective dynamic range of this half-wheel array is shown in Fig. 5. These results indicate that the desired 10 dB effective dynamic range was attained in the effective region of 400 Hz – 2.5 kHz.

## 6. Measurement Accuracy in This Method with Dummy Noise Source

An actual 42-channel microphone array was built and a test was carried out with a dummy noise source of a loud speaker to verify the basic performance of the method.

### 6.1. Accuracy of Single Noise Source Location

The position error was investigated in a dummy noise source test of the beamforming array in order to study the error of the array in identifying the location of the real

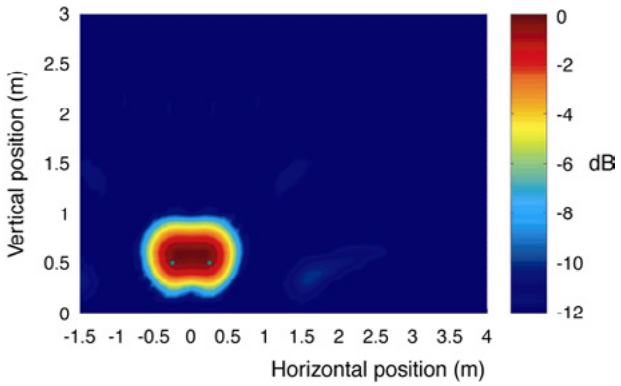



Fig. 4 Result of simulation (42 microphones)

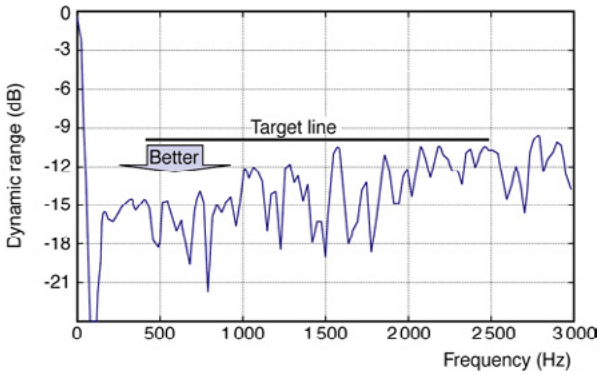



Fig. 5 Maximum side lobe response (42 microphones)

source. Figure 6 provides some typical results. The source was placed at a height of 5 cm above the floor in a semi-anechoic room and the noise signals generate 1 kHz pink noise. The distance between the noise source and the microphone array was 4 m. The results are shown as a noise contour map with a center frequency of 1 kHz 1/3-octave band. The region for which calculations were carried out measured 5 m wide x 2.5 m high. These results indicate that the accuracy of location of noise sources was within the target of 25 cm. Also, the contour map is marked in 10 dB ranges relative to the maximum noise level, but there were no ghost images. It was thus verified that the dynamic range of 10 dB had been realized.

### 6.2. Capability to Distinguish Two Noise Sources

Next, the sound field from two loud speaker noise sources (1 kHz band passed uncorrelated pink noise signals) 50 cm apart was observed with the beamforming array to verify the system's ability to resolve separate sources. The distance between the noise source and the microphone array was 4 m. The resulting noise contour map with a center frequency of 1 kHz 1/3-octave band is presented in Fig. 7. These show that distinct 1 kHz sources separated by the target distance of 50 cm were successfully distinguished by the system.

### 6.3. Verifying Transient Phenomena Performance

It is necessary to be able to carry out a noise source location analysis on an accelerating automobile, whose engine is operating at an arbitrary speed. For this purpose, the analytical method must be applicable to transient as well as to stationary phenomena; this can impose discrepancies in results for measurements of stationary phenomena. The discrepancies were investigated by using two speaker dummy noise sources, in supplying a stationary signal, and a transient signal.

The results under stationary sources are provided in Fig. 8 in a noise contour map with a center frequency of 1 kHz 1/3-octave band. Both loud speakers were emitting 1 kHz uncorrelated pink noise; source-microphone array distance was 2 m.

Figure 9 shows the results under a transient 2-source signal in the form of a noise contour map with a center frequency of 1 kHz 1/3-octave band. The noise signals were set to generate in frequency from 100 Hz to 5.1 kHz in 5 sec; a higher speed than will occur in noise frequency from accelerating vehicle engines. The analysis was carried out for the transient 1 kHz signal during that process. The distance between the noise source and the array and the location of the speakers were the same as in the stationary tests. The results obtained in this test, shown in Figs. 8 and 9, were similar to those in the stationary tests. It was verified that this system would provide valid results for transient phenomena.

## 7. Application of System in Bench Analyses

An example of application of the system proposed in this paper to measurements of an actual vehicle is given here.

A vehicle with a 1.5L in-line 4-cylinder engine and automatic transmission was used.

The vehicle was placed on a chassis dynamo in a semi-

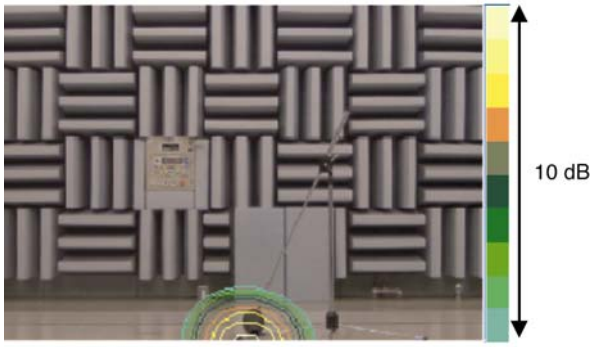



Fig. 6 Result of single source test (loudspeaker, 1 kHz)




Fig. 8 Result of stationary tone test
(×: Noise source)

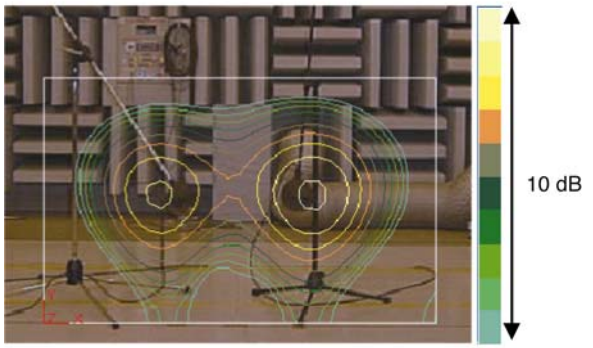



Fig. 7 Result of two-source test (loudspeaker, 1 kHz)

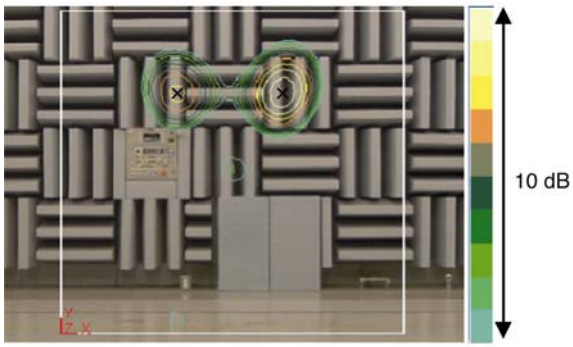



Fig. 9 Result of sweep tone test
(×: Noise source)

anechoic room and the dynamo was operated to enact a driving test with a controlled rolling resistance, simulating real driving conditions. The microphone array used for the analysis was arranged 4 m from the side of the vehicle, so that a single test could be performed; simultaneously, a single microphone was placed 7.5 m from the center of the vehicle at a height of 1.2 m to evaluate a far field (Fig. 10). The engine speed was reported by a sensor and recorded as well as the signals from the microphones by the analytical system.

The vehicle was accelerated at full power from an initial speed of 50 km/h during the same drive range as a driving mode specified in ISO 362 acceleration test, and time signal recording was done for about 1.5 sec as the vehicle passed through the measurement area (over 20 m long).

The analysis of the noise source location results and evaluation point results was conducted on the time signal at the engine speed at which the acceleration noise was the maximum (3 600 rpm).

Figure 11 shows the frequency spectrum observed from the original vehicle at the evaluation point. The frequency component showing the maximal level was 1 184 Hz, so this frequency was examined more closely. A noise source location analysis was also performed at 1 184 Hz on the microphone array signal, which had been taken at the same time; the results are shown in Fig. 12. These indicated that the main noise sources were the rear side of the front tires.

On the basis of these results, the test was re-performed after sound barriers had been installed behind the front tires. Figure 13 shows the results of the analysis performed at the same frequency as before. It is clear that the noise radiated by the main source component had been attenuated. Figure 14 presents a comparison of the analytical results for the frequency response, taken at the evaluation point at the same time, with the original frequency spectrum. This confirmed a roughly 12 dB reduction in noise at the target frequency, 1 184 Hz.

Next, the vehicle condition was changed and the exhaust noise radiated from the rear part of the exhaust system was recorded during the same driving range. The frequency analysis results at the evaluation point in this experiment are shown in Fig. 15. Prominent peaks in the spectrum are seen at 1 760 Hz and 1 880 Hz. These frequencies were chosen for closer examination. Figure 16 displays the noise source location results at these frequencies; it is clear that the source of this radiated noise was the rear part of the exhaust system.

The results of noise source location without the exhaust noise radiation and a comparison of the spectrums at the evaluation point with and without the exhaust noise radiation, are given in Figs. 17 and 18, respectively. There was a correlation between the noise source location results and the sound pressure level in the evaluation point. Thus, these analytical results for the vehicle showed that the location results are effective when the sound pressure level at evaluation points is reduced. Also, the time necessary for this task, from the measurement to the noise source location analysis, was within the target of 30 min.

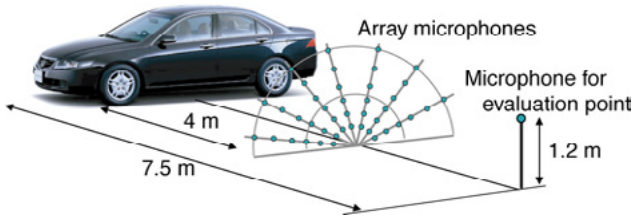



Fig. 10 Measurement condition

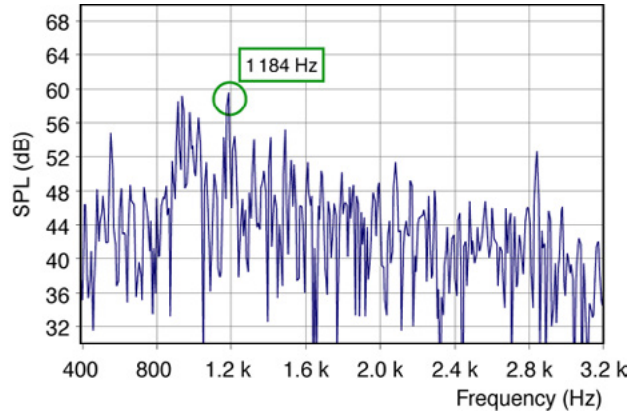



Fig. 11 Sound pressure spectrum at evaluation point




Fig. 12 Result of beamforming analysis

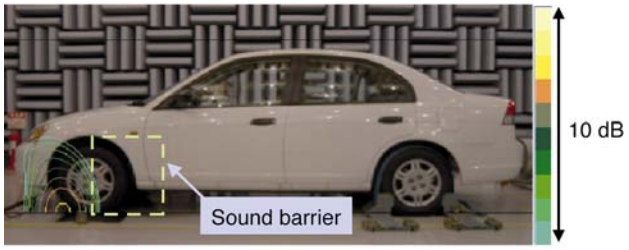



Fig. 13 Result of beamforming analysis (with sound barrier)

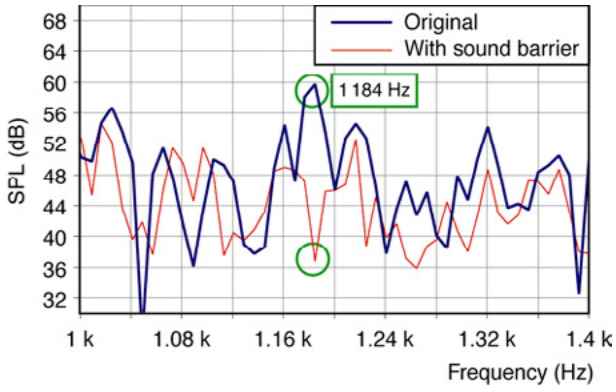



Fig. 14 Sound pressure spectrums at evaluation point

## 8. Conclusion

This paper reports the results of the application of the beamforming method of noise source location, which is one way for performing bench analysis of vehicle pass-by noise. A microphone array appropriate for analysis of pass-by noise was investigated as part of this effort. Tests of noise source location were carried out to examine the effectiveness of both the loud speakers and the vehicle noise source identification. As a result:

(1) A beamforming system incorporating a microphone array was created which met the targets for accuracy of noise source location, one-shot measurements, adequate processing time and effective dynamic range.

(2) It was confirmed that this method is effective for reducing noise by its application for noise source analysis of pass-by noise.

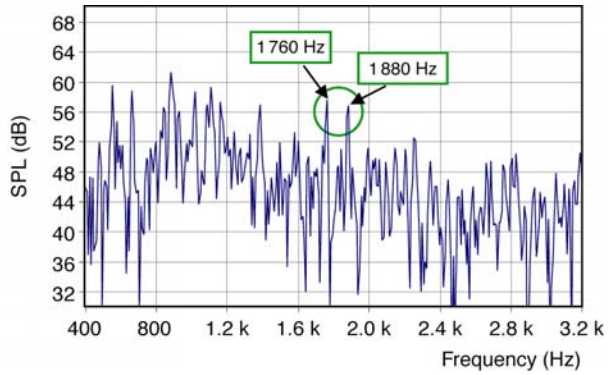



Fig. 15 Sound pressure spectrum at evaluation point

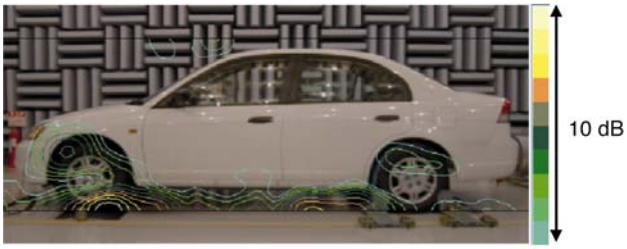



Fig. 16 Result of beamforming analysis (with exhaust noise radiation)




Fig. 17 Result of beamforming (without exhaust noise radiation)

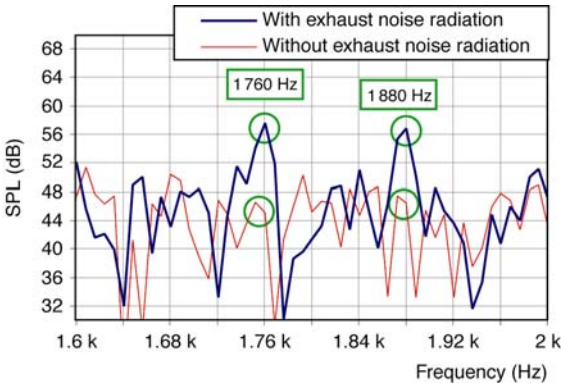



Fig. 18 Sound pressure spectrums at evaluation point

## Acknowledgements

The authors extend their deep gratitude to B&K Japan (Spectris Co., Ltd./BK Division) and Brüel & Kjaer for their assistance in this project.

## References

(1) Sawai, et al.: Measurement method for contribution of pass-by noise, JSAE, Vol. 35, No. 12, p. 1428-1432 (1981)

(2) Kashiwagi, H., et al.: Development of Noise Measurement System Using Microphones Array in Anechoic Camber, JSAE, Vol. 936, p. 281-284 (1993)

(3) Sakamoto, I., et al.: Noise Source Identification on an Operating Vehicle by Acoustic Holography, JSAE, Vol. 953, p. 145-148 (1995)

(4) Fleszar, A.R.: Combining Vehicle and Test-Bed Diagnosis Information to Guide Vehicle Development for Pass-By Noise, SAE 2001-01-1565 (2001)

(5) Stoker, R.W., et al.: Investigations of Airframe Noise in Pressurized Wind Tunnels, AIAA/CEAS 2001-2107 (2001)

(6) Takano, Y.: Visualizing Noise Sources of High Speed Train, Japan Society of Mechanical Engineers, Vol. 99, No. 931, p. 433-436 (1996)

(7) Takano, Y.: Development of Visualization System for High-Speed Noise Source with a Microphone Array and a Visual Sensor, Inter Noise 2003 Seogwipo, Korea, August 25-28 (2003)

(8) Hald, J.: A class of optimal broadband phased array geometries designed for easy construction, Inter Noise 2002 Dearborn, MI, USA. August 19-21 (2002)

## ■ Authors ■



Yukihiko HANZAWA



Jun KITAHARA



Shinichi NISHIMURA

# Establishment of Method for Analyzing Radiation Noise in Intake System

Hideaki ITOH* Mototaka MAEDA*
Fumihiko IDE* Jiro UEDA**

## ABSTRACT

Radiation noise in an air cleaner is determined by acoustic excitation due to internal pressure and also by the structural resonance characteristics. A calculation method was developed for predicting radiation noise by acoustic and structural coupling calculation analysis, and for designing the structure of the air cleaner to be as light as possible. This method was applied to the development of a new air cleaner. As a result, it was verified that the prediction accuracy of the radiation noise was within 300 Hz, which was adequate, and also it was possible to reduce the weight of the air cleaner by 12%, thus proving the effectiveness of this method.

## 1. Introduction

The need for a requirement to reduce the weight of the intake system has increased with the need to lighten automobiles themselves. Since the air cleaner accounts for much of the volume and weight of the intake system, this is certainly one of the components for which weight reduction should be required. The market appeal of automobiles with lower noise and vibration makes it more important to structure air cleaners to control radiation noise. Formerly, the generally used method for reducing radiation noise was to stiffen the exterior surface of the air cleaner by thickening the plate, adding reinforcing ribs, and other approaches. These tended to increase the weight of the air cleaner. Thus, there tends to be a contradiction between the goals of reducing the weight of the intake system and of reducing the radiation noise from it.

A simulation method was developed for predicting radiation noise from the air cleaner by an acoustic-structural coupled analysis, based on its acoustic and structural characteristics. In addition, a method was constructed for optimizing the structure for reduced weight while accomplishing the primary goal of a specified level of radiation noise.

* Tochigi R&D Center
** CDH Japan Ltd.

## 2. Factors Affecting Radiation Noise Characteristics

The noise radiated from an air cleaner is usually generated in the following process: Pulsations of the intake air occur in the intake passage, which give rise to pressure fluctuations, which propagate through the passages and provide the energy for acoustic inputs in the air cleaner.

An air cleaner was installed in a rig for a component test under acoustic excitation to analyze its characteristics that influence the radiation noise. The correlation between its vibration and radiation noise was examined.

### 2.1. Initial Component Test under Acoustic Excitation

In order to identify factors affecting the characteristics of radiation noise from air cleaners, a test air cleaner was removed from a completed vehicle and installed in a rig so that the acoustic excitation test could be carried out in a simpler manner with lower interference from other noise sources. The correlation between the results of this test and those from a test on a completed vehicle were examined.

Figure 1 compares the findings for the sound pressure level of the radiation noise from the air cleaner during engine

firing while installed in an actual vehicle and the sound level near the air cleaner in a component acoustic excitation test. The spectrum in the actual vehicle test was virtually the same as that in the component test. It was verified that the radiation noise characteristics of the air cleaner in an actual vehicle could be assessed using component tests.

## 2.2. Correlation between Air Cleaner Surface Vibration and Radiation Noise

Air cleaner surface vibration and the characteristics of radiation noise were compared in a component test to look for a relationship. The vibration characteristics of the surface were observed under vibration excitation (inertance) and under acoustic excitation (acoustic inertance).

### 2.2.1. Vibration due to vibration excitation and radiation noise characteristics

A comparison of inertance under vibration excitation and the frequency characteristics of radiation noise indicated that although the resonance peaks in the inertance were at frequencies neighboring the radiation noise peaks, these did not always occur together; the inertance could not really be described as showing the same frequency response as the radiation noise (Fig. 2). There was, at best, a minimal relationship between surface vibration due to vibration input into the air cleaner and radiation noise.

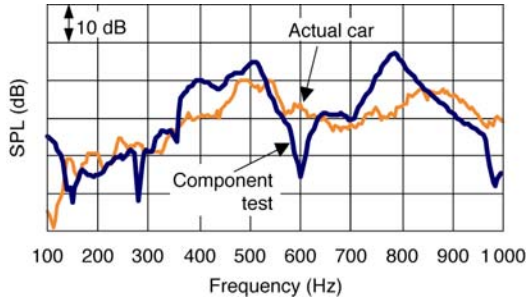



Fig. 1 Comparison of results between specification test and acoustic excitation test

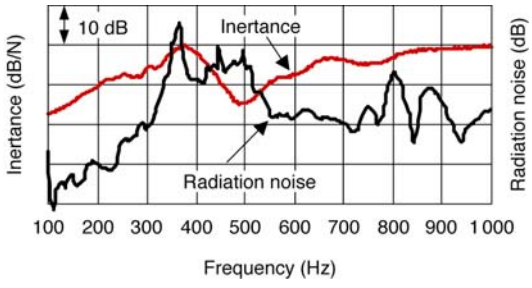



Fig. 2 Comparison of inertance and radiation noise

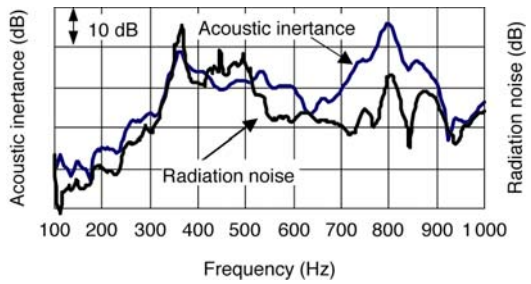



Fig. 3 Comparison of acoustic inertance and radiation noise

### 2.2.2. Surface vibration due to acoustic excitation (acoustic inertance) and radiation noise characteristics

Figure 3 compares the vibration frequency response under acoustic excitation (acoustic inertance) and the spectrum of radiation noise. These results show two matching peaks in the spectra, a high correlation between the acoustically-excited vibration and the radiation noise frequency response. It therefore seems necessary to analyze coupling between the internal acoustic input and the response due to vibration in the air cleaner radiation noise.

## 2.3. Examples of Generation of Air Cleaner Radiation Noise

Figures 4 – 7 present examples of air cleaner radiation noise. As shown in Fig. 4, during engine firing, the main components of the radiation noise from the air cleaner were between 300 and 400 Hz and above 500 Hz. Figure 5

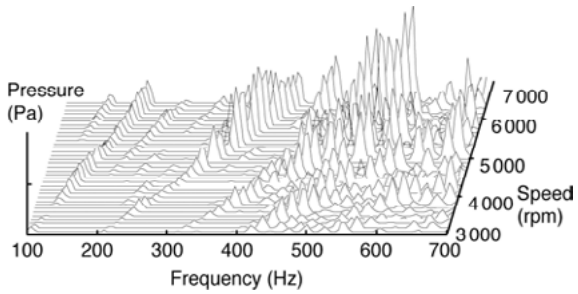



Fig. 4 Radiation noise spectrum

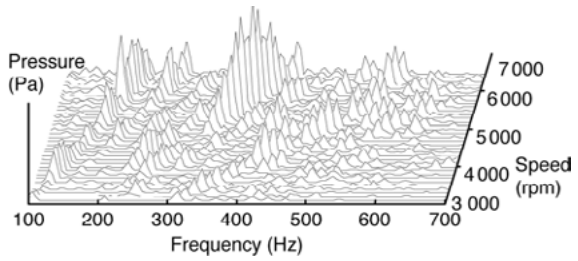



Fig. 5 Cabin noise spectrum including radiation noise

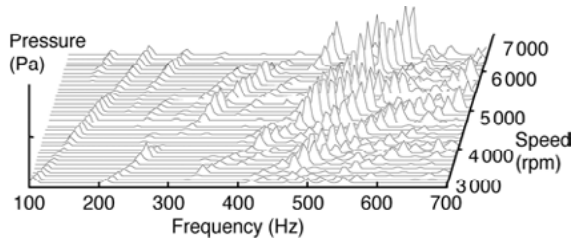



Fig. 6 Spectrum of reduced radiation noise spectrum

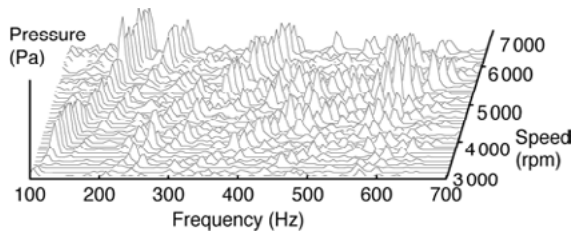



Fig. 7 Cabin noise spectrum including reduced radiation noise

demonstrates the noise occurring in the cabin at the same time. When the air cleaner in the engine compartment was covered with noise insulation to thoroughly mask its contribution to cabin noise, the spectrum changed by the magnitudes shown in Fig. 6; Fig. 7 shows the actual spectrum in the cabin, featuring much lower noise levels in the 300 – 400 Hz range. This indicates that the air cleaner is the source for much of the cabin noise in the 300 – 400 Hz range.

Thus, it was determined to concentrate on the region below 400 Hz in this study.

## 3. Construction of the Analytical Method

The radiation noise from an air cleaner was calculated in the method described below. This method uses acoustic-structural coupled analysis between the acoustic characteristics of the air intake passages and the vibration characteristics of the air cleaner.

### 3.1. Acoustic Characteristics of Air Intake Passages

The acoustic model of the entire air intake system shown in Fig. 8 was created with solid elements. It extended from the engine side, the excitation source, to the intake port. The excited panel (Fig. 9), which exerted an acceleration equivalent to the acoustic input, was made of shell elements and attached to a cross section of the throttle section of the intake system where it connected to the engine side. The excited panel was constrained in all but one direction so that its translation was in a direction parallel to the passages.

An acoustic input $P_{in}$ was applied to the excited panel, and the pressure $P_{(n)}$ corresponding to the pressure acting on the air cleaner wall was calculated using the transfer function $H_{ac(n)}$:

$$P_{(n)} = H_{ac(n)} P_{in} \quad (1)$$

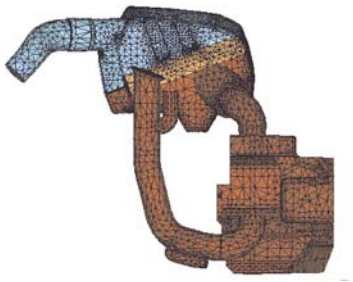


Fig. 8 Acoustic model

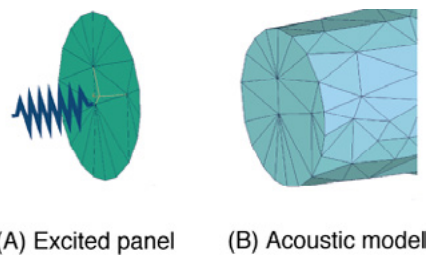



Fig. 9 Model of excited panel and acoustic model

### 3.2. Vibration Characteristics of the Air Cleaner

A shell model of the air cleaner structure was constructed of finite elements. The exterior structure of the case and cover as well as the rubber seals, filter, and fastener locations for the cover were made of fine shell models in order to improve calculation accuracy.

### 3.3. Creation of the Model of the Acoustic-Structural Boundary

In order to create the acoustic-structural model boundary, it is essential for the elements at the boundaries between the two models to meet up with each other one-for-one. Ordinarily, however, the structural model is made with a much finer mesh than the acoustic model. This makes it unlikely for the elements to match up with each other at the boundary. Therefore, it is necessary to use a large number of matrices (coupling matrices, defined in Eq. (2)) in order to approximately compensate the mismatches in the boundary where the acoustic model and structural model are in contact. In other words, the force $V_{(m,n)}$, exerted on every element in the structural model, is given by the product of this coupling matrix $M_{(m,n)}$ with $P_{(n)}$, as depicted in Fig. 10.

$$V_{(m,n)} = M_{(m,n)} P_{(n)} \quad (2)$$

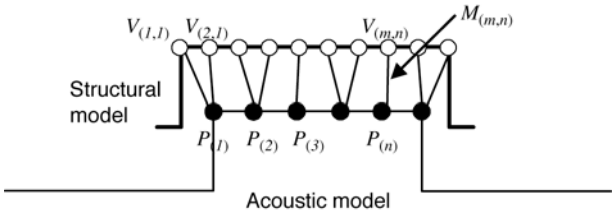



Fig. 10 Coupling matrix

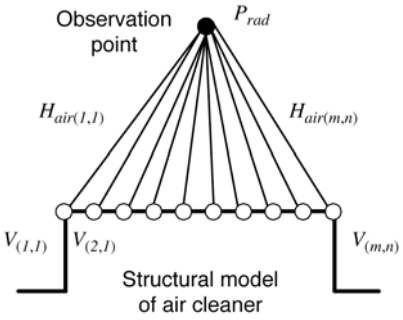



Fig. 11 Acoustic transfer function

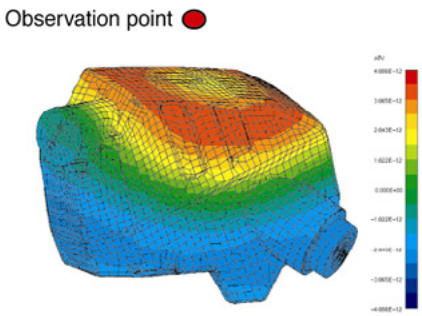



Fig. 12 Example of calculation of acoustic transfer function

### 3.4. Calculation of the Acoustic Transfer Function

In order to find the noise $P_{rad}$ radiated by the air cleaner surface at the observation point, as shown in Fig. 11, the acoustic transfer functions $H_{air(m,n)}$ from each element of the model surface to the observation point are calculated. Figure 12 demonstrates some results using the acoustic transfer functions for an actual air cleaner. The locations showing high contributions are colored in red. In this example, it is clear that there are high contributions from the upper surface down onto the sides.

### 3.5. Calculation of Radiation Noise

The radiation noise at the observation point can be calculated using Eq. (3), inserting the air intake path transfer function $H_{ac}$, the coupling matrix $M_{(m,n)}$, and the acoustic transfer functions $H_{air(m,n)}$.

$$P_{rad} = \Sigma H_{air(m,n)} V_{(m,n)} = \Sigma [H_{air(m,n)} M_{(m,n)} H_{ac(n)} P_{in}] \quad (3)$$

## 4. Optimization Calculations

In the previous sections, the radiation noise from an air cleaner was seen to be determined by the acoustic transfer function of the passages in the intake system and the structural characteristics of the air cleaner. Thus, one can develop two methods for optimizing an air cleaner to accomplish both an objective radiation noise level and a reduced weight air cleaner. One method is to improve the acoustic characteristics, while the other method is to improve the structural characteristics of an intake passage system. For this study, it was decided to optimize the structural characteristics, rather than the acoustic characteristics, to obtain reduced radiation noise and reduced weight.

This method consists of tuning the vibration eigenvalues of a system, avoiding coupling with acoustic resonance. It assumes that there exists an optimized structure capable of low radiation noise; the optimization calculations seek both the objective function for the radiation noise and the objective function for reduced weight.

For the variables in the optimization calculations, the plate thickness of the air cleaner exterior wall and the reinforcing material were used. In the first stage, the weight of the air cleaner was constrained to seek the structure which yielded the desired sound pressure level of the radiation noise in the target frequency band. In the second stage, the radiation noise level was constrained while seeking a structure of minimal weight. A β mesh was used for the optimization algorithm in order to minimize the peak sound pressure level within the frequency band of interest.

The exterior wall and reinforcing rib thickness, which were used as parameters, were each divided into several sections. An example is shown in Fig. 13. This section was divided with reference to parameters from the acoustic transfer function (Fig. 11) and the modes of vibration of the structural model.

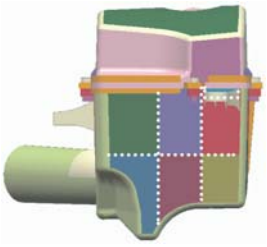


Fig. 13 Example of divided sections

## 5. Application Results

An example of application of these analytical method and optimization calculations to radiation noise and weight reduction in an air cleaner during development of a new intake system is described below.

### 5.1. Verification of Precision of Calculated Radiation Noise Level

Figure 14 presents a comparison of the calculated radiation noise and the measured results in an acoustic excitation test. Below 300 Hz, the characteristics were well reproduced by the simulation. This showed that the method described above is able to predict radiation noise.

### 5.2. Application to Optimization Calculations

The structure model of an air cleaner was sectioned in accordance with its modes of vibration and optimized for light weight while meeting radiation noise performance requirements.

As shown in Fig. 15, the first stage concerned the initial acoustic response: Setting objective levels in an objective function for radiation noise; optimizing the wall thickness of each section; and identifying the structure which met the objective levels. In this example, the ninth iteration achieved the radiation noise targets. The optimized structure obtained in the first stage was used as the initial structure for the second stage, and the radiation noise level was constrained. A

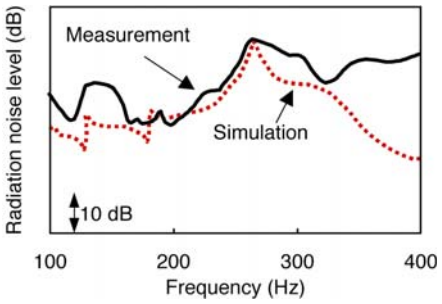



Fig. 14 Correlation of experimental and simulation results

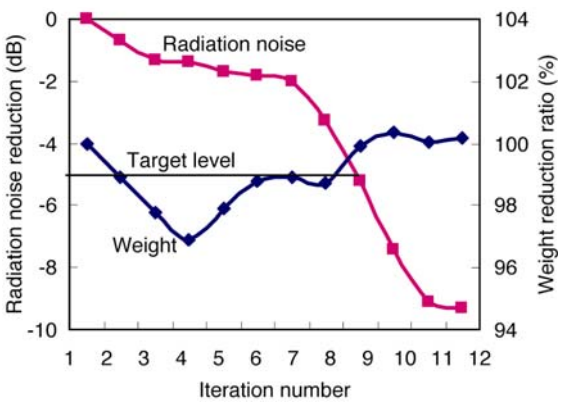



Fig. 15 First step of optimization

structure with reduced weight was obtained, as shown in Fig. 16; in this example, the final weight was about 85% of the initial weight.

### 5.3. Verification of Optimization Results

The brackets and other fittings attached to the air cleaner described in the previous section were manufactured and the weight and radiation noise level of the actual air cleaner were checked. The results are shown in Fig. 17; the radiation noise level was reduced by 8 dB, and the total weight by 12% in a completed vehicle.

## 6. Conclusion

The internal acoustic characteristics of an air cleaner and its structural characteristics were used in an acoustic-structural coupled analysis to predict the noise radiated from the air cleaner. A method was constructed to optimize the structure and the following results were obtained.

(1) This calculation method allowed prediction of radiation noise at frequencies below 300 Hz.
(2) This method was verified to enable development of new air cleaners meeting radiation noise targets while maintaining low component weight.

Also, this method was used to develop a new air cleaner whose radiation noise met the objective and which was 12% lighter than the initial design.

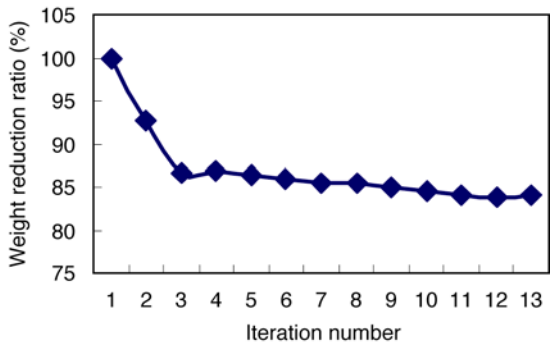



Fig. 16 Second step of optimization

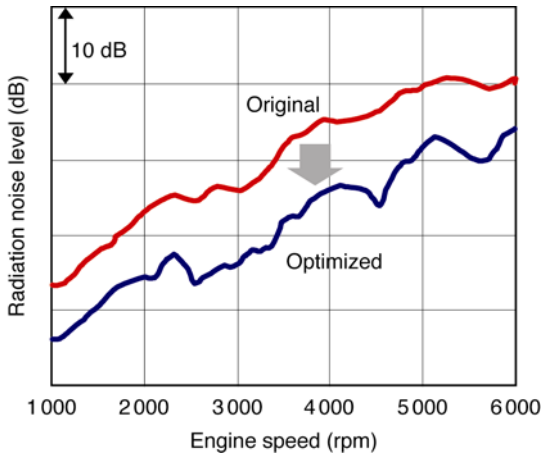



Fig. 17 Radiation noise reduction effect in the vicinity of actual car

## References

(1) Amago. T.: Sizing Optimization Using Response Surface Method in FOA, R&D Review of Toyota CRDL, Vol. 37, No. 1, p. 31-36 (2002)

(2) Taguchi: Methods for planning experiments, 3rd ed. Vol. 1 (1976)

(3) M. Alex: Air Intake Development-Effects of Coupled Fluid/Structure Modes, SAE paper n. 20011919

(4) Mladen Chargin: Optimization of frequency response with β equations, www.cdh.co.jp/technical/beta.pdf

■ Authors ■


Hideaki ITOH


Mototaka MAEDA


Fumihiko IDE


Jiro UEDA

# Verification of Modal Arrangement for Reduction of Body Response

Koichi TAKAHASHI* Masafumi KYUSE* Tatsuhide SAKAI *


## ABSTRACT

This report describes a verification of cabin noise reduction for a medium class sedan at engine speeds lower than 2 000 rpm. Mode frequencies and mode shapes are defined as a modal arrangement, and a target arrangement is established to achieve significant body response reduction. In order to realize the target arrangement, a FE model of a semi-white body structure is modified, and an actual vehicle is modified as well. As a result, overall body response is reduced, and as desired a relationship between phases in the upper and lower parts of the cabin is improved. Thus, the modal arrangement is proven to be effective to reduce body noise and vibration.


## 1. Introduction

System characteristics related to cabin noise of a vehicle are diverse, including engine vibration, engine mount characteristics, sub-frame characteristics, drive train and suspension transfer characteristics, body characteristics and cabin acoustics. This report examines cabin noise associated with the body frame of a medium class sedan with an in-line 4 cylinder engine (displacement 2.41 – 5 AT) for engine speeds under 2 000 rpm, focusing on body characteristics. The modes that make the largest contribution to body vibration are defined as S-class modes and have been selected for further study. The mode frequency and mode shape of each of the modes is defined as its modal arrangement. A target for a set of modal arrangements that greatly reduce body vibration has been defined. In order to realize the target arrangement, the structure was analyzed using a finite element (FE) model. After making modifications to a semi-white body, it was possible to meet the target of reduction in body vibration and the target for the phase relationship of the upper and lower parts of the cabin. The arrangement example that is being described here shows that it is feasible to reduce body vibration.

* Tochigi R&D Center

## 2. Experimental Modal Analysis

In order to obtain modes for the vehicle under running condition, operational experimental modal analysis (operational EMA) was performed on a vehicle. In order to better grasp the body modes, modal analysis was performed on a semi-white body, which is a white body with both the windshield and the rear window installed.

### 2.1. Operational Experimental Modal Analysis

A vehicle was placed on a chassis dynamometer and as can be seen in Fig. 1, there were two excitation points, the front portion of the sub-frame and the knuckle of the right front wheel. Vibration data was taken at 213 different locations, including on the doors, the suspension, the sub frame, and on the body.

The vertical axis of Fig. 2 is vehicle speed and the horizontal axis is frequency. The green dotted lines are wheel harmonics and the black solid line is the first order harmonic from the engine with the vehicle running in $5^{th}$ gear. The intersections of the red solid line and blue solid line are 90 km/h and 100 km/h respectively, with the green dotted

lines and black solid line showing where the frequencies meet the first order harmonic of the engine and the wheel harmonics.

In this manner, two speeds where the wheel harmonics and the first engine harmonic do not overlap were arbitrarily chosen within a frequency range for measurement. While holding speed steady, an excitation test using two exciters and frequency response function measurement at 213 locations was performed.

The frequency response functions for the two speeds are shown in Fig. 3. In the frequency response function measured, a noise peak can be seen for a frequency that overlaps one of the wheel harmonics; however, a frequency response function without peaks was obtained through processing of the data.

The modes during vehicle operation were obtained through performing modal analysis using frequency response functions in this manner.

Figure 4 shows synthesized frequency response functions from each mode that has a large contribution to body vibration levels (S-class modes) and actual frequency response function data from the upper part of the cabin. As can be seen from this figure, the contributions of the 4 modes S1, S2, S3, and S4 are large. The frequency of each mode is shown in Table 1.

For reference, there are modes other than these S-class modes that have large contributions; however, they are not body vibration modes, they are modes of the suspension, doors, etc.

As an example, the S1 mode shape has been placed in Fig. 5. A characteristic of this mode is that along with bending of the body, the upper and lower parts of the cabin are out of phase, which is considered an unfavorable mode shape for changing the volume of the cabin.



Fig. 1 Excitation points in operational EMA

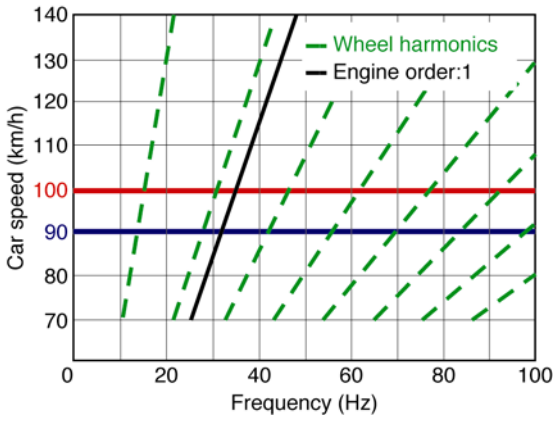



Fig. 2 Condition of operational EMA

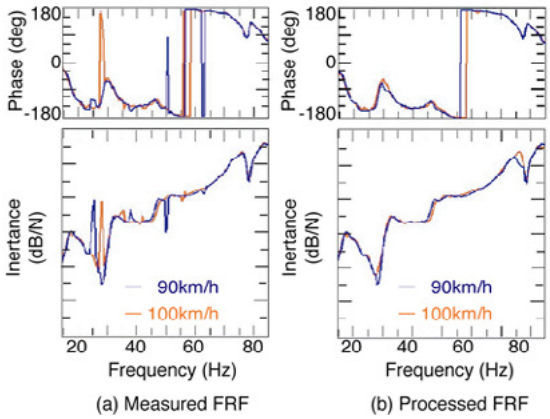



Fig. 3 Post processing of operational EMA

Table 1 S class mode frequency obtained from operational experimental modal analysis

| Mode number | Frequency |
|---|---|
| S1 | 31.5Hz |
| S2 | 45.7Hz |
| S3 | 51.7Hz |
| S4 | 77.7Hz |

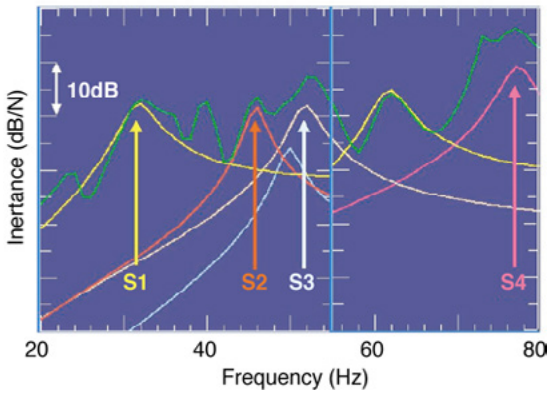



Fig. 4 Contribution of S class modes to measurement frequency response function

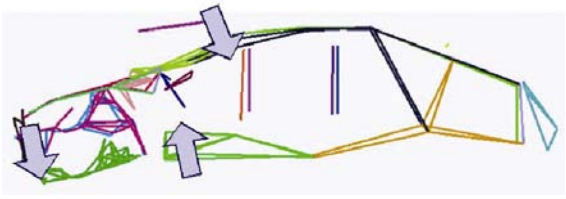


Fig. 5 Mode shape of S1

Similar to the S1 mode, the S2 mode shape is a mode that exhibits out of phase vibration of the upper and lower parts of the cabin. In order to reduce interior sound pressure, changes in the mode frequency and/or improving the mode shape such that the vibration of the upper and lower parts of the cabin change from being out of phase to in phase are considered.

## 2.2. Experimental Modal Analysis

In order to more clearly grasp body modes, modal analysis of a semi-white body was performed. The semi-white body was placed on an air mount. Exciters were set in 2 places, one at the front right connection point of the front sub frame and the other at the left rear connection point. Frequency response functions were measured at 131 locations in 3 axes. Modes were extracted using modal analysis.

Figure 6 shows synthesized frequency response functions from each of the modes that have a contribution to semi-white body vibration levels (W-class modes) and actual frequency response function data from the upper part of the cabin in the 40 – 60 Hz region. This diagram shows that the contributions of the 5 modes W1, W2, W3, W4 and W5 are large.

The W-class modes have been listed in Table 2. From their mode shape characteristics, it was judged that there is a high correlation between S1 and W1, S2 and W3, and S3 and W4.

As an example, the W1 mode shape is shown in Fig. 7. Similar to S1, the upper and lower parts of the cabin are out of phase and it is clear that this is an unfavorable mode shape for changing the volume of the cabin. It was confirmed that the W3 characteristics matched those of W1.

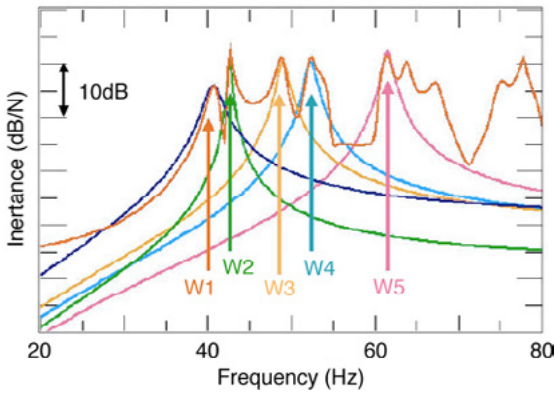



Fig. 6 Contribution of W class modes to measurement frequency response function

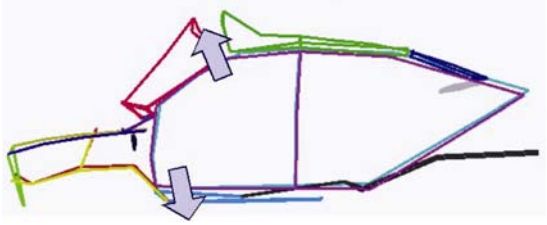


Fig. 7 Mode shape of W1

Table 2 W class mode frequency obtained from experimental modal analysis

| Mode number | Mode number | Frequency |
|---|---|---|
| S1 | W1 | 40.8Hz |
| | W2 | 42.6Hz |
| S2 | W3 | 48.9Hz |
| S3 | W4 | 52.8Hz |
| | W5 | 60.8Hz |

# 3. Change in Modal Arrangement

A modal arrangement is defined to be the combination of the mode frequency and mode shape. Experimental changes to the modal arrangement for reduction in the vibration of the upper part of the cabin and for improvement in the phases of the upper and lower parts of the cabin were tried.

## 3.1. Target for Changes to the Modal Arrangement

Targets were set based on the results of the previous paragraph.

For the W1 mode, in order to reduce underbody vibration the stiffness line was lowered and a target of a 20% increase in mode frequency, 49 Hz, was set.

As can be seen in Fig. 8, for the W2 mode, improvements have been made to the mode shape to change the phases of the upper and lower parts of the cabin from an out of phase to an in-phase relationship. In order to couple it with the W1 mode, it was targeted at 49 Hz.

The W3 mode, similar to the W1 mode, has a mode shape where the upper and lower parts of the cabin are out of phase. Through a synthesis of the frequency response function from modal parameters, it was confirmed that a frequency difference of 9 Hz or greater was needed, therefore the target frequency for W3 was set at 58 Hz.

As the W4 mode has a similar mode shape as the W2 mode, it was given the same percentage increase in frequency, 14%, for a calculation of 60 Hz.

For W5, it was confirmed that a frequency difference of 4 Hz or greater than W4 was needed through a synthesis of the frequency response function from modal parameters, therefore the target frequency for W5 was set at 64 Hz.

The target frequency for each of the W-class modes is shown in Table 3.

## 3.2. Frequency Response Function Synthesized from Target Arrangements

Using the results of the experimental modal analysis, the modal arrangement was changed into the target arrangement. Then a synthesis of the frequency response functions was

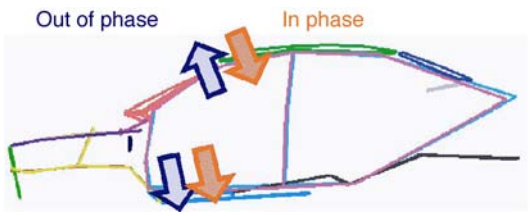



Fig. 8 Concept of mode shape change

Table 3 Target mode frequency determined by refining modal arrangement

| Mode number | Base frequency | Target frequency |
|---|---|---|
| W1 | 40.8Hz | 49Hz |
| W2 | 42.6Hz | 49Hz |
| W3 | 48.9Hz | 58Hz |
| W4 | 52.8Hz | 60Hz |
| W5 | 60.8Hz | 64Hz |

performed. Figure 9 shows the frequency response function for the front area of the side frame, which is the front body, and the frequency response function for the upper part of the cabin, which has a large contributor to cabin noise. The vibration peak level of the front area of the side frame was not changed. It is estimated that the lowering of the stiffness line would reduce body vibration for lower engine speeds. Through coupling of the different phase modes in the upper part of the cabin it was possible to reduce the vibration level by 6 dB.

As can be seen in Fig. 10, it was also possible to confirm that the phase relationship of the upper and lower parts of the cabin was changed from out of phase to in-phase for the range of 40 – 50 Hz.

From these results it was verified that it is possible to achieve targeted vibration reduction levels through making changes to the modal arrangements in accordance with the above targets.

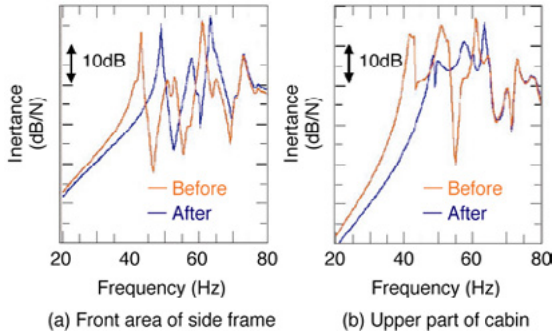



Fig. 9 Estimation of response levels by refining modal arrangement

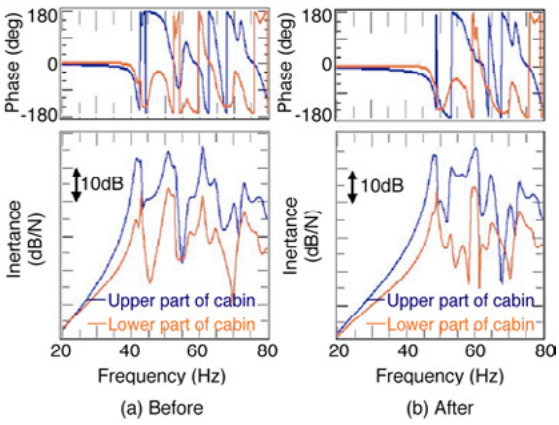



Fig. 10 Estimation of phases in upper and lower parts of cabin by refining modal arrangement

## 4. Changes to Structure with the FE Model

In order to implement the target modal arrangement established in the previous paragraph, a sensitivity analysis was performed for target modes using an FE model of a semi-white body. An estimation of performance was completed after structural changes were made based on these results.

### 4.1. Sensitivity Analysis and Structural Changes

For targeted modes, stiffness sensitivity, mass sensitivity, and sheet metal thickness sensitivity analyses were performed. This identified the places where changes to the structure are needed.

Figure 11 shows the results of the stiffness sensitivity analysis of W1 mode. This diagram shows that the mode frequency can be increased through increasing the stiffness of the yellow and pink areas. It has been found that increasing the stiffness around the window and the upper and lower weld areas of the center pillar is effective at changing this mode's modal arrangement.

Figure 12 shows the results of the mass sensitivity analysis of mode W2. This diagram shows that the mode frequency can be increased through decreasing the mass of the brown and blue areas. For this mode, reduction in the weight of the front area of the side frame and the front bulkhead was found to be effective in changing the modal arrangement.

For all of the W-class modes, structural changes were made in a FE model while monitoring the strain energy distribution and stiffness and mass sensitivity analyses. Structural changes were made at the joints of each pillar, of the side sill, of the roof side rail, of the roof rail, etc., for an approximate total of 20 places.

### 4.2. Performance Achievement Estimation

A refined FE model investigated previously was used to estimate performance.



Fig. 11 Stiffness sensitivity analysis



Fig. 12 Mass sensitivity analysis

Table 4 Estimated mode frequencies with refined FE mode

| Mode number | Target frequency | Estimated with refined FE model |
|---|---|---|
| W1 | 49Hz | 52Hz |
| W2 | 49Hz | 49Hz |
| W3 | 58Hz | 57Hz |
| W4 | 60Hz | 59Hz |
| W5 | 64Hz | 64Hz |

Table 4 shows the mode frequencies for the performance estimation from a refined FE model and targeted modal arrangements. Concerning the modal arrangement, the W1 mode is 3 Hz higher than the target and the W3 mode is 2 Hz lower. Figure 13 shows the synthesized frequency response function for the front area of the side frame and the upper part of the cabin with the base and refined FE model. It also shows a 6 dB reduction was achieved for the front area of the side frame and a 12 dB reduction was achieved for the upper part of the cabin.

The phase relationship of the upper and lower parts of the cabin is shown in Fig. 14. Prior to the changes they were out of phase in the 40 – 52 Hz region. After the change they now have an in-phase relationship in this region.

Through the structural changes discussed previously, it is expected that the modal arrangement will be improved and a reduction in vibration level will be achieved when the changes are also made to an actual vehicle.

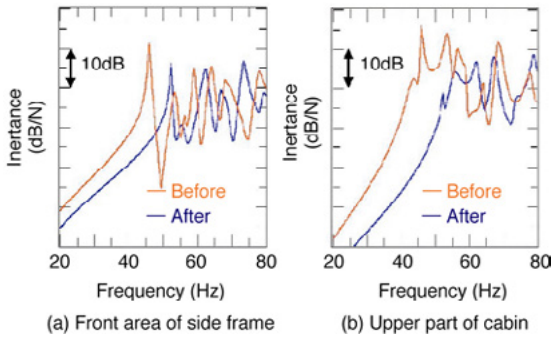



Fig. 13 Estimation of response levels by refining FE model

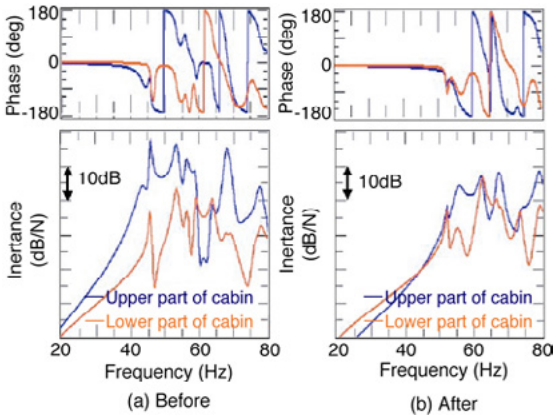



Fig. 14 Estimation of phases in upper and lower parts of cabin by refining FE model

Table 5 Verified mode frequencies with modified semi-white body

| Mode number | Estimated with FE model | Verified with modified semi-white body |
|---|---|---|
| W1 | 52Hz | 51.9Hz |
| W2 | 49Hz | 49.2Hz |
| W3 | 57Hz | 56.3Hz |
| W4 | 59Hz | 59.1Hz |
| W5 | 64Hz | 63.5Hz |

## 5. Verification of a Modified Semi-white Body

The changes that were made in the FE model were used to make modifications to a semi-white body. Verification of the changes to the modal arrangement, developed by these modifications, was performed through experimental modal analysis, using the conditions described in section 2.2. The information in Table 5 confirms that the mode frequencies estimated by the FE model match the results of the experimental modal analysis.

The frequency response functions of the upper part of the cabin and the front area of the side frame for the base and modified condition of the semi-white body are shown in Fig. 15. Through moving the stiffness line down the vibration level of the front area of the side frame was lowered 6 dB. The upper part of the cabin's vibration level was lowered 7 dB at the peak frequency under 60 Hz and was lowered 10 dB at other frequencies.

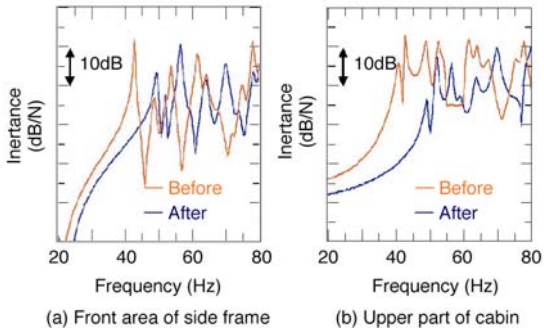



Fig. 15 Verification of response levels by modifying semi-white body

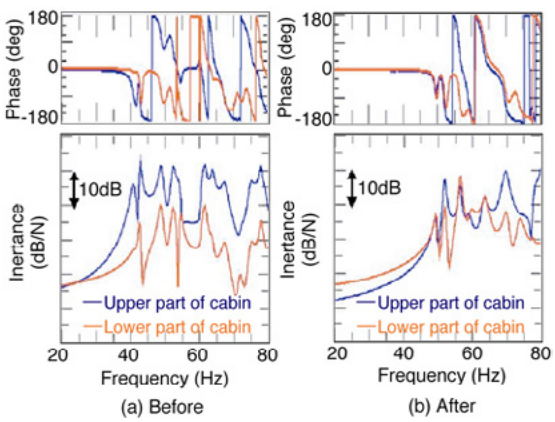



Fig. 16 Verification of phases in upper and lower parts of cabin by modifying semi-white body

The phase relationship for the upper and lower parts of the cabin is shown in Fig. 16. Prior to changes made to the semi-white body, the upper and lower parts of the cabin were out of phase over the broad region of 42 – 60 Hz. After making the targeted changes to the mode shape, the upper and lower parts of the cabin became in phase for the ranges below 52 Hz and above 60 Hz.

## 6. Conclusion

This report focused on the reduction of cabin noise for engine speeds under 2 000 rpm for a medium class sedan with an in-line 4 cylinder engine. This was done through investigation of the modal arrangement of a semi-white body. The following results were achieved.

(1) The modal arrangement was changed with a focus on the phases of the upper and lower parts of the cabin. Through analysis it was estimated that by coupling the different modes of specific target areas, the body vibration level could be reduced.

(2) Structural changes that could achieve the targeted mode shapes and frequencies were first investigated through analysis and then verified through modifications to a semi-white body.

This verifies that the examination of the modal arrangement is effective at reducing the level of body vibration.

The changes described in this report will be applied to the trimmed body and vehicle. This will be done in order to further verify that the modal arrangements used in this report are effective at reducing cabin noise levels.

This method has been exhibited to be a useful tool to reduce the overall vehicle weight while improving noise and vibration performance, crash performance, and driving stability.

## References

(1) Banner, A.: Development of the 2002 Buick Rendezvous Body Structure, Proceeding SAE Noise & Vibration Conference, 2001-01-1414 (2001)

(2) Deweer, J.: Identification of the Best Modal Parameters and Strategies for FE Model Updating, Proceeding SAE Noise & Vibration Conference, 2001-01-1439 (2001)

(3) Sakurai, T.: Study on Weight Reduction for a Vehicle Body in Design Process, Proc. of JSAE Autumn Convention 20015525 (2001) (in Japanese)

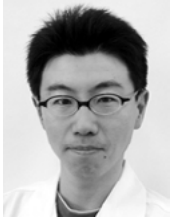
(4) Liu, L.: Application of FRF-Based Inverse Substructuring Analysis to Vehicle NVH Problems, Proceeding SAE Noise & Vibration Conference, 2003-01-1607 (2003)

(5) Akanda, A.: Modal Overlap at Low Frequencies – A Stochastic Approach for Vehicle System Modal Management, Proceeding SAE Noise & Vibration Conference, 2003-01-1612 (2003)

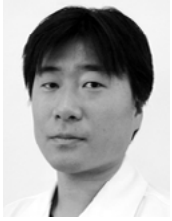
(6) Sakai, T.: Development Procedure for Interior Noise Performance by Virtual Vehicle Refinement, Proceeding SAE Noise & Vibration Conference, 2001-01-1538 (2001)

(7) Sakai, T.: Improvement of Engine Noise for the 2003 Accord Using Hybrid CAE Technology, Proceeding SAE Noise & Vibration Conference, 2003-01-1427 (2003)

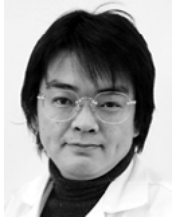
■ Authors ■



Koichi TAKAHASHI



Masafumi KYUSE



Tatsuhide SAKAI

# Improving Suspension and Engine Mount Transfer Path Analysis Accuracy with Respect to Low Frequency Noise and Vibration

Masafumi KYUSE* Koichi TAKAHASHI* Tatsuhide SAKAI*

## ABSTRACT

This paper describes a transfer path analysis method used to analyze the low frequency noise and vibration contribution of suspension and engine mounts caused by second order engine vibration. This transfer path analysis method is capable of removing transmitted forces from other paths (residual forces) besides the main path at a particular degree of freedom. Compared to the conventional methods, results from this analysis method showed improved accuracy with respect to vehicle measurements. From the results of the transfer path analysis performed by using this method, frequency range and contribution by the suspension paths for low frequency noise and vibration are clarified.

## 1. Introduction

In the analysis of automotive noise and vibration, Transfer Path Analysis (TPA) provides a means to determine an effective countermeasure; due to the fact that the contribution, input force, and sensitivity that constitute each path, are well-defined. Because of these characteristics, TPA is used in various cases of analyses[(1), (2)].

However, when the systems are coupled at mutually adjacent points, as is the case with some engine and suspension mounts which are coupled to a sub-frame, multiple transfer forces affect a single connecting degree of freedom, making it difficult to separate the transfer paths. Thus, even if TPA is performed, the measurement results will not agree with the analysis results, and it will be difficult to construct a highly accurate model. Consequently, the contribution of each system for an event will not be well defined, and it will be difficult to determine system level target values in order to achieve global targets, such as interior noise and steering vibration, without excess or deficiency.

This paper describes an example of using the conventional TPA method for low-frequency vibration and noise caused by engine combustion forces, and clarifies issues related to accuracy. Next, it describes a method (residual method) in which transfer forces (residual forces) from paths other than the main path are removed, and indicates the theoretical equations involved. It also suggests a practical judgment criterion for the connecting degree of freedom to which this method is applicable. In addition, it clarifies the advantages compared to conventional methods, and also clarifies the contribution of the suspension to low-frequency vibration and noise.

## 2. Description of the TPA Method

As shown in Eq. (1), the TPA method obtains the composite noise and vibration $S_{All}$ by multiplying the input force $F_i$ of the connecting degree of freedom of the object of analysis by the sensitivity $S_i/F_i$ from the connecting degree of freedom to the targeted noise and vibration $S_i$, and then calculating the vector sum[(3)]. This permits an analysis of the extent to which each connecting degree of freedom contributes to the target.

* Tochigi R&D Center

$$S_{All} = \sum_{i}^{n} F_i \times S_i / F_i \quad (1)$$

Conventional methods of obtaining transfer forces are the mount stiffness and the inverse matrix methods. The points to note when using each of these methods and the results of analysis obtained are described below.

### 2.1. Mount Stiffness Method

As shown in Eq. (2), the mount stiffness method derives the transfer force by multiplying mount stiffness $K$ of the coupled mount rubber by the relative displacement $x_a - x_p$ between the input and response sides.

$$F_{MS\text{-}path} = K \cdot (x_a - x_p) \quad (2)$$

The mount stiffness method performs coupling between each input and response side by using the mount dynamic stiffness characteristics, so the contribution of each coupling becomes clear. However, in the case of a highly rigid spring-coupled path that cannot be isolated, such as the suspension, the predicted value for the transfer force does not agree with the measured vehicle result, so the accuracy is low.

### 2.2. Inverse Matrix Method

On the other hand, the inverse matrix method measures the frequency response $[\ddot{x}_{Mlk} / F_{Mlj}]$ and acceleration $[\ddot{x}_{Mlk}]$ at which all of the connecting degrees of freedom are taken as the input and response, performs the inverse matrix calculation of Eq. (3), and derives the transfer force $[F_{Mlj}]$.

$$\begin{bmatrix} F_{Ml1} \\ \vdots \\ F_{Mlj} \end{bmatrix} = \begin{bmatrix} \ddot{x}_{Ml1}/F_{Ml1} & \cdots & \ddot{x}_{Ml1}/F_{Mlj} \\ \vdots & \ddots & \vdots \\ \ddot{x}_{Mlk}/F_{Ml1} & \cdots & \ddot{x}_{Mlk}/F_{Mlj} \end{bmatrix}^{-1} \cdot \begin{bmatrix} \ddot{x}_{Ml1} \\ \vdots \\ \ddot{x}_{Mlk} \end{bmatrix} \quad (3)$$

The inverse matrix method enables accurate results to be obtained in a system containing a highly rigid spring coupling. However, in order to stabilize the inverse matrix calculation, it is necessary to over determine the matrix by at least twice the number of connecting degrees of freedom. Also, if multiple transfer forces affect a single connecting degree of freedom, such as in the case of the engine mount and suspension which are coupled to a sub-frame, it is not possible to extract the contribution for that path alone.

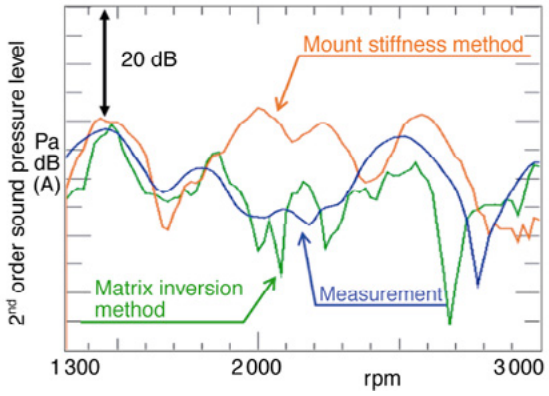



Fig. 1 Comparison of measured response with response calculated using two methods

Figure 1 shows the result of a comparison performed between the composite sound pressure derived from the above methods, and the measured value. As can be seen from the figure, the calculated result derived from the mount stiffness method is at least 10 dB higher than the result of measurement in the vicinity of 2 000 rpm. This is due to the fact that the suspension transfer force increases in this region, becoming a major contributing factor. Also, the calculated result derived from the inverse matrix method was 7 dB lower than the vehicle measurement result in the vicinity of 2 500 rpm. This is due to multiple transfer forces acting upon a single connecting degree of freedom.

### 2.3. Combination of the Mount Stiffness and the Inverse Matrix Methods

Analysis consisting of a combination of two methods, namely the inverse matrix and mount stiffness methods was carried out. This appears to have the merits of both methods that comprise it. The engine mount side to which the mount stiffness method is applied is isolated, and the calculation accuracy is high, however at the suspension mount to which the inverse matrix method is applied, the calculation accuracy is reduced. On the sub-frame, the suspension and engine mount are adjacent to each other. The connecting degree of freedom of the suspension is affected not only by the suspension transfer force, but also by the engine mount transfer force as well. This engine mount transfer force component constitutes a residual force, preventing an accurate transfer force calculation at the suspension coupling point. As a result, as shown in Fig. 2, the calculated value does not agree with the result obtained from vehicle measurements, so the calculation accuracy is low.

## 3. Description of TPA Using the Residual Method

In the conventional combined method, the matrix inversion calculation accuracy was poor due to the influence of the engine mount transfer force (residual force) upon the suspension connecting degree of freedom; therefore, the engine mount residual force will be removed by using the residual method as described below[4].

As shown in Eq. (4), in order to obtain the vibration $[\ddot{x}_{MSm}]$ of the connecting degree of freedom at which the inverse matrix method was used, the transfer force $[F_{MSn}]$ of the

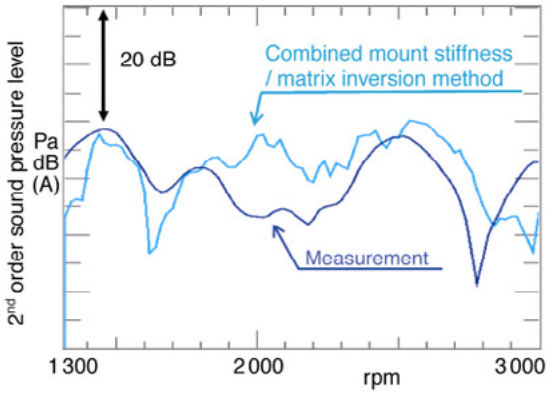



Fig. 2 Comparison of measured response with response calculated using combination of two methods

connecting degree of freedom at which the mount stiffness method was used is multiplied by the vibration sensitivity $[\ddot{x}_{MSm} / F_{MSn}]$ to the connecting degree of freedom at which the inverse matrix method was used.

$$\begin{bmatrix} \ddot{x}_{MS1} \\ \vdots \\ \ddot{x}_{MSm} \end{bmatrix} = \begin{bmatrix} \ddot{x}_{MS1}/F_{MS1} & \cdots & \ddot{x}_{MS1}/F_{MSn} \\ \vdots & \ddots & \vdots \\ \ddot{x}_{MSm}/F_{MS1} & \cdots & \ddot{x}_{MSm}/F_{MSn} \end{bmatrix} \cdot \begin{bmatrix} F_{MS1} \\ \vdots \\ F_{MSn} \end{bmatrix} \quad (4)$$

Next, as shown in Eq. (5), $[\ddot{x}_{MSm}]$ is subtracted from measured value $[\ddot{x}_{measm}]$, enabling the vibration $[\ddot{x}_{MIm}]$ from which the influence of other connecting degrees of freedom was removed, to be obtained.

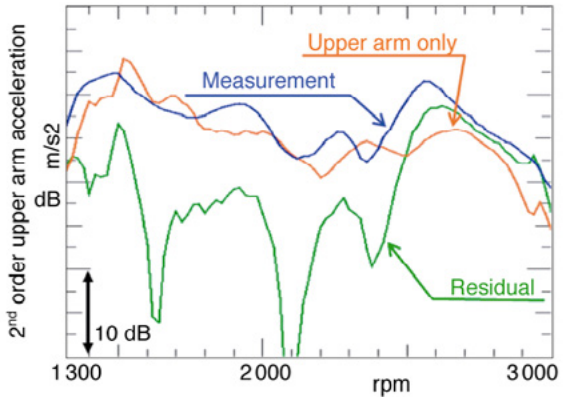



Fig. 3 Residual acceleration on upper arm

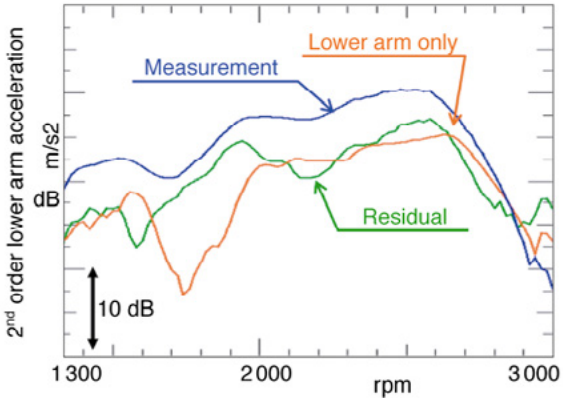



Fig. 4 Residual acceleration on lower arm

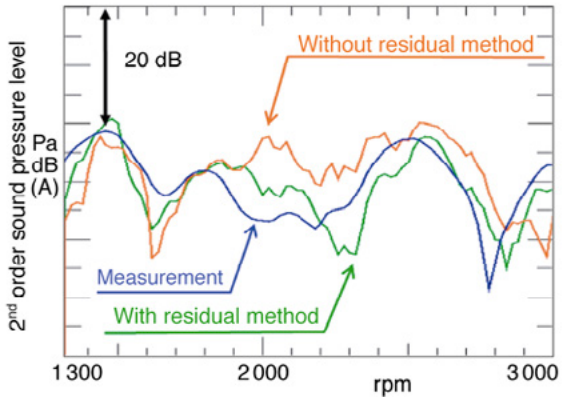



Fig. 5 Improvement of calculated response resulting from use of residual method

$$\begin{bmatrix} \ddot{x}_{MI1} \\ \vdots \\ \ddot{x}_{MIm} \end{bmatrix} = \begin{bmatrix} \ddot{x}_{meas1} \\ \vdots \\ \ddot{x}_{measm} \end{bmatrix} - \begin{bmatrix} \ddot{x}_{MS1} \\ \vdots \\ \ddot{x}_{MSm} \end{bmatrix} \quad (5)$$

As shown in Eq. (6), by performing an inverse matrix calculation on the vibration sensitivity, it is possible to obtain the transfer force $[F_{MIn}]$ from which residual forces have been removed, for that path alone.

$$\begin{bmatrix} F_{MI1} \\ \vdots \\ F_{MIn} \end{bmatrix} = \begin{bmatrix} \ddot{x}_{MI1}/F_{MI1} & \cdots & \ddot{x}_{MI1}/F_{MIn} \\ \vdots & \ddots & \vdots \\ \ddot{x}_{MIm}/F_{MI1} & \cdots & \ddot{x}_{MIm}/F_{MIn} \end{bmatrix}^{-1} \cdot \begin{bmatrix} \ddot{x}_{MI1} \\ \vdots \\ \ddot{x}_{MIm} \end{bmatrix} \quad (6)$$

Next, the method of selecting the connecting degree of freedom at which the residual method is to be used is described below. In the coupling between the suspension, the body, and the sub-frame, the effect of the engine mount transfer force differs depending upon the coupling point. For example, the upper arm is coupled to the body, which is isolated from other connecting degrees of freedom, and the lower arm and the engine mount are coupled to the sub-frame adjacent to each other.

Figure 3 shows the measured value of the upper arm, the result obtained using the residual method, and the calculated vibration result from the lower arm transfer force alone. At the upper arm connecting degree of freedom, the upper arm is relatively unaffected by the engine mount transfer force, so the vibration generated due to residual forces is at least 20 dB lower. Also, the phase of the vibration at the suspension and body side upper arm connection is stable. Consequently, it is appropriate to use the mount stiffness method for the coupling of the upper arm.

In contrast, in Fig. 4, the lower arm is greatly affected by the engine mount transfer force, and a large difference arises between the measured vibration and the calculated vibration for the lower arm path alone. For this reason, the residual method is applied to the lower arm to remove the effect of engine mount residual forces, thus enabling the transfer force for the lower arm path alone to be obtained.

In this way, by selecting a method that is suitable for each connecting degree of freedom, it is possible to obtain a more accurate model.

Figure 5 shows a comparison of the results obtained by combining the conventional mount stiffness and inverse matrix methods, and the results obtained using the residual method. It can be seen that the results obtained using the residual method are closer to the measured results, indicating improved accuracy of this method.

## 4. Transfer Path Contribution Analysis Results

The results of transfer path contribution analysis using the residual method for cabin low-frequency sound pressure level caused by engine secondary vibration are described below.

It can be seen from Fig. 6 that the main contribution is from the engine mount path, and also that there is a contribution from the suspension path at 1 500, 2 400, and 2 600 rpm. Particularly, it was confirmed empirically that the contribution from the suspension at 1 500 rpm (50 Hz) is due to the mode of the damper inner shaft shown in Fig. 7.

## 5. Conclusion

Transfer contribution analysis concerning a path that is affected by multiple transfer forces, such as in the case of engine and suspension mounts closely coupled to a sub-frame, was carried out, and the following results obtained.

(1) It was found that by using the residual method, the results approximated the measured results more closely than those of conventional methods, thus indicating the analysis accuracy improved.
(2) It was confirmed how to judge the methods to be selected for each connecting degree of freedom.
(3) The residual method was used in the contribution analysis of the suspension and engine mounts to low-frequency vibration and noise caused by engine secondary vibration, and as a result the extent of suspension path contribution was clarified.

In the future, in order to perform low-frequency drive system vibration and noise analysis, the authors intend to create a finite element model for the suspension including the drive transfer system, and carry out a study aimed at deriving a suspension construction that halves the transfer force of low-frequency vibration and noise.

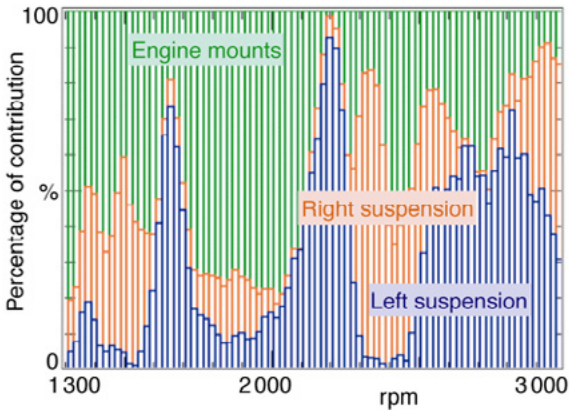



Fig. 6 Percentage path contribution of 2nd order sound pressure

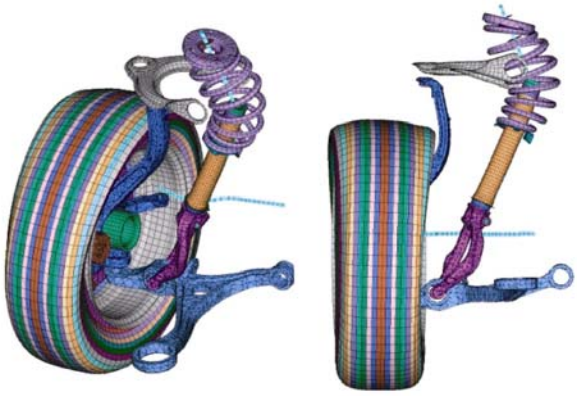


Fig. 7 Damper inner shaft mode

## References

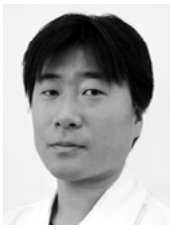
(1) Plunt, J.: Strategy for transfer path analysis (TPA) applied to vibro-acoustic systems at medium and high frequencies, ISMA 23 (1998)

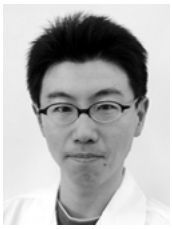
(2) Dubbaka, K.: Application of Noise Path Target Setting Using the Technique of Transfer Path Analysis, SAE Noise & Vibration Conference, 2003-01-1402 (2003)

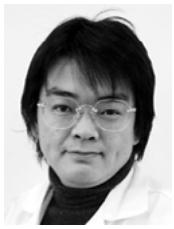
(3) LMS International, “Transfer Path Analysis”: The Qualification and Quantification of Vibro-Acoustic Transfer Paths, LMS International, Application Notes (1995)

(4) Sakai, T.: Development Procedure for Interior Noise Performance by Virtual Vehicle Refinement, Proceedings of SAE Noise & Vibration Conference, 2001-01-1538 (2001)

■ Authors ■


Masafumi KYUSE


Koichi TAKAHASHI


Tatsuhide SAKAI

# Development of Simulation Model for Active Controlled Engine Mount

Kosuke SAKAMOTO* Tatsuhide SAKAI*

## ABSTRACT

This paper presents the development of an active control engine mount (ACM) model required to study passive characteristics and control inputs of an ACM, which absorbs increased 1.5 order vibrations caused by three-cylinder operation in a V6 engine. By integrating a dynamic model of the moving parts of an actuator into a conventional hydraulic engine mount model, resonance due to two fluid orifices are expressed. As a result, the ACM model capable of reproducing passive, active and unit characteristics with high accuracy is established. In addition, this actuator force value is obtained with this model to cancel the sub-frame transfer load generated by engine vibrations.

## 1. Introduction

To improve fuel economy, the engine employed in the 2003 model INSPIRE has been provided with cylinder-on-demand type enabling combustion to be stopped in one bank of cylinders when the vehicle is cruising or decelerating. However, while it has improved fuel economy, it has also increased the 1.5 order component of engine vibrations over approximately 10 dB. Front and rear active control engine mounts (ACM)[(1)] have been employed in the new INSPIRE to absorb the increased vibrations. These ACM apply feed-forward control by detecting variations in the engine crank angle and determining the level of control input on that basis. Because the basic specifications of the feed-forward control system, such as gain and control waveform, were designed using a model that expressed physical phenomena in a simplified form, it was essential to achieve accuracy in the model. At present, the heuristic method is most commonly employed for this purpose, but this method posed issues in terms of reproducing the high-order components of the ACM driving frequency as found in an actual vehicle. A review of the literature concerning ACM shows that almost no research has been conducted on ACM models[(2) - (5)]. The aim of the research discussed in this paper was to construct an ACM model capable of reproducing the high-order components of the driving frequencies by integrating a dynamic model of a structure with two fluid orifices, and to determine the actuator force required to minimize transfer load by using the ACM model.

## 2. Constructing a Calculation Model

Figure 1 shows a cutaway view of the ACM. To increase the ride comfort performance, an electromagnetic solenoid actuator has been added to the conventional hydraulic mount, which employs fluid orifices. It has been possible to locate the actuator in the lower section of the ACM by positioning the main fluid chamber in the center and the secondary fluid chamber in the upper section. The actuator controls the displacement of the engine mounting points by means of the fluid in the main fluid chamber. It operates to maintain the displacement of the mounting points in phase as engine vibrations in order to reduce the subframe transfer load.

* Tochigi R&D Center

Figure 2 shows the dynamic model proposed in this research. The former ACM model was a simple model in which an actuator force component was added to a hydraulic mount model[6]. The newly developed model employs the former hydraulic mount model, in which the engine was expressed as a simple mass with the main rubber and a fluid orifice positioned below, as a base. New terms for the mass of the moving parts of the actuator, dynamic spring constant, damping coefficient and force have been added to the lower section of the former model. In addition, the mass for the moving sections of the actuator includes the fluid mass passing through the filter orifice located in the upper section.

Equations (1a), (1b), (1c), (1d) and (2) are derived from this model. (1a) is the dynamic equation for the inertial mass of the engine, (1b) is the dynamic equation for the fluid mass passing through the orifice established to improve the ride comfort performance, (1c) is the dynamic equation for the inertial mass of the actuator, and (1d) shows the constrained conditions derived from the law of conservation of mass of a fluid under fixed pressure conditions in the main liquid cabin. Equation (2) is a coefficient substituted to simplify the equations. Subframe transfer load is expressed by Eq. (3).

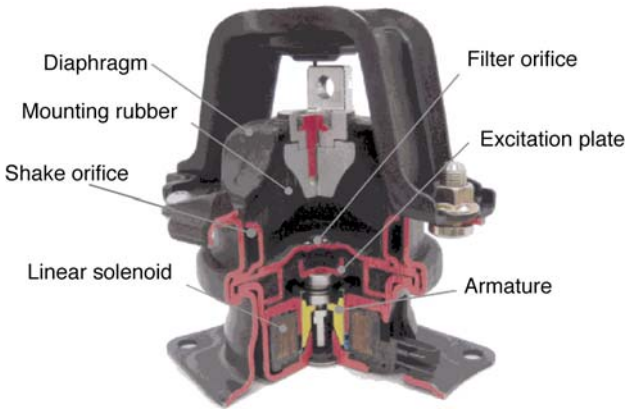



Fig. 1 Cutaway view of ACM

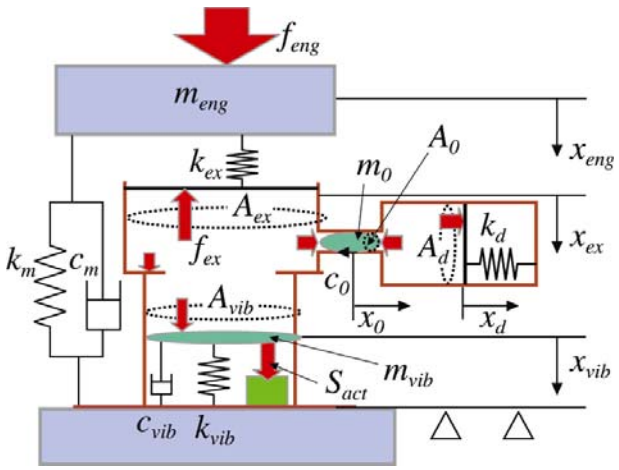



Fig. 2 ACM model

$$\begin{cases} \ddot{x}_{eng}+2\xi_{eng}\omega_{eng}\dot{x}_{eng}+\omega_{eng}^2 x_{eng}=\frac{1}{m_{eng}}\{f_{eng}-f_{ex}\} & (1a) \\ \ddot{x}_0+2\xi_0\omega_0\dot{x}_0+\omega_0^2 x_0=\frac{1}{m_0}\left(\frac{A_0}{A_{ex}}\right)f_{ex} & (1b) \\ \ddot{x}_{vib}+2\xi_{vib}\omega_{vib}\dot{x}_{vib}+\omega_{vib}^2 x_{vib}=\frac{1}{m_{vib}}\left\{s_{act}+\left(\frac{A_{vib}}{A_{ex}}\right)f_{ex}\right\} & (1c) \\ f_{ex}=k_{ex}\left\{-\left(\frac{A_0}{A_{ex}}\right)x_0-\left(\frac{A_{vib}}{A_{ex}}\right)x_{vib}+x_{eng}\right\} & (1d) \end{cases}$$

However,

$$\begin{cases} \omega_{eng}=\sqrt{\frac{k_m}{m_{eng}}}, \quad \xi_{eng}=\frac{c_m}{2\sqrt{m_{eng}k_m}} \\ \omega_0=\left(\frac{A_0}{A_{ex}}\right)\sqrt{\frac{k_d}{m_0}} \quad \xi_0=\frac{c_0}{2\left(\frac{A_0}{A_{ex}}\right)\sqrt{m_0 k_d}} \\ \omega_{vib}=\sqrt{\frac{k_{vib}}{m_{vib}}} \quad \xi_{vib}=\frac{c_{vib}}{2\sqrt{m_{vib}k_{vib}}} \end{cases} \qquad (2)$$

$$LOAD=f_{ex}+k_m x_{eng}+c_m \dot{x}_{eng} \qquad (3)$$

$x_{eng}$ : Displacement of engine mass (m)
$x_0$ : Displacement of fluid mass passing shake orifice (m)
$x_{vib}$ : Displacement of moving parts of actuator (m)
$m_{eng}$ : Engine mass (kg)
$m_0$ : Fluid mass passing shake orifice (kg)
$m_{vib}$ : Mass of moving parts of actuator (kg)
$k_m$ : Main spring constant (N/m)
$k_d$ : Spring constant of diaphragm (N/m)
$k_{vib}$ : Spring constant of excitation plate (N/m)
$k_{ex}$ : Extended spring constant of main rubber (N/m)
$A_{ex}$ : Effective area of main rubber ($m^2$)
$A_0$ : Cross-sectional area of shake orifice ($m^2$)
$A_{vib}$ : Effective area of excitation plate ($m^2$)
$A_d$ : Effective area of diaphragm ($m^2$)
$LOAD$ : Subframe transfer load (N)

## 3. Verification of Calculation Model

A study was conducted to verify the accuracy of the model described in Section 2 above. The accuracy of passive characteristics was verified in the dynamic spring constant, and the accuracy of active characteristics was verified in the displacement of moving parts during operation of the actuator.

### 3.1. Passive Characteristics

Equations (1a) – (1d) were transposed as shown in Eq. (4) to express frequency response. This expression was solved for $X_{eng}$, $X_0$ and $X_{vib}$, and Eq. (3) was used to generate Eqs. (5) and (6). These equations express the dynamic spring constant.

$$\begin{aligned} & x_{eng}=X_{eng}e^{j\omega t},\ x_0=X_0 e^{j\omega t},\ x_{vib}=X_{vib}e^{j\omega t} \\ & f_{eng}=s_{act}=0 \end{aligned} \qquad (4)$$

$$\begin{aligned} |K_*|= abs\Big[k_{ex}\Big\{-\left(\frac{A_0}{A_{ex}}\right)\left(\frac{AH_{22}-BH_{12}}{H_{11}H_{22}-H_{12}H_{21}}\right) \\ -\left(\frac{A_{vib}}{A_{ex}}\right)\left(\frac{BH_{11}-AH_{21}}{H_{11}H_{22}-H_{12}H_{21}}\right)\Big\}+1+k_m+j\omega c_m\Big] \end{aligned} \qquad (5)$$

However,

$$\begin{cases} H_{11} = -\omega^2 + 2j\omega\xi_0\omega_{n_0} + \omega_{n_0}^2 + \frac{k_{ex}}{m_0}\left(\frac{A_0}{A_{ex}}\right)^2 \\ H_{12} = \frac{k_{ex}}{m_0}\left(\frac{A_0}{A_{ex}}\right)\left(\frac{A_{vib}}{A_{ex}}\right) \\ H_{21} = \frac{k_{ex}}{m_{vib}}\left(\frac{A_{vib}}{A_{ex}}\right)\left(\frac{A_0}{A_{ex}}\right) \\ H_{22} = -\omega^2 + 2j\omega\xi_{vib}\omega_{vib} + \omega_{vib}^2 + \frac{k_{ex}}{m_{vib}}\left(\frac{k_{ex}}{m_{vib}}\right)^2 \\ A = \frac{k_{ex}}{m_0}\left(\frac{A_0}{A_{ex}}\right) \\ B = \frac{k_{ex}}{m_{vib}}\left(\frac{A_{vib}}{A_{ex}}\right) \end{cases} \quad (6)$$

Figure 3 shows a comparison of the dynamic spring constant calculated using Eq. (5), and values measured in tests. Employing parameters based on design values, a good correlation between calculated values and measured values was obtained. The effect of resonance of the fluid orifices appears as peaks in the region of several Hz, and the effects of resonance in the moving parts of the actuator and the fluid which passes through the filter orifice appear as peaks between 100 and 150 Hz.

### 3.2. Active Characteristics

A time series simulation was conducted based on Eq. (1), and the results were compared with values measured in tests. Actuator force was found from a polynomial approximation of the non-linearity of the relationship between force characteristic and current as shown in Fig. 4 and the measured current shown in Fig. 5. Figure 6 shows the calculated force.

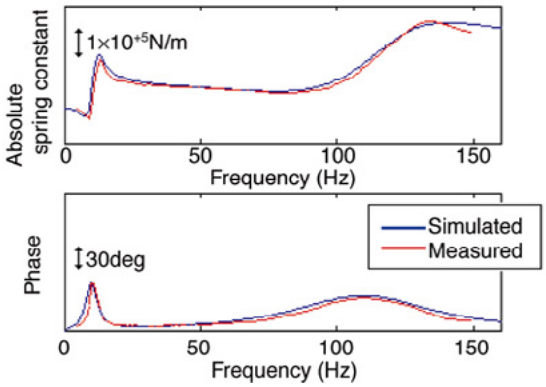



Fig. 3 Passive characteristic

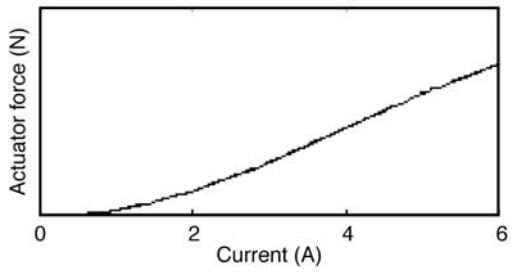



Fig. 4 Force characteristic of solenoid actuator

Figure 7 shows time series data for displacement of the moving parts of the actuator, and Fig. 8 shows a comparison of simulation results and measurements of the frequency characteristics of the displacement. There is a disparity of 0.4% in 1st-order components of driving frequencies and 9.4% in 2nd-order components between the simulation results and the measured values, enabling the model to be judged as possessing a sufficient degree of accuracy. The disparity in 3rd-order components is larger at 119%, and this is considered to be a result of the simplification of the friction loss characteristic of the moving parts of the actuator and the actuator force characteristics in the polynomial approximation.

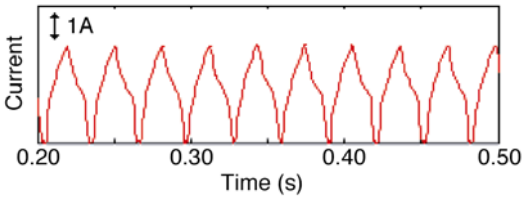



Fig. 5 Measured current

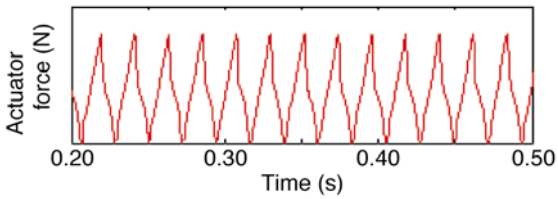



Fig. 6 Calculated force

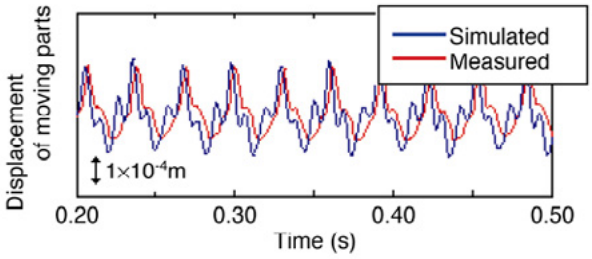



Fig. 7 Displacement of moving parts

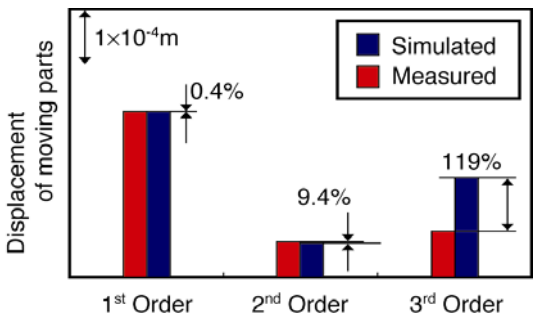



Fig. 8 Frequency characteristic of moving parts

## 4. Required Force Characteristic of ACM

Using this model, it is possible to determine the required actuator force to cancel engine vibrations. Substitution of Eq. (7) into Eqs. (1a) – (1d) enables the actuator force ($S_{act}$) at which subframe transfer load is at its minimum (LOAD → minimum) to be found. This generates Eqs. (8) and (9).

$$\begin{aligned} &x_{eng} = X_{eng}e^{j\omega t},\ x_0 = X_0 e^{j\omega t},\ x_{vib} = X_{vib}e^{j\omega t} \\ &f_{eng} = 0,\ s_{act} = S_{act}e^{j\omega t},\ LOAD \to 0 \end{aligned} \tag{7}$$

$$\begin{aligned} S_{act} &= \{RFA + RFB\,(RFC + RFD)\}X_{eng} \\ &= RF(\omega)X_{eng} \end{aligned} \tag{8}$$

However,

$$\left\{\begin{aligned} RFA &= \left(\frac{A_0}{A_m}\right)\left(k_m + j\omega c_m\right) \\ RFB &= -m_{vib}\left(\omega^2 - 2j\omega\xi_{vib}\omega_{vib} - \omega_{vib}^2\right) \\ RFC &= \left(\frac{A_m}{A_{vib}}\right)\frac{k_m + k_a + j\omega c_a}{k_a} \\ RFD &= -\frac{1}{m_0}\frac{k_a + j\omega c_a}{\omega^2 - 2j\omega\xi_0\omega_0^2}\left(\frac{A_0}{A_m}\right)^2 \end{aligned}\right\} \tag{9}$$

Figure 9 shows the required force function calculated using Eqs. (8) and (9). The actuator force required to minimize subframe transfer load against any given engine vibrations can be determined, enabling study of actuator specifications and control current to the ACM.

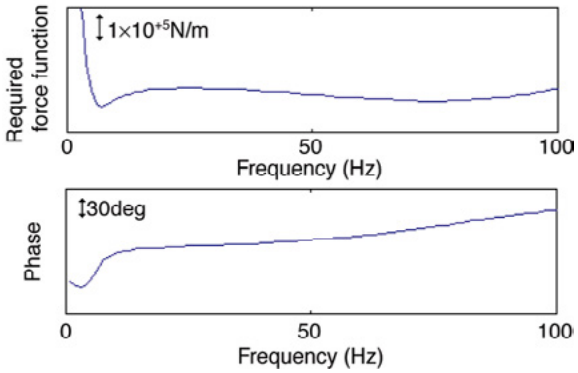



Fig. 9 Required force function

## 5. Conclusion

The research described in this paper constructed a detailed ACM model. The following results were achieved:

(1) The addition of a dynamic model of the moving parts of the actuator to a conventional hydraulic mount model and the expression of resonance in two fluid orifices enabled the construction of a model in which the passive characteristics (dynamic spring constant) were expressed with a high degree of accuracy.

(2) The model expresses the high-order components of driving frequency, which normally represent an issue in achieving consistency with the characteristics of actual vehicles, with a high degree of accuracy.

(3) The ACM model enables the actuator force required to cancel subframe transfer load to be determined.

## References

(1) Matsuoka, H., et al.: Development of Active Control Engine Mount, Honda R&D Technical Review Vol. 15, No. 2, p. 209-213 (2003)

(2) C. R. Fuller, et al.: Active Control of Vibration, ACADEMIC PRESS (1996)

(3) Sakai, T., et al.: CAE Strategy in Development of Engine Mount System, Japan Modal Analysis Conference, 8th Conf. (1994)

(4) Ozaki, H., et al.: Development of an Active Control Engine Mount, 1998 JSAE Annual Congress Proceedings, 983, p. 141-144 JSAE 9833269 (1998)

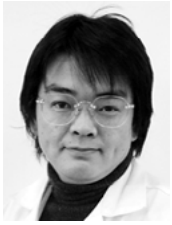
(5) Aoki, K., et al.: Quietness Improvement of Diesel Engine Automobile with Active Control Engine Mount (ACM), 1998 JSAE Annual Congress Proceedings, 983, p. 133-136 JSAE 9833241 (1998)

(6) Y.W. Lee: Dynamic analysis and control of an active engine mount system, J Automobile Engineering, Vol. 216 Part D (2001)

■ Authors ■



Kosuke SAKAMOTO



Tatsuhide SAKAI

# Hybrid SEA Modeling Scheme for Analysis of High-frequency Noise in Passenger Car

Kazuhito MISAJI* Hiroko TADA* Tsuyoshi YAMASHITA*

## ABSTRACT

A Hybrid SEA modeling method has been developed and applied to increase the accuracy of the SEA model for a passenger car. This paper will discuss the detailed workflow of the modeling method and the method employed to verify the accuracy of the model during development. In addition, to provide an example of the high level of accuracy of the results, the paper will discuss a road noise (interior cavity sound pressure level) analysis conducted with a complete vehicle SEA model constructed using the method.

## 1. Introduction

Reduced noise in the interior cavity is one of the prime selling points for automobiles. In order to consider the noise and vibration phenomena in the early stages of the design of an automobile, it is essential to create an analytical model capable of accurately expressing the dominant paths for transmission of acoustic and vibratory power, which comes to the cabin from a variety of sources. Using this kind of model allows one to design in features for reducing interior cavity noise due to road noise. However, the large number of both vibration sources and transfer paths complicates noise and vibration issues.

Nowadays, it has become possible to use Statistical Energy Analysis (SEA) to analyze the propagation of noise in the 400 – 5 000 Hz frequency range through both acoustic spaces in the vehicle and its structure[(1) – (3)]. In addition, there are cases[(4)] showing how SEA has proven effective for solving vibration issues in the 200 – 400 Hz frequency band. However, in the past, it had not been possible to model propagation from sources to the interior cavity through the main transfer paths of the air and structural members.

This report describes details of analyses and the verification of a Hybrid SEA model of an automobile body capable of predicting transfer paths for road noise in the 200 – 5 000 Hz frequency range. The model precisely predicts interior cavity noise by accurate reproduction of the main transfer paths through the air and through the structure.

* Tochigi R&D Center

## 2. Method of Hybrid SEA Modeling

The “Hybrid SEA model” proposed in this report is a combination of a conventional analytical SEA model and a test-based SEA model which accurately reproduces the energy flow that occurs in an actual automobile. This section of the report describes the process of assembling the model, in the following six steps:

(1) Analytical SEA model is constructed.
(2) Input subsystems are defined.
(3) Main transfer path network is graphed.
(4) SEA parameters are set on the basis of test measurements.
(5) The obtained SEA parameters are written to the analytical SEA model created in (1).
(6) Hybrid SEA model is created.

The processes in the steps are summarized in the above order.

### 2.1. Construction of Analytical SEA Model

Each subsystem is defined so that it contains a sufficient number of modes in the analytical frequency band. An actual finished vehicle can be divided into about 100 structural subsystems and 20 acoustic subsystems. Since subsystems can be defined where SEA parameters cannot be measured, more subsystems may be defined in this stage than could be defined in the test-based SEA model.

SEA parameters are theoretically determined for the defined subsystems to create the model. The commercially available package AutoSEA-2 was used for this step.

## 2.2. Definition of Input Subsystems

The input subsystems are selected. In an actual finished vehicle, 14 subsystems were selected from among the acoustic (Figs. 1 and 2) and the structural subsystems (Fig. 3) as input subsystems. The total number of subsystems and input subsystems depends on the vehicle model (sedan, 1 BOX, 2 BOX) and the type of suspension.

## 2.3. Construction of Main Transfer Path Network Diagrams

The main transfer path is selected for each input subsystem defined in section 2.2. Next, a diagram of the network for each path is created on the basis of the analytical SEA model results. The example in Fig. 4 is the network diagrams for power inputs into the front damper housing (Dpr housing up).

## 2.4. Measurement of SEA Parameters

The energy ratios between each of the subsystems in the constructed network diagram are measured. The ratios are used to find the Coupling Loss Factors (CLF) between each subsystem pair. The Total Damping Loss Factor (TDLF) for each subsystem is also measured, using the decay rate method[3), (4)], at the same time as the energy ratios.

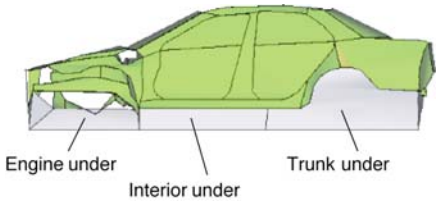



Fig. 1 Acoustic input subsystems (under car body)

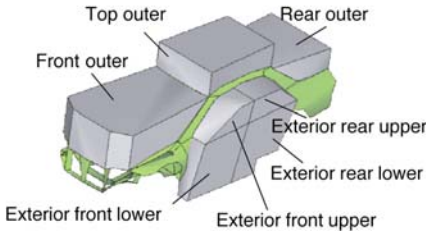



Fig. 2 Acoustic input subsystems (around car body)

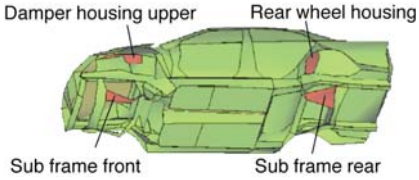



Fig. 3 Structural input subsystems

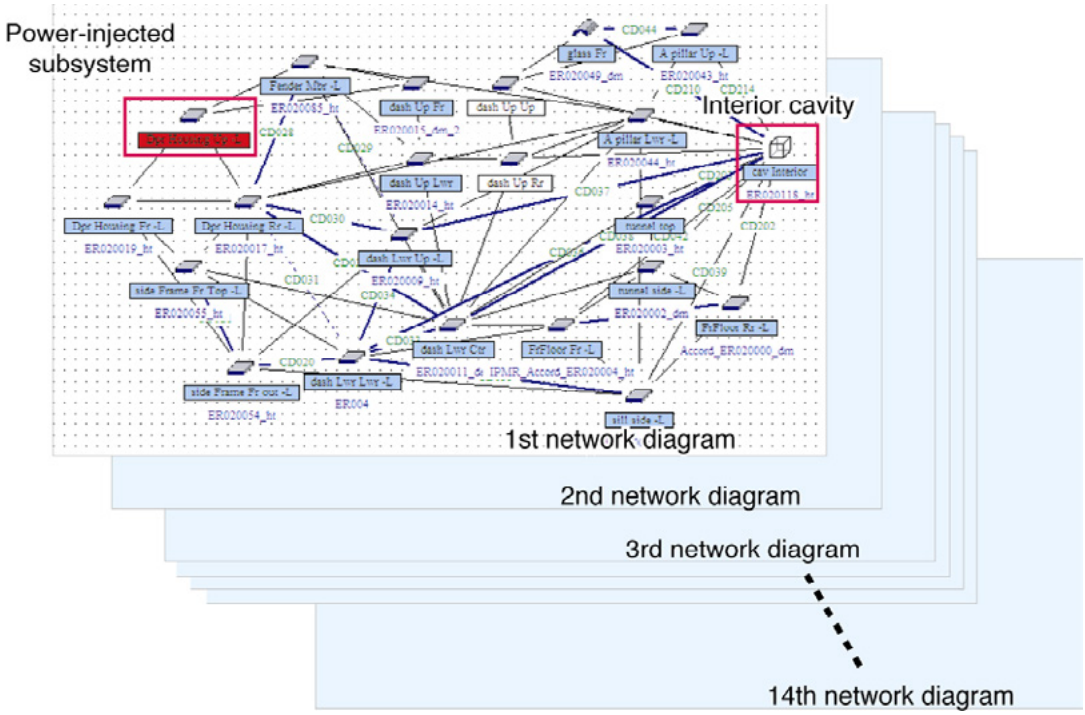



Fig. 4 14 Network diagrams (“Dpr housing up- left” is power injected subsystem)

### 2.5. Writing Obtained SEA Parameters to Analytical SEA Model

The parameters for the constructed analytical SEA model are converted to the corresponding parameters (TDLF, CLF) measured in the test-based SEA model.

### 2.6. Creation of Hybrid SEA Model

The energy ratios between each input subsystem and other subsystems are calculated using the models created in 2.5. The resulting values for energy ratios are then compared with the values measured in 2.4. In Fig. 5, the first number appearing under each subsystem name in the network diagram is the test-determined value in dB, and the second number shows the differences in dB between the test-determined value and the calculated value.

The CLF's are adjusted in order to minimize the magnitude of the differences. A "Hybrid Process" is used to adjust CLF. The Hybrid Process is performed until all the differences are reduced to within ±3 dB. Figure 6 shows a network in which the differences in energy ratio have been sufficiently minimized. With the completion of the above steps 2.1 – 2.6, the Hybrid SEA model is complete.

## 3. Verification of Accuracy

The predicted values and the measured values of the energy ratios of each subsystem are compared as the first step in verifying the accuracy of the SEA model by the Hybrid Process. Next, the interior cavity sound pressure levels resulting from road noise at 80 kph are compared between

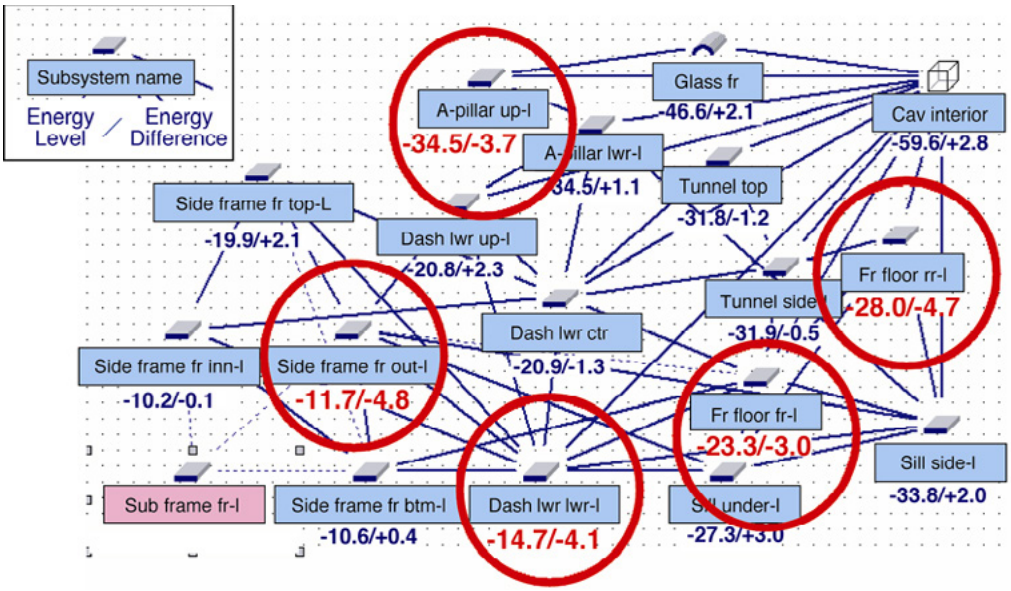



Fig. 5 Network diagram with difference of energy ratio (before hybrid process)

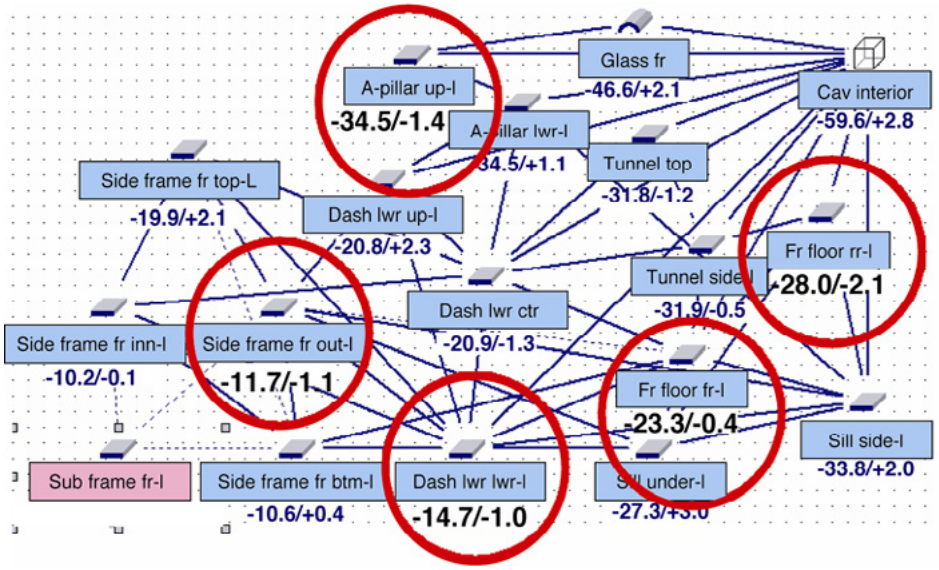



Fig. 6 Network diagram with correct energy flow (after hybrid process)

the predicted values and the measured values. The results of the comparison are described below.

### 3.1. Comparison of Energy Ratios between Subsystems

The first example shows the energy ratios for the floor front, a structural element, and the interior cavity, an acoustic space, as a result of input to the front sub-frame (Fig. 7a).

From Fig. 7a, it is clear that the energy flow between the structural subsystems have been reproduced within ±3 dB at frequencies above 200 Hz. Also, from Fig. 7b, it is clear that the energy flow between the structural subsystem and the acoustic subsystem have been reproduced within ±3 dB at frequencies above 200 Hz. Next, as an example of energy flows between acoustic subsystems, Fig. 8 shows the results for acoustic propagation from interior-under cavity to interior cavity. These findings also show a correlated model of the energy flow between the acoustic subsystems of within ±3 dB above 200 Hz.

### 3.2. Comparison of Predicted and Measured Levels of Interior Cavity Sound Pressure Levels

In order to verify accuracy of the SEA model constructed using the hybrid process, road noise generated by inputs during driving at a speed of 80 kph was analyzed. The predicted interior cavity sound pressure levels were compared with the measured levels. Figure 9 provides the results of the comparison.

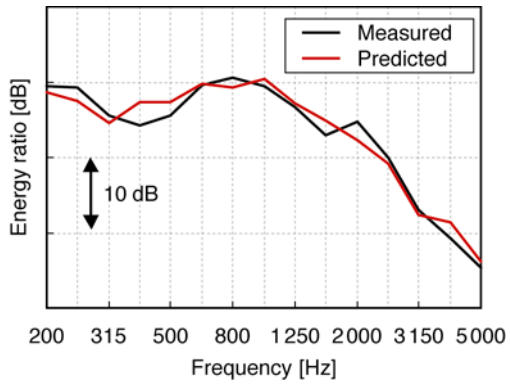



Fig. 7-a Energy ratio (Floor front/Front sub frame)

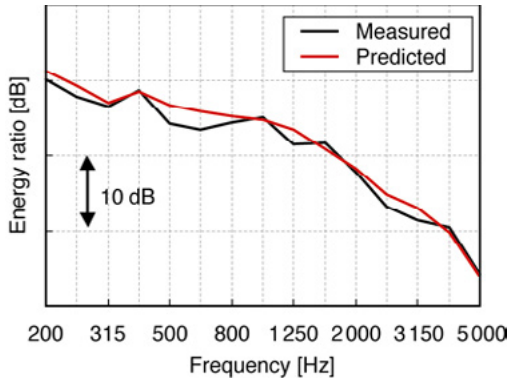



Fig. 7-b Energy ratio (Interior cavity/Front sub frame)

The results confirmed that the differences are consistent within ±3 dB.

## 4. Uniqueness of Solutions

The method proposed here succeeded in accurately predicting interior cavity noise pressure level due to road noise. However, the authors had defined the uniqueness of the model solution by reproduction of the vibration and noise characteristics, including reproduction of the dominant power paths, by the constructed Hybrid SEA model in response to road noise. The authors also conceived that verifying the uniqueness is an important element for assessing the model's accuracy[6]. The main input correlation coefficient $r_1$, a measure of the solution accuracy for power flow between subsystems, was defined as shown in Eq. (1). Similarly, the total correlation coefficient $R$, which used $r_1$ values, was defined as in Eq. (2)[6].

$$r_1 = \frac{n_1}{N_1} W_1 \tag{1}$$

$$R = \sum_{i=1}^{M} r_i \tag{2}$$

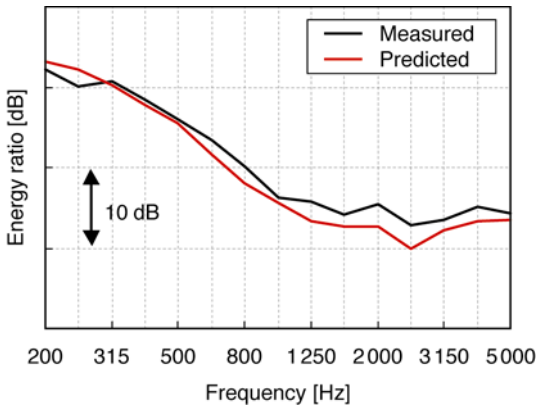



Fig. 8 Energy ratio (Interior cavity/Interior under cavity)

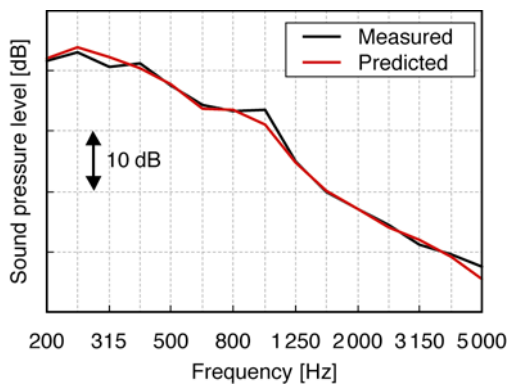



Fig. 9 Interior cavity sound pressure level (road noise analysis 80 km/h)

Here, $n$ is the number of subsystems common to both the main input found by the test model and the main input found by the hybrid SEA model in the specified frequency band. $N$ is the number of all the subsystems which do *not* receive power inputs. $W_i$ is the contribution of the interior cavity noise made by the $i^{th}$ main input, to the total noise. $M$ is the total number of contributors.

As an example of this calculation, consider the transfer paths shown in Fig. 10. Here, $n$ = 2 (SS2, interior cavity), $N$ = 6 (SS1 – SS5, interior cavity). When 0.9 is selected as the most important input, the main input correlation coefficient $r_1$ in Eq. (1) is 0.3. (The solid lines in Fig. 10 represent the main input predicted by Hybrid SEA, the dashed lines, the main input according to the test model.) The verification was carried out by comparing the test-based SEA, whose accuracy for specifying the transfer paths is increased in stages with a Hybrid SEA model created by the method proposed above. The test-based SEA model was used for comparison in the 3-stage method described below, by progressive tuning of the energy ratio differences.

- Test Model 1: A model with consistent characteristics was constructed in the method described above, using only the CLF characteristics for acoustic radiation from all the panels directly adjoining the interior cavity.
- Test Model 2: A model was created whose inter-subsystem energy ratio differences were within ±0.5 dB of measured results for the paths from the four dominant subsystems affecting the interior cavity which accounted for approximately 90% of the input into the interior cavity.
- Test Model 3: Test Model 2 was further refined to reduce the energy ratio difference from the fifth most dominant subsystem to within ±0.5 dB.

Next, the interior cavity road noise levels were compared between Test Model 1 and the Hybrid SEA model (source of the "Predicted" figures in Fig. 11) and an actual test vehicle. Both models (Fig. 11) showed levels within ±3 dB of results from an actual automobile; however, they showed significantly different contributions to the interior cavity from adjoining panels (analytical results for contributions at 200 Hz, Fig. 12). This illustrates that even if a good match with measured interior cavity levels seems to have been obtained, it is misleading; there is not some single unique model that can provide this. This indicates that the Hybrid SEA model must be confirmed to reproduce the dominant power transfer paths that exist in the actual vehicle.

That confirmation is illustrated below using the total correlation coefficient $R$, defined above, to confirm the analytical accuracy of the power transfer paths. Figures 13 and 14 show $R$ for Test Models 1, 2 and 3 for propagation through structural members. Figure 13 shows the $R$ values for structure-borne noise from the front-left side of Front Subframe, and Fig. 14 shows those for noise from the left side of the Front damper housing.

These results indicate that $R$ of Test Model 3 approaches unity at frequencies above 1 kHz and remains above 0.8 at lower frequencies. Figure 15 shows a comparison between Test Model 3 and the Hybrid SEA model for indicated power contributions from panels adjoining the interior cavity.

This indicates a superior correlation, in comparison to the results presented in Fig. 12. Not only can the Hybrid SEA model constructed by the proposed method provide accurate predictions of interior noise, actual power flows are also well reproduced. This model was therefore considered to be effective for reproducing road noise.

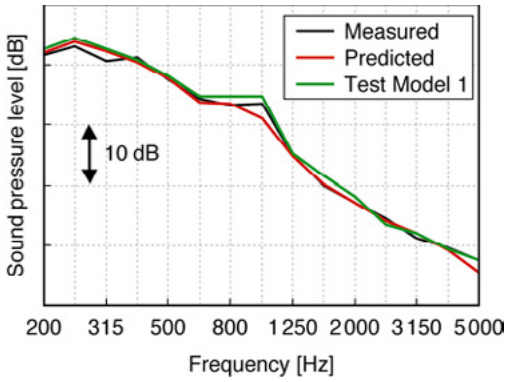



Fig. 11 Interior cavity sound pressure level for main transfer path (road noise analysis 80 km/h)

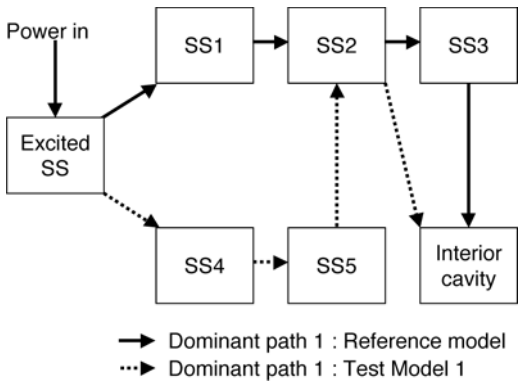



Fig. 10 Simple model for dominant power path investigation

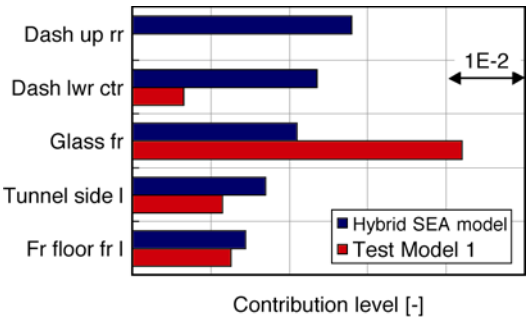



Fig. 12 Power contribution to interior cavity (before hybrid process)

## 5. Example of Application of Analysis

### 5.1. Separation of Contributions by Structural Members and Acoustic Spaces to Interior Cavity Noise

An attempt was made to distinguish between structural inputs and acoustic inputs to road noise using the Hybrid SEA model described above that is capable of identifying the unique solution to acoustic issues. First, the structure-borne cavity noise was estimated; then, the air-borne cavity noise was estimated. The results are shown in Fig. 16.

The results indicate that the structural contribution is higher up to about 500 Hz, and the acoustic system accounts for most noise at higher frequencies. This expresses the qualitative character of automobile road noise very well.

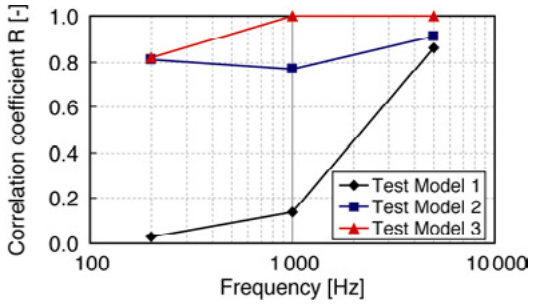



Fig. 13 Correlation coefficient (from Sub frame fr-l to Interior cavity)

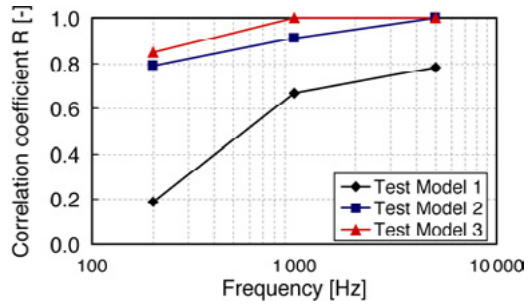



Fig. 14 Correlation coefficient (from Dpr housing to Interior cavity)

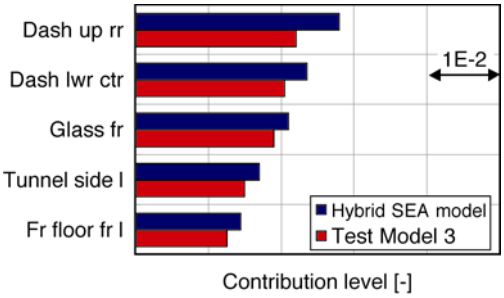



Fig. 15 Power contribution to interior cavity (after hybrid process)

### 5.2. Power Contributions to Interior Cavity Noise by Adjoining Subsystems

Figure 17 illustrates the power contributions of various adjoining subsystems to interior cavity noise, according to the Hybrid SEA model.

They indicate that the structural subsystems of the rear wheel house, floor, dashboard and tunnel are dominant in the 200 – 500 Hz band. Leaks from around the doors and door windows and the acoustic radiation from the front windshield dominate above 2 kHz. Thus, the analytical results gained from the use of this method will allow efficient decision-making about specifications for the reduction of road noise.

## 6. Conclusion

A method for creating a Hybrid SEA model has been proposed. The model is capable of predicting structurally-propagated road noise in the 200 – 5000 Hz frequency range with an accuracy of ± 3 dB and reproduces power flows among subsystems. Use of the Hybrid SEA model

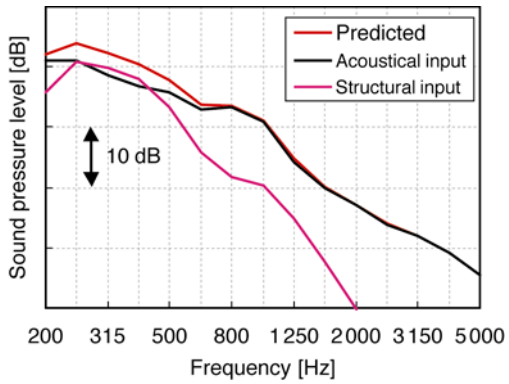



Fig. 16 Contribution to interior cavity sound pressure level

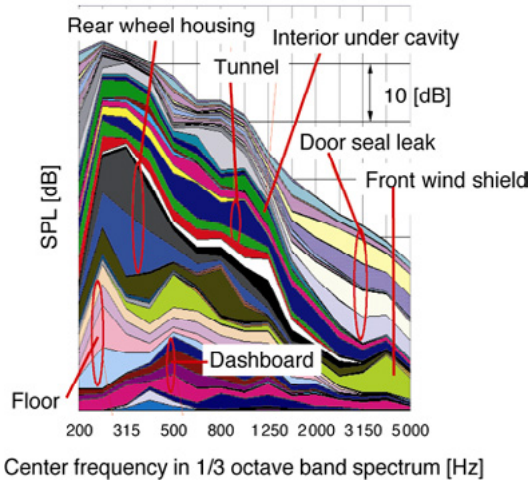



Fig. 17 Power contribution to interior cavity sound pressure level

constructed under this method enabled structural noise propagations to be distinguished from air-borne propagations. Also obtained was the contribution of noise passing through acoustic systems as well as the contribution of acoustically radiated noise to the interior cavity. Therefore, the model is expected to streamline the process of counter measuring road and other noise.

## References

(1) Onsay, T., et al.: Transmission of Structure-Borne Road Noise in a Mid-size Car: Statistical Energy Analysis (SEA), NOISE-CON 98, Ypsilanti, Michigan (1998)

(2) Dong, B., et al.: Road noise modeling using statistical energy analysis, Proc. SAE N&V Conf. (1995)

(3) Misaji, K., et al.: Analysis of Vehicle Road-Noise Using Statistical Energy Analysis, JSAE Conference, No. 71-99, 9939730, p. 9-12 (1999) (in Japanese)

(4) Lyon R. H., Dejong R. G.: Theory and Application of Statistical Energy Analysis, Butterworth-Heinemann (1995)

(5) Misaji, K., et al.: Development of a Hybrid SEA Modeling Scheme for a Passenger Car, 2003 SAE World Congress (2003)

(6) Misaji, K., et al.: Testing Uniqueness of Hybrid SEA Modeling Solution for a Passenger Car, 2003 SAE Noise & Vibration Conference & Exhibition (2003)

■ Authors ■


Kazuhito MISAJI


Hiroko TADA


Tsuyoshi YAMASHITA

# Analysis of Suspension System Vibration Using Finite Element Model

Youichi KAMIYAMA*


## ABSTRACT

A technique enabling the level of vibration in a suspension to be predicted has been developed to improve road noise performance. Individual parts were defined and modeled to more accurately reproduce their shape and structure, and a method of assembling the component models was then formulated to enable middle-frequency vibrations to be predicted. In addition, to allow the prediction of vibration in an operating suspension, a method of experimentally identifying the force transmitted to the suspension by the road surface was developed. Measured values and predicted values were compared to verify the accuracy of the prediction technique. In addition, the technique was employed to study the reduction of vibration in an actual suspension, confirming its effectiveness in predicting the effects of structural change.


## 1. Introduction

With the recent pressure to shorten automotive development periods, there is a growing demand for technologies that will enable the prediction of the performance of completed vehicles at the design stage, before prototypes are built. Some examples of the application of such systems for the analysis of collision performance and of the dynamic characteristics of automobile bodies in frequencies typical for noise and vibration have been presented[1), 2)]. However, there have been few actual examples[3)] of applications of vibration analysis using finite element (FE) models of complete suspension systems to reduce road noise.

In spite of the fact that tire acoustic cavity noise and resonance of the complete suspension system often couple and cause issues in the middle-frequency band (200 – 300 Hz), it is still common to conduct vibration analyses of suspension components in isolation from each other[4)]; one almost never sees examples of analyses of complete suspension systems.

In this research, a technique using FE models of the suspension components was created and used to predict forces from the suspension on the automobile body in the middle-frequency range. And then a technology was developed for modeling the complete suspension system and employed as a method for reducing vibration.

## 2. Outline of Technologies for Predicting Suspension Vibrations

### 2.1. Approach to Modeling

The most important consideration for efficient creation of a suspension system model is how to define the components and their interconnections in the target frequency range. For example, it has been shown possible to make analyses in the low-frequency “drumming” range using comparatively small FE models (Fig. 1). However, faithful reproduction of mass and of the distribution of stiffness is essential to the accuracy of models for analysis at middle-range frequencies. This research has resulted in the development of a method for predicting middle-frequency vibration in a suspension with a large elastic FE model which reproduces the 3-dimensional shapes of components of the complete suspension system (Fig. 2).

* Tochigi R&D Center

## 2.2. Part Modeling Technology

In modeling the components, top priority was given to faithful reproduction of the shape, mass and stiffness of the originals. The models of each part were defined as shown in Table 1.

Table 1 Elements list of FE model

| Component | Parts | FE model | Component | Parts | FE model |
|---|---|---|---|---|---|
| Damper | Rod<br>Outer pipe<br>Inner pipe<br>Rod guide<br>Valve<br>Oil<br>Gas | CBAR, CSHELL, CONM, CELAS, CDAMP | Arm | Arm<br>Collar<br>Bracket | CBAR, CSHELL, CTETRA, CONM |
| | | | Spring | Coil spring<br>Seat rubber | CBEND, CELAS |
| | | | Bush | Rubber<br>Outer collar<br>Inner collar | CONM, CELAS |
| Drum brake | Drum<br>Pad<br>Base plate<br>Other parts<br>Spring<br>Contact area | CSHELL, CTETRA, CONM, CELAS | Ball joint | Stud<br>Outer case<br>Ball | CBAR, CTETRA, CONM, CELAS |
| | | | Stabilizer | Rink<br>Rink ball<br>Holder<br>Holder bush | CBAR, CSHELL, CTETRA, CONM, CELAS |
| Hub & bearing & spindle | Hub<br>Bearing<br>Spindle | CBAR, CSHELL, CTETRA, CELAS | Subframe | Body<br>Bracket<br>Collar | CSHELL, CTETRA, CONM |
| Wheel | Rim<br>Disk | CSHELL, CTERTA | | | |

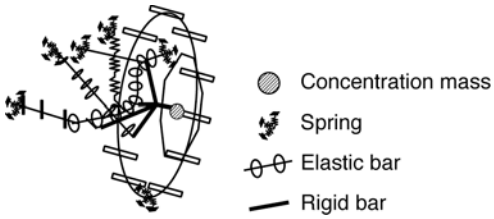



Fig. 1 Low frequency FE model

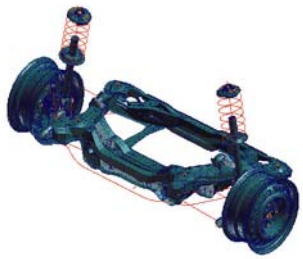


Fig. 2 Mid frequency FE model

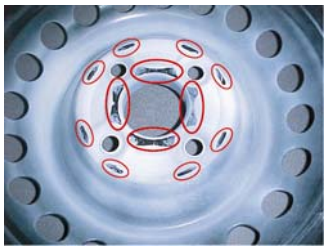


Fig. 3 Contact area of wheel disk and hub

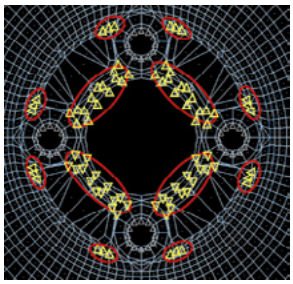


Fig. 4 Connection area of wheel disk and hub in model

## 2.3. Part Assembly Technology

For bushings and joints at the connections between components, the dynamic spring characteristics, were determined experimentally, and then modeled as 6-degree of freedom (DOF) scalar springs. For the other connections where direct characteristics were difficult to determine, or contact area locations, the joint characteristics were determined by inserting provisional spring elements to the model and updating it until the natural frequencies and mode shapes obtained from the calculation matched those of the experimental modal analysis.

The accuracy of the model in the surface contact locations was ensured by, first, precise measurements of dimensions and locations of the static contact areas in an actual part, as shown in the example of a wheel disk tightening in Fig. 3. The connection areas of the model were then more accurately reproduced to match the characteristics of the contact areas in the actual part, as shown in Fig. 4. Finally, spring elements were placed between the areas to connect them.

## 2.4. Technologies for Identifying Exciting Forces

It is essential to identify the excitation forces from the road surface on the suspension during operating conditions, in order to obtain the best possible accuracy in predictions of suspension behavior.

Examples of applying road surface displacement and the exciting forces on the tire contact patch have been described[5, 6], but since either more accurate models of tires or complicated analytical procedures must be employed, the methods described above cannot be considered practical for application in automobile development. That is why assigning the experimentally determined exciting forces to the driving points on the wheel disk, a method which requires no models of the tire, was used in this study. In the method, the suspension vibration in actual operating conditions during driving on the road surface generating road noise was measured and the frequency response function at the same reference point was used when the wheel was excited. Thus, the exciting forces on the suspension exerted by the road surface were identified using the inverse matrix solution by the least-squares approximation shown in Eq. (1).

$$\{F_j\} = [H_{ij}]^{-1}\{x_i\} \quad (1)$$

$F_j$ : Identified exciting force vector at selected driving point
$H_{ij}$ : Matrix defining frequency response function from driving point to reference point
$x_i$ : Response vector to vibration at reference point during operation

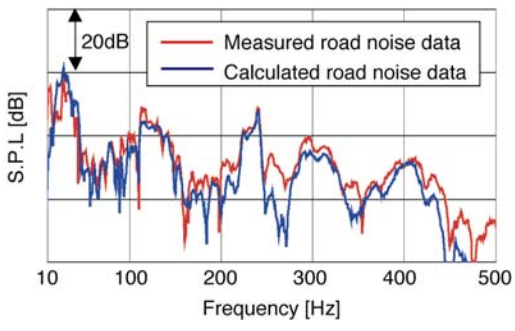



Fig. 5 Precision verification of force identification

Each driving point was assumed to be subject to 3-axis translational forces and was offset so that two moment components could also be expressed, except in the direction of tire rotation.

Figure 5 shows the results obtained when the composite sound pressure levels (SPL) calculated according to the identified exciting forces were compared with the measured cabin SPL due to road noise. It is clear that the actual SPL was well reproduced up to around 450 Hz.

### 2.5. Correlation with an Actual Suspension System

Figure 6 presents a comparison of the calculated and measured frequency response functions (FRF) of the suspension when the wheels are excited, and Fig. 7, the modal assurance criteria (MAC) values, which are indices of correlation between the mode shapes. The FRF were nearly identical up to about 300 Hz, and the MAC values also matched well. The present prediction technique can clearly be applied for analysis of the frequency band of tire acoustic cavity noise (200 – 300 Hz).

## 3. Example of Application in Prediction and Analysis of Suspension Vibrations

This section describes examples in which this technique was employed to investigate ways to upgrade performance of the rear suspension in mass-produced automobiles.

### 3.1. Results of Analysis of Modes of Interest

Analysis of vibratory frequency response characteristics of a suspension in the tire acoustic cavity noise band was carried out using a FE model; as visible in Figs. 8 and 9, the main mode, coupled with the tire acoustic cavity resonance, was the mode in which the wheel disk was bending and simultaneously the hub and knuckle was bending 180° out of phase (camber mode).

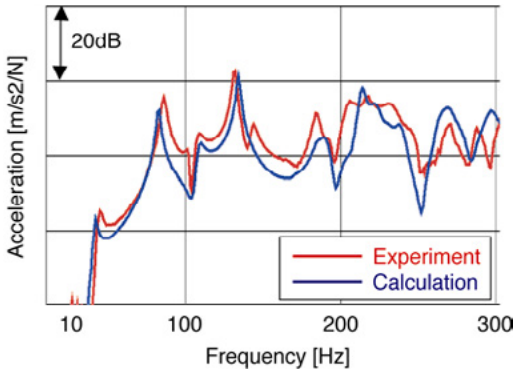



Fig. 6 Precision verification of FRF

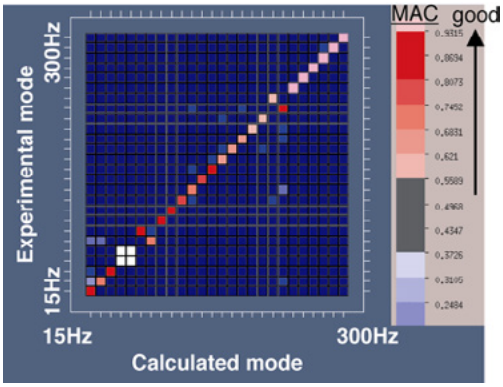



Fig. 7 Precision verification of MAC

### 3.2. Improvement of Performance in Individual Parts of Suspension

Next, the individual parts making up the suspension were investigated for ways to improve performance under excitation at the camber mode natural frequency. Focus was placed on the wheel disk, the component that absorbs the most strain energy in the camber mode. The goal was non-coupling of this component with tire acoustic cavity noise. A stiffer version of the disk was designed and vibratory frequency response characteristics of suspension were calculated (Fig. 10).

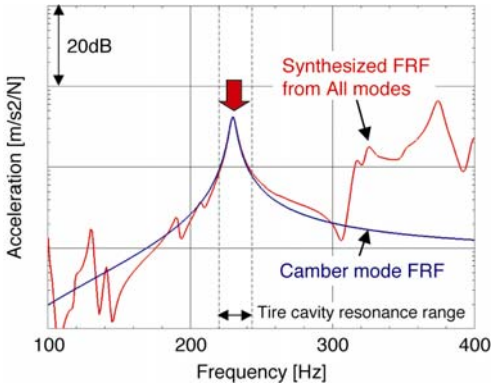



Fig. 8 Mode contribution of target point FRF

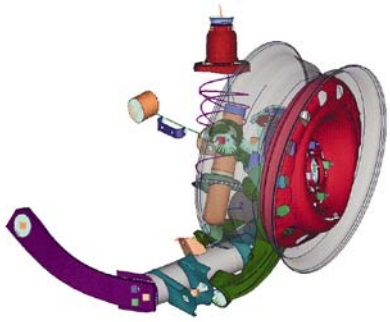


Fig. 9 Mode shape of Camber mode

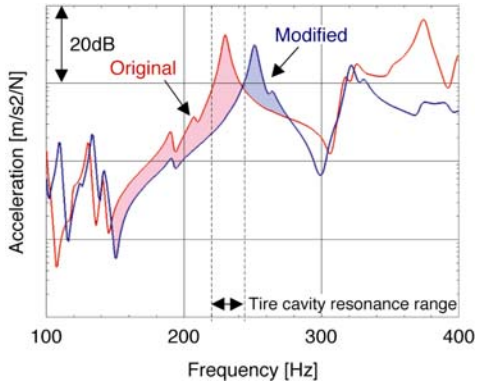



Fig. 10 Improvement of camber mode by increased wheel disk stiffness

Vibration level was substantially reduced in the tire acoustic cavity noise band, but since examination of the entire medium-frequency band showed that the peak in the camber mode response spectrum remained nearby, simply shifted to a slightly higher frequency, it was clear that this approach had not completely succeeded.

### 3.3. Improvement of Performance in Complete Suspension Systems

An analysis of the contributions of stiffness and mass of every component of the suspension system was carried out with the objectives of reducing mode amplitude and re-adjusting the camber mode peak to lower levels. The analysis showed that the highest contributions were by the knuckle stiffness and the mass of the trailing arm end (Fig. 11).

One constraint was to avoid increases of the weight of the overall suspension system. As a countermeasure, a structural change was tried, with a move of the shock absorber location from the middle of the trailing arm to the end, to allow modification of the knuckle geometry and shape and to increase the mass of the trailing arm end (Fig. 12).

The resulting changes in the suspension FRF were estimated. The conversion to the mode shape in which mass efficiency was improved and the increase in modal mass effected a large reduction in the amplitude of the camber mode. Dramatic reductions in vibration acting on the suspension are expected from this result (Fig. 13).

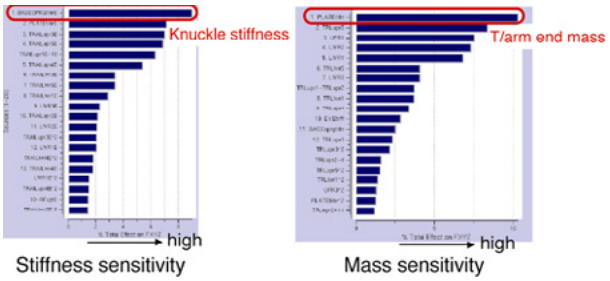



Fig. 11 Sensitivity of suspension components to changes in stiffness and mass

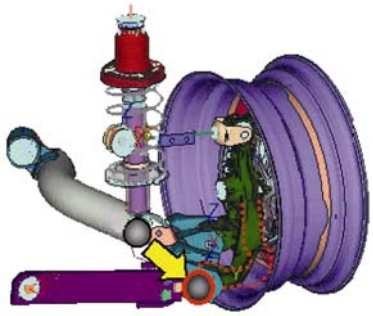


Fig. 12 Case of structure change for improvement of road noise

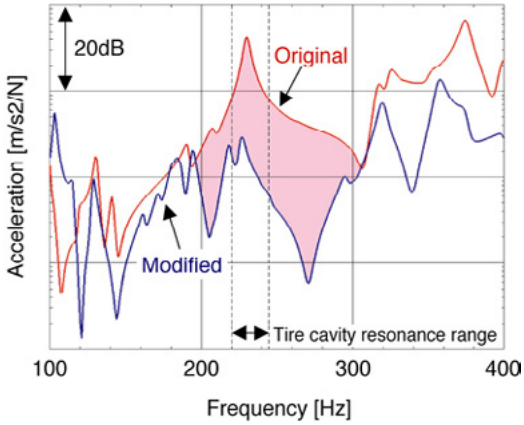



Fig. 13 Improvement of camber mode by optimization of stiffness and modal mass

### 3.4. Results of Verification in Actual Assembly

A prototype was constructed to verify the validity of the prediction for improved performance. A knuckle with modified geometry was installed and a weight was attached to the trailing arm end corresponding to the mass of the shock absorber. Figure 14 shows the predicted results, and Fig. 15, the measured results. These confirm the effectiveness of this method. It was also found that the new suspension system offers reduced road noise in the cabin (Fig. 16).

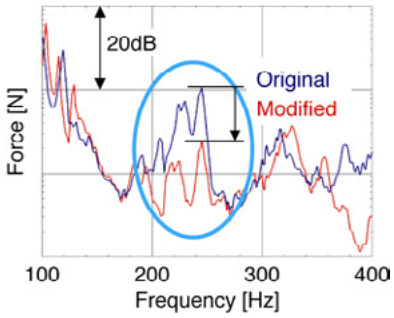



Fig. 14 Estimate of improvement using FE model

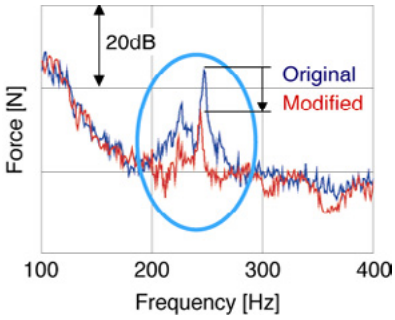



Fig. 15 Verification of improvement by experiment

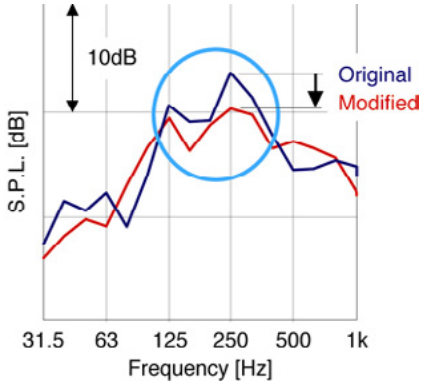



Fig. 16 Improvement of road noise by optimization of modal mass

## 4. Observations on Modal Masses

It has been shown that vibration forces which contribute greatly to road noise can be reduced at its driving points by modifying the mass distribution to increase the modal mass of a selected mode. Next, some observations of the differences between suspension types in vibratory frequency response characteristics were made, with reference to modal mass.

### 4.1. Suspension Types and Modal Masses

The sums of suspension vibratory forces in different suspension types were analyzed for comparison, as shown in Fig. 17. It is clear in the figure that the torsion-beam type offered much lower absolute spectral line values in the middle-range frequencies. The frequency response of the torsion-beam suspension was superior to the multi-link suspension.

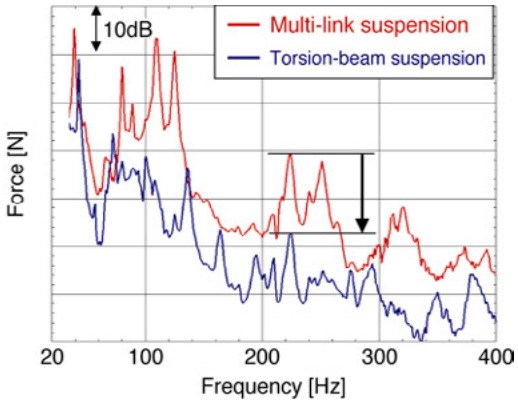



Fig. 17 Comparison of different suspension systems as calculated by FE model

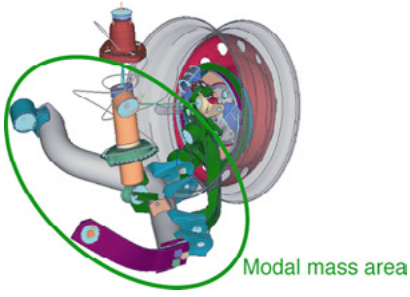



Fig. 18 Modal mass area of multi-link suspension in camber mode

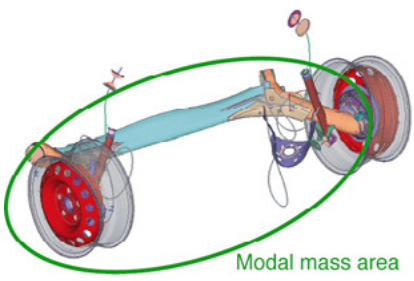



Fig. 19 Modal mass area of torsion-beam suspension in camber mode

The camber mode was the contributory mode in the region for tire acoustic cavity noise in both systems. The mode shapes in the systems were compared; Fig. 18 shows that only part of the system for one wheel in each pair vibrates in the rear multi-link type; this makes for a low modal mass, and in turn, high mode amplitude. In contrast, vibration occurs over a large portion of both wheels in the pair in the rear torsion-beam type (Fig. 19); vibratory forces are exerted on both wheel masses, so the modal mass is high, causing low mode amplitude.

### 4.2. Increase of Modal Mass in Multi-link Suspension

In order to increase the modal mass in the multi-link suspension, whose modal mass would otherwise be excessively low, the mass distribution in one side wheel of the suspension must be optimized. Even after this re-design, however, the absolute value of its modal mass is still nowhere near that of the torsion beam system in which both wheels can act as masses. The present method was therefore used to predict the behavior of a sub-frame floating version of the multi-link system, which incorporated the masses of both wheels and a sub-frame. The results are presented in Fig. 20. The suspension response was comparable to that of a torsion-beam system.

## 5. Conclusion

The following results were obtained using this technology for predicting suspension system vibration.

(1) The development of this technology for finite element modeling of suspensions and experimental identification of suspension excitation forces has provided a method for reproducing suspension vibration comparable to the actual automobile operation.

(2) This technology also allows analysis of complete suspension systems and prediction of improvements in performance. Its effectiveness was verified in tests of an actual assembly.

(3) It was shown, both in predictions and tests with an actual assembly that optimizing the modal mass distribution of a suspension system is an effective method for reducing suspension vibration, and that vibratory forces can be reduced at the suspension attachment points.

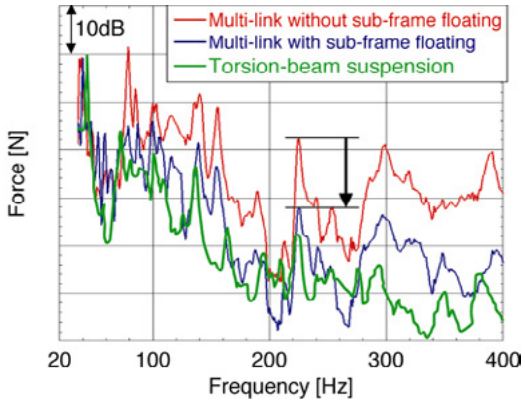



Fig. 20 Comparison between sub-frame floating and torsion-beam suspension as calculated by FE model

(4) The rear torsion-beam suspension was shown to be superior to the rear multi-link type, from the viewpoint of the modal mass and of its effect on the frequency response function of each type of suspension.

## References

(1) Yasuki, T., Watanabe, N.: Safety Vehicle Crash Analysis Applications to a Vehicle Development, Toyota Technical Review, Vol. 51, No. 1, p. 54-59 (2001)

(2) Matsumoto, K., Suzuki, M., et al.: Idle Vibration Analysis Using a Full Vehicle Simulation Model, 2003 JSAE Annual Congress Proceedings, No. 39-03, 182, p. 1-4 (2003)

(3) Kido, I., Nakamura, A., et al.: Suspension Vibration Analysis for Road Noise Using Finite Element Model, SAE, No. 99-01-A1788, p. 1053-1060 (1999)

(4) Yamauchi, H., Akiyoshi, Y.: Theoretical Analysis of Tire Acoustic Cavity Noise and Proposal of Improvement technique, Transactions of Society of Automotive Engineers of Japan, Vol. 32, No. 2, 20014169, p. 79-84 (2001)

(5) Yamada, H., Ishiyama, O., et al.: Development of road noise prediction method, 2000 JSAE Annual Congress Proceedings, No. 65-00, 20005007, p. 1-4 (2000)

(6) Nakagawa, T., Sugiura, N., et al.: An Analyzing Method of the Exciting Force on Tire for Road Noise, 1998 JSAE Annual Congress Proceedings, No. 78-98, 79, p. 13-16 (1998)

■ Author ■



Youichi KAMIYAMA

# Vibration Characteristics Analysis in Vehicle Body Vertical Plane of Motorcycle during Turning

Yoshitaka TEZUKA* Shinichi KOKUBU*
Yoshinobu SHIOMI* Satoru KIYOTA*

## ABSTRACT

A vibration phenomenon generated in the vertical plane of a motorcycle during high-speed turning has been analyzed using actual running tests and simulation. As a result, it was found that the phenomenon is a self-excited vibration caused by the sprung part resonance and the unsprung part resonance of the rear wheel coupled with a frictional force variation at the contact patch of the tire. The simulation model developed reproduced the same vibration phenomenon.

## 1. Introduction

Motorcycles sometimes generate a vibration during high-speed turns. The dominant component of the vibration is in the vertical plane of the motorcycle. Riders have complained that it is uncomfortable and that it slows down the turning velocity or interferes with other active performances. Few studies of this vibration have been carried out; currently, it is handled by adjusting the motorcycle dimensions, in accordance with experience and the rider's preferences, by adjustment of the suspension parameters, by choice of tires, and by other measures.

The authors have conducted actual running tests under conditions which are known to cause the vibrations. The test results allowed an investigation of the mechanisms underlying the vibration and creation of a simulation model for reproducing similar vibrations.

## 2. Measurement Method for Actual Running Tests

As depicted in Fig. 1, 14 accelerometers were mounted on the test motorcycle, 7 in the sprung portions and 7 in the unsprung portions to obtain rigid-body behavior of the motorcycle. Motorcycle conditions were simultaneously observed: Engine speed, throttle opening, rotation velocity of the front and rear wheels, motorcycle body roll angle, and lap marker (in order to grasp which area of the course the motorcycle is being run). These were transmitted over a data link for measuring vibration.

The vibratory phenomenon does not derive until the motorcycle turns at a limit causing lateral tire slip, so the measurement device was installed inside the fuel tank. This was due to considerations of its effect on motorcycle body conditions including additional weight to the motorcycle and the change in weight distribution on the wheels, and reducing the inconvenience to the rider.

## 3. Actual Running Test Results and Analysis

### 3.1. Analysis of Time Domain Data

Figure 2 shows the time domain waveforms for front axle vertical acceleration, engine speed, velocity difference between the front and rear wheels, and the throttle opening during the vibration event observed in the running test.

The vibration was prominent over the period (for about 2 seconds) as shown in the figure. There is a visible increase in the vertical acceleration trace amplitude for the front axle in comparison with time before and afterward. The throttle was opened just before the event began, and when the throttle was closed slightly, the vibration converged toward normal levels. Then, the vibration began again as the throttle was re-opened. Rear wheel slip was visible as the difference in wheel velocities appeared in sequence with the throttle opening changes. The motorcycle body roll angle has been nearly constant throughout this period.

* Asaka R&D Center

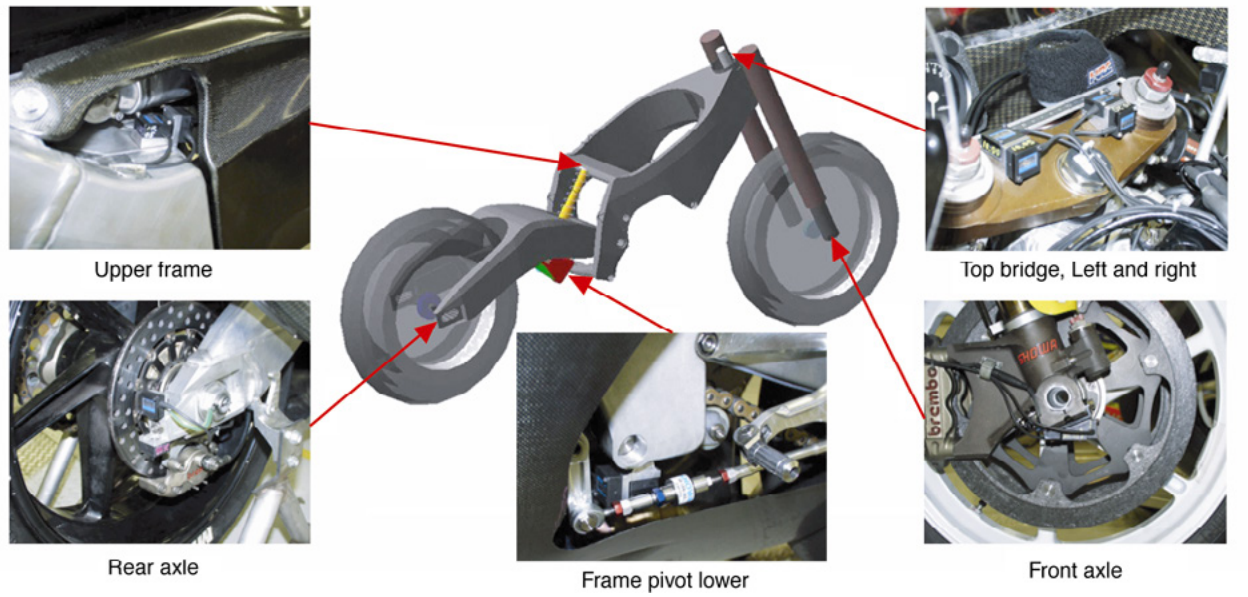



Fig. 1 Locations for acceleration meter

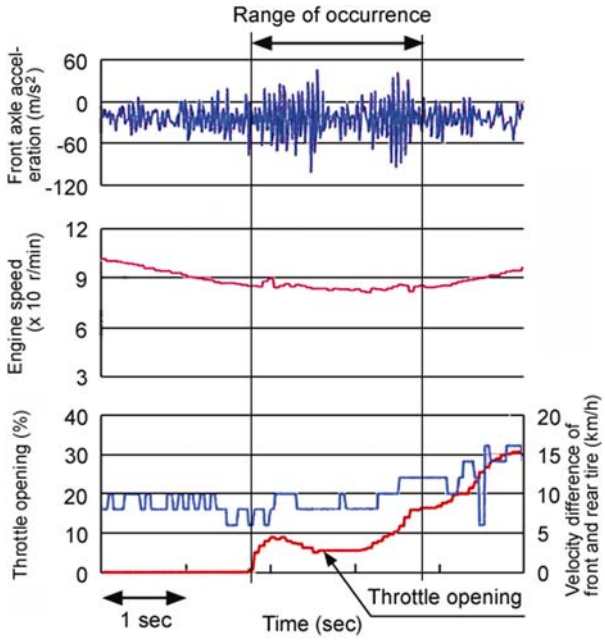



Fig. 2 Time domain data

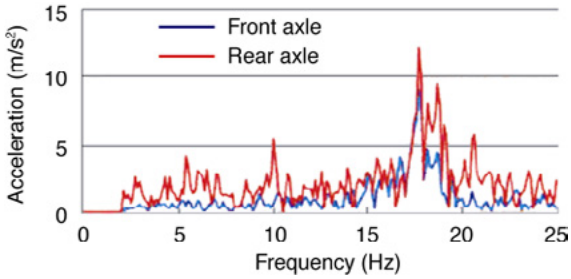



Fig. 3 Front and rear axle acceleration

### 3.2. Analysis of Real Vibratory Motion

A frequency analysis of the data observed during the running test showed vibrations occurring around a prominent peak at 17.7 Hz, as shown in the power spectrum density (PSD) of the vertical acceleration for the front and rear axles in Fig. 3. A motion animation of the 17.7 Hz vibration was made, using a transfer function in reference to the vertical acceleration of the rear wheel (see Fig. 4).

Observations of the actual vibration motion showed that it could be decomposed into three motions, in a continually repeated sequence. Motion 1: The entire body moves forward, forcing the front wheel against the ground. Motion 2: The body moves back, forcing the rear wheel against the ground. Motion 3: The front wheel moves upward, followed after a slight delay by the rise of the rear wheel. It is assumed that the sprung resonance of the body accompanying the vertical motion of the front wheel couples with the resonance in vertical motion of the rear wheel, and the two modes excite each other; the combination appears to act as a self-excited system with a continuous energy input.

Close consideration of the time domain data in the running tests and the analysis of the vibration modes indicated that these are self-excited vibrations that occur during the steepest body roll angle with the driving force applied to the rear wheel, and that mutually promote the behavior of the resonance body modes.

## 4. Models Used for Simulation

### 4.1. Motorcycle Body Model

A spring and rigid-body mass model with nine degrees of freedom (DOF) was constructed, on the basis of the authors' deductions about the frequency of the actual vibration that the chassis, front fork, and swing arm accompany no elastic behavior.

Figure 5 shows the model used for the simulation. It was composed of ten elements: Sprung steering components, unsprung steering components, front tire, engine, frame body, rider body, rear suspension, and its linkage portion, swing arm, and rear tire. The nine DOF consisted of six DOF for the body component, one DOF for steering and two DOF for

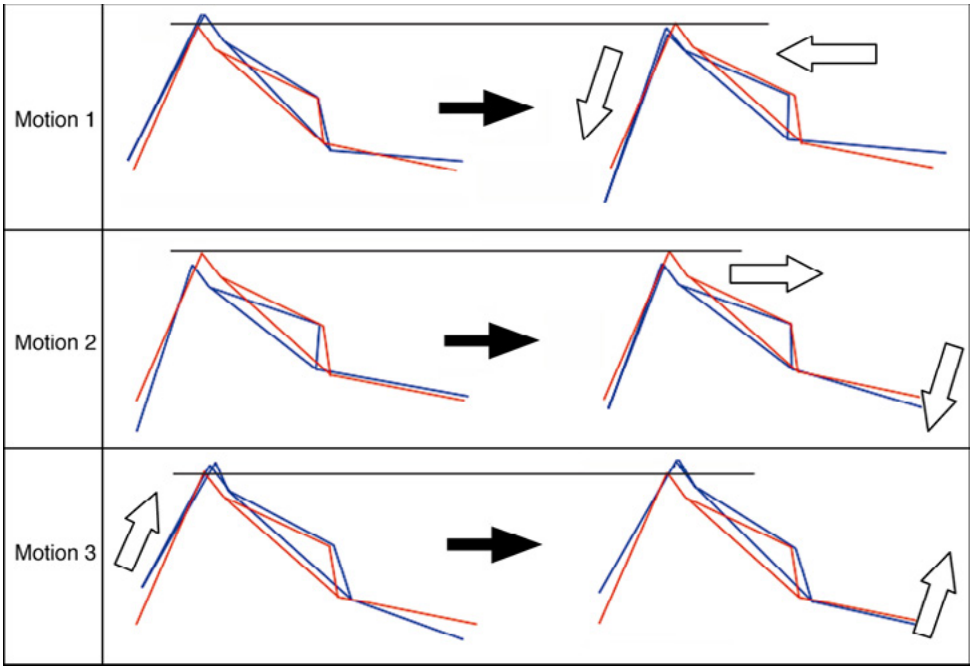



Fig. 4 Sample of modes animation

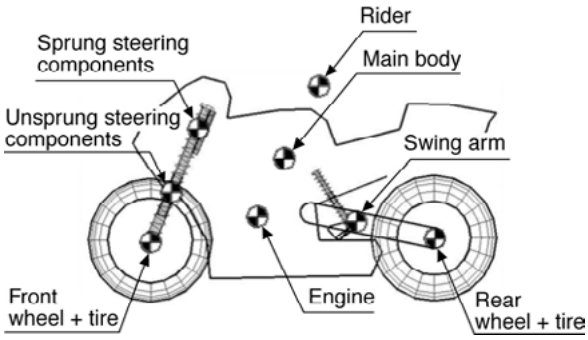



Fig. 5 Motorcycle model

the front and rear suspensions. The actual spring and damping parameters for suspension are non-linear, but since the vibration occurred while the motorcycle was in a stable configuration, these were approximated with linearized parameters. The motorcycle body was assumed rigidly bound, including the rider, who was considered only as a single mass.

## 4.2. Tire Model

The vibration is caused by a frictional interaction between the tires and the road surface, so modeling of the tires was an essential part of this simulation. Since this model was linearized, however, the tire characteristics do not express dynamic attitude such as cornering characteristics and defines spring constant and damping factor of the tire from the tire tester. The roll angle is high in this model and the motorcycle is in the midst of cornering, so frictional forces act at the contact patch between the tire and the ground in the centripetal direction. Analysis of the time domain data showed evidence of the driving force at the rear tire, in addition to the centripetal force, during the period when the vibration was occurring. The frictional force $F_\mu$ was defined as shown in Fig. 6[(1) - (3)].

$$F_\mu = \mu * F_z \quad (1)$$

$$F_z = K_g * u_z \quad (2)$$

Here,
$\mu$ : Friction coefficient
$u_z$ : Vertical displacement of tire

Figure 7 shows the definitions of the vertical direction spring constant $K_g$, the spring constants of the tires in terms of the vehicle coordinate system Y, Z axes $K_Y$, $K_Z$, and the camber angle $\theta$. These are required to solve Eq. (3):

$$K_g = K_z \cos\theta + K_y \sin\theta \quad (3)$$

## 4.3. Equation of Motion for Motorcycle Body Model

Since the vibration was attributed to self-excitation by the analysis of the running test results, a stability criterion analysis was carried out using complex eigenvalues analysis to investigate the potential for reproduction of the actual phenomenon[(4), (5)].

In the first stage of a complex eigenvalue modal analysis, the real parts of the eigenvalues are sought, assuming no damping or exterior loads on the system. In the second stage, these real eigenmodes are used to transform the asymmetric equation of motion in the physical coordinate system into modal coordinate system and execute complex eigenvalue analysis. The complex eigenmode thus obtained expresses the extent to which each real mode is excited. By showing the displacement components of the complex modes as vectors, it is easily seen how much each real-component mode contributes to the unstable mode[(6) - (9)]. The equation of motion for the body model is given in Eq. (4):

$$[M]\{\ddot{x}\} + [K]\{x\} = \{F\} + \{F_\mu\} \quad (4)$$

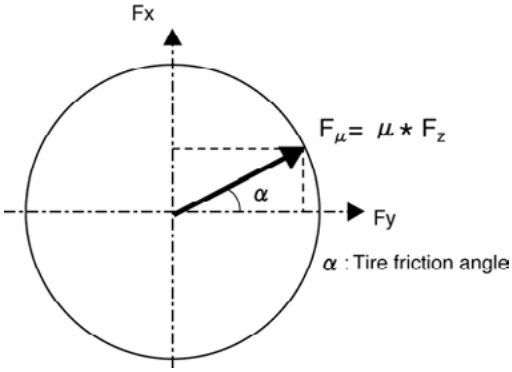



Fig. 6 Tire friction circle concept

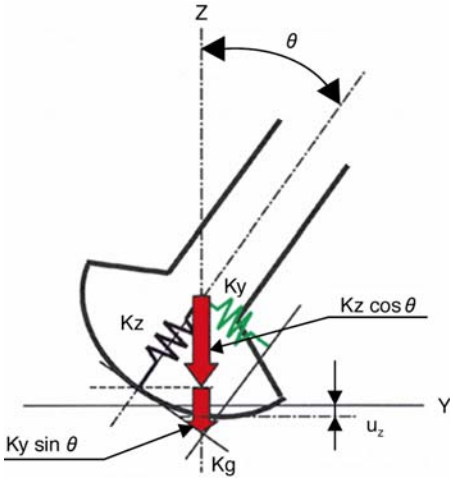



Fig. 7 Tire condition

Here,
$\{F\}$ : Force vector
$[M]$ : Mass matrix
$[K]$ : Stiffness matrix
$\{x\}$ : Displacement vector

Exterior forces due to friction $\{F_\mu\}$ are calculated using Eq. (5):

$$\{F_\mu\} = [\Delta K]\{x\} \quad (5)$$

$[\Delta K]$ is an asymmetric modal stiffness matrix since $\mu * k_g$ expressing the frictional force exerted on the tire, contains a row with the Y-direction component and a column with the Z-direction component only in the respective body-coordinate directions.

$$[\Delta K] = \begin{bmatrix} & & \\ & \mu * k_g & \\ & & \end{bmatrix} \quad (6)$$

Substituting Eq. (5) into Eq. (4) and moving the force term which is a function of position onto the left side, the asymmetric equation of motion in Eq. (7) is obtained:

$$[M]\{\ddot{x}\} + [K - \Delta K]\{x\} = \{F\} \quad (7)$$

If we examine the real eigenmodes of a symmetric version of Eq. (7), with the asymmetric stiffness term $[\Delta K]$ removed, we obtain the relational expression between the physical and modal DOF in Eq. (8).

$$\{x\} = [\phi]\{\lambda\} \quad (8)$$

Here,
$[\phi]$ : Mode shape matrix
$\{\lambda\}$ : Modal vector

Substituting Eq. (7) into Eq. (8) and multiplying both sides by the transposed matrix $[\phi]^T$, Eq. (9) is obtained:

$$[m]\{\ddot{\lambda}\} + [k - \Delta k]\{\lambda\} = \{f\} \quad (9)$$

This equation uses the terms
$[m]$ : Modal mass matrix
$[k]$ : Modal stiffness matrix
$[\Delta k]$ : Asymmetric modal stiffness matrix
$\{f\}$ : Modal force

where each term is composed of the following:

$$[m] = [\phi]^T[M][\phi] \quad (10)$$

$$[k] = [\phi]^T[K][\phi] \quad (11)$$

$$[\Delta k] = [\phi]^T[\Delta K][\phi] \quad (12)$$

$$\{f\} = [\phi]^T\{F\} \quad (13)$$

To add a little further explanation of Eq. (9): Complex eigenvalue analysis reveals complex eigenmodes, which consist of the complex eigenvalue and the real eigenmodes modal DOF for the model. This allows the real eigenmodes which cause the unstable mode(s) to be identified.

## 5. Results of Simulation and Observations

A parametric study was conducted in an attempt to identify the variables which had correlations with the vibration phenomenon in order to assess the validity of this model. Since the vibration occurred under a combination of circumstances of near-the steepest roll angle, driving force applying to the rear wheel and low throttle opening of around 10%, the body roll angle and the angle α which establishes the frictional force $F_\mu$ under driving force at high body roll angles (hereafter called the “tire friction angle”) were chosen as the parameters. The body roll angle was varied in steps of 5° from 30° to 60° and the tire friction angle was varied from 0° to 10° for each body roll angle.

Figure 8 shows the root loci of the parameter study results. The real part of the complex eigenvalues becomes unstable around the roll angle of 45° and the tire friction angle of 8°. This clearly was the region in which the self-excitation began. The resonance frequency was indicated at around 19 Hz here, a value reasonably close to that observed in the running test. No vibration was indicated at lower body roll angles, regardless of the tire friction angle; the real part of the complex results was stable. These results vindicate the model as valid for reproducing the vibration.

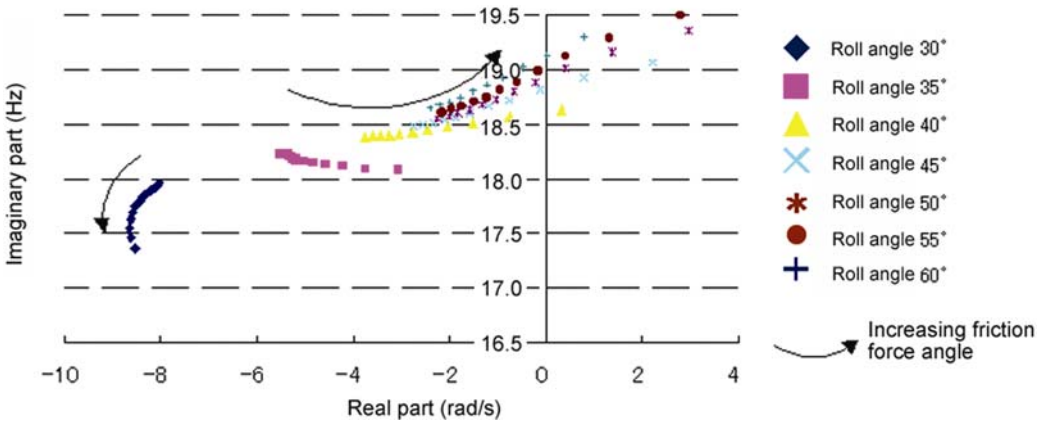



Fig. 8 Simulation result

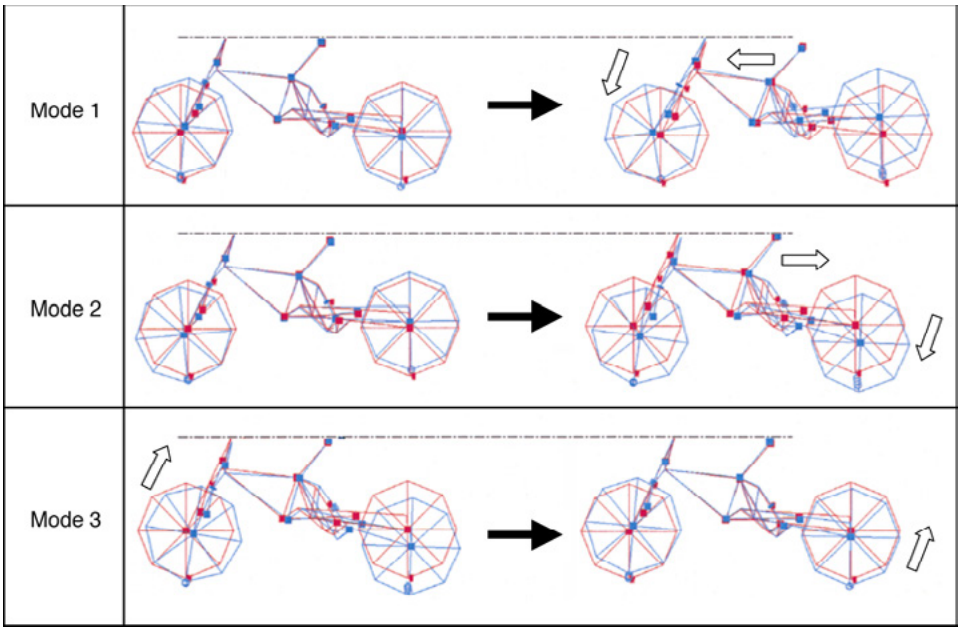



Fig. 9 Sample of simulation result animation

Next, the causes of the vibration were analyzed.

The modal complex eigenvalue analysis allows quantitative identification of the contribution ratios of the real eigenvalues, which cause the unstable eigenmodes. Figure 9 shows the results of a simulation at the roll angle of 50° and the tire friction angle of 8°. These are nearly the same as the vibration modes seen in the running test, and the resonance frequency was 19 Hz. The components of the complex eigenmode displacements were obtained by the analysis. It is indicated that the vibratory phenomenon is mainly made up from three real eigenmodes A, B and C, which are shown as vectors in Fig. 10.

Table 1 provides these real eigenmodes and their strain energy ratios. Real eigenmode A was the opposite phase mode of the sprung components on both the front and rear wheels; the strain energy chart indicates a high contribution from the front suspension. Mode B, the opposite phase mode of the unsprung components on both the front and rear wheels, showed a dominant contribution from the rear tire. Mode C, the in-phase mode of the unsprung components on both wheels, showed a dominant contribution from the front tire. The vector relations depicted in Fig. 10 show that Modes B and C were nearly equal in magnitude and were mixed. Since they were out of phase with each other and chiefly affected the front tire, the two phases cancelled, reducing displacement of the front tire. They appear to have formed a synthetic mode of the unsprung components of the

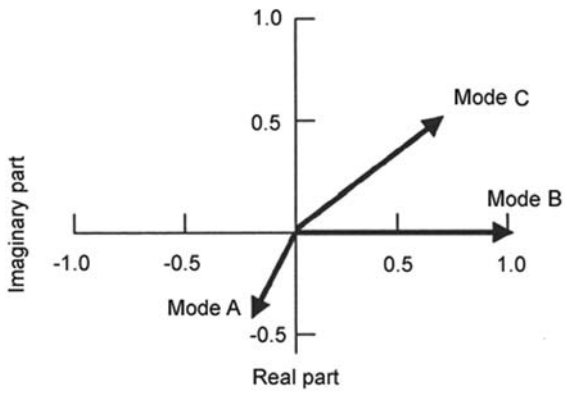
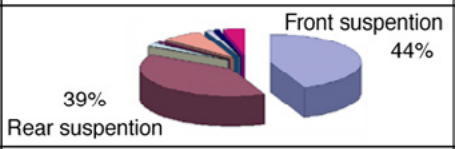
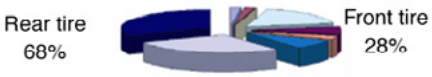
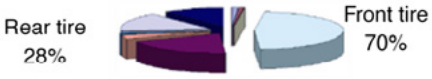



Fig. 10 Mode vector

Table 1 Real inherence mode of simulation model

| | Modes | Percent of strain energy |
|---|---|---|
| A |  Opposite phase mode of sprung |   |
| B |  Opposite phase mode of unsprung |   |
| C |  Inphase mode of unsprung |   |

rear tire. Thus, the vibratory phenomenon appears to have been caused by friction at the tires, resulting in coupling of the sprung components' Mode A and a combination of the unsprung components' Modes B and C.

## 6. Conclusion

(1) It was found that the motorcycle vertical-plane vibration observed in a motorcycle during high-speed turns was the self-excited vibration, in which the opposite phase mode of sprung components on the vehicle body and the mode of unsprung components on the rear wheel excited each other by friction at the tires' contact patches.
(2) Actual running tests and simulation provided results which revealed the mechanisms of the vibration and enabled reproduction of the vibratory phenomenon in a simulation.

## References

(1) Kageyama, K.: Soujyusei Anteisei ni Kakawaru Taiya no Tokusei, Handling and Stability, Chapter 2, p. 7-44 (1992) (in Japanese)

(2) Kageyama, K.: Soujyusei Anteisei no Kihon Jikou (5), Handling and Stability, Chapter 3, p. 70-71 (1992) (in Japanese)

(3) Yokohamagomu Co., Ltd.: Taiya no Kounaringu Tokusei (7) Kudoryoku Seidoryoku no Eikyou, Pneumatic Tire Technology, Chapter 4.2, p. 140-142 (1995) (in Japanese)

(4) Nagai, M., Kageyama, I., Tagawa, Y.: Jireishindo to Hisenkei Shindo 6.2 Anntei Hanbetsu, Shindo Kougaku Tsuuron, Chapter 6, p. 107-112 (1995) (in Japanese)

(5) Inoue, Y., et al.: Shindo no Kangaekata Toraekata, Chapter 5, p. 71-94 (1998) (in Japanese)

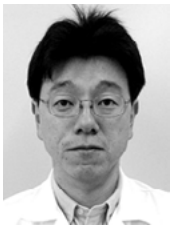
(6) Nagamatsu, A.: Modo Kaiseki, Tajiyuudokei, Chapter 3, p. 53-60 (1991) (in Japanese)

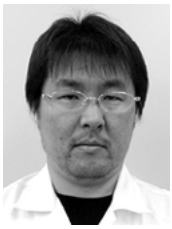
(7) Suzuki, K., et al.: Fukuso Koyuch Kaiseki ni Yoru Bureiki Naki Shimuraeshon, MSC Yuza Kaigi, Vol. 11 (1993) (in Japanese)

(8) Nakata, H., Kobayashi, K., Kajita, M.: A New Analysis Method for Motorcycle Brake Squeal Noise and Its Adaptation, Honda R&D Technical Review, Vol. 13, No. 2, p. 159-166 (2001)

(9) Nihon MSC Co., Ltd.: MSC/NASTRAN Basic Dynamic Analysis User's Guide V68, Chapter 3.2 (1993) (in Japanese)

## ■ Authors ■


Yoshitaka TEZUKA


Shinichi KOKUBU


Yoshinobu SHIOMI


Satoru KIYOTA

# Chain Load Simulation for Turbo Diesel Engine

Hiroshi TAKAGISHI* Kazuaki SHIMOYAMA* Kenji FUJIKI*
Masaru ASARI* Yasuhiro KAWAMURA* Atsushi NAGAKUBO*

## ABSTRACT

Fluctuation of crankshaft speed in a turbo charged direct-injection diesel (i-CTDi) engine significantly increases the load on the timing chain.

A simulation method was developed that calculates the load on the chain caused by these fluctuations. All moving parts, centered on the crankshaft, are connected in the simulation, which is able to more accurately reproduce a working engine on a computer. The model was simplified by focusing on the frequency response of each component when it was being assembled, enabling calculation accuracy to be maintained with a reduction in calculation time.

This enabled the load on the chain in an i-CTDi engine to be both accurately and rapidly predicted. The virtual engine contributed significantly to the optimization of the design of the timing chain in an actual engine.

## 1. Introduction

The load applied to the rotating parts inside an i-CTDi engine is larger than that of a gasoline engine because of the high combustion pressure used. Also, if a fuel injection pump is installed on the end of the camshaft of an i-CTDi engine, the torque fluctuation on the camshaft will increase, causing the load on the timing chain and oil pump chain to increase as well. For this reason, technology for performing a simulation to accurately predict the transmission load generated inside the engine was necessary.

In a conventional chain load simulation, it was general practice to employ a method in which modeling was performed on a limited number of parts. For example, in the case of the timing chain, simulation was previously performed using a model in which the parts responsible for generating the main vibromotive force were limited[(1)], such as the chain and valve train parts. This method was effective in cases where fluctuations of the crankshaft speed were small, such as in the case of a naturally aspirated gasoline engine.

However, in actual engine development, maximum priority is placed on obtaining an accurate grasp of phenomena concerning a working engine, so virtually all analysis consisted of behavioral and load measurement on a combustion operation engine. For this reason, analysis using the conventional simplified model produced a large discrepancy between measurement and simulation, and was inadequate for quantitatively predicting the transmission load.

Simulation has become large in scale. Figure 1 shows an example of large-scale analysis. Simulation includes calculations for determining the crankshaft behavior from the abridged results of FEM rigidity of the cylinder block and crankshaft, and takes into account various factors including each link in the chain, making it quite complicated. In order to simulate the chain load when linking these large-scale analyses, much calculation time was required and it was difficult to coordinate the results of simulation with actual development.

To overcome these issues, technology was established for predicting the chain load that can contribute to i-CTDi engine development. A description of this technology is reported below.

* Tochigi R&D Center

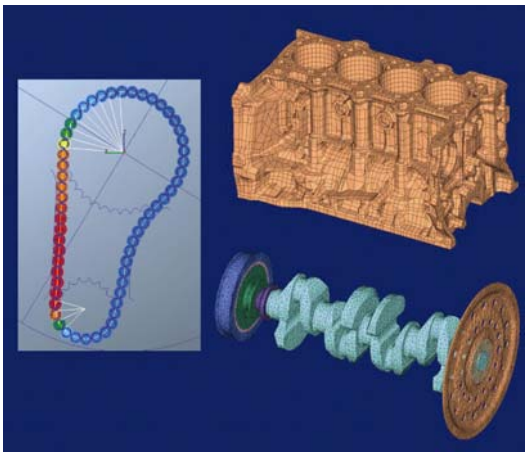


Fig. 1 Large-scale simulation model

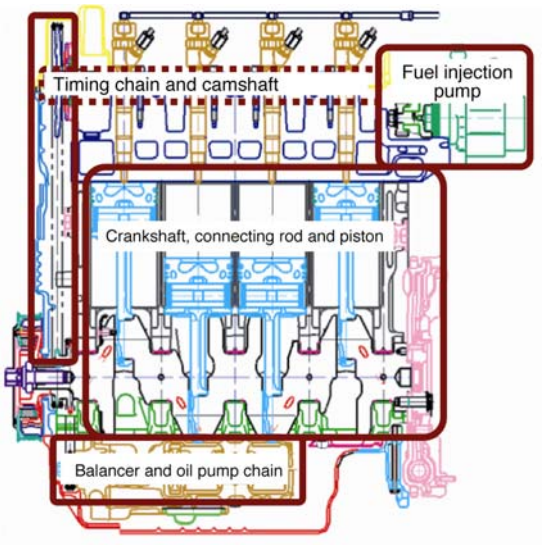



Fig. 2 i-CTDi engine

Table 1 General specification of i-CTDi engine

| | |
|---|---|
| Number of cylinders | 4 cylinders |
| Flywheel | Dual mass flywheel |
| Crank pulley | Isolation pulley |
| Balancer | Balancer driven by roller chain |
| Cam drive | Roller chain and gear |
| Number of cams | 2 camshafts |
| Number of valves | Intake: 2 valves / Exhaust: 2 valves |
| Valve train | Roller rocker arm with hydraulic adjuster |
| Fuel injection pump | Common rail injection pump |
| Auxiliary belt | Serpentine poly-V belt |

In the development, attention was paid to simulation technology that simultaneously coupled all moving parts centered about the crankshaft. Also, a study was carried out concerning the high prediction accuracy of the transmission system chain load and a practical calculation time.

## 2. Simulation Model

### 2.1. Configuration of a Virtual i-CTDi Engine

Table 1 shows the main specifications of the i-CTDi engine, and Fig. 2 is a cross-sectional diagram. Also, Fig. 3 shows the overall simulation model developed on this occasion. In this model, all of the moving parts were coupled, and a working engine was more accurately constructed on a computer. In the simulation model, the combustion pressure acted on the pistons, driving the crankshaft via the connecting rod, and the chains, gears, and belts coupled to

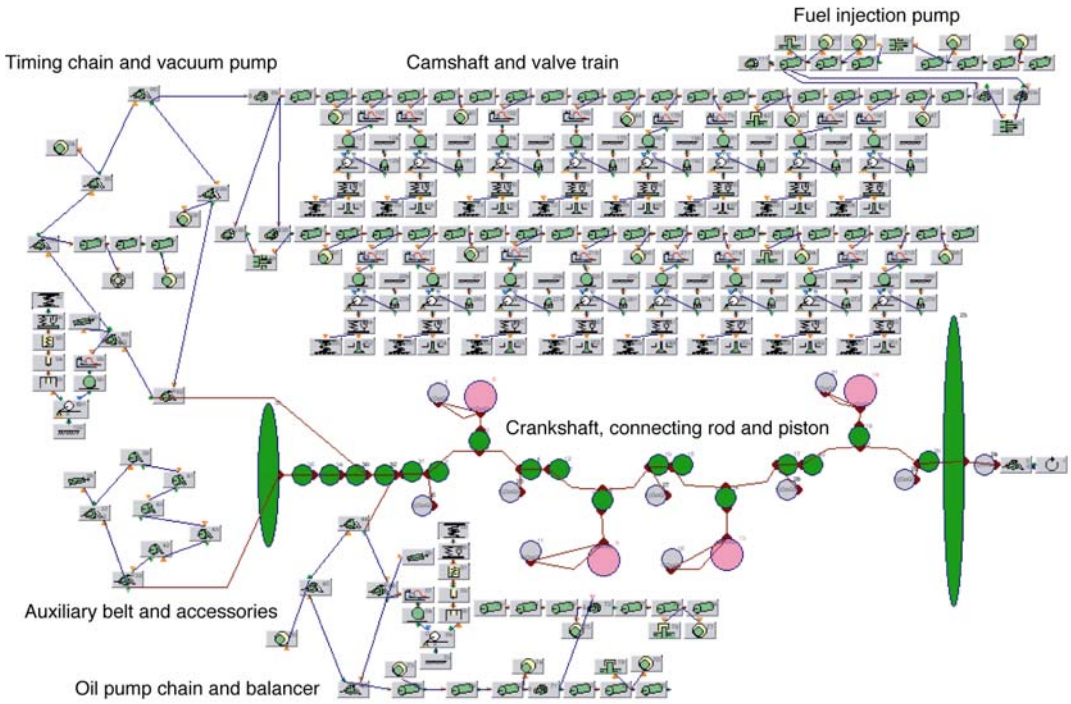



Fig. 3 Virtual i-CTDi engine

the crankshaft drove all of the parts including the cams, valves, fuel injection pump, vacuum pump, balancer and accessories simultaneously.

In this development, a highly accurate and unique model was constructed based on the TYCON software made by AVL, which most closely matched the objective. Details of this modeling technology are given below.

## 2.2. Crankshaft

The fluctuation of the rotational speed of the crankshaft of an i-CTDi engine is larger than that of a gasoline engine, and greatly increases the chain load. In the conventional simulation, the crankshaft model had six degrees of freedom and was intended mainly for studying details including stress evaluation. However, fluctuations of rotational speed exert the greatest effect on each part. For this reason, in order to reduce calculation time, it was decided to construct a crankshaft model that had degrees of freedom only in the direction of rotation and ignored bending deformation. Details of this crankshaft model are described below.

Figure 4 shows the crankshaft model. A link point for connecting the connecting rod was set on the crankpin, and the piston was connected to this point via the connecting rod. The cylinder was offset from the rotating axis of the crankshaft. A pressure load was applied to the piston, causing the crankshaft to be driven. Also, in order to simulate steady-state running, a constant brake torque was applied to the flywheel side.

The torsional rigidity of the crankshaft was calculated using the FEM-P method, as shown in Fig. 5.

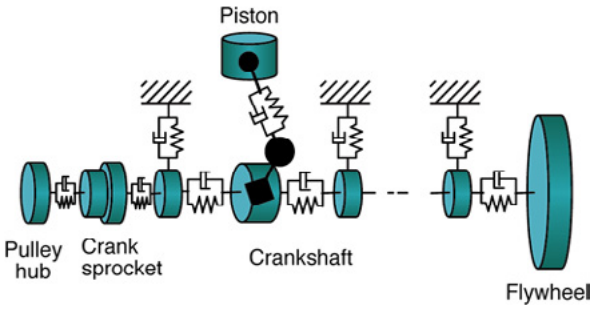



Fig. 4 Crankshaft simulation model

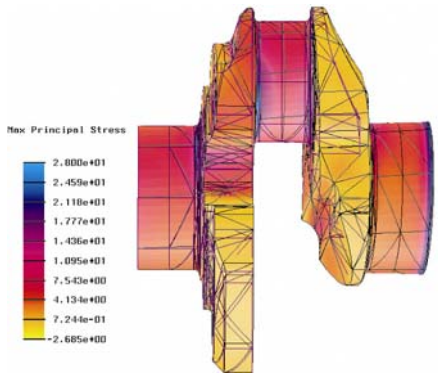



Fig. 5 Crankshaft rotational stiffness analysis

The dynamic behavior in the rotational direction of the crankshaft is determined by the torsional natural frequency characteristics of the crankshaft. The accuracy of the simulation model was guaranteed by confirming the accuracy of the torsional natural frequency of the crankshaft. The method of doing this is described below.

In order to check the frequency response, the crankshaft was excited by means of an impulse function to perform frequency analysis on the fluctuations of rotational speed. Eq. (1) shows the Fourier transformation equation for the impulse function.

$$F[\delta(t)] = \int_{-\infty}^{\infty} \delta(t) e^{-j\omega t}\, dt = 1 \tag{1}$$

Thus, the ideal impulse function when a Fourier transformation is performed is 1 over the entire area. Consequently, in an actual test, the eigen value is checked using a pseudo frequency response such as that produced by hammering. In the case of simulation as well, it is considered ideal to obtain the frequency response over the entire area. A pseudo impulse function should ideally have as narrow an impulse width as possible. For this reason, it is necessary that the time during which the impulse is applied be as short as possible, as shown in Eq. (2).

$$\delta(t) = \begin{cases} 0, & t \neq 0 \\ \infty, & t = 0 \end{cases} \qquad \int_{-\infty}^{\infty} \delta(t)dt = 1 \tag{2}$$

However, this simulation is calculated using a 2nd order predictor-corrector method. An extremely short step response brings about fineness of the calculation step, and as a result the calculation time increases. Here, the crankshaft was excited using step function. The Fourier transformation of the step function is shown in Eq. (3).

$$F[u(t)] = \int_{-\infty}^{\infty} u(t) e^{-j\omega t}\, dt = \pi\delta(\omega) + \frac{1}{j\omega} \tag{3}$$

The Fourier transformation of the step function is a function that is inversely proportional to frequency, so the input becomes large in the low-frequency area. However, it was considered that if the frequency range to be studied was limited, there should be no problem in identifying the frequency response. Also, like an impulse function, a step function enables the width definition to be omitted, and thus has the merits of simplifying the definition and reducing the calculation time.

The torsional natural frequency of the crankshaft of an in-line 4-cylinder engine is between about 300 and 500 Hz, so it is important that the simulation reproduces this frequency. The frequency was checked in two stages to take into account the effect of the crankshaft damper. First, a pure torsional resonance check of the crankshaft was performed using a fixed pulley model without a damper, and next the torsional resonance was checked using a damper model that simulated the condition in which a damper was fitted.

### 2.2.1. Fixed pulley model

The green line in Fig. 6 indicates the step response results. Because of the effect of the soft spring of the dual mass flywheel, a high value was obtained on the low frequency side, but a clear peak was seen at 437 Hz.

The green line in Fig. 7 indicates the results of measuring the 10th order component of the rotational acceleration of the crankshaft pulley hub in one rotation of crankshaft. It can be seen that torsional resonance of the shaft occurs at 2 600 rpm. In other words, 2 600/60*10 = 433 Hz is the torsional natural frequency of the fixed pulley shaft, thus indicating that the simulation accurately reproduces the shaft torsional resonance.

### 2.2.2. Damper model

A damper is installed in this engine in order to reduce the torsional resonance of the crankshaft. Consequently, the main resonance is reduced but a small resonance frequency appears instead. It was confirmed that this peak could be reproduced in the simulation.

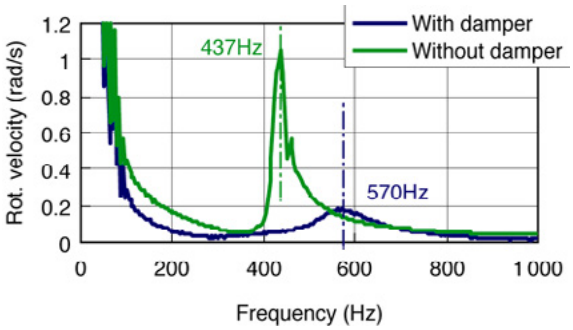



Fig. 6 Response of unit function

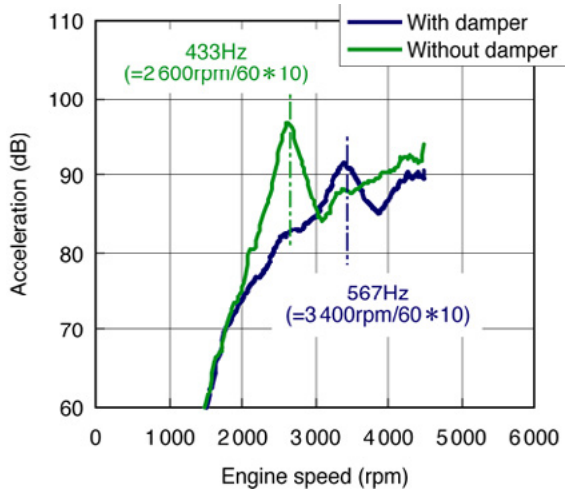



Fig. 7 Crankshaft rotational acceleration (order 10)

The blue line of Fig. 6 shows the step response results. The peak has shifted to 570 Hz. It can be seen that even for the measurement results indicated by the blue line in Fig. 7, the resonance has shifted to 3 400 rpm. In other words, 3 400/60*10 = 567 Hz is the torsional natural frequency, thus indicating that the simulation accurately reproduces the torsional resonance of a shaft on which a damper is installed.

In this way, it was possible to complete a simple crankshaft model that could reproduce the frequency response. The rotational speed fluctuation was verified using the completed crankshaft model. For the measurement, an optical rotary encoder was installed on the hub of the crankshaft pulley. Figure 8 shows the measurement results and the simulation results at 3 500, 4 000 and 4 500 rpm. In the i-CTDi engine, which produces a large explosive force, the effect of rotational speed fluctuation appears prominently when a combustion occurs in the cylinder nearest the crankshaft pulley. The torsional vibration of the crankshaft, which occurs as a result of this combustion, determines the speed fluctuation of the crankshaft. The simulation accurately reproduces not only the maximum speed fluctuation due to this combustion, but also the torsional vibration of the crankshaft as well. This was achieved by model verification based on the step response frequency. It was also found that the simulation accurately followed differences in rotational speed.

This model enabled the calculation for 10 revolutions of the crankshaft when rotating at 1 000 rpm in several minutes by a PC that had a CPU processing speed of 1.5 GHz. Because the model has degrees of freedom only in the direction of rotation, it was possible to construct a highly accurate crankshaft simulation model that permitted analysis to be performed in a short time such as this.

## 2.3. Balancer, Oil Pump and Oil Pump Chain

The balancer is excited by the fluctuation of the crankshaft speed. This speed fluctuation, which constitutes the excitation force, could be simulated accurately as mentioned above. Next in importance for predicting the transmission load is accurate prediction of resonance in the chain system. Accordingly, modeling was performed using a simple 1-dimensional chain model in the vertical direction that could accurately predict the transmission load. As a result, it was possible to reduce the calculation time.

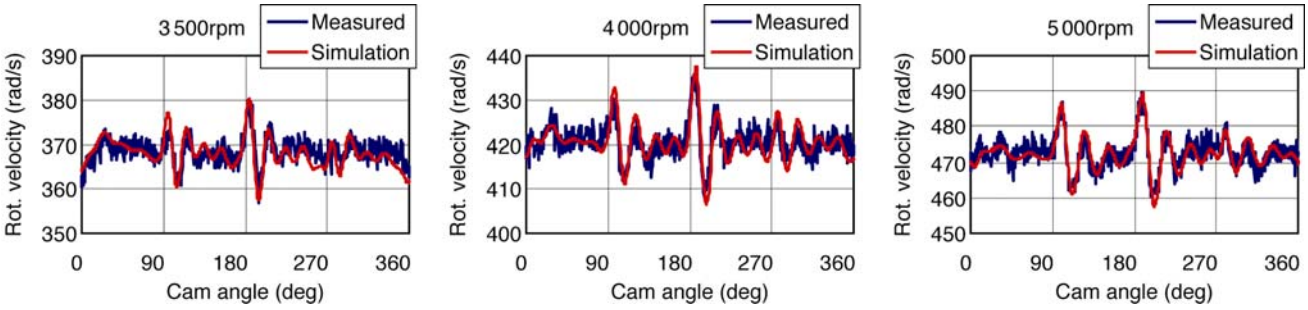



Fig. 8 Crankshaft rotational speed

Figure 9 shows the layout of the balancer and the oil pump. In order to cancel the 2nd order inertial force due to the mass of the reciprocating parts, such as the pistons, two balancer shafts are installed. The trochoid type oil pump that supplies oil to the entire engine is installed on the front shaft. It is driven by the rear shaft via gears. Figure 10 shows the balancer and oil pump model. Like the cams, the two balancers are supported by the journal. Also, a fixed pump drive torque is applied to the pump.

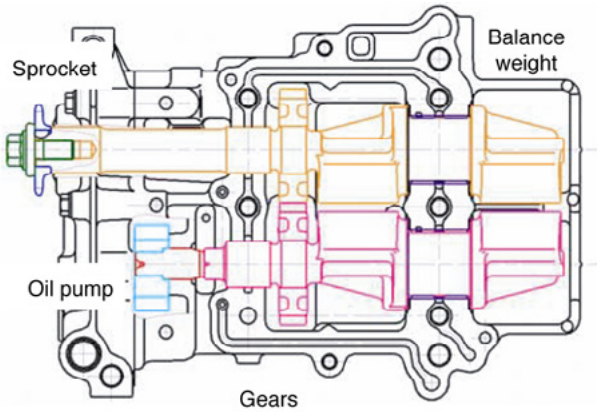



Fig. 9 Balancer shafts and Oil pump

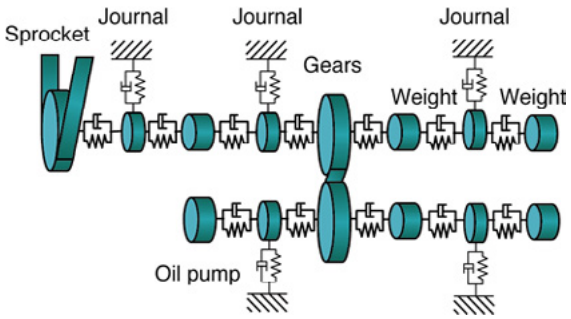



Fig. 10 Balancer shafts and oil pump simulation model

Figure 11 shows the layout of the oil pump chain. The sprocket drives the oil pump that is integral with the balancer shaft at twice the rotational speed of the crankshaft, via an 8 mm pitch roller chain. Figure 12 shows the oil pump chain model. If the tensioner is operating normally, the vertical vibration will constitute the main cause of chain load

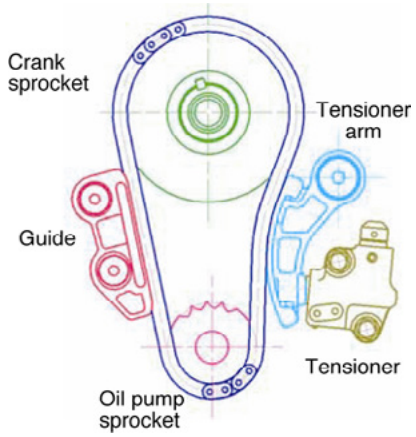



Fig. 11 Oil pump chain

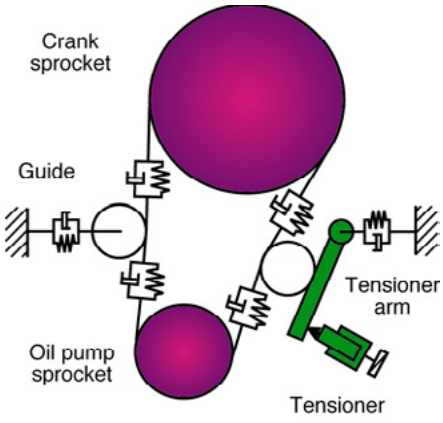



Fig. 12 Oil pump simulation model

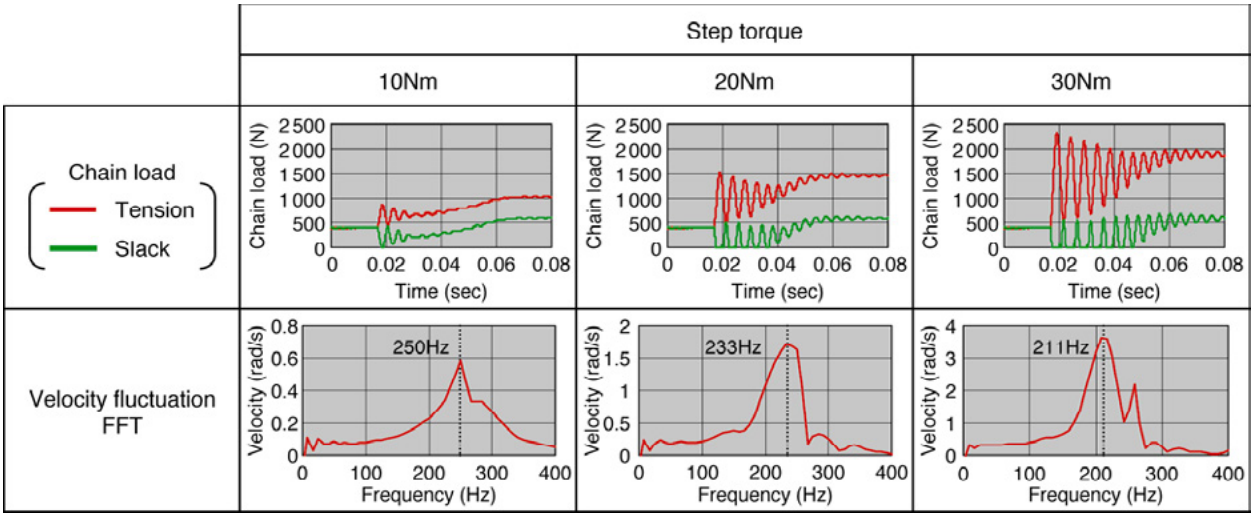



Fig. 13 Influence of step torque on chain resonance

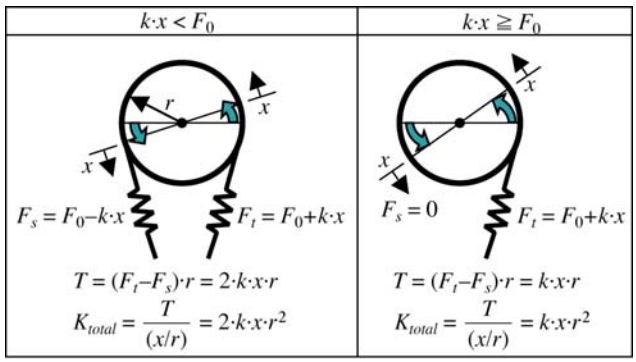
fluctuation. For this reason, the chain was simulated by a vertical direction 1-dimensional model. The moments of inertia of each part were linked by the chain rigidity and an attenuation element. Also, in the model, the tensioner with relief valve maintains the chain tension via the arm.

The oil pump chain has a resonant frequency in the normal rotation range. This resonance exerts a large effect on the chain load. For this reason, the frequency constituents of the step response of the chain were checked in the same way as for the crankshaft. When checking the frequency response of the chain, it is necessary to be careful of the size of the step function. As shown in Fig. 13, the change in the resonance point due to differences in the step torque was verified by simulation. It was predicted that the resonant frequency would vary between 213 and 250 Hz depending upon the magnitude of the step torque. This is due to the non-linearity of the chain system. If the chain load vibrates within the preload, it is possible to maintain the chain tension at both the tension and slack sides. However, if the step function is too large, the chain load on the slack side will be lost, and the load will be maintained only by the chain on the tension side. In this case, as shown in Fig. 14, the spring constant of the chain system will decrease, causing the resonant frequency to fall as well.

Figure 15 shows the result of performing a check of measurement of rotational speed of the actual sprocket on the balancer side. From this graph it was possible to confirm that the resonant frequency in the high rotational speed range shifted to the low frequency side. In actual measurement, the resonant frequency varied between 215 and 250 Hz, which matched the simulation. Thus, when estimating the rotational speed at which the chain resonates, it is necessary to take into account the reduction of rigidity of the chain system due to the loss of the load. As described above, it was confirmed that the frequency response of the simulation model was correct.

The oil pump chain load was verified. Measurement was performed by providing a thin wall area on the crankshaft sprocket and mounting a strain gauge on it. The torque measured here was multiplied by the effective radius of the sprocket and converted into chain tension. Figure 16 shows the measurement results and the simulation results at 2 000, 3 000 and 4 000 rpm. It was found that the simulation could reproduce the measurement results with good accuracy. Consequently, it was verified that the load transmitted to the oil pump chain and the balancer could be reproduced with high accuracy using a simple model.

In addition, the reduction of the chain load was verified using this simulation model. It was established that the chain load could be reduced by optimizing the relief pressure of the tensioner. Figure 17 shows the effect of the relief pressure on the chain load. By thus optimizing the relief pressure of the tensioner, it was possible to reduce the oil pump chain load.




$F_t$ : Chain load at tension side
$F_s$ : Chain load at slack side
$F_0$ : Pre-load
$x$ : Displacement of chain
$k$ : Stiffness of chain
$r$ : Effective radius of sprocket
$T$ : Torque
$K_{total}$ : Equivalent torsional stiffness

Fig. 14 Equivalent torsional stiffness of chain

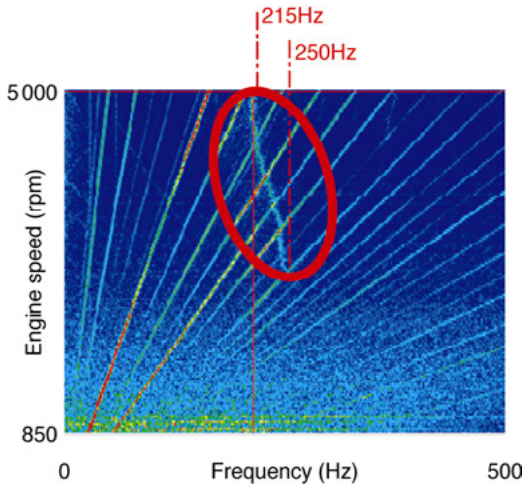



Fig. 15 Rotational velocity fluctuation FFT of balancer sprocket

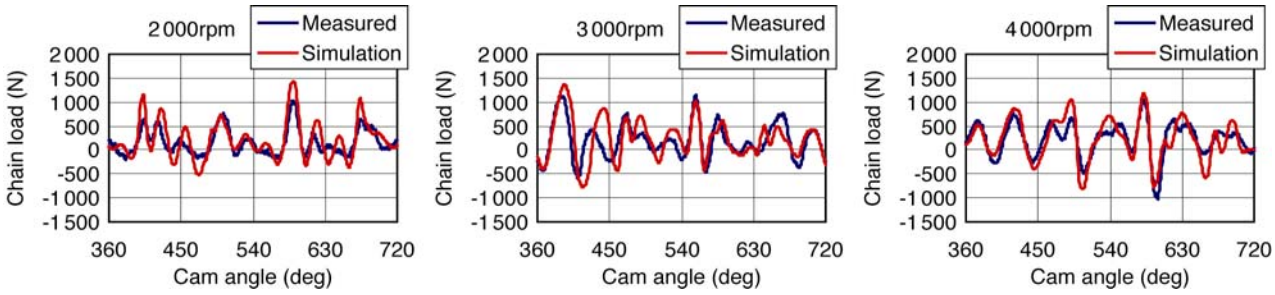



Fig. 16 Oil pump chain load

## 2.4. Valve Train

Conceivably, the next largest source of excitation following the crankshaft is the valve train. Particularly, in the case of the i-CTDi engine, the fuel injection pump is installed on the end of the cam, and also constitutes a large source of excitation. This excitation force is superimposed on the resonance of the timing chain, generating a high chain load. Details of the valve train model are described below.

Figure 18 shows the layout of the valve train. There are two intake valves and two exhaust valves for each cylinder. The cam has a roller bearing, and drives each valve via the rocker arm. The rocker arm is supported by a hydraulic lash adjuster for freedom from maintenance.

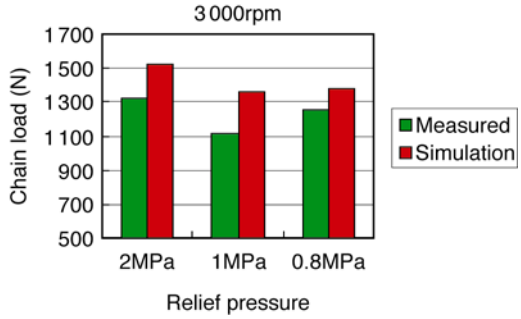



Fig. 17 Oil pump chain load

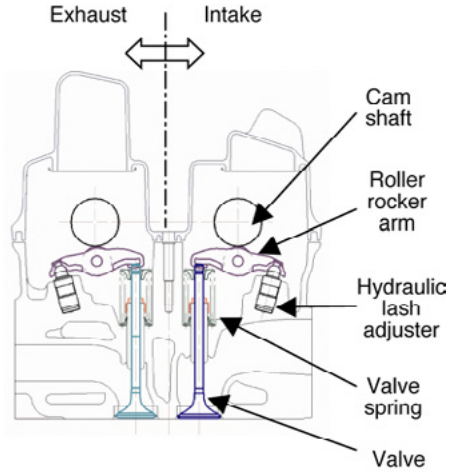



Fig. 18 Valve train

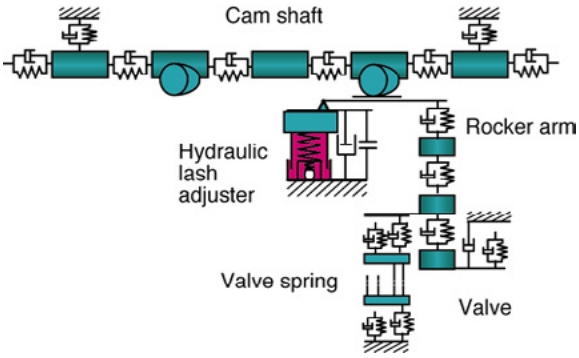



Fig. 19 Valve train simulation model

Figure 19 shows the valve train model. The calculation model consists of the rocker arm that is supported by a hydraulic lash adjuster, the valve and the valve spring. A detailed model was made because the hydraulic lash adjuster exerts a large effect on the valve train excitation force. The oil in the high-pressure chamber is supplied via a check ball by the motion of the plunger. The model also takes into account oil leakage from the gap between the plunger and the housing when load is applied, as well as the dependence on pressure of the oil rigidity due to ingress of air[2].

Figure 20 shows the results of verifying the valve lift. An optical type measuring device was used for measurement. The simulation accurately reproduces both the timing and the maximum lift.

Figure 21 shows the cam layout. There are two cams, one for the intake and the other for the exhaust. First, the exhaust cam is driven by the crankshaft via the cam sprocket and the timing chain. In addition, the exhaust cam drives the intake cam via scissors gears located adjacent to the cam sprocket, and simultaneously drive the fuel injection pump via the intermediate shaft by means of the gear installed on the opposite side of the sprocket and the cam.

Figure 22 shows the camshaft model. In this model, the cam was divided into multiple mass points coupled together by beam elements. Regarding the gears, the meshing reaction is simulated 3-dimensionally, enabling the 3-dimension deformation behavior of the cam to be accurately simulated. In addition, the journal is supported by an oil film model to simulate fluctuations of the shaft in the clearance. Like the crankshaft, the frequency response of the camshaft was

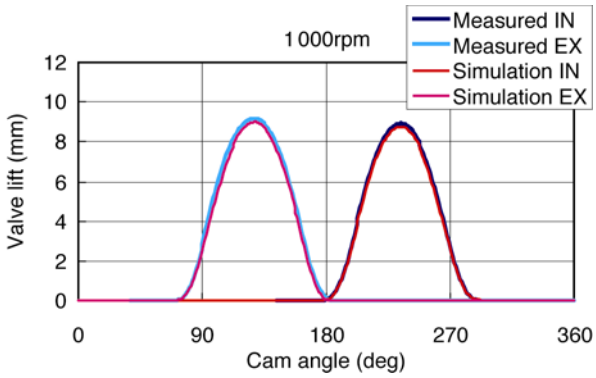



Fig. 20 Valve lift verification

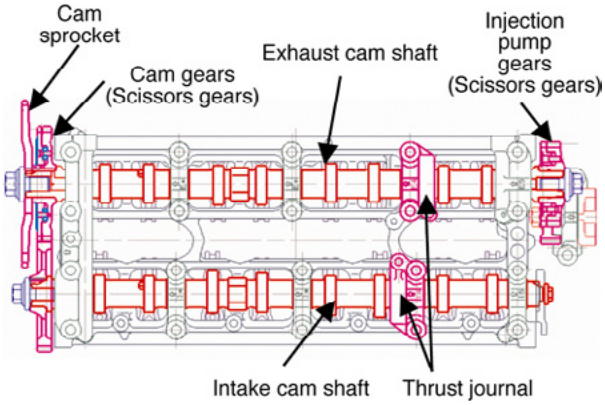



Fig. 21 Cam shafts

checked using the step response results in order to raise the accuracy.

Figure 23 shows the layout of the fuel injection pump and the drive system. The injection pump is mounted on the intermediate shaft installed obliquely beneath the exhaust cam, via an Oldham joint. This intermediate shaft is driven from the exhaust camshaft via scissors gears at a speed of 5/3 times that of the camshaft.

Figure 24 shows the drive system model of the fuel injection pump. In the model, the Oldham joint transmits only torque. Also, the clearance in the rotational direction of the Oldham joint is equivalent to that in an actual engine. In the model of the intermediate shaft, the shaft is supported by the journal, as in the case in an actual engine, and like the camshaft, it is supported by an oil film. The drive resistance torque of the pump is applied to the shaft of the fuel injection pump.

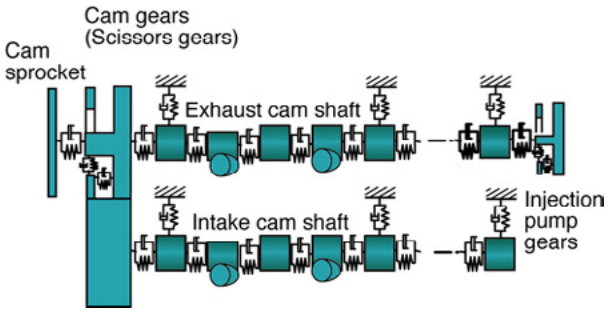



Fig. 22 Cam shafts simulation model

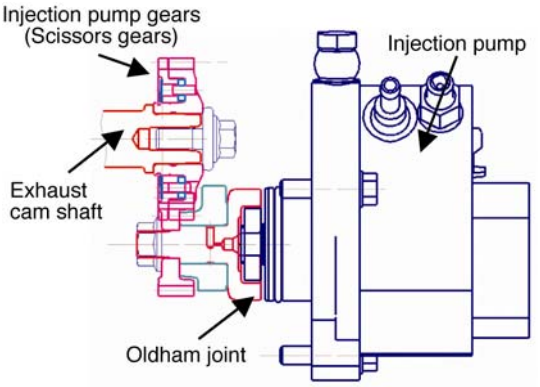



Fig. 23 Fuel injection pump driving system

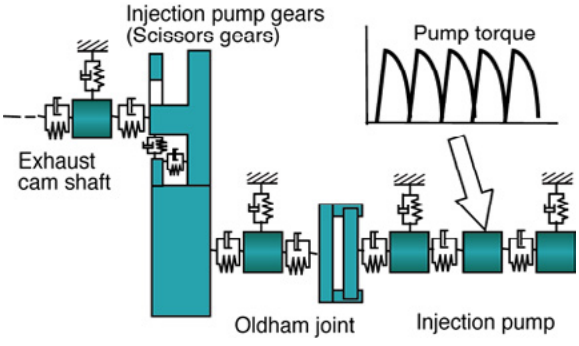



Fig. 24 Fuel injection pump driving system simulation model

By using these models, the thrust load generated in the camshaft holder was verified. The analysis results are shown in Fig. 25. In the simulation, the occurrence of a high impact thrust reaction was confirmed. The cause was found to be due to the high reaction of the fuel injection pump gears causing the cam to strike the holder. Similar measurement results were obtained from stress measurement of the cam holder as well, enabling the appropriateness of the simulation to be verified. The measurement results are shown in Fig. 26. Based on the impact load obtained, the optimum shape of cam holder was designed, and it was confirmed that the stress generated at the cam holder was within the guaranteed range of the material strength.

## 2.5. Timing Chain

Figure 27 shows the layout of an actual chain. The chain used was a roller chain that had a pitch of 9.525 mm. It

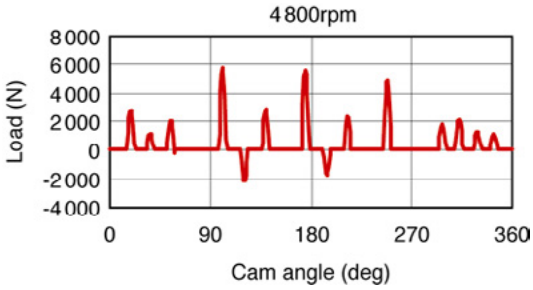



Fig. 25 Simulated camshaft thrust journal load

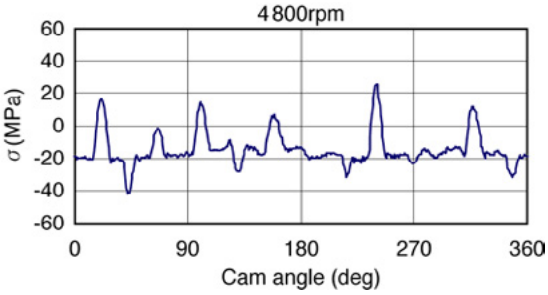



Fig. 26 Measured camshaft thrust journal load

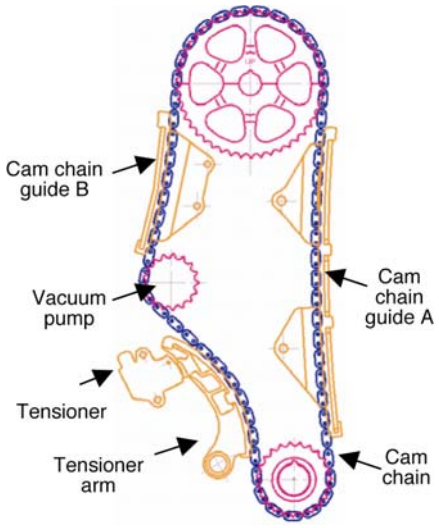



Fig. 27 Timing chain system

simultaneously drives the exhaust cam and the vacuum pump. There is a chain guide between the crankshaft sprocket and the camshaft sprocket, and also between the camshaft sprocket and the vacuum pump. Between the vacuum pump and the crankshaft sprocket, the tensioner maintains the chain tension via an arm. Because the chain is supported by the guide and the tensioner, a 1-dimensional model that ignored the transverse vibration of the chain took account only of vertical vibration in the chain tension direction.

Figure 28 shows the chain model. The inertias of each part are coupled by the chain rigidity and an attenuation element. The model simulated the maintenance of the chain tension by a tensioner with a relief valve via the tensioner arm[(2), (3)].

As in the case of the oil pump chain, the frequency response of the timing chain was verified from the step response.

Attention was focused on the timing chain, which is subjected simultaneously to the effects of these drive torques and crankshaft rotation fluctuations, and verification was done. Measurement was performed by providing a thin wall area on the crankshaft sprocket and mounting a strain gauge on it. The torque measured here was multiplied by the effective radius of the sprocket and converted into chain tension. Figure 29 shows the measurement results and the simulation results at 3 000 and 4 000 rpm. The 2.5$^{th}$ order fluctuation of the fuel injection pump torque and the 2$^{nd}$ order component of the cam drive torque and the crankshaft speed fluctuation overlap each other, resulting in a 0.5$^{th}$ order wave of the timing chain load.

In addition, Fig. 30 shows the change in the minimum and maximum values of the chain load with the engine speed. The simulation was done by performing a comparison using a model without a crankshaft and a full-engine model. If there is no crankshaft model, the accuracy of the chain load in the low rotational speed range will be insufficient. On the other hand, it can be seen that the full-engine model accurately reproduces the measurement results through the entire range, thus verifying its accuracy. It was thus possible to construct a highly accurate timing chain model that enabled an analysis to be carried out in a short time.

Table 2 shows a comparison of calculation time using the large-scale model and that using the new model. This table shows an example in which calculation for 10 revolutions of the crankshaft rotating at 1 000 rpm is performed using a PC that has a CPU processing speed of 1.5 GHz. Compared to large-scale analysis, the new model enables the calculation time to be significantly reduced. By thus adopting independent simple models, it was possible to carry out a full-engine simulation, which is considered to require several weeks when using the conventional complicated method, in several hours. It also enables the load on the chain in the transmission system to be predicted with high accuracy.

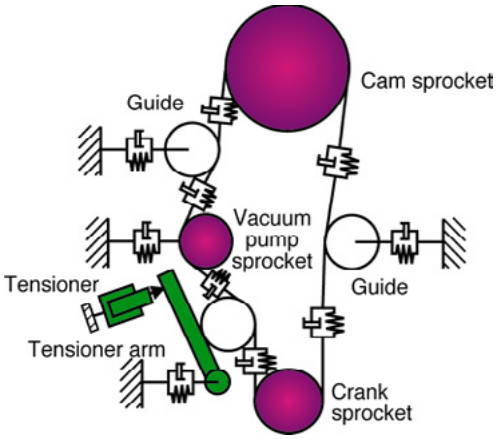



Fig. 28 Timing chain simulation model

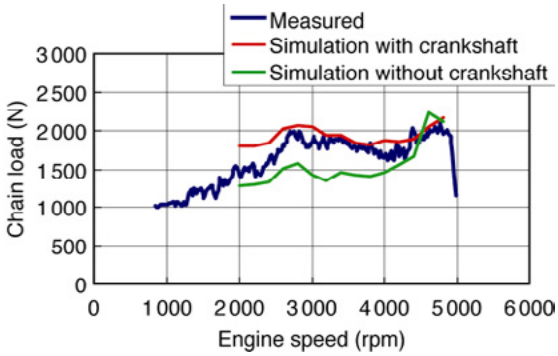



Fig. 30 Maximum and minimum load of timing chain

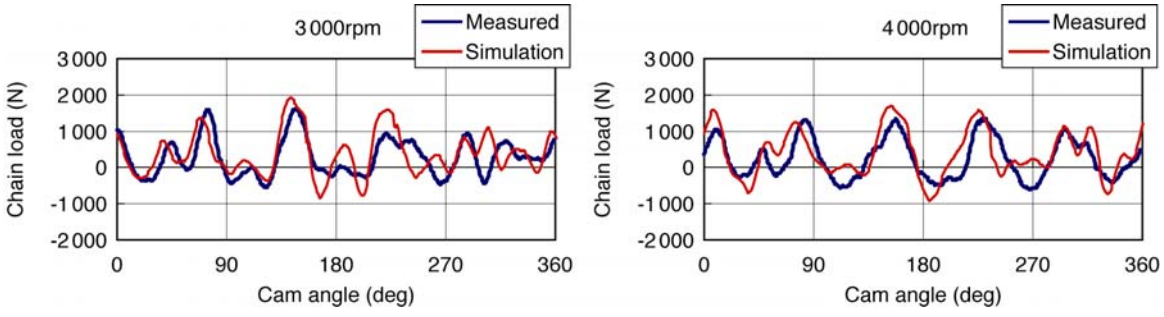



Fig. 29 Time history of timing chain load

Table 2 Calculation time

T: Time (h)

| | Crankshaft fluctuation | Timing chain load | Oil pump chain load | Auxiliary belt load | Full engine |
|---|---|---|---|---|---|
| Large-scale model | T > 48 | T > 48 | T > 24 | T > 48 | ——— |
| New model | 0.1 > T | 0.5 > T | 0.2 > T | 0.1 > T | 1 > T |

## 3. Conclusion

The following facts were acquired through the establishment of simulation for predicting the load on the chain in the transmission system of the i-CTDi engine.

(1) In order to obtain a grasp of the resonant frequency of the crankshaft, impact excitation simulation using a step function was carried out. The simulation results were compared with the actual measurement, and it was found possible to verify the torsional resonant frequency of the crankshaft. In this way, it was confirmed that the new model enables fluctuations of the rotational speed of the crankshaft to be accurately predicted.

(2) In order to obtain an accurate grasp of the oil pump chain as well, impact excitation simulation using a step function was carried out. In the case of the chain, the resonant frequency varies according to the input torque. It was established that this phenomenon could be predicted using this simulation.

(3) An accurate model of the valve train and the fuel injection pump, which are major sources of excitation of the timing chain, was made. As a result, it was possible to clarify the phenomenon of impact of the camshaft on the cam holder due to motion in the axial direction.

(4) By coupling the crankshaft and all moving parts, it was possible to simultaneously and accurately predict the timing chain load and the oil pump load, which are affected by the crankshaft rotational speed fluctuation, the cam drive torque, and the fuel injection pump drive torque.

(5) The calculation model could be simplified while maintaining accuracy, and realized a reduction in calculation time. As a result, it enabled the transmission system chain load to be predicted in a practical time.

## Acknowledgements

The authors would like to thank Dr. Hellinger, Mr. Sopouch and Mr. Vock of AVL for their kind cooperation in helping us establish this simulation technology.

## References

(1) Takagishi, H., Sugawara, H.: Prediction of Chain Load in Timing Chain System, Honda R&D Technical Review, Vol. 14, No. 1

(2) Sopouch, M., Hellinger, W., Priebsch, H.H.: Simulation of Engines Structure Borne Noise Excitation due to the Timing Chain Drive, SAE paper 2002-01-0451

(3) Hellinger, W., Priebsch, H.H., Rainer, G. Ph.: Auslegung von Ventiltrieben für Hochleistungsmotoren – Rechnerische und Experimentelle Verfahren. 16. Internationales Wiener Motorensymposium 1995 4

■ Authors ■


Hiroshi TAKAGISHI


Kazuaki SHIMOYAMA


Kenji FUJIKI


Masaru ASARI


Yasuhiro KAWAMURA


Atsushi NAGAKUBO

# Practical Application of Combustion Simulation Using CFD for Two-wheeled Vehicle Small Engine

Yasuo MURAKAMI* Hitoshi KUROSAKA*


## ABSTRACT

The Computational Fluid Dynamics simulation of the flame propagation phenomena in a cylinder is carried out to visualize the combustion condition in a small displacement, high-speed 4-stroke motorcycle engine. For verifying the simulation results, steady-state in-cylinder flow, fuel injection behavior, and flame propagation behavior were compared. Each experimental result verifies the simulation results, validating that the CFD simulation is an effective and useful tool to visualize the inside of the cylinder of the engine. This CFD visualizing technology is applied to study the combustion condition of a commercial motorcycle engine, and clarified that the technology is effective to reduce the fuel consumption and expand the lean combustion limit. This technology was applied to the development of the 4-stroke 50 cc PGM-FI (Programmed Fuel Injection) Engine.


## 1. Introduction

In recent years, demands for motorcycles with greater fuel economy and reduced exhaust emissions have been steadily increasing. For that purpose, measures to protect the environment, such as the adoption of 4-stroke engines and PGM-FI systems for mass-production motorcycles, are being promoted, and also increased research is being carried out for improving the combustion condition in the engine cylinder. In order to improve the combustion condition, it is important to obtain a detailed grasp of physical phenomena such as the gas mixture formation process inside the cylinder, and the flame propagation. Previously, it was common practice to observe these phenomena using an optically accessible engine[(1)] installed with quartz windows. However, such an engine did not have adequate durability under high temperature and pressure, particularly when running at high engine speeds, so observation of the inside of the cylinder of a small motorcycle engine, which is a high-speed type, is not necessarily the an optimal way for monitoring conditions inside an engine such as this.

Meanwhile, along with amazing progress of computer performance in recent years, Computation Fluid Dynamics (CFD) technology has come into wide use, particularly, in the development of an in-cylinder direct injection engine. For example, there are many papers[(2), (3)] where CFD simulation is being used for the visualization of the gas mixture formation in order to study the shape of the combustion chamber. Nowadays, it has become an important method for visualization of the inside of the cylinder. However, in a port injection engine, the overall crankshaft displacement angle duration necessary for analyzing the gas mixture formation process is two or three times longer than that of an in-cylinder direct injection engine in which fuel injection starts during the compression stroke. In addition, the combustion speed is greatly affected by the gas flow condition inside the cylinder. Consequently, there are many issues concerning the calculation accuracy, and to date there are only a few reported cases[(4), (5)] of verifications having been performed both experimentally and by CFD analysis including the combustion process as well.

In this research, we targeted port injection type motorcycle engines featuring small displacement and high engine speed, and we verified and clarified the fact that CFD analysis of the gas mixture formation process and the combustion process in these engines can be used as a method of visualization of the inside of the cylinder. These results were used in the development of an actual mass production engine, and the effectiveness of this method for optimizing the specifications of the combustion system was confirmed. In addition, some actual applications of the simulation visualizing method are described.

## 2. Calculation Method

### 2.1. Gas Flow

In order to calculate the gas flow condition in the cylinder and also the inlet and exhaust ports, it is necessary to discretize the calculation space and to solve the continuity equation of gas flow at each element, the conservation equations for the momentum, the energy and each reaction

* Asaka R&D Center

component, and the equation of state. When the engine is running, the calculation space change varies constantly due to the reciprocating piston and the moving inlet and exhaust valves. Consequently, it is necessary to use a special sliding grid, called a moving boundary grid, in the calculation space. There are several methods for this moving boundary grid. The method used in this research involved many preset periods during which each grid expands or contracts following the deformation of the calculation space, and switching over to the next grid before the grid quality becomes low due to the grid deformation. Some of the computational grids are shown in Fig. 1. Twenty nine grids were used for one cycle. Each grid used a boundary-fitted grid consisting of hexahedron cells. Two-layers of boundary grids were installed inside the inlet and exhaust ports, and one-layer of the boundary grid was installed inside the cylinder. The k – ε turbulence model was adopted, which was based on the turbulence kinetic energy k, and the rate of turbulent energy dissipation ε. FIRE (AVL List Co.), which is a commercially available 3D CFD code, was used for these calculations.

### 2.2. Fuel Spray Behavior

The Discrete Droplet Model (DDM) method[6] was adopted for the spray particle behavior calculations. The DDM method divides the several million fuel droplets supplied to the inlet port into several thousand droplet groups called parcels that have equivalent characteristics (position, droplet diameter, velocity and temperature), do not have mutual interaction, and are used for behavior calculation by tracing these groups using a Lagrangian method. Calculation of the flow in the injector was not performed and the nozzle hole was set to be a boundary condition. Experimental parameters, such as the initial injection velocity, injection rate, spray cone angle and particle size distribution obtained from an open spray experiment using a constant capacity box, were assigned to this model. For the breakup of the droplets, the Taylor Analogy Breakup (TAB) model[7] was adopted. Regarding the impingement and coalescence of the droplets in the spray, a collision frequency based on a Poisson distribution was assigned only for the droplets in the same calculation call. In this sub-model, the state of a droplet after impingement (coalescence or momentum exchange) was determined by the criterion value at the moment of collision. In addition, the wall film model was adopted to calculate the behavior of reflex and adhered, resulting from droplets impinging with the wall, and also for the flow and evaporation of the fuel liquid film in the inlet port.

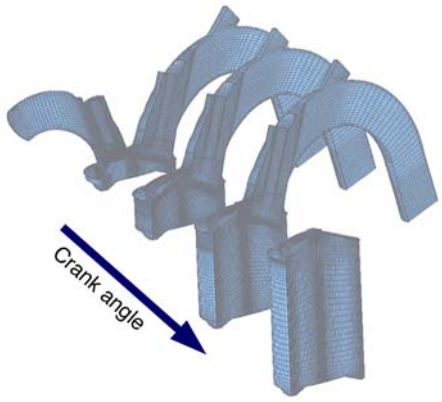



Fig. 1 Computational grids

### 2.3. Combustion Reaction

Concerning combustion in a spark ignition engine, the combustion reaction starts as a result of the activation of a high-voltage discharge by a spark plug to the mixture gas formed inside the cylinder. When performing a combustion simulation, it is necessary to create some kind of chemical reaction model to calculate the thermodynamic quantity due to the chemical reaction in the energy conservation equation and each generated quantity in the chemical species conservation equation. In the case of a spark ignition engine, the chemical reaction takes place in an extremely short time along the flame surface, so it was considered adequate to take into consideration the chemical equilibrium after combustion, and hence the Eddy Dissipation Model[8] propounded by Magnussen was used. With this model, the mean reaction rate $R_{fu}$ that determines the quantity of a generated chemical species was calculated by Eq. (1).

$$R_{fu} = A(\rho\varepsilon/k)\min\{y_{fu}, y_{ox}/S, B\cdot y_{pr}/(1+S)\} \quad (1)$$

Here, A and B are constants, $y_{fu}$, $y_{ox}$, and $y_{pr}$ are the mass fractions of fuel, oxygen and combustion products respectively, $S$ is the theoretical quantity of oxygen, and ρ is the density. In an actual engine, heat generates rapidly after an ignition delay time subsequent to the spark discharge. However, this model cannot take into account the oxidation reaction such as the cool flame that occurs at low temperature during the ignition delay period. Thus in the simulation, it is necessary to estimate the ignition delay by experience and set the ignition timing delayed by this amount.

### 2.4. Boundary Conditions

At the flange of the inlet port and exhaust port, which are the ends of the calculation area, the time history gas pressure and temperature obtained by experiments were defined as boundary conditions. Also, on the walls of the combustion chamber, piston and inlet and exhaust ports, the temperature obtained by experiments was defined, so that boundary conditions were set more closely approaching the operating conditions in an actual engine. In addition, the residual gas concentration subsequent to the valve overlap was taken into account by starting the calculation from the exhaust stroke.

## 3. Experimental Investigation of Correlation

### 3.1. Test Engine

Figure 2 shows the shape of the test engine, and Table 1 shows the main specifications of the engine. A two-valve, side ignition plug type engine was used as a typical small-displacement motorcycle engine, and squish is located only in part of the hemispherical type combustion chamber. The inlet port is U-shaped, and the tumble ratio according to the Ricardo measurement method is slightly less than 1. This engine was used to investigate the correlation between the simulations and experiments about the steady-state flow field of the inlet port, the behavior of the fuel spray and the combustion process.

### 3.2. Verification in the Inlet Port Steady State Flow Field

The inlet port is an important part that affects the output performance of the engine, and the effective valve opening area Z[9] is used as an index for evaluating it. Generally, the

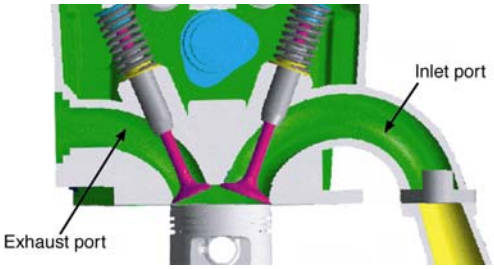



Fig. 2 Sample engine

Table 1 Test engine specifications

| | | |
|---|---|---|
| Engine type | | 4-stroke single cylinder, spark ignition |
| Bore × Stroke | (mm) | 36 × 49 |
| Displacement | ($cm^3$) | 49.8 |
| Valve layout | | 1 inlet and 1 exhaust valve |
| Compression ratio | | 12.0 |
| Combustion chamber | | Hemispherical type |

inlet port is measured under constant pressure using a steady state flow test rig, but recently there are an increasing number of cases in which this measurement is being replaced by CFD instead. Before an unsteady state flow was calculated, a flow of the inlet port was calculated under steady state conditions, and the correlation between the calculated value and the measured value was verified. The verification items were Z and the velocity distribution at the horizontal cross-section of the cylinder. Laser Doppler Velocimetry (LDV) shown in Fig. 3 was used for measuring the air flow velocity. Multi-point measurement was performed on the same plane, and a comparison with the calculated values was made. Figure 4 shows the results of the comparison of Z, and Fig. 5 shows the results of a comparison of the velocity distribution at the cross-section of the cylinder. It was found that the value of Z obtained by the simulation agreed closely with the measured value, and also that the tendency of Z that reaches its peak off in the high valve lift area could be accurately reproduced. For a velocity distribution at the horizontal cross-section of the cylinder, the changing velocity distribution according to the increase of the valve lift was well estimated. In addition, it was found that the strong downstream flow generated along the cylinder wall, the upstream flow generated directly beneath the inlet valve, the flow pattern divided by the valve stem, and other detailed flow features agreed closely with the experimental results. In this way, adequate correlation concerning the steady state flow calculations was obtained.

### 3.3. Validity Verification of the Fuel Spray Model

Figure 6 shows a comparison between the results of the open spray test performed in a constant capacity box, and the results of calculation using a spray model that was set based on data, such as the injection velocity, injection rate, spray corn angle and particle size distribution, obtained from this test. The test conditions were a fuel injection pressure of 250 kPa, a fuel injection time of 10 ms, and an atmospheric pressure equal to ambient pressure.

From the results of the calculation, it was confirmed that the spread of the spray, its penetration, the profile of the spray at the end of injection, and so on, obtained by the DDM method was consistent with the experimental results, thus validity of the spray model was confirmed.

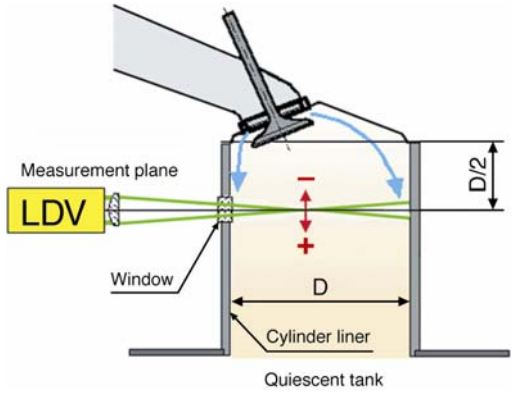



Fig. 3 Schematic diagram of LDV measurement

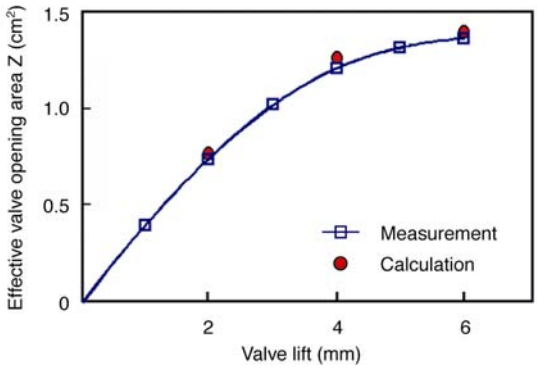



Fig. 4 Comparison of effective valve opening area between measurement and calculation

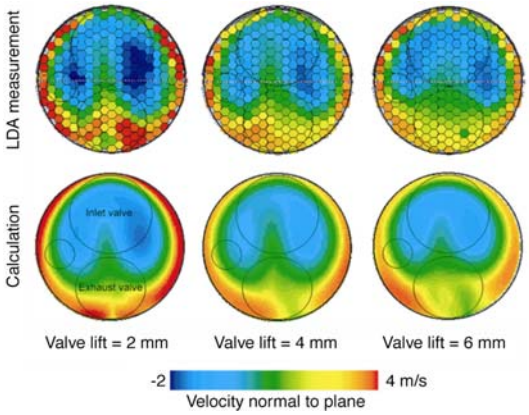



Fig. 5 Comparison of flow field structure on horizontal plane between measurement and calculation

### 3.4. Verification of Flame Propagation Correlation

#### 3.4.1. Flame behavior observation apparatus

A Tomographic Combustion Analyzer[10] (TCA) produced by AVL List Co. was used to verify the flame behavior. The TCA uses one hundred and several tens of optical fibers arranged in a circle in the cylinder head gasket for measuring the luminescence intensity emitted by the combustion flame. The obtained luminescence intensity signal is used to observe the behavior of the flame. Figures 7 and 8 show the measurement concept and configuration of the apparatus, and Fig. 9 shows the special gasket containing the optical fibers. The apparatus has the following features.

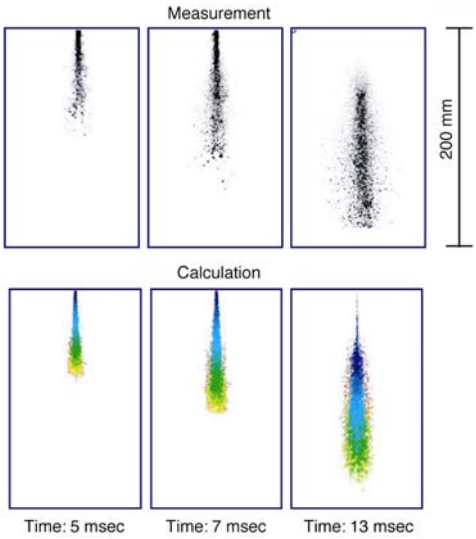



Fig. 6 Comparison of spray form between measurement and calculation (Ambient pressure)

(1) It enables the actual engine to be used without modification, so there is no change in the combustion condition due to the visualization.
(2) It has high strength and durability, enabling the flame to be observed over a long period under a wide range of engine operating conditions.
(3) It enables quantitative flame observation and data processing to be performed in a short time.
(4) It is necessary to prepare an individual special gasket for each engine bore diameter.
(5) It is possible to observe only the 2-dimensional flame propagation structure on the cross-sectional face of the gasket.

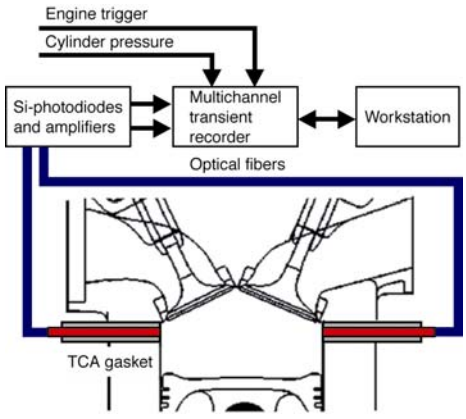



Fig. 7 Schematic diagram of TCA measurement

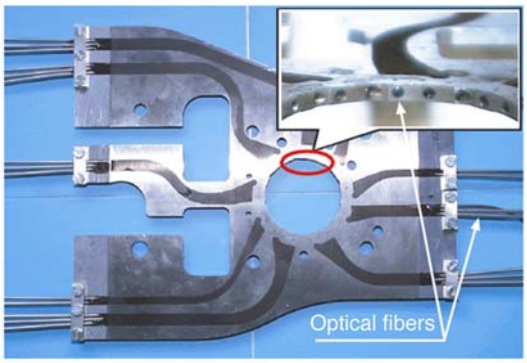



Fig. 9 Photograph of TCA gasket

Compared to conventional visualizing methods, the TCA method has many advantages. However, it is considered to be disadvantageous compared to visualization by CFD, because of the relatively small amount of data obtained by analysis and the high cost of analysis; therefore, in this research it was used only for the purpose of performing a correlation investigation.

### 3.4.2. Comparison of results

Figure 10 shows the spread of the flame surface obtained by simulation. The operating conditions were an engine speed of 4 900 r/min, an equivalence ratio of 1.13, a brake mean effective pressure of 135 kPa at a partial load, and an ignition timing of 20° BTDC. From the calculation results, it can be seen that the expansion of the initial flame surface at 10° ATDC agrees closely with the experimental results. At 20° ATDC where the combustion reaction increases, the experimental result of the flame speed in the direction of the inlet valve was high, whereas the calculated result was high in the direction of the center of the squish area, thus indicating that there were also parts where the calculated and experimental result were not consistent with each other. At 30° ATDC where the flame surface reaches the squish area furthest from the ignition plug, the phenomenon, whereby the flame propagation to the squish center is fast and conversely the flame propagation toward both ends of the squish is slow, was well simulated. Overall, it was confirmed that the macroscopic spread of the flame surface was consistent with the experimental results obtained using TCA.

Next, the comparison results of the cylinder pressure history (Fig. 11) and the mass fraction burned (Fig. 12) are shown below. As comparison conditions, the engine load was changed in several patterns, and the test was carried out under different combustion conditions. From the calculation results, the early combustion duration tended to be shorter under all load conditions. This tendency was seen especially at a high engine speed and a high load. This is due to the fact that the eddy dissipation model does not include the

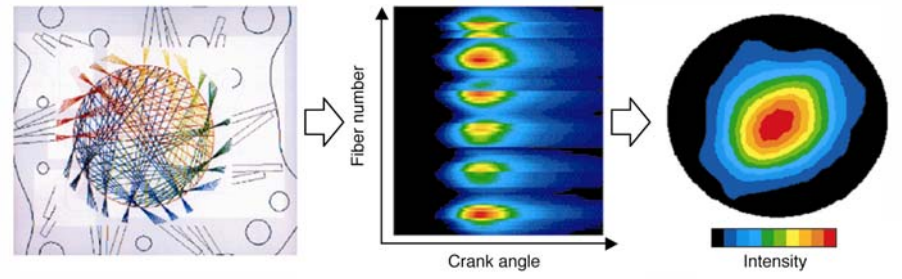



Fig. 8 Schematic flow of TCA measurement

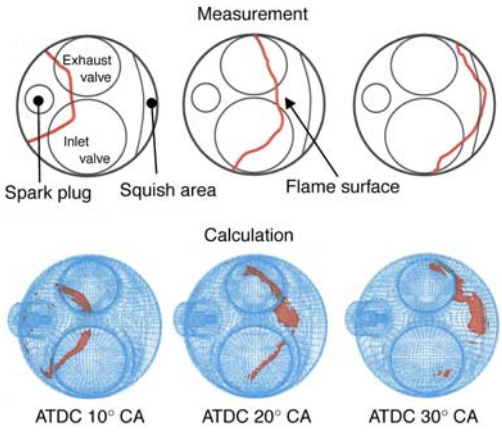



Fig. 10 Comparison of flame propagation between experiment and calculation (4 900 r/min, POT, $\phi$=1.13, Ignition timing=20° BTDC)

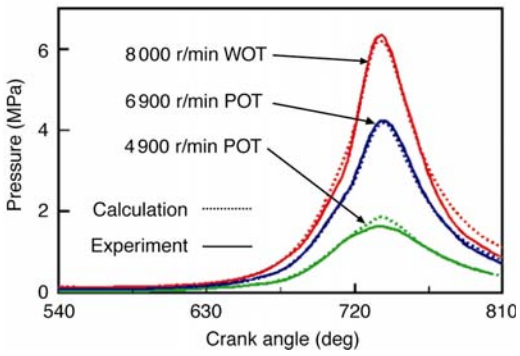



Fig. 11 Comparison of cylinder pressure between experiment and calculation

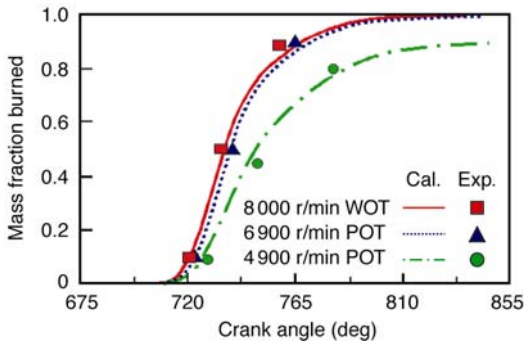



Fig. 12 Comparison of MFB between experiment and calculation

generation of activated chemical species, which occurs at low temperature during the ignition delay period, and the subsequent abrupt high temperature oxidation reaction. It is considered necessary to re-select the combustion model under combustion conditions such that the reaction under delayed ignition greatly affects the main combustion formation. However, it can be said that the selection of this model is appropriate if the main purpose of the model is visualizing flame propagation. Overall, the maximum generated pressure and the crank angle are roughly equal, and there is good correlation between the experimental results and the calculated results.

From the above verified results, it was confirmed possible to estimate the flame propagation behavior in a small displacement motorcycle engine by performing a simulation based on CFD.

## 4. Case Study Applicable to Engine Development

### 4.1. Improvement of the Lean Limit

Generally, cylinder pressure cycle fluctuations are evaluated according to their deviations. When the mixture ratio is made leaner, combustion becomes unstable and the pressure deviation becomes larger. As a result of the vibration and noise levels increasing, the lean limit is assessed by the combustion coefficient of variation, which is the deviation divided by the mean value of the cylinder pressure. This sub-section describes a case study in which CFD is used to visualize the flame propagation in order to analyze the cause of combustion fluctuations and to improve the lean limit.

The engine used in the test was a 4-valve, small displacement engine that had a pent roof type combustion chamber and a center plug layout. It was designed under the concept of lean combustion by means of a strengthened tumble flow, however as shown in Fig. 13 the combustion fluctuation of the prototype engine deteriorated abruptly when the equivalence ratio was 0.7 or less, which prevented the lean limit from being expanded (Fig. 14). For this reason, CFD was used to visualize the flame propagation so the cause could be investigated.

Figure 15 shows the results of analyzing the flame propagation both under partial load and under full load. It can be seen that when the engine is operating under full load, the flame spreads concentrically in a circle centered about the ignition plug, and conversely when the engine is operating under partial load the initial flame elongates in the direction toward the exhaust valve, thus indicating that the flame propagation is not uniform.

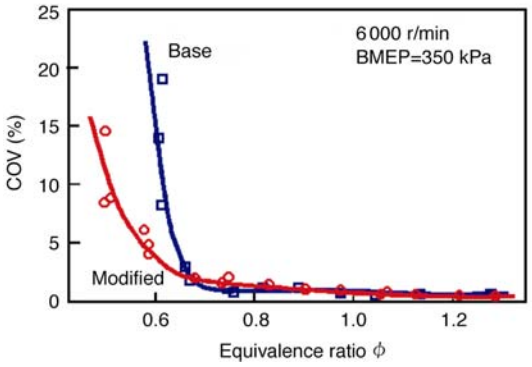



Fig. 13 Comparison of coefficient of variation between base engine and modified

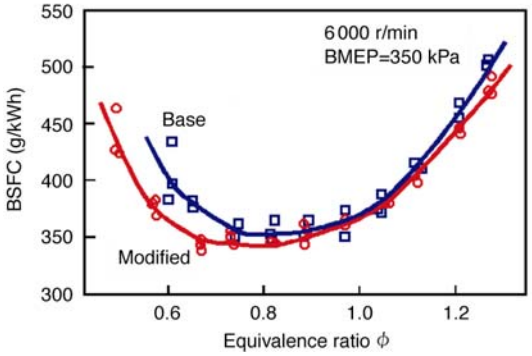



Fig. 14 Comparison of fuel consumption between base engine and modified

Figure 16(a) shows the distribution of the flow gas velocity vector in the cylinder before and after the ignition timing when the engine is operating under partial load. Figure 16(b) shows the distribution of the equivalence ratio. The tumble flow does not collapse even when the ignition timing (BTDC 45°) is reached, and the ignition plug is exposed to a bulk flow. Also, the gas mixture forms a rich band along the bulk flow, so it is thought that this causes the flame to propagate in the direction of the exhaust valve. This situation is extremely unstable for the early flame, and is likely to result in a misfire, so it was judged to be the main cause of combustion fluctuations. It is thought that a misfire does not occur under a full-load because the ignition delay period is shorter than that for partial load operation and also the ignition timing is 15° retarded, so that disintegration of the tumble flow proceeds and the flow velocity falls down.

Next, a study for a countermeasure was carried out using CFD. As a means of restraining the flow velocity around the ignition plug, which is the cause of flame elongation, a method[11] of slanting the axial center of the tumble flow has been reported by Kaneko and others. However, in this research, a study of a countermeasure proceeded without a control device. The flow velocity of the vertical eddy remaining at the ignition timing was high along the wall face, however it was slow around the center of the eddy. Attention was focused on these facts, and the ignition plug was made to protrude 2.5 mm, aiming at reducing the flow velocity. However, the closer one gets to the center of the eddy, the leaner the gas mixture becomes, which makes a misfire more likely to occur. To overcome this, the initial timing of the fuel injection was advanced, and an adjustment performed so that an ignitable gas mixture band would be formed in the vicinity of the ignition plug. Figures 17 and 18 show the comparison of the calculated history of the flow velocity and the equivalence ratio around the ignition plug before and after the countermeasure was adopted. It was found that the flow velocity at ignition timing could be reduced from 18 m/s to 15 m/s, and also obtained the same equivalence ratio as before the countermeasure by advancing the start of the fuel injection timing. From these results, it was confirmed in advance that a countermeasure by which misfire did not readily occur could be investigated by using simulation. Next, physical validation was performed on an actual engine with the specifications of the proposed countermeasure. As a result, it was found that the lean limit could be expanded to about 1 in terms of an equivalence ratio, and the fuel consumption rate improved by about 3%.

### 4.2. Study of the Injection Direction

It is well known that the emission values vary according to the installing position and angle of the injector. Particularly, it is known empirically that exhaust hydrocarbon (HC) can be reduced by directing the fuel spray at the port wall to collide with the wall. Previously, a study of these

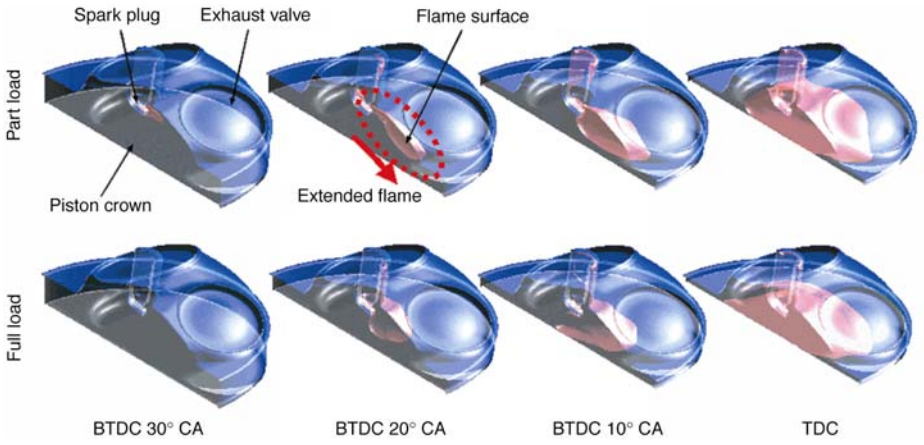



Fig. 15 Calculation results of flame propagation

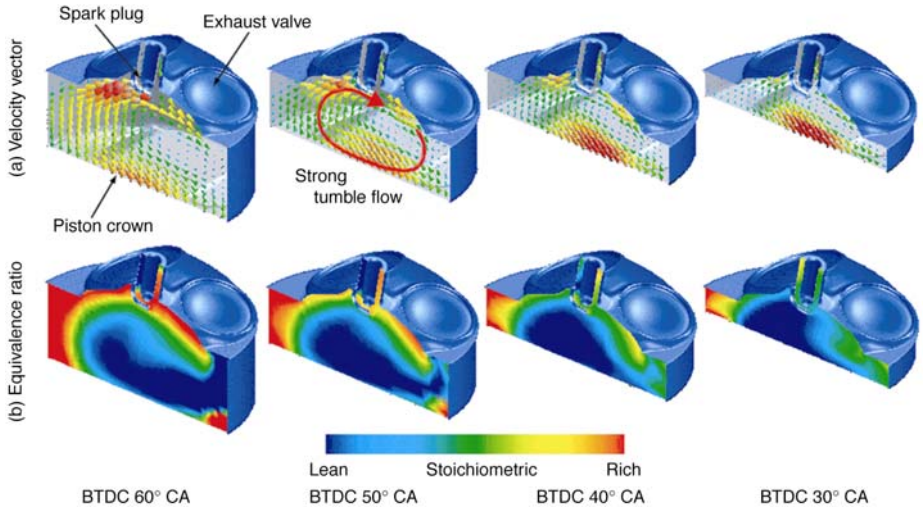



Fig. 16 Calculation results of gas behavior: (a) Gas velocity vector (b) Equivalence ratio distributions

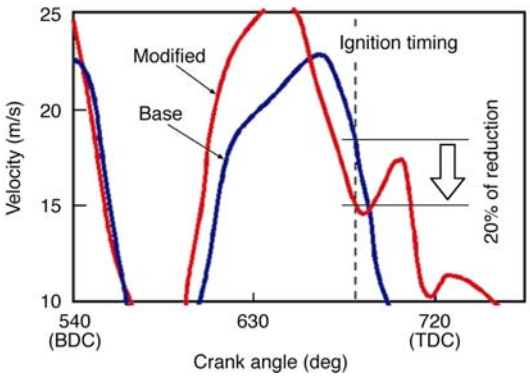



Fig. 17 Time history of mean velocity around spark plug

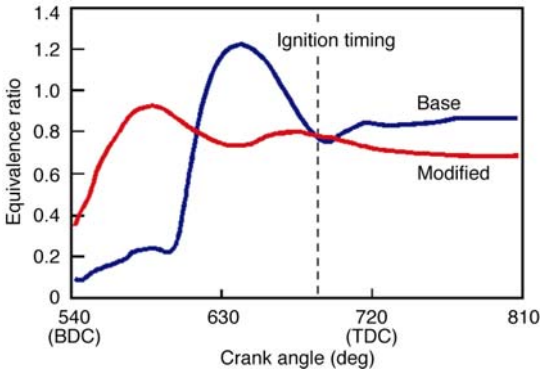



Fig. 18 Time history of equivalence ratio around spark plug

detailed specifications was carried out each time a new engine was being developed. This sub-section describes an example in which CFD visualization was used to verify the mechanism of reduction of unburnt HC, thereby facilitating the selection of the specifications.

The test engine was a 4-valve engine with an injector at an intermediate position on the inlet port. The injection angle of the injector was initially set at 48° (Type 1), aiming at the center of the inlet valve head, then to Type 2, which is 10° higher, Type 3, which is 20° higher, and so on, while keeping the collision of the spray with the port wall to a minimum, and the amount of HC at each angle was measured. The results of the measurements are shown in Fig. 19.

It was found that HC decreased as the injection angle was increased and became a minimum at Type 3, and then it started to rise again gradually as the injection angle was increased further. From this trend, it was found that the difference in the blow-out behavior of the gas mixture when the valves overlap was more dominant than the worsening of HC resulting from the inflow into the combustion chamber of the fuel liquid film at the bottom wall of the port, which increases as the injection angle is raised. In order to validate this trend more qualitatively, CFD was used to visualize the blow-out behavior of the gas mixture and to enable a detailed understanding of the phenomenon to be obtained. As the analysis condition, a partial load equivalent to a constant speed of 50 km/h was applied. Figure 20 shows the distribution of the equivalence ratio for each specification obtained by calculation. In case of Type 1, there is a rich gas mixture near the valve seat before the inlet valve opens (ATDC −26°). Part of this gas mixture is blown off to the exhaust port after the inlet valve opens, and is exhausted as unburnt HC together with the burnt gas.

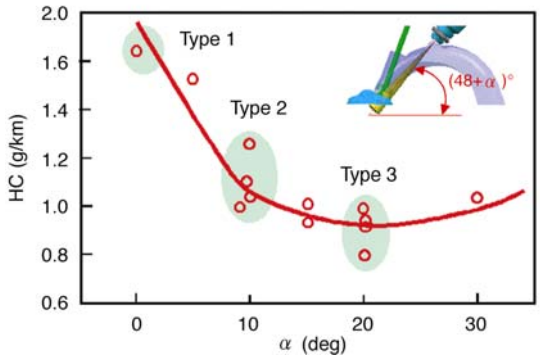



Fig. 19 Effects of injection angle on emission

In the case of Type 2 and Type 3, all of the injected droplets collide with the bottom wall of the port, and are either reflected or become a wall-film. Consequently, almost no droplets directly reach around the valve seat. The fuel that becomes a liquid film is warmed and gasified by the wall temperature of the inlet port, however a delay in reaching around the valve seat occurs. Consequently, it was confirmed that when the inlet valve is open, a rich gas mixture does not exist around the valve seat, and the amount of HC blown off to the exhaust port is less. From the above analysis, it was possible to understand the characteristics of the HC according to the direction of the injector, and it became easier to perform the specification selection.

### 4.3. Application to the Development of the First 4-stroke 50 cm$^3$ PGM-FI Engine

This technology was used in the development of the first 4-stroke 50 cm$^3$ PGM-FI engine in the world. The resulting engine was installed in a scooter for the Japanese market in the spring of 2004. The new engine (Fig. 21) has 8% higher maximum output and 10% better fuel economy in the actual running mode (in-house test value comparison that assumes actual conditions of use) than the 2-valve, twin carburetor specification engine of the Crea SCOOPY, on which this machine is based. Table 2 shows the main specifications of the engine.

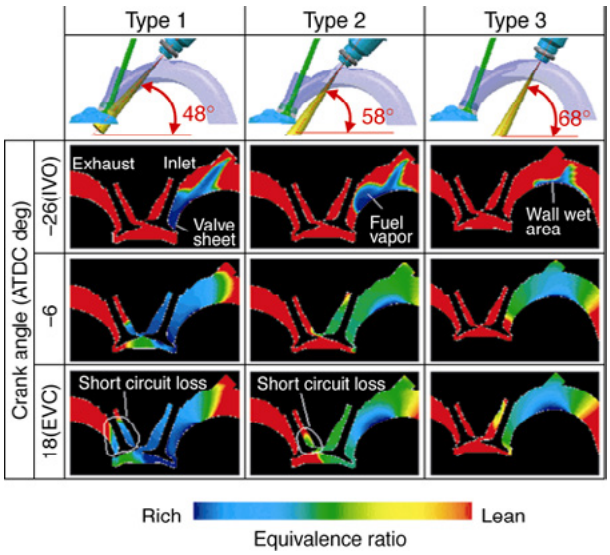



Fig. 20 Calculation results of equivalence ratio distributions



Fig. 21 Cutaway model of 50cm$^3$ four stroke engine with PGM-FI system

Table 2 Developed engine specifications

| | |
|---|---|
| Engine type | 4-stroke single cylinder, spark ignition |
| Bore × Stroke (mm) | 38 × 44 |
| Displacement (cm$^3$) | 49.9 |
| Valve layout | 2 inlet and 2 exhaust valve |
| Compression ratio | 12.0 |
| Combustion chamber | Pentroof type |

## 5. Conclusion

A combustion simulation based on CFD was carried out in order to visualize the inside of the cylinder of a small motorcycle engine that features small displacement and high engine speed. Experimental investigation of correlation was performed and the effectiveness of this simulation was set forth below.

(1) The results of simulating the steady-state flow in the cylinder and the behavior of the fuel spray generally were consistent with the measured results.

(2) Under the common-use operating load conditions of a small 4-stroke motorcycle engine, the macroscopic flame propagation behavior can be estimated by using an Eddy Dissipation Model as the combustion model. In order to estimate the microscopic combustion behavior including a cool flame, which occurs during the ignition delay period, it is necessary to re-select the combustion model appropriate to the particular phenomenon.

(3) As a result of visualization of in-cylinder behavior using CFD, it was possible to improve the fuel economy and also expand the lean burn zone, thus indicating that it can be applied effectively to the development of an actual mass-production engine.

## References


(1) Sasaki, T., Yoshida, K., Urata, Y., Ohno, T., Ishii, K.: Introduction of Optically Access Engine to Investigate in Cylinder Phenomena, HONDA R&D Technical Review, Vol. 10, p. 78-89 (1998)

(2) Yamada, T.: Current Status of Development and Application of CFD, ENGINE TECHNOLOGY, Vol. 04, No. 05, p. 10-11 (2002)

(3) Sadakane, S., Abe, S.: Present and Future of Direct Injection Gasoline Engine, Journal of Society of Automotive Engineers of Japan, Vol. 57, p. 49-50 (2003)

(4) Naitoh, K., Itoh, T., Takagi, Y., Kuwahara, K.: Large Eddy Simulation of Turbulent Premixed-Flame in Engine by Using the Multi-Level Formation, JSME, B, 59-559, p. 289-295 (1993)

(5) Miyagawa, H., Kojima, S., Katsumi, N., Ueda, T., Okumura, T.: Numerical Analysis of the Effects of Squish Geometry on a Newly Developed 4-Valve Gasoline Engine Combustion Process, International Symposium COMODIA 98, p. 227-232 (1998)

(6) Dokowicz, J. K.: Particle-Fluid Numerical Model for Liquid Spray, J. of Computational Physics 35, p. 229-253 (1980)

(7) O'Rourke P. J., Amsden A. A.: The Tab Method for Numerical Calculation of Spray Droplet Breakup, SAE Paper 872089 (1987)

(8) Magnussen, B. F.: On the Structure of Turbulence and a Generalized Eddy Dissipation Concept for Chemical Reactions in Turbulence Flow, 19th AIAA Sc. Meeting (1981)

(9) Takahashi, Y., Murakami, Y.: Establishment of an Intake Port Design Support Tool Using CFD, Honda R&D Technical Review, Vol. 15, No. 1, p.104 (2003)

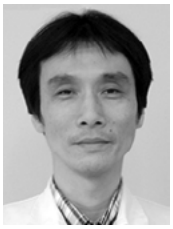
(10) Philipp, H., Plimon, A., Femitz, G., Hirsch, A., Fraidl, G., Winklhofer, E.: A Tomographic Canera System for Combustion Diagnostics in SI Engines, SAE Paper 950681 (1995)

(11) Kaneko, M., Kato, S., Saisyu, Y.: Combustion Control Technologies for SI Engines by Controlling Tumble Generation and Dispersion, The 17th Internal Combustion Engine symposium, Japan (2002)


## ■ Authors ■




Yasuo MURAKAMI



Hitoshi KUROSAKA

# Autocoding of Power Plant Control Software

Shintaro MINOWA* Toshiaki HIROTA* Hiroki YOKOYAMA*
Tetsuya ISHIGURO* Satoru OHTSUKA*

## ABSTRACT

An autocoding system has been developed for use in CAD of control systems. This system conducts simulations of fixed point calculations equivalent to those used in ECU implementation, and autocodes the designed control specifications. The use of this system enables simple formulation of the data accuracy (LSB) and data type required for software coding. In addition to coding software in a Honda format, the system autocodes the label information required in setting parameters and monitoring for vehicle tests. As a result, the autocoded software can be employed in ECU implementation without alteration. Verification of the accuracy of calculations using a coverage check enables ECU malfunctions to be prevented before implementation. This has reduced the time spent in correcting the software, and autocoding has shortened the period to ECU implementation by one-third. A level of performance equivalent to the simulation has been achieved with no malfunctions in a single implementation.

## 1. Introduction

Power plants require complex, large scale and high accuracy control such as environmental compliance, fuel economy enhancement, and on-board diagnosis. However, shortening the development period, increasing the number of development models and otherwise increasing development efficiency are also important issues. Therefore, the use of software libraries has begun in order to ensure power train ECU software quality and increase the development efficiency. This has separated the portions dependent on the hardware from the application portions, and allows the development of applications by combining existing software.

Applications are designed using simulation tools (MATLAB, SimuLink), and the established control logic was formerly compiled into control specification sheets and then manually coded in the Honda format. However, this process had the following concerns.

(1) Discordant design aims due to manual coding
(2) Conflict between simulations and actual calculations during implementation

As a means of realizing a method that does not produce these conflicts, a system was developed for performing the calculations used for implementation in the Honda format on the simulation tools, and then autocoding these results.

## 2. System Development Goals

The goals of software autocoding are as follows.

(1) Eliminating conflicts in logic interpretation between logic designers and programmers
(2) Reducing software description errors
(3) Reducing the development time by automating the work

### 2.1. Shortening the Development Process

The ECU performs fixed point calculations instead of the more commonly used floating point calculations in consideration of processing speed and memory capacity, etc. Figure 1 shows a comparison of floating point and fixed point wave forms. Fixed point calculations differ from floating point calculations in that the parameter size and LSB

* Tochigi R&D Center

must be set properly in order to obtain the required calculation accuracy. In the conventional development process, software coding (manual coding) is performed for the model diagram after the floating point operation check. This meant that fixed point calculations were first performed after implementation, and the software had to be revised in order to correct any operation discrepancies found. The control logic design tools used with the newly developed system are a control design CAD (SimuLink)[1] and a general-purpose integer type autocoding tool (TargetLink)[2]. These tools perform fixed point calculations on the model diagram and automatically code the software for that logic. Applying this system makes it possible to complete the series of correction processes on a PC, so a reduction in the ECU development time can be expected. Figure 2 compares the conventional ECU development process with the process when applying the newly developed system.

### 2.2. Development Environment without a Correction Process

The general-purpose integer type autocoding tool has an optimum software coding function suited to ANSI-C and Target (ECU chip). However, this differs from the Honda format, so manual corrections are necessary for software implementation. The label name, LSB, data type and other parameter information in the sensor outputs and other parameters normally used by Honda are registered and managed in an original library as shared information. For this reason, the following functions were created as a system linked to this library and as a development environment that does not produce correction time from logic construction to software coding.

(1) A function for acquiring label information from the library and reflecting it to the model
(2) A function for describing the label form for fixed point calculations in the Honda format

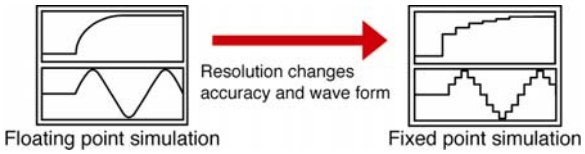



Fig. 1 Comparison of floating point and fixed point wave form

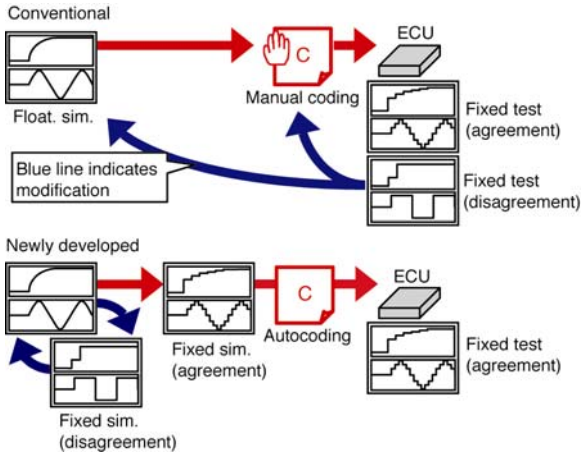



Fig. 2 Comparison of ECU design processes

(3) A function for checking operation through a coverage check
(4) An autocoding function that conforms to the Honda format
(5) A function for generating documents to take the place of conventional specification sheets

Figure 3 shows an outline of the newly developed system. This system eliminates the need for manual corrections during fixed point calculations and implementation of the autocoded software, etc.

## 3. Adapting Model Diagrams to Honda Format

The functions of the newly developed system are described below.

### 3.1. Label Information Setting Function

The library registers not only the label information, but also the control logic specification sheets that use those labels and the software that is based on these specification sheets. Therefore, when creating new control logic, the registered control logic and software can be reused in accordance with the application. The library centrally manages and shares the label information used in the logic as CSV files, and the same label name is used for labels that handle the same information, even if the logic differs. This makes it possible to set the LSB, data type and other parameters without having to set the label information for each logic. In addition, when the original library label information is changed (renewed), these changes are reflected to all the logic that uses that label. The following functions were created to match these settings with the label information settings made using the newly developed system.

(1) A function for referencing the library label information when creating model diagrams
(2) A function for renewing model label information when the library label information is renewed
(3) A function for creating new label information and registering it in the library

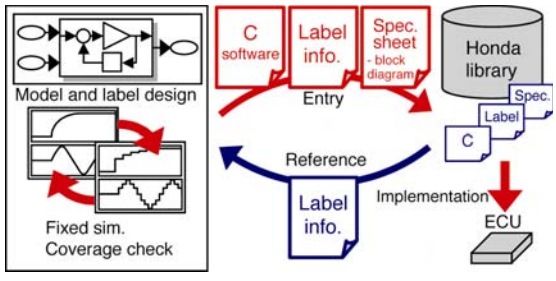



Fig. 3 Newly developed process

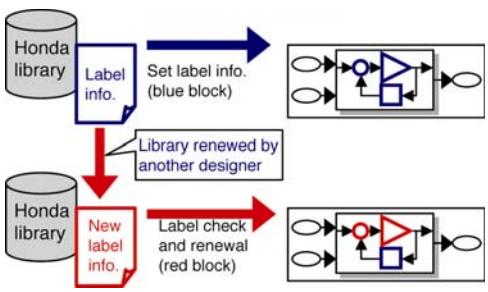



Fig. 4 Label information check and renewal tool

This makes it possible to automatically set the LSB and other label information for existing labels even when creating new models, and allows auto renewal of that label information to the latest library information. In addition, the label information auto renewal function can also be used to avoid the risk that newly created labels in a model might overlap with existing label information. Figure 4 shows this function.

### 3.2. Auto Switching of Data Classes

In fixed point calculations using the general-purpose integer type autocoding tool, the labels used by the logic must be defined within the logic. However, in the actual logic, sensor signal values and other parameters are sometimes provided by extern labels, which make it necessary to change the data class declaration each time the calculations are performed. Therefore, a label type was created that automatically switches the data class declaration according to the autocoding setting, with global labels for simulations and extern labels for autocoding. This made it possible to perform fixed point calculations without changing the data class used in software coding. Figure 5 shows an outline of the data class auto switching function.

### 3.3. Replacement of Map Search Routines

Normally when using maps and tables, the blocks provided for the general-purpose integer type autocoding tool are used. However, Honda defines and uses original map search routines, so the general-purpose integer type autocoding tool blocks cannot be used as is. Therefore, a function was created for replacing the search routines and outputting in the Honda format during autocoding. The search routines are original, but the blocks used for model creation use the same blocks as the general-purpose integer type autocoding tool, so replacement can be performed without any awareness on the part of control logic designers. The search routines are replaced from the standard search routines not only during software coding, but also from the control logic investigation calculations to ensure uniformity of operation with implementation.

### 3.4. Stipulation of Data Types

In the same manner that general labels are shared as a library, the data types used by Honda are also stipulated. The general-purpose integer type autocoding tool has an extremely large number of standard data types to ensure generality, so human error may occur when selecting the type. Therefore, the newly developed system uses a format where only Honda original data types can be selected. In addition, type information was added to the label name to allow users to know the data type being used. This work was formerly done manually, but automatically adding this information during the data type selection reduces errors and increases efficiency of the work.

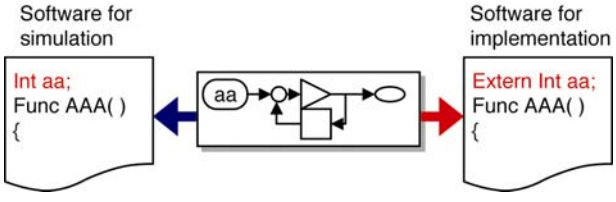



Fig. 5 Auto switch of C software generation

### 3.5. Initialize Statement

When constructing the control logic, it is sometimes necessary to initialize the labels in specific operation modes such as engine start or stop. However, each company has its own initialization method and there is no standardization, so this function is not provided in the general-purpose integer type autocoding tool. Therefore, an initialize statement block was created using the existing label definition block, and a function was created for automatically adding initialize logic during source coding as a C function in accordance with the library rules.

### 3.6. Inclusion of Existing Software

When constructing the control logic, logic may be developed which uses the output values of existing software as the inputs. Existing software may not have a model diagram, and may exist only as manually coded software. In these cases it is necessary to understand the software contents and create a model diagram in order to use this software in logic development. Therefore, a function was created for including software without edit as a block within the model diagram. Figure 6 shows an outline of this function. The included software follows the coding rules stipulated by the library, so the block inputs and outputs are generated automatically and the software is included as a model diagram block. In addition, linking with the data file allows operation to set the coefficient setting values of the included software.

### 3.7. Model Library

Some block structures such as counters and switches are used frequently when constructing model diagrams, and thus far designers had created model diagrams of these blocks each time they were used. Therefore, these blocks were created in advance, converted to subsystems, and used as a

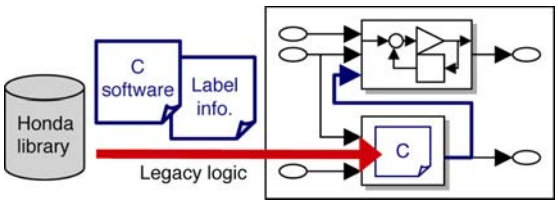



Fig. 6 Embedded function of legacy C software to new system

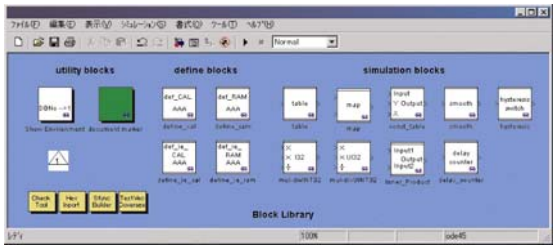



Fig. 7 New system model library

model library. Figure 7 shows the model library. This reduced the modeling time, eliminated the need to check the operation of portions registered in the model library, and allowed standardization of model diagram descriptions. In addition, the functions created using the new system can be easily called up from the library.

## 4. Validation Check

Operation is checked by preparing optional input data. In most cases, measurement data obtained from vehicle tests is generally used as the input data. In addition, autocoded software is basically not checked manually, and the LSB settings are also made automatically except for blocks where succession is performed manually. This naturally increases the importance of the input data used when making the settings. That is to say, if the data input and output values during actual use exceed the input and output values used to make the LSB settings, or if combinations of these values are not tested, this may cause issues because overflow or other phenomena could not be checked until vehicle tests or after the product is introduced to the market. Likewise, if all branches generated by operation switching of "if" branches or flags within the software are not checked, it is possible that logic overflow up to those branches will not be checked, and also that the validity or even the need for the logic will not be checked. Therefore, the following functions were created to increase the software reliability.

(1) A function for generating input data (test vectors) with optional upper and lower limit values
(2) A function for investigating branch coverage
(3) A function for forcibly switching branches that have not been executed

### 4.1. Test Vector Generation Function

The test vector generation function was created to generate inputs for the coverage check function. This function generates two-level data that allows the amplitude to be set and changed freely. There are two types of wave form shapes: an all pattern and design of experiment (DOE)[3] type that is expressed by a combination of the two-level data, and a pulse width modulation (PWM) type that expresses this same data as a PWM waveform. Figure 8 shows the generated wave forms.

#### 4.1.1. Wave form types

The all pattern input consists of all patterns for two levels, where the number of input ports n for the target control logic is used as the number of factors, and covers all combinations for the case where the input data is thought of as two levels. However, this means that as the number of input ports increases, the generated input data volume also increases significantly. Therefore, DOE was included to allow the construction of data signifying an experimental amount equivalent to all patterns even with a small amount of input data. However, the selection of orthogonal factors is left to the designer constructing the logic, and the orthogonal Latin squares, that is to say the input data bases, are created using a function provided for the control design CAD.

The PWM wave form generates two-level data by pulse width modulation based on the fixed values of the frequency and the frequency variation for each input port. The generated wave form takes a shape where the output cycle of the wave form for other ports repeats in accordance with the amount of data for the longest cycle among the PWM waveforms for each input port.

#### 4.1.2. Repeating wave form amplitude

In logic that performs the high order filtering and multi delay data hold used in modern control, no matter how the data is handled, the data is rounded at the filter output stage, and cannot be used for subsequent logic checks. In addition, there are also fundamental concerns such that as the order increases, the amount of data becomes insufficient. Therefore, a function was created for amplifying the input data generated by repeating the above wave forms. Figure 9 shows the test vector wave form for 5-time repeat mode. The amplitude when repeating can be selected from the following three types.

(1) Optionally set maximum and minimum values for each input port (Fig. 9 (a))
(2) Changing the maximum and minimum values while maintaining a fixed amplitude in accordance with the number of repeat times (Fig. 9 (b))
(3) Changing the set maximum and minimum values in accordance with the number of repeat times and gradually reducing the amplitude (Fig. 9 (c))

This makes it possible to check the LSB toughness by detecting overflow, and also to check performance near values that are important for actual logic operation.

The test vector generation function generates input data according to the number of input ports for the model. However, the specifications make it possible to further reduce the amount of input data by excluding the corresponding input ports from the factor combinations when values that have no effect on the logic are present in the model configuration or when two-level values exist in the flag information, etc.

### 4.2. Coverage Check Function

The coverage check results are generated automatically by the control design CAD when the test vector simulation ends. At this time if the process did not pass through all the branches within the logic, the coverage results are displayed as less than 100%. Therefore, a function was created to display the pertinent locations in the model and to optionally

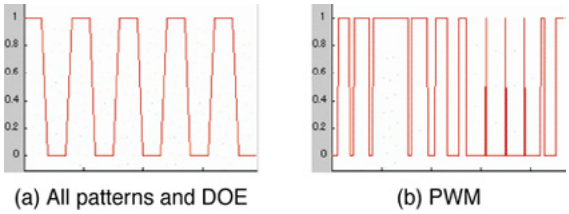



Fig. 8 Shape of test vector

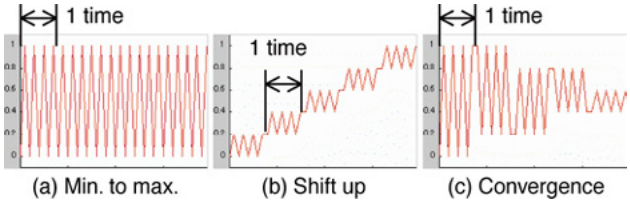



Fig. 9 Shape of test vector (5-time-repeat mode)

change the thresholds for the branch blocks. Figure 10 shows the coverage check flow. This makes it possible to change the branch conditions for the second simulation to cover the branch blocks that were not completed in the first simulation, resulting in an ultimate coverage of 100%.

### 4.3. Test Vector Coverage Check Results

Table 1 shows an example of test vector application. Note that the model used for application was modern control logic with branching and filters, and LSB matching by measurement values had been completed. In addition, the test vector amplitudes used the physical upper and lower limit values of each input data, and were the results before using branch switching. Overflow was detected for all test vectors with an input data level of 1/10 or less with respect to the measurement values, thus confirming the validity. A comparison of test vectors showed that DOE had fewer detected overflows than the other test vectors, but the amount of input data was also extremely small, so the detection rate increased. However, the number of detected overflows did not increase even when the amount of data was increased by subsequent repeats. Also, the orthogonal factor selection produced a marked difference in the results, and in some cases does not necessarily contribute to increasing efficiency, which indicates that factor selection is the key to efficiency.

The use of test vectors made it possible to detect overflows that could not be detected with measurement values, and also enhanced the model toughness, but the coverage did not increase.

## 5. Software Coding

When coding software, in addition to the label information added to each block in the model diagram, the creator, creation date, revision information and other information described when creating the specification sheet by the conventional method, must also be described separately. This is because it is important not only to include information as Honda specifications for the coded software, but also to have the document generation results correspond with the conventional specification sheets. Therefore, a function was created for describing the above information in the function definition blocks. These blocks are provided by the general-purpose integer type autocoding tool and enable to divide and code the software in units positioned within the model. Autocoding of software first codes in the standard format using the general-purpose integer type autocoding tool, and then converts this format to Honda specification software by performing the following processes based on the information added by the newly developed system.

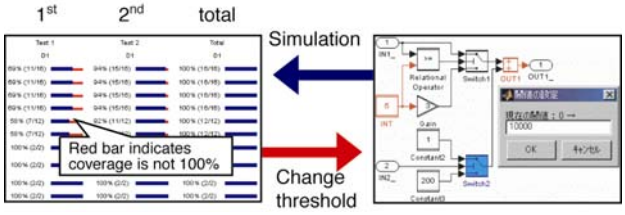



Fig. 10 Verification of coverage

Table 1 Result of coverage tool

| Mode | Measure-ment | Test vector | | |
|---|---|---|---|---|
| | | All patterns | DOE | PWM |
| Number of step times | 27 500 | 1 540 | 96 | 2 470 |
| Coverage [%] | 95 | 60 | 58 | 60 |
| Number of detected overflows | 0 | 6 | 5 | 8 |
| Detected overflows per step time | 0 | 0.39 | 5.21 | 0.32 |

(1) Description of model information (creator, creation date, etc.)
(2) Correction of label declarations
(3) Description of initialized functions
(4) Generation of label information files for registration in the library

When implementing the coded software, the size and execution speed can become issues, so these were compared with manually coded software. Model diagrams were created and autocoding was performed for specifications with existing software. The results confirmed that the average size for autocoded software excluding vector processing was 1.8 times, and the average execution speed was 1.1 times that of manually coded software, which are levels that can be applied to mass production ECU without edit.

## 6. Document Generation

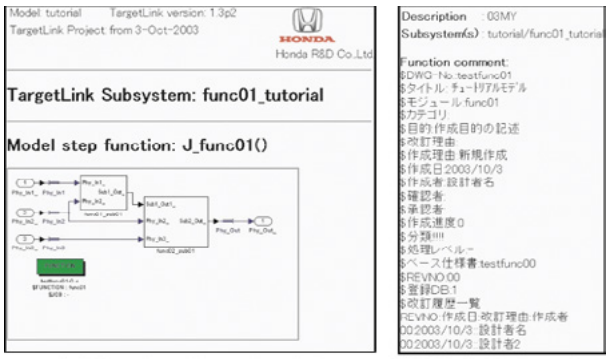
Logic was formerly checked using the model diagram based on the specification sheet, and then manual coding was performed. In contrast, the newly developed method places priority on the model diagram, and there is no specification sheet. However, as mentioned above, the library comprises a database that includes the specification sheet, so a specification sheet is required for registration. This means that even when logic is created using a model diagram, a separate specification sheet must also be created, but this is not practical time-wise. The general-purpose integer type autocoding tool has a function for outputting the model diagram as an html file, so a study was made to determine whether this is equivalent to a specification sheet. However, it was found that the html file output function of the general-purpose integer type autocoding tool essentially outputs only specific upper levels and levels where the function definition blocks are located. Therefore, the following items were developed to facilitate an understanding of the model structure.

(1) Output instruction blocks that also output optionally located levels
(2) Successive display of the model diagram from the upper levels of the block diagram
(3) Description of creator and other information in function definition block units between model diagrams

Figure 11 shows an example of document output.

Points for caution when converting model diagrams to documents include the model scale reduction rate and line overlapping, which affect legibility. The Japan MATLAB Advisory Board (J-MAAB) is investigating guidelines for model description methods using block diagrams, so Honda

original expanded guidelines were created for using the general-purpose integer type autocoding tool, and diagrams and documents are generated based on these guidelines.




(a) Function title and model (b) Model information

Fig. 11 Spec. sheet produced by auto document generation

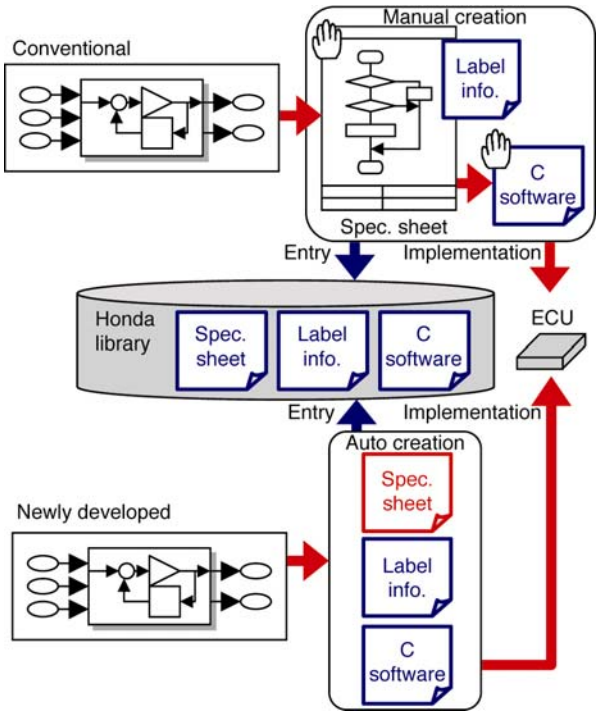



Fig. 12 Comparison of flows of model data up-load

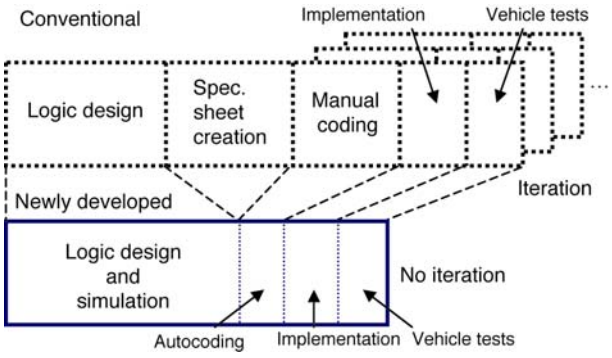



Fig. 13 Reduction of flow of design logic and load to ECU

Figure 12 shows a comparison of library registration flows. Auto document generation has further shortened the process time, and allows automatic output of all the information registered in the library. This has reduced the period from logic construction to ECU implementation by one-third compared to the conventional method. Figure 13 compares a breakdown of ECU implementation periods.

## 7. Conclusion

Development of this new system produced the following results.

(1) ECU implementation is possible without edits to software autocoded from model diagrams.
(2) A level of performance equivalent to the simulation has been achieved in a single implementation.
(3) Time formerly spent in correcting the software following implementation has been eliminated, thus shortening the period from logic development to ECU implementation by one-third.

## References

(1) The MathWorks, Inc.: Using Simulink Version 5, USA, The MathWorks, Inc., p. 476 (2002)

(2) dSPACE GmbH: TargetLink Production Code Generation Guide for TargetLink 1.3, Germany, dSPACE GmbH, p. 748 (2001)

(3) Nakamura, G.: Understanding Design of Experiment, Tokyo, Kindaikagakusya, p. 82-108 (1997)

■ Authors ■


Shintaro MINOWA


Toshiaki HIROTA


Hiroki YOKOYAMA


Tetsuya ISHIGURO


Satoru OHTSUKA

# Development of Rolling Bearing Model for Mechanical Dynamic Analysis Considering Elastic Properties

Junya SAITO* Tatsuya IWAMOTO* Osamu KUDO*

## ABSTRACT

To enhance the simulation accuracy for mechanical dynamic analysis of an assembled crankshaft often used in single cylinder, small displacement engines, it is important to make a detailed model of the rolling bearings simulating physical phenomena such as deformation, contact, and damping. A rolling bearing model that permits simulation of a three-dimensional contact considering elastic properties was developed, and the analysis accuracy was enhanced. By applying the rolling bearing model to the mechanical dynamic analysis of the assembled crankshaft, the correlation between the crankshaft displacement and the strain during actual engine operation was confirmed. As a result, it was confirmed that the rolling bearing model is accurate enough for a practical strength evaluation in the design stage of an assembled crankshaft system.

## 1. Introduction

In recent years, mechanical dynamic analysis of the crankshaft system has been an essential tool for the specifications of an engine to reach a level of maturity during the initial design stages. As for the one-piece crankshaft of multi-cylinder engines, the mechanical analysis technologies[(1)] have been constructed and applied to actual development as the investigation design tool. This is not only within Honda, many kinds of versatile CAE packages have been released and are widely used within the industry. On the other hand, the assembled crankshafts are widely adopted in small single-cylinder motorcycle engines, and differ from multi-cylinder engines in that rolling bearings are used in the main journal.

In the case of one-piece crankshafts, sliding bearings are used, where fluid film lubrication theory is incorporated in order to enhance analytical accuracy. On the other hand, conventional methods of rolling bearings consist simply of linear or non-linear simple springs and dampers. These are much too low to attain acceptable accuracy for analysis of crankshaft behavior, where the journal bearings are affected by heavy fluctuating loads.

In this paper, a new model for a rolling bearing is developed, considering the elastic properties of the rolling elements and the bearing rings and simulating three-dimensional contact between them. This model was then applied to mechanical dynamic analysis of assembled crankshaft systems.

## 2. Model of Rolling Bearing

Figure 1 shows the structure of a single-cylinder motorcycle engine with an assembled crankshaft. Rolling bearings are installed in the main journal of the crankcase to support the crankshaft. At the running condition, rolling bearings show very complex behavior. They contain multiple rolling elements that are held between the inner and outer rings by retainers and are in constantly changing contact conditions due to the changing conditions of the crankshaft (engine speed, torque fluctuations). Many papers have been published by the bearing companies[(2), (3)] about bearing behavior, but the purpose of these is to analyze behavior of the bearings themselves, detailed behavior such as influences by a rolling contact surface and tolerance of rolling elements are analyzed; they are not suitable for mechanical dynamic analysis of whole crankshaft systems. Therefore, this rolling bearing model was developed under several assumptions, while the behavior of the bearing itself was not considered because it would be relatively unaffected by heavy fluctuating loads.

* Asaka R&D Center

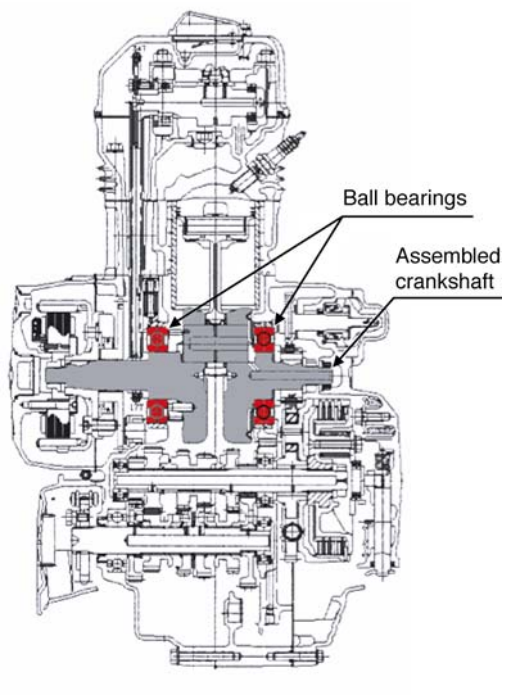



Fig. 1 Structure of single-cylinder engine

## 2.1. Requirements for Development

It was mentioned above that the conventional methods for a bearing model adopt simple linear or non-linear springs and dampers. In these methods, the properties of contact stiffness between the rolling element and the raceway of inner and outer rings, both radially and axially, are converted to simple spring properties. These methods were used in an initial attempt at mechanical dynamic analysis of an assembled crankshaft, but the accuracy of calculated crankshaft behavior was insufficient. Therefore, requirements for the new model were decided, with regard to all the factors necessary to provide enhanced analytical accuracy.

The rolling bearings chosen as the object for this development were deep groove ball bearings (ball bearings, hereafter). The requirements included the following:

(1) This model (ball bearing model, hereafter) must be installed in the existing mechanical dynamic analysis of crankshaft systems using general mechanical analysis software. It must enable strength evaluations of crankshafts during development of actual engines.
(2) Three-dimensional contact between the rolling elements (balls) and the inner and outer ring raceway must be accurately calculated.
(3) The elastic properties (stiffness and damping) of the balls and rings must be accurately calculated.

## 2.2. Outline of Model

The modeling method in which the ball bearing model is used for the mechanical dynamic analysis was comprised of two systems, the creation of the ball bearing properties and the main calculations. The overall system flow for creating the ball bearing model is shown in Fig. 2.

### 2.2.1. Creation system of ball bearing property

This defines the three-dimensional contacts for one ball in the ball bearing model and creates the property file. As shown in Fig. 2, the creation system of the ball bearing property consists of three component sub-systems, the pre-processor, the execution of linear static analysis, and the contact processor.

- Pre-processor

In this sub-system, the specifications for the ball bearing are input and the finite element method (FEM) data required for linear static analysis of the balls and rings are generated. The FEM data includes the geometric mesh, the loads and the boundary conditions.

- Execution of linear static analysis

This sub-system uses general structural analysis software to execute a linear static analysis of the bearing using the FEM data generated by the pre-processor. It creates the nodal stiffness data set used by the contact processor.

- Contact processor

This sub-system executes the analysis of the three-dimensional contact between the balls and the rings, using the nodal stiffness data created by the linear static analysis. As shown in Fig. 3, the orbital position angle $\alpha$ is determined by the number of balls, and the contact on a radial plane defined by the bearing axis and angle $\alpha$[(4)]. The penetration $\delta$ and the contact angle $\beta$ between the ball and the raceway are defined, and the contact load f, a function of $\delta$ and $\beta$, is calculated using the nodal stiffness data. Next, the

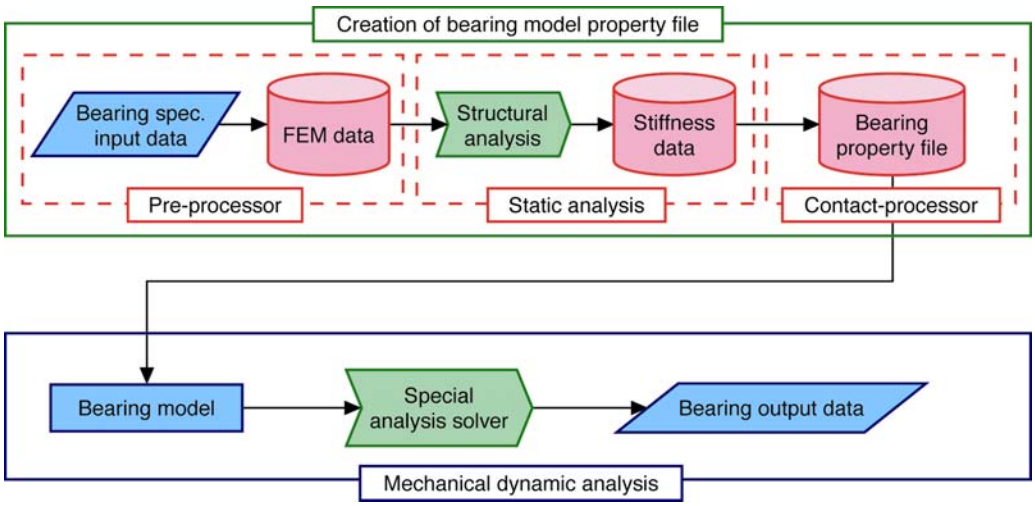



Fig. 2 System flow

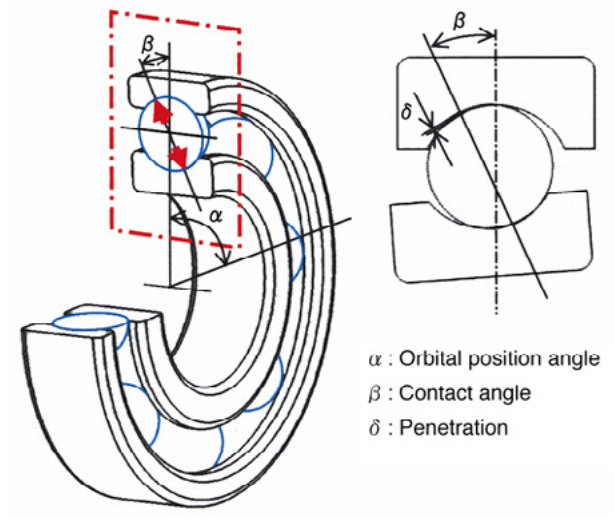



Fig. 3 Figure of contact method

three-dimensional contact loads in the inner and outer rings are calculated using δ, β and f. Then the contact processor finds the three-dimensional contact function of the inner and outer rings. This function is exported as a ball bearing model property file.

#### 2.2.2. Main calculation system

The method to apply the ball bearing model to a mechanical dynamic analysis must be applied to numerical integration methods in the time domain. Also, the loads in six axes must be calculated considering the bearing loads caused by the deformation and the behavior of the crankshaft as they are transmitted to the crankcase. An exclusive built-in solver based on user subroutines was newly developed and applied to the existing general mechanical analysis software.

Output of the loads in six axes by the built-in solver follows this procedure:

(1) The displacements, angles, velocities and angular velocities from the center of the case journal to the center of the shaft journal are calculated.
(2) The contact loads and damping for one ball are calculated by using the ball bearing model property file.
(3) The contact loads, torque around the axis and the damping for all the balls are calculated. Then the loads in six axes are exported as a ball bearing model.

A definitional Eq. (1) of the contact load vector {F} of the ball bearing model is shown below. Here, $\{F_i\}$ is the contact load vector for one ball, f is the contact load obtained from the property file, C is the damping parameter, and $\{v_i\}$ is the translational velocity vector.

$$\{F\}=\sum_{i=1}^{n}\{F_i\}=\sum_{i=1}^{n}\{f(\delta_i,\beta_i)+C(f(\delta_i,\beta_i))\cdot\{v_i\}\} \quad (1)$$

In the same way, a definitional Eq. (2) for the torque vector {T} around the axis of the ball bearing model is shown below. Here, $\{T_i\}$ is the torque vector around the axis for one ball and $\{l_i\}$ is the distance vector from the case journal center point to the contact point.

$$\{T\}=\sum_{i=1}^{n}\{T_i\}=\sum_{i=1}^{n}\{\{f(\delta_i,\beta_i)+C(f(\delta_i,\beta_i))\cdot\{v_i\}\}\cdot\{l_i\}\} \quad (2)$$

## 3. Verification of Model

The function of the developed ball bearing model was verified. This process consisted of two steps, one is verification of the component function of the ball bearing model itself, and the other is verification of the assembly function of the model applied to the mechanical dynamic analysis of the crankshaft system.

### 3.1. Verification of Component Function

Static stiffness of the actual ball bearing and the FEM model had been verified in advance. By the results, it was clarified that there is good correlation between the load and the displacement. Therefore, verification of static stiffness analysis of the ball bearing model and the FEM model was applied to that of the component function.

#### 3.1.1. Verification method

As shown in Fig. 4, two directional loads were applied and linear static analysis was executed. A radial load Fr was applied perpendicular to the axis, and an axial load Fa was applied parallel to the axis.

In the radial direction analysis, function was verified on layout (a) and (b) as shown in Fig. 5, because the initial number of contacting balls and radial clearance are changed by the ball orbital angles.

#### 3.1.2. Verified results

Table 1 shows the specifications of the ball bearing used for the verification test of the component function. When the static load was applied to the shaft model installed inside of the inner ring, elastic deformation occurred in the balls and raceway surface at the contact areas. The elastic deformation

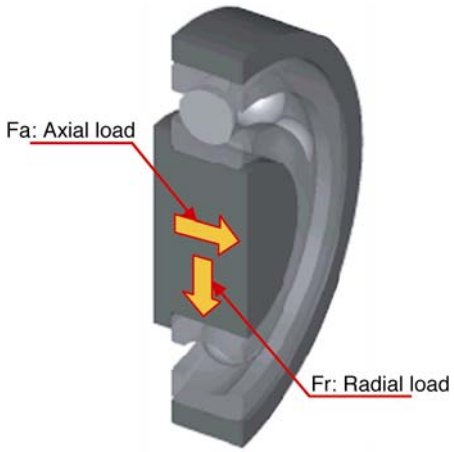



Fig. 4 Figure of component static analysis

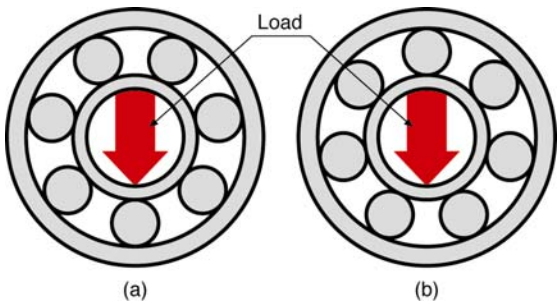



Fig. 5 Figure of balls layout

Table 1 Ball bearing specifications

| | |
|---|---|
| Outside diameter | 72 mm |
| Inside diameter | 35 mm |
| Width | 15 mm |
| Diameter of ball | 7/16 inch |
| Number of balls | 9 |

δr in the radial direction and the radial clearance clr were summed to define the radial displacement dr. Similarly, the axial elastic deformation δa was summed with the axial clearance cla to define the axial displacement da. The obtained displacement results are shown in Fig. 6.

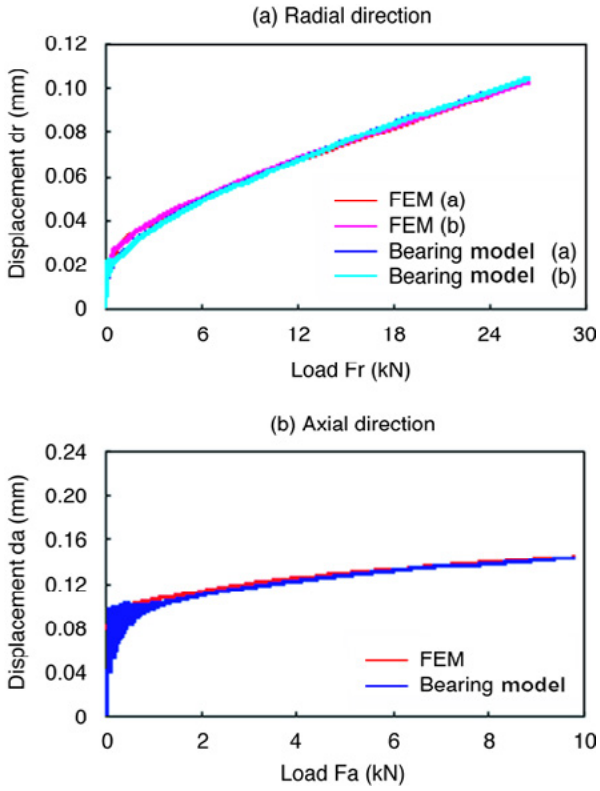



Fig. 6 Results of component static analysis

The displacement results from the FEM and ball bearing model showed good correlation, indicating the three-dimensional contact behavior properly by the new model, from low loads up to high loads. The ball bearing model satisfied the static functional requirement for mechanical dynamic analysis.

### 3.2. Verification of Assembly Function

The ball bearing model used in the component verification process was applied for the assembly verification. Test equipment with a simplified crankshaft and crankcase was made and correlation between experiments and calculations was verified. Figure 7 shows a picture of the whole test system and the model of measurement device.

"L" and "R" refer to the "left" and "right" sides of the measurement device below. The yellow components in the crankcase are gap sensors; these were fixed in the upper portion on the L and R sides, and next to the crank web on the L and R sides, for a total of four sensors.

#### 3.2.1. Verification method

A bolt was screwed in the crank pin of the crankshaft and a tensile load was applied with a hydraulic tester. A notch was machined in the bolt before assembly so that the bolt would break at specified load; the impact load test is a method of using the impact caused by the break of the bolt as the exciting force. The pre-break behavior was defined as the static zone, and the post-break behavior, as the dynamic zone. The displacements of each area of the crankshaft were measured by four gap sensors fixed in the crankcase.

#### 3.2.2. Static verification results

Figure 8 is a displacement result at the gap sensor on the upper L side of the assembly, until the bolt breaks under the tensile load.

There was good correlation between the experiments and the calculated results. The displacement increased with tensile load. The stiffness and three-dimensional contact conditions were calculated very accurately by the ball bearing model in the static analysis of the assembly. The function of the ball bearing model has successfully satisfied the requirement.

#### 3.2.3. Dynamic verification results

The bolt breaks at the specified load, and the impact by the breaking and the elastic deformation excites the crankshaft. Figure 9 shows the time series of crankshaft displacement, indicating the dynamic behavior of this system.

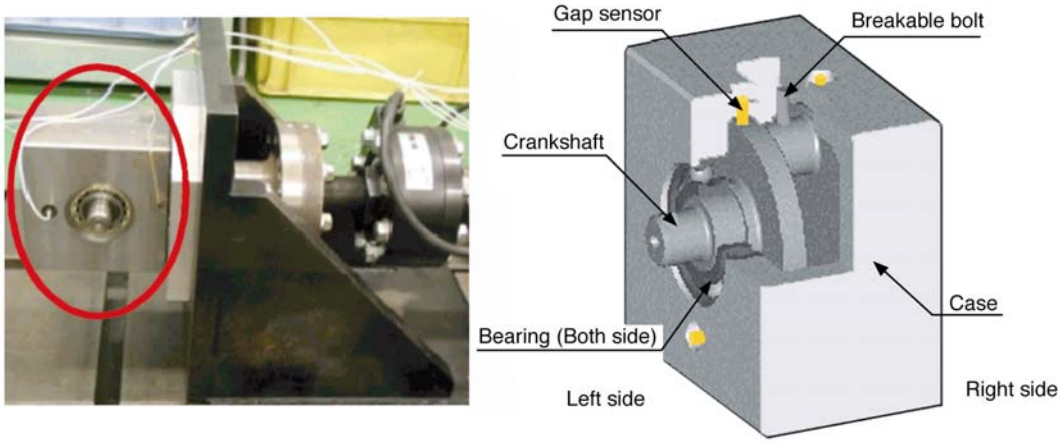



Fig. 7 Figure of test system and measuring device model

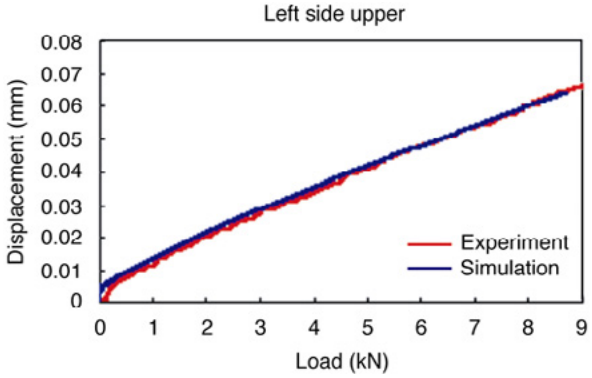



Fig. 8 Result of static assemble analysis

## 4. Application Example

The mechanical dynamic analysis model of the assembled crankshaft of a motorcycle engine was created as shown in Fig. 1, and the correlation was verified by an actual experiment. Table 2 shows the test engine specifications. Figure 11 shows the figure of the mechanical dynamic analysis model used for the analysis.

### 4.1. Details of Verification Test

The engine was operated in a constant speed mode from 4 000 to 10 000 r/min with increments of 2 000 r/min.

As shown in Fig. 12, the displacement of the crank-web was measured by a gap sensor fixed in the crankcase, with the Y direction defined from the crank center through the crank pin, and X defined at a perpendicular angle to that. In order to measure crankshaft strain during the maximum combustion load, a strain gauge was attached on the crank pin fillet on the delayed angle side as shown in Fig. 13.

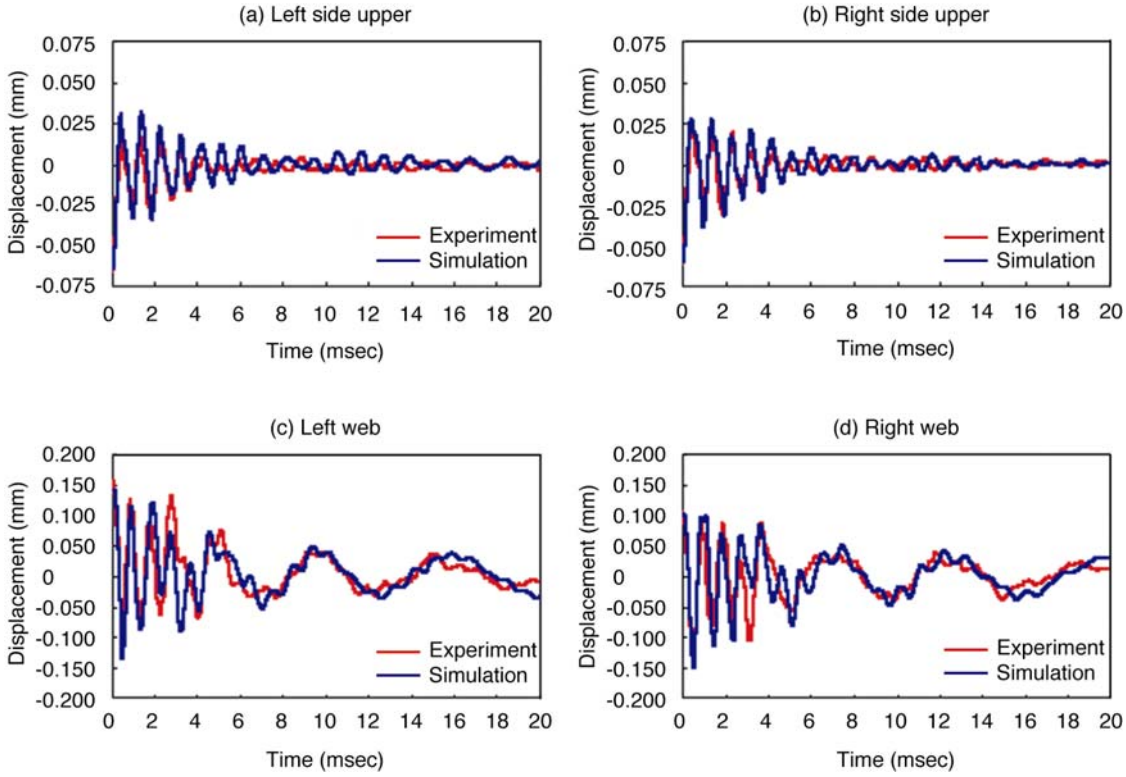



Fig. 9 Results of dynamic assemble analysis

The displacement results at the conditions where the impact excitation and vibration converge show a very good correlation.

Next, the time series of the displacement was used to analyze a power spectral density, which is a standard frequency analysis. Figure 10 shows power spectral density results for dynamic behavior of the crankshaft. The experiments and the calculation matched particularly well around 1 kHz, and the correlation is generally good. This indicated that the dynamic properties of the ball bearing model were also sufficiently accurate.

### 3.3. Summary of Model Verification

The function of the ball bearing model in the component and assembly tests satisfied the requirements in both static and dynamic properties. It was therefore applied to a mechanical dynamic analysis of an actual assembled crankshaft.

### 4.2. Displacement and Strain during One Cycle at Engine Operation

The calculated and measured waveforms for displacement of the crank web on the L side in the Y direction during one cycle at engine speeds of 4 000 and 8 000 r/min are shown in Fig. 14. Figure 15 shows the corresponding waveforms for strain at the crank pin fillet, L side, during one cycle.

At both the low speed of 4 000 r/min and the high speed of 8 000 r/min, the calculated displacement waveform, which included the considerations of the combustion load and inertia, showed a good correlation with the measured waveform. The calculated strain at the fillet during the combustion stroke also showed good correlation with the measured results.

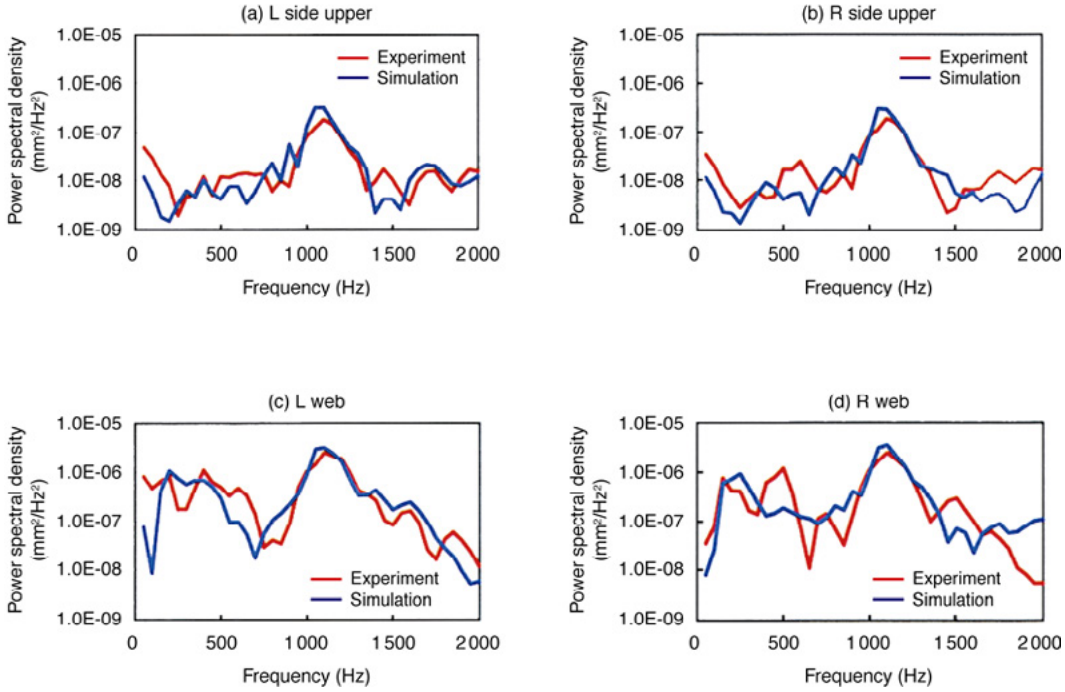



Fig. 10 Results of power spectrum

Table 2 Major specifications of test engine

| Items | Specifications |
|---|---|
| Engine type | 4-stroke, single cylinder |
| Displacement | 149.4 $cm^3$ |
| Valve train | DOHC 4-valves |
| Clutch type | Multiplate wet clutch |
| Transmission | 6 speeds constant mesh |

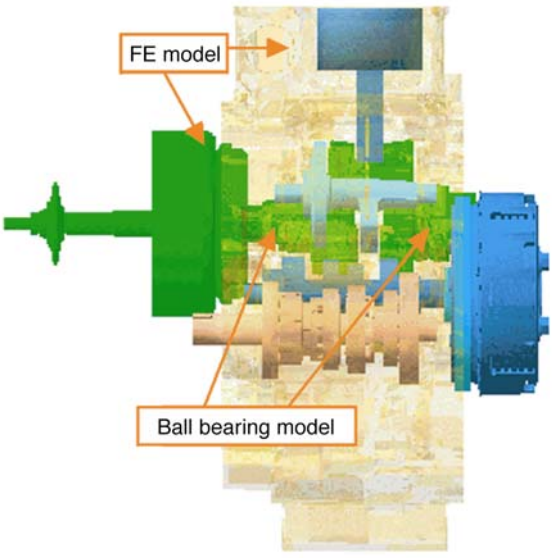



Fig. 11 Figure of mechanical dynamic analysis model

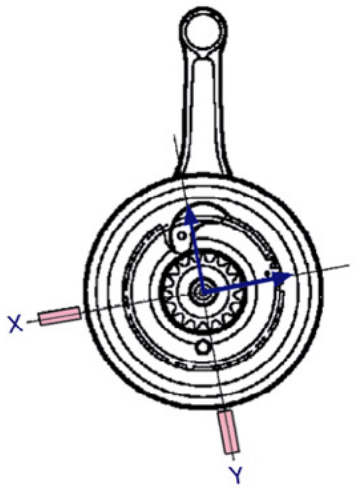



Fig. 12 Position of displacement sensor of Crankshaft-web

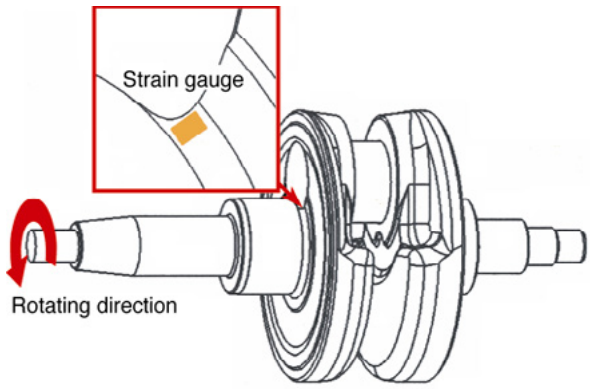



Fig. 13 Strain gage position

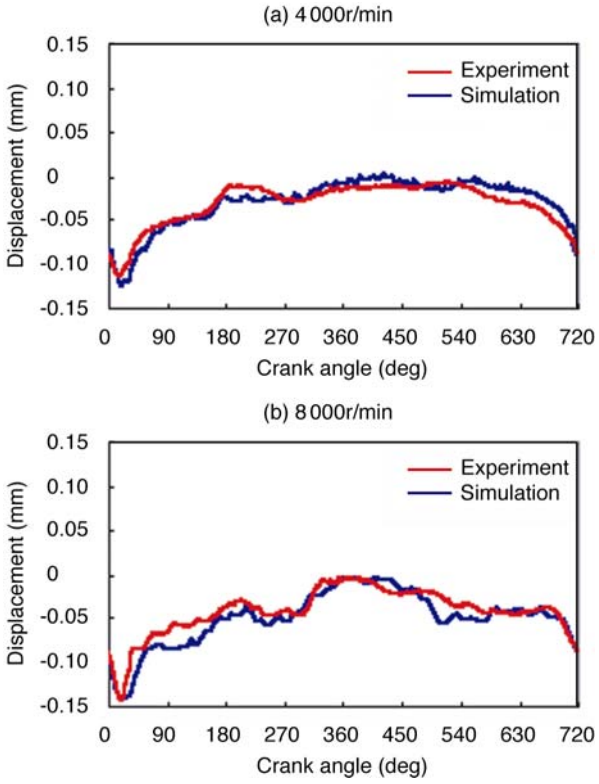



Fig. 14 Correlation results of displacement

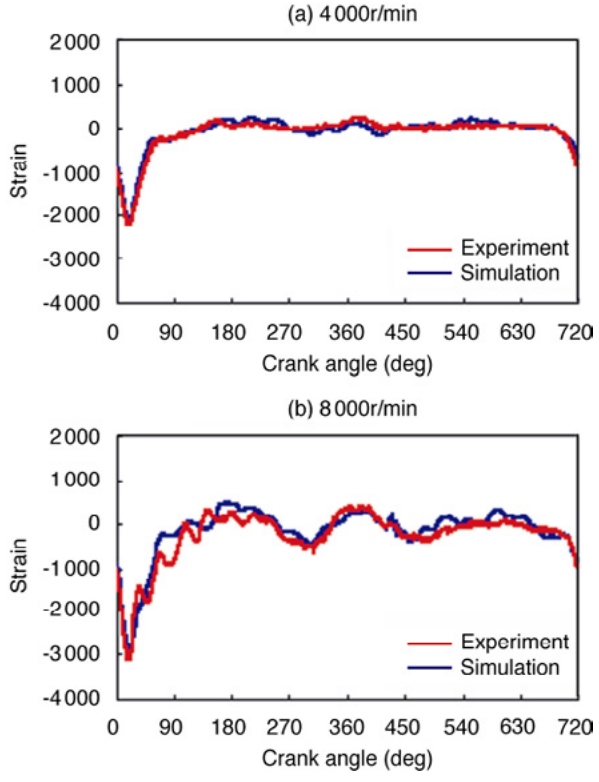



Fig. 15 Correlation results of strain

The above results showed good correlation between the calculated and measured values for displacement and strain at low and high speeds, and sufficiently high accuracy for the strength evaluation of assembled crankshafts.

### 4.3. Comparison of Bearing Model and Conventional Methods

Figure 16 shows the strain waveforms at the crank pin fillet, L side, during one cycle at 10 000 r/min. These data results were taken in an actual engine and calculated both with the ball bearing model and with a conventional spring-damper model.

The conventional spring-damper model indicated a maximum strain right after the combustion load about 30% higher than that calculated by the ball bearing model and measured in the actual experiment. Its high-frequency vibration results were also much more prominent than those in the actual experiment.

Thus, the ball bearing model showed more accurate results for mechanical dynamic analysis of the assembled crankshaft than the conventional model.

### 4.4. Summary of Application Results

The mechanical dynamic analysis of an assembled crankshaft, where ball bearings are used under severe condition, was conducted. The ball bearing model in this development has been verified that is the effective method to analyze with high accuracy.

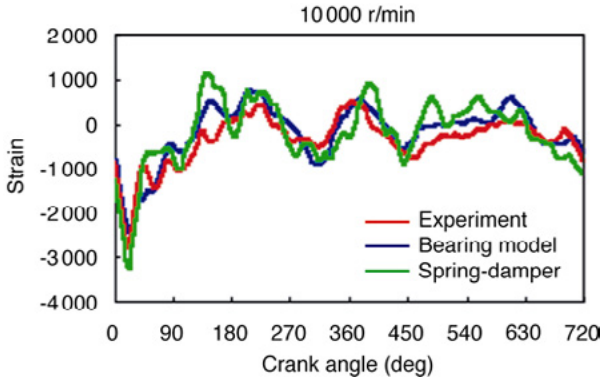



Fig. 16 Comparison of ball bearing model with spring-damper model

## 5. Conclusion

(1) A new model of the rolling bearing (ball bearing model) was developed considering elastic properties of the rolling elements (balls) and the rings. The model simulates three-dimensional contact conditions between them.

(2) The ball bearing model was applied to a mechanical dynamic analysis of the assembled crankshaft. The crankshaft displacement and strain in the firing operation was compared with those of an actual engine. Correlation between them was sufficiently accurate. It was verified that the analysis is suitable for use in a strength evaluation of the crankshaft in the design stages during development of engines.

## References

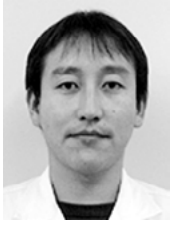
(1) Niino, T., et al.: Development of simulation technology for dynamic behavior of crankshaft systems in motorcycle engines, JSAE Review, Vol.23, Issue 1, p. 127-131 (2002)

(2) Sakaguchi, T., Akamatsu, Y.: Simulation for Ball Bearing Vibration, NTN Technical Review, No. 69, p. 69-75 (2001) (in Japanese)

(3) Tada, S.: Dynamic Analysis of Sound, Vibration and Motion of Cages in High Speed Ball Bearings, Koyo Engineering Journal, No. 160, p. 31-38 (2001)

(4) Nakahara, I.: Sessyoku Ouryoku, Zairyou Rikigaku-Gekan, Tokyo, Yokendo, p. 116-132 (1966) (in Japanese)

■ Authors ■



Junya SAITO



Tatsuya IWAMOTO



Osamu KUDO

# Estimation of Durability of Nickel-Metal Hydride Batteries for Hybrid Electric Vehicles

Tatsuo MINAMI*


## ABSTRACT

A method of estimating the durability of the nickel-metal hydride batteries employed in hybrid electric vehicles was studied based on factors contributing to their deterioration. The factors in battery deterioration are battery temperature, current load and state of charge. Based on the expectation that the formulation of a reaction rate equation employing chemical kinetics would enable the durability of the battery to be estimated, the Eyring equation, which enables consideration of temperature and another stress factor was focused on. The number of stress factors in the equation was increased to study the applicability of current load and state of charge.

It was shown that the values of frequency factors which are obtained in durability tests performed under various conditions of battery deterioration factors were the same. These results confirmed that the modified equation enabled multiple factors to be employed in estimations of battery life. The use of this reaction rate equation through quantification of each factor has enabled the estimation of battery life.


## 1. Introduction

One of the main elements of electric vehicles and hybrid electric vehicles (HEV) is the battery, which needs to have long life. Battery life is greatly affected by deterioration factors such as temperature, current load and state of charge band (SOC band).

For estimation of some type of battery life, it is generally understood that up until now the life of batteries follows the reaction theory Arrhenius equation based on the temperature. In the report of reaction kinetics type estimation for estimating battery life, deterioration reaction rate equation or an approximation equation using the battery temperature as its fundamental factor, were used to estimate battery life[(2),(3)]. Other deterioration factors have only been added to this equation as singular factor. It is guessed that this is because the equations were developed for commercial batteries where normal use provides a steady current load for which consideration of other factors is not necessary. Recently, with the increase in HEV sales, a database of market information for battery temperature, current load, SOC band and of how the battery is used, is being developed. Research[(4)] has begun on a method that will provide an estimation of battery life using these deterioration factors. However, as in the case of HEV batteries, a reaction rate equation that targets systems (including not only changes in the environment, but also changes in current load, and that includes battery deterioration factors of battery temperature, current load and SOC band) has not yet been reported.

The reaction rate equation that is focused on is the Eyring equation, which includes dependence on both temperature and other types of stress. As an example of the application of the Eyring equation, stress factors other than temperature, such as humidity and current, were used in the evaluation of life expectancy for semiconductor devices and rubber[(5),(6)]. There is only one stress factor in the Eyring equation; however, in the case of batteries, there are two stress factors other than temperature, current load and SOC band. More

* Tochigi R&D Center

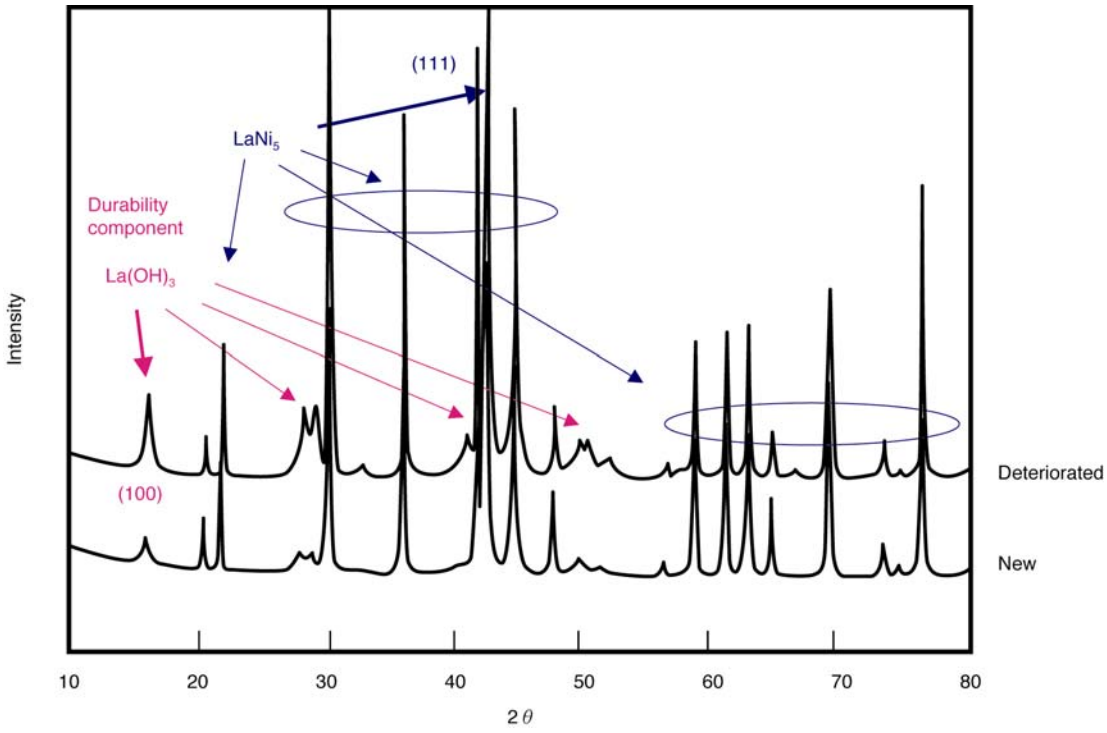



Fig. 1 XRD spectra of new and deteriorated negative

stress factors have therefore been added to the Eyring equation and a battery deterioration reaction rate equation that has more than one stress factor has been developed. Experiments to verify this equation's formation have been performed.

## 2. Correlation Between Chemical Reaction Induced Electrode Deterioration and the Deterioration of the Battery

The battery that is being primarily used for HEVs is the Nickel Metal Hydride (Ni–MH) battery. The main deterioration mechanisms for the Ni-MH battery are: hydroxidation of the hydrogen-storing alloy active material on the negative electrode, oxidation and change of crystal structure of the oxy nickel hydride active material on the positive electrode, the drying out of the electrolyte in the separator due to swelling of the electrode and elimination of active material on the electrodes. These mechanisms cause a loss of power and capacity. In this manner, the deterioration of Ni-MH batteries are expected to follow reaction kinetics theory, as the main causes of deterioration chemical reaction of the electrodes such as the oxidation and the hydroxidation of the active material. In order to determine if this interpretation is correct, the relationship between battery deterioration and chemical reaction induced electrode deterioration was analyzed.

As high current is required of the battery, internal resistance was chosen as a deterioration dispersion coefficient. Concerning chemical reactions leading to electrode deterioration, the structure of the electrode was analyzed and the behavior of deterioration elements was studied. The differences between the structure of the negative electrode before and after deterioration were analyzed using X-Ray diffraction (XRD). The results of this analysis are shown in Fig. 1. The negative electrode of this battery is a hydrogen-storing alloy of rare earth metals, primarily made up of lanthanum nickel ($LaNi_5$). The amount of one of the deterioration elements, lanthanum hydroxide ($La(OH)_3$), was found, at its peak, to have increased as compared to before deterioration.

Furthermore, the relationship between the increase in elements of deterioration and the increase in internal resistance was considered. The structure of the negative electrodes that had various internal resistances was similarly analyzed using XRD. The amount of the deterioration component $La(OH)_3$ was shown by dividing its peak intensity by that of $LaNi_5$. The peaks used for comparison were the maximum intensity peaks for both $La(OH)_3$ and $LaNi_5$, the peak of $La(OH)_3$ being the (100) plane and the peak of $LaNi_5$ being the (111) plane. The index used for the increase in internal resistance is the ratio of increase in internal resistance, defined as the increase in internal resistance after deterioration divided by the original internal resistance. Lastly, the relationship between the amount of the deterioration component $La(OH)_3$ and the increase in internal resistance was analyzed. The results of this analysis are shown in Fig. 2. This analysis confirmed that there is a

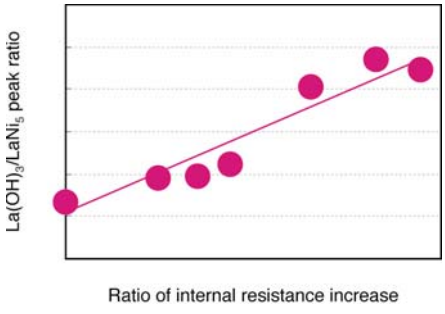



Fig. 2 Relation between $La(OH)_3$ / $LaNi_5$ peak ratio and ratio of internal resistance increase

correlation between the amount of the deterioration component $La(OH)_3$ and the increase in internal resistance ratio. This correlation shows that the chemical reaction induced electrode deterioration contributes to the battery deterioration mechanism; therefore, it can be treated similar to reaction kinetics. This also leads to the understanding that the amount of chemical reaction induced electrode deterioration is proportionate to the ratio of increase in internal resistance. Therefore it is possible to use the ratio of increase in the internal resistance in place of the battery deterioration reaction rate.

## 3. Battery Deterioration Reaction Rate Equation

The Eyring equation has been chosen as the reaction rate equation for development of a battery deterioration reaction rate equation. This equation has been generalized through using the original reaction temperature dependence and adding stresses other than temperature as well. Defining the amount of deterioration as $x$ and the rate of reaction as $K$ gives the following equation:

$$dx/dt = K,\ K = a(kT/h) \cdot \exp(-\Delta E/kT) \cdot S^{\alpha} \quad (1)$$

$a$ : Constant
$k$ : Boltzmann's constant
$h$ : Planck's constant
$\Delta E$ : Activation energy
$T$ : Absolute temperature
$S$ : Stress factors other than temperature
$\alpha$ : Constant

The following equation can be used for a small range of temperature $T$.

$$K = \Lambda \cdot \exp(-\Delta E/kT) \cdot S^{\alpha} \quad (2)$$

$\Lambda$ : Constant

On the other hand, using the Arrhenius equation, which only provides dependence on temperature gives the following equation:

$$K = A \cdot \exp(-\Delta E/kT) \quad (3)$$

$A$ : Constant

Comparing the Eyring equation with the Arrhenius equation, the Eyring equation has had stress factors added. Furthermore, focusing on just the stress factors in Eq. (2) gives the following equation:

$$K = B \cdot S^{\alpha} \quad (4)$$

$B$ : Constant

Therefore, Eq. (4) is used when there are stresses other than temperature such as thermal fatigue (hot-cold cycle) deterioration etc. The constants $\Lambda$, $A$, and $B$ are termed frequency factors[7] in reaction kinetics.

Applying the Eyring equation, Eq. (5) has been developed as an estimate for a reaction rate equation using 2 stress factors other than temperature. These 2 stresses are current load and SOC band.

$$K = \Lambda \cdot \exp(-\Delta E/kT) \cdot S_1^{\alpha} \cdot S_2^{\beta} \quad (5)$$

$S_1$ : The 1st stress factor
$\alpha$ : Constant
$S_2$ : The 2nd stress factor
$\beta$ : Constant

## 4. Verification and Results

### 4.1. Verification Method

The constants in Eq. (5) are determined in the following manner. First of all, deterioration reaction rate $K$ is the amount of deterioration, or the amount of increase in internal resistance $x$ divided by the life cycle test time $t$. Next, the temperature factor constant $-\Delta E/k$ and the other stress factor constants $\alpha$ and $\beta$ are defined by conducting analysis for each stress factor. Placing each of these deterioration stress factor constants in Eq. (5) completes the deterioration reaction rate equation except for the frequency factor $\Lambda$. Finally, through substituting each of the deterioration factor conditions used in testing, it is possible to solve for the unknown frequency stress factor $\Lambda$.

In order to establish Eq. (5) as a battery deterioration reaction rate equation, it is necessary for the frequency factor to remain the same through various conditions of temperature, current load, and SOC band. Confirmation is possible through performing life cycle tests while changing conditions of the deterioration factors.

Next a particular method for deriving each of the deterioration factor constants will be shown. The deterioration reaction of the HEV Ni-MH battery is the chemical reaction production of $La(OH)_3$. The reaction rate increases with temperature because the reaction components collide more frequently at higher temperature. Larger current load and SOC band leads to larger reaction surface area on the electrode, which increases the reaction rate. From this discussion, it can be easily understood that if each single factor is separated, the current load and the SOC band load factors follow Eq. (4) while the temperature follows Eq. (3).

The temperature factor constant $-\Delta E/k$ is found by focusing only on the temperature, allowing use of Eq. (3), the Arrhenius equation. Taking the logarithm of both sides gives the following equation.

$$\ln K = \ln A - \Delta E/kT \quad (6)$$

The deterioration reaction rate $K$ can be shown to be $K = x/t$, therefore Eq. (6) becomes the following when $x = 1$.

$$\ln(1/t) = \ln A - \Delta E/kT \quad (7)$$

This shows both the inverse of temperature and the logarithm of the reaction rate in a first order equation. If it is possible to determine the relationship between the temperature and reaction rate at 2 or more points, it will be possible to find the slope $-\Delta E/k$. In a life cycle test, the temperature is varied while other stresses are held constant.

It is also possible to determine individual influences of the current load constants and the SOC band constants through focusing only on their stress characteristics. Taking the logarithm of both sides of Eq. (4), which focuses only on individual stress factors, gives the following equation.

$$\ln K = \ln B + \alpha \ln S \quad (8)$$

Table 1 Test conditions and test times

| No. | Test classification for constant calculation | | | Test conditions | | | Test time (hr) |
|---|---|---|---|---|---|---|---|
| | Battery temperature (−ΔE/k) | Current (α) | SOC band (β) | Battery temperature (°C) | Hour rate of charge and discharge current (C) | SOC band (SOC%) | |
| 1 | ○ | | | 35 | 2 | 20 | 2800 |
| 2 | ○ | | ○ | 45 | 2 | 20 | 1800 |
| 3 | ○ | ○ | | 55 | 2 | 20 | 1100 |
| 4 | | ○ | | 55 | 3 | 20 | 700 |
| 5 | | ○ | | 55 | 5 | 20 | 400 |
| 6 | | | ○ | 45 | 2 | 40 | 1500 |
| 7 | | | ○ | 45 | 2 | 60 | 1200 |

The deterioration reaction rate $K$ can be shown to be $K = x/t$, therefore Eq. (8) becomes the following when $x = 1$.

$$\ln(1/t) = \ln B + \alpha \ln S \quad (9)$$

This shows both the logarithm of the stress factors and the logarithm of the reaction rate in a first order equation. If it is possible to determine the relationship between the stress factors and the reaction rate at 2 or more points, it will be possible to find the slope α. In a life cycle test, one of the stress constants is varied while the other stress constants and temperature are held constant.

## 4.2. Life Cycle Test

With the battery mounted in a vehicle, in order to make a final, accurate estimate of battery life expectancy, a charge/discharge profile was used from actual driving profile for the life cycle test. And in order for the reaction surface area on the electrode surface to become as large as possible, the profile with a high frequency of switching between current input and current output was chosen. The charge/discharge profile is a control value sent to the charge/discharge battery test equipment and is shown as a current charge/discharge value request per unit time.

The values of each of the deterioration factors are: temperature is the average battery temperature during the tests, the average absolute value of current during the tests for the current load, and the difference between the highest SOC and lowest SOC for the SOC band. The unit used for the average absolute current is C and is the time rated charge/discharge current. It means that 1C is the current value that the battery can be discharged in 1 hour. The unit of SOC is defined to be SOC%. During the driving cycle test the current load of charge/discharge profile was set to 2C and the SOC band set to 20 SOC%. This is called the standard profile.

Also, using this standard profile as a base life cycle test, testing was performed at 2 or more test conditions for each of the stress factors. During this test, the temperatures that were used were 35 °C, 45 °C, and 55 °C. The average current loads that were used are: the standard profile 2C and using the standard profile charge/discharge frequency with the different current load settings of 3C and 5C. The SOC bands that were used are: the standard profile of 20 SOC% and an expanded setting of 40 SOC% and 60 SOC%. These profiles were used repetitively for the life cycle tests. The conditions and test time for each of the deterioration factors is shown in Table 1. For each of the deterioration factors, higher loads lead to a faster rate of increase in internal resistance and shorter test times.

## 4.3. Deterioration Factor Constants

Using the life cycle test results, each of the deterioration factor constants were derived from the relationship between the reaction rate and the deterioration factors. The reaction rate unit is defined to be (R%/hr). First, the temperature characteristic results are shown in Fig. 3. In order to

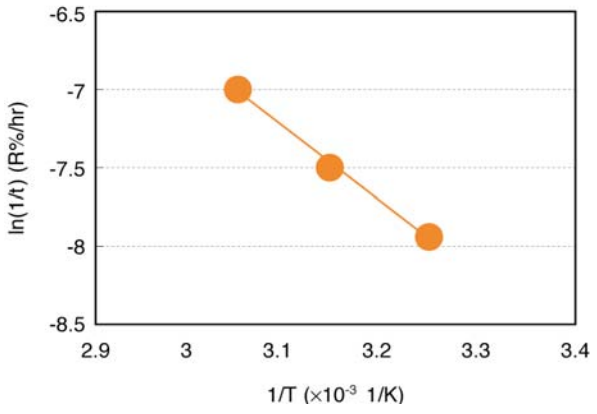



Fig. 3 Relation between inverse of battery temperature and logarithm of reaction rate

determine the values of the constants using Eq. (7), the relationship between the inverse of the absolute temperature for the test and the logarithm of the deterioration reaction rate ln(1/$t$) was investigated. For the temperature factor constant $-\Delta E/k$: –4 700(K) was obtained from the slope of the first order straight line approximation.

Next, the current load characteristic results are shown in Fig. 4. In order to determine the values of the constants using Eq. (9), the relationship between the logarithm of the current load $S_1$ and the logarithm of the deterioration reaction rate ln(1/$t$) was investigated. For the current load constant $\alpha$: 1.1(1/C) was obtained from the slope of the first order straight line approximation.

Next, the SOC band characteristic results are shown in Fig. 5. In order to determine the values of the constants using Eq. (9), the relationship between the logarithm of the current load $S_2$ and the logarithm of the deterioration reaction rate ln(1/$t$) was investigated. For the SOC band constant $\beta$: 0.36(1/SOC%) was obtained from the slope of the first order straight line approximation.

This shows how the deterioration factor constants were determined from analysis for the constants on the individual deterioration factors.

### 4.4. Verification of the Battery Deterioration Reaction Rate Equation

Placing the values for the deterioration factor constants obtained in 4.3 in Eq. (5) gives the following equation.

$$K = x/t = \Lambda \cdot \exp(-4\,700/T) \cdot S_1^{1.1} \cdot S_2^{0.36} \qquad (10)$$

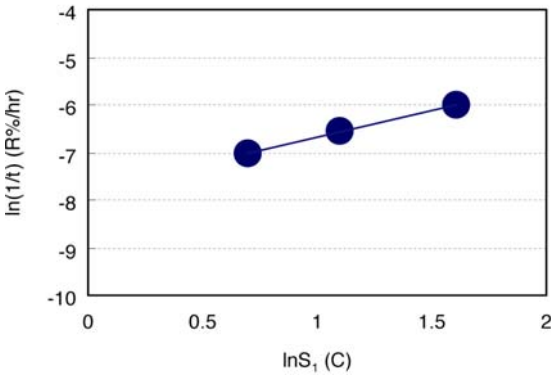



Fig. 4 Relation between logarithm of hour rate of charge and discharge current and logarithm of reaction rate

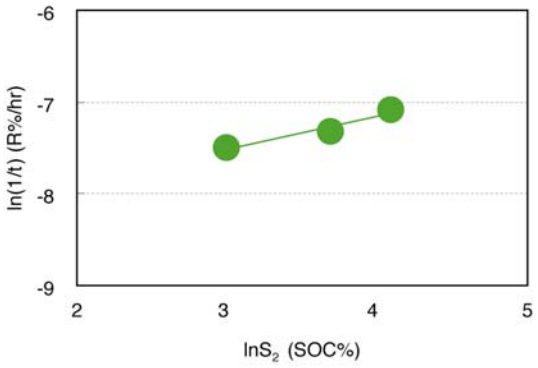



Fig. 5 Relation between logarithm of SOC band and logarithm of reaction rate

Table 2 Test conditions and frequency factors

| No. | Test conditions | | | Frequency factor (R%/hr) |
|---|---|---|---|---|
| | Battery temperature (°C) | Hour rate of charge and discharge current (C) | SOC band (SOC%) | |
| 1 | 35 | 2 | 20 | 240 |
| 2 | 45 | 2 | 20 | 230 |
| 3 | 55 | 2 | 20 | 240 |
| 4 | 55 | 3 | 20 | 240 |
| 5 | 55 | 5 | 20 | 240 |
| 6 | 45 | 2 | 40 | 220 |
| 7 | 45 | 2 | 60 | 230 |

The value of the frequency factor $\Lambda$ can be found using each of the known life cycle conditions, with $x$ = 1. The results are shown in Table 2.

Throughout the tests, the frequency factor $\Lambda$ remains the same for the most part. The average value was found to be 240 (R%/hr). As the frequency factor was stable throughout tests where the conditions of each of the deterioration factors were changed, the battery deterioration reaction rate equation can be expressed as it is written in Eq. (5), an application of the Eyring equation with stress factors added. The following equation has been defined for the battery used in this life cycle test.

$$K = x/t = 1/t = 240 \cdot \exp(-4\,700/T) \cdot S_1^{1.1} \cdot S_2^{0.36} \qquad (11)$$

The frequency factor is interpreted as the number of collisions that the reaction molecules make in the chemical reaction[8]. The stability of the frequency factor means that the chemical reaction is the same and that the deterioration mechanism does not change. After the life cycle test, the structure of the electrodes was analyzed and the deterioration condition was found to be the same as could be seen in Fig. 1. And, the deterioration effects of the battery deterioration factors are synergism as can be seen in Eq. (11).

Furthermore, if the test time $t$ is solved for, the following equation results from Eq. (11).

$$t = 1/\{240 \cdot \exp(-4\,700/T) \cdot S_1^{1.1} \cdot S_2^{0.36}\} \qquad (12)$$

Therefore, if the vehicle speed during the test mode is known, it is possible to determine the range by multiplying the test time and the vehicle speed. In the application to a vehicle, quantifying values for the average temperature, average absolute current load value and the SOC band for a representative drive cycle mode, makes it possible to estimate the expected time and therefore vehicle range before reaching a specified deterioration amount.

## 5. Conclusion

Through estimating the life expectancy of HEV batteries, an investigation was performed for the application of the Eyring equation to deterioration reaction rate equation that includes the battery deterioration factors temperature, current load and SOC band. The following were obtained:

(1) Because the deterioration reaction rate equation frequency factor was stable through changes in each of the deterioration factors, the deterioration reaction rate equation was established as correct.
(2) The stability of the deterioration reaction rate equation frequency factor through changing conditions of the deterioration factors means that the deterioration mechanism is likewise stable.
(3) It is possible to estimate the battery life through quantifying each of the deterioration factors and using this deterioration reaction rate equation. It can now be used in the practical application of estimating the battery life for vehicles.

## References

(1) Kanuma, Y., et al.: Sinraisei Kasokusiken no Kouritsuteki na Susumekata to sono Jissai, J-Techno Co., Ltd., p. 11-12 (2002) (in Japanese)

(2) Matsushita Electric, Fukunaga Hidemi, Chiku Denchi no Jyumyou Yokoku houhou oyobi Jyumyou Yokoku Souchi: Tokkyo Dai 3136981 go, 2001-02-19

(3) Toyota Motor Corporation, Okayama Shinobu: Denchi Youryou Yosoku Souchi, Tokkai 2000-228227, 2000-08-15

(4) Nissan Motor Co., Ltd.: Li Ion Denchi no EV Shijyo Tekiousei to EV/HEV Denchi Jyumyou Suiteihou no Kensho, EV forum, http://www.itsev.com/j/tech/tech_j24.html, (2000) (in Japanese)

(5) Ajiki, T., Matsusita Electric Industrial Co., Ltd.: Handoutai Debaisu no Shinraisei Gijyutsu, JUSE Press. Co., Ltd., p. 40-43 (1993) (in Japanese)

(6) Tamura, M., et al.: Gomu Jyushi Seihin niokeru Koshou Kaiseki to Jyumyou Yosoku, J-Techno Co., Ltd., p. 201-202 (2002) (in Japanese)

(7) Keii, T.: Hannousokudoron dai 3 pan, Tokyo Kagaku Dozin Co., Ltd., p. 5 (2001) (in Japanese)

(8) Keii, T.: Hannousokudoron dai 3 pan, Tokyo Kagaku Dozin Co., Ltd., p. 43-45 (2001) (in Japanese)

■ Author ■



Tatsuo MINAMI

# Technical Papers Submitted to Out-of-company: July, 2003 to December, 2003

(English Papers only)

| Date | Conference | Title | Author | Organization |
|---|---|---|---|---|
| 2003.7.06～10 | ASME, JSME/ 4th ASME/ JSME Joint Fluid Engineering Conference (HONOLULU, HAWAII/USA) | DEVELOPMENT OF THE EXHAUST SYSTEMS RADIATION NOISE SIMULATION TECHNOLOGY | Masato Sakurai<br>Masaki Endo<br>Fred PERIE | Tochigi R&D Center<br>Tokyo Denki Univ.<br>Mcube S.A.R.L |
| 2003.7.14～17 | AIAA (The American Institute of Aeronautics and Astronautics)/ International Air & Space Symposium and Exposition - The Next 100 Years - (Dayton Convention Center, Dayton, USA) | Design and Development of the HondaJet (AIAA-2003-2530) | Michimasa Fujino | Honda R&D Americas |
| 2003.7.14～18 | ASC (American Society for Composites); CMA (Composites Manufacturing Association of SME)/ SME (Society of Manufacturing Engineers)/ The 14th. International Conference on Composite Materials (ICCM-14) (Grand Hyatt San Diego, USA) | Research Work of the All-Composite Fuselage Structure | Nobuo Matsui<br>Keiichi Sato | Wako Research Center<br>Wako Research Center |
| 2003.8.12～13 | SAE/SAE Emerging Transmission Technologies TOPTEC Symposium (Troy, USA) | Development of the CVT for Honda Civic Hybrid | Masahiro Kanda | Tochigi R&D Center |
| 2003.8.25～28 | The Japan Society of Mechanical Engineers/ The 18th IAVSD Symposium (Atsugi, Japan) | Proposal on Variable Gear-ratio Characteristics of Cable-type EPS | Katsuhiro Sakai<br>Atsuhiko Yoneda<br>Yasuo Shimizu | Tochigi R&D Center<br>Tochigi R&D Center<br>Tochigi R&D Center |
| | | On-Center Steer Feel Evaluation based on Non-linear Vibration Analytical Method | Hiroyuki Tokunaga<br>Kazuhito Misaji<br>Yasuo Shimizu | Tochigi R&D Center<br>Tochigi R&D Center<br>Tochigi R&D Center |
| | | Yaw Rate Control by Using Tire Force Information to Stabilize Vehicle Motion with Independent ABS Wheel Control | Nobuyoshi Asanuma<br>Masato Abe | Tochigi R&D Center<br>Kanagawa Institute of Technology |
| | | A Theoretical Study of Influence of Roll Center Height on Vehicle Dynamics | Minoru Higuchi<br>Kazuhiro Taneda<br>Yasuji Shibahata<br>Masaaki Minakawa | Tochigi R&D Center<br>Tochigi R&D Center<br>Tochigi R&D Center<br>Honda R&D Europe(Deutschland) Gmbh |
| | International Institute of Noise Control Engineering (I-INCE)/ The 32nd International Congress and Exposition on Noise Control Engineering (Seogwipo, Korea) | Tooth Profile Optimizing System for Spur Gears in View of Tooth Profile Error | Akira Sonohata<br>Satoru Nojima | Asaka R&D Center<br>Asaka R&D Center |
| 2003.9.1 | European Union Control Association, IEEE Control Systems Society/European Control Conference 2003 (Cambridge, UK) | Steering Assistance System for Driver Characteristics using Gain Scheduling Control | Yukihiro Fujiwara<br>Shuichi Adachi | Tochigi R&D Center<br>Utsunomiya Univ. |
| 2003.9.10～13 | The Japan Society of Mechanical Engineers Materials and Mechanics Division/ International Conference on Advanced Technology in Experimental Mechanics 2003 (ATEM'03) (Nagoya, Japan) | Ultrasonic bending fatigue testing method for thin sheet materials | Hitoshi Ishii<br>Youhei Taguchi<br>Kazuo Ishii<br>Hirofumi Akagi | Shizuoka Univ.<br>Shizuoka Univ. Graduate School<br>Tochigi R&D Center<br>Tochigi R&D Center |
| 2003.9.15～18 | SAE International, JSAE/ SAE 2003 Small Engine Technology Conference and Exhibition (SETC) (Madison, USA) | Interconnection Technology for Engine Generators | Yoshiaki Kotani<br>Yoshihisa Shinogi<br>Yasuhiro Nakada<br>Yoshinori Nakagawa | Asakahigashi R&D Center<br>Asakahigashi R&D Center<br>Asakahigashi R&D Center<br>Asakahigashi R&D Center |
| | | Modeling the Sound Source of an Intake and Predicting the Intake Sound Pressure Level for a Motorcycle | Hideki Kido<br>Hiroyuki Kuwahara<br>Eike Brechlin<br>Rene Boonen | Asaka R&D Center<br>Asaka R&D Center<br>LMS International<br>Katholieke Universiteit Leuven |

| Date | Conference | Title | Author | Organization |
|---|---|---|---|---|
| 2003.9.15～18 | SAE International, JSAE/ SAE 2003 Small Engine Technology Conference and Exhibition (SETC) (Madison, USA) | Development of Hollow, Weld-able Die-cast Parts for Alminum Motorcycle Frames | Eitaro Koya<br>Toshimitsu Suzuki<br>Masahiko Nakagawa<br>Gunpachi Fujimoto<br>Mitsunori Murakami<br>Kunikazu Murata | Asaka R&D Center<br>Asaka R&D Center<br>Asaka R&D Center<br>Kyushu Yanagawa Seiki Co., Ltd.<br>Kyushu Yanagawa Seiki Co., Ltd.<br>Kyushu Yanagawa Seiki Co., Ltd. |
| | | A Computer Simulation for Motorcycle Rider-motion in Collision | Hideo Namiki<br>Toyokazu Nakamura<br>Satoshi Iijima | Asaka R&D Center<br>Asaka R&D Center<br>Asaka R&D Center |
| | | Development of a Lightweight Seat Bottom Frame for Two-wheeled Vehicles Utilizing Injection Foam Molding | Tetsuharu Tanaka<br>Takeshi Yoshida<br>Tomohisa Chiba | Asaka R&D Center<br>Asaka R&D Center<br>TS TECH CO., LTD. |
| | | Optimization of Turbocharger Characteristics for Personal Watercraft | Kazuhiko Tomoda<br>Kazunori Okada<br>Takaharu Kurosaki | Asaka R&D Center<br>Asaka R&D Center<br>Asaka R&D Center |
| 2003.10.1 | JSAE/JSAE Review Vol.24, No.4 | Development of a Tire Pressure Monitoring System for Motorcycles | Toshio Yamagiwa<br>Masayoshi Orita<br>Satoshi Harada | Asaka R&D Center<br>Asaka R&D Center<br>Asaka R&D Center |
| 2003.10.9 | Technical University Berlin/ 5th Berlin Workshop Man-Machine Systems (Berlin, Germany) | Cognitive Maps of Automobile Cockpits as Basic Design Tool | Miklos Kiss<br>Marc Wittmann<br>Peter Gugg<br>Elke Deubzer<br>Martina Neidhart<br>Ernest Poppel<br>Hiroyuki Kamiya | Generation Research Program Ludwig-Maximilians-University<br>Generation Research Program Ludwig-Maximilians-University<br>Generation Research Program Ludwig-Maximilians-University<br>Generation Research Program Ludwig-Maximilians-University<br>Generation Research Program Ludwig-Maximilians-University<br>Generation Research Program Ludwig-Maximilians-University<br>Tochigi R&D Center |
| | The Japan Society of Applied Physics/Japanese Journal of Applied Physics Vol.42 (2003) Part 1, No.10, October 2003 | Molecular Patterns of Alkyl-Aryl Amides Self-assembled on a Graphite Surfaces/ STM Observation of Alkyl and Aryl Amides | Pu Qian | Wako Research Center |
| 2003.10.27～29 | JSAE/International Body Engineering Conference 2003 (IBEC 2003) (Makuhari, Japan) | Object Oriented Formulation of the 3D Large Deformation Beam Element for Crash Applications | Kenji Takada<br>Wlodek Abramowicz | Tochigi R&D Center<br>Impact Design, EUROPE |
| | | Lead Free Cationic Electro-Deposition for Automobile Body in White | Hiroyuki Morishita<br>Katsuyoshi Kaneko | Tochigi R&D Center<br>Tochigi R&D Center |
| | | A Study of Development Indices Established Quantification of Road Load | Tsuneyasu Aoki<br>Kenji Imai<br>Yuji Nakahara<br>Masaki Haraguchi<br>Shinji Watanabe<br>Yuji Uchiyama<br>Shinji Yamakawa | Tochigi R&D Center<br>Tochigi R&D Center<br>TOYOTA MOTOR CORPORATION<br>TOYOTA MOTOR CORPORATION<br>SUZUKI MOTOR CORPORATION<br>Mitsubishi Motors Corporation<br>Kogakuin Univ. |
| | | A New Concept for Occupant Deceleration Control during Vehicle Crashes -Study of the Vehicle Mass Separation Model | Yasuki Motozawa<br>Junya Noguchi<br>Yasushi Kawamura<br>Makoto Tsuruta | Tochigi R&D Center<br>Tochigi R&D Center<br>Tochigi R&D Center<br>Tochigi R&D Center |
| | | Sensitivity Analysis Method of Scatter Factors Based on Cyclic Plastic Zone Size for Fatigue Life of Arc-Welded Joint | Akira Okubo<br>Atsushi Kawamoto<br>Shuichi Magara<br>Tsuyoshi Shiozaki<br>Nobutaka Kurosawa<br>Yukio Iizuka<br>Koji Koibuchi | Tochigi R&D Cener<br>PRESS KOGYO Co.,LTD.<br>PRESS KOGYO Co.,LTD.<br>JFE Steel Corporation<br>JFE Steel Corporation<br>Hino Motors, Ltd.<br>Shonan Institute of Technology |
| 2003.11.2～7 | Gas Turbine Society of Japan/ International Gas Turbine Congress 2003 Tokyo (Tokyo, Japan) | Performance of a Micro-Scale Radial-Flow Compressor Impeller made of Silicon Nitride | James P. Johnston<br>Sangkyun Kang<br>Toshiyuki Arima<br>Minoru Matsunaga<br>Hideaki Tsuru<br>Fritz B. Prinz | Stanford University<br>Stanford University<br>Wako Research Center<br>Wako Research Center<br>Wako Research Center<br>Stanford University |

| Date | Conference | Title | Author | Organization |
|---|---|---|---|---|
| 2003.11.15～19 | World Electric Vehicle Association (WEVA), The Electric Drive Transportation Association (EDTA)/The 20th International Electric Vehicle Symposium (EVS-20) (Long Beach, USA) | Application Studies of Electric Double-Layer Capacitor System for Fuel Cell Vehicle | Naohiko Oki<br>Koji Tamenori<br>Kouichi Yamamoto | Wako Research Center<br>Wako Research Center<br>Wako Research Center |
| | | Development of New Power Train for Fuel Cell Vehicle | Takayuki Ogawa<br>Kenichiro Kimura<br>Kenji Uchibori<br>Kiyoshi Shimizu<br>Sachito Fujimoto | Wako Research Center<br>Wako Research Center<br>Wako Research Center<br>Wako Research Center<br>Wako Research Center |
| | | Introduction to Honda's Hydrogen Refueling Station with Photovoltaic Modules | Masaki Ueyama<br>Shiro Matsuo<br>Steven Mathison | Wako Research Center<br>Honda R&D Americas<br>Honda R&D Americas |
| | | Honda's Challenges toward the Sustainable Automotive Society | Tomohiko Kawanabe | Tochigi R&D Center |
| 2003.11.17～20 | ITS World Congress/10th World Congress (Madrid, Spain) | The method of a driver assistance system and analysis of a drive's behavior | Shinnosuke Ishida<br>Jun Tanaka<br>Satoshi Kondou<br>Masahito Shingyoji | Tochigi R&D Center<br>Tochigi R&D Center<br>Tochigi R&D Center<br>Tochigi R&D Center |
| | | Front Wheel Active Steering for Lane Keeping of the Vehicle with Minimized Stopping Distance ABS Control | Nobuyoshi Asanuma<br>Masato Abe | Tochigi R&D Center<br>Kanagawa Institute of Technology |
| | | SS24:Telematics in The Future | Akira Iihoshi | Tochigi R&D Center |
| 2003.11.20～21 | Fahrzeug-und Verkehrstecnik/ Innovative Occupant and Partner Crash Protection -Vehicle Safety 2010- (Berlin, Germany) | Honda's approach to pedestrian protection | Tomiji Sugimoto | Tochigi R&D Center |
| 2003.12.1～3 | The Japan Society of Mechanical Engineers/ International Symposium on Micro-Mechanical Engineering－Heat Transfer, Fluid Dynamics, Reliability and Mechanical Engineering－ (Tsukuba, Japan) | Challenges to Develop Miniature Gas Turbine Engine with Ceramic Unitary Compressor/Turbine Rotor | Hideaki Tsuru<br>James P. Johnston<br>Sangkyun Kang<br>Toshiyuki Arima<br>Minoru Matsunaga<br>Fritz B. Prinz | Wako Research Center<br>Stanford University<br>Stanford University<br>Wako Research Center<br>Wako Research Center<br>Stanford University |
| 2003.12.8～10 | Florida Educational Seminars, Inc/ The 13th International Seminar on Double Layer Capacitor And Similar Energy Storage Device (Deerfield Beach FLORIDA/USA) | Application Studies of Ultracapacitor System for Honda FCV | Koji Tamenori<br>Kouichi Yamamoto<br>Akihiro Anekawa<br>Naohiko Oki<br>Minoru Noguchi | Wako Research Center<br>Wako Research Center<br>Wako Research Center<br>Wako Research Center<br>Wako Research Center |
| | | Development of High-power Electric Double-layer Capacitor for Fuel Cell Vehicle | Manabu Iwaida<br>Shigeki Oyama<br>Kenichi Murakami<br>Eisuke Komazawa<br>Naohiko Oki | Wako Research Center<br>Wako Research Center<br>Wako Research Center<br>Wako Research Center<br>Wako Research Center |

# Editor’s Postscript

Today marks the coldest period of winter according to the old lunar calendar. Here in Senzui it is bone-chilling cold now, but by the time this issue comes out, the cherry blossoms will be in full bloom, and at that time I expect that everyone at the R&D Center will find their creative activity accelerating still further.

The *Analects* contain Confucius' saying, “If I can hear the Tao in the morning, in the evening I can die content.” I doubt that there is anybody who would not mind dying in the evening just because they had acquired some new knowledge in the morning. New knowledge causes people to evolve. That evolution should contribute to the evolution of humanity and society. The activity of acquiring new knowledge is extremely important for engineers, in that constant effort is necessary to raise their creativity to still higher levels.

Many people today are absorbed in trying to keep up with events in the increasingly efficient and evolved research and development system. They rack their brains seeking out any and all new knowledge they can to further their own evolution. My greatest joy as an editor of the *Honda R&D Technical Review* is that this journal can be of assistance to people like this in their search. The present issue contains much knowledge obtained through a wide variety of R&D activity. R&D has an extremely important position in the activity of a company that society wants to exist. It is key to environmental and safety technology, first of all, but the crucial role of R&D is to create the various technologies for producing attractive products that are acceptable to our customers and societies around the world.

Just as Honda intends to sustain the creativity of its R&D centers in the future, so we intend for the *Honda R&D Technical Review* to continue serving as a medium for further raising the creativity of both its authors and readers.

(Kashiwagi)

Honda R&D Technical Review English Version Vol.16 No.1
The following associates provided us with their cooperation and expertise:

| | | |
|---|---|---|
| Karen | Arneson | American Honda Motor Co., Inc. |
| Bill | Bezilla | Honda R&D Americas, Inc. Ohio Center |
| Jeff | Brown | Honda R&D Americas, Inc. Ohio Center |
| Mary | Christopherson | Honda North America Inc. |
| Kimberly | Clavin | Honda R&D Americas, Inc. Ohio Center |
| Jared | Cox | Honda R&D Americas, Inc. Ohio Center |
| Dan | Croasmun | Honda R&D Americas, Inc. Ohio Center |
| Marcos | DeLeon | Honda R&D Americas, Inc. Ohio Center |
| Andrew | Fox | Honda R&D Americas, Inc. Ohio Center |
| Charles | Gagliano | Honda R&D Americas, Inc. Ohio Center |
| Brian | Gillespie | Honda R&D Americas, Inc. Ohio Center |
| Lee | Goldring | Honda North America Inc. |
| Chad | Harrison | Honda R&D Americas, Inc. Ohio Center |
| Derrick | Holmes | Honda R&D Americas, Inc. Ohio Center |
| Dan | Leibovitz | Honda R&D Americas, Inc. Ohio Center |
| Ryan | Mahn | Honda R&D Americas, Inc. Ohio Center |
| Skye | Malcolm | Honda R&D Americas, Inc. Ohio Center |
| Andrea | Martin | Honda R&D Americas, Inc. Ohio Center |
| Daniel | McCain | Honda R&D Americas, Inc. Ohio Center |
| Jake | McKeegan | Honda R&D Americas, Inc. Ohio Center |
| Chad | Nere | Honda R&D Americas, Inc. Ohio Center |
| Marc | Odell | Honda R&D Americas, Inc. Ohio Center |
| Ronald | Petrus | Honda R&D Americas, Inc. Ohio Center |
| Jason | Ray | Honda R&D Americas, Inc. Ohio Center |
| Philip | Reale | Honda R&D Americas, Inc. Ohio Center |
| Jason | Ruminski | Honda R&D Americas, Inc. Ohio Center |
| Randy | Skiles | Honda R&D Americas, Inc. Ohio Center |
| Hideharu | Takemoto | Honda R&D Americas, Inc. L.A. Center |
| Dan | Turk | Honda R&D Americas, Inc. Ohio Center |
| William | Willen | American Honda Motor Co., Inc. |
| Jun | Xin | Honda R&D Americas, Inc. Ohio Center |

